

In Situ and *Ex Situ* Hydrogenation Studies of
Zintl Phases Containing Tetrelides or Gallium

Von der Fakultät für Chemie und Mineralogie

der Universität Leipzig

genehmigte

DISSERTATION

zur Erlangung des akademischen Grades

DOCTOR RERUM NATURALIUM

(Dr. rer. nat.)

vorgelegt

von M. Sc. Henry Auer

geboren am 09.07.1989 in Leipzig

Angenommen aufgrund der Gutachten von:

Prof. Dr. Holger Kohlmann

Prof. Dr. Caroline Röhr

Tag der Verleihung: 29.06.2018

Für Remy

Bibliographische Beschreibung / Bibliographic description

Henry Auer:

In situ and *ex situ* Hydrogenation Studies of Zintl Phases Containing Tetrelides or Gallium,

Universität Leipzig, Institut für Anorganische Chemie, Dissertation, 2018,
235 Seiten, 125 Abbildungen, 12 Schemata, 59 Tabellen, 338 Referenzen.

Leipzig University, Department of Inorganic Chemistry, Ph.D. thesis, 2018,
235 pages, 125 figures, 12 schemes, 59 tables, 338 references.

Betreuung / Supervision

Die vorliegende Dissertation entstand im Zeitraum von Januar 2014 bis März 2018 unter Betreuung von Prof. Dr. Holger Kohlmann.

This Ph.D. thesis has been written between January 2014 and March 2018 under supervision of Prof. Dr. Holger Kohlmann.

Danksagung

Auch wenn die restliche Arbeit in englischer Sprache verfasst ist, möchte ich meinen Dank in deutsch aussprechen.

Zu aller erst möchte ich Prof. Dr. Holger Kohlmann danken. Seine Antrittsvorlesung in Leipzig hat meine Neugier für die Festkörperchemie geweckt. Er begleitet meinen wissenschaftlichen Werdegang jetzt seit meiner Masterarbeit und hat mir auch schon in diesem frühen Stadium die Möglichkeit gegeben in Grenoble Neutronen zu beugen. Das hat mich darin bestärkt eine Promotion unter seiner Betreuung anzustreben. Seine Tür stand jederzeit offen, sodass man Probleme oft direkt besprechen und lösen konnte. Unter seiner Betreuung hatte ich viele Freiheiten, sodass ich mein Thema eigenständig entwickeln konnte. Er zeigte immer viel Verständnis, vor allem auch wenn mein Sohn mit zur Besprechung kommen musste, weil die Tagesbetreuung ausgefallen ist.

Außerdem möchte ich mich bei meinen Kollegen bedanken, allen voran André, der seit der ersten Stunde das Büro mit mir geteilt hat. Unsere kleine Gruppe führte vor allem in der Anfangszeit dazu, dass oft mehr Studenten als Betreuer anwesend waren, weswegen wir uns oft gegenseitig vertreten mussten. Nach und nach sind dann Christian, Anton, Raphael und Nico als Doktoranden nachgekommen und haben die Gruppe bereichert. Auch mit unserer Laborantin Elisabeth kam eine große Entlastung in Sachen Labororganisation und -verwaltung. Es gab immer sehr produktive Gespräche, oft auch in einer Kuchenrunde (bei ausführlicher Kuchenbewertung), auf langen Fahrten nach Grenoble, oder während langer Nächte an verschiedenen Beamlines. Die gemeinsamen Seminare mit Prof. Dr. Oliver Oeckler und seiner Gruppe waren sehr hilfreich um weitere Anregungen für das Thema zu bekommen. Darüber hinaus gab es hier auch instrumentell eine enge Zusammenarbeit, sodass wir Geräte von Prof. Oeckler nutzen konnten.

Es herrschte immer ein gutes Arbeitsklima, wobei das Klima bei mittlerweile sechs Leuten auf eigentlich fünf Plätzen und noch extra Studenten schon mal etwas stickig werden konnte. Ich schulde auch allen meinen Kollegen großen Dank dafür, dass Sie immer kurzfristig eingesprungen sind, wenn mein Sohn mal nicht zur Tagesmutter gehen konnte, sei es indem sie sich um meine Studenten gekümmert haben oder gleich direkt um Remy, sodass ich noch schnell eine Messung starten konnte. Vor allem Anton hat deswegen auch mindestens ein Seminar für mich übernommen.

Ich muss mich auch bei den Studenten bedanken, die zu meinem Thema gearbeitet haben. An erster Stelle stehen hier Sebastian und Lena, die auch Anteil an einigen der Publikationen haben. Die Ergebnisse von Anton, der nach einem kurzen Ausflug zu den Laves-Phasen jetzt mein Thema in einer Doktorarbeit weiterführt, Orlette und Paul haben direkt oder indirekt zu dieser Arbeit beigetragen. Abschließend ist noch Fang zu nennen, dessen kürzlich abgeschlossene Bachelorarbeit zum CaSiH_y den Bogen schließt und wieder zum Ursprung des Themas zurückgeführt hat.

Wissenschaftlich zum Thema beigetragen haben auch André durch Messungen am SEM, sowie Dr. Wagner und Robert aus der Gruppe von Prof. Oeckler durch Messungen am TEM. Die Physiker Marko, Robin und Manuel haben für mich eine ganze Reihe an Verbindungen ins NMR gehalten. Dirk und Nico vom Helmholtz-Zentrum Berlin haben extra für unsere Experimente einen Aufbau gebastelt und zum Teil auch für etwas unkonventionelle Messzeiten gesorgt.

Außerdem möchte ich dem Fond der Chemischen Industrie für ein Promotionsstipendium danken, sowie dem Institut Laue-Langevin, Grenoble, dem Helmholtz-Zentrum Berlin und der Advanced Photon Source für die Bereitstellung von Messzeit.

Ich möchte meinen Eltern und meinen Freunden danken, die mich die ganze Zeit unterstützt und die auch dafür gesorgt haben, dass ich zwischendurch etwas anderes mache. Peter, als nicht Wissenschaftler und vor allem nicht Chemiker, hat sogar den kompletten Teil I Korrektur gelesen.

Meiner Frau Anja möchte ich danken, dass sie mich die ganze Zeit unterstützt und ermutigt hat auch wenn es mal stressig und ich ziemlich unleidlich war und abschließend noch meinem Sohn: Mit ihm hat es zwar alles länger gedauert, ohne ihn wäre es aber nur halb so schön gewesen.

Abstract

The hydrogenation of Zintl phases leads to interstitial hydrides that are coordinated exclusively by cations, polyanionic hydrides that exhibit a covalent bond to the more electronegative element, or a combination of both motifs. A series of new compounds is prepared and structurally characterised by laboratory X-ray, synchrotron and neutron powder diffraction. Most examples can be derived via hydrogenation of CrB- or FeB-type Zintl phases. These structure types are closely related and characterised by polyanionic zigzag chains. The interstitial hydrides $LnTtH$ ($Ln = La, Nd$, $Tt = Si, Ge, Sn$) are oxidation products of the formally metallic Zintl phases $LnTt = Ln^{3+}Tt^{2-}e^-$. Hydrogen occupies tetrahedral Ln_4 -voids. The products occur as a filled FeB-type phase (P -phase, LaGeH-structure type) or a filled CrB-type phase (C -phase, ZrNiH-structure type). The hydrogenation of electron-precise Zintl phases $AeTt$ ($Ae = Sr, Ba$, $Tt = Ge, Sn$, CrB-structure type) leads to hydrogen-poor ($AeTtH_y$, $y < 1$) and hydrogen-rich phases ($AeTtH_y$, $1 < y \leq 2$). The first show partially hydrogen-filled Ae_4 -voids. For low contents $y < 0.4$, hydrogen is statistically distributed over the voids (α -phases). Slightly increased hydrogen contents lead to partial (β -SrGeH $_y$, $0.47 \leq y \leq 0.75$) or full ordering (β -BaGeH $_{0.5}$). The hydrogen-rich phases $AeTtH_y$, $1 < y \leq 2$ (γ -phases), combine interstitial and polyanionic hydride motifs. The literature-known phases SrSiH $_{1.6}$ and BaSiH $_{1.9}$ could be structurally characterised for the first time. The homologue series was extended to SrGeH $_{1.2}$, BaGeH $_{1.6}$ and BaSnH $_{1.3}$. Tetrahedral Ae_4 -voids are totally filled with hydride anions. The additional hydrogen binds to the polyanions. Furthermore, some of the zigzag chains are interconnected perpendicular to the chain direction. Three different structure types exhibiting a close structural relationship were identified. This leads to difficulties in structure determination from powder diffraction. The covalent character of the bond is characterised by solid-state nuclear magnetic resonance and density functional theory calculations. Typical tetrel-hydrogen bond lengths are 155(2) pm (Si-H), 163(2) pm (Ge-H) and 186(1) pm (Sn-H). *In situ* neutron, X-ray and synchrotron powder diffraction were used to elucidate reaction schemes. The $AeTt-H_2$ systems ($Ae = Sr, Ba$, $Tt = Ge, Sn$) show several reversible reaction steps between γ -, β - and α -phases upon heating under hydrogen pressure. Finally, an irreversible decomposition into the binary hydrides AeH_2 and Tt -rich Zintl phases $AeTt_2$ occurs. *In situ* diffraction of the reaction of NdGa with hydrogen leads directly to NdGaH $_{1+x}$ (isostructural to γ -AeTtH $_y$) which shows a large compositional range from at least $x = 0.17$ to 0.80. Ga-H distances are long (about 200 pm) and, thus, not classical 2-electron-2-center bonds. *In situ* diffraction of the reactions of KSi and CsSi with hydrogen show a one step formation of the corresponding hydrides KSiH $_3$ and CsSiH $_3$. They exhibit SiH $_3^-$ -anions which are isoelectronic to PH $_3$. Further heating under hydrogen pressure leads to decomposition into KH and K $_8$ Si $_{46}$ or reformation of CsSi, respectively. Finally, further compounds were tested for reactivity towards hydrogen. The phases $AeTt_2$ ($Ae = Ca, Sr, Ba$, $Tt = Si, Ge$), AGe and ASi_xGe_{1-x} ($A = K, Rb, Cs$) do not form corresponding hydrides under the investigated conditions (at least 5 MPa H $_2$, 700 K). The gallides CaGa, Sr $_8$ Ga $_7$ and Ba $_8$ Ga $_7$ show reactivity towards hydrogen. They decompose into binary hydride and the gallium-rich phases Ca $_3$ Ga $_8$, SrGa $_4$ or BaGa $_4$. Furthermore, laboratory *in situ* diffraction of the reaction of CaGa with hydrogen indicates the formation of a new, crystalline phase. Formation and decomposition occur in a relative small temperature window. The new phase could not be characterised, yet.

Kurzzusammenfassung

Die Hydrierung von Zintl-Phasen führt zur Bildung von Einlagerungshydriden, die ausschließlich von Kationen koordiniert sind, zu polyanionischen Hydriden, bei denen Wasserstoff kovalent an das stärker elektronegative Element bindet, oder zu einer Kombination von beiden Motiven. Es wurde eine Reihe neuer Verbindungen dargestellt und mittels Laborröntgen-, Synchrotron- und Neutronenpulverbeugung strukturell charakterisiert. Die meisten Beispiele werden durch die Hydrierung von Zintl-Phasen im CrB- oder FeB-Strukturtyp erhalten. Die beiden Typen sind strukturell eng verwandt. Sie sind durch das Auftreten von polyanionischen Zickzackketten gekennzeichnet. Die Einlagerungshydride $LnTtH$ ($Ln = La, Nd$, $Tt = Si, Ge, Sn$) sind Oxidationsprodukte der formal metallischen Zintl-Phasen $LnTt = Ln^{3+}Tt^{2-}e^-$. Wasserstoff besetzt dabei Ln -Tetraederlücken. Die Produkte treten als gefüllter FeB- (P -Phase, $LaGeH$ -Strukturtyp) oder als gefüllter CrB-Strukturtyp (C -Phase, $NiZrH$ -Strukturtyp) auf. Die Hydrierung der elektronenpräzisen Zintl-Phasen $AeTt$ ($Ae = Sr, Ba$, $Tt = Ge, Sn$, CrB-Strukturtyp) führt zu wasserstoffarmen ($AeTtH_y$, $y < 1$) und wasserstoffreichen ($AeTtH_y$, $1 < y \leq 2$) Phasen. Erstere weisen partiell gefüllte Ae_4 -Lücken auf. In Phasen mit kleinem y (< 0.4) wird der Wasserstoff statistisch über die Lücken verteilt (α -Phasen). Etwas höhere Gehalte führen zu partieller (β - $SrGeH_y$, $0.47 < y < 0.75$) oder vollständiger (β - $BaGeH_{0.5}$) Ordnung. Die wasserstoffreichen Phasen $AeTtH_y$, $1 < y \leq 2$ (γ -Phasen), zeigen sowohl die Struktur motive von Einlagerungs- als auch von polyanionischen Hydriden. $SrSiH_{1.6}$ und $BaSiH_{1.9}$ als literaturbekannte Verbindungen wurden das erste mal strukturell charakterisiert. Die homologe Reihe konnte um $SrGeH_{1.2}$, $BaGeH_{1.6}$ und $BaSnH_{1.3}$ erweitert werden. Die Ae_4 -Tetraeder sind in diesen Phasen vollständig mit Hydridionen besetzt. Zusätzlicher Wasserstoff bindet kovalent an die Polyanionen. Außerdem verknüpfen sich die Zickzackketten z. T. senkrecht zur Kettenrichtung. Es wurden insgesamt drei Strukturtypen differenziert, die alle strukturell eng verwandt sind. Das führt zu Problemen bei der Strukturbestimmung aus Pulverdaten. Der kovalente Charakter der Bindung wurde durch Festkörperkernresonanzspektroskopie und Dichtefunktionaltheorierechnungen charakterisiert. Typische Tetrel-Wasserstoff-Bindungslängen sind 155(2) pm (Si-H), 163(2) pm (Ge-H) und 186(1) pm (Sn-H). *In situ*-Neutron, Röntgen- und Synchrotronpulverbeugung wurden angewandt um Reaktionsabläufe aufzuklären. Beim Heizen unter Wasserstoffdruck treten im $AeTt-H_2$ -System ($Ae = Sr, Ba$, $Tt = Ge, Sn$) verschiedene reversible Reaktionen zwischen den γ -, β - und α -Phasen auf, bevor ein irreversibler Zersetzungsschritt in die binären Hydride AeH_2 und die Tt -reichen Zintl-Phasen $AeTt_2$ beobachtet wird. Ein *In situ* Beugungsexperiment der Reaktion von $NdGa$ mit Wasserstoff zeigt direkt die Bildung von $NdGaH_{1+x}$ (isostrukturell zu γ - $AeTtH_y$), das eine Zusammensetzung von mindestens $x = 0.17$ bis 0.80 aufweist. Die Ga-H Abstände sind lang (ca. 200 pm) und darum keine klassischen 2-Elektronen-2-Zentrenbindungen. *In situ* Beugung an den Reaktionen von KSi und $CsSi$ mit Wasserstoff konnte gezeigt werden, dass die Hydride $KSiH_3$ und $CsSiH_3$ in einem Schritt gebildet werden. Diese Phasen weisen SiH_3^- -Anionen auf, die isoelektronisch zu PH_3 sind. Weiteres Heizen unter Wasserstoffdruck führt zur Zersetzung in KH und K_8Si_{46} oder zur Rückbildung von $CsSi$. Außerdem wurde eine Reihe weiterer Verbindungen auf die Reaktivität gegenüber Wasserstoff untersucht. Die Phasen $AeTt_2$, AGe und ASi_xGe_{1-x} ($A = K, Rb, Cs$) bilden keine Hydride unter den untersuchten Bedingungen (mindestens 5 MPa H_2 , 700 K). Die Gallide $CaGa$, Sr_8Ga_7 und Ba_8Ga_7 weisen Reaktivität gegenüber Wasserstoff auf. Diese Beispiele zersetzen sich in binäres Hydrid und die galliumreichen Phasen Ca_3Ga_8 , $SrGa_4$ und $BaGa_4$. *In situ* Laborröntgenbeugung der Reaktion von $CaGa$ mit Wasserstoff führt zur Bildung einer neuen, kristallinen Phase. Bildung und Zersetzung laufen in einem sehr schmalen Temperaturfenster ab. Die neue Phase konnte noch nicht charakterisiert werden.

Conventions

In the following some naming and formatting conventions are given. They strictly apply to Part I of this thesis. The published articles printed in Part II might deviate.

Group names

Triel, Tetrel, Pentel: For most of the main groups there are common trivial names like alkaline and alkaline earth metals or chalcogens and halogens. Within generalised chemical formulas they are easy to abbreviate, i.e. *A*, *Ae* or simply *X*. Unfortunately such common names are missing for groups 13 and 14. The *IUPAC* recommends to name them by the first element as boron- and carbon-group, respectively (Red Book¹). This is quite tedious and furthermore does not imply a viable abbreviation. Another standard work of inorganic chemistry *Holleman* and *Wiberg's "Lehrbuch der Anorganischen Chemie"*² calls them by their main group number, i.e. triel, tetrel, pentel, etc. This scheme will be used in this work as well. Therefore the following names and abbreviations will be used:

- group 1 = alkaline metal (*A*)
- group 2 = alkaline earth metal (*Ae*)
- group 13 = triel (*Tr*)
- group 14 = tetrel (*Tt*)
- group 15 = pentel³ (*Pn*)

Lanthanides vs. lanthanoids: Within the chemical community there is some controversy about the naming convention of lanthanum and the subsequent elements. The *IUPAC* recommends to avoid the old fashioned term *lanthanide* since the suffix *-ide* implies a negatively charged ion (Red Book¹). Otherwise, the alternative *lanthanoid* literally means lanthanum-like and, thus, excludes lanthanum itself. Still the latter one is the recommended term since "*lanthanum has become included by common usage* (Red Book¹, Sec. IR-3.5)". A compromise would be calling this group of elements *rare earth elements* implying scandium and yttrium as well. Since these two are of no relevance of this work the following will be used:

- lanthanoid (*Ln*) = La, Ce, Pr, Nd, Pm, Sm, Eu, Gd, Tb, Dy, Ho, Er, Tm, Yb, Lu

Hydrogen and deuterium

This thesis deals with hydrides of Zintl phases. Part I deals with general their structures and properties. There are techniques that need or at least prefer to use deuterated samples instead of hydrides, e.g. quadrupolar NMR or neutron diffraction. Since most chemical properties are independent of the isotope, Part I mainly talks about hydrides implying the use of deuterium if necessary. More details are given in the published works in Part II.

PXRD vs. XRPD and related terms

The terms used for different diffraction techniques sometimes cause some controversy. On the one hand there is powder and single crystal diffraction. On the other hand the methods can be distinguished by the radiation applied, i.e. X-ray, neutron or electron diffraction. Combining both leads either to X-ray powder diffraction (XRPD) or powder X-ray diffraction (PXRD) to name one example. There is no reference recommending one or the other. Single crystal or powder diffraction should be considered as the used method, which is specified by the radiation applied as prefix. Thus, the following terms will be used:

- X-ray powder diffraction (XRPD)

¹ Connelly, N. G.; Damhus, T.; Hartshorn, R. M.; Hutton, A. T., *NOMENCLATURE OF INORGANIC CHEMISTRY - IUPAC Recommendations 2005 (Red Book)*; IUPAC: 2005.

² Holleman, A. F.; Wiberg, N.; Wiberg, E., *Lehrbuch der Anorganischen Chemie*, 102nd ed.; de Gruyter: 2008.

³ Pentel will be used instead of pnictogen (or pnictogen) as applied in ². The abbreviation *Pn* works in both cases.

- synchrotron powder diffraction (SPD)
- neutron powder diffraction (NPD)

Sections and referencing of articles within this thesis

The sections of Part I are numbered. Part II includes the published as well as unpublished work. Printed as well as accepted articles are labelled by a capital *A* followed by a number. Unpublished work is indicated by a capital *U*. References to these articles and manuscripts are given according to this label.

Figures and tables

To get a unique identifier for each figure, table or scheme of this thesis different numbering-schemes are applied

- Figures, tables and schemes of Part I are labelled by the section number followed by the figure, caption or scheme number.
- Figures, tables and schemes of Part II are labelled by the article number, i.e. *A#* for published or accepted articles and *U#* for unpublished content, followed by the figure, caption or scheme number as used in the original article. Figures, tables and schemes of supplementary material are labelled by an additional *S* (*A#.S#*) to match the published version.

Color code of crystal structures

This thesis deals with Zintl phases and their hydrides. They are composed of a less electropositive metal *M* (*A*, *Ae* or *Ln*) and a more electronegative element *X* (*Tr*, *Tt*, *Pn*). They can be described as $M_m X_x H_h$. This general expression is represented by the colour-code of crystal structure figures as well. For Part I the following scheme is used

- large, green spheres: $M = A, Ae$ or Ln
- medium, grey spheres: $X = Tr, Tt, Pn$
- small, white spheres: H

Contents

Danksagung	i
Abstract	ii
Kurzzusammenfassung	iii
Conventions	iv
Table of Contents	vii
I Hydrogenation of Zintl phases	1
1 Introduction	3
1.1 Outline of the thesis	4
2 Polyanionic compounds, Zintl phases and hydrogen	6
2.1 The general (8-N) rule for polyanions	6
2.2 Zintl phases	7
2.3 Hydrides of Zintl phases	8
2.3.1 Interstitial hydrides and related phases	11
2.3.2 Polyanionic hydrides and related phases	12
2.3.3 Zintl ion hydrides	15
2.4 Relevance and open questions	15
3 Methods	16
3.1 Synthesis	16
3.2 <i>Ex situ</i> characterisation and quantum chemical calculations	16
3.2.1 Single crystal diffraction	16
3.2.2 Powder diffraction	16
3.2.3 Spectroscopy	17
3.2.4 Density functional theory (DFT) calculations	17
3.2.5 Further measurements	18
3.3 <i>In situ</i> characterisation	18
3.3.1 Diffraction	18
3.3.2 Thermal analysis	20
3.4 Limitations and outlook	20
4 Hydrogenation of CrB-structure type Zintl phases and related systems	22
4.1 CrB- and FeB-structure type	22
4.2 Examples of CrB- and FeB-structure type Zintl phases	23
4.3 Hydrogen filling tetrahedral voids	24
4.3.1 $LnTtH$, $Ln = La, Nd$, $Tt = Si, Ge, Sn$	24
4.3.2 α - and β - $AeTtH_y$, $AeTt = SrGe, BaGe, BaSn$, $y < 1$	26
4.3.3 Geometrical restrictions for hypothetical $AeTtH_1$ -phases, $Ae = Ca, Sr, Ba$, $Tt = Si, Ge, Sn$	29
4.4 Hydrogen bound to polyanions	29
4.4.1 $CaSiH_y$ - a starting point	30
4.4.2 $AeTtH_y$ - structure types, $Ae = Ca, Sr, Ba$, $Tt = Si, Ge, Sn$, $1 < y < 2$	31
4.4.3 $AeTtH_y$ - bond lengths by diffraction and NMR spectroscopy	34
4.4.4 $AeTtH_y$ - decomposition and infra-red spectroscopy	36
4.4.5 $NdGaH_y$ - similar but different	38
4.4.6 $CaGa$ - a candidate for chain hydrogenation	39
4.5 Reaction schemes of the $AeTt-H_2$ -systems, $Ae = Ca, Sr, Ba$, $Tt = Si, Ge, Sn$	40

5	Reactivity of tetrahedral and other three-binding polyanions towards hydrogen	42
5.1	Examples of three-binding Zintl phases	42
5.2	Hydrogenation of ATt ($A = \text{K-Cs}$; $Tt = \text{Si, Ge}$)	42
5.2.1	ASi ($A = \text{K-Cs}$)	42
5.2.2	The homologue systems ASi_xGe_{1-x} ($A = \text{K-Cs}$)	43
5.3	Hydrogenation of Sr_8Ga_7 and Ba_8Ga_7	44
5.4	Hydrogenation of $AeTt_2$ -systems ($Ae = \text{Ca, Sr, Ba}$; $Tt = \text{Si, Ge}$)	44
6	Structural relationship between the structures	45
6.1	Group-subgroup relations	48
7	Conclusion	52
8	Index of crystal structures	53
9	References	55
II	Published articles and unpublished results	65
A1	Hydrides of alkaline earth-tetrel ($AeTt$) Zintl phases: covalent Tt-H bonds from silicon to tin	67
A1.1	Authors' contributions	68
A1.2	Abstract	68
A1.3	Article	69
A1.4	Supplement	82
A1.5	References	86
A2	Structural and electronic flexibility in hydrides of Zintl phases with tetrel-hydrogen and tetrel-tetrel bonds	89
A2.1	Authors' contributions	90
A2.2	Abstract	90
A2.3	Article	91
A2.4	Supplement	95
A2.5	References	107
A3	From metallic $LnTt$ ($Ln = \text{La, Nd}$; $Tt = \text{Si, Ge, Sn}$) to electron-precise Zintl phase hydrides $LnTtH$	109
A3.1	Authors' contributions	110
A3.2	Abstract	110
A3.3	Article	111
A3.4	Supplement	120
A3.5	References	131
A4	<i>In situ</i> hydrogenation of the Zintl phase SrGe	135
A4.1	Authors' contributions	136
A4.2	Abstract	136
A4.3	Article	137
A4.4	Supplement	147
A4.5	References	152
A5	A sapphire single-crystal cell for <i>in situ</i> neutron powder diffraction of solid-gas reactions	155
A5.1	Authors' contributions	156
A5.2	Abstract	156
A5.3	Article	157
A5.4	References	164

A6 Reversible hydrogenation of the Zintl phases BaGe and BaSn studied by <i>in situ</i> diffraction	167
A6.1 Authors' contributions	168
A6.2 Abstract	168
A6.3 Article	169
A6.4 Supplement	180
A6.5 References	185
A7 <i>In situ</i> investigations on the formation and decomposition of KSiH₃ and CsSiH₃	187
A7.1 Authors' contributions	188
A7.2 Abstract	188
A7.3 Article	189
A7.4 References	196
U1 <i>In situ</i> neutron powder diffraction of the Zintl phase NdGa	199
U1.1 Authors' contributions	199
U1.2 Manuscript	200
U1.3 Supplement	209
U2 Collection of unpublished results	213
U2.1 Hydrogenation of CaGa	213
U2.2 Hydrogenation of Ae ₈ Ga ₇ , Ae = Sr, Ba	217
U2.3 Hydrogenation of AeTt ₂ (Ae = Ca, Sr, Ba; Tt = Si, Ge)	222
U2.4 Hydrogenation of AGe, A = K, Cs	223
U2.5 References	226
III Curriculum vitae and list of publications	229
Curriculum vitae	231
List of publications	232
Conference contributions	234

Part I

Hydrogenation of Zintl phases

1 Introduction

There are about 94 elements on earth⁴. Stable isotopes only exist for 80 of them. Just 24 are non-metals and only 12 of them do not occur as solids (at ambient conditions). Still solid state chemistry has a quite small scientific community compared to other inorganic chemical disciplines like molecular or coordinational chemistry. It focuses on investigations like preparation and characterisation of new extended solids. Due to its lack of molecules, it is more related to material science. Thus, *Roald Hoffmann* said, “*to state it provocatively, many solid state chemists have isolated themselves (no wonder that their organic or even inorganic colleagues aren’t interested in what they do) by choosing not to see bonds in their materials*” (Roald Hoffmann in [2, p. 3]).

The chemistry of molecules (organic as well as inorganic) is much easier to understand by chemical intuition than the chemistry of extended solids. All compounds that are able to exist are local minima of the potential energy surface (PES) with respect to composition, temperature, pressure, etc. Generally speaking, a global PES is too complicated to predict. This problem can be reduced by assuming special boundary conditions. The main advantage of molecular, especially organic synthesis, is that for every reaction step, only a limited number of bonds is formed or broken. Thus, the PES often can be approximated by only a few reaction coordinates. Since solvent chemistry has a large repertoire of highly selective reaction schemes, such a problem can usually be solved with pen and paper. By contrast, the major problem of solid state chemistry is the lack of such rational synthesis design. Solid state reactions are usually limited by diffusion and need high temperatures. Therefore, they are thermodynamically controlled. Furthermore, it is usually difficult to predict the structure or even the existence of a solid state compound by chemical intuition. Advanced computational methods can help to find new structures [3–6], or *in situ* monitoring of reactions can help to understand and gain control of the formation of desired products [7–9]. The latter approach is one topic this thesis.

Still, to come back to *Roald Hoffmann* cited in the beginning, all chemistry, molecular and extended solid, is the realm of electrons. Structures, properties and reactivity heavily depend on the electronic configuration. Thus, one of the simplest chemical principles states that the same electron count (isoelectronicity) of an equal number of atoms leads to the same structures (isosterism)⁵. More general speaking, only the valence electrons count (isovalenceelectronicity). The simple connection of electron number and configuration leads to several models describing compounds. This is fruitful in perspective of directed (covalent) interactions and therefore for molecular structures. For example, the extension of this idea by geometric aspects directly leads to the *valence shell electron pair repulsion (VSEPR)* theory [11] (Review: [12]) describing the spatial arrangement of ligands around a central atom. Usually being applied to molecular gas phase structures, the concept works for extended solids as well. A trivial example is a $(\text{SiO}_4)^{4-}$ -tetrahedron. A more unconventional example might be the structure of (red) PbO. Pb(II) possesses a lone pair (*E*) and is coordinated by four oxygen atoms ($\text{PbO}_{4/4}E$). Thus, the structure of PbO_4^{6-} can be described as a quadratic pyramid with lead at the center and the lone pair pointing at the top⁶. This structural motif can be found in the solid state structure and the lone pair orientation was confirmed by electron localization function (ELF) calculations [13–15].

A more sophisticated description than simply considering the valence electrons was introduced by *Fukui* with his description of frontier orbitals [16], the highest occupied as well as the lowest unoccupied orbitals, which determine the reactivity of compounds (Nobel lecture: [17], overview: [18]). Based on this idea, *Hoffmann* came up with the isolobal analogy that accounts for the chemical behaviour of metal complexes [19]. By dividing structures into fragments, a calculation or even estimation by chemical intuition of the frontier orbitals of transition metal complexes can be interpreted in terms of organic molecules. In his Nobel lecture, *Hoffmann* calls this “building bridges between inorganic and organic chemistry” [20].

The idea of frontier orbitals works for solids as well, translating them into bands [2, 21, 22]. Thus, at this point we can build the bridge between molecular and solid state chemistry. But still, a main difference is that in molecular chemistry atomic size plays a subordinate role, except for instance in terms of possible coordination numbers (e.g. coordination chemistry) or polarisability (e.g. *hard and*

⁴ Considering plutonium as the last one occurring in traces naturally [1].

⁵ This description differs from the IUPAC definition of isoelectronicity, which presumes the same number of electrons and the same structure for this term [10].

⁶ The first *VSEPR* guess of an AX_4E would be a seesaw structure as in SF_4 , i.e. *E* in the equatorial plane of a trigonal bipyramid.

soft acids and bases (HSAB) concept [23]). In the chemistry of extended solids the roles are inverted. Directed, covalent bonds as commonly drawn have a much stronger ionic character, i.e. in SiO_4^{4-} bond character is about half covalent and half ionic. The packing of spheres of different sizes is the driving force of the formation of intermetallics (metallic bonding) and the so gained Coloumb energy for salts (ionic bonding). The ratio of radii plays a role e.g. for Laves phases (intermetallics). Ionic packings were described by *Goldschmidt* [24] and elaborated on through coordination rules by *Pauling* [25]. More recently, *Beck* described a coordination-based concept [26, 27]. Within an ionic framework, the concepts of iso(valence)electronicity are reformulated as electron counting rules. Some of these ideas are even older than their molecular counterparts. So, the Grimm-Sommerfeld rule [28] describes cubic or hexagonal diamond-like structures with an average electron count of four electrons per atom. Another example are Hume-Rothery phases [29]. Their formation strongly depends on the total number of valence electrons (“*valence electron concentration (VEC)*”) of a compound. A more sophisticated formulation was given by *Mooser and Pearson* [30] by describing general semiconductor compounds through electron counting rules (Details in Sec. 2.1).

This thesis deals with a class of compounds that links the molecular world and the solid state: the Zintl phases (details and general definitions in Sec. 2.2). To cite *Hoffmann* again: “*The simple notion, introduced by Zintl and popularized by Klemm, Busmann, Herbert Schäfer, and others, is that in some compounds A_xB_y , where A is very electropositive relative to a main group element B, one could just think, that’s all, think that the A atoms transfer their electrons to the B atoms, which then use them to form bonds. This very simple idea, in my opinion, is the single most important theoretical concept (and how not very theoretical it is!) in solid state chemistry of this [the 20th, note from the author] century. And it is important not just because it explains so much chemistry, but because it forges a link between solid state chemistry and organic, or main group, chemistry.*” (Roald Hoffmann in [2, p. 3]). By this definition, the Zintl-concept describes the formation of anionic (B^{n-}) pseudo-element partial structures. They can be understood by simple comparison to isoelectronic elements. This concept was extended to the occurrence of heteropolar element-hydrogen bonds (called polyanionic hydrides, see Sec. 2.3) in the works of *Gingl et al.* [31] and *Fahlquist et al.* [32–34]. A proper classification and terminology was provided by *Häussermann et al.* [35]. This pseudo-elemental or even pseudo-molecular view describing the polyanionic partial structure got a new name from a couple of physical chemists. In a much more narrow definition they call this version of iso(valence)electronicity simply pseudo- or electronic transmutation⁷[36, 37]. Unfortunately, the authors lack to draw the connection to the Zintl concept. While chemists cannot transform one element into another, they can mimic this effect by forming ionic species as originally found by *Zintl*.

As stated in the beginning these are all facets of isoelectronicity. This simple notion can be used to search for new binary, anionic pseudo-element hydrides packed in a cationic framework. They can form new molecular or extended structures not present for their isoelectronic, electric neutral counterparts. Thus, the preparation of polyanionic hydrides is a field of chemistry that allows to prepare new structural motives. To further prove this solid state concept, this work offers new experimental examples of hydrides of Zintl phases that show the formation of pseudo-element hydrides. The compounds presented show novel polyanions with element-hydrogen bonds that represent structures of hypothetical binary compounds that do not exist (yet). Furthermore, this thesis illuminates the reaction paths followed by these phases and gives spectroscopic evidence for the formed bonds. The reaction behaviour of phases that were supposed to follow this concept but do not show classical 2-electron-2-center element-hydrogen bonds is investigated as well.

1.1 Outline of the thesis

This work is a publication-based thesis. Articles within this thesis are cited with a capital *A* in front of the article number, i.e. [A1] - [A7]. Furthermore, unpublished content is indicated by a capital *U*. There is a manuscript [U1] and a collection of experimental results [U2].

The thesis deals with the incorporation of hydrogen into Zintl phases. Therefore, this work aims to provide further evidence for the occurrence of polyanionic hydrides and the applicability of the Zintl concept on this type of compounds. As an introduction to the topic, general definitions are provided regarding different formalisms (Sec. 2.1 (Mooser-Pearson) and Sec. 2.2 (Zintl phases)). Furthermore, the

⁷ Transmutation as the physical process of changing an element into another, e.g. by a radioactive decay or by fusing nuclei.

different possibilities of hydrogen incorporation are described and several examples from literature are given (Sec. 2.3). A motivation of the scientific work is derived in Sec. 2.4.

Since this is a publication-based thesis, experimental procedures are described within the articles. Nevertheless, an overview of the used methods is given in Sec. 3. Some limitations of the applied techniques are discussed as well.

The main focus of this work rests on CrB-structure type and related Zintl phases with two-binding polyanions and their hydrogenation (Sec. 4). The formation of interstitial hydrides is described in Sec. 4.3 and summarises results from [A3] as well as from the works on *in situ* diffraction [A4], [A5] and [A6]. The related polyanionic hydrides are discussed in Sec. 4.4. The presented findings are mainly taken from the articles [A1], [A2] as well as from the unpublished content [U1]. Results from solid state nuclear magnetic resonance were obtained as private communication and are directly included in this section. The reaction schemes described in Sec. 4.5 summarize the results from [A4] and [A6].

Sec. 5 deals with three-binding, especially tetrahedral polyanions. These phases appear to be unreactive or decompose. Therefore, this section summarizes experiments given in [U2]. Systems known to take up hydrogen are ASi ($A = K, Rb, Cs$). These reactions were investigated by *in situ* diffraction which is topic of the article [A7].

Finally, Sec. 6 gives an overview of the structural relationship of the new structures beyond the discussion of the published works. It also relates them to examples known in literature.

An index of all crystal structure data given within this work is displayed in Sec. 8.

Published articles, manuscripts as well as unpublished results are given in Part II. The articles are not ordered chronologically but by *ex situ* ([A1], [A2], [A3]), *in situ* ([A4], [A5], [A6], [A7]) and unpublished works ([U1], [U2]).

2 Polyanionic compounds, Zintl phases and hydrogen

2.1 The general (8-N) rule for polyanions

Our view on molecular systems and solid state structures that are no (or, as we will see later, at least poor) metals is strongly influenced by the concept of valences and the octet rule. Considering main group elements only, the most stable electron configurations have eight valence electrons, which corresponds to the noble gases. The only exceptions are hydrogen and helium since they only possess the 1s orbital. These concepts were already developed in the early 20th century. At the same time *Lewis* and *Kossel* described two valid concepts for the formation of stable compounds. While *Lewis* drew the covalent picture of electron sharing between two elements to gain an eight valence electron configuration [38], *Kossel* considered an electrovalent (or ionic) model of exchanged electrons to gain a noble gas configuration [39]. For elements of groups 14 to 17, *Hume-Rothery* then came up with the (8-N) rule to explain the elemental structures [40]:

Definition 1 ((8-N) rule for elements of group 14 to 17) *The structure of an element X can be described by the number of covalent bonds ($b(XX)$) to its next neighbours as:*

$$b(XX) = 8 - N,$$

where N is the main group number.

As mentioned above, this is strongly correlated with the concept of valences:

Definition 2 (Valence (IUPAC [10])) *The maximum number of univalent atoms (originally hydrogen or chlorine atoms) that may combine with an atom of the element under consideration, or with a fragment, or for which an atom of this element can be substituted.*

Thus, in general we can differentiate between (normal) valence compounds that fulfil the octet rule by forming covalent or electrovalent bonds and metallic systems that are governed by metallic bonding. These are just the boundary cases and the transitions are fuzzy.

Since valence compounds follow the octet principle, their connectivity can be described by the (8-N) rule in a more general form as introduced mainly by *Mooser* and *Pearson* [30, 41–43]. The formalism used here is adapted from *Müller* [44]. For an binary main group element compound



with M being a less electronegative metal⁸ and X a more electronegative element as well as $e(M)$ valence electrons per M and $e(X)$ valence electrons per X , we can define a valence electron concentration per anion, $VEC(X)$, as

Definition 3 (Valence electron concentration per anion [44])

$$VEC(X) = \frac{m \cdot e(M) + x \cdot e(X)}{x}.$$

Thus, formally the metal M transfers all its electrons to the element X . To fulfil the octet rule for a simple ionic compound, i.e. without additional covalent bonds, the following relation holds:

$$VEC(X) = 8$$

which is in principle the concept proposed by *Kossel* [39]. Allowing element-element bonding ($b(XX)$) leads to the general (8-N) rule as originally proposed by *Mooser* and *Pearson* [30]:

Definition 4 (general (8-N) rule)

$$b(XX) = 8 - VEC(X).$$

⁸ The main group metal can be replaced by a lanthanoid which typically forms three-valent cations; in exceptions also two-valent.

This relation was later extended for cation-cation bonding and non-bonding electrons [42, 43]. They can be explicitly added to the relation mentioned above (see [45] or [44] for details). We will treat excess electrons implicitly using a correction to the transferred electrons $e(M)$:

$$e(M)' = e(M) - n. \quad (1)$$

The remaining electrons n are available for cation-cation bonding, non-bonding, or metallic states.

Hydrogen as a special case was already mentioned in the original work of *Mooser* and *Pearson* [30]. It might seem trivial but Def. 4 holds for hydrogen ($X = \text{H}$) as well, replacing the required octet by a duplet [45]:

$$b(\text{HH}) = 2 - \text{VEC}(\text{H}). \quad (2)$$

This directly leads to the conclusion that hydrogen either needs to form a covalent bond (H^0) or an anion (H^-).

2.2 Zintl phases

Zintl phases are a class of compounds at the border between ionic salts and intermetallics (Some reviews are [46–54]). They are sometimes referred to as intermetallic compounds with strong heteropolar bonding [1] or just polar intermetallics. They are typically composed of main group elements. Keeping the formalism from above, a Zintl phase



consists of a less electronegative metal M from group one, two or the lanthanoids and a more electronegative element X from group 13 to 16. The structures can be described by a formal ionic picture with an electron transfer to the p-block element. This either leads to classical salt-like compounds with monomeric anions which, in a quite narrow definition, are not Zintl phases, or to polyanionic compounds. According to their formal charges, the anions form structures (isosterism) of the iso(valence)electronic elements or new structure motifs that are not known from the elements but follow valence rules as described above. Therefore, we can define

Definition 5 (Zintl phase) *Zintl phases $M_m X_x$ are solid state structures of a less electronegative element (group one, two or lanthanoid metal) and a more electronegative p-block element that form (poly-) anions, i.e. $b(X-X) \geq 0$. The limiting case $b(X-X) = 0$ leads to monomeric anions (classical salts) that will be referred to as Zintl phases as well. Extended polyanionic partial structures can be explained by the general (8-N) rule.*

The first example showing an extended (three-dimensional) polyanion was NaTl^9 . The structure of this textbook example of a Zintl phase was determined by *Zintl* and *Dullenkopf* [56]. Since the thallium partial structure shows an extended polyanion, they counted it as intermetallic phase. The formally Tl^- is isoelectronic to a group 14 element and resembles the diamond structure while Na^+ occupies interstitial sites.

Originally, Zintl introduced a line or a boundary between group 13 and 14. He stated that elements from groups which are one to four positions in front of the noble gases are able to form negatively charged (poly-)anions [46, 57]. Furthermore, he showed the existence of monomeric anions and thus, classical salt-like compounds for the corresponding magnesium compounds which do not exist for group 13 elements [46]. *Laves* later introduced the term *Zintl Linie* (Zintl line or Zintl boundary) and also named main group element phases with polyanions *Zintl phases* [58]. The Zintl boundary also corresponds to the formation of polyanionic clusters (which we today call “naked” Zintl ions) which are soluble or directly prepared in solution. In contrast to the extended, pseudo-element like structures, the isolated, deltahedral Zintl ions might be described by the Wade-rules [59, 60]¹⁰, or its generalisation by *Mingos* [61]. Therefore, we can define

⁹ *Zintl* and *Dullenkopf* compared the structure of NaTl to β -brass (Hume-Rothery phases [29]) and recognised a strong deviation from $\text{VEC} = 1.5$ for this type of intermetallics and thus, interpreted it as an salt-like compound. The comparison was extended in [55].

¹⁰ deltahedral clusters exhibiting $2n + (2, 4, 6, \dots)$ skeletal-electrons form *closo*-, *nido*-, *arachno*-, ... structures, respectively; $n = (v+l-2)$, v = valence electrons, l = ligand electrons (usually two, in case of H one); formalism taken from [1].

Definition 6 (Zintl ion) *Zintl ions are isolated, deltahedral polyanions, that can exist in solution or as a Zintl phase in the solid state. The structures can be explained by Wade-rules.*

In his first work on this topic, Zintl describes the titration of sodium in liquid ammonia with PbI_2 that leads to polyanionic compounds Na_4Pb_7 and Na_4Pb_9 [57]. This was extended by several examples right of the Zintl boundary [62–66]. It was shown later that the Zintl boundary is to be considered less strict when examples of group 13 Zintl ions occurred (as a review see [49]). An example of a typical Zintl ion is the $[\text{Tt}_9^{4-}]$ -cluster (Tt = tetrel). According to Wade-rules, it exhibits $22 = 2n + 4$ skeletal-electrons. Thus, it is the *nido*-form of a bicapped square-antiprism. Furthermore, the structure of tetrahedral Tt_4^{4-} can either be explained by the Wade-rules as *nido*-cluster¹¹, or as pseudo-white phosphorous (P_4). Typical solvents for Zintl ions are liquid ammonia, ethylenediamine or dimethylformamid. The solubility can be improved by complexation of the cations using cryptant ligands or crown-ethers (Some reviews on Zintl ions are: [49, 50, 53]). While Zintl phases containing extended polyanions can be found on the electron rich side reaching to the limit of monomeric anions, Zintl ions refer to the electron deficient region and therefore, mark the transition to intermetallics.

While the general concept dates back to the 1930's and *Eduard Zintl* [46, 57], it was extended by *Klemm* and *Busmann* [67, 68]. Therefore, it is sometimes referred to as Zintl-, Zintl-Klemm, or Zintl-Klemm-Busmann concept. According to the formalism of *Mooser* and *Pearson* as described above, this leads to decent semi-conductors. In fact, Zintl phases are often poor metals, e.g. AeTt (Ae = alkaline earth metal, Tt = tetrel) exhibit partially oxidized *Tt*-zigzag chains (pseudo μ -sulfur) with depopulated π^* -bands due to covalent interaction between polyanion and cationic d-states as shown by density functional theory (DFT) calculations [69–71] and experimental electron density studies [72]. This deviation from the formally pure ionic formulation does not spoil the model. In fact, the main difference between the two concepts is the focus on the electronic structure of semi conductors (Mooser and Pearson) or the crystal structure prediction using a pseudo-atom approach (Zintl concept).

In contrast to the poor metallic conductivity of electron precise Zintl phases (formally valence compounds), there are Zintl phases with excess electrons, e.g. LnTt (Ln = lanthanoid, Tt = tetrel). The structures of these phases show infinite zigzag chains of two-binding *Tt*-atoms. Thus, they need to be formulated as Tt^{2-} , leading to $\text{Ln}^{3+} + \text{Tt}^{2-} + e^-$. The additional electron stays part of the cationic partial structure (Ln -d-states [73], [A3]) and thus, formally counts as non-bonding or metallic electron (see Eqn. 1, p. 7). We can then formulate

$$\begin{aligned}\text{VEK}(\text{Tt}) &= \frac{(3-1)+4}{1} = 6, \\ \text{b}(\text{Tt-Tt}) &= 2\end{aligned}$$

and give the following definition

Definition 7 (Metallic Zintl phase) *Metallic Zintl phases are characterised by excess electrons that can be attributed as metallic states of the cationic partial structure. Structure and bonding of the polyanion can be described according to the Zintl-concept and the general (8-N) rule (counting the metallic electrons as non-bonding).*

This definition introduces a formal metallic character by excess electrons. The actual physical property (i.e. the poor metallic conductivity of an electron precise Zintl phase) is not considered here.

2.3 Hydrides of Zintl phases

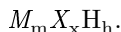
Hydrides of Zintl phases can be prepared by direct synthesis using binary hydrides, elements and optionally hydrogen gas pressure, or by hydrogenation of a precursor Zintl phase. Especially the latter case stays in the focus of this work and will be picked up when reaction schemes are discussed.

Talking about Zintl phases, hydrogen plays a special role. Its electronegativity is comparable to most of the p-block elements. Therefore, it can be readily incorporated into Zintl phases as part of the anionic partial structure.

In Sec. 2.1 the Mooser and Pearson concept of polyions was discussed for binary systems. A general definition for multinary systems can be found elsewhere [45]. Let us consider the special case of a ternary

¹¹ $12 = 2n + 4$ skeletal electrons; a tetrahedron is the *nido*-form derived from a trigonal bipyramid.

system with hydrogen as one component,



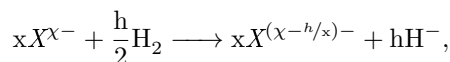
Since hydrogen is usually the most electronegative element in Zintl phases, cationic protons can be excluded from the discussion. Thus, we need to consider two types of hydrogen incorporation into Zintl phases:

- (i) as monoatomic hydride, or
- (ii) covalently bound to the polyanion.

$VEC(X)$ is considered as the averaged electron count of the Zintl anion X . The formation of h hydride anions H^- leads to a reduction of the absolute value of $VEC(X)$ compared to the corresponding (hypothetical) hydrogen free compound:

$$\begin{aligned} VEC(X)' &= \frac{m \cdot e(M) + x \cdot e(X) - h}{x} \\ VEC(X)' &= VEC(X) - \frac{h}{x} \end{aligned}$$

Considering this formation as a (hypothetical) redox reaction of a binary Zintl phase with hydrogen, the polyanion is then oxidized, i.e. starting with an anionic charge $-\chi$



and the number of bonds needs to be increased:

$$b(XX) = 8 - VEC(X)' = 8 - VEC(X) + \frac{h}{x}.$$

Since a hydride anion has the electron configuration of a He, it cannot form additional covalent bonds and, therefore, needs to be coordinated by the cationic part of the structure. According to *Häussermann* [74] and *Häussermann et. al* [35] who introduced this classification in regard to Zintl phases, we can use the following definition¹²:

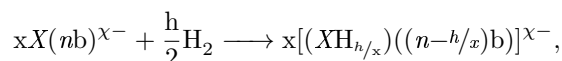
Definition 8 (Interstitial hydrides) (I - as structure motif) *An interstitial hydride is an anionic hydrogen atom, that is solely coordinated by the less electronegative metal M of a Zintl phase and thus, part of the cationic partial structure. (In this context salt-like partial structure seems more appropriate.)* (II - as a phase) *An interstitial hydride phase is a Zintl phase that incorporates interstitial hydrides according to (I).*

At the end of this hypothetical oxidation reaction a decomposition into binary metal hydride and the element or an element-rich Zintl phase might occur (Scheme 2.1)[35].

Since the electronegativity of hydrogen is similar to the p-block elements, it can bind covalently to the polyanion. As shown above (Eqn. 2, p. 7), only a formally neutral H^0 can form a covalent bond. Thus, $VEC(X)$ does not change and, therefore, the overall charge and connectivity of X stays the same. Since there are element-element bonds ($b(XX)$) next to element-hydrogen bonds ($b(XH)$), the overall number of binding partners of X will be called $b(X\{X,H\})$ with

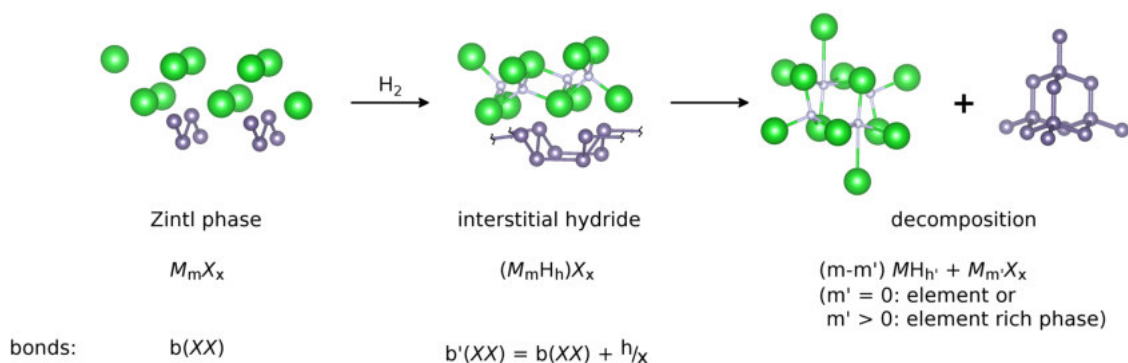
$$\begin{aligned} b(X\{X,H\}) &= b(XX) + b(XH) \quad \text{and} \\ b(X\{X,H\}) &= 8 - VEC(X). \end{aligned}$$

Considering a formal reaction of a binary Zintl phase with molecular hydrogen, the n -binding $X(nb)^{\chi-}$ of a polyanionic network is truncated and saturated by hydrogen:

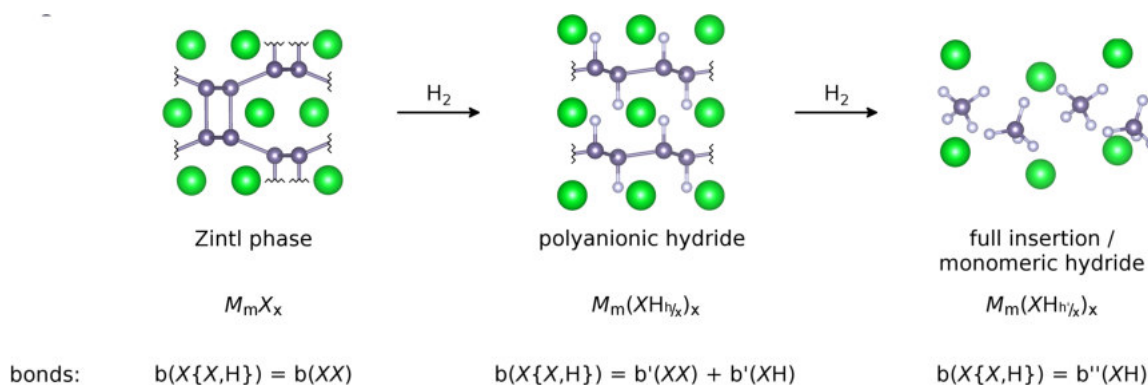


with $n-h/x$ the remaining $X-X$ bonds. Since hydrogen is the more electronegative part, this can be considered as oxidative insertion into an element-element bond. These phases are defined as follows:

¹² *Häussermann* [74] and *Häussermann et al.* [35] established these terms to distinguish two types of hydrides of Zintl phases. Originally the term *Zintl phase hydride* was established to describe phases with cation-coordinated hydride anions [74]. Subsequently, the term *interstitial hydride* was defined to be equivalent [35]. In later works only the term *interstitial hydride* occurs, thus, it seem appropriate to redefine *Zintl phase hydride* (Def. 11, p. 11) as a more general term.



Scheme 2.1: Hydrogenation of Zintl phases leading to interstitial hydrides followed by a decomposition. The polyanion is oxidised and its connectivity increases. Large, green spheres: M ; medium, grey spheres: X ; small, white spheres: H . Scheme adapted from [35].



Scheme 2.2: Hydrogenation of Zintl phases leading to polyanionic hydrides and finally to a monomeric complex hydride. The overall connectivity of the anions does not change. Large, green spheres: M ; medium, grey spheres: X ; small, white spheres: H . Scheme adapted from [35].

Definition 9 (Polyanionic hydrides) (I - as structure motif) *A polyanionic hydride is a polyanionic partial structure that exhibits X-H bonds next to X-X bonds.* (II - as a phase) *A polyanionic hydride phase is a Zintl phase that incorporates polyanionic hydrides according to (I).*

If the hypothetical oxidative insertion reaction goes on, it will lead to monomeric $(\text{XH}_{h/x})^{X-}$ units, with $(n = h/x)$ -binding X atoms and, thus, only X-H bonds remaining (Scheme 2.2).

Formally, interstitial hydride formation is possible as long as the sum of the charges of the hydrides is smaller than the sum of the charge of the cations leading to an overall positive charge (n) of the $M_m H_h^{n+}$ -partial structure¹³. Considering polyanionic hydrides is less simple. From the considerations above, some conclusions can be drawn

- Phases with mono-atomic anions cannot form polyanionic hydrides directly, since they do not exhibit X-X bonds. They need to form interstitial hydrides in a first (formal) step to increase $b(\text{XX})$.
- Assuming an integer negative charge per element atom¹⁴, i.e. X^{n-} with $n = 1, 2, 3, \dots$, can lead to
 - pseudo group 14 units (Tr^- , four-bonding),
 - pseudo group 15 units (Tr^{2-} , Tt^- , three-bonding) or

¹³ A compensation of charges, i.e. $n = 0$, does not lead to the formation a Zintl phase. This border case might be considered as a co-crystallization of metal hydride and the p-block element.

¹⁴ A non-integer average charges lead to intermediate case with different types of atoms X , i.e. with different numbers of bonds.

- pseudo group 16 units (Tr^{3-} , Tt^{2-} , Pn^- , two-bonding)
(Tr = triel, Tt = tetrel, Pn = pentel).

Where hydrogen can be incorporated into X - X -bonds. Especially the last example allows only polyanions with small hydrogen content. In this case, it might truncate chains forming anionic $(HX)_2X_n$ -groups.

Another class that was not considered by *Häussermann et. al.* [35] are Zintl ions that incorporate or bind hydrogen. Examples of this type are rare and not relevant for this thesis. Still, we will regard them as

Definition 10 (Zintl ion hydrides) *Zintl ions that incorporate an hydride ion (H^-) inside the cage or that have a negatively polarised hydrogen ($H^{\delta-}$) as ligand. In both cases the two electrons or one electron, respectively, are part of the framework according to Wade-rules.*

Finally, we can introduce another term deviating from the original definition:

Definition 11 (Zintl phase hydrides) *The term Zintl phase hydrides is supposed to describe a Zintl phase that incorporates hydrogen in general and does not specify the type of hydride as defined above.*

2.3.1 Interstitial hydrides and related phases

The occurrence of hydrogen in Zintl phases with fully reduced, monomeric anions is well known. Mixtures of Ae , AeH_2 , and Tt ($Ae = Ca$ or Yb , $Tt = Sn$ or Pb) react to form Ae_3TtH_2 which can be formally described as $Ae_2Tt + AeH_2$ showing hydrogen filled Ae_4 -tetrahedra as well as mono-atomic Tt^{4-} -anions [75]. As expected, such phases show semi-conducting behaviour or poor metallic conductivity. Density functional theory (DFT) calculations on Ca_3SnH_2 support this view and show a small band gap [76]. The interstitial hydride $LiCa_7Ge_3H_3$ was prepared in a calcium-lithium flux under addition of CaH_2 [77]. Due to excess of reducing agent Ge^{4-} -anions are present while the hydride resides in octahedral voids formed by calcium and lithium. An example of a fully reduced pentel element is Sr_3LiAs_2H which can be formulated according to the Zintl concept as $(Sr^{2+})_3(Li^+)(As^{3-})_2H^-$ [78]. Hydrogen is coordinated tetrahedrally by strontium. In contrast to the Zintl-like formulation, there is considerable covalent interaction between arsenic and lithium. DFT calculations and magnetic measurements show that the compound is a proper diamagnetic semi-conductor [78].

Even the non-observance of hydrogen in Zintl phases was not unusual. Hydrogen typically occurred as an impurity in alkaline-earth metals up to 20 mol-% [79]. Thus, there are several studies, typically from the *Corbett*-group pointing out hydrogen sites [80–85], i.e. in the structure families Ae_5Pn_3H and Ae_5Tt_3H ($Ae =$ alkaline earth metal or two-valent lanthanoid; $Pn =$ pentel; $Tt =$ tetrel): There are phases that have an odd electron count, e.g. an excess electron, like Ae_5Pn_3 ($Ae = Ca, Sr, Ba$ or two-valent Eu, Sm, Yb ; $Pn = As, Sb, Bi$). In terms of the Zintl concept these phases still show fully reduced anions and can be described as $Ae_5^{2+}Pn_3^{3-}e^-$. They crystallize either as β - Yb_5Sb_3 - or Mn_5Si_3 -structure type. In fact, these phases are hydrogen stabilized and show a large homogeneity range of hydrogen incorporation. Careful evaluation showed that the hydrogen free phases (Ae_5Pn_3 [81, 84, 85]) only exist in Mn_5Si_3 -structure type, while fully hydrogenated phases (Ae_5Pn_3H [80, 81, 84, 85]) exhibit a stuffed β - Yb_5Sb_3 -structure type which is equivalent to the Ca_3Sb_5F -structure type. Upon evacuation and rehydrogenation the phases can be transformed into each other. Most structural work was done by single crystals and X-ray diffraction. Hydride sites were assigned to tetrahedral Ae_4 -voids. For $Ca_5Bi_3D_{0.93}$ deuterium positions were determined by powder neutron diffraction [85]. There are also Ae_5Tt_3 -phases ($Ae = Ca, Sr, Ba$ or two-valent Eu, Yb , $Tt = Si-Pb$) that crystallize in Cr_3B_3 -structure type and fulfil the Zintl-concept as $(Ae^{2+})_5Tt_2^{6-}Tt^{4-}$ forming dumbbells and monomeric anions. These phases feature a Tt - Tt -bond. Nevertheless, most of them are not stable in this form and need an additional anion like fluorine or hydrogen, forming oxidized Zintl phases $Ae_5Tt_3\{H,F\}$ [82, 83] in Ca_5Sn_3F -structure type. In this structure type fluorine (hydrogen) occupies tetrahedral Ae_4 -voids again. Considering extended Hückel calculations and crystal orbital overlap population (COOP) results, the oxidation of the Zintl anions refers to a depopulation of π^* -bands that belong to the Tt - Tt -dumbbells [83]. Such a bonding motif will play a role again later. Density of states (DOS) calculations on Ca_5Sn_3H also confirmed a depopulation of Sn-p states due to the hydrogen incorporation and did not show a band gap at the Fermi level [76].

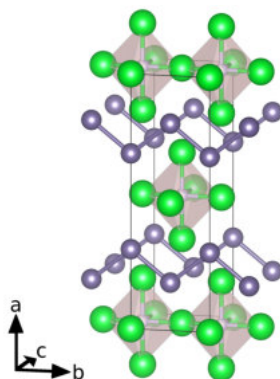


Figure 2.1: The interstitial hydride $\text{Li}_4\text{Si}_2\text{H}$ exhibiting HLi_8 -octahedra (shaded) and ${}_{\infty}[\text{Si}^{1.5-}]$ -polyanions. Large, green spheres: Li ; medium, grey spheres: Si ; small, white spheres centring the octahedra: H .

An example exhibiting an extended polyanion is $\text{Li}_4\text{Tt}_2\text{H}$ ($\text{Tt} = \text{Si}, \text{Ge}$) [86, 87] with ${}_{\infty}[\text{Tt}]$ -zigzag chains (Fig. 2.1). The hydride is coordinated octahedrally by lithium. Counting electrons according to the Zintl-concept, the polyanion lacks $1/2 e^-$ per Tt atom, i.e. $\text{Tt}^{1.5-}$ instead of a Zintl precise Tt^{2-} . Comparing bond length with other zigzag-chain Zintl phases, they appear shortened with 253 pm. The electron precise Zintl phases AeGe ($\text{Ae} = \text{Ca-Ba}$) show Ge-Ge bond lengths of 260 - 265 pm [88]. The shorter distance can be attributed to a depopulation of π^* -bands as again.

Interstitial hydrides also exist in solid state compounds that exhibit Zintl ions. In $\text{Ba}_5\text{Ga}_6\text{H}_2$ [89] hydrogen is coordinated tetrahedrally by barium which is similar to the structures above. Therefore, we can distribute charges according to the Zintl concept as $(\text{Ba}^{2+})_5(\text{Ga}_6)^{8-}(\text{H}^-)_2$. In accordance with the Wade-rules, the gallium partial structure forms a *closo*-cluster ($14 = 2n + 2$ skeletal-electrons) and therefore, an octahedron.

The Zintl phase Ba_3Si_4 contains a butterfly-shaped $(\text{Si}^-)_2(\text{Si}^{2-})_2$ -anion with two- and three-binding silicon atoms. According to Wade-rules, it can also be described as *arachno*- Si_4^{6-} ($14 = 2n + 6$ skeletal-electrons, derived from an octahedron). Upon mild hydrogenation hydride fills barium-voids oxidizing the polyanion under formation of $\text{Ba}_3\text{Si}_4\text{H}_x$, $1 \leq x \leq 2$ [90]. According to transmission electron microscopy (TEM) investigations, the structure is strongly disordered. A preliminary structure model assumes the formation of $\text{Si}_4^{\approx 4-}$ -tetrahedra as pseudo-white phosphorous [90].

The phase $\text{Ba}_{21}\text{Tt}_2\text{O}_5$, $\text{Tt} = \text{Si}, \text{Ge}$ originally described as suboxide [91] was shown to be stabilized by hydrogen ($\text{Ba}_{21}\text{Tt}_2\text{O}_5\text{H}_{24}$)[92]. This phase would be described as an electron precise Zintl phase with monomeric, barium-coordinated Ge^{4-} -anions. Oxygen is coordinated octahedrally, while hydrogen is coordinated tetrahedrally, square-pyramidally or octahedrally by barium. Unfortunately, the structure shows unreasonably short H-H distances which renders the structure solution questionable. Similar phases are described as $\text{Ba}_{21}\text{Tr}_2\text{O}_5\text{H}_x$ ($\text{Tr} = \text{Ga}, \text{In}, \text{Tl}, x \approx 22$) [92]. The structures were reevaluated as $\text{Sr}_{21}\text{Si}_2\text{O}_5\text{H}_{12+x}$ and $\text{Ba}_{21}\text{M}_2\text{O}_5\text{H}_{12+x}$ ($\text{M} = \text{In}, \text{Tl}, \text{Si}, \text{Ge}, \text{Sn}, \text{Pb}, \text{As}, \text{Sb}, \text{Bi}$ (Zintl-like) and $\text{Zn}, \text{Cd}, \text{Hg}$ (not Zintl-like), $x \approx 2$) [93]. Thus, they are better characterised as sub-hydride-oxides and not as Zintl phases. An other hydride-oxide that can be formulated as a Zintl phase is $(\text{Rb}^+)_2(\text{Ba}^{2+})_6(\text{Sb}_2^{4-})_2(\text{Sb}^{3-})(\text{H}^-)(\text{O}^{2-})$ [94] showing monomeric antimony anions as well as antimony-dumbbells.

2.3.2 Polyanionic hydrides and related phases

The works above were mainly motivated by the clarification of structures that incorporated hydrogen accidentally. The search for new Zintl phase hydrides gained momentum when the first polyanionic hydride¹⁵ was described by *Gingl et al.* [31]. They prepared SrAl_2H_2 from the CeCu_2 -structure type Zintl phase SrAl_2 by mild oxidation with hydrogen at 5 MPa and less than 475 K. Upon hydrogenation one Al-Al-bond of the four-binding Al^- cleaves and is saturated by hydrogen. Thus, each Al-atom keeps its overall number of bonds and the reaction can be considered an oxidative insertion as discussed above. The polyanion exhibits two-dimensional ${}_{\infty}[\text{AlH}^-]$ puckered honey-comb layers. The hydrogenation of

¹⁵ The authors claimed the preparation of the first *Zintl phase hydride*. According to more recent practice [35, 74] it would be referred to as first *polyanionic hydride*.

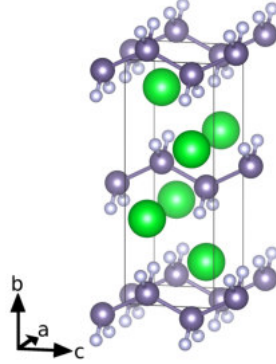


Figure 2.2: The polyanionic hydride KGaH_2 exhibiting polyethylene-like $\frac{1}{\infty}[(\text{GaH}_2)^-]$ -polyanions. Large, green spheres: Cs; medium, grey spheres: Ga; small, white spheres: H.

the homologue series AeTr_2 ($\text{Ae} = \text{Ca}, \text{Sr}, \text{Ba}$; $\text{Tr} = \text{Al}, \text{Ga}, \text{In}$) leads to the compounds SrGa_2H_2 , BaGa_2H_2 which are isotypic to SrAl_2H_2 [95]. *In situ* neutron powder diffraction (NPD) on the formation of SrGa_2D_2 under 5-6 MPa D_2 pressure shows a one step reaction, i.e. there is neither an interstitial deuterium incorporation in SrGa_2 , nor a phase width for the polyanionic hydride phase [96, 97]. The Al-H bond length is 170.6(4) pm, the Ga-H bond lengths are 169 pm. Thus, they are longer than in monomeric AlH_4^- in AAIH_4 ($A = \text{alkaline metal}$), where Al-H distances reach from 157 pm to 165 pm [98–100] or in monomeric GaH_4^- (RbGaH_4 , $d(\text{Ga-H}) = 150 - 154$ pm [101]).

Furthermore, the mixed trielide-tetrelide phases AeTrTt ($\text{Ae} = \text{Ca}, \text{Sr}, \text{Ba}$; $\text{Tr} = \text{Al}, \text{Ga}, \text{In}$; $\text{Tt} = \text{Si}, \text{Ge}, \text{Sn}$) were hydrogenated to form AeTrTtH ($= \text{AeTr}(\text{H})\text{Tt}$) [102–106]. The precursors show a statistical distribution of Tr and Tt and are isopointal to AeGa_2 phases ($\text{Ae} = \text{Sr}, \text{Ba}$; AlB_2 -structure type). The polyanions shows graphite-like hexagonal layers. While a graphite-like structure fits the Zintl description of AeGa_2 , the AeTrTt phases are electronically imbalanced. Upon hydrogenation the triel and tetrel positions order and a polyanionic hydride similar to the SrAl_2H_2 -structure is formed. It exhibits two-dimensional puckered honey-comb layers as well, but only Tr is saturated by hydrogen. Since Tt^- was already three-binding, it does not bind a hydrogen atom. Thus, the layers can be described as $\frac{2}{\infty}[\text{Tr}(\text{H})\text{Tt}^{2-}]$. The Tr-H -bonds are even longer than in AeTr_2H_2 ($d(\text{Al-H}) = 173 - 177$ pm, $d(\text{Ga-H}) = 171 - 173$ pm, $d(\text{In-H}) = 176$ pm). The formation of a distinct covalent Tr-H bond was further confirmed by inelastic neutron scattering (INS). Especially the formation of a In-H bond is a rare example in the solid state [106]. In SrGa_2H_2 and BaGa_2H_2 the Ga-H stretching mode is assigned to a band from 1200-1400 cm^{-1} while bending modes show peaks at about 800 cm^{-1} [107]. In the mixed gallide-tetrelides the stretching mode shows at 1155-1190 cm^{-1} and bending mode at about 900 cm^{-1} [108]. The Al-H bond in BaAlSiH shows a similar bond strength as for the gallides with bending and stretching modes at about 900 cm^{-1} and 1200 cm^{-1} , respectively [103]. The stretching mode of the In-H bond is shifted down to 1000 cm^{-1} [106]. According to the elongated Tr-H distances, the bonds are weaker and thus, shifted to lower frequencies compared to the stretching modes of AlH_4^- (1650 - 1700 cm^{-1}) and GaH_4^- (1700 - 1800 cm^{-1}) [109]. Based on density functional theory (DFT) calculations a mainly ionic H^- and only weak covalent interaction was discussed [110]. Further DFT calculations showed that the trielides SrAl_2H_2 , SrGa_2H_2 and BaGa_2H_2 are poor metals that exhibit a pseudo-gap at the Fermi level [76, 95]. The mixed phases AeTrTtH are semi-conducting with small band gaps. For AeAlTtH ($\text{Tt} = \text{Si}, \text{Ge}$) the band gap reaches from 0.3 eV (Ca) to 0.8 eV (Ba) [102, 103, 105]. The corresponding gallium-containing compounds show smaller band gaps from 0.1 eV (BaGaSiH) to 0.6 eV (BaGaGeH , BaGaSnH) [104].

Trielides and especially gallium show an even richer polyanionic hydride chemistry. Mainly by direct synthesis using the elements under hydrogen gas pressure, pseudo-alkane like moieties could be prepared. In $\text{A}_8\text{Ga}_5\text{H}_{15}$ ($A = \text{Rb}, \text{Cs}$) a neopentane like $\text{Ga}(\text{GaH}_3)_4^{5-}$ -unit was found [32, 33]. Additional hydrogen atoms are located in Rb_6 -octahedra. Thus, this is the first example of a Zintl phase hydride featuring polyanionic and interstitial hydride motifs next to each other. $\text{Cs}_{10}\text{Ga}_9\text{H}_{25}$ exhibits a propane-like $\text{Ga}_3\text{H}_8^{3-}$ -group and additional hydrogen atoms located in Cs_6 -octahedra. The possible existence of aluminium based pseudo-alkane structures was recently shown by *ab initio* calculations. Investigation of the potential energy surfaces of $\text{Li}_2\text{Al}_2\text{H}_6$ and $\text{Li}_3\text{Al}_3\text{H}_8$ suggests the existence of ethane-like $\text{Al}_2\text{H}_6^{2-}$ and propane-like $\text{Al}_3\text{H}_8^{3-}$ [111]. A lithium coordinated pseudo-propane $\text{Li}_2[\text{Al}_3\text{H}_8]^-$ moiety could be

verified in a molecular beam experiment using photo electron spectroscopy and *ab initio* calculations [112]. A corresponding solid state bulk compound is still lacking. The existence of pseudo-alkane like $(B_nH_{2n+2})^{n-}$ -groups was predicted by *ab initio* methods as well [36]. An other experimental example is a polyethylene-like $^1_\infty[\text{GaH}_2^-]$ -unit in AGaH_2 ($A = \text{K}, \text{Rb}$), crystallizing in two different structure types [32, 34] (Fig. 2.2). The heavy metal partial structures can be related to the CrB- or FeB-structure type, which will be relevant later. In RbGaH_2 Wyckoff positions are similar to the FeB-structure type, but the a/c -ratio is inverted. KGaH_2 without hydrogen positions can be described as CrB-structure type. In both cases, hydrogen is situated on a mirror-plane perpendicular to the chain direction with a H-Ga-H angle of $97\text{--}98^\circ$. Potassium can be partially exchanged by rubidium ($\text{Rb}_x\text{K}_{1-x}\text{GaH}_2$, $0 \leq x \leq 0.5$) keeping its structure. Higher rubidium contents lead to a separation into RbGaH_2 and $\text{Rb}_{0.5}\text{K}_{0.5}\text{GaH}_2$ [34]. KGaH_2 was also prepared by hydrogenation of the K_2Ga_3 [113]. The samples prepared by direct synthesis are colorless powders. Thus, Ga-H bond vibrations can be analysed by infra red (IR) spectroscopy. There are broad bands of the stretching-mode at about 1400 cm^{-1} (RbGaH_2 , $\text{Rb}_x\text{K}_{1-x}\text{GaH}_2$) or 1500 cm^{-1} ($\text{Cs}_{10}\text{Ga}_9\text{H}_{25}$, $\text{Rb}_8\text{Ga}_5\text{H}_{15}$) [33, 34]. These values are smaller than the corresponding vibrations in pseudo-methane like GaH_4^- -moieties at $1700\text{--}1800\text{ cm}^{-1}$ [109], indicating weaker bonds for the higher homologues of pseudo-alkane like structures. The Ga-H distance reach from 149 to 167 pm and are therefore between GaH_4^- and AlGa_2H_2 .

Recently, the CrB-structure type Zintl phases NdGa and GdGa were hydrogenated forming $\text{NdGaH}_{1.66}$ and isotypic GdGaH_x [114, 115]. Hydrogen positions of the first one were determined by neutron diffraction using the corresponding deuteride. One hydrogen per formula unit is incorporated in tetrahedral Nd_4 -voids. The additional $2/3$ hydrogen atoms fill trigonal-bipyramidal Nd_3Ga_2 -voids. Therefore they bridge gallium zigzag chains which are already present in the parent Zintl phases. DFT calculations of ordering variants suggest the formation of a $^1_\infty[(\text{Ga}-\text{H}-\text{Ga}-\text{H}-\text{Ga})^{6-}]$ -moiety. Due to the location of hydrogen in the middle of two zigzag chains, Ga-H distances are rather long ($\approx 200\text{ pm}$) beyond a classical covalent bond.

There are plenty of examples that feature polyanionic hydrides exhibiting a triel-hydrogen bond. A proper description of polyanions with tetrel-hydrogen bond was still elusive and is given in this work (Sec. 4.4 as well as [A1] and [A2]). The description of hydrogen atoms coordinating silicon in CaSiH_y ($1 \leq y \leq 1.33$) caused some controversy about the character of the interaction [116, 117]. The preparation of a homologue series $\text{SrSiH}_{1.6}$, $\text{BaSiH}_{3.4}$ and $\text{EuSiH}_{1.8}$ is possible but a localisation of hydrogen atoms was still missing [118, 119]. A reinvestigation by the *Kohlmann*-group could determine some preliminary hydrogen positions [97], but the interpretation of the bonding character is still ambiguous. *In situ* diffraction of the reaction of CaSi under hydrogen pressure and elevated temperatures showed that the $\text{CaSi}-\text{H}_2$ system is even more complex [97]. More details about these systems are given below (Sec. 4).

The existence of monomeric tetrel-hydride units prepared from solution chemistry is well documented. Reactions of alkaline metal and tetrel-tetrahydrides in liquid ammonia, mono- or diglyme lead to the formation of ASiH_3 ($A = \text{Na-Cs}$) [120–122], AGeH_3 ($A = \text{Li-Cs}$) [121–125], or KSnH_3 [121]. In ATtH_3 all three bonds that are expected for a formally Tt^- are saturated by hydrogen. The silicides ASiH_3 ($A = \text{K}, \text{Rb}, \text{Cs}$) can also be prepared by hydrogenation of the corresponding Zintl phases ASi under 5 MPa hydrogen pressure and 373 K [126, 127]. Therefore, according to Scheme 2.2, p. 10 the SiH_3^- -moiety can be considered as the end-product of an oxidative insertion reaction. In liquid ammonia dissolved Si_4^{4-} reacts as strong base slowly deprotonating NH_3 to form SiH_3^- [128]. Another solution-based method for the preparation of KSiH_3 is the hydrogenation of potassium triphenylsilyl under 0.1 MPa hydrogen pressure [129]. This reaction leads to the precipitation of a white powder. The hydrogenations of LiSi and NaSi lead to decompositions into $\text{LiH} + \text{Si}$ and $\text{NaH} + \text{Na}_8\text{Si}_{46}$, respectively [130, 131]. In contrast to the solution-based synthesis that leads to colourless to pale yellow crystals [121, 132], the solid-gas reaction leads to grey powders. High temperature α - KSiH_3 crystallizes in a NaCl-type structure with SiH_3^- -units occupying the anion site [133]. The silanide is rotationally disordered mimicking a hydrogen sphere around the silicon and is only weakly bound to the cation [125, 134, 135]. Solution chemical based crystallization of 18-crown-6-ligand coordinated $\text{K}^+-\text{SiH}_3^-$ leads to the formation of a *tet*-conformer with direct K-Si or an *inv*-conformer with K-H electrostatic interactions underlying this weak bonding [136]. Similar crown-ether derivatives could be crystallized for the GeH_3^- -anion [137]. The high temperature form of α - ASiH_3 as well as KGeH_3 and RbGeH_3 are isotypic. There are β -phases of the silicides at low temperatures. The phase transition shows a hysteresis of about 50 K and occurs between 240 - 300 K [127, 135, 138]. β - KSiH_3 shows ordered SiH_3^- anions [138]. It can be described as FeB-structure type with A^+ occupying the iron- and SiH_3^- occupying the boron-site. The structure of CsGeH_3 is closely

related since it crystallizes in CrB-structure type [124]. Hydrogen positions have not been determined yet. The low temperature forms β -RbSiH₃ and β -CsSiH₃ [127] are isostructural. They crystallize in the monoclinic space group $P2_1/m$ which can be derived from CrB-structure type by a group-subgroup relation. The determination of hydrogen positions of CsGeH₃ might lead to the same structure. The pseudo spherical rotational disorder of SiH₃⁻ and GeH₃⁻ in NaCl-structure type phases is reduced to a rotational disorder around the internal C_{3v}-axis, when changing to the low temperature form. At even lower temperatures (≈ 100 K for CsGeH₃ [125], ≈ 200 K for KSiH₃ [135, 139]) the anion rotation freezes, which was determined by solid-state nuclear magnetic resonance (SSNMR).

2.3.3 Zintl ion hydrides

Examples that show a hydride interacting with Wade-like Zintl ions are rare and will not be considered relevant for this work. Nevertheless, there are two examples. Hydrogen can be incorporated as hydride inside the cluster and thus, contributes two electrons. There is Na₁₅K₆Tl₁₈H [140] containing two types of cluster ions. The more interesting one is an hydrogen-stuffed [H@Tl₆]⁷⁻ octahedron. This clusters has $14 = 2n + 2$ skeletal-electrons and therefore, forms an octahedral *closo*-cluster. Hydrogen can also bind as a ligand to the cluster. The Zintl ion HSn₉³⁻, in solution or as [K(2,2,2-crypt)]₃HSn₉·1.5en-salt (en = ethylenediamine), contains an exo-hydrogen bound to an 9-vertex *nido*-cluster [141]. Since hydrogen is a ligand, it contributes one electron to the framework giving $22 = 2n + 4$ electrons.

2.4 Relevance and open questions

The Zintl concept explains crystal structures considering formal valence compounds. Zintl phases in fact cover a wide range of electrical properties, reaching from semi-conducting to metallic conductivity. Thus, they became relevant e.g. as thermoelectric material [142]. Incorporating hydrogen changes the bonding situation drastically. Especially interstitial hydrides often allow a variable hydrogen content which might be exploited to tune electrical properties. Furthermore, a theoretical work predicts a bulk photovoltaic effect for the moisture-stable polyanionic hydrides $AeTrTtH$ ($Ae = \text{Ca-Ba}$, $Tt = \text{Al, Ga}$ and $Tt = \text{Si-Sn}$) [143]. Another aspect is hydrogen storage. Interstitial hydrides build a bridge between Zintl phases and salt-like s-block metal hydrides (e.g. MgH₂). Polyanionic hydrides however link the hydrogen-free compounds with complex main group hydrides (e.g. AlH₄⁻ or BH₄⁻). These are classes of potential hydrogen storage materials. Zintl phase hydrides can combine both motifs. Thus, the hydrogenation of Zintl phases often shows good reversibility combined with low absorption and desorption temperatures. An early example of a Zintl phase in the field hydrogen storage was CaSi which was investigated by the *Toyota R & D Lab* [144]. While the hydrogenation behaviour was studied in detail [144–147], there is still ambiguity about the structure of the corresponding hydride [116, 117]. Further systems that were investigated as possible hydrogen storage materials are the polyanionic hydride SrAl₂H₂ [148] or KSiH₃, that features monomeric SiH₃⁻-units and can be prepared from the Zintl phase KSi [126, 149].

An advantage for future applications is the availability of Zintl phases as precursors that consist of cheap and abundant elements. Still, our knowledge of the hydrogenation behaviour or even the existence of corresponding hydrides is still limited. While the Zintl-concept is well established to describe polyanionic structures, the validity especially for polyanionic hydrides is not clear yet. There are some examples of covalent Tr -H bonds ($Tr = \text{triel}$), but also exceptions like NdGaH_{1.66} [114] and GdGaH_{1.66} [115] which show a Ga-H interaction that is not simply covalent. Furthermore, there is still a controversy about the Si-H bonding in CaSiH_{1+x} ($x \leq 0.3$) [116, 117]. (for details see Sec. 4.4.1). The final prove of a polyanionic hydride with a covalent Tt -H bond next to a Tt - Tt ($Tt = \text{tetrel}$) is still elusive.

This work aims to close some gaps by extending the experimental foundation. Thus, one focus lies on the preparation of Zintl phase hydrides with a Tt -H bond. Known as well as new phases were prepared and characterised experimentally and by quantum chemical calculations to prove the covalent character of the bond. A second focus lies on the investigation of reaction mechanisms. *In situ* diffraction is applied to study the reversible hydrogenation of Zintl phases. It provides insight into the formation of intermediate phases and helps to distinguish line phases from phases of variable hydrogen content. Especially the latter case is not easily reconcilable with a Zintl-like view of the structures and might need some idealisations. A deeper knowledge of reaction mechanisms is a prerequisite for the search and fine tuning of systems for possible applications.

3 Methods

This section gives an overview of the applied techniques and also some limitations. Details are given in the publications in Part II.

3.1 Synthesis

Most educts and samples are air- and moisture-sensitive. Thus, all manipulations were done in an argon-filled glovebox ($\text{H}_2\text{O} < 1\text{ppm}$, $\text{O}_2 < 1\text{ppm}$). Typically, Zintl phases were prepared from the elements. Stoichiometric mixtures of the elements were placed into metal jackets which were then sealed by arc-melting. Stainless steel, niobium or tantalum were used as container material. While steel ampoules could be placed directly into the oven, the other metal jackets were either sealed inside a fused silica tube, or placed under primary vacuum. Samples were typically heated above the melting point and cooled down by the internal rate of the oven. If phases show a peritectical decomposition the samples were quenched in cold water and subsequently annealed below the decomposition temperature.

Hydrogenation reactions were done in *Nicrofer*[®] 5219Nb-alloy 718-autoclaves which were set under hydrogen pressure up to 30 MPa. A maximum temperature of 825 K can be realised using these autoclaves. Typically polyanionic hydrides were prepared at temperatures of about 475 K to 525 K. Samples for neutron diffraction were prepared using deuterium gas to avoid a strong background from incoherent scattering of hydrogen.

Details of the preparation of the different samples can be found in Part II. All samples were prepared by the author or under his supervision except for

- $\text{SrSiH}_y(\text{D}_y)$, $\text{BaSiH}_y(\text{D}_y)$ and precursors (by P. Wenderoth, Saarland University, Germany),
- $\text{LaGeH}(\text{D})$, LaSnH , $\text{NdSiH}(\text{D})$, $\text{NdGeH}(\text{D})$ and precursors (by A. Werwein, Leipzig University, Germany), and
- NdGa (by the Häussermann group, Stockholm University, Sweden)

3.2 *Ex situ* characterisation and quantum chemical calculations

The first aspect of this thesis is the description of new Zintl phase hydrides and the clarification of the crystal structures of already known but crystallographically poorly described phases. The articles [A1], [A2] and [A3] deal with this topic.

3.2.1 Single crystal diffraction

Single crystal diffraction of the prepared Zintl phase hydrides is typically not feasible. The samples are prepared from Zintl phase precursors under hydrogen pressure and moderate temperatures, often below 550 K. Higher temperatures that might allow proper crystal growth lead to decomposition. There is a report about X-ray single crystal diffraction of a poor CaSiH_y crystal [118]. Own Laue diffraction experiments showed strongly developed powder rings for this type of sample [150].

Since macroscopic single crystals could not be obtained, transmission electron microscopy (TEM) using a Philips STEM CM 200 ST with 23 pm point resolution was applied to gain single crystal diffraction patterns. Due to moisture sensitive samples and no possibility to transfer TEM samples under inert atmosphere into the instrument, only a limited number of compounds was investigated successfully. One example can be found in [A2]. Selected area electron diffraction (SAED) of $\text{AeTtH}_{5/3-x}$ ($\text{AeTt} = \text{SrSi}$, BaSi , BaGe) was used to determine a superstructure not recognised before. Diffraction patterns were evaluated qualitatively by comparing them to simulated pattern of crystal structure candidates.

3.2.2 Powder diffraction

Since single crystal diffraction was not possible, crystal structures were determined and refined using powder methods, i.e. laboratory X-ray, synchrotron, and neutron diffraction or a combination of them. Laboratory X-ray diffraction patterns were indexed and structural candidates for Rietveld refinement were found by group-subgroup relations [151]. The used instruments were a Stoe Stadi P Debye-Scherrer diffractometer equipped with a Mythen 1k detector, or a Huber G670 Guinier diffractometer with image

plate detector. Both instruments use monochromatic Cu-K $_{\alpha 1}$ ($\lambda = 154$ pm) radiation. To improve data quality, synchrotron diffraction data of BaSiH $_y$ and its deuteride, SrGeH $_y$ and BaGeH $_y$ were obtained. Except for the latter one they are published in [A1]. Data were collected on the 11-BM beamline of the advanced photon source (APS) of the Argonne National Laboratory (ANL), USA. The samples were handled via the mail-in service under the general user proposal (GUP) 41649. Measurements were conducted at a wavelength $\lambda = 45.8997$ pm.

Neutron powder diffraction is mandatory to determine hydrogen positions, since most samples contain heavy metals and do not allow a refinement of them from X-ray data. Experiments were done at the Institut Laue-Langevin (ILL), Grenoble, France at the high intensity diffractometer two-axis diffractometer D20 [152] ($\lambda = 186.6$ pm). Another instrument used is the fine resolution powder diffractometer (FIREPOD/ E9 [153], $\lambda = 179.7$ pm) of the reactor neutron source BERII of Helmholtz-Zentrum Berlin (HZB), Germany. Due to large incoherent scattering contribution of hydrogen, deuterated samples were supplied. Deuterium sites in the crystal structures were obtained by a difference Fourier analysis or by chemical reasoning. Crystal structures were evaluated using the Rietveld method [154, 155] using *FullProf* [156, 157] or *TOPAS* [158]. Structure pictures were prepared with *VESTA* [159, 160].

3.2.3 Spectroscopy

Phases of the *AeTtH $_y$* -family (*Ae* = alkaline earth metal, *Tt* = tetrel) that exhibit polyanionic hydrides were investigated. Since one goal of this work is the characterisation of element-hydrogen bonds, vibrational spectroscopy is a natural choice. Samples are opaque powders, thus measurements need to be done in reflecting geometry. Unfortunately standard laboratory measurements, i.e. Raman- and Infra red¹⁶-spectroscopy did not yield any signals except for BaSiH $_y$. The most probable reason is the lack of a band gap. This was not determined experimentally, but the non-stoichiometry regarding hydrogen as well as the behaviour of hydrogen free Zintl phases suggests the existence of metallic states. After decomposition in air or in cold hydrochloric acid, element-hydrogen bonds can be measured by IR-spectroscopy [161]. The results are summarized in Sec. 4.4.4.

Another quantity that is sensitive to distances is the interaction of a quadrupole moment of an atomic nucleus with the electric field gradient (EFG)¹⁷ as measured by solid state nuclear magnetic resonance (SSNMR). Measurements on the *AeTtH $_y$* -family were conducted in cooperation with the department of experimental physics¹⁸. Since information of the structure of the polyanion are of interest, the deuterium (²H) nucleus was chosen as local probe. Hydrogen (¹H) as a $I = 1/2$ nucleus does not feature a quadrupole moment. First results of the magnitude of the quadrupole interaction (C_Q) were already presented in [A1]. In Sec. 4.4.3 they are set into relation of the bond length.

3.2.4 Density functional theory (DFT) calculations

DFT calculations of extended solids were done applying periodic boundary conditions. Either the *Abinit* [162–166] or the *Quantum Espresso (QE)* [167, 168] open source package was used. The calculations were done in the generalised gradient approximation (GGA) using the PBE-functional [169] with projector augmented waves (PAW) [170]. Atomic data sets were obtained from *JTH*-library (*Abinit*, [171, 172]) or the *pslibrary* (*QE*, [173]). Prior to the productive calculations, typical parameters were converged, e.g. energy cut-offs, k-grids (Monkhorst-Pack type [174]) and smearing parameters that control the electronic occupations at the Fermi-level for metallic systems.

Crystal structures were optimised and reproduced experimental values up to a few percent deviation. Calculations were done for structures of the *AeTtH $_2$* -system as well as LaSi and LaSiH. Non-stoichiometric systems were treated with an idealised occupation and still reproduced experimental structures with reasonable accuracy.

Density of states (DOS) as well as fatband structures¹⁹ were calculated. Since these electronic properties were calculated on the DFT level, band gaps are usually underestimated or do even vanish. This arises

¹⁶ Attenuated total reflection (ATR) technique.

¹⁷ The EFG is a matrix (tensor) since it is the gradient of the electric field, i.e. the second derivative of the potential $\partial^2/\partial x_i \partial x_j V(x)$, $x \in \mathbb{R}^3$

¹⁸ Robin Guehne, Manuel Lindel, Dr. Marko Bertmer, Prof. Jürgen Haase, Leipzig University, Department of Experimental Physics II, Linnéstraße 5, 04103 Leipzig, Germany.

¹⁹ Band structures that emphasize the contribution of an atomic state by the dot size.

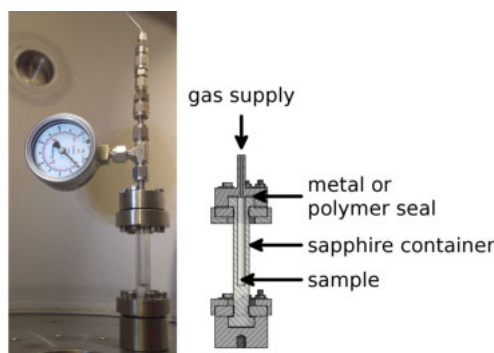


Figure 3.1: (Leuco-)sapphire single crystal cell used for *in situ* diffraction. Details are given in [179] or [A5].

from the lack of a proper description of unoccupied states. Still, calculated quantities are qualitatively correct.

Quadrupole interactions were calculated with the *Abinit* package using a deuterium quadrupole moment of $2.86 \cdot 10^{-3}$ barn (0.286 fm^2) [175, 176]. Experimental quadrupole interaction values (C_Q) can be reproduced adequately. Furthermore, a systematic variation of bond lengths and angles can be calculated to get an idea how to interpret experimental data. Results are mainly unpublished yet and are discussed directly in Sec. 4.4.3.

3.2.5 Further measurements

The hydrogen contents of the hydrides were determined by elemental analysis using the carrier gas-hot extraction method in triplicate repetition. Air sensitive samples were handled in a glove box. Tin containers were filled with the samples and sealed by crimping.

The heavy metal ratios were determined by energy-dispersive X-ray spectroscopy either using a scanning or transmission electron microscope.

3.3 *In situ* characterisation

The second aspect of this thesis is the investigation of reaction schemes. The articles [A4], [A5], [A6], [A7] and the manuscript [U1] deal with this topic. On the search for intermediate phases the solid state-gas reactions are monitored by *in situ* powder diffraction and thermal analysis. For a general overview of *in situ* diffraction see [177] (neutrons) or [178] (synchrotron).

3.3.1 Diffraction

***In situ* neutron powder diffraction (*in situ* NPD)** was done at the high-intensity two axis diffractometer D20 [152], Institut Laue-Langevin (ILL), Grenoble, France. The high flux of this neutron source combined with a reasonable resolution allows real time studies with small samples. Furthermore, the position-sensitive detector (PSD) allows the collection of diffraction data to a maximum 2θ -angle of 150° in one measurement. The shortest measuring time we realised was 10 s per frame (see Article [A6], Fig. A6.10) and still allowed to extract limited structural data. Samples sizes are about 0.3 cm^3 , which is less than $1/3$ of the size of a typical neutron diffraction sample. As sample container a (leuco-)sapphire single crystal reaction chamber is used, which was developed by our group [179] (Fig. 3.1). A more recent description as well as a number of examples are given in [A5]. The cell is connected to a gas supply system. The set-up can realise pressures up to about 10 MPa D_2 gas, which is limited by the pressure of available deuterium gas bottles. Since the reaction chamber is a single crystal, it can be oriented towards the primary beam in a way, that no reflection hits the detector. Thus, it provides a flat diffraction background. *In situ* experiments were conducted under the proposals 5-22-734 [180], 5-21-1096 [181] and 5-24-576 [182]. Data were evaluated qualitatively or by Rietveld refinements [154, 155] using *FullProf* [156, 157] or *TOPAS* [158].

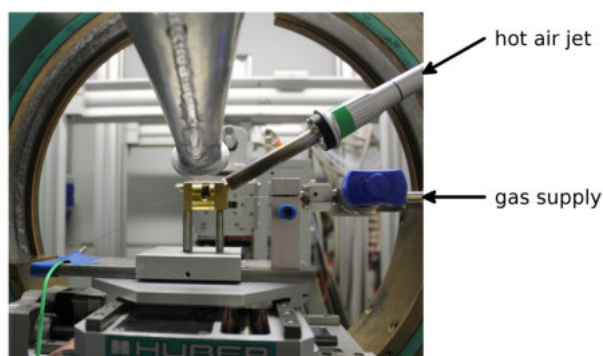


Figure 3.2: *In situ* synchrotron diffraction at KMC-2 beamline, BESSY II, HZB, Berlin. Picture is taken in direction of the primary beam. Heating is realised by a hot air jet.

Serial Rietveld refinement was used to evaluate *in situ* neutron diffraction data. Typical counting times to get a diffraction pattern of sufficient intensity for structural analysis were one to five minutes. Serial refinements could be done semi-automatically. During the experiments different phases occur that change during the reaction, i.e. show a phase width in regard to hydrogen incorporation. A suitable diffraction pattern was chosen and refined manually. Constraints were set if necessary, i.e. for Debye-Waller factors of like elements. The converged refinement was used as input for the following diffraction pattern. This was automatically repeated either forward or backward in time. If a refinement diverged or run into a local, to say chemically unreasonable, minimum, constraints were adjusted. This procedure allows to extract structural data during the whole experiment. Changes of the unit cell, i.e. anisotropic lattice parameter changes are a good indicator for structural changes. They did typically not correlate with other parameters. Structural parameters, i.e. bond lengths and hydrogen contents, were evaluated more carefully. Due to complex diffraction patterns including several phases, they easily correlate. Furthermore, at elevated temperatures the sapphire single crystal cell (NPD) can cause a considerable background signal due to inelastic scattering.

***In situ* synchrotron powder diffraction (*in situ* SPD)** was realised at the multi purpose beamline KMC-2 [183] at BESSYII, Helmholtz-Zentrum Berlin (HZB), Germany. Measurements were done in 0.3 mm fused silica capillaries at $\lambda = 100$ pm. They were glued into a $1/4$ in VCR dummy plug that was modified with a bore hole (top: 3 mm, bottom 1 mm) using two-component epoxy glue. A sample mounting and the attachment to the gas supply system were constructed by *D. Wallacher* and *N. Grimm*²⁰ (See Fig. 3.2). Heating is realised by a hot air jet. Temperatures up to 825 K and pressures up to 20 MPa are possible. This extends the conditions available for *in situ* diffraction. Fast experiments (fast heating rate) using only small amounts of sample are possible. Thus, they are comparable to *in situ* thermal analysis (see below).

The first set up did not allow sample rotation (Proposal 15202481) which was improved for later measurements (Proposal 17104825). The instrument is equipped with a two-dimensional detector, that covers about 12° in 2θ . The collection of a diffraction pattern over the whole angular range takes about 30 min. Time-resolved measurements were done at a fixed detector position with an typical time resolution of about 20 s. (The detector has a software-related dead time of 4 s.)

Data were evaluated qualitatively to show reactions upon isobaric heating or isothermic pressurizing.

An *in situ* laboratory X-ray powder diffraction (*in situ* XRPD) set-up was developed in the course of this thesis and successfully tested for the reaction $\text{KSi} \xrightarrow{\text{H}_2} \text{KSiH}_3$ [A7]. The assembly is based on suggestions given in [184], which deals with *in situ* diffraction using capillary geometry at a synchrotron. Some details of the laboratory set-up are given in [A7]. See also Fig. 3.3. The standard capillary heating systems of a Huber G670 Guinier diffractometer was adapted to allow gas supply from the top. For a typical *in situ* experiment, 0.2-0.5 mm fused silica capillaries were used. They were glued with two-component epoxy glue either into a $1/8$ in Swagelok- or $1/8$ in VCR-fitting. At room temperature,

²⁰ Dirk Wallacher, Nico Grimm, HZB, Department Sample Environment, Hahn-Meitner-Platz 1, 14109 Berlin, Germany



Figure 3.3: Laboratory *in situ* X-ray powder diffraction; Sample mounting and gas attachment (left) and set up at the Giunier camera (right). Heating is realised by a resistivity heater.

0.3 mm capillaries support more than 20 MPa H_2 pressure (maximum pressure available for testing). At elevated temperatures up to 700 K, a pressure of 10 MPa was successfully tested. Measurements were done with monochromatic $Mo-K_{\alpha 1}$ -radiation in a static set up without sample rotation. Texture effects were no major issue. Nevertheless, due to possibly poor crystallite statistics and limited resolution data were evaluated qualitatively.

The G670 instrument is equipped with an image plate detector. Depending on the sample, a collection time of 5 to 30 min is necessary. Thus, pressure and temperature are increased as step functions. The evaluation of reaction kinetics appears possible applying even shorter counting times, but need further testing. There is a dead time of about 20 s to read the image plate.

3.3.2 Thermal analysis

Another valuable tool is differential scanning calorimetry (DSC) under up to 7 MPa hydrogen gas pressure and 725 K (referred to as *in situ* thermal analysis or H_2 -DSC). Measurements were done on a TA Instruments Q1000. Less than 20 mg of sample are placed in an aluminium crucible which is crimped afterwards. The sealed containers are tight against air and moisture but allow hydrogen to penetrate. H_2 -DSC allows to collect the reaction heat during hydrogen uptake or release qualitatively. Since some reactions are rather slow, they show broad peaks or no signal at all. Thus, the determination of a proper onset or baseline for integration is often ambiguous. Typically, quantitative signal evaluation is not conducted. This technique is convenient to screen the reactivity of samples and identify systems for *in situ* diffraction, e.g. systems with reversible signals. It allows to investigate several temperature-pressure regimes to estimate proper reaction conditions for subsequent experiments.

3.4 Limitations and outlook

Crystal structures were evaluated using the Rietveld method [154, 155]. This method inherently assumes three-dimensional periodicity. Similar to single crystal diffraction, the intensity of a Bragg reflections is integrated. However, in the powder case, due to strong overlap, it is combined with an on-the-fly partitioning of reflections according to the crystal structure model and a whole pattern fitting procedure. This technique neglects local effects (that are not described by periodicity) and averages the structure over the whole bulk. Especially for non-stoichiometric compounds like the investigated $AeTtH_y$ -systems, this procedure can lead to sometimes artificial bond lengths as discussed in detail in Sec. 4.4.3 in conjunction with SSNMR.

A method to overcome this type of artefacts is the total scattering (total diffraction) approach [185, 186]. A careful determination of the total scattering factors $S(Q)$ and its Fourier-transformation leads to the pair distribution function (pdf) that directly correlates to distances within the crystal structure. This technique is more sensitive to the local structure. Since neutron radiation needs to be used again to evaluate the proper lengths of element-hydrogen distances, this is not a standard experiment and beam

time at a large scale facility is needed. The total scattering approach is beyond the scope of this work, but a beam time proposal is in preparation based on the results of this thesis and the already published articles.

Another problem of these samples is the insensitivity toward vibrational spectroscopy, i.e. Raman and IR. Inelastic neutron scattering (INS or neutron vibrational spectroscopy) also can probe vibrational modes of the crystal. This was extensively done for Tr -H bonds ($Tr = \text{Al, Ga, In}$) [103, 105–108]. Measurements of CaSiH_y [117] showed that these results are still ambiguous for our type of compounds (see Sec. 4.4.1 for a discussion). Thus, INS experiments were not considered yet.

4 Hydrogenation of CrB-structure type Zintl phases and related systems

4.1 CrB- and FeB-structure type

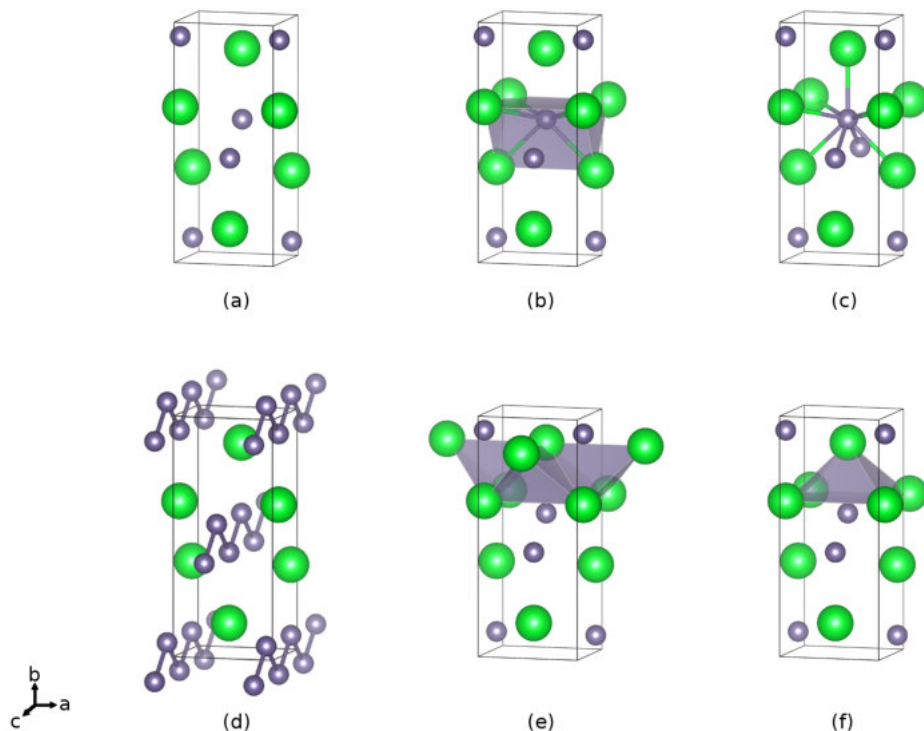
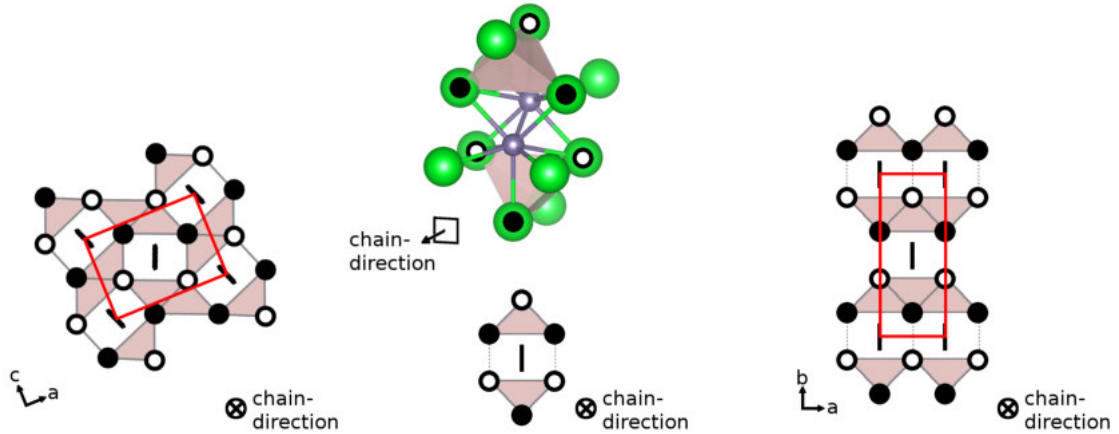


Figure 4.1: CaSi in CrB-structure type: (a) Unit cell. (b) Trigonal prismatic coordination of silicon. The faces of the prisms are capped by another calcium and two silicon atoms leading to (c) a 7+2 coordination. (d) Polyanionic $\frac{1}{\infty}[\text{Si}^{2-}]$ -zigzag chain. (e) Tetrahedral voids already present in the Zintl phase. (f) A possible quadratic-pyramidal void. The center of the void exhibits a quite short distance to the silicon atom below. Large green spheres: Ca; small grey spheres: Si.

CrB-structure type: The CrB-structure type (B33-structure regarding *Strukturberichte*) is widespread. While CrB is an intermetallic compound, it is also known as TII- (ionic), CaSi- (Zintl phase) or AlTh-type (intermetallic), thus covering ionic, covalent and metallic bonding.

For the discussion we will use CaSi as model system, which is a typical Zintl phase (Fig. 4.1). Each Si-atom is trigonal-prismatic coordinated by Ca (Fig. 4.1 (b)) with one Ca- and two Si-atoms capping the three faces of the prism. This results in a 7+2 coordination (Fig. 4.1 (c)). The structure can be understood according to the Zintl-Klemm concept: The formally Si^{2-} -anions are two-binding and form zigzag chains (Fig. 4.1 (d)) that are isoelectronic to μ -sulfur. The prisms as shown in Fig. 4.1 (b) are stacked perpendicular to the chain direction and share faces in chain direction. This leads to 2D-sheets in the a - c -plane. They are stacked in crystallographic b direction with a translation of $\frac{1}{2}a$ which is represented by a C -centred lattice. The chain separating Ca-layer can be described as two intersecting nets of edge-sharing tetrahedra (Fig. 4.1 (e)) and edge-sharing quadratic pyramids (Fig. 4.1 (f)).

Upon hydrogenation tetrahedral voids can get filled. The pyramidal voids cannot be filled without a strong distortion of the structure since they are already part of the Si coordination sphere and exhibit a small Si-Ca distance (Fig. 4.1 (c) and (f)). For Part I all CrB-type derived crystal structures will be described due to the axes system of CaSi. In the following, crystal structures will be discussed exhibiting zigzag chains and 2D sheets of tetrahedral M_4 -voids (M = alkaline earth or lanthanoid metal). Some of them develop superstructures that, in general, run perpendicular to the chain direction. Therefore, the



Scheme 4.1: Schematic FeB- (**left**) and CrB-structure type (**right**) as well as the common coordination motif of the zigzag chain (**middle**; large green spheres cation-site; small grey spheres (poly-)anion-site). The schematic representations show full circles as atoms in the front ($y(\text{FeB})/z(\text{CrB}) = 3/4$) and open circles as atoms in the back ($y/z = 1/4$). Polyanionic chains are indicated as a bar.

following definition will be used:

Definition 12 (Normalised axes of CrB-structure type derived phases) *The axes are defined with regard to the CrB-structure type of the parent Zintl phases:*

- crystallographic $\mathbf{a} = [100]$ = superstructure direction (if present)*
- crystallographic $\mathbf{b} = [010]$ = stacking direction of the layers*
- crystallographic $\mathbf{c} = [001]$ = chain direction*

Thus, spacegroups will be given in non-standard setting. Standard setting and number are added in parentheses.

Attention: This definition might not hold for the published articles (Part II).

FeB-structure type: Closely related to the CrB- is the FeB-structure type. As already mentioned for polyanionic hydrides (Sec. 2.3.2), some of them occur either as CrB- ($\text{Rb}_{0.5}\text{K}_{0.5}\text{GaH}_2$, CsGeH_3) or FeB-derived structures (RbGaH_2 , $\beta\text{-KSiH}_3$). The coordination of the chains is equal for both structure types but the alignment is different. Due to the zigzag character of the chains, they lie in a plane. In CrB-type phases, these planes run parallel to each other, while, in FeB-type phases, these planes are tilted in different directions. The coordination around the chain and the different packings together with the tetrahedral voids are shown in Scheme 4.1.

4.2 Examples of CrB- and FeB-structure type Zintl phases

There is a rich diversity of CrB- and FeB-structure type Zintl phase. They can be electron-precise according to the Zintl concept, formally metallic Zintl phases as defined in Sec. 2.2 or even lack electrons. The main feature of these phases (in respect to the Zintl concept) is the formation of $\frac{1}{\infty}[\text{X}^{x-}]$ zigzag chains. Therefore, these phases are supposed to be isoelectronic to group 16 elements with $\text{VEC}(\text{X}) = 6$ and $b(\text{XX}) = 2$.

There are binary examples (MX) for at least three types of phases:

- (i) formally valence compounds:
 $\text{Ae}^{2+}\text{Tt}^{2-}$ and $\text{Ln}^{3+}\text{Ga}^{3-}$ (CrB-structure type)
- (ii) phases with one electron in excess:
 $\text{Ln}^{3+}\text{Tt}^{2-}\text{e}^-$ (CrB- and FeB-structure type)

- (iii) an electron deficient phase:
 CaGa (CrB-structure type)
 (Ae = alkaline earth metal, Ln = lanthanoid, Tt = tetrel)

In fact, even the formally electron-precise phases of these systems show poor metallic conductivity and no band gaps. The chain structure can be described by a simple (local) scheme using a molecular orbital (MO)-diagram (Scheme 4.2). Due to $M(d)$ - $X(p)$ interactions, the π^* -bands are partially depopulated causing the metallic conductivity. This effect has been shown for CaSi by density functional theory (DFT) calculations as well as an experimental charge density determination [72]. A DFT Si- p_x fatband representation, which represents the π -band is given in Scheme 4.2. Bonding and antibonding contributions were calculated qualitatively according to the crystal orbital hamilton population [189] and are shown for reference. Such interactions were also calculated for SrSi and BaSi and lead e.g. to Pauli-paramagnetism in these phases [69, 70, 118] or for LaGa [73]. The formal metallic Zintl phases $LnTt$ show an excess electron that can be mainly attributed to Ln -d bands as shown by DFT calculations for ht-LaSi (FeB-structure type) and hypothetical CrB-type LaSi [73], [A3]. The electron-deficient phase CaGa shows metallic conductivity and Pauli-paramagnetism as well, which is attributed to “holes” in the π -band (Scheme 4.2) [190]. This phase is considerably contracted in crystallographic a and elongated in chain-direction c . DFT fatband calculations showed that the Ga- p_x states that form the π -band entirely lie above the Fermi level. Instead, there is a σ -like stacking interaction of p_x -states, which explains the shortening in a [71, 191].

4.3 Hydrogen filling tetrahedral voids

As described above, the CrB- and FeB-structure types exhibit tetrahedral M_4 -voids in the cationic partial structure. They can be partially or totally filled by hydrogen. There is one void per formula unit. Thus, phases that incorporate hydrogen only in such sites lead to a chemical formula $MXH_{\leq 1}$. To distinguish them from phases with additional hydrogen site, these phases will be called hydrogen-poor:

Definition 13 (Hydrogen-poor (CrB- or FeB-structure type derived) phases) *Zintl phase hydrides derived from the CrB- or FeB-structure type that contain a maximum of one hydrogen atom per formula unit, usually incorporated in a tetrahedral void of cations (interstitial hydrides).*

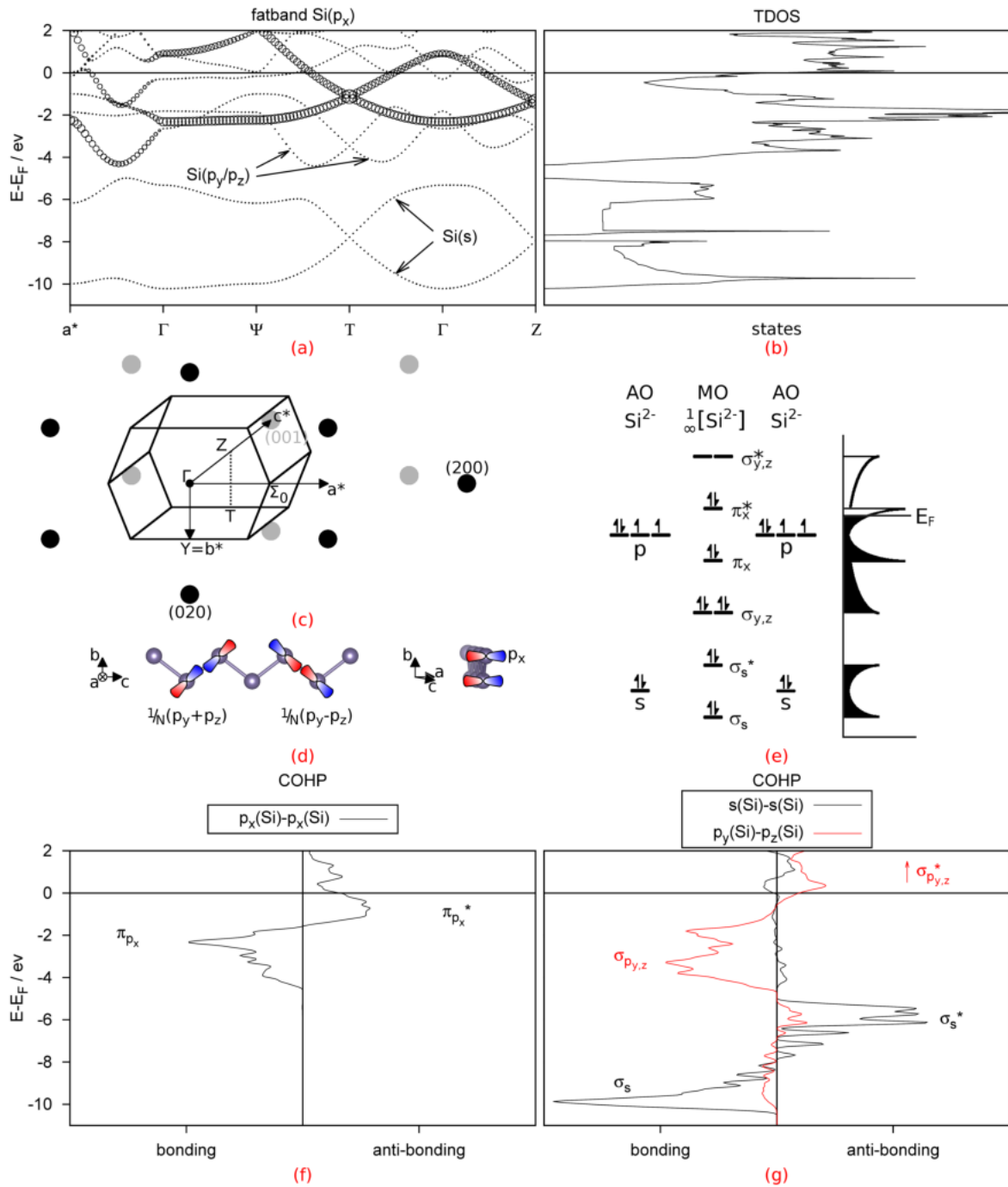
4.3.1 $LnTtH$, $Ln = La, Nd$, $Tt = Si, Ge, Sn$

The hydrogenation of $LnTt$, $Ln = La, Nd$, $Tt = Si, Ge, Sn$, is described in [A3]. The phases LaSi, LaGe and NdSi crystallize in FeB-, LaSn and NdGe in CrB-structure type. These phases can be characterised as formally metallic Zintl compounds, since they exhibit an excess electron and can be formulated as $Ln^{3+} Tt^{2-} e^-$. According to density functional theory (DFT) calculations the additional electron can be attributed to Ln -d-states [71], [A3]. This effect will be regarded as d-metallicity. Furthermore these systems show Ln -d- Tt -p interaction that leads to a depopulation of Tt - π^* -states as explained above (cf. CaSi, Scheme 4.2). This second effect will be called π -metallicity.

The hydrogenation of LaSi was described before. A hydrogenation at low temperatures leads to a phase with low hydrogen content keeping the structure of the parent phase and is denoted as solubility of hydrogen in the lattice [192, 193]. Furthermore they describe the formation of a phase LaSiH but could not determined the crystal structure. We could reproduce the diffraction pattern presented by *Henneberg* [193] qualitatively. It can be described as a two phase system of a FeB-type as well as a CrB-type hydride. The same effect was observed for the remaining FeB-type phases. The FeB-derived hydrides are always the minor fraction of the sample. The CrB-type Zintl phases show only one hydrogenation product keeping the structure type.

Hydrogen sites and their occupations were determined using neutron powder diffraction data. Both structure types show a filling of tetrahedral Ln_4 -voids. Thus, the CrB-structure type derived hydrides $LnTtH$ crystallize in ZrNiH-structure in space group type $Cmcm$ ²¹. Filled FeB-structure types (space group type $Pnma$) are less numerous and an isotypic representative was not found. Thus, these phases will

²¹ ZrNiH was originally predicted as a stuffed CrB-structure type [194]. Neutron powder diffraction data showed a triclinic distortion with metrical angles near to 90°[195]. The ICSD database regards the structure type as space group type $Cmcm$ and thus, the structure type name was adopted in [A3].



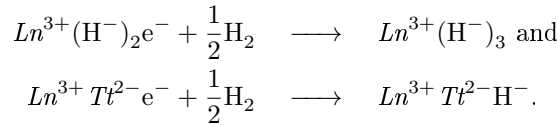
Scheme 4.2: Qualitative electronic structure of CaSi calculated using *Abinit* [162, 166] and *LOBSTER* [187, 188]. **(a)** Fatband structure emphasizing the partially occupied π^* -band and **(b)** corresponding total density of states (TDOS). **(c)** First Brillouin zone and reciprocal lattice (hk0 in black, hk1 in grey). **(d)** Polyanionic ${}^1_\infty[\text{Si}^{2-}]$ -chain showing possible orbital overlap and **(e)** translation in a (local) molecular orbital (MO)-scheme. The transfer into a qualitative density of states is given, indicating the partially depopulated π^* -band again. **(f,g)** Crystal orbital Hamilton populations (COHP) showing bonding and antibonding states as expected from the MO-scheme.

Table 4.1: Tt - Tt bond lengths ($Tt = \text{Si, Ge, Sn}$) within the zigzag chains of $\text{La}Tt$ and $\text{Nd}Tt$ and their corresponding hydrides.

precursor	$d(Tt-Tt)$ /pm	hydride	$d(Tt-Tt)$ /pm
FeB-structure type precursor			
LaSi	251.7(4)	C -LaSiD _{0.92(1)}	242.6(9)
NdSi	259.7(5)	P -NdSiD _{0.88(6)}	245(4)
		C -NdSiD	231.4(8)
LaGe	266.73(9)	P -LaGeD _{0.96(4)}	245.4(10)
		C -LaGeD _{0.88(1)}	257.7(4)
CrB-structure type precursor			
NdGe	268.5(5)	NdGeD _{0.95(1)}	250.2(5)
LaSn	299.13(7)	LaSnH _x	283.19(9)
DFT structure optimisation			
LaSi (FeB)	251.8	P -LaSiH	245.1
LaSi (CrB)	251.4	C -LaSiH	242.7

be called LaGeH-structure type. For simplicity the phases are referred to as C - and P -phase, respectively. Crystal structures (Fig. 4.2 (a) and (b)) data are deposited²².

Metrical ratios change upon hydrogenation to allow more regular Ln_4 -tetrahedra. The volume hardly increases. Such an effect or even a negative volume effect upon hydrogenation can be seen from a metal to salt or semiconductor transition as observed e.g. for Na/NaH or LnH_2/LnH_3 ($Ln = \text{lanthanoid}$) [196]. Especially the latter case resembles the electronic situation of our systems:



The hydrogenation of FeB-type Zintl phases always leads to a mixture of P - and C -phase hydride. DFT calculations of both types of LaSiH shows a 47 meV lower total energy for the latter one which is the main fraction of the reaction. Considering the results of *Henneberg* [193] it is most likely that at first the FeB-type Zintl phase takes up hydrogen. Subsequently a phase transition into the ZrNiH-structure type occurs which needs a high activation energy. Due to experimental limitation a complete formation of the C -phase was not observed, yet.

The electronic structure changes upon hydrogenation were studied by DFT calculations of the LaSi-H system. The parent phase shows La-d-state dominated metallic behaviour as well as partially depopulated Si- π^* -states. The formation of an anionic hydride leads to a reduction of d-metallicity as main effect. Still the π^* -states are lifted in regard to the Fermi edge increasing the bond order. This can be seen experimentally by a shortening of the Tt - Tt -bond lengths of all systems (Tab. 4.1). Thus, the hydrogenation of $LnTt$ can be described as a transition from a metallic to electron precise Zintl phase. A similar situation was described for the Ae_5Pn_3/Ae_5Pn_3H -systems (cf. Sec. 2.3.1).

4.3.2 α - and β - $AeTtH_y$, $AeTt = \text{SrGe, BaGe, BaSn}$, $y < 1$

In situ neutron diffraction experiments of SrGe [A4], [A5] and BaTt ($Tt = \text{Ge, Sn}$) [A6] showed several intermediate phases with a hydrogen content corresponding to $AeTtH_y$, $y < 1$. There are two types of compounds present, denoted as α -phases that incorporate up to 0.35 hydrogen atoms per formula unit and β -phases with an intermediate hydrogen content of about 0.5 to 0.75 hydrogen atoms (Fig. 4.3). Structures were determined from *in situ* neutron diffraction data²³.

²² Further details on the crystal structure investigations may be obtained from the Fachinformationszentrum Karlsruhe, 76344 Eggenstein-Leopoldshafen, Germany (fax: (+49) 7247-808-666; e-mail: crysdata@fiz-karlsruhe.de), on quoting the depository numbers CSD-434191 (C -LaGeD_{0.87}), CSD-434192 (P -LaGeD_{0.96}), CSD-434193 (C -LaSiD_{0.92}), CSD-434194 (C -LaSnH_x), CSD-434195 (C -NdGeD_{0.95}), CSD-434196 (C -NdSiD), CSD-434197 (P -NdSiD_{0.88}).

²³ Further details on the crystal structure investigations may be obtained from the Fachinformationszentrum Karlsruhe, 76344 Eggenstein-Leopoldshafen, Germany (fax: (+49) 7247-808-666; e-mail: crysdata@fiz-karlsruhe.de), on quoting the depository numbers CSD-432668 (α -SrGeD_{0.20}), CSD-432669 (β -SrGeD_{0.53}), CSD-433794 (α -BaGeD_{0.09}), CSD-433795

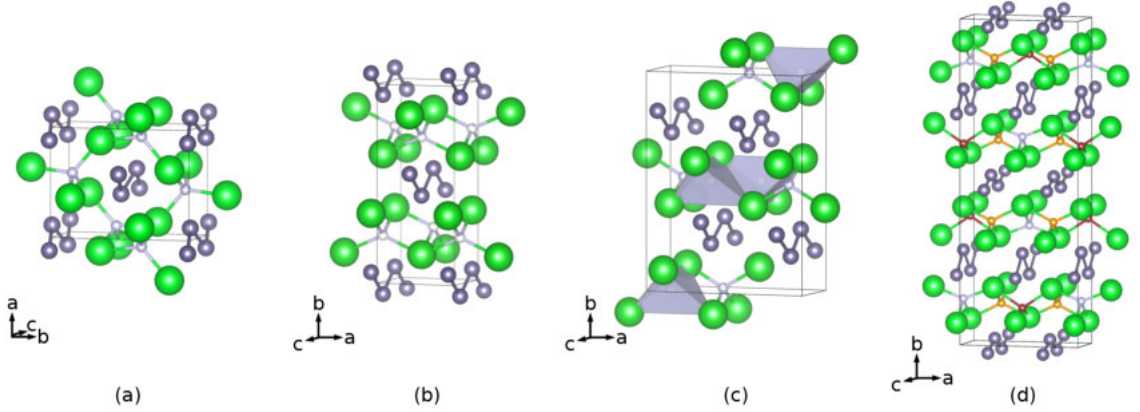


Figure 4.2: Crystal structures of hydrogen-poor phases $MXH_{\leq 1}$. (a) P - $LnTtH$, $Ln = \text{La, Nd}$, $Tt = \text{Si, Ge, Sn}$ in LaGeH-structure type ($Pnma$); (b) C - $LnTtH$ in ZrNiH-structure type ($Cmcm$) and isotypic α - $AeTtH_y$, $y < 0.4$, $Ae = \text{Sr, Ba}$, $Tt = \text{Ge, Sn}$, with partial hydrogen occupation of tetrahedral Ae_4 -voids; (c) β - $BaGeH_{0.5}$ in $Pbnm$ -setting (No. 62 $Pnma$) with ordered hydrogen sites. The almost (SOF = 0.05(1)) empty tetrahedra are shaded in grey; (d) β - $SrGeH_y$, $0.47 < y < 75$ ($Cmcm$) with partially occupied hydrogen sites. Different sites are marked with different colours. Large green spheres: Ln or Ae ; medium grey spheres: Tt ; small white (yellow or red) spheres: H.

The α -phases show a statistical distribution of hydrogen over all tetrahedral Ae_4 -voids (Fig. 4.2 (b)). The heavy elements resemble the structure of the parent Zintl-phase. Therefore, these phases are isotypic to C - $LnTtH$ as described above. Since the Zintl phases exhibit compressed tetrahedra, the unit cell needs to expand in crystallographic b direction to form more regular voids. The other lattice parameters are hardly effected. In general, lattice parameter c , which runs in chain direction does hardly change for any observed hydrogen content. Therefore, the b/c -ratio is a good measure for the formation of the α -phases (Tab. 4.2).

As described above, the CrB-structure-type Zintl phases are poor metals with partially filled π^* -bands. Incorporation of hydrogen into tetrahedral Ae_4 -voids causes a further oxidation of the anti-bonding states. Thus, the zigzag chains needs to contract. As shown in Tab. 4.2, α -phases shows about 1-2% shorter Tt - Tt distances which is at least three time as large as the combined estimated standard uncertainties (e.s.u.). Furthermore, the shorter lengths correspond to higher measuring temperatures, thus, a temperature effect is unlikely. The ternary CrB-structure-type phase $Na_{0.14}Sr_{0.86}Ge$ [197] has a similar formal electron count per germanium as the α - $AeGeH_y$ phases. The bond length of 260.2 pm (293 K) is comparable to our results with 261.6(6) (α - $BaGeH_{0.13}$, 325 K) and 262.6(3) pm (α - $SrGeH_{0.20}$, 618 K).

The *in situ* experiments described in [A4], [A5] and [A6] show that the α -phases exhibit a large homogeneity range (Fig. 4.3). Upon heating under primary vacuum or even under up to 5 MPa hydrogen pressure, hydride can be removed from the tetrahedral voids. However, a total dehydrogenation was not observed. Only α - $BaGeH_y$ was heated under vacuum during an *in situ* neutron diffraction experiment. The lowest hydrogen content ($y = 0.09$) was reached after 30 min heating at 502(2) K. Higher temperatures were not realised but might lead the a further dehydrogenation.

From *in situ* diffraction experiments an additional phase in the $SrGe$ - H_2 [A4], [A5] and the $BaGe$ - H_2 system [A6] is known. These phases show superstructures with at least partial hydrogen ordering and were called β -phases [A4], [A6]. In contrast to the α -phases, β - $BaGeH_{0.5}$ appears to be a line phase with fully ordered hydrogen sites. β - $SrGeH_y$ shows a considerable phase width with $0.47(8) \leq y \leq 0.75(8)$. Both phases correspond to different structure types and therefore, need different hydrogen ordering schemes.

β - $BaGeH_{0.5}$ shows a low-angle reflection that corresponds to a twofold superstructure in crystallographic a direction (Fig. 4.2 (c)). Rietveld refinement of a structure model in spacegroup type $Pbnm$ (No. 62, $Pnma$) leads to two possible $4c$ hydrogen sites in tetrahedral voids that are occupied (92.5(13)%) and empty (5.0(10)%), respectively (Fig. 4.2). Due to an increased π -bonding within the zigzag chain,

(α - $BaGeD_{0.13}$), CSD-433797 (β - $BaGeD_{0.49}$), CSD-433796 (α - $BaSnD_{0.19}$),

The crystal structures are also deposited in the Crystallography Open Database (COD) by the following depository numbers: COD-ID 4345256 (α - $SrGeD_{0.20}$), COD-ID 4345049 (β - $SrGeD_{0.53}$),

Table 4.2: Lattice parameters and Tt - Tt bond lengths ($Tt = \text{Si, Ge, Sn}$) of the pristine Zintl phases and the α - and β -hydrides. SG = space group: $C = Cmc21$; $C2 = Cmc21$ ($a' = 2a$, $b' = 2b$), $P = Pbnm$ ($a' = 2a$; standard setting $Pnma$). Unit cells are given in regard to the hydrogen free phases.

phase	Ref	SG	T / K	a / pm	b / pm	c / pm	b/c	$d(Tt-Tt)$ / pm
SrGe	[A5] ^a	C	298(1)	482.58(2)	1138.26(4)	417.41(2)	2.73	265.0(2)
α -SrGeH _{0.204(4)}	[A4]	C	618(2)	476.59(5)	1182.80(14)	415.42(5)	2.85	262.6(3)
β -SrGeH _{0.53(4)}	[A4]	$C2$	538(2)	$a'/2 =$ 466.84(10)	$b'/2 =$ 1250.1(3)	411.64(8)	$b'/(2c) =$ 3.04	228.0(11)- 271(3)
BaGe	[A6]	C	298(2)	506.58(2)	1195.5(2)	430.27(2)	2.78	267.6(4)
BaGe	[A6]	C	502(2)	507.50(4)	1206.0(2)	431.65(4)	2.79	269.5(4)
α -BaGeH _{0.131(5)}	[A6]	C	325(6)	503.09(3)	1221.5(2)	427.38(4)	2.86	261.6(6)
α -BaGeH _{0.095(7)}	[A6]	C	502(2)	505.66(4)	1218.0(2)	429.85(4)	2.83	266.5(6)
β -BaGeH _{0.488(11)}	[A6]	P	502(2)	$a'/2 =$ 495.77(4)	1319.5(2)	421.46(2)	3.13	257.1(7)
BaSn	[A6]	C	298(2)	532.79(5)	1251.10(10)	465.89(4)	2.69	301.0(5)
α -BaSnH _{0.188(4)}	[A6]	C	478(5)	522.72(6)	1293.6(2)	463.97(6)	2.79	294.0(3)

^a Not given in the publication; extracted from rawdata used for the production of this article.

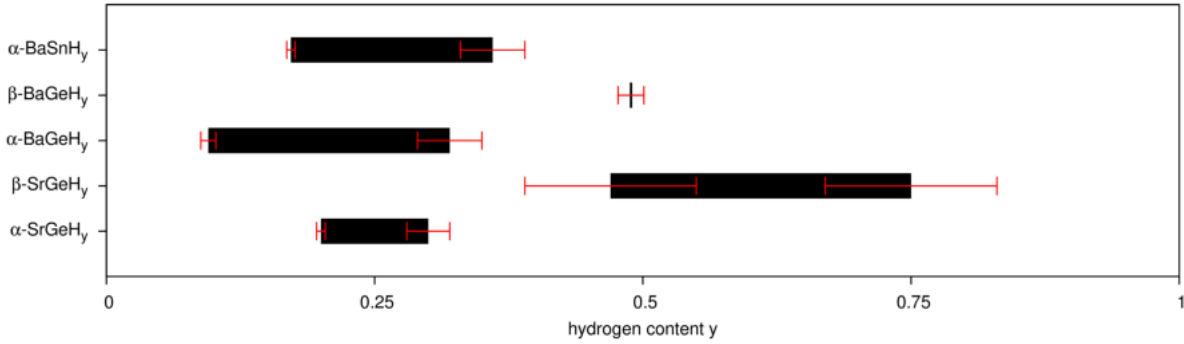
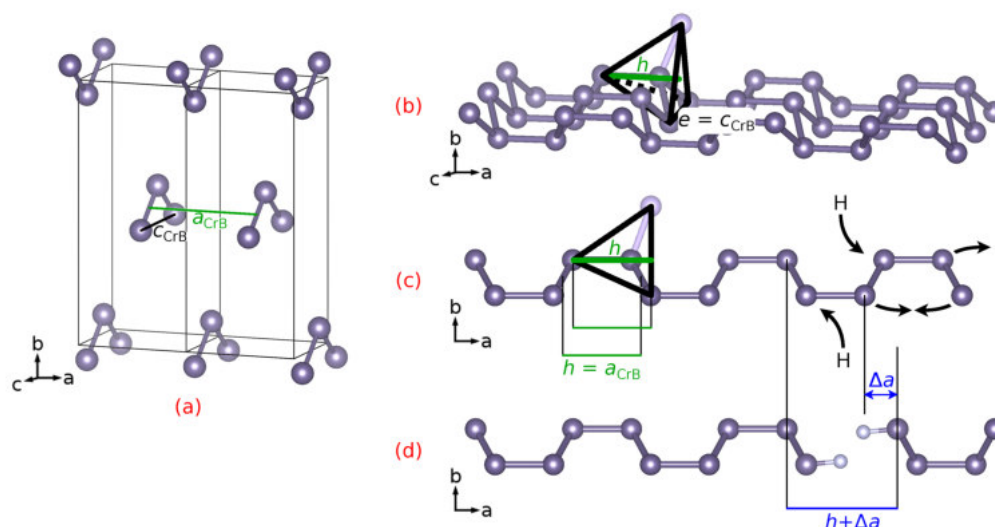


Figure 4.3: Hydrogen content of the α -phases and β -phases, as obtained according to [A4], [A5] (SrGeH_y) and [A6] (BaGeH_y, BaSnH_y).

the Ge-Ge distance is considerably shortened with 257.1(7) pm (502 K) compared to the hydrogen-free Zintl phase (269.5(4) pm, 502 K). The interstitial hydride Li₄Ge₂H [86, 87] has the same formal electron count per germanium (Ge^{1.5-}) as β -BaGeH_{0.5}. Its chain-bond length (253 pm) shows a value that fits our observation.

β -SrGeH_y shows a low-angle reflection that corresponds to a 2x2-superstructure in crystallographic a and b direction (Fig. 4.2 (d)). A structure model in $Cmc21$ ($a' = 2a$, $b' = 2b$, $c' = c$) was proposed that allows hydrogen ordering on two $4c$ (24(4)% and 65(4)%) and one $8g$ (61(3)%) site. A total ordering seems not probable due to the large homogeneity range (Fig. 4.3) as seen by the strong change in lattice parameters during the *in situ* experiment [A4]. There might be an ordered model that is overlain by another disordered phase. Thus, the proposed model is considered preliminary and bond lengths need to be considered cautiously. There is a large (271(3) pm) and a short (228.0(11)) Ge-Ge distance. Due to data quality, these values are not interpreted any deeper here.

The electronic situation of α - and β -phases lies between $AeTt$ that already show π^* -depopulation and CaGa that does not show π -interaction any longer, but σ -bonding perpendicular to the chain (see Sec. 4.4.6). This is reflected by an inverted a/c -ratio smaller than unity [71, 191]. A similar situation was experimentally investigated for the solid solution CaSi-CaGa and CaSn-CaGa. On the Ca Tt side, significant amounts of tetrel can be substituted by gallium up to CaSi_{0.4}Ga_{0.6} and CaSn_{0.6}Ga_{0.4}, respectively [71, 191]. Due to the change of the covalent radius going from Tt to Ga, it was difficult to discuss the shortening of the bonds within the zigzag chain unambiguously. Using the hydride systems, changing atomic sizes do not play a role any longer. Thus, the shortening can be confirmed. According to a/c -ratios, which are larger than unity, our systems are still characterised by π -bonding interaction.



Scheme 4.3: Polyanionic chains (grey spheres) of the CrB-structure type (a) related to a hypothetical condensation to form a net of six-membered rings in boat-configuration (b/c). This leads to an ideal $a_{\text{CrB}}/c_{\text{CrB}}$ -ratio of 0.816 which is derived from a hypothetical tetrahedron as depicted in light grey. The corresponding edges are drawn in black. The ideal ratio corresponds to height (h) and edge (e) of a tetrahedron, i.e. $a_{\text{CrB}}/c_{\text{CrB}} = h/e = \sqrt{6}/3$. Incorporating hydrogen (white spheres) between the chain (c/d), i.e. a truncation of the hypothetical 2D-net, increases a and thus the a/c -ratio.

4.3.3 Geometrical restrictions for hypothetical $AeTtH_1$ -phases, $Ae = \text{Ca, Sr, Ba}$, $Tt = \text{Si, Ge, Sn}$

The hypothetical phases $AeTtH_1$ were not observed, yet. These phases could still be present as a filled CrB-structure type as observed for α - $AeTtH_y$ -phases. The electron count of a Tt^- then formally corresponds to a total depopulation of the π^* -band and, thus, to a double-bonded chain. Covalent interaction between Tt -p- and Ae -d- states renders this scenario unlikely. CaGa realises such an electron count, but π -bonding is abandoned for a σ -like stacking interaction. The a/c -ratio is smaller than unity and, thus, inverted compared to the $AeTt$ -systems.

A third binding mode according to the Zintl-concepts seems more intuitive: Tt^- would be supposed to act as a pseudo-pentel and to form three single bonds. Considering the geometry of the hydrogen free phases, the parallel zigzag chains need to incline towards each other forming an additional bond. This scenario leads to a two-dimensional layer of condensed six-rings in boat configuration (Scheme 4.3). Such a structure motif is known from the boron partial structure of RuB_2 [198–200]. An idealised structure needs an a/c -ratio of 0.816. As a comparison, CaGa only reaches 0.956. On the contrary, the hydride-filled cationic partial structure requires an a/c -ratio of exactly one to provide proper tetrahedral voids. This conflict can be solved by a truncation of the two-dimensional polyanionic layer in crystallographic a direction by hydrogen as described for the formation polyanionic hydrides (Scheme 4.3 (d)). Since σ -bonding along crystallographic a direction seems to become more important than π -bonding for Tt^- , the hypothetical $AeTtH_1$ phases directly convert to the hydrogen-rich phases described below (Sec. 4.4).

4.4 Hydrogen bound to polyanions

In addition to the interstitial hydride phases that were described above there are several phases $AeTtH_y$ ($Ae = \text{alkaline earth metal}$, $Tt = \text{tetrel}$) or $LnGaH_y$ ($Ln = \text{lanthanoid}$) with a hydrogen content $y > 1$. These phases will be referred to as hydrogen-rich phases:

Definition 14 (Hydrogen-rich (CrB-/FeB-structure type derived) phases) *Zintl phase hydrides derived from the CrB- (or FeB-) structure type that contain more than one hydrogen atom per formula*

unit, typically contained in a tetrahedral void of cations (interstitial hydride) as well as bound to the polyanion (polyanionic hydride).

In the case of $AeTtH_y$, the hydrogen-rich phases are also called γ -phases. This term was introduced in the works on *in situ* diffraction [A4], [A6]. There are additional hydrogen sites next to the polyanionic zigzag chain that may or may not form a covalent bond to the chain. In the $AeTt-H_2$ system there are at least three distinct structure types occurring that can be described by the Zintl-concept. [A1] and [A2] deal with this topic. Furthermore, non-published solid-state nuclear magnetic resonance (SSNMR) and density functional theory (DFT) data substantiate the covalent character of the bond between polyanion and hydrogen. There is a set of phases in the $LnGa-H_2$ system that show a non-classical bonding situation [114, 115]. The *in situ* work [U1] deals with the hydrogenation of NdGa as one example of this compound class.

4.4.1 $CaSiH_y$ - a starting point

The hydrogenation of CaSi leads to the formation of hydrogen-rich $CaSiH_{\approx 1-1.33}$ (Fig. 4.4), which was originally described by the *Toyota-Central R&D Labs* as a possible hydrogen storage material [144–146]. Several structure descriptions followed, i.e. [97, 116–119, 150]. Details of the crystal structure are still unclear, especially the position of hydrogen atoms that coordinate the polyanionic chain and the structure of the polyanionic backbone are contradictory in these works. Therefore, the Si-H bond length is ambiguous. The models known by literature are isopointal but show different hydrogen content reaching from $CaSiH_{1.06}$ [118, 119] to $CaSiH_{1.3}$ [116] and have slightly different unit cell parameters which indicates at least a phase width for this compound. In general, it crystallizes in space group type $Pbnm$ (No. 62, $Pnma$). The structure shows a three-fold superstructure along crystallographic a direction regarding the parent Zintl phase. Hydride anions fully occupy tetrahedral Ca_4 -voids which leads to one hydrogen atom per formula unit as a common feature for the whole homologue series (see below). This leads to an hypothetical intermediate $CaSiH_1$ as discussed in Sec. 4.3.3. Due to the superstructure, there are three ${}^{\infty}[\text{Si}^-]$ -zigzag chains per polyanionic layer in one unit cell. They are inclined to each other forming additional Si-Si bonds. Therefore, the formally Si^- -ions become three-binding as expected from the Zintl-concept, but some of the silicon atoms have only two silicon neighbours and thus, are undersaturated. This is compensated by additional hydrogen atoms next to these atoms and corresponds to the truncation in crystallographic a direction discussed before (see Sec. 4.3.3, Scheme 4.3 or Fig. 4.4). The chain coordinating hydrogen site (sometimes referred to as chain position) is not fully occupied. This leads to the different compositions determined. Since the two-dimensional layer is terminated after three chains, the maximum hydrogen content allowed for this structure type leads to the chemical formula $CaSiH_{4/3}$.

The main discrepancy between the different works regards the description of the additional hydrogen site either as binding to the polyanion ($d(\text{Si-H}) = 158$ pm [116]) which is supported by DFT calculations and synchrotron diffraction or as being coordinated in a $Ca_3\text{Si}$ -void without covalent interaction ($d(\text{Si-H}) = 182$ pm [117]) which was refined from neutron diffraction data. Unfortunately, both referenced works shows some inconsistencies. While *Ohba et al.* [116] describe a proper DFT model, they lack to show their experimental synchrotron diffraction data and even do not clarify whether they did powder or single crystal diffraction (from context it seems to be powder diffraction). They reference an unpublished work as *Noritake et al.* for synchrotron data which is untraceable. On the other side, *Wu et al.* [117] conducted neutron powder diffraction (NPD) and vibrational spectroscopy where in the first case, they did not show a series of excluded data points and in the latter case, the result is not unambiguous. The other works lack to determine hydrogen positions [118, 119], or applied *in situ* neutron diffraction that did not reach a phase-pure product [97]. A single crystal determination of poor quality was done. Since the diffraction frames showed strongly developed powder rings, no detailed refinement was possible [118]. Laue diffraction patterns collected in our group led to the same result [150]. Thus, single crystal diffraction is no practical technique for these systems.

Although the true structure of $CaSiH_y$ is still elusive, there are some indications that *Ohba et al.* properly described the structure as will be seen later. Therefore, this work (as most of the published articles within this work do as well) will refer to the $CaSiH_{1.3}$ -structure type.

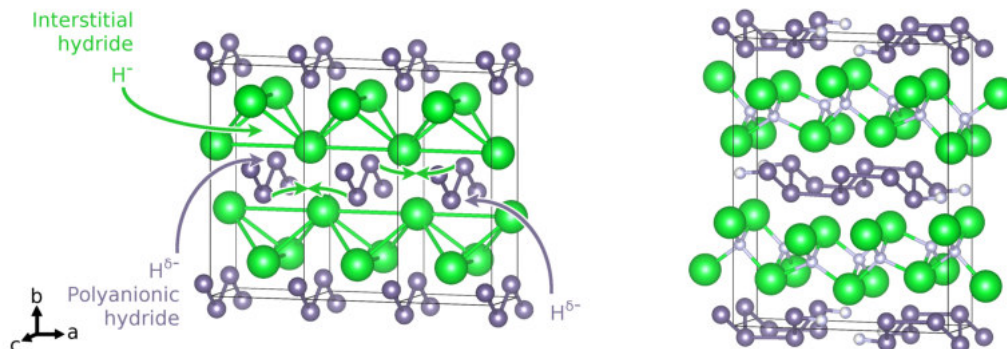


Figure 4.4: The hydrogenation of CaSi (**left**) leads to the formation of CaSiH_y (**right**), $1.06 < y < 1.3$, *Pbnm*-setting (No. 62, *Pnma*). The incorporation of an interstitial hydride leads to an increased connectivity within the polyanion (green arrows). Furthermore a polyanionic hydride partial structure is formed (grey arrows). The chain coordinating hydrogen site is underoccupied leading to a variable hydrogen content. Large green spheres: Ca; medium grey spheres: Si, small white spheres: H.

4.4.2 *AeTtH_y* - structure types, *Ae* = Ca, Sr, Ba, *Tt* = Si, Ge, Sn, $1 < y < 2$

The hydrogenation of SrSi, BaSi and EuSi leads to products that were initially described as SrSiH_{1.6}, BaSiH_{3.4} and EuSiH_{1.8} [118, 119]. From X-ray powder diffraction (XRPD) patterns the heavy metal partial structures were assumed to be isostructural to the CaSiH_{1.3}-structure type even though this structure type allows a maximal hydrogen content of *AeTtH*_{4/3}. NPD data could show that the structures deviate from the CaSiH_{1.3}-model but no proper structure was described [97].

Thus, the hydrogenation of *AeTt* Zintl phases of the heavier tetrel elements germanium, tin and lead was investigated and is presented in [A1], [A2]. While the homologue series could be extended to SrGeH_y, BaGeH_y and BaSnH_y, the phases SrPb and BaPb tend to decompose into SrPb₃ and SrH₂ or Ba₃Pb₅ and BaH₂, respectively. In addition, the reactivity of CaGe was tested but did not show any changes as investigated by *ex situ* XRPD. This confirmed earlier hydrogenation attempts of this compound [118].

The structures of SrSiH_y [A2], BaSiH_y [A1]/[A2], SrGeH_y [A1], BaGeH_y [A2] and BaSnH_y [A1] were determined²⁴. They crystallize in three distinct structure types that allow different hydrogen contents. With increasing radius of the alkaline earth metal the polyanion is stretched. Thus, the ideal *a/c*-ratio for condensed boat-like six-membered rings cannot be fulfilled and the polyanion is truncated by hydrogen in crystallographic *a* direction (see Sec. 4.3.3). This leads to a termination

- (i) after three chains (CaSiH_{1.3}-structure type),
- (ii) alternating after one or two chains (SrSiH_{5/3-x}-structure type) or
- (iii) after every chain (BaSiH_{2-x}-structure type)

as shown in Fig. 4.5. These phases show a non-stoichiometry due to partially occupied hydrogen positions at the polyanions. This leads to a hydrogen content of $n/3$ ($n = 4, 5, 6$) per formula unit reduced by x with $x \ll 1$ as indicated by the chemical formula. Thus, these phases will be denoted as *AeTtH* _{$n/3-x$} or as hydrogen-rich *AeTtH_y* (γ -phases). The increasing hydrogen content can be seen from the *a/c*-ratio (Tab. 4.3). Due to the hydrogen incorporation at the polyanion, the ratio is about unity which allows the formation of more regular tetrahedral voids than in the hydrogen-free phases.

²⁴ Further details on the crystal structure investigations may be obtained from the Fachinformationszentrum Karlsruhe, 76344 Eggenstein-Leopoldshafen, Germany (fax: (+49) 7247-808-666; e-mail: crysdata@fiz-karlsruhe.de), on quoting the depository numbers CSD-432665 (γ -SrGeD_{1.20}), CSD-432666 (BaSiD_{1.89}), CSD-432667 (γ -BaSnD_{1.28}), CSD-433047 (γ -BaGeD_{1.56}) and CSD-433048 (SrSiD_{1.49}).

The crystal structures are also deposited in the Crystallography Open Database (COD) by the following depository numbers: COD-ID 4345254 (γ -SrGeD_{1.20}), COD-ID 4345054 (BaSiD_{1.89}), COD-ID 4345255 (γ -BaSnD_{1.28}), COD-ID 1547274 (γ -BaGeD_{1.56}) and COD-ID 1547275 (SrSiD_{1.49}).

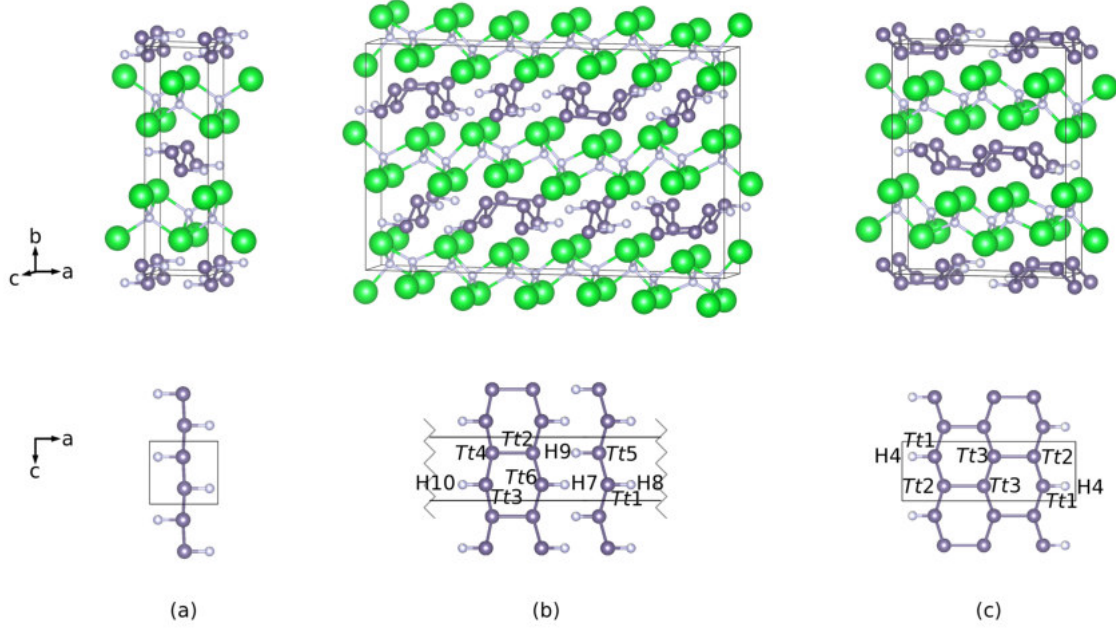


Figure 4.5: Crystal structures of (a) BaSiH_{2-x} , (b) $\text{AeTtH}_{5/3-x}$ ($\text{AeTt} = \text{SrSi}, \text{BaGe}$), and (c) $\text{AeTtH}_{4/3-x}$ ($\text{AeTt} = \text{CaSi}, \text{SrGe}, \text{BaSn}$) regarding $Pbnm$ -setting (No. 62, $Pnma$). Additionally the polyanions are shown and labelled. Large green spheres: Ca, Sr or Ba; medium grey spheres: Si, Ge or Sn; small white spheres: H.

Table 4.3: Structure type and a/c -ratio matrix of the γ - AeTtH_y , $1 < y < 2$ system. The ratio is given regarding space group type $Pbnm$. The limiting composition is given as a classification. The y -value corresponds to the hydrogen content of the chemical formula AeTtH_y .

	Si		Ge		Sn	
	expx.	DFT	expx.	DFT	expx.	DFT
Ca	$\text{AeTtH}_{4/3}$ [116]					
	$y = 1.3$ $a/c = 0.980$	$y = 4/3$ $a/c = 0.962$				
Sr	$\text{AeTtH}_{5/3}$ [A2]		$\text{AeTtH}_{4/3}$ [A1]			
	$y = 1.49$ $a/c = 1.040$	$y = 5/3$ $a/c = 0.989$	$y = 1.20$ $a/c = 0.978$	$y = 4/3$ $a/c = 0.958$		
Ba	AeTtH_2 [A1]		$\text{AeTtH}_{5/3}$ [A2]		$\text{AeTtH}_{4/3}$ [A1]	
	$y = 1.89$ $a/c = 1.087$	$y = 6/3$ $a/c = 1.069$	$y = 1.56$ $a/c = 1.019$	$y = 5/3$ $a/c = 1.006$	$y = 1.28$ $a/c = 0.945$	$y = 4/3$ $a/c = 0.937$

The $\text{CaSiH}_{1.3}$ -structure type family - γ - SrGeH_y and γ - BaSnH_y : γ - SrGeH_y and γ - BaSnH_y crystallize in the $\text{CaSiH}_{1.3}$ -structure type as originally described by *Ohba et al.* [116] (Fig. 4.5 (c)). Rietveld refinement applying this model to NPD patterns of deuterated samples gave a composition of $\text{SrGeD}_{1.19}$ and $\text{BaSnD}_{1.28}$ [A1]. Due to the three connected *Tt*-chains that are saturated by hydrogen and filled tetrahedral voids, the structure allows a maximal hydrogen content of $\text{AeTtH}_{4/3} \approx \text{AeTtH}_{1.33}$. The reduced hydrogen content is a result of an under-occupation of the *Tt*-binding site as reported for CaSiH_y [116, 117] as well. The *in situ* work [A4] regarding the hydrogenation of SrGe clearly showed that the γ -phase shows a variable hydrogen content. In contrast, the *in situ* work [A6] on the hydrogenation of BaSn suggests no homogeneity range for the γ -phase. Tetrahedral voids are completely filled within 3 estimated standard uncertainties (e.s.u.) with hydrogen. The Ge-D distance is 151.7(3) pm and the Sn-D distance is 185.8(8) pm as determined by Rietveld refinement of the crystal structure. Compared to molecular compounds GeH_4 ($d = 151.7$ pm at 5 K [201]) and SnH_4 ($d = 170.6$ pm at 5 K [201]), covalent bonding can be assumed here. Thus, the description of *Ohba et al.*[116] is supported, while it contradicts the findings of *Wu et al.*[117]. A detailed discussion of bonds is given below including all structure types. DFT density of states (DOS) calculations of the idealized compounds $\text{SrGeH}_{4/3}$ and $\text{BaSnH}_{4/3}$ show small band gaps of about 10 meV. This fits the findings regarding $\text{CaSiH}_{4/3}$ [116].

The BaSiH_{2-x} -structure type: The determination of the BaSiH_y structure was done evaluating synchrotron powder diffraction (SPD) and NPD data [A1]. In contrast to the assumptions by the literature [97, 118, 119], diffraction patterns show no hint of any superstructure regarding the parent Zintl phase BaSi. Thus, indexation could be done in the orthorhombic crystal system with contracted *a* and strongly elongated *b* lattice parameter, while *c* is hardly affected. The symmetry needed to be lowered to *Pbnm* (*Pnma*, No. 62) to describe all reflections (see Part II, Fig. A1.2 (top), p. 73). The crystal structure shows a new structure type with similarities to the $\text{CaSiH}_{1.3}$ -structure (Fig. 4.5). Tetrahedral voids are filled but show a site occupation factor (SOF) of 95%. Since there is no superstructure, no additional Si-Si bonds can be formed as expected from three-binding $\text{Si}^{\approx 1-}$. Hydrogen saturation of the chain satisfies the demand of an additional bond and leads to the formation of $\frac{1}{\infty}[\text{SiH}^-]$ -zigzag single-chains. This hydrogen site is under-occupied as well (SOF = 91%) leading to the composition $\text{BaSiH}_{1.87}$, while the structure type would support a hydrogen content corresponding to BaSiH_2 . Carrier hot-gas extraction gave a hydrogen content of 1.83 mol-% per formula unit BaSi and, thus, supports the refinement. These values are much lower than the proposed one ($\text{BaSiH}_{3.4}$ [118, 119]). Since lattice parameters do not deviate much this indicates that in our work the same compound was formed²⁵. The refined Si-H distance is 164.1(5) pm. Molecular $\text{Si}_2\text{H}_{6(g)}$ (200 K) shows a shorter bond length with 149 pm [202]. The SiH_3^- units in KSiH_3 have an elongated Si-H distance with 152-155 pm [127, 203] but still do not reach the refined value. Nevertheless, it is much nearer to the determination of *Ohba et al.* [116] and was interpreted as covalent interaction. A detailed discussion of the bonds is given below in the context of all three structure types and additional measurements. According to a DFT calculation of an idealised BaSiH_2 , this compound shows no band gap [A1].

The $\text{SrSiH}_{5/3-x}$ -structure type family - SrSiH_y , γ - BaGeH_y and another BaSiH_y : The third structure type of the homologue series corresponds to an intermediate hydrogen content according to $\text{AeTtH}_{5/3}$ realised by $\text{SrSiH}_{1.49}$ and $\text{BaGeH}_{1.56}$ [A2]. The samples show a pronounced non-stoichiometry again. *In situ* NPD monitoring the hydrogenation of BaGe suggests no variable hydrogen content for the γ -phase [A6]. The structure is related to the structure types described previously. One hydrogen atom per formula unit corresponds to occupied tetrahedral Ae_4 -voids leaving $2/3$ hydrogen atoms to saturate the chains. XRPD as well as NPD show a threefold superstructure regarding the parent Zintl phase. Structure determination led to a model with two partially occupied hydrogen sites that exclude each other due to an unreasonably short H-H distance. Furthermore, the model did not lead to additional chain-connecting *Tt-Tt* bonds (for details see Part II, Sec. A2.4: “Averaged crystal structure model in *Cmcm* (threefold superstructure)”). This first model describes XRPD data well, but shows deviations applied to neutron diffraction data.

²⁵ Nevertheless, a BaSiH_4 can be rationalised considering the literature of polyanionic hydrides and related structures. One hydrogen atom per formula unit can be expected to occupy tetrahedral voids. That leaves SiH_3^- . According to the Zintl concept, this needs to be a monomeric anion. A structure candidate is β - CsSiH_3 which crystallizes in a monoclinic subgroup of the CrB-structure type [127]. The hypothetical BaSiH_4 might be a filled variant of these structure. Lattice parameters are expected to change strongly compared to BaSiH_{2-x} .

Selected area electron diffraction (SAED) could be applied to SrSiH_y as well as BaGeH_y and BaSiH_y [A2]. Diffraction patterns of SrSiH_y clearly showed that the superstructure needs to be doubled again leading to the structure shown in Fig. 4.5. The Zintl concept demands three-binding Si^- atoms. A consideration of the sixfold superstructure regarding the parent Zintl phase allowed some educated guesses for possible structure candidates with hydrogen order. DFT structure optimizations on such hydrogen ordered models led to a crystal structure in space group type $Pbnm$ (No. 62, $Cmcm$). Two out of three chains are inclined to each other, forming an additional covalent bond. The remaining Tt -atoms are hydrogen-saturated, except for the non-stoichiometry. The structure type then shows two types of polyanions:

- (i) Hydrogen saturated single chains ${}^1_{\infty}[\text{TtH}^-]$ as in BaSiH_{2-x} , and
- (ii) Hydrogen saturated double chains ${}^1_{\infty}[\text{H Tt}_2\text{H}^{2-}]$.

Due to the complex model and limited data quality, Ge-H and Si-H bond length cover a wide range with large e.s.u. On average they are 162 pm and 158 pm, respectively. Thus, they are in a covalent range. A detailed discussion is given below. DFT calculation on the idealised compounds $\text{SrSiH}_{5/3}$ and $\text{BaGeH}_{5/3}$ lead to metallic behaviour with a pseudo-band gap at the Fermi level.

Using SAED patterns, a second phase of a BaSiH_y sample (about 10% phase content) could be shown to have the same superstructure and is therefore assumed to be isotypic to this structure model.

4.4.3 AeTtH_y - bond lengths by diffraction and NMR spectroscopy

Rietveld refined bond lengths affected by non-stoichiometry: The compounds described above are non-stoichiometric. Furthermore, $\gamma\text{-SrGeH}_{4/3-x}$ also allows for different hydrogen contents. The chain binding hydrogen site is always underoccupied. Thus, locally, there are two cases for the affected tetrel atom:

- (i) Tt^- is three-binding with two Tt and one H neighbour, or
- (ii) Tt^- is only two-binding coordinated by a void and undersaturated

For a stoichiometric compound only case (i) is relevant. This can easily be simulated by a DFT calculation using an idealised composition. Based on this assumption, the structure relaxations have been performed using *Quantum Espresso*[167, 168]. Lattice parameters were reproduced with a reasonable accuracy better than 2.5%, except for $\text{SrSiH}_{5/3-x}$ where the deviations are smaller than 5%. Distances and DOS regarding the optimised structures and computational details were presented for all examples in [A1] and [A2]. Case (ii) is less clear. Similar to the hydrogen-poor phases (Sec. 4.3.2), π -bonding can compensate the lack of a hydrogen neighbour. Furthermore, an unordered additional connection of Tt -chains might be possible. The absence of a chain-coordinating hydrogen atom needs to have an effect on the Tt -chain. A relaxation towards the void is most likely. These hydrogen voids seem to be statistically distributed over a sample, thus, Rietveld refinement leads to an averaged structure model which influences bond lengths. The effect can be expected to be largest in crystallographic a direction, i.e. perpendicular to the chain. Tt -H bond lengths and chain connecting Tt - Tt bonds might be biased. Comparing Rietveld-refined results with DFT calculations of compounds with idealised composition underlines this effect. Tab. 4.4 lists all Tt - Tt distances. It can be seen that in chain direction, distances fit DFT calculations, while the perpendicular-, chain-connecting distances are systematically longer than calculated. This can be considered to be the result of the averaging due to the non-stoichiometry of the compounds. Still, bond-lengths are all comparable to the pristine Zintl phases ($d(\text{Si-Si}) = 250\text{-}251$ pm [204], [A1]; $d(\text{Ge-Ge}) = 265\text{-}268$ pm [A1], [A6]; $d(\text{Sn-Sn}) = 300\text{-}301$ pm [A1], [A6]). Thus, the formation of a single bond as expected by the Zintl-description can be assumed. In fact, the bonds are systematically shorter than in the hydrogen-free phases, but longer than in the elements (Si: 235 pm, Ge: 245 pm, α -Sn: 281 pm [1]). Thus, the changing atomic/ionic radius affects the covalent bond length as well.

The Tt -H bonds also run perpendicular to the chains. Therefore, bond lengths derived from Rietveld refined crystal structures are affected by the non-stoichiometry effects as well. Proper bond lengths can be established using solid-state nuclear magnetic resonance (SSNMR) as a local probe sensitive to hydrogen and distances as described below.

Table 4.4: Bond lengths of the polyanionic hydrides of $AeTtH_y$ ($Ae = \text{Sr, Ba}$; $Tt = \text{Ge, Sn}$) as determined from the crystal structures derived from Rietveld refinement and DFT structure optimisation. Labels are used according to Fig. 4.5.

phase	in chain direction				perpendicular, chain connecting		
	chain		refined d / pm	DFT d / pm	chain	refined d / pm	DFT d / pm
SrGeH _{4/3-x}	outer	Ge1-Ge2	251.1(5)	255.6	Ge2-Ge3	274.3(6)	269.5
	middle	Ge3-Ge3	254.7(4)	257.7			
BaSnH _{4/3-x}	outer	Sn1-Sn2	289.3(7)	292.2	Sn2-Sn3	308.5(8)	305.2
	middle	Sn3-Sn3	296.5(6)	294.1			
SrSiH _{5/3-x}	double (1)	Si2-Si6	239(3)	242	Si2-Si4	259(5)	244.3
	double (2)	Si3-Si4	239(3)	242			
	single	Si1-Si5	246(3)	248			
BaGeH _{5/3-x}	double (1)	Ge2-Ge6	264(2)	261	Ge2-Ge4	273(3)	268
	double (2)	Ge3-Ge4	255(2)	261			
	single	Ge1-Ge5	255(2)	263			
BaSiH _{2-x}			248.9(10)	248.3			

DFT and SSNMR study - refine the bonding picture: The problems regarding the bond lengths within the polyanionic hydride described above arise from the general property of the Rietveld method being a bulk technique. It averages over local, or more precise, non-periodic effects. SSNMR is a local technique. Using the $^2\text{H}=\text{D}$ nucleus²⁶ as a probe allows the evaluation of the interaction of its quadrupole moment with the electric field gradient (EFG) generated by the surrounding nuclei and the electron density. Furthermore, this is a quantity that can be evaluated by DFT-methods. In general, the $AeTtH_y$ -systems show two hydrogen species that lead to different types of signals. The interstitial hydride has a filled $1s^2$ -shell. Furthermore, the cationic surrounding is resembling a tetrahedron (in fact, two dihedra). Thus, the EFG almost vanishes and signals are narrow. By contrast, the polyanionic hydride is dominated by covalent and, therefore, directed interactions leading to a large EFG-component in direction of the bond. Thus, quadrupole interaction leads to a signal splitting. Its magnitude C_Q is proportional to the largest component of the diagonalised EFG (principle axis system). These systems show values in the range of $C_Q \approx 40\text{-}80$ kHz. The different character of the signals was already shown for SrGeH_{4/3-x} and BaSiH_{2-x} in [A1] (see Fig. A1.6, p. 78). Experimental values can be interpreted in more detail with the aid of DFT-methods. The *Abinit*-package [162–166] was used to calculate quadrupole splittings²⁷. Experimental and previously DFT-optimised structures were used as given in [A1], [A2].

The following results are unpublished. Before discussing them, some additional considerations need to be done. To establish a length scale, two model systems were considered. Molecular SiH₄ placed in a large box, and the DFT-optimized structure of BaSiH₂ were used. In both cases, Si-H distances were varied systematically. For BaSiH₂ the dihedral-angle of hydrogen towards the zigzag-chain plane (δ) was screened as well (Fig. 4.6). As long as hydrogen does not interfere with the Si-Si bond (small δ in Fig. 4.6), which is not reasonable to assume anyway, the distance dependence of the quadrupole splitting is equal for both systems. This further underlines the covalent character of the Si-H bond. Furthermore, experimental data of molecular silanes as well as the Zintl phase hydride β -KSiH₃ fit the curve well. An empirical formula was determined from both sets (SiH₄ and BaSiH₂ at optimised δ -angle) of DFT

²⁶ This will be implied talking about SSNMR results. In the text only hydride (H) will be used.

²⁷ Calculations were performed using the generalized gradient approximation (GGA) and the Perdew-Burke-Ernzerhof (PBE) functional [169]. Projector-augmented wave (PAW) [170] atomic data were taken from the *JTH PAW atomic dataset table* [171, 172]. Electron density and, therefore, the electric field gradient (EFG) were calculated with a SCF threshold of 10^{-9} hartree regarding total energy (*toldfe*) on a $12 \times 4 \times 12$ (no superstructure, *Pbnm*-BaSiH₂), $4 \times 4 \times 12$ (threefold superstructure, *Pbnm*- $AeTtH_{4/3}$) or $2 \times 4 \times 12$ (sixfold superstructure, *Pbnm*- $AeTtH_{5/3}$) Monkhorst-Pack [174] k-point grid which corresponds to about 0.01 bohr^{-1} k-point accuracy. Molecular SiH₄ and GeH₄ were placed in a large box ($a = 200$ pm) with Γ as single k-point. Since previous DOS calculations showed no or just pseudo band gaps, the systems were treated metallic with 0.001 hartree Gaussian smearing. This value was tested for chemically similar systems and seemed appropriate. The kinetic energy cut-off (*ecut*) was set to 25 hartree which is the suggested *high* value for hydrogen. The corresponding *pwecutdg* was set to $2 \cdot \textit{ecut}$. To calculate the magnitude of the quadrupole splitting C_Q , an electric quadrupole moment of $2.86 \cdot 10^{-3}$ barn [175, 176] was used.

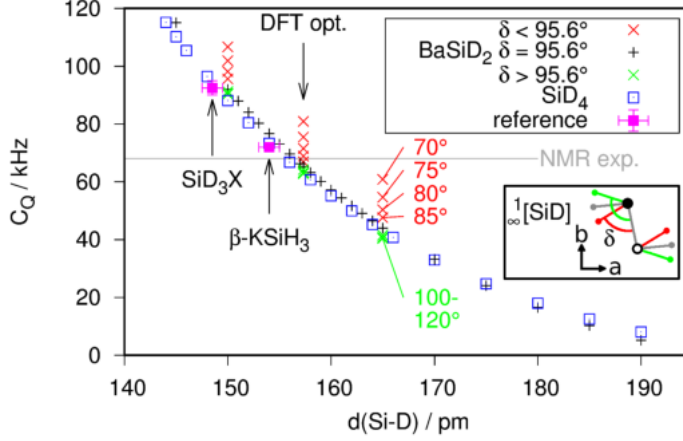


Figure 4.6: DFT calculation derived quadrupole interactions of BaSiD_2 and SiD_4 given as C_Q as function of the Si-D distance. The experimental C_Q of a BaSiD_{2-x} sample (NMR exp.) and the DFT structure optimised Si-D distance (DFT opt.; for $\delta = 95.6^\circ$) are given. Reference values are: $\beta\text{-KSiD}_3$: $C_Q = 72.0(5)$ kHz at 200 K [135], $d(\text{Si-D}) = 153$ pm at 1.5 K [127]; SiD_3X : $C_Q = 95$ kHz at 48 K for $X = \text{H}$ [205], $C_Q = 90(2)$ kHz for $X = \text{CH}_3$ [206], $C_Q = 91(2)$ kHz for $X = \textit{phenyl}$ [207], $d(\text{Si-D}) = 148.1$ pm $X = \text{H}$ [1] (Si-D distance of SiH_4 are ambiguous in the literature, a better reference might be $d(\text{Si-D}) = 147.3 - 149.2$ pm in Si_2H_6 [202, 208]). Inset shows the dihedral angle δ towards the zigzag chain (full circle: $z = 3/4$, open circle $z = 1/4$).

calculations:

$$C_Q/\text{kHz} = 2.0(4) \cdot 10^4 (d(\text{Si-H})/\text{pm})^{-1} - 1.34(13) \cdot 10^7 (d(\text{Si-H})/\text{pm})^{-2} + 1.85(11) \cdot 10^9 (d(\text{Si-H})/\text{pm})^{-3} \quad (3)$$

Thus, this relation can be used to interpret experimental SSNMR data and estimate errors of DFT-derived quantities regarding experimental structure models. A similar calculation was done for GeH_4 , leading to the empirical formula:

$$C_Q/\text{kHz} = 4.557(7) \cdot 10^4 (d(\text{Ge-H})/\text{pm})^{-1} - 2.199(2) \cdot 10^7 (d(\text{Ge-H})/\text{pm})^{-2} + 2.612(2) \cdot 10^9 (d(\text{Ge-H})/\text{pm})^{-3} \quad (4)$$

In Tab. 4.5 experimental and DFT-derived data regarding the Si-H interactions and distances are summarized²⁸. Especially, $\text{SrSiH}_{5/3-x}$ and $\text{BaGeH}_{5/3-x}$ show two quadrupole splitted lines, which further proves the existence of two types of polyanionic hydrides, i.e. a single chain $\frac{1}{\infty}[\textit{TtH}^-]$ and a double chain $\frac{1}{\infty}[\textit{Tt}_2\text{H}_2^-]$. Experimental SSNMR and Rietveld-refined bond lengths fit moderately. Unfortunately e.s.u. are large, especially for the $\text{AeTtH}_{5/3-x}$ -systems. DFT structures shown a higher agreement. Using the SSNMR results under the aid of the DFT-derived distance dependency, bond lengths can be estimated as:

- $d(\text{Si-H}) = 155(2)$ pm
- $d(\text{Ge-H}) = 163(2)$ pm
- $d(\text{Sn-H}) = 186(1)$ pm

Considering the presented results, the covalent character of the \textit{Tt} -H bond becomes clear.

4.4.4 AeTtH_y - decomposition and infra-red spectroscopy

The majority of the investigated Zintl phase hydrides do not show any infra red (IR) spectroscopic signal. Only for BaSiH_y a weak signal is obtained. The measurement was done under air for a hydride and a deuteride sample. The isotope shift can be used as an indicator for vibrations of hydrogen. Fig. 4.7

²⁸ The author thanks *R. Guehne*, *M. Lindel*, *M. Bertmer* and *J. Haase* (Leipzig University, Institute of Experimental Physics II, Linnéstr. 4, 04103 Leipzig) for providing SSNMR measurements of all samples of the AeTtH_y -family including CaSiH_y as private communication.

Table 4.5: Tt -D distances as obtained from Rietveld refinement, DFT optimisations and SSNMR quadrupole interactions (C_Q). Calculated C_Q values are given for the DFT- and the diffraction-derived structure models. The SSNMR distances are calculated from a calibration curve derived from systematic DFT calculations.

compound -bond ^e	exp. structure d(Tt -D) / pm	NMR cal. ^a C_Q / kHz	DFT structure ^b d(Tt -D) / pm	NMR cal. ^c C_Q / kHz	NMR exp. C_Q / kHz	NMR dist. ^d d(Tt -D) / pm
CaSiD _{4/3-x}	182 [117]	16	158 [116]	64	61 ^f	157
SrSiD _{5/3-x}					63 & 77 ^f	157 & 152
-double-chain	150(4)-182(4) [A2]	95-20	160 [A2]	57		
-single-chain	143(4)-158(4) [A2]	124-63	158 [A2]	64		
BaSiD _{2-x}	164.1(5) [A1]	47	157 [A1]	65	68 [A1] ^g	155
SrGeD _{4/3-x}	152.1(9) [A1]	95	167 [A1]	48	52 [A1] ^g	164
BaGeD _{5/3-x}					51 & 61 ^f	165 & 161
-double-chain	155(6)-157(6) [A2]	86-77	164 [A2]	55		
-single-chain	161(5)-175(5) [A2]	62-31	166 [A2]	50		
BaSnD _{4/3-x}	185.8(8) [A1]	40	187 [A1]	37	39 [A1] ^g	

^a Unpublished calculations using the experimental structure.

^b As optimized elsewhere, neglecting the nonstoichiometry, i. e. $x=0$.

^c Unpublished calculation using the DFT derived structure.

^d NMR derived distance according to the empirical formulas given in Eqn. (3), p. 36 and Eqn. (4), p. 36.

^e Describes the Tt -D bond if necessary.

^f Private communication (see text).

^g The published value is given as $3/2C_Q$.

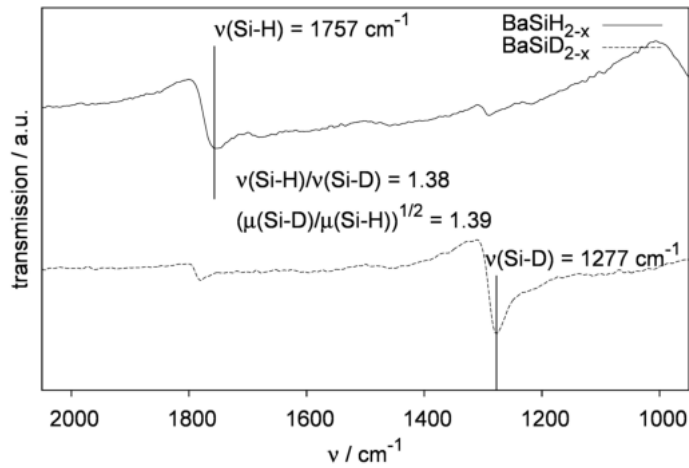


Figure 4.7: ATR-IR spectra of BaSiH_{2-x} and BaSiD_{2-x} shown as transmission. The ratio of the wavenumbers (ν) and the reduced mass (μ) are given to show the expected isotope shift.

shows the stretching modes at 1757 cm^{-1} (Si–H) and 1277 cm^{-1} (Si–D), respectively. These vibrations occur at considerably lower wavenumbers than molecular silanes, i.e. about 2200 cm^{-1} in silane and derivatives [209, 210], and in KSiH_3 (1910 cm^{-1}) [203]. This fits well into our findings of an even longer bond in BaSiH_{2-x} . It also corresponds to the lowered quadrupole interaction determined by SSNMR.

Decomposition in air or cold hydrochloric acid leads to white (silicides) or orange (germanides) amorphous powders. This was investigated in a practical course [161] and supervised by the author. The degradation product can be characterised by IR spectroscopy. The signals correspond to the formation of polysiloxanes and -germanes as obtained by decomposing hydrogen-free Zintl phases CaGe and CaGe_2 [211–214]. SrAlGeH behaves similarly [105]. Starting from Zintl phase deuterides, decomposition leads to partially deuterated products, which suggest the existence of an element-hydrogen bond before decomposition [161]. The isotope shift is a good indicator for vibrations of hydrogen atoms. The Ge–H stretching vibration occurs at 2000 cm^{-1} (Ge–D at 1450 cm^{-1}). Bending vibrations can be seen at about $770\text{--}820\text{ cm}^{-1}$ (Ge–D bending at $700\text{--}730\text{ cm}^{-1}$). The decomposition products of the silicides show strong Si–O vibrations at 1000 cm^{-1} . A weak Si–H vibration can be assigned to a peak at 2200 cm^{-1} (Si–D at 1600 cm^{-1}). These values are typical for molecular silanes and germanes.

4.4.5 NdGaH_y - similar but different

The trivalent lanthanoid metals and gallium form electron-precise Zintl phases $Ln\text{Ga}$ crystallizing in CrB-structure type. They take up hydrogen as shown for $\text{NdGaH}_{1.66}$ [114] and $\text{GdGaH}_{1.66}$ [115]. For the latter one no hydrogen positions were determined. There are two coordination environments for hydrogen in $\text{NdGaH}_{1.66}$. Similar to the $AeTtH_y$ -systems, tetrahedral Ln_4 -voids are filled. The additional hydrogen atoms do not bind to the polyanion forming truncated σ -bonded bands as described above, but bridge the gallium zigzag chains almost in the middle. The coordination can be described as a Nd_3Ga_2 trigonal bipyramid. This leads to quite long ($\approx 190\text{ pm}$) Ga–H distances. There are two alternative descriptions of the crystal structure of $\text{NdGaH}_{1.66}$ (Fig. 4.8). The original work suggested a monoclinic subgroup of space group type $Cmcm$ given by the pristine Zintl phase. An almost equivalent result can be obtained keeping the original symmetry (For details see [114] or [U1]).

In situ NPD was applied to monitor the reaction of NdGa with D_2 and to establish a compositional range for the hydride phase. The results are given as unpublished manuscript [U1]. The samples already takes up hydrogen at low pressures of about 0.1 MPa and ambient temperature. The gallium chain coordinating site shows a large range of occupation. Thus, the phases needs to be described as NdGaH_{1+x} and x describing this site. The compositional range was found to reach from at least $x = 0.137(7)$ to $0.799(11)$. This is a major difference to the hydrogen-rich $AeTtH_y$, $1 < y < 2$, systems. *In situ* diffraction of the hydrogenation of BaGe and BaSn did not show any sign of a compositional range. SrGeH_y shows only a small compositional range from $y = 1.16$ to 1.23 . This finding fits the structural differences. The hydrogen-rich $AeTtH_y$ -systems show covalent Tt -H bonds. A variable hydrogen content at the chain binding site needs breaking and forming of bonds. The crystal structure of NdGaH_{1+x} shows a large Ga–H bond. Thus, hydrogen is only loosely bound to the gallium zigzag chain allowing uptake and release much easier.

Upon hydride formation the cell expansion is small with about 1% volume increase. Within the compositional range of NdGaH_{1+x} from $x = 0.137(7)$ to $0.799(11)$ the volume change is even much smaller. The unit cell change is strongly anisotropic. Lattice parameter a which runs perpendicular to the zigzag chains strongly decreases upon hydrogen incorporation. This supports a bonding interaction between hydrogen and gallium. Lattice parameter b increases, while c which runs in chain direction is hardly effected.

At occupations of the Ga-chain coordinating site from 0.53 to 0.66 a two-fold superstructure can be identified, at occupations above 0.73 a three-fold one occurs²⁹. In the latter case a structure model could be refined, that shows hydrogen ordering. The refined composition is $\text{NdGaH}_{5/3}$. A resembling situation occurred for $\text{BaGeH}_{5/3-x}$ and $\text{SrSiH}_{5/3-x}$ that could be solved by another doubling of the superstructure indicated by selected area electron diffraction (SAED). The resulting sixfold superstructure model worked well for the alkaline earth systems, but does not lead to a satisfactory Rietveld refinement for NdGaH_y . Instead, the crystal structure shows a $\frac{1}{\infty}[(\text{Ga}-\text{H}-\text{Ga}-\text{H}-\text{Ga})^{6-}]$ -unit as predicted for $\text{NdGaH}_{1.66}$ or $\text{GdGaH}_{1.66}$ [114, 115]. The gallium zigzag chains show a Ga–Ga distance of 257 pm to 259 pm which is

²⁹ These occupations are refined using a structure model with a simple unit cell, i.e. no superstructure regarding the parent phase.

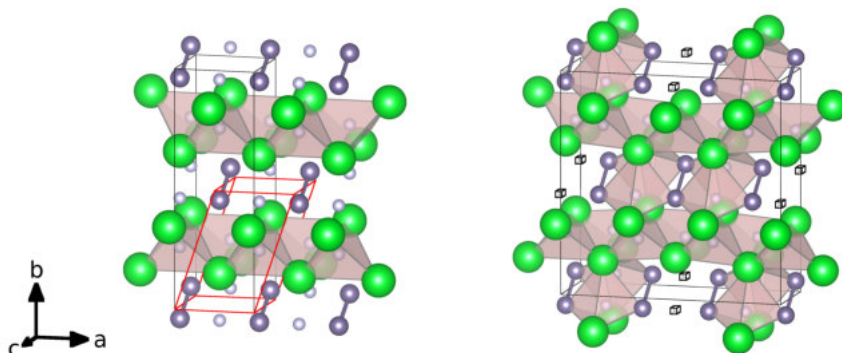


Figure 4.8: Crystal structures of NdGaH_{1+x} in general (**left**) and an ordered $\text{NdGaH}_{1.66}$ (**right**). Large green spheres: Nd, medium grey spheres: Ga, small white spheres: H. Hydrogen occupies Nd_4 -voids (shaded tetrahedra, full occupation) and coordinates the Ga-zigzag chain in with a variable site occupation (shown as white small sphere, **left** or as shaded trigonal bipyramid, **right**). NdGaH_{1+x} (**left**) was also described in a monoclinic setting [114] which is shown as are unit cell. Hydrogen has an additional degree of freedom in crystallographic a direction in this description. The ordered superstructure $\text{NdGaH}_{1.66}$ (**right**) exhibits a ${}^1_{\infty}[(\text{Ga}-\text{H}-\text{Ga}-\text{H}-\text{Ga})^{6-}]$ -moieties that are separated by a hydrogen void (\square).

shorter than 262 pm in the pristine Zintl phase. There is a short Ga-H distance of 205 pm and a long one of 225 pm, both larger than typical covalent distances, e.g. 169 pm in SrGa_2H_2 . After desorption the Nd_4 -tetrahedra still show full occupations. 0.14 hydrogen atom per formula unit stay between the Ga-chains.

A simple covalent interaction between gallium and hydrogen can be excluded. Due to the large homogeneity range an idealisation of the chemical formula NdGaH_{1+x} as discussed for the hydrogen-rich AeTtH_y phases seems not appropriate here. Thus, this phase is an exception from the Zintl concept as defined in Sec. 2.3.

4.4.6 CaGa - a candidate for chain hydrogenation

As described above, CaGa is an electron-deficient phase in CrB-structure type. From a Zintl-like picture, one would expect a π -bonded system with short Ga-Ga distances within the zigzag chains. The crystal structure as well as DFT-fatband calculations show that π -bonding is abandoned in favour of a σ -stacking interaction in crystallographic a direction [71, 191]. Still, the systems do not show a σ -bonded 2D network as discussed before (Sec. 4.3.3, Scheme 4.3, p. 29). The ideal a/c -ratio of such a layer is $\sqrt{6}/3 \approx 0.816$. The CaGa-structure only reaches a ratio of 0.956. Thus, the unit cell is still about 17% too long in crystallographic a direction. The hydrogen-rich AeTtH_y -systems compensate this effect by introducing hydrogen between the chains upon formation of (mainly) σ -bonded systems. These systems show an a/c -ratio of about 1 that allows more regular tetrahedra (see Tab. 4.3, p. 32). With increasing ratio the number of chain connections decreases. The value of CaGa fits to the $\text{AeTtH}_{4/3}$ -systems. Therefore, it is a reasonable candidate for a polyanionic hydride formation that does not show interstitial hydride ions. The bonding situation might either correspond to the treltel systems or to LnGaH_{1+x} , $x \leq 1$. The filling of tetrahedral voids and formation of an ionic layer is an important step of the hydrogenation of AeTt - or LnTt -systems. Thus, a second reaction scheme of CaGa seems possible that leads to a filling of tetrahedral voids. The resulting formal Ga^- requires four covalent bonds according to the Zintl concept. This was already realised for AGaH_2 ($A = \text{K}, \text{Rb}$) [32, 34, 113]. The solid solution $\text{Rb}_x\text{K}_{1-x}\text{H}_2$ ($0 \leq x \leq 0.5$) is an example of a variant of the CrB-structure type. In the case of CaGa, this structure could be realised by a CaGaH_3 with with additionally filled tetrahedral voids. Therefore the formation of two structures seems reasonable for the hydrogenation of CaGa:

- (i) CaGaH_y with a polyanionic hydride partial structure equal to the $\text{AeTtH}_{4/3}$ -system or similar to NdGaH_{1+x} ($x \leq 1$), but without an interstitial hydride site occupied. This reaction scheme leads to a composition $\text{CaGaH}_{\leq 1}$.

- (ii) CaGaH_3 with one hydrogen per formula unit filling tetrahedral Ca_4 -voids and two hydrogen forming a $\frac{1}{\infty}[\text{GaH}_2^-]$ polyethylene-like chain.

All experimental data of the hydrogenation of CaGa are summarized in Sec. U2.1. Laboratory *in situ* diffraction of the hydrogenation reaction shows the occurrence of an intermediate phase that is followed directly by a decomposition into CaH_2 and Ca_3Ga_8 . Thermal analysis (H_2 -DSC) under hydrogen pressure shows only one broad exothermic signal that can be attributed to the decomposition and might cover the reaction step. Since the segregation of binary hydride leads to $5\text{CaH}_2 + \text{Ca}_3\text{Ga}_8 \approx \text{Ca}_8\text{Ga}_8\text{H}_{10}$, the product of case (i) can be expected to have a lower hydrogen content, while the product discussed for case (ii) has a much higher hydrogen content. Screening the pressure from 1.5 to 5 MPa could not separate any other H_2 -DSC signals. *Ex situ* hydrogenation always leads to the same decomposition products. The temperature window for the formation of the intermediate phase seems quite small which makes *ex situ* preparation demanding.

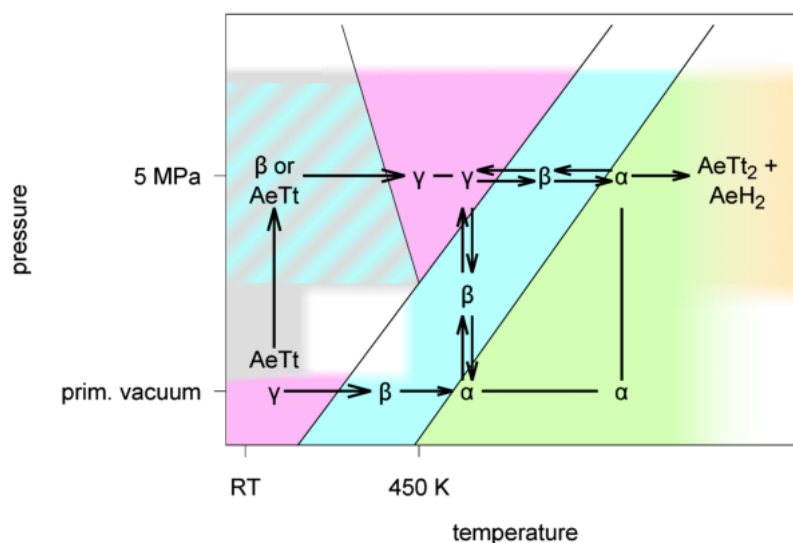
Further evaluations need high-resolution laboratory *in situ* diffraction with more accurate temperature control than realised at the moment. This screening is mandatory to establish a proper protocol for the preparation of this phase. If this phase can be traced, a heavy metal partial structure model from X-ray data can be determined. Considering previous research the target phase can be assumed to be structurally related to the parent phase. *In situ* thermal analysis does not appear to be a helpful tool to reach the target phase. If the reaction and the decomposition step can be separated, this system is ideally suited for *in situ* neutron diffraction.

4.5 Reaction schemes of the AeTt-H_2 -systems, $\text{Ae} = \text{Ca, Sr, Ba}$, $\text{Tt} = \text{Si, Ge, Sn}$

Until now, the focus lay on structures and bonding. In the following, the reaction schemes will be the topic of discussion. The SrGe- , BaGe- , and BaSn-H_2 systems have been studied in detail as presented in [A4] and [A6]. Furthermore, there are *in situ* neutron powder diffraction (NPD) data available for the reaction of CaSi under deuterium pressure and elevated temperatures which are already part of a previous PhD-thesis [97]. Differential scanning calorimetry under hydrogen pressure (H_2 -DSC) is a valuable tool to probe different temperature-pressure conditions. *In situ* diffraction then can be used to determine the structures of the different occurring phases since some of them cannot be collected at ambient conditions yet. To decrease the incoherent background, typically deuterium gas was used.

Scheme 4.4 reflects the reactions of the AeTt-H_2 -systems ($\text{Ae} = \text{Sr, Ba}$; $\text{Tt} = \text{Ge, Sn}$) in general. For the corresponding silicides, only the formation of γ -phases is clear yet. The marked pressure (5 MPa) and temperature (450 K) are typical values for the formation of the hydrogen-rich phases. An crease in pressure facilitates the formation but the effect might be quite small. From thermal analysis data, the starting temperature of the hydrogenation reaction is difficult to determine due to broad DSC-peaks. *In situ* diffraction of BaGe showed that $\beta\text{-BaGeH}_{0.5}$ is formed already at room temperature. This formation is always incomplete and cannot be facilitated by increasing pressure, thus, it might be a particle size or passivation effect. The formation of α -phases at ambient temperature and gas pressure cannot be assigned unambiguously for these systems due to insufficient data. Furthermore, a formation of γ -phases is not obtained for low pressures. When the reaction still takes place at 3 MPa (tested for SrGe and BaGe), it stops working at 2 MPa. The reaction scheme at low pressures is not clear yet. According to the trends shown in Scheme 4.4, a formation of hydrogen-poor phases seems most probable. $\gamma\text{-SrGeH}_y$ clearly showed a variable hydrogen content. This can be assumed from *in situ* neutron diffraction and *ex situ* diffraction after storing the sample for 70 days under argon [A4]. $\gamma\text{-BaGeH}_y$ and $\gamma\text{-BaSnH}_y$ do not give any signs towards a homogeneity range regarding hydrogen incorporation [A6]. These phases show the smallest deviation from a stoichiometric composition as well.

A decomposition at high pressures (typically 5 MPa hydrogen) takes place in several steps. The formation of hydrogen-poor phases is reversible. It is followed by an irreversible formation of binary hydride and tetrel-rich Zintl phase. While at 5 MPa hydrogen pressure $\gamma\text{-SrGeH}_y$ reacts to form $\beta\text{-SrGeH}_y$ (570 K) and $\alpha\text{-SrGeH}_y$ (590 K), $\gamma\text{-BaGeH}_y$ only shows the formation of $\beta\text{-BaGeH}_y$ (550 K). $\gamma\text{-BaSnH}_y$ directly turns into $\alpha\text{-BaSnH}_y$ (480 K). The decomposition of the polyanionic hydride and, thus, the breaking of the Tt-H bonds appears at considerably lower temperature for tin than for germanium, reflecting the weaker covalent bond. For all systems it is accompanied by a release of hydrogen from interstitial sites. The reversible formation of the γ -phases can show considerable hysteresis (see SrGe-H_2 -system [A4]). An irreversible decomposition was not observed for the BaSn-H_2 reaction yet. In the



Scheme 4.4: Hydrogenation and dehydrogenation conditions of the $AeTt$ -Zintl phases ($Ae = Sr, Ba$; $Tt = Ge, Sn$). Typical temperatures and pressures are indicated. Colours correspond to different phases as indicated in the graph. White regions are still unclear.

case of the germanides, it leads to the formation of $AeGe_2$ ($Ae = Sr, Ba$). There is no proper DSC signal for this irreversible step. *In situ* diffraction showed that the decomposition is slow and leads to broad reflections. Increasing temperature improves crystallinity. Irreversible decomposition typically starts at 600-700 K.

γ -BaGeH_y was also dehydrogenated under primary vacuum [A6]. It showed the subsequent formation of β - and α -phase. Upon further heating the hydrogen content in α -BaGeH_y decreases from $y = 0.3$ to $y = 0.1$. The hydrogen-free Zintl phase could not be obtained up to 500 K. Pressurizing α -BaGeH_y at 500 K from vacuum to 0.2 MPa immediately leads to the formation of β -BaGeH_{0.5}. The reaction is completed in less than a minute.

In general, the silicides do not show proper H_2 -DSC signals [97]. An *in situ* diffraction study on CaSi was conducted before [97]. The reaction of CaSi at high temperature (> 550 K) leads to the formation of a new, yet not finally solved structure [97]. The system reacts fast, within seconds, on pressure changes, reforming CaSi or maybe an α -phase at hydrogen release and forming another phase upon pressurization. Upon cooling, the hydrogen rich phase is formed [97]. In analogy to the germanides and the stannide, the existence of an α - or a β -phase is possible here.

5 Reactivity of tetrahedral and other three-binding polyanions towards hydrogen

5.1 Examples of three-binding Zintl phases

The previous section dealt with Zintl phases exhibiting two-binding polyanions that became three-binding upon hydrogenation. Now, the connectivity of the precursor phases is going to be increased. Thus, triel Tr^{2-} and tetrel Tt^- anions were considered for hydrogenation reactions. A starting point is the known reaction $KSi + 3/2H_2 \longrightarrow KSiH_3$ that works for the heavier alkaline metals as well. Three-binding polyanions feature two general motifs: either isolated X_4 -tetrahedra as present in white phosphorous or two- or three-dimensional networks.

Within the ATt -system (A = alkaline metal; Tt = tetrel) the light metals exhibit MgGa- (LiSi and LiGe), NaSi- or NaGe-structure types. Silicides and germanides of the larger alkaline metals are isotypic and crystallize in cubic KGe-type structures. Only the tetragonal LiSi-structure exhibits a three-dimensional network of three-binding Si^- -anions forming condensed puckered eight-membered rings. The other structures are monoclinic (NaSi, NaGe) or cubic (KGe-type structures) and show tetrahedral Tt_4^{4-} -anions. The ternary phases $ASi_{0.5}Ge_{0.5}$ (A = Na, K, Rb) and $K_{0.5}Rb_{0.5}Si$ [215] show the same structural units. Density functional theory (DFT) calculations of all silicides (Li-Rb) showed semiconducting behaviour with band gaps larger than 1 eV [216].

SrGa and BaGa do not exist, but the isotypic phases Ba_8Ga_7 , Sr_8Ga_7 and Sr_8Al_7 [217] show Tr_4^{8-} -tetrahedra, Tr = Al, Ga, as expected from the 1:1 compounds. Additionally, there are Tr_3^{8-} -triangles. According to the Zintl-electron counting rules, the triangular moieties are electron-deficient since two-binding trielides should formally possess six valence electrons (i.e. Tr^{3-}). Applying Wade rules leads to the same result, since an *arachno*-cluster ($2n+6$) requires 12 skeleton electrons instead of the remaining 11 electrons of this moiety.

The $AeTt_2$ -systems, Ae = Ca, Sr, Ba; Tt = Si, Ge, crystallizes in several structure types. They all show three-binding polyanions as expected from the Zintl-concept. Only the $BaSi_2$ -structure type [218] shows isolated Si_4^{4-} tetrahedra. $SrGe_2$ and $BaGe_2$ isotypic to it. DFT as well as experimental data show that these phases are semiconductors with a band gap of about 1 eV [219–221]. The $CaSi_2$ -structure type [222], which is realized by $CaGe_2$ as well, is a layered structure. Three-binding Si^- forms a 2D-net of condensed six-membered rings in armchair configuration. The rings are connected like *trans*-decalin and, therefore, each sheet corresponds to the structure of grey arsenic. A layer of cations separates the polyanions. The structure is rhombohedral with 6 polyanion layers (6R-structure). There are two crystallographic independent silicon atoms leading to an AA'BB'CC' stacking sequence. For $CaSi_2$ another rhombohedral structure type with one silicon site and an ABC stacking is discussed (3R-structure) [223, 224]. The occurrence of the 3R-polymorph can probably be related to some residual hydrogen that might have been present in the used calcium metal. The phase transition from 6R- to 3R-structure was shown to be promoted by a hydrogen atmosphere [225]. $SrSi_2$ crystallizes in an own structure type [218] that exhibits a three-dimensional network of three-binding silicon atoms. $CaSi_2$, $CaGe_2$ and $SrSi_2$ were shown to be metallic conductors [219].

5.2 Hydrogenation of ATt (A = K-Cs; Tt = Si, Ge)

5.2.1 ASi (A = K-Cs)

The hydrogenation of the silicide phases ASi (A = Li-Rb) was extensively studied already. Hydrogenation either leads to decomposition

- $LiSi + \frac{1}{2}H_2 \longrightarrow LiH + Si$ [130]
- $46NaSi + 19H_2 \longrightarrow 38NaH + Na_8Si_{46}$ [131]

or to the formation of monomeric SiH_3^- -anions

- $ASi + \frac{3}{2}H_2 \longrightarrow ASiH_3$ (A = K, Rb, Cs) [126, 127, 226]

Hydrogenation of small particles of KSi [131] or KSi at high temperatures [A7] also leads to the formation of the clathrate phase K_8Si_{46} . These clathrate formation is typical for oxidation reactions of NaSi or KSi with gaseous HCl or H_2O [227].

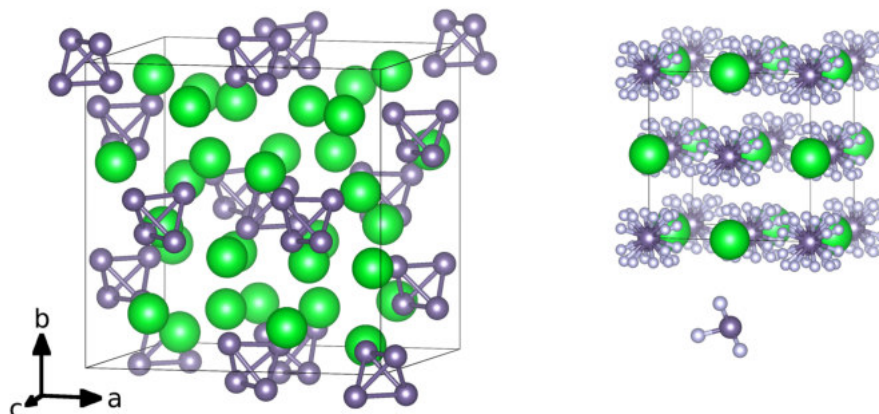


Figure 5.1: Crystal structures of KSi (left) and α -KSiH₃ (right). The SiH₃⁻-units are rotationally disordered. A single SiH₃⁻-group is shown below the structure. Large green spheres: K, medium grey spheres Si, small white spheres: H.

The crystal structure of high temperature or α -KSiH₃ corresponds to the NaCl-structure type with rotationally disordered SiH₃⁻ on the anion sites [133]. The low temperature or β -form corresponds to FeB-structure type [138]. The Rb- and Cs-analogues crystallize in a CrB- type related crystal structure, with SiH₃⁻-units on the anion site and a monoclinic distortion [127]. These structure types also allow the formation of several different polyanions, i.e. polyethylene-like GaH₂⁻ [32, 34] or polyphosphane-like ${}_{\infty}^1[\text{SiH}^-]$ [A1]. Thus, it is legitimate to speculate about intermediate phases during the hydrogenation of ASi, i.e. ${}_{\infty}^1[\text{SiH}^-]$ or even a dimeric species ${}_{\infty}^2\text{HSi-SiH}_2^-$ would be candidates.

In situ neutron powder diffraction (NPD) at 5 MPa deuterium pressure and at elevated temperatures was applied to probe this hypothesis [A7]. It could be shown that the reaction $\text{KSi} \xrightarrow{\text{H}_2} \text{KSiH}_3$ under the stated conditions is an one step reaction. The structure of the Zintl phase can be refined during the whole experiment and does not indicate any solubility of hydrogen. The lattice expands due to heating without any further effects during isothermal steps. The formed KSiH₃ appears to be a line phase as expected from an electron precise phase with isolated anionic moieties. The formation of an intermediate phase during the diffraction experiment can be excluded. *Ex situ* as well as laboratory *in situ* X-ray powder diffraction (XRPD) showed the decomposition to KH and K₈Si₄₆ upon further heating. Furthermore, the reaction of the heavier homologue CsSi under equivalent conditions was monitored by *in situ* NPD [A7]. The reaction to form CsSiH₃ does not show any intermediates as well. In contrast to KSiH₃, the caesium compound decomposes to form the Zintl phase CsSi again. Clathrate and binary hydride are not obtained. This correlates with *ex situ* experiments at 5 MPa H₂ pressure up to 700 K that always showed single phases CsSiH₃ after cooling down. The different reaction behaviour can be explained by the higher thermodynamical stability of KH, in contrast to CsH which is the major component during the clathrate formation.

5.2.2 The homologue systems $\text{ASi}_x\text{Ge}_{1-x}$ ($A = \text{K-Cs}$)

The existence of AGeH_3 ($A = \text{Li-Cs}$) and even KSnH_3 is well established [121, 123, 124]. They are prepared by solutional chemistry. A solid state route is still missing. Thus, a hydrogenation similar to the reaction of KSi was tested. The investigated systems KGe and CsGe showed no formation of AGeH_3 at pressures of 5 MPa H₂ and temperatures up to 500 K. There are first hints towards the decomposition reaction of CsGe into the clathrate phase Cs₈Ge₄₄. This would open up a new preparative route to the formation of this phase since only a high temperature, high pressure protocol is described yet. For details see Sec. U2.4.

Furthermore, solid solutions of $\text{RbSi}_x\text{Ge}_{1-x}$ and $\text{CsSi}_x\text{Ge}_{1-x}$ were prepared and attempted to be hydrogenated during a practical course that was supervised by the author [228]. The preparation of a solid solution row of the rubidium system is possible in accordance with the literature [215]. The caesium system always shows the presence of CsSi as well as a second compound with a cubic lattice parameter

between CsSi and CsGe. Hydrogenation experiments either show no reactions at all or lead to the formation of ASiH_3 (according to the lattice parameter) and a second phase $\text{ASi}_x\text{Ge}_{1-x}$ that shows an increased lattice parameter. This can be interpreted as a formal dissolution of ASi from the ternary phases that reacts to form ASiH_3 . Thus, a solid state route to AGeH_3 or isotypic ternary phases that show a covalent Ge-H bond is still elusive.

5.3 Hydrogenation of Sr_8Ga_7 and Ba_8Ga_7

There is no study about the reactivity of Sr_8Ga_7 or Ba_8Ga_7 towards hydrogen known to the author. Thus, a preliminary study of the hydrogenation of Sr_8Ga_7 and Ba_8Ga_7 was conducted. Both phases show decompositions into $\text{SrGa}_4 + \text{SrH}_2$ or $\text{BaGa}_4 + \text{BaH}_2$, respectively (for experimental details see U2.2). The Sr_8Ga_7 -sample contained considerable amounts of SrGa_2 . Thermal analysis under hydrogen pressure (H_2 -DSC) showed two reaction steps. Stopping the DSC right after the first signal (550 K) showed the formation of SrGa_2H_2 as well as decomposition products. While SrGa_2 reacts with hydrogen to form a polyanionic hydride, Sr_8Ga_7 already segregates into binary SrH_2 and the more gallium-rich phase SrGa_4 . H_2 -DSC experiments of Ba_8Ga_7 only showed one signal, that is attributed to the formation of the gallium-rich phase. Decomposition into AeGa_4 ($\text{Ae} = \text{Sr}, \text{Ba}$) was obtained for the hydrogenation of AeGa_2 at high temperatures as well [95].

5.4 Hydrogenation of AeTt_2 -systems ($\text{Ae} = \text{Ca}, \text{Sr}, \text{Ba}$; $\text{Tt} = \text{Si}, \text{Ge}$)

The samples AeTt_2 , $\text{Ae} = \text{Ca}, \text{Sr}, \text{Ba}$, $\text{Tt} = \text{Si}, \text{Ge}$, do not show any reactivity towards hydrogen under all applied conditions³⁰. Differential scanning calorimetry experiments at 5 MPa hydrogen starting pressure (H_2 -DSC) only show a baseline up to 720 K (see Sec. U2.3). Diffraction patterns taken after the hydrogenation procedure are identical to powder diffraction data gained after synthesis of the Zintl phase. There are no reflections vanishing or appearing. Profiles do not show any broadening. BaGe_2 and BaSi_2 were also hydrogenated in an autoclave at moderate temperatures (550 K) and high pressure (18 MPa H_2). Diffraction patterns do not show any effect as well. As it turned out later for the germanium systems, AeGe_2 occurs as a decomposition product of the reaction $\text{AeGe} + \text{H}_2$ at high temperatures and hydrogen pressure. This process might finally lead to the formation of elemental germanium. Experimentally, we observe that the reaction stops at AeGe_2 . This seems thermodynamically more favourable since it is the most stable compound of the Ae-Ge -phase systems.

³⁰ A phase transition from 6R- CaSi_2 into 3R- CaSi_2 was described to be mediated by hydrogen [225]. The latter polymorph might be stabilised by residual hydrogen within the crystal structure.

6 Structural relationship between the structures

This thesis deals with new hydrogen-poor (α - and β -) as well as literature known ($AeSiH_y$) or new (γ - $SrGeH_y$, γ - $BaGeH_y$ and γ - $BaSnH_y$) hydrogen-rich Zintl phase hydrides of the $AeTt-H_2$ -systems ($Ae = Ca, Sr, Ba, Tt = Si, Ge, Sn$). These phases are related to the CrB-structure type. This and the related FeB-type can support several motifs of hydrogen incorporation. Considering examples known by literature as presented in the beginning, a large ensemble of Zintl phase hydrides can be described with regard to these structure types. In general, the structures can be categorized in the following three classes:

- (i) interstitial hydrides,
- (ii) polyanionic hydrides, or
- (iii) interstitial + polyanionic hydrides.

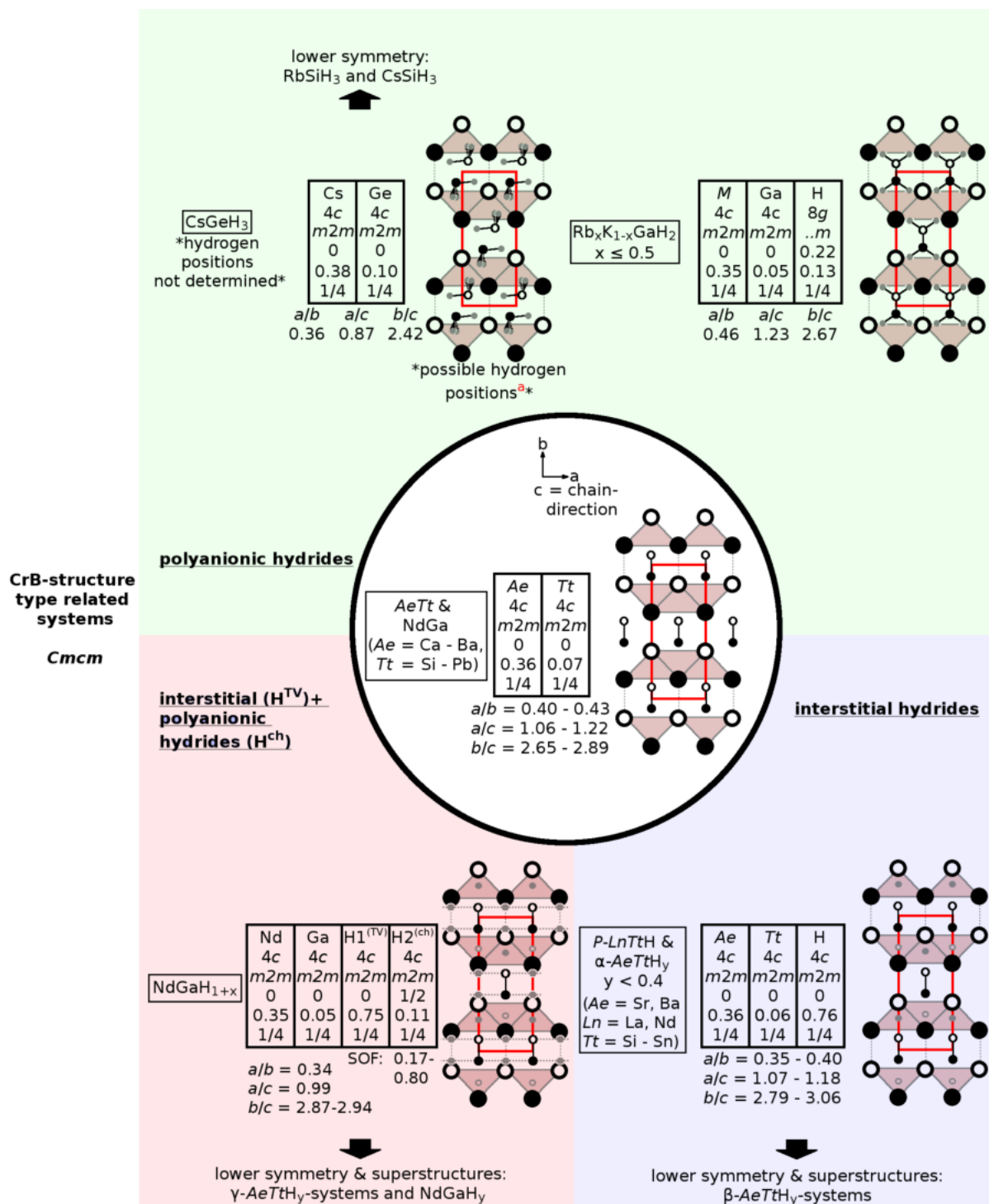
This is shown in Scheme 6.1 (CrB) and Scheme 6.2 (FeB). Neglecting hydrogen, the shown phases are isotypic, except for $RbGaH_2$ where the a/c -ratio is inverted. Depending on the space requirements of the different polyanions, the original unit cells are enlarged anisotropically as can be seen from the lattice parameter ratios given in the schemes.

The new interstitial hydrides $LnTtH$, $Ln = La, Nd, Tt = Si, Ge, Sn$, crystallize in ZrNiH- (C -phase according to [A3]) or LaGeH-structure type (P -phase according to [A3]). They can be derived from CrB- and FeB-structure type by filling tetrahedral Ln_4 -voids with hydrogen, respectively. The phases are electron precise Zintl phases. The hydrogen poor phases α - $AeTtH_y$, $y < 1$, $Ae = Sr, Ge, Tt = Ge, Sn$ are isotypic but occur only in ZrNiH-type. The polyanions are partially oxidized, i.e. the anionic charge is reduced regarding the expected Zintl like formulation ($Tt^{(2-y)-}$).

Furthermore, there are several polyanionic or mixed polyanionic and interstitial hydrides fitting into the scheme. The cationic partial structure of CrB- or FeB-type derived phases can house:

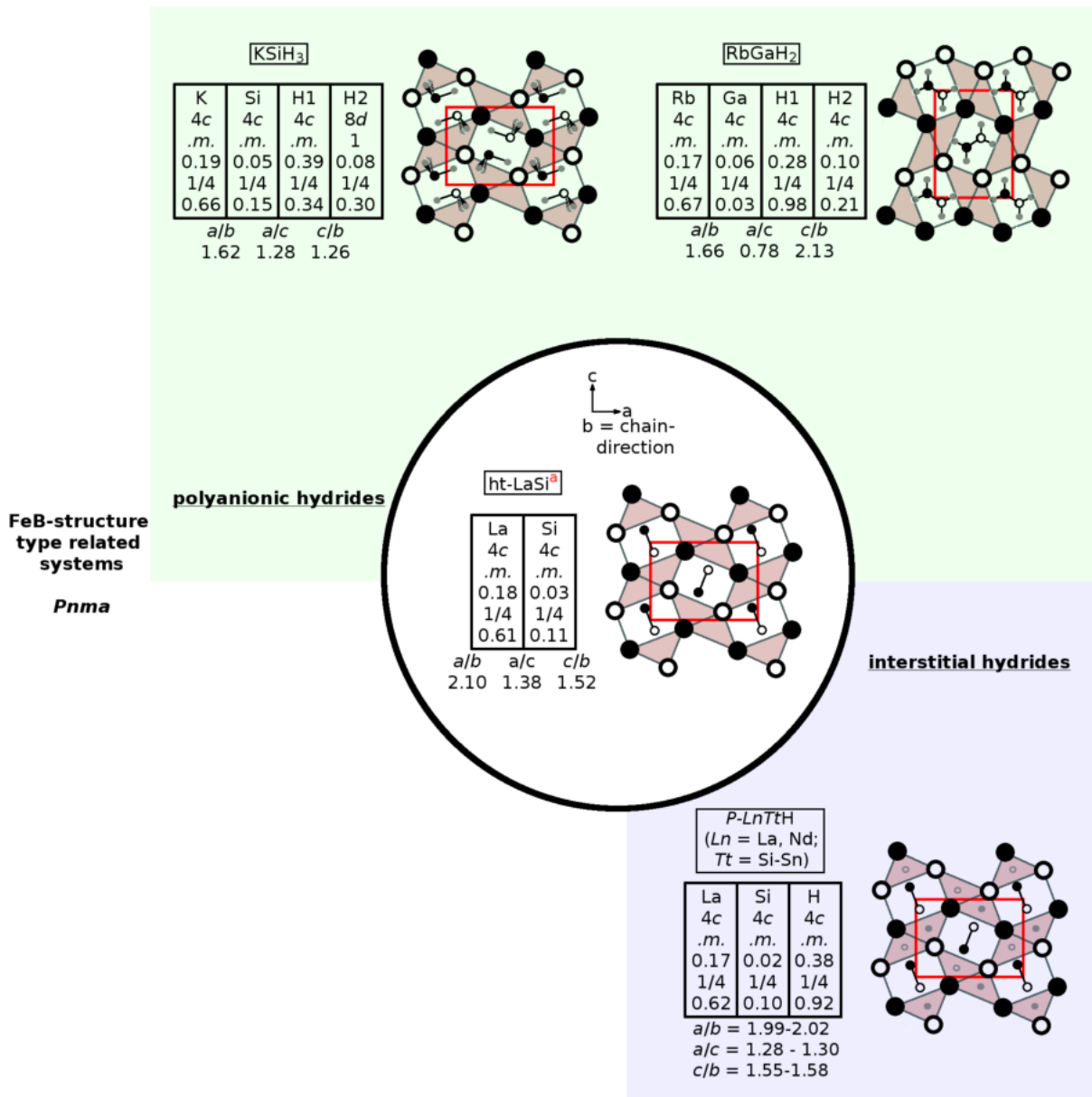
- ammonia-like, monomeric SiH_3^- ,
- polyethylene-like chains ${}^1_\infty[GaH_2^-]$,
- polyphosphene-like chains ${}^1_\infty[SiH^-]$,
- condensed polyphosphene-like bands ${}^1_\infty[HSi_4H^{4-}]$ and ${}^1_\infty[HSi_6H^{6-}]$, or
- GaH_x^{2-} , where the bonding is still unclear.

The literature examples $AGaH_2$, $A = K, Rb$, β - $KSiH_3$ and $CsGeH_3$ fit into the scheme. In the latter case, hydrogen positions are still unclear. Most likely, the symmetry needs to be reduced. The structure might be isotypic to monoclinic β - $CsSiH_3$ (see below). Orthorhombic $NdGaH_{1+x}$, $x < 1$, is an example of a mixed interstitial and polyanionic hydride and can be described as filling variant of the CrB-structure type. It is the aristotype of the more complex pseudo-polyphosphene like polyanions and monoclinic $NdGaH_{1+x}$ as discussed below.



Scheme 6.1: CrB-structure type related Zintl phase hydrides MXH_h . Full spheres: front, $z = 3/4$; open spheres: back, $z = 1/4$; large, black spheres: $M =$ alkaline, alkaline earth (Ae) or lanthanoid metal (Ln); medium, black spheres: $X =$ tetrel (Tt) or gallium; small, grey spheres: hydrogen; H^{TV} : hydrogen in a tetrahedral void, H^{ch} : hydrogen coordinating the chain.

^a The schematic hydrogen positions do not fit to $Cmcm$ symmetry. They are taken from the monoclinic structures of RbSiH₃ and CsSiH₃. See Fig. 6.3.



Scheme 6.2: FeB-structure type related Zintl phase hydrides MXH_h . Full spheres: front, $z = 3/4$; open spheres: back, $z = 1/4$; large, black spheres: M = alkaline, alkaline earth (Ae), lanthanoid metal (Ln); medium, black spheres: X = tetrel (Tt) or gallium; small, grey spheres: hydrogen.

^a High temperature (ht) modification of LaSi crystallizing in FeB structure type.

6.1 Group-subgroup relations

This section finally relates the more complex structures to the CrB-structure type. The given group-subgroup trees [151] start with a standardized setting [229] of the aristotype. The sub-group setting is derived according to the transformations given in the tree, but atomic coordinates are presented according to experimental structures. Within the given accuracy, all named examples fit the description. In Sec. 8 there is an index of all crystal structures given in Part II.

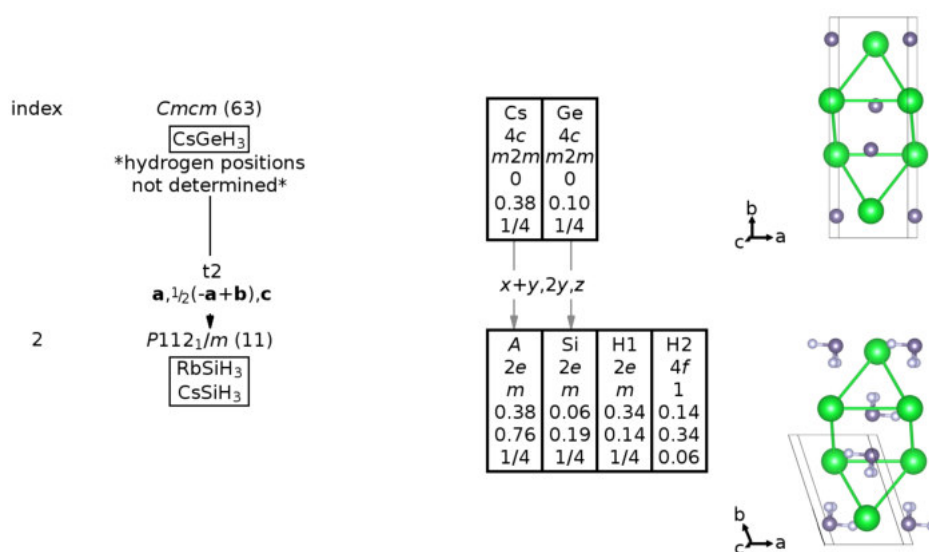
At the end of this section a table is given, referencing the original structure data regarding Part II of this work (Tab. ??).

The CrB-type structures show a rich diversity. As a matter of completeness the literature-known TtH_3^- ($Tt = Si, Ge$) containing structures are briefly discussed at first. $CsGeH_3$ was described to crystallize in CrB-structure type. Hydrogen positions were not determined. Later, the structures β - $RbSiH_3$ and β - $CsSiH_3$ followed. These low temperature measurements lead to a description using a model in a monoclinic subgroup as derived in Scheme 6.3.

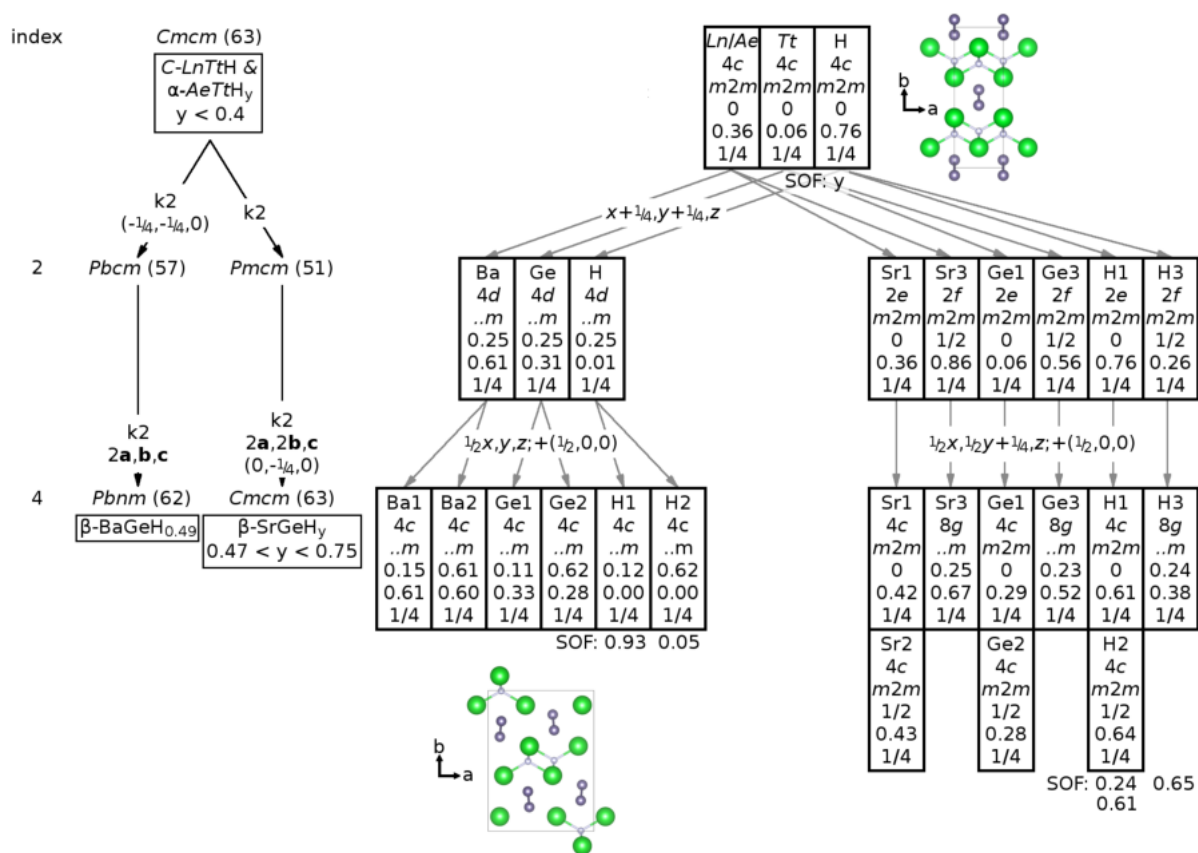
The hydrogen-poor $AeTtH_y$ systems can be derived from the C - $LaGeH$ -structure ($ZrNiH$ -type). The α -phases are isotypic to the given aristotype but show only partial hydrogen occupation. The two phases β - $BaGeH_{0.5}$ and β - $SrGeH_y$, $0.47 < y < 0.75$, exhibit superstructures. The latter case shows a large homogeneity range. A preliminary model was proposed that shows a preference for hydrogen incorporation on different sites. In the case of β - $BaGeH_{0.5}$, a line phase is assumed. The structure model allows full hydrogen order. The relation to the aristotype is given in Scheme 6.4.

Finally, the hydrogen-rich phases are shown (Scheme 6.5). As aristotype, the orthorhombic structure of $NdGaH_{1+x}$, $x < 1$, is given as used in the manuscript [U1]. The published monoclinic structure $NdGaH_{1.66}$ is closely related to orthorhombic $BaSiH_{2-x}$. Both structure types allow a tilting of the zigzag chains out of the b - c -plane, but in different directions for consecutive layers. While for $NdGaH_{1.66}$ all chains rotate (around crystallographic c direction) in the same direction, this rotation changes after each salt-like Ba-H-layer in $BaSiH_{2-x}$. Tripling lattice parameter a and keeping $Cmcm$ space group type leads to the averaged structure of the $AeTtH_{5/3-x}$ -systems. The hydrogen chain-site needs to be described as a split position, doubling the $8g$ site. From this intermediate step, two structure types can be derived. Further symmetry reduction leads to the $CaSiH_{1.3}$ -structure (A branch) or the ordered model (B branch). The hydrogen occupied chain sites and the remaining voids are inverted between these two structure types. The transition between the $AeTtH_y$ structure types can be related to different space requirements. The salt-like Ae -H-layers are quite rigid. A representation of the group-subgroup tree showing projections of the structures is given in Scheme 6.6 to emphasize the topological similarities.

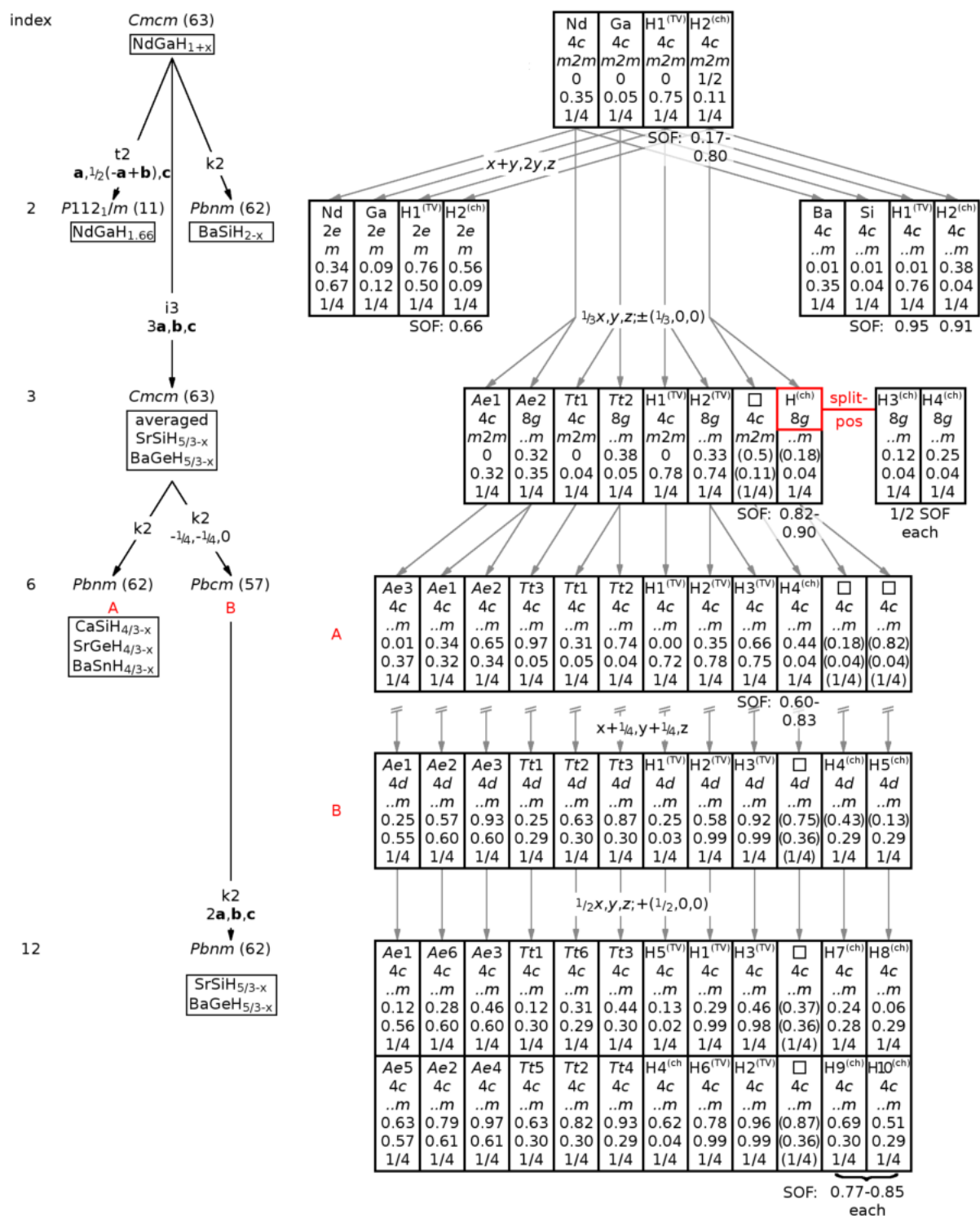
As a consequence of the structural richness of these systems some problems with the structure determination occur as previously described. All these structures are closely related and show a lot of pseudo-symmetry. Increasing the cationic size from Ca to Ba also increases the amount of hydrogen incorporated, changing the structure type. A sharp transition between the structure types or a floating one exhibiting a mixture of different polyanionic hydrides statistically distributed over the crystal is hard to distinguish for these systems and not clear yet. Due to the superstructures, peak overlap is already severe. The reactions might be topotactically. The anisotropic unit cell change upon hydrogenation would then lead to stress and strain of the structure resulting in broad reflections as we observe them. Furthermore the structures are layered and different stackings might be possible. An example of different variants are the structures of orthorhombic $BaSiH_{2-x}$ and monoclinic $NdGaH_{1.66}$. In all of these cases, evaluating powder diffraction data by the Rietveld methods averages over the local effect which caused problems with the refinement this work tries to solve.



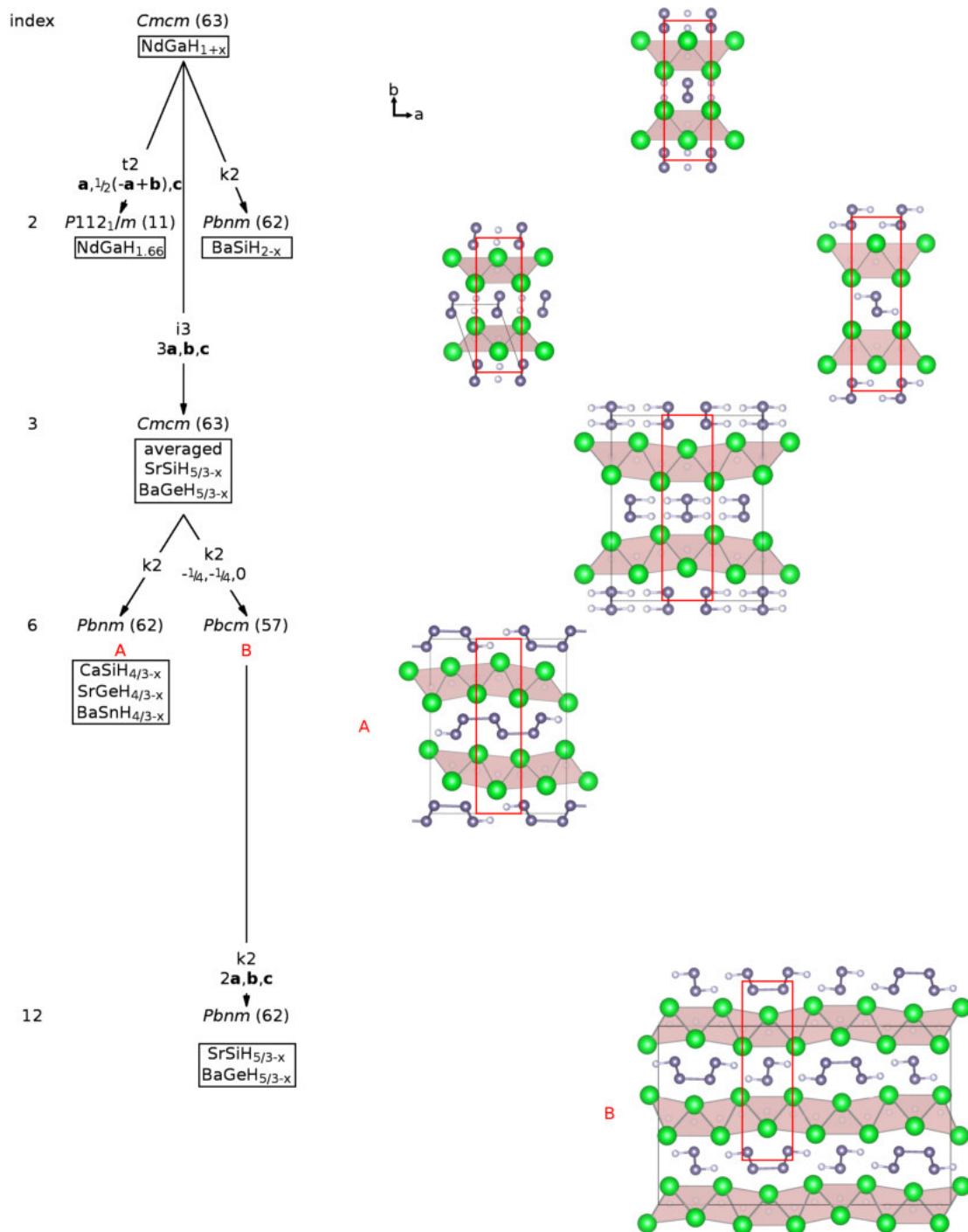
Scheme 6.3: Group-subgroup tree of the CrB-structure type derived hydrides with $Tt\text{H}_3^-$ -anions, $Tt = \text{Si, Ge}$. The A_4 -tetrahedra, $A = \text{Rb, Cs}$, are empty. Large green spheres: A ; medium grey spheres: Tt ; small white spheres: H.



Scheme 6.4: Group-subgroup tree of the hydrogen-poor phases that show tetrahedral-void filling by hydrogen. Large green spheres: A ; medium grey spheres: Tt ; small white spheres: H.



Scheme 6.5: Group-subgroup tree of the hydrogen-rich phases. H^{TV}: hydrogen in a tetrahedral void, H^{ch}: hydrogen coordinating the chain. The averaged crystal structure model of SrSiH_{5/3-x} and BaGeH_{5/3-x} is described by a split-position of the chain-binding hydrogen (H^{ch}). The splitting is indicated in red.



Scheme 6.6: Group-subgroup tree of the hydrogen-rich phases showing projections of the crystal structures. The shaded tetrahedra are filled with hydrogen atoms (H^{TV} according to Scheme 6.5). The unit cell of the aristotype is depicted in red for all structures. Large green spheres: cations; medium grey spheres: anions; small white spheres: H.

7 Conclusion

Hydrogen can act as an oxidizing agent for Zintl phases. The CrB-structure type with linear polyanionic zigzag-chains turned out to be convenient for hydride formation. Hydrogen can be used to oxidize formally metallic Zintl phases $LnTt = Ln^{3+}Tt^{2-}e^{-}$ (Ln = lanthanoid, Tt = tetrel) to electron precise compounds $LnTtH$. Since the metallic states can be associated to the cationic partial structure (Ln -d-states), the polyanion is hardly affected. Furthermore, electron-precise Zintl phases $AeTt = Ae^{2+}Tt^{2-}$ (Ae = alkaline earth metal, Tt = tetrel) can be oxidized. In this case the electronic situation of the polyanion is changed. It can increase its bond order (α - and β - $AeTtH_y$, $y < 1$ with depopulated π^* -states) or its connectivity (γ - $AeTtH_y$, $1 < y < 2$). Considering formally a two-step process, the demand of an additional bond can be satisfied by the formation of a new Tt - Tt -bond (hypothetical $AeTtH$). Then hydrogen can be incorporated into such a bond (oxidative insertion). The ratio of the cation to anion correlates with the amount of hydrogen bound to the polyanion. That leads to a connection of either three or two chains perpendicular to their running direction or even to no additional Tt - Tt bond and a saturation of each Tt by hydrogen. Considering examples from the literature, even a total breakdown into monomeric TtH_3^- is possible ($ASiH_3$, A = alkaline metal). Thus, this work gives examples how hydrogen can be used to systematically increase the bond order or connectivity of polyanions by incorporation of an interstitial hydride anion. Moreover, the polyanion can be truncated by inserting hydrogen into an element-element bond. The hydrogenation of Zintl phases can be used to change their electronic properties. This can be utilized to prepare new motifs of pseudo-elemental structures or pseudo-binary hydrides.

Furthermore, some of the given compounds exhibit a Tt -H bond next to Tt - Tt -bonds. This is the first proper characterisation of a Tt -H distance of a polyanionic hydride in a covalent range. The quadrupolar interaction of deuterium measured by solid state nuclear magnetic resonance is a valuable tool to evaluate the bond lengths. Under the aid of density functional theory calculations this leads to the following values:

- $d(\text{Si-H}) = 155(2)$ pm
- $d(\text{Ge-H}) = 163(2)$ pm
- $d(\text{Sn-H}) = 186(1)$ pm

The established bond lengths are, therefore, about 10% longer than in molecular compounds.

The experimental foundation of the concept of Zintl phase hydrides is, thus, extended. Still, some limitations are obvious. Especially the hydrogen-rich phases exhibiting a Tt -H bond show an under-occupation of hydrogen that does not fit the concept but needs idealisation. An exception from the Zintl concept is $NdGaD_{1+x}$ which shows a large compositional range for hydrogen incorporation from $x = 0.17$ to 0.80. In all cases, the partially occupied hydrogen site bridges two gallium chains exhibiting large Ga-H distances. Although the Zintl concept would predict a covalent bond comparable to the isovalence-electronic $AeTtH_y$, $1 < y < 2$, phases, the coordination within a Nd_3Ga_2 -trigonal bipyramid contradicts such a covalent picture.

In situ studies give mechanistic insight into the formation of Zintl phase hydrides. The $AeTtH_y$, $1 < y < 2$, phases show features of salt-like hydrides, i.e. HAe_4 -tetrahedra, as well as complex hydrides, i.e. a covalent Tt -H bond. These structural motifs relate them to hydrogen storage materials. The combination of them leads to a good reversibility as well as low desorption temperatures. *In situ* studies of the hydrogenation show that the filling of cationic voids is accompanied by the formation of a polyanionic hydride. The low desorption temperatures are typical for complex hydrides. The element-hydrogen bonds break at moderate temperatures. In our case, this goes along with a release of hydrogen from an anionic site which can be traced back to geometrical restrictions of the crystal structure.

The knowledge of the formation of new hydrides, understanding their bonding schemes and the conceptual description are prerequisites for the rational synthesis planning and the search for new functional materials. This work extends our understanding of Zintl phase hydrides in all three fields. It opens perspectives in the synthesis of new compounds containing anionic hydrides and element-hydrogen bonds.

8 Index of crystal structures

Index of crystal structures

Index of crystal structure data given in the articles and manuscripts of Part II.

Methods are: NPD - neutron powder diffraction, XRPD - X-ray powder diffraction, SDP - synchrotron powder diffraction, DFT - density functional theory structure optimised model; DFT does not differentiate between hydrogen or deuterium.

compound	alternative description	method	article	table	page
BaGe		NPD, <i>in situ</i>	A6	A6.S1	180
		NPD, <i>in situ</i>	A6	A6.S2	181
BaGeD _y	y = 0.095(7) α-BaGeD _y	NPD, <i>in situ</i>	A6	A6.S3	182
	y = 0.131(5) α-BaGeD _y	NPD, <i>in situ</i>	A6	A6.1	171
	y = 0.488(12) β-BaGeD _y	NPD, <i>in situ</i>	A6	A6.4	174
	y = 1.61(2) γ-BaGeD _y , averaged model	NPD	A2	A2.S2	98
	y = 5/3 γ-BaGeD _y , ordered model	DFT	A2	A2.S6	103
	y = 1.57(3) γ-BaGeD _y , ordered model	XRPD+NPD	A2	A2.S7	104
BaSiD _y	y = 2 γ-BaSiD _y	DFT	A1	A1.S2	83
	y = 1.87(2) γ-BaSiD _y	NPD	A1	A1.2	72
	y ≈ 1.9 γ-BaSiD _y	SPD	A1	A1.S1	83
BaSn		NPD, <i>in situ</i>	A6	A6.S4	183
BaSnD _y	y = 0.188(4) α-BaSnD _y	NPD, <i>in situ</i>	A6	A6.2	171
	y = 4/3 γ-BaSnD _y	DFT	A1	A1.S4	84
	y = 1.278(2) γ-BaSnD _y	NPD	A1	A1.3	74
CsSiD _y	y = 3.05(3)	NPD, <i>in situ</i>	A7	A7.1	192
	y = 3.22(8)	NPD, <i>in situ</i>	A7	A7.1	192
KSiD _y	y = 3.23(5)	NPD, <i>in situ</i>	A7	A7.1	192
	y = 3.27(7)	NPD, <i>in situ</i>	A7	A7.1	192
LaGeD _y	y = 0.878(9) C-LaGeD _y	NPD	A3	A3.2	114
	y = 0.96(4) P-LaGeD _y	NPD	A3	A3.3	114
LaSi	CrB-type LaSi	DFT	A3	A3.S8	127
	FeB-type LaSi	DFT	A3	A3.S7	127
LaSiD _y	y = 1 C-LaSiD _y	DFT	A3	A3.S10	127
	y = 0.918(11) C-LaSiD _y	NPD	A3	A3.S1	122
	y = 1 P-LaSiD _y	DFT	A3	A3.S9	127
	y = 0.61(3) P-LaSiD _y	NPD	A3	A3.S2	122
LaSnH _y	y ≈ 1 C-LaSnH _y	XRPD	A3	A3.S6	125
NdGa		NPD	U1	U1.S2	210
NdGaD _y	y = 1.137(7)	NPD, <i>in situ</i>	U1	U1.4	208
	y = 1.172(8)	NPD, <i>in situ</i>	U1	U1.S4	212
	y = 1.226(9)	NPD, <i>in situ</i>	U1	U1.S3	211
	y = 1.595(11)	NPD, <i>in situ</i>	U1	U1.2	206
	y = 5/3	NPD, <i>in situ</i>	U1	U1.1	205
NdGeD _y	y = 0.951(13) C-NdGeD _y	NPD	A3	A3.S5	124
NdSiD _y	y = 1 C-NdSiD _y	NPD	A3	A3.S3	123
	y = 0.88(6) P-NdSiD _y	NPD	A3	A3.S4	123

(Index of crystal structures - continued)

Methods are: NPD - neutron powder diffraction, XRPD - X-ray powder diffraction, SDP - synchrotron powder diffraction, DFT - density functional theory structure optimised model; DFT does not differentiate between hydrogen or deuterium.

compound		alternative description	method	article	table	page	
SrGeD _y	y = 0.204(4)	α-SrGeD _y	NPD, <i>in situ</i>	A4	A4.1	139	
	y = 0.53(4)	β-SrGeD _y	NPD, <i>in situ</i>	A4	A4.2	141	
	y = 4/3	γ-SrGeD _y	DFT	A1	A1.S4	84	
	y = 1.197(3)	γ-SrGeD _y	NPD	A1/	A1.3/	74/	
				A4	A4.S1	148	
	y = 1.228(3)	γ-SrGeD _y	NPD	A4	A4.S1	148	
	y = 1.205(4)	γ-SrGeD _y	NPD, <i>in situ</i>	A4	A4.S1	148	
	y = 1.214(4)	γ-SrGeD _y	NPD, <i>in situ</i>	A4	A4.S1	148	
	y = 1.224(3)	γ-SrGeD _y	NPD, <i>in situ</i>	A4	A4.S1	148	
	y ≈ 1.2	γ-SrGeD _y	SPD	A1	A1.S3	83	
	SrSiD _y	y = 1.554(12)	γ-SrSiD _y , averaged model	NPD	A2	A2.S1	97
		y = 5/3	γ-SrSiD _y , ordered model	DFT	A2	A2.S4	102
y = 1.493(14)		γ-SrSiD _y , ordered model	XRPD+NPD	A2	A2.S5	103	

9 References

- (1) Holleman, A. F.; Wiberg, N.; Wiberg, E., *Lehrbuch der Anorganischen Chemie*, 102nd ed.; de Gruyter: 2008.
- (2) Hoffmann, R., *SOLIDS and SURFACES - A Chemist's View of Bonding in Extended Structures*; Wiley-VCH: 1988.
- (3) Schön, J. C.; Jansen, M. *Angew. Chem.* **1996**, *108*, 1358–1377, DOI: 10.1002/ange.19961081204.
- (4) Schön, J. C.; Jansen, M. *Angew. Chem., Int. Ed.* **1996**, *35*, 1286–1304, DOI: 10.1002/anie.199612861.
- (5) Schön, J. C.; Jansen, M. In *Modern Methods of Crystal Structure Prediction*; Wiley-VCH: 2010, pp 67–105, DOI: 10.1002/9783527632831.ch4.
- (6) Schön, J. C.; Doll, K.; Jansen, M. *Phys. Status Solidi B* **2010**, *247*, 23–39, DOI: 10.1002/pssb.200945246.
- (7) Pienack, N.; Bensch, W. *Angew. Chem.* **2011**, *123*, 2062–2083, DOI: 10.1002/ange.201001180.
- (8) Pienack, N.; Bensch, W. *Angew. Chem., Int. Ed.* **2011**, *50*, 2014–2034, DOI: 10.1002/anie.201001180.
- (9) Yang, J.; Muhammad, S.; Jo, M. R.; Kim, H.; Song, K.; Agyeman, D. A.; Kim, Y.-I.; Yoon, W.-S.; Kang, Y.-M. *Chem. Soc. Rev.* **2016**, *45*, 5717–5770, DOI: 10.1039/c5cs00734h.
- (10) *IUPAC Compendium of Chemical Terminology - Gold Book*; Nič, M., Jirát, J., Košata, B., Jenkins, A., McNaught, A., Eds.; IUPAC: 2009, DOI: 10.1351/goldbook.
- (11) Gillespie, R. J.; Nyholm, R. S. *Q. Rev. Chem. Soc.* **1957**, *11*, 339, DOI: 10.1039/qr9571100339.
- (12) Gillespie, R. *Coord. Chem. Rev.* **2008**, *252*, 1315–1327, DOI: 10.1016/j.ccr.2007.07.007.
- (13) Galy, J.; Meunier, G.; Andersson, S.; Åström, A. *J. Solid State Chem.* **1975**, *13*, 142–159, DOI: 10.1016/0022-4596(75)90092-4.
- (14) Matar, S. F.; Galy, J. *Prog. Solid State Chem.* **2015**, *43*, 82–97, DOI: 10.1016/j.progsolidstchem.2015.05.001.
- (15) Galy, J.; Matar, S. F. *Prog. Solid State Chem.* **2016**, *44*, 35–58, DOI: 10.1016/j.progsolidstchem.2016.04.001.
- (16) Fukui, K.; Yonezawa, T.; Shingu, H. *J. Chem. Phys.* **1952**, *20*, 722–725, DOI: 10.1063/1.1700523.
- (17) Fukui, K. *Science* **1982**, *218*, 747–754, DOI: 10.1126/science.218.4574.747.
- (18) Fukui, K., *Frontier Orbitals and Reaction Paths*; Fukui, K., Fujimoto, H., Eds.; WORLD SCIENTIFIC: 1997, DOI: 10.1142/2731.
- (19) Elian, M.; Chen, M. M. L.; Mingos, D. M. P.; Hoffmann, R. *Inorg. Chem.* **1976**, *15*, 1148–1155, DOI: 10.1021/ic50159a034.
- (20) Hoffmann, R. *Angew. Chem., Int. Ed.* **1982**, *21*, 711–724, DOI: 10.1002/anie.198207113.
- (21) Hoffmann, R. *Angew. Chem.* **1987**, *99*, 871–906, DOI: 10.1002/ange.19870990907.
- (22) Hoffmann, R. *Rev. Mod. Phys.* **1988**, *60*, 601–628, DOI: 10.1103/revmodphys.60.601.
- (23) Pearson, R. G. *J. Am. Chem. Soc.* **1963**, *85*, 3533–3539, DOI: 10.1021/ja00905a001.
- (24) Goldschmidt, V. M. *Naturwissenschaften* **1926**, *14*, 477–485, DOI: 10.1007/bf01507527.
- (25) Pauling, L., *The Nature of the Chemical Bond and the Structure of Molecules and Crystals*, 3rd; Cornell University Press: New York, 1960.
- (26) Beck, H. P. *Z. Kristallogr. - Cryst. Mater.* **2014**, *229*, 24–38, DOI: 10.1515/zkri-2013-1705.
- (27) Beck, H. P. *Z. Kristallogr. - Cryst. Mater.* **2014**, *229*, 473–488, DOI: 10.1515/zkri-2014-1735.
- (28) Grimm, H. G.; Sommerfeld, A. *Z. Phys.* **1926**, *36*, 36–59, DOI: 10.1007/bf01383924.
- (29) Hume-Rothery, W. *J. Inst. Met.* **1926**, *35*, 295–361.

- (30) Mooser, E.; Pearson, W. B. *J. Electron. Control* **1956**, *1*, 629–645, DOI: 10.1080/00207215608961467.
- (31) Gingl, F.; Vogt, T.; Akiba, E. *J. Alloys Compd.* **2000**, *306*, 127–132, DOI: 10.1016/S0925-8388(00)00755-6.
- (32) Fahlquist, H.; Noréus, D.; Callear, S.; David, W. I. F.; Hauback, B. C. *J. Am. Chem. Soc.* **2011**, *133*, 14574–14577, DOI: 10.1021/ja2067687.
- (33) Fahlquist, H.; Noréus, D. *Inorg. Chem.* **2013**, *52*, 7125–7129, DOI: 10.1021/ic400714e.
- (34) Fahlquist, H.; Noréus, D.; Sørby, M. H. *Inorg. Chem.* **2013**, *52*, 4771–4773, DOI: 10.1021/ic400224a.
- (35) Häussermann, U.; Kranak, V. F.; Puhakainen, K. *Struct. Bond.* **2010**, *139*, 143–161, DOI: 10.1007/430_2010_20.
- (36) Olson, J. K.; Boldyrev, A. I. *Chem. Phys. Lett.* **2012**, *523*, 83–86, DOI: 10.1016/j.cplett.2011.11.079.
- (37) Zhang, X.; Lundell, K.; Olson, J.; Boldyrev, A.; Bowen, K. H. *Chem. - Eur. J.* **2018**, DOI: 10.1002/chem.201800517.
- (38) Lewis, G. N. *J. Am. Chem. Soc.* **1916**, *38*, 762–785, DOI: 10.1021/ja02261a002.
- (39) Kossel, W. *Ann. Phys.* **1916**, *354*, 229–362, DOI: 10.1002/andp.19163540302.
- (40) Hume-Rothery, W. *Philos. Mag. (1798-1977)* **1930**, *9*, 65–80, DOI: 10.1080/14786443008564982.
- (41) Mooser, E.; Pearson, W. B. *Acta Crystallogr.* **1959**, *12*, 1015–1022, DOI: 10.1107/S0365110X59002857.
- (42) Hulliger, F.; Mooser, E. *J. Phys. Chem. Solids* **1963**, *24*, 283–295, DOI: 10.1016/0022-3697(63)90133-1.
- (43) Pearson, W. B. *Acta Crystallogr.* **1964**, *17*, 1–15, DOI: 10.1107/S0365110X64000019.
- (44) Müller, U., *Anorganische Strukturchemie*, 6th ed.; Vieweg+Teubner: 2008.
- (45) Kjekshus, A. *Acta Chem. Scand.* **1964**, *18*, 2379–2384.
- (46) Zintl, E. *Angew. Chem.* **1939**, *52*, 1–6, DOI: 10.1002/ange.19390520102.
- (47) Schäfer, H.; Eisenmann, B.; Müller, W. *Angew. Chem.* **1973**, *85*, 742–760, DOI: 10.1002/ange.19730851704.
- (48) Schäfer, H. *Annu. Rev. Mater. Sci.* **1985**, *15*, 1–42, DOI: 10.1146/annurev.ms.15.080185.000245.
- (49) Corbett, J. D. *Angew. Chem., Int. Ed.* **2000**, *39*, 670–690, DOI: 10.1002/(SICI)1521-3773(20000218)39:4<670::AID-ANIE670>3.0.CO;2-M.
- (50) Scharfe, S.; Kraus, F.; Stegmaier, S.; Schier, A.; Fässler, T. F. *Angew. Chem., Int. Ed.* **2011**, *50*, 3630–3670, DOI: 10.1002/anie.201001630.
- (51) Nesper, R. *Z. Anorg. Allg. Chem.* **2014**, *640*, 2639–2648, DOI: 10.1002/zaac.201400403.
- (52) *Zintl Phases*; Fässler, T. F., Ed.; Struct. Bond. Vol. 139; Springer Berlin Heidelberg: 2011, DOI: 10.1007/978-3-642-21150-8.
- (53) *Zintl Ions*; Fässler, T. F., Ed.; Springer Berlin Heidelberg: 2011, DOI: 10.1007/978-3-642-21181-2.
- (54) Janka, O.; Kauzlarich, S. M. In *Encyclopedia of Inorganic and Bioinorganic Chemistry*; John Wiley & Sons, Ltd: 2011, DOI: 10.1002/9781119951438.eibc0244.pub2.
- (55) Zintl, E.; Brauer, G. *Z. Phys. Chem.* **1933**, *20B*, 245–71, DOI: 10.1515/zpch-1933-2023.
- (56) Zintl, E.; Dullenkopf, W. *Z. Phys. Chem.* **1932**, *16B*, 195–205, DOI: 10.1515/zpch-1932-1616.
- (57) Zintl, E. *Naturwissenschaften* **1929**, *17*, 782–783, DOI: 10.1007/bf01507600.
- (58) Laves, F. *Naturwissenschaften* **1941**, *29*, 244–255, DOI: 10.1007/bf01479157.
- (59) Wade, K. *J. Chem. Soc. D* **1971**, 792, DOI: 10.1039/c29710000792.

-
- (60) Wade, K. *Inorg. Nucl. Chem. Lett.* **1972**, *8*, 559–562, DOI: 10.1016/0020-1650(72)80141-7.
- (61) Mingos, D. M. P. *Nature, Phys. Sci.* **1972**, *236*, 99–102, DOI: 10.1038/physci236099a0.
- (62) Zintl, E.; Goubeau, J.; Dullenkopf, W. *Z. Phys. Chem.* **1931**, *154A*, 1–46, DOI: 10.1515/zpch-1931-15402.
- (63) Zintl, E.; Harder, A. *Z. Phys. Chem.* **1931**, *154A*, 47–91, DOI: 10.1515/zpch-1931-15403.
- (64) Zintl, E.; Dullenkopf, W. *Z. Phys. Chem.* **1932**, *16B*, DOI: 10.1515/zpch-1932-1615.
- (65) Zintl, E.; Kaiser, H. *Z. Anorg. Allg. Chem.* **1933**, *211*, 113–131, DOI: 10.1002/zaac.19332110113.
- (66) Brauer, G.; Zintl, E. *Z. Phys. Chem.* **1937**, *37B*, DOI: 10.1515/zpch-1937-0125.
- (67) Klemm, W. *Proc. Chem. Soc.* **1958**, 329, DOI: 10.1039/ps9580000329.
- (68) Klemm, W.; Busmann, E. *Z. Anorg. Allg. Chem.* **1963**, *319*, 297–311, DOI: 10.1002/zaac.19633190511.
- (69) Reyes, E. C.; Stalder, E. D.; Mensing, C.; Budnyk, S.; Nesper, R. *J. Phys. Chem. C* **2011**, *115*, 1090–1095, DOI: 10.1021/jp106169h.
- (70) Reyes, E. C.; Nesper, R. *J. Phys. Chem. C* **2012**, *116*, 2536–2542, DOI: 10.1021/jp205825d.
- (71) Harms, W.; Wendorff, M.; Röhr, C. *J. Alloys Compd.* **2009**, *469*, 89–101, DOI: 10.1016/j.jallcom.2008.02.020.
- (72) Kurylyshyn, I. M.; Fässler, T. F.; Fischer, A.; Hauf, C.; Eickerling, G.; Presnitz, M.; Scherer, W. *Angew. Chem., Int. Ed.* **2014**, *53*, 3029–3032, DOI: 10.1002/anie.201308888.
- (73) Dürr, I.; Bauer, B.; Röhr, C. *Z. Naturforsch. B* **2011**, *66*, 1107–1121.
- (74) Häussermann, U. *Z. Kristallogr.* **2008**, *223*, 628–635, DOI: 10.1524/zkri.2008.1016.
- (75) Huang, B.; Corbett, J. D. *Inorg. Chem.* **1997**, *36*, 3730–3734, DOI: 10.1021/ic970289u.
- (76) Orgaz, E.; Aburto, A. *Int. J. Quantum Chem.* **2005**, *101*, 783–792, DOI: 10.1002/qua.20338.
- (77) Lang, D. A.; Lattturner, S. E. *Eur. J. Inorg. Chem.* **2011**, *2011*, 4006–4011, DOI: 10.1002/ejic.201100325.
- (78) Feng, X.-J.; Prots, Y.; Bobnar, M.; Schmidt, M. P.; Schnelle, W.; Zhao, J.-T.; Grin, Y. *Chem. - Eur. J.* **2015**, *21*, 14471–14477, DOI: 10.1002/chem.201501236.
- (79) Peterson, D. T. *JOM* **1987**, *39*, 20–23, DOI: 10.1007/bf03258986.
- (80) Leon-Escamilla, E.; Corbett, J. D. *J. Alloys Compd.* **1994**, *206*, L15–L17, DOI: 10.1016/0925-8388(94)90025-6.
- (81) Leon-Escamilla, E.; Corbett, J. D. *J. Alloys Compd.* **1998**, *265*, 104–114, DOI: 10.1016/s0925-8388(97)00320-4.
- (82) Leon-Escamilla, E.; Corbett, J. D. *J. Solid State Chem.* **2001**, *159*, 149–162, DOI: 10.1006/jssc.2001.9144.
- (83) Leon-Escamilla, E. A.; Corbett, J. D. *Inorg. Chem.* **2001**, *40*, 1226–1233, DOI: 10.1021/ic0010306.
- (84) Leon-Escamilla, E. A.; Corbett, J. D. *Chem. Mater.* **2006**, *18*, 4782–4792, DOI: 10.1021/cm0612191.
- (85) Leon-Escamilla, E. A.; Dervenagas, P.; Stassis, C.; Corbett, J. D. *J. Solid State Chem.* **2010**, *183*, 114–119, DOI: 10.1016/j.jssc.2009.10.024.
- (86) Wu, H.; Zhou, W.; Udovic, T. J.; Rush, J. J.; Yildirim, T.; Hartman, M. R.; Bowman, R. C.; Vajo, J. J. *Phys. Rev. B* **2007**, *76*, 224301, DOI: 10.1103/PhysRevB.76.224301.
- (87) Wu, H.; Hartman, M. R.; Udovic, T. J.; Rush, J. J.; Zhou, W.; Bowman Jr, R. C.; Vajo, J. J. *Acta Crystallogr., Sect. B* **2007**, *63*, 63–68, DOI: 10.1107/s0108768106046465.
- (88) Merlo, F.; Fornasini, M. *J. Less-Common Met.* **1967**, *13*, 603–610, DOI: 10.1016/0022-5088(67)90105-1.

- (89) Henning, R. W.; Leon-Escamilla, E. A.; Zhao, J.-T.; Corbett, J. D. *Inorg. Chem.* **1997**, *36*, 1282–1285, DOI: 10.1021/ic9612966.
- (90) Kranak, V. F.; Benson, D. E.; Wollmann, L.; Mesgar, M.; Shafeie, S.; Grins, J.; Häussermann, U. *Inorg. Chem.* **2015**, *54*, 756–764, DOI: 10.1021/ic501421u.
- (91) Röhr, C. *Z. Anorg. Allg. Chem.* **1995**, *621*, 1496–1500, DOI: 10.1002/zaac.19956210910.
- (92) Huang, B.; Corbett, J. D. *Inorg. Chem.* **1998**, *37*, 1892–1899, DOI: 10.1021/ic971339y.
- (93) Jehle, M.; Hoffmann, A.; Kohlmann, H.; Scherer, H.; Röhr, C. *J. Alloys Compd.* **2015**, *623*, 164–177, DOI: 10.1016/j.jallcom.2014.09.228.
- (94) Boss, M.; Petri, D.; Pickhard, F.; Zönnchen, P.; Röhr, C. *Z. Anorg. Allg. Chem.* **2005**, *631*, 1181–1190, DOI: 10.1002/zaac.200400546.
- (95) Björling, T.; Noréus, D.; Häussermann, U. *J. Am. Chem. Soc.* **2006**, *128*, 817–824, DOI: 10.1021/ja054456y.
- (96) Wenderoth, P.; Kohlmann, H. *Inorg. Chem.* **2013**, *52*, 10525–10531, DOI: 10.1021/ic401480b.
- (97) Wenderoth, P. Untersuchungen zur Hydridbildung von Zintl-Phasen der Erdalkalimetalle mit Aluminium, Gallium und Silicium., Ph.D. Thesis, Saarbrücken: Universität des Saarlandes, 2014.
- (98) Hauback, B.; Brinks, H.; Fjellvåg, H. *J. Alloys Compd.* **2002**, *346*, 184–189, DOI: 10.1016/s0925-8388(02)00517-0.
- (99) Hauback, B.; Brinks, H.; Heyn, R.; Blom, R.; Fjellvåg, H. *J. Alloys Compd.* **2005**, *394*, 35–38, DOI: 10.1016/j.jallcom.2004.10.028.
- (100) Bernert, T.; Krech, D.; Kockelmann, W.; Felderhoff, M.; Frankcombe, T. J.; Weidenthaler, C. *Eur. J. Inorg. Chem.* **2015**, *2015*, 5545–5550, DOI: 10.1002/ejic.201500841.
- (101) Bakum, S.; Irodova, A.; Kuznetsova, S.; Lyakhovitskaya, O.; Nozik, Y.; Somenkov, V. *Koord. Khim.* **1990**, *16*, 1210–1214.
- (102) Björling, T.; Noréus, D.; Jansson, K.; Andersson, M.; Leonova, E.; Edén, M.; Hålenius, U.; Häussermann, U. *Angew. Chem., Int. Ed.* **2005**, *44*, 7269–7273, DOI: 10.1002/anie.200502090.
- (103) Lee, M. H.; Björling, T.; Hauback, B. C.; Utsumi, T.; Moser, D.; Bull, D.; Noréus, D.; Sankey, O. F.; Häussermann, U. *Phys. Rev. B* **2008**, *78*, 195209, DOI: 10.1103/PhysRevB.78.195209.
- (104) Evans, M. J.; Holland, G. P.; Garcia-Garcia, F. J.; Häussermann, U. *J. Am. Chem. Soc.* **2008**, *130*, 12139–12147, DOI: 10.1021/ja803664y.
- (105) Kranak, V. F.; Evans, M. J.; Daemen, L. L.; Proffen, T.; Lee, M. H.; Sankey, O. F.; Häussermann, U. *Solid State Sci.* **2009**, *11*, 1847–1853, DOI: 10.1016/j.solidstatesciences.2009.08.007.
- (106) Evans, M. J.; Kranak, V. F.; Garcia-Garcia, F. J.; Holland, G. P.; Daemen, L. L.; Proffen, T.; Lee, M. H.; Sankey, O. F.; Häussermann, U. *Inorg. Chem.* **2009**, *48*, 5602–5604, DOI: 10.1021/ic9005423.
- (107) Lee, M. H.; Evans, M. J.; Daemen, L. L.; Sankey, O. F.; Häussermann, U. *Inorg. Chem.* **2008**, *47*, 1496–1501, DOI: 10.1021/ic7019318.
- (108) Evans, M. J.; Lee, M. H.; Holland, G. P.; Daemen, L. L.; Sankey, O. F.; Häussermann, U. *J. Solid State Chem.* **2009**, *182*, 2068–2073, DOI: 10.1016/j.jssc.2009.05.023.
- (109) Kurbakova, A.; Leites, L.; Gavrilenko, V.; Karaksin, Y.; Zakharkin, L. *Spectrochim. Acta, Part A* **1975**, *31*, 281–286, DOI: 10.1016/0584-8539(75)80022-5.
- (110) Subedi, A.; Singh, D. *J. Phys. Rev. B* **2008**, *78*, 045106, DOI: 10.1103/PhysRevB.78.045106.
- (111) Gish, J. T.; Popov, I. A.; Boldyrev, A. I. *Chem. - Eur. J.* **2015**, *21*, 5307–5310, DOI: 10.1002/chem.201500298.
- (112) Popov, I. A.; Zhang, X.; Eichhorn, B. W.; Boldyrev, A. I.; Bowen, K. H. *Phys. Chem. Chem. Phys.* **2015**, *17*, 26079–26083, DOI: 10.1039/c5cp04148a.
- (113) Reichert, C. Untersuchungen zu Synthese und Hydrierverhalten von Verbindungen der Triele (B, Al, Ga) mit Lithium und Kalium., Ph.D. Thesis, Saarbrücken: Universität des Saarlandes, 2013.

-
- (114) Ångström, J.; Johansson, R.; Sarkar, T.; Sørby, M. H.; Zlotea, C.; Andersson, M. S.; Nordblad, P.; Scheicher, R. H.; Häussermann, U.; Sahlberg, M. *Inorg. Chem.* **2016**, *55*, 345–352, DOI: 10.1021/acs.inorgchem.5b02485.
- (115) Nedumkandathil, R.; Kranak, V. F.; Johansson, R.; Ångström, J.; Balmes, O.; Andersson, M. S.; Nordblad, P.; Scheicher, R. H.; Sahlberg, M.; Häussermann, U. *J. Solid State Chem.* **2016**, *239*, 184–191, DOI: 10.1016/j.jssc.2016.04.028.
- (116) Ohba, N.; Aoki, M.; Noritake, T.; Miwa, K.; Towata, S.-i. *Phys. Rev. B* **2005**, *72*, 075104, DOI: 10.1103/PhysRevB.72.075104.
- (117) Wu, H.; Zhou, W.; Udovic, T. J.; Rush, J. J.; Yildirim, T. *Phys. Rev. B* **2006**, *74*, 224101, DOI: 10.1103/PhysRevB.74.224101.
- (118) Armbruster, M. M. Reaktionen von Wasserstoff mit Zintl-Phasen., Ph.D. Thesis, Zürich: Eidgenössische Technische Hochschule (ETH) Zürich, 2008, DOI: 10.3929/ethz-a-005645188.
- (119) Armbruster, M.; Wörle, M.; Krumeich, F.; Nesper, R. *Z. Anorg. Allg. Chem.* **2009**, *635*, 1758–1766, DOI: 10.1002/zaac.200900220.
- (120) Ring, M. A.; Ritter, D. M. *J. Am. Chem. Soc.* **1961**, *83*, 802–805, DOI: 10.1021/ja01465a013.
- (121) Amberger, E.; Römer, R.; Layer, A. *J. Organomet. Chem.* **1968**, *12*, 417–423, DOI: 10.1016/S0022-328X(00)88694-5.
- (122) Lobreyer, T.; Oeler, J.; Sundermeyer, W. *Chem. Ber.* **1991**, *124*, 2405–2410, DOI: 10.1002/cber.19911241105.
- (123) Emeleus, H. J.; Mackay, K. M. *J. Chem. Soc.* **1961**, 2676–2680, DOI: 10.1039/JR9610002676.
- (124) Thirase, G.; Weiss, E. *Z. Naturforsch., B* **1974**, *29*, 800.
- (125) Thirase, G.; Weiss, E.; Hennig, H. J.; Lechert, H. *Z. Anorg. Allg. Chem.* **1975**, *417*, 221–228, DOI: 10.1002/zaac.19754170306.
- (126) Chotard, J.-N.; Tang, W. S.; Raybaud, P.; Janot, R. *Chem. - Eur. J.* **2011**, *17*, 12302–12309, DOI: 10.1002/chem.201101865.
- (127) Tang, W. S.; Chotard, J.-N.; Raybaud, P.; Janot, R. *J. Phys. Chem. C* **2014**, *118*, 3409–3419, DOI: 10.1021/jp411314w.
- (128) Neumeier, M.; Fendt, F.; Gärtner, S.; Koch, C.; Gärtner, T.; Korber, N.; Gschwind, R. M. *Angew. Chem., Int. Ed.* **2013**, *52*, 4483–4486, DOI: 10.1002/anie.201209578.
- (129) Leich, V.; Spaniol, T. P.; Okuda, J. *Chem. Commun.* **2015**, *51*, 14772–14774, DOI: 10.1039/C5CC06187C.
- (130) Tang, W. S.; Chotard, J.-N.; Janot, R. *J. Electrochem. Soc.* **2013**, *160*, A1232–A1240, DOI: 10.1149/2.089308jes.
- (131) Tang, W. S.; Chotard, J.-N.; Raybaud, P.; Janot, R. *Phys. Chem. Chem. Phys.* **2012**, *14*, 13319, DOI: 10.1039/c2cp41589e.
- (132) Amberger, E.; Mühlhofer, E. *J. Organomet. Chem.* **1968**, *12*, 55–62, DOI: 10.1016/s0022-328x(00)90897-0.
- (133) Ring, M. A.; Ritter, D. M. *J. Phys. Chem.* **1961**, *65*, 182–183, DOI: 10.1021/j100819a506.
- (134) Österberg, C.; Fahlquist, H.; Häussermann, U.; Brown, C. M.; Udovic, T. J.; Karlsson, M. *J. Phys. Chem. C* **2016**, *120*, 6369–6376, DOI: 10.1021/acs.jpcc.6b00363.
- (135) Nedumkandathil, R.; Jaworski, A.; Fischer, A.; Österberg, C.; Lin, Y.-C.; Karlsson, M.; Grins, J.; Pell, A. J.; Edén, M.; Häussermann, U. *J. Phys. Chem. C* **2017**, *121*, 5241–5252, DOI: 10.1021/acs.jpcc.6b12902.
- (136) Wolstenholme, D. J.; Prince, P. D.; McGrady, G. S.; Landry, M. J.; Steed, J. W. *Inorg. Chem.* **2011**, *50*, 11222–11227, DOI: 10.1021/ic201774x.
- (137) Teng, W.; Allis, D.; Ruhlandt-Senge, K. *Chem. - Eur. J.* **2007**, *13*, 1309–1319, DOI: 10.1002/chem.200601073.
- (138) Mundt, O.; Becker, G.; Hartmann, H.-M.; Schwarz, W. *Z. Anorg. Allg. Chem.* **1989**, *572*, 75–88, DOI: 10.1002/zaac.19895720109.

- (139) Weiss, E.; Hencken, G.; Kühr, H. *Chem. Ber.* **1970**, *103*, 2868–2872, DOI: 10.1002/cber.19701030924.
- (140) Dong, Z.-C.; Corbett, J. D. *Inorg. Chem.* **1995**, *34*, 5709–5710, DOI: 10.1021/ic00127a005.
- (141) Kocak, F. S.; Downing, D. O.; Zavalij, P.; Lam, Y.-F.; Vedernikov, A. N.; Eichhorn, B. *J. Am. Chem. Soc.* **2012**, *134*, 9733–9740, DOI: 10.1021/ja3018797.
- (142) Kauzlarich, S. M.; Brown, S. R.; Snyder, G. J. *Dalton Trans.* **2007**, 2099, DOI: 10.1039/b702266b.
- (143) Brehm, J. A. *J. Mater. Chem. C* **2018**, DOI: 10.1039/c7tc04091a.
- (144) Ohba, N.; Aoki, M.; Noritake, T.; Miwa, K.; Towata, S.-i. *R&D Review of Toyota CRDL* **2004**, *39*, 40–45.
- (145) Aoki, M.; Ohba, N.; Noritake, T.; Towata, S. *Appl. Phys. Lett.* **2004**, *85*, 387–388, DOI: 10.1063/1.1773930.
- (146) Aoki, M.; Ohba, N.; Noritake, T.; Towata, S.-i. *J. Alloys Compd.* **2005**, *404*, 402–404, DOI: 10.1016/j.jallcom.2004.11.104.
- (147) Miyoshi, M.; Kinoshita, K.; Aoki, M.; Ohba, N.; Miwa, K.; Noritake, T.; Towata, S. *J. Alloys Compd.* **2007**, *446–447*, 15–18, DOI: 10.1016/j.jallcom.2006.11.196.
- (148) Zhu, Y.; Zhang, W.; Hua, F.; Li, L. *J. Alloys Compd.* **2009**, *485*, 439–443, DOI: 10.1016/j.jallcom.2009.05.130.
- (149) Zhang, J.; Yan, S.; Qu, H.; Yu, X.; Peng, P. *Int. J. Hydrogen Energy* **2017**, *42*, 12405–12413, DOI: 10.1016/j.ijhydene.2017.03.132.
- (150) Yang, F. Synthese, Hydrierung und Deuterierung der Zintl phase CaSi., Bachelor’s thesis, Leipzig: Universität Leipzig, 2017.
- (151) Bärnighausen, H. *MATCH: Commun. Math. Comput. Chem.* **1980**, *9*, 139–175.
- (152) Hansen, T. C.; Henry, P. F.; Fischer, H. E.; Torregrossa, J.; Convert, P. *Meas. Sci. Technol.* **2008**, *19*, 034001.
- (153) Töbrens, D.; Stüßer, N.; Knorr, K.; Mayer, H.; Lampert, G. *Mater. Sci. Forum* **2001**, *378–381*, 288–293.
- (154) Rietveld, H. M. *Acta Crystallogr.* **1967**, *22*, 151–152, DOI: 10.1107/S0365110X67000234.
- (155) Rietveld, H. M. *J. Appl. Crystallogr.* **1969**, *2*, 65–71, DOI: 10.1107/S0021889869006558.
- (156) Rodríguez-Carvajal, J. *Phys. B* **1993**, *192*, 55–69, DOI: 10.1016/0921-4526(93)90108-I.
- (157) Rodríguez-Carvajal, J. FULLPROF (version 5.30): A Program for Rietveld Refinement and Pattern Matching Analysis; Institut Laue-Langevin, Grenoble (France)., 2012.
- (158) Bruker AXS, TOPAS[®] version 5, www.bruker-axs.com.
- (159) Momma, K.; Izumi, F. *J. Appl. Crystallogr.* **2011**, *44*, 1272–1276, DOI: 10.1107/S0021889811038970.
- (160) VESTA - Visualisation for Electronic and Structural Analysis, version 3.3.1.
- (161) Mkhari, O. Synthesis of poly-GeH_x(D_x), SiH_x(D_x) by hydrolysis of their Zintl phases and hydrides/deuterides Zintl phases., Practical course, Leipzig: Universität Leipzig, 2016.
- (162) <http://www.abinit.org>, Abinit v. 8.2.2, GNU General Public License.
- (163) Gonze, X. et al. *Comput. Mater. Sci.* **2002**, *25*, 478–492, DOI: 10.1016/S0927-0256(02)00325-7.
- (164) Gonze, X. *Z. Kristallogr.* **2005**, *220*, DOI: 10.1524/zkri.220.5.558.65066.
- (165) Gonze, X. et al. *Comput. Phys. Commun.* **2009**, *180*, 2582–2615, DOI: 10.1016/j.cpc.2009.07.007.
- (166) Gonze, X. et al. *Comput. Phys. Commun.* **2016**, *205*, 106–131, DOI: 10.1016/j.cpc.2016.04.003.

-
- (167) <http://www.quantum-espresso.org>, QUANTUM ESPRESSO v. 5.1.2, , GNU General Public License.
- (168) Giannozzi, P. et al. *J. Phys.: Condens. Matter* **2009**, *21*, 395502.
- (169) Perdew, J. P.; Burke, K.; Ernzerhof, M. *Phys. Rev. Lett.* **1996**, *77*, 3865–3868, DOI: 10.1103/physrevlett.77.3865.
- (170) Blöchl, P. E. *Phys. Rev. B* **1994**, *50*, 17953–17979, DOI: 10.1103/physrevb.50.17953.
- (171) <https://www.abinit.org/downloads/PAW2>, JTH PAW atomic datasets, version 1.0.
- (172) Jollet, F.; Torrent, M.; Holzwarth, N. *Comput. Phys. Commun.* **2014**, *185*, 1246–1254, DOI: 10.1016/j.cpc.2013.12.023.
- (173) <http://www.qe-forge.org/gf/project/pslibrary>, version 0.3.1.
- (174) Monkhorst, H. J.; Pack, J. D. *Phys. Rev. B* **1976**, *13*, 5188–5192, DOI: 10.1103/physrevb.13.5188.
- (175) Bishop, D. M.; Cheung, L. M. *Phys. Rev. A* **1979**, *20*, 381–384, DOI: 10.1103/physreva.20.381.
- (176) Stone, N. *At. Data Nucl. Data Tables* **2005**, *90*, 75–176, DOI: 10.1016/j.adt.2005.04.001.
- (177) Hansen, T. C.; Kohlmann, H. *Z. Anorg. Allg. Chem.* **2014**, *640*, 3044–3063, DOI: 10.1002/zaac.201400359.
- (178) Möller, K. T.; Hansen, B. R. S.; Dippel, A.-C.; Jørgensen, J.-E.; Jensen, T. R. *Z. Anorg. Allg. Chem.* **2014**, *640*, 3029–3043, DOI: 10.1002/zaac.201400262.
- (179) Kohlmann, H.; Kurtzemann, N.; Wehrich, R.; Hansen, T. *Z. Anorg. Allg. Chem.* **2009**, *635*, 2399–2405, DOI: 10.1002/zaac.200900336.
- (180) Kohlmann, H.; Auer, H.; Götze, A.; Hansen, T.; Weber, S. Reaction pathways to the Zintl phase hydrides CaSiH and MGeH_x (M = Sr, Ba)., Institut Laue-Langevin, 2015, DOI: 10.5291/ILL-DATA.5-22-734.
- (181) Kohlmann, H.; Auer, H.; Götze, A.; Hansen, T.; Werwein, A. Formation and decomposition of deuterides of the Zintl phases KSi and CsGe., Institut Laue-Langevin, 2015, DOI: 10.5291/ILL-DATA.5-21-1096.
- (182) Kohlmann, H.; Auer, H.; Götze, A.; Hansen, T.; Werwein, A. Reaction pathways to the Zintl phase hydride NdGaD_{1.66} by *in situ* neutron diffraction., Institut Laue-Langevin, 2016, DOI: 10.5291/ill-data.5-24-576.
- (183) Többens, D. M.; Zander, S. *Journal of large-scale research facilities* **2016**, *2*, A49, DOI: 10.17815/jlsrf-2-65.
- (184) Jensen, T. R.; Nielsen, T. K.; Filinchuk, Y.; Jørgensen, J.-E.; Cerenius, Y.; Gray, E. M.; Webb, C. J. *J. Appl. Crystallogr.* **2010**, *43*, 1456–1463, DOI: 10.1107/S0021889810038148.
- (185) Hibble, S. J.; Hannon, A. C.; Fawcett, I. D. *J. Phys.: Condens. Matter* **1999**, *11*, 9203–9219, DOI: 10.1088/0953-8984/11/47/307.
- (186) Billinge, S. J. L.; Levin, I. *Science* **2007**, *316*, 561–565, DOI: 10.1126/science.1135080.
- (187) <http://www.cohp.de/>, LOBSTER version 2.1.0.
- (188) Maintz, S.; Deringer, V. L.; Tchougréeff, A. L.; Dronskowski, R. *J. Comput. Chem.* **2016**, *37*, 1030–1035, DOI: 10.1002/jcc.24300.
- (189) Dronskowski, R.; Blöchl, P. E. *J. Phys. Chem.* **1993**, *97*, 8617–8624, DOI: 10.1021/j100135a014.
- (190) Zhao, J.-T.; Seo, D.-K.; Corbett, J. D. *J. Alloys Compd.* **2002**, *334*, 110–117, DOI: 10.1016/S0925-8388(01)01784-4.
- (191) Harms, W. F. Polare intermetallische Phasen AM und AM_2 (A = Ca, Sr, Ba; M = Ga, In, Zn, Cd, Hg, Cu, Ag, Au) - Kristallchemie, chemische Bindung und Eigenschaften., Ph.D. Thesis, Freiburg: Albert-Ludwigs-Universität Freiburg, 2008.

- (192) Bohmhammel, K.; Henneberg, E. *Solid State Ionics* **2001**, *141-142*, 599–602, DOI: 10.1016/S0167-2738(01)00774-3.
- (193) Henneberg, E. Thermodynamische und kinetische Untersuchung im System La-Si-H-(Cl)., Ph.D. Thesis, Freiberg: Technische Universität Bergakademie Freiberg, 2003.
- (194) Westlake, D. *J. Less-Common Met.* **1980**, *75*, 177–185, DOI: 10.1016/0022-5088(80)90115-0.
- (195) Westlake, D.; Shaked, H.; Mason, P.; McCart, B.; Mueller, M.; Matsumoto, T.; Amano, M. *J. Less-Common Met.* **1982**, *88*, 17–23, DOI: 10.1016/0022-5088(82)90005-4.
- (196) Bronger, W. *Z. Anorg. Allg. Chem.* **1996**, *622*, 9–16, DOI: 10.1002/zaac.19966220103.
- (197) Xie, Q.-X.; Nesper, R. *Z. Kristallogr. - New Cryst. Struct.* **2003**, *218*, 291–292, DOI: 10.1524/ncrs.2003.218.3.291.
- (198) Aronsson, B.; Stenberg, E.; Åselius, J. *Nature* **1962**, *195*, 377–378, DOI: 10.1038/195377a0.
- (199) Roof, R. B.; Kempter, C. P. *J. Chem. Phys.* **1962**, *37*, 1473–1476, DOI: 10.1063/1.1733309.
- (200) Frotscher, M.; Hölzel, M.; Albert, B. *Z. Anorg. Allg. Chem.* **2010**, *636*, 1783–1786, DOI: 10.1002/zaac.201000101.
- (201) Maley, I. J.; Brown, D. H.; Ibberson, R. M.; Pulham, C. R. *Acta Crystallogr., Sect. B* **2008**, *64*, 312–317, DOI: 10.1107/S0108768108010379.
- (202) Beagley, B.; Conrad, A.; Freeman, J.; Monaghan, J.; Norton, B.; Holywell, G. *J. Mol. Struct.* **1972**, *11*, 371–380, DOI: 10.1016/0022-2860(72)85004-x.
- (203) Kranak, V. F.; Lin, Y.-C.; Karlsson, M.; Mink, J.; Norberg, S. T.; Häussermann, U. *Inorg. Chem.* **2015**, *54*, 2300–2309, DOI: 10.1021/ic502931e.
- (204) Currao, A.; Curda, J.; Nesper, R. *Z. Anorg. Allg. Chem.* **1996**, *622*, 85–94, DOI: 10.1002/zaac.19966220113.
- (205) Lähteenmäki, U.; Niemelä, L.; Pyykkö, P. *Phys. Lett. A* **1967**, *25*, 460–461, DOI: 10.1016/0375-9601(67)90080-1.
- (206) Ader, R.; Loewenstein, A. *Mol. Phys.* **1974**, *27*, 1113–1116, DOI: 10.1080/00268977400100991.
- (207) Fung, B.-M.; Wei, I. Y. *J. Am. Chem. Soc.* **1970**, *92*, 1497–1501, DOI: 10.1021/ja00709a009.
- (208) Brockway, L. O.; Beach, J. Y. *J. Am. Chem. Soc.* **1938**, *60*, 1836–1846, DOI: 10.1021/ja01275a036.
- (209) Wang, X.; Andrews, L. *J. Am. Chem. Soc.* **2003**, *125*, 6581–6587, DOI: 10.1021/ja0298621.
- (210) Robietti, A.; Thompson, J. *Spectrochim. Acta* **1965**, *21*, 2023–2030, DOI: 10.1016/0371-1951(65)80219-3.
- (211) Royen, P.; Schwarz, R. *Z. Anorg. Allg. Chem.* **1933**, *211*, 412–422, DOI: 10.1002/zaac.19332110409.
- (212) Vogg, G.; Brandt, M. S.; Stutzmann, M. *Adv. Mater.* **2000**, *12*, 1278–1281, DOI: 10.1002/1521-4095(200009)12:17<1278::aid-adma1278>3.0.co;2-y.
- (213) Vogg, G.; Meyer, L. J.-P.; Miesner, C.; Brandt, M. S.; Stutzmann, M. *Monatsh. Chem.* **2001**, *132*, 1125–1135, DOI: 10.1007/s007060170028.
- (214) Bianco, E.; Butler, S.; Jiang, S.; Restrepo, O. D.; Windl, W.; Goldberger, J. E. *ACS Nano* **2013**, *7*, 4414–4421, DOI: 10.1021/nn4009406.
- (215) Waibel, M.; Raudaschl-Sieber, G.; Fässler, T. F. *Chem. - Eur. J.* **2011**, *17*, 13391–13394, DOI: 10.1002/chem.201102095.
- (216) Imai, Y.; Watanabe, A. *J. Alloys Compd.* **2009**, *478*, 754–757, DOI: 10.1016/j.jallcom.2008.11.149.
- (217) Fornasini, M. L. *Acta Crystallogr., Sect. C* **1983**, *39*, 943–946, DOI: 10.1107/S0108270183006940.
- (218) Janzon, K. H.; Schäfer, H.; Weiss, A. *Z. Anorg. Allg. Chem.* **1970**, *372*, 87–99, DOI: 10.1002/zaac.19703720110.

-
- (219) Evers, J.; Weiss, A. *Mater. Res. Bull.* **1974**, *9*, 549–553, DOI: 10.1016/0025-5408(74)90124-x.
- (220) Migas, D. B.; Shaposhnikov, V. L.; Borisenko, V. E. *Phys. Status Solidi B* **2007**, *244*, 2611–2618, DOI: 10.1002/pssb.200642556.
- (221) Imai, M. *Phys. Status Solidi C* **2013**, *10*, 1728–1731, DOI: 10.1002/pssc.201300375.
- (222) Böhm, J.; Hassel, O. *Z. Anorg. Allg. Chem.* **1927**, *160*, 152–164, DOI: 10.1002/zaac.19271600115.
- (223) Janzon, K. H.; Schäfer, H.; Weiss, A. *Z. Naturforsch., B* **1968**, *23*, 1544.
- (224) Dick, S.; Öhlinger, G. *Z. Kristallogr. - New Cryst. Struct.* **1998**, *213*, DOI: 10.1524/ncrs.1998.213.14.246.
- (225) Nedumkandathil, R.; Benson, D. E.; Grins, J.; Spektor, K.; Häussermann, U. *J. Solid State Chem.* **2015**, *222*, 18–24, DOI: 10.1016/j.jssc.2014.10.033.
- (226) Tang, W. S.; Dimitrievska, M.; Chotard, J.-N.; Zhou, W.; Janot, R.; Skripov, A. V.; Udovic, T. J. *J. Phys. Chem. C* **2016**, *120*, 21218–21227, DOI: 10.1021/acs.jpcc.6b06591.
- (227) Böhme, B.; Guloy, A.; Tang, Z.; Schnelle, W.; Burkhardt, U.; Baitinger, M.; Grin, Y. *J. Am. Chem. Soc.* **2007**, *129*, 5348–5349, DOI: 10.1021/ja0705691.
- (228) Kemmesies, P. Untersuchung von Alkali-Silizium-Zintl-Phasen mit Germaniummischbesetzungen, und deren Verhalten bei Hydrierung., Practical course, Leipzig: Universität Leipzig, 2017.
- (229) Gelato, L. M.; Parthé, E. *J. Appl. Crystallogr.* **1987**, *20*, 139–143, DOI: 10.1107/s0021889887086965.

Part II

Published articles and unpublished results

A1 Hydrides of alkaline earth-tetrel (*AeTt*) Zintl phases: covalent *Tt*-H bonds from silicon to tin

Henry Auer^a, Robin Guehne^b, Marko Bertmer^b, Sebastian Weber^a, Patrik Wenderoth^c, Thomas Christian Hansen^d, Jürgen Haase^b, Holger Kohlmann^{a*}

^a *Leipzig University, Department of Inorganic Chemistry, Johannisallee 29, 04103 Leipzig, Germany*

^b *Leipzig University, Department of Experimental Physics II, Linnéestraße 5, 04103 Leipzig, Germany*

^c *Saarland University, Department of Inorganic Solid-State Chemistry, Am Markt, Zeile 3, 66125 Saarbrücken, Germany*

^d *Institut Laue-Langevin, 71 Avenue des Martyrs, CS 20156, 38042 Grenoble cedex 9, France*

* *Corresponding author*

— Dedicated to Prof. Lothar Beyer on the occasion of his 80th birthday. —

Reprinted with permission from

H. Auer, R. Gühne, M. Bertmer, S. Weber, P. Wenderoth, T. C. Hansen, J. Haase, H. Kohlmann, *Inorg. Chem.* **2017**, *56*, 1061-1071. DOI:10.1021/acs.inorgchem.6b01944

© 2017 American Chemical Society.

This is the accepted version with minor adaptations for use with L^AT_EX and one column printing.

A1.1 Authors' contributions

The synthesis of BaSi and its deuteride was done by P. Wenderoth and a preliminary crystal structure was given in his PhD thesis^a. The reactivity of SrGe and BaSn towards hydrogen were shown by H. Auer. He also prepared the deuteride of SrGe for neutron diffraction. S. Weber then investigated the reactivity of the stannides and plumbides towards hydrogen in detail in course of his B.Sc. thesis^b. He also prepared a deuterided sample of BaSnD_y for neutron diffraction. The neutron diffraction experiments were done by H. Kohlmann, H. Auer and S. Weber. T. Hansen assisted during the neutron beamtime. H. Auer did the final evaluation of all the diffraction data and the quantum chemical modelling. H. Kohlmann supervised the diffraction part of this work. Solid state nuclear magnetic resonance measurements (SSNMR) were done and evaluated by R. Guehne. M. Bertmer and J. Haase supervised the SSNMR part of the work.

The manuscript was mainly written and edited by H. Auer. R. Guehne provided the text concerning SSNMR data and interpretation. This part was revised edited by M. Bertmer and J. Haase. H. Kohlmann revised the whole manuscript.

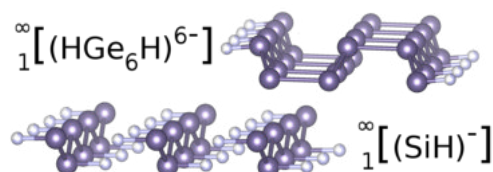
Some further minor contributions are given in the acknowledgements.

^a Wenderoth, P. *Untersuchungen zur Hydridbildung von Zintl-Phasen der Erdalkalimetalle mit Aluminium, Gallium und Silicium*, PhD thesis, Saarbrücken: Universität des Saarlandes, 2014.

^b Weber, S. *Synthese und Untersuchung der Reaktivität der Zintl-Phasen EaTt mit Ea = Sr, Ba und Tt = Sn, Pb gegenüber Wasserstoff*, Bachelor's thesis, Leipzig: Universität Leipzig, 2015.

A1.2 Abstract

Zintl phases form hydrides either by incorporating hydride anions (interstitial hydrides) or by covalent bonding of hydrogen to the polyanion (polyanionic hydrides), which yields a variety of different compositions and bonding situations. Hydrides (deuterides) of SrGe, BaSi and BaSn were prepared by hydrogenation (deuteration) of the CrB-type Zintl phases *AeTt* and characterized by laboratory X-ray, synchrotron and neutron diffraction, NMR spectroscopy and quantum chemical calculations. SrGeD_{4/3-x} and BaSnD_{4/3-x} show condensed boat-like six-membered rings of *Tt* atoms, formed by joining three of the zig-zag chains contained in the Zintl phase. These new polyanionic motifs are terminated by covalently bound hydrogen atoms with $d(\text{Ge-D}) = 1.521(9) \text{ \AA}$ and $d(\text{Sn-D}) = 1.858(8) \text{ \AA}$. Additional hydride anions are located in Ae_4 tetrahedra, thus both features of interstitial hydrides and of polyanionic hydrides are represented. BaSiD_{2-x} retains the zig-zag Si-chain as in the parent Zintl phase, but in the hydride (deuteride) it is terminated by hydrogen (deuterium) atoms, thus forming a linear (SiD)-chain with $d(\text{Si-D}) = 1.641(5) \text{ \AA}$.



A1.3 Article

Introduction

Zintl phases are polar intermetallic compounds of a group one or two metal and a group 13 to 16 element. According to the Zintl-Klemm concept[1–7] the more electronegative element forms polyanionic partial structures that resemble features of the formally isoelectronic element structure, e.g., CrB-structure type Zintl phases $AeTt$, $Ae = \text{Ca-Ba}$, $Tt = \text{Si-Pb}$, form linear $\infty[Tt^{2-}]$ zig-zag chains like in chalcogens.

The reactions of hydrogen with Zintl phases have only recently started to be explored systematically. According to Häussermann two general types of Zintl phase hydrides may be distinguished: (i) interstitial hydrides, where ionic hydride (H^-) is coordinated by the cationic framework exclusively and (ii) polyanionic hydrides, where hydrogen binds covalently to the Zintl polyanion [8].

Gallium shows a rich chemistry of polyanionic hydrides that can be rationalized by an extended Zintl concept, e.g., it forms neopentane-like $(\text{Ga}[\text{GaH}_3]_4)^{5-}$ [9], propane-like $(\text{Ga}_3\text{H}_8)^{3-}$ [10], or polyethylene-like $([\text{GaH}_2]_n)^{n-}$ structures [9, 11]. The Zintl phases $AeTr_2$, $Ae = \text{Sr, Ba}$, $Tr = \text{Al, Ga}$ react with hydrogen (deuterium) to form $AeTr_2\text{H}_2$, which show hydrogen (deuterium) puckered Tr honeycomb layers (6^3 nets) [12–14]. This can be rationalized since $(Tr\text{H})^-$ has the same valence electron configuration as polysilicon hydride $(\text{SiH})_\infty$.

While Zintl phases containing group 13 elements show a strong trend in forming polyanionic hydrides, the existence of such motifs for group 14 elements is still under discussion. Covalent Si-H bonds could be shown for ASiH_3 , $A = \text{K-Cs}$, but the tetrahedral Si_4^{4-} units of the parent phases ASi are broken up and we find isolated SiH_3^- -groups [15–18]. The Zintl phase Ba_3Si_4 that shows distorted butterfly tetrahedral $(\text{Si}^{2-})_2(\text{Si}^-)_2$ -polyanions behaves differently forming an interstitial hydride [19]. The mixed compounds $AeTrTt$, $Ae = \text{Ca-Ba}$, $Tr = \text{Al, Ga, (In)}$, $Tt = \text{Si-Sn}$, that are electronically imbalanced Zintl phases, form electron precise polyanionic hydrides $Ae(Tr\text{H})Tt$, where hydrogen only binds to the group 13 element [20–23].

Most promising candidates for polyanionic hydrides of group 14 are the phases derived from CrB-structure type Zintl phases. Early work by Ohba *et al.* claimed covalently bound hydrogen in $\text{CaSiH}_{1.3}$ next to hydride filled tetrahedral Ca_4 -voids [24]. This was denied by Wu *et al.* relying on neutron vibrational spectroscopy as well as neutron diffraction data [25]. Since then a couple of similar hydride (deuteride) phases were described, e.g., $\text{SrSiH}_{1.6}$ and $\text{BaSiH}_{3.4}$ [26, 27], as well as $\text{NdGaH}_{1.66}$ [28] and GdGaH_x [29].

In this contribution we reinvestigate the barium compound and classify it as BaSiH_{2-x} . We also show the existence of two new hydride phases $\text{SrGeH}_{4/3-x}$ and $\text{BaSnH}_{4/3-x}$. SrSn does not show any reactivity towards hydrogen, while SrPb and BaPb decompose into $\text{SrH}_2 + \text{SrPb}_3$ and $\text{BaH}_2 + \text{Ba}_3\text{Pb}_5$. There are at least two additional hydrogen (deuterium) poor phases in the SrGe-H_2 system, which will be discussed in a forthcoming paper [30]. Therefore, as it is the hydrogen (deuterium) richest compound, $\text{SrGeH}_{4/3-x}$ will alternatively be called $\gamma\text{-SrGeH}_y$. A combination of diffraction methods (laboratory X-ray, synchrotron and neutron), solid-state nuclear magnetic resonance spectroscopy as well as quantum chemical calculations strongly suggest a covalent bond between Si/Ge/Sn and hydrogen (deuterium) and therefore show the first examples for well established polyanionic hydrides of the tetrrels.

Experimental Section

Synthesis

All manipulations were done in an argon filled glovebox. Oxygen and moisture content were both monitored and kept below 1 ppm.

BaSi was prepared from the elements (Si: ChemPur, 99.9999%; Ba rod: 99.3%) in an electric arc furnace. A 5% barium excess was used to compensate the evaporation of alkaline earth metal. Samples were remelted several times to improve homogeneity. SrGe was prepared from the elements (Ge: ChemPur, 99.9999%; Sr: ChemPur, 99%, under oil, washed in dry hexane) in welded niobium or tantalum jackets sealed in quartz ampules. The sample was melted at 1560 K and annealed at 1370 K for 48 h. As tin and lead react with the niobium or tantalum, for the other samples steel jackets were used. BaSn and SrSn were prepared from the elements (Sn powder: ChemPur, 99+%; Ba, Sr: as above). They were annealed at 1270 K for 48 h, then ground and annealed at 1270 K for 48 h again. BaPb and SrPb were prepared from the elements (Pb powder: Alfa Aesar, 99.95%; Ba, Sr: as above). They decompose peritectically

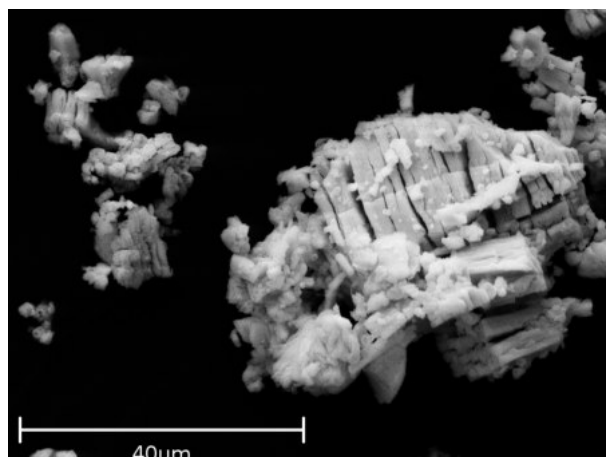


Figure A1.1: Scanning electron microscope (secondary electron detector) picture of $BaSnD_{4/3-x}$. The crystals are brittle and easily cleave to form plates.

Table A1.1: Hydrogenation conditions for Zintl phases $AeTt$, $Ae = Sr, Ba$; $Tt = Si-Pb$. Deuterides were prepared under the same conditions.

Sample	H_2 -pressure/ bar	temperature/ K	time/ h	hydride	molar content by EDX	
					Ae	Tt
BaSi	90	450	24	$BaSiH_{2-x}$	51(3)%	48(3)% ^a
SrGe	50	470	10	$SrGeH_{4/3-x}$	47(2)%	53(2)% ^a
SrSn	50	720	10	no reaction		
BaSn	50	470	10	$BaSnH_{4/3-x}$	51.5(7)%	48.5(7)% ^b
SrPb	50	550	2	decomposition to $SrPb_3 + SrH_2$		
BaPb	50	570	2	decomposition to $Ba_3Pb_5 + BaH_2$		

^a TEM-EDX

^b SEM-EDX

and thus they were melted at 1270 K and quenched in cold water. Subsequently, SrPb was annealed at 970 K for 48 h and BaPb was annealed at 1010 K for 48 h.

Hydrides (H_2 : Air Liquide, 99.9%) and deuterides (D_2 : Air Liquide, 99.8% isotope purity) of BaSi, SrGe and BaSn were prepared using an autoclave made from hydrogen resistant Nicrofer[®] 5219Nb-alloy 718. Tab. A1.1 summarizes the hydrogenation conditions for the syntheses. The corresponding deuterides were prepared under the same conditions as the hydrides. The alkaline earth metal to tetrel ratio of the hydrides was confirmed by EDX.

Zintl phases as well as their hydrides are grey brittle powders. The hydrides easily cleave (Fig. A1.1) as described by Armbruster for $CaSiH_x$ [26, 27]. While the hydride of BaSi decomposes slowly in air, the hydrides of SrGe and BaSn rapidly react with moisture. The decomposition products of the hydrides are powders that are amorphous to X-ray diffraction. In the case of SrGe the color changes to yellow.

Characterization

Laboratory powder X-ray diffraction (PXRD) was used to monitor phase purity of the precursor Zintl phases as well as hydride formation. Measurements were done on a Huber G670 diffractometer in Guinier geometry and with copper $K_{\alpha 1}$ radiation. Flat samples were prepared by grinding the moisture sensitive powders in an argon atmosphere, mixing with grease, and putting the sample between two sheets of capton foil.

Powder neutron diffraction (PND) was performed at Institut Laue Langevin (ILL), Grenoble, France at the high-intensity diffractometer D20 [31]. Measurements were done at a take off angle of 120° and a wavelength of $\lambda = 1.86613(16)$ Å or a take off angle of 90° and $\lambda = 2.41538(19)$ Å. Wavelengths

were calibrated using silicon-NIST640b as an external standard. Samples were loaded in an argon filled glovebox with oxygen and moisture content below 1 ppm each. Measurements were done in indium sealed vanadium containers with 6 mm inner diameter at a temperature of 297(2) K.

Powder synchrotron diffraction (PSD) was done using the mail-in service of the Advanced Photon Source (APS), Argonne, USA. Measurements were performed at 11-BM beamline at a wavelength $\lambda = 0.458997 \text{ \AA}$ and 295 K. Samples were sealed in glass capillaries of 0.3 mm inner diameter which were placed in 0.8 mm capton tubes.

Rietveld refinement [32, 33] was done using the TOPAS[®] software package [34] for synchrotron data. The Stephens model[35] for anisotropic line broadening was used. FULLPROF[36, 37] software package was used for neutron diffraction data.

Structure pictures were prepared by VESTA[38, 39]. Structural data were normalized using STRUCTURE TIDY[40] as implemented in VESTA.

Solid-State Nuclear Magnetic Resonance (SSNMR) measurements of powdered samples sealed under argon atmosphere in glass tubes were carried out in static magnetic fields of 9.4 T, 11.7 T, and 17.6 T with *BRUKER AVANCE* spectrometers. Both, a static home-built and BRUKER 4 mm and 2.5 mm MAS probes were used. Static spectra were recorded with a solid-echo sequence [41, 42] ($\pi/2$ pulse length 3 μs , recycle delay 500 s). For exciting free induction decays under MAS the pulse length was 5 μs (recycle delay 500 s) and the spinning frequencies were 1.5 kHz and 25 kHz at 11.7 T and 17.6 T, respectively. For data analysis we used either *BRUKER Topspin* or *ORIGINLab* software. Measurements were done on the ^2H nucleus of the Zintl phase deuterides $\text{SrGeD}_{4/3-x}$ and BaSiD_{2-x} . Deuterated water ($\text{D}_2\text{O} = ^2\text{H}_2\text{O}$) was used for setup optimization and referencing. Chemical shifts are given on the δ -scale in regard to TMS.

Energy dispersive X-ray spectroscopy (EDX) was done for chemical analysis of the heavy atoms of the hydrides (deuterides). Either an EDX INCA SYSTEM from Oxford Instruments mounted on a Zeiss LEO 1530 scanning electron microscope (SEM) with 20 kV acceleration voltage and a working distance of 15 mm or an EDAX EDX system mounted on a Philips STEM CM 200 ST transmission electron microscope (TEM) was used.

Quantum Chemical Calculations were done using the QUANTUM ESPRESSO package[43, 44]. Calculations were performed in the DFT framework applying the generalized gradient approximation (GGA) and the functional from Perdew-Burke-Ernzerhof (PBE)[45]. The projector augmented wave method (PAW)[46] was used and base sets were obtained from the PSLibrary[47]. The plane wave kinetical energy cutoff was tested on convergence and set to 60 ry. Marzari-Vanderbilt cold smearing [48] was used with 0.005 ry for structure relaxations. Density of states (DOS) calculations were done on relaxed structures using the tetrahedron method [49]. Partial density of states (pDOS) were calculated using Gaussian smearing since the tetrahedron method is not implemented.

Hydrogen free Zintl phases were constructed without applying a superstructure. All hydride structures were set in a three-fold superstructure regarding to the parent Zintl phase. An idealized hydrogen content neglecting any nonstoichiometry effect as obtained by neutron diffraction was used. Structures as well as lattice parameters were relaxed without applying any symmetry restraints but all unit cell angles were constraint to 90° . Density of states (DOS) calculations were done on the relaxed structures. After structure relaxation a pseudo-symmetry search using the PSEUDO module[50–52] of Bilbao Crystallographic Server[53–56] was done. Structural data of the structure relaxations can be found in the supplementary information (Tab. A1.S1, Tab. A1.S4). They are given in the high symmetry setting as obtained from the pseudo-symmetry search. For hydrides the k-space was sampled over a $4 \times 4 \times 12$ mesh for structural relaxations and a $8 \times 8 \times 24$ mesh for an electronic structure calculation on the final structures. Structure relaxation of the hydrogen free Zintl phases were done on a $12 \times 4 \times 12$ mesh. The grids were produced according to the Monkhorst-Pack scheme [57].

Table A1.2: Structural parameters of BaSiD_{2-x}, x = 0.13(2) in space group type *Pbnm* (No 62, *Pnma*) from Rietveld refinement on powder neutron diffraction data. Debye-Waller factors for Ba and Si are fixed to reasonable values.

BaSiD _{2-x} , x = 0.13(2)						
<i>Pbnm</i> (No. 62), <i>a</i> = 4.4732(8) Å, <i>b</i> = 15.622(2) Å, <i>c</i> = 4.1112(7) Å						
Atom	Wyckoff	x	y	z	B _{iso} /Å ²	SOF
Ba1	4 <i>c</i>	0.0060(20)	0.3496(5)	1/4	0.3	1
Si1	4 <i>c</i>	0.01044(20)	0.0448(8)	1/4	0.7	1
D1	4 <i>c</i>	0.5100(20)	0.2566(4)	1/4	3.1(3)	0.948(12)
D2	4 <i>c</i>	0.3773(11)	0.0442(6)	1/4	2.4(3)	0.914(12)

Results

The Zintl phases BaSi, SrGe, as well as *AeTt*, *Ae* = Sr, Ba and *Tt* = Sn, Pb, were attempted to hydrogenate or deuterate (Tab. A1.1). BaSi forms a hydride (deuteride) phase as described in the literature [27]. In the following a structure model for this phase will be presented. SrGe and BaSn form new hydride (deuteride) phases that are structurally closely related to the CaSiH_{1.3} structure type [24]. SrSn shows no reactivity towards hydrogen, while SrPb and BaPb decompose under formation of SrH₂ and SrPb₃ or BaH₂ and Ba₃Pb₅, respectively.

Crystal structures of BaSiD_{2-x}, SrGeD_{4/3-x} and BaSnD_{4/3-x}

The PXRD patterns of the hydrides (deuterides) BaSiD_{2-x}, SrGeD_{4/3-x} and BaSnD_{4/3-x} can be indexed in the orthorhombic crystal system. BaSi was hydrogenated by Armbruster *et. al.* before [26, 27]. They could index the powder pattern but did not present a structure solution due to poor crystallinity. We reinvestigated BaSiD_{2-x} and extended the scheme to SrGeD_{4/3-x} and BaSnD_{4/3-x}. The corresponding Zintl phases, *AeTt*, *Ae* = alkaline earth metal, *Tt* = tetrel element, crystallize in the orthorhombic CrB-structure type and the *Tt*-polyanion can be described with the Zintl concept as infinite linear *Tt*²⁻-chains.

The hydride (deuteride) phases can be described in a metrically distorted cell of the parent structure. **Thus, in the following, all structures are discussed with regard to the corresponding Zintl phases. For the sake of simplicity all space groups are set with the same axes system as the Zintl phase, e.g., *Tt*-zig-zag chains run along the crystallographic *c* axis. Standard settings are given in brackets.** (For the cell transformation see Tab. A1.4)

Synchrotron and neutron diffraction data suggest space group type *Pbnm* (No. 62, *Pnma*) for BaSiD_{2-x}, SrGeD_{4/3-x} and BaSnD_{4/3-x}. For the latter two the crystallographic *a* axis is tripled with respect to the Zintl phase. The crystal structures of all three compounds could be solved and refined from powder data (Fig. A1.2). For details of the structure determination and synchrotron powder patterns (Fig. A1.S1 and Fig. A1.S2) please see the supplementary information.

In general the structures of these Zintl phase hydrides show features of interstitial as well as polyanionic hydrides. There is one *Ae*₄-tetrahedral void per alkaline-earth metal. In addition, voids between the *Tt*-chains may be occupied as well resulting in a *Tt*-H bond, which is confirmed by calculations and fits the SSNMR data well. In the following, two distinct structure types resulting from different occupation of such voids will be described in detail.

BaSiD_{2-x}: BaSiD_{2-x}, x=0.13(2) has the highest hydrogen (deuterium) content within the *AeTt*-H system and represents a new structure type. The deuterium content is much lower than the literature value of BaSiH_{3.4} [26, 27]. The structure may be described in space group type *Pbnm* (No. 62, *Pnma*) and does not show any superstructure with regard to the parent Zintl phase. There are two deuterium positions. The deuterium site in the tetrahedral Ba₄-void is refined to 95% occupation (Tab. A1.2, D1). Crystal chemical consideration suggest an additional deuterium atom that binds to the Si-chain and forms a $\overset{\ominus}{\text{r}}[(\text{SiH})^-]$ moiety. This additional site (Tab. A1.2, D2) was refined to 91% occupation.

The Si-Si chain shows a bond length (DFT calculated values in brackets) of 2.489(10) Å [2.483 Å] and an Si-Si-Si angle of 111.4(4)° [112.0°]. The silicon-hydrogen (deuterium) distance is 1.641(5) Å [1.573 Å]. The H(D)-Si-Si angle is 92.0(3)° [93.1°]. Fig. A1.3 shows the polyanionic partial structure as well as different projections of the crystal structure.

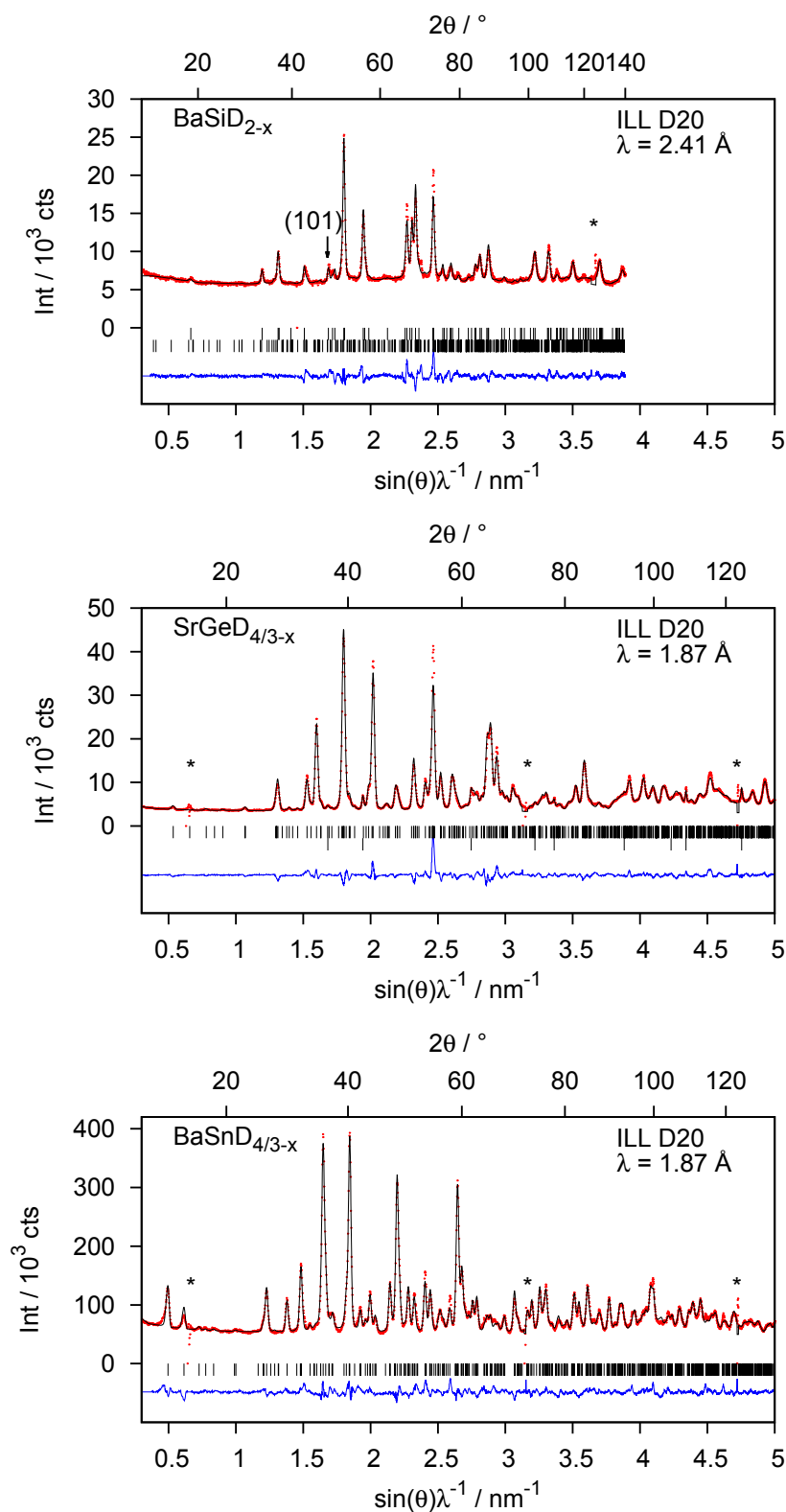


Figure A1.2: Rietveld refinement of the crystal structures of BaSiD_{2-x} , $x = 0.13(2)$, $\text{SrGeD}_{4/3-x}$, $x = 0.139(3)$ and $\text{BaSnD}_{4/3-x}$, $x = 0.055(2)$ using powder neutron diffraction data. (*) excluded due to detector failure. **BaSiD_{2-x} :** $R_p = 3.02\%$, $R_{wp} = 4.12\%$, $R_{Bragg} = 6.29\%$, $\text{GoF} = 2.35$; **$\text{SrGeD}_{4/3-x}$:** $R_p = 4.13\%$, $R_{wp} = 5.59\%$, $R_{Bragg} = 4.46\%$, $\text{GoF} = 4.63$. **$\text{BaSnD}_{4/3-x}$:** $R_p = 3.58\%$, $R_{wp} = 4.62\%$, $R_{Bragg} = 5.63\%$, $\text{GoF} = 2.06$.

Table A1.3: Structural parameters of SrGeD_{4/3-x}, x = 0.139(3), *Pbnm* (No 62, *Pnma*) and BaSnD_{4/3-x}, x = 0.055(2), *Pbnm* (No 62, *Pnma*) as obtained by Rietveld refinement using powder neutron diffraction data. Debye-Waller factors were constraint for equal elements. For deuterium occupying tetrahedral voids the site occupancy factor refined to 1.0 within 1 e.s.u., thus, occupation was fixed to 1 during the last refinement cycle.

SrGeD _{4/3-x} , x = 0.139(3)						
<i>Pbnm</i> (No. 62), <i>a</i> = 11.9113(9) Å, <i>b</i> = 15.2692(11) Å, <i>c</i> = 4.0600(2) Å						
Atom	Wyckoff	x	y	z	B _{iso} /Å ²	SOF
Sr1	4c	0.3414(6)	0.3152(4)	1/4	0.35(9)	1
Sr2	4c	0.6480(6)	0.3397(3)	1/4	0.35	1
Sr3	4c	0.0122(4)	0.3655(4)	1/4	0.35	1
Ge1	4c	0.3125(3)	0.0469(4)	1/4	0.66(7)	1
Ge2	4c	0.7409(3)	0.0403(4)	1/4	0.66	1
Ge3	4c	0.5287(4)	0.5451(3)	1/4	0.66	1
D1	4c	0.5040(5)	0.2240(4)	1/4	1.21(10)	1
D2	4c	0.1570(6)	0.2546(4)	1/4	1.21	1
D3	4c	0.8382(6)	0.2765(4)	1/4	1.21	1
D4	4c	0.4397(7)	0.0380(8)	1/4	1.21	0.592(8)
BaSnD _{4/3-x} , x = 0.055(2)						
<i>Pbnm</i> (No. 62), <i>a</i> = 12.9169(7) Å, <i>b</i> = 16.3097(10) Å, <i>c</i> = 4.5554(2) Å						
Atom	Wyckoff	x	y	z	B _{iso} /Å ²	SOF
Ba1	4c	0.3461(7)	0.3075(4)	1/4	0.94(13)	1
Ba2	4c	0.6520(7)	0.3323(4)	1/4	0.94	1
Ba3	4c	0.0156(6)	0.3697(5)	1/4	0.94	1
Sn1	4c	0.3026(4)	0.0527(5)	1/4	1.02(11)	1
Sn2	4c	0.7308(4)	0.0533(5)	1/4	1.02	1
Sn3	4c	0.5303(5)	0.5530(4)	1/4	1.02	1
D1	4c	0.5014(7)	0.2208(3)	1/4	1.92(11)	1
D2	4c	0.1581(6)	0.2531(4)	1/4	1.92	1
D3	4c	0.8410(6)	0.2787(4)	1/4	1.92	1
D4	4c	0.4447(5)	0.0357(5)	1/4	1.92	0.834(6)

Table A1.4: Lattice parameters of the Zintl phases BaSi, SrGe, BaSn and their corresponding deuterides. The unit cell volume is normalized to formula units (fu).

Compound	x =	Spgr.	Super- str. ^a a =	Lattice parameter	V/fu / Å ³		
				a / Å	b / Å	c / Å	
silicides							
BaSi [58]		<i>Cmcm</i>		5.0430(8)	11.933(2)	4.1395(8)	62.3
BaSi		<i>Cmcm</i>		5.0342(2)	11.9171(3)	4.1335(2)	62.0
BaSi ^b		<i>Cmcm</i>		4.953	11.961	4.085	60.5
BaSiH _{3.4}		<i>Pbnm</i> ^c	3 \tilde{a}	13.43(8)	15.73(15)	4.13(3)	72.7
BaSiD _{2-x} ^d		<i>Cmcm</i>	none	4.48485(5)	15.66599(18)	4.12256(3)	72.4
BaSiD _{2-x} ^e	0.13(2)	<i>Pbnm</i> ^c	none	4.4732(8)	15.622(2)	4.1112(7)	71.8
BaSiD ₂ ^b			none ^f	4.3996	15.332	4.1156	69.3
germanides							
SrGe [59]		<i>Cmcm</i>		4.820(5)	11.39(1)	4.167(2)	57.0
SrGe		<i>Cmcm</i>		4.82389(6)	11.37955(11)	4.17265(4)	57.3
SrGe ^b		<i>Cmcm</i>		4.756	11.325	4.143	55.8
SrGeD _{4/3-x} ^d		<i>Pbnm</i> ^c	3 \tilde{a}	11.84848(12)	15.3938(2)	4.06561(4)	61.8
SrGeD _{4/3-x} ^e	0.139(3)	<i>Pbnm</i> ^c	3 \tilde{a}	11.9113(9)	15.2692(11)	4.0600(2)	61.5
SrGeD _{4/3} ^b			3 \tilde{a}	11.624	15.152	4.046	59.4
stannides							
BaSn [59]		<i>Cmcm</i>		5.316(5)	12.55(1)	4.657(2)	77.7
BaSn		<i>Cmcm</i>		5.3168(2)	12.5037(5)	4.6534(2)	77.3
BaSn ^b		<i>Cmcm</i>		5.263	12.537	4.644	76.6
BaSnD _{4/3-x} ^e	0.055(2)	<i>Pbnm</i> ^c	3 \tilde{a}	12.9169(7)	16.3097(10)	4.5554(2)	80.0
BaSnD _{4/3} ^b			3 \tilde{a}	12.814	16.034	4.5564	78.0

^a \tilde{a} refers to the basis structure of the parent Zintl phase.

^b DFT; for calculated structures an ideal occupation was assumed.

^c nonstandard setting, standard setting is *Pnma* with $a' = b$, $b' = c$ and $c' = a$.

^d synchrotron diffraction.

^e neutron diffraction.

^f structure relaxation using $a = 3\tilde{a}$; From a pseudo symmetry search a smaller cell was obtained.

SrGeD_{4/3-x} and BaSnD_{4/3-x}: We describe the compounds SrGeD_{4/3-x} (x = 0.139(3)) and BaSnD_{4/3-x} (x = 0.055(2)). They show a three-fold superstructure with regard to the Zintl phase and are isotypic to the CaSiH_{1.3}- structure type[24]. The structures may be described in space group type *Pbnm* (No. 62, *Pnma*). Structural data are summarized in Tab. A1.3.

The tetrahedral Ae_4 -voids are fully occupied with deuterium. The tetrel chains are tilted with respect to the Zintl phase and three of them are connected by an additional *Tt-Tt* bond (DFT in brackets) with $d(\text{Ge2-Ge3}) = 2.743(6)$ Å [2.695 Å] and $d(\text{Sn2-Sn3}) = 3.085(8)$ Å [3.052 Å] (Fig. A1.3). In zig-zag chain direction (*c* direction regarding *Pbnm* setting) the bonds are $d(\text{Ge1-Ge2}) = 2.551(5)$ Å [2.556 Å] or $d(\text{Sn1-Sn2}) = 2.893(7)$ Å [2.922 Å] (hydrogen terminated chain) and $d(\text{Ge3-Ge3}) = 2.547(4)$ Å [2.577 Å] or $d(\text{Sn3-Sn3}) = 2.965(6)$ Å [2.941 Å] (middle chain). Thus, the tetrel atoms form condensed six rings in boat configuration (see Fig. A1.3). There are two condensed boats running in an infinite chain in crystallographic *c* direction, which are hydrogen (deuterium) terminated (D4 site) forming a $1^\infty[\text{D-(Ge)}_6\text{-D}]$ moiety. This D4 site is not fully occupied with SOF = 59% (SrGeD_{4/3-x}) and 83% (BaSnD_{4/3-x}). The angles in chain connecting direction are 105.54(13)° [100.3°] (Ge1-Ge2-Ge3) and 104.76(16)° [106.6°] (Ge2-Ge3-Ge3) and 101.8(3)° [96.3°] (D4-Ge1-Ge2) or 98.52(14)° [99.5°] (Sn1-Sn2-Sn3) and 105.41(16)° [105.6°] (Sn2-Sn3-Sn3) and 93.3(2)° [94.0°] (D4-Sn1-Sn2). In chain direction the angles are 107.9(3)° [103.8°] (Ge1-Ge2-Ge1) and 105.68(18)° [102.5°] (Ge3-Ge3-Ge3) and for the corresponding BaSnD_{4/3-x} compound angles are 103.9(3)° [102.4°] (Sn1-Sn2-Sn1) and 100.37(18)° [101.6°] (Sn3-Sn3-Sn3). Fig. A1.3 shows the polyanionic partial structure as well as different projections of the crystal structure including the labeling of the polyanion.

Density of States (DOS)

All presented compounds are non-stoichiometric Zintl phase hydrides. For DFT calculations an idealized composition of $AeTtH_n$, n = 4/3 (SrGeH_n, BaSnH_n), 2 (BaSiH_n) was used. Then they can formally

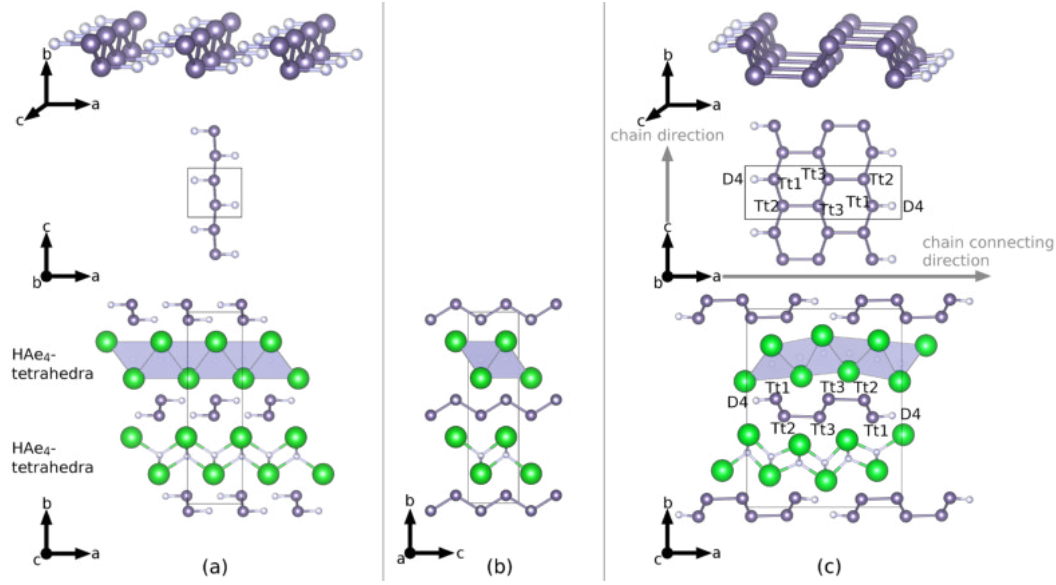


Figure A1.3: Different projections of the polyanion as well as the crystal structure of (a,b) BaSiD_{2-x} and (c) AeTtD_{4/3-x} (SrGeD_{4/3-x} and BaSnD_{4/3-x}). (b) shows the [100] view of BaSiD_{2-x} to emphasize on the tetrahedral voids and the zig-zag chains. This projection looks similar for both structure types. Large spheres: Alkaline earth metal (*Ae*); medium spheres: Tetrel element (*Tt*); small spheres: Hydrogen/deuterium (H/D).

be considered to be comprised of ions $Ae^{2+} + H^{-} + (n-1)(TtH)^{-} + (2-n)Tt^{-}$. DOS calculations were performed on these idealized structures without vacancies in the hydrogen partial structure. The Zintl like view is supported by the DOS. SrGeH_{4/3} and BaSnH_{4/3} show a small band gap while BaSiH₂ is a poor metal with a pseudo-gap at the Fermi level (Fig. A1.4). Partial-DOS for SrGeH_{4/3} and BaSiH₂ are shown in Fig. A1.5 for selected atoms and orbitals. The s-band of hydrogen atoms in tetrahedral Ae₄-voids shows only a low dispersion and lies below the Fermi level indicating a hydridic species. In contrast, the hydrogen which terminates atoms of the Si(Ge)-chain mix with Si(Ge)-bands and also shows a fraction above the Fermi level. The structure of SrGeH_{4/3} shows Ge-atoms that bind only to three other Ge-atoms and Ge-atoms that bind to both, hydrogen and germanium. The main direction for the interaction with hydrogen is the crystallographic *a* axis. Thus, the p_x derived bands of the hydrogen terminated Ge-atoms are lowered while the p_y and p_z components as well as all components of the other germanium atoms form bands at higher energies above and below the Fermi level. Since all Si-atoms of BaSiH₂ are terminated by hydrogen in *a* direction all Si-p_x derived bands are lowered. Only the Si-p_y and -p_z derived bands show electron density at the Fermi level.

Solid-state nuclear magnetic resonance (SSNMR)

In Fig. A1.6 we show the static (a) ²H NMR spectra of BaSiD_{2-x} (*left*) and SrGeD_{4/3-x} (*right*), together with their simulations (b), and low-spinning MAS (c) spectra. For both materials, we observe a narrow line in addition to a broad spectrum. Note that for ²H (spin-1 nucleus) there is no central transition. Thus, the narrow lines for BaSiD_{2-x} (SrGeD_{4/3-x}) of 1.3 kHz (3.9 kHz) widths point to nuclear sites with nearly cubic local charge symmetry, i.e., vanishing electric field gradient (EFG). On the other hand, broad powder patterns must originate from ²H nuclei with very different local charge symmetry, which causes a substantial EFG. All widths are found to be independent of the magnetic field in frequency units (data not shown), which points to quadrupolar linewidths for the broad powder pattern, which is also borne out in the slow-spinning MAS spectra (A1.6(c)). The quadrupole frequencies that characterize the found isotropic EFGs are 51(1) kHz and 39(1) kHz for BaSiD_{2-x} and SrGeD_{4/3-x}, respectively.

Careful evaluations of the relative intensities within each sample revealed ratios of 1:1 (BaSiD_{2-x}) and about 3:1 (SrGeD_{4/3-x}), for narrow vs. broad spectra. This means, as one can already guess from Fig. A1.6, that there are three times as many ²H nuclei occupying the sites of higher charge symmetry in SrGeD_{4/3-x} compared to the crystallographic site that shows a substantial EFG, while for BaSiD_{2-x} the number of nuclei in both type of sites is similar.

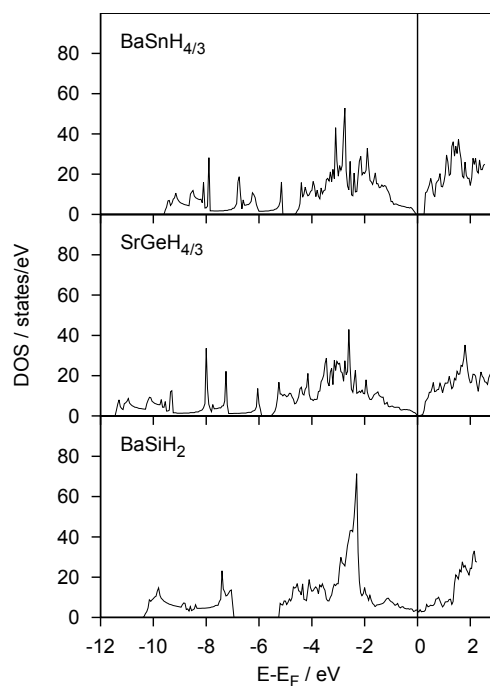


Figure A1.4: Total density of states (DOS) of hydrides of BaSn, SrGe and BaSi

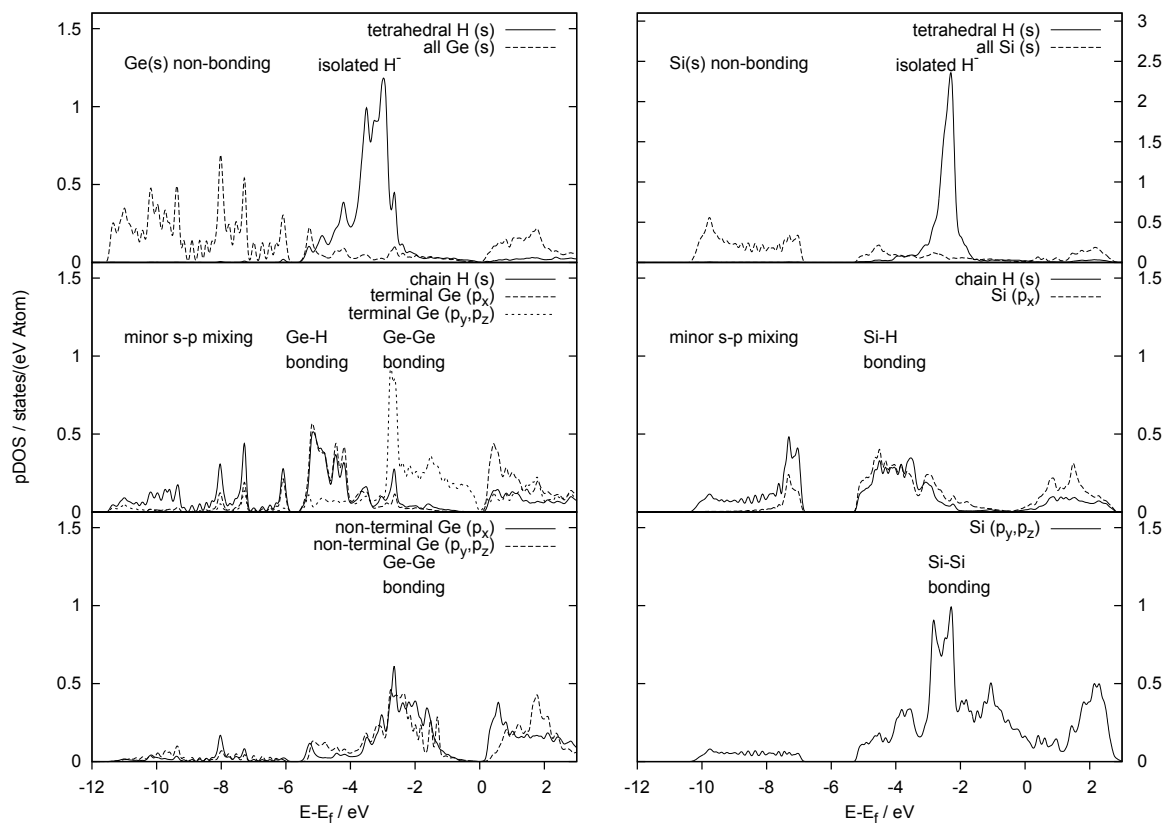


Figure A1.5: Partial density of states (pDOS) for selected atoms and orbitals **Left:** SrGeH_{4/3} **Right:** BaSiH₂.

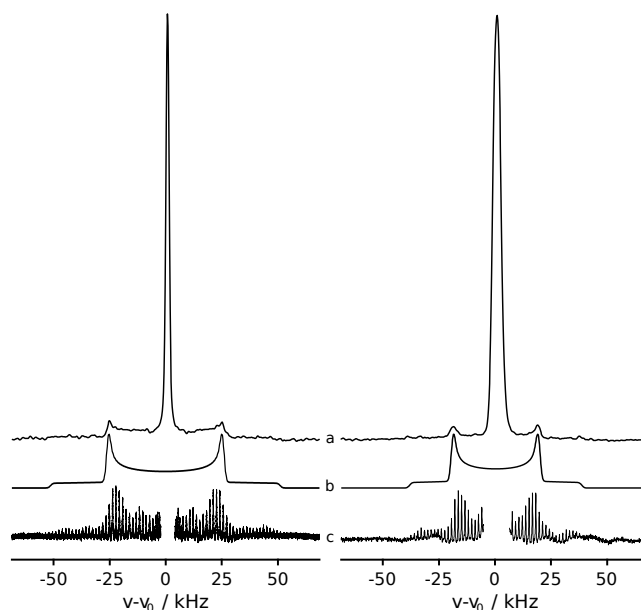


Figure A1.6: (a) Static solid-echo ^2H NMR spectra of BaSiD_{2-x} (left) and $\text{SrGeD}_{4/3-x}$ (right) obtained at 9.4 T. (b) Simulated first order quadrupole powder pattern that fits the broad component of the static spectra in (a). (c) Slow MAS spectra (1.5 kHz) at 11.4 T are in agreement with the assumed powder pattern from quadrupole interaction. The intense central line is cut out for better visualization.

The field independent width of the narrow line in BaSiD_{2-x} (1.3 kHz) is in agreement with what one expects from homonuclear dipole-dipole coupling between ^2H nuclei (derived from the crystal structure). The much broader line in $\text{SrGeD}_{4/3-x}$ (3.9 kHz), however, is probably caused by a very weak quadrupole coupling (or indirect nuclear coupling), and the subject to further investigation.

Substantial line narrowing under fast MAS (17.6 T, 25 kHz spin rate, not shown) gives isotropic shifts for the nuclei with strong quadrupole coupling of about $\delta = 0$ ppm, while the narrow lines are clearly displaced at $\delta = 11(1)$ ppm with regard to TMS.

Spin lattice relaxation times on the order of 10^2 s with slight differences among the various resonance lines (at most a factor of two) may be typical for insulating compounds, but a definite assignment of the involved mechanisms is still under investigation.

Discussion

This paper describes two new compounds $\text{SrGeD}_{4/3-x}$, $x = 0.139(3)$ and $\text{BaSnD}_{4/3-x}$, $x = 0.055(2)$ in the $\text{CaSiH}_{1.3}$ -structure type and it assigns a new structure type to BaSiD_{2-x} , $x = 0.13(2)$. According to the classification of Häussermann [8] these phases show features of interstitial hydrides due to filled tetrahedral Ae_4 -voids ($\text{Ae} = \text{Sr}, \text{Ba}$) as well as features of polyanionic hydrides due to short *Tt*-D (*Tt* = Si-Sn) distances which according to bond lengths are all in the region of covalent interaction.

The polyanionic partial structure is strongly geometrically constraint since it lies between ionically dominated sheets of edge connected HAe_4 -tetrahedra. Therefore *a*- and *c*-directions are rigidly coupled to the size of the tetrahedra. A hypothetical *AeTtH*, *Ae* = alkaline earth metal, *Tt* = group 14 element, can be formulated according to the Zintl concept as $\text{Ae}^{2+}\text{H}^- \text{Tt}^-$. Thus, for the group 14 element (Tt^-) we can expect sheets in between the salt like tetrahedral layers similar to the structure of black phosphorus or grey arsenic. Each *Tt* atom is then covalently bound to three other *Tt* atoms and the bonds can be suspected to have single bond character. Indeed we find a structure motif of condensed boat configurations in contrast to the armchair configuration in black phosphorus. Due to the rigidity of the salt like layers a totally condensed *AeTtH*-structure was not obtained yet. To comply with the predetermined required space additional *Tt*-H(D) bonds are formed (Fig. A1.3).

In $\text{SrGeD}_{4/3-x}$ and $\text{BaSnD}_{4/3-x}$ two thirds of the tetrel atoms form an additional *Tt*-*Tt* bond compared to the hydrogen (deuterium) free Zintl phase. With this additional bond tetrel atoms form condensed six-rings in boat configuration. In crystallographic *a*-direction two boats are condensed, while an infinite

chain of these double row of boats runs along crystallographic c axis. The last third of the tetrel atoms is hydrogen (deuterium) terminated and therefore separates the condensed boats spatially (Fig. A1.3). Both compounds are non-stoichiometric and furthermore for $\text{SrGeD}_{4/3-x}$ it was shown that x changes slightly over time [30]. The tetrahedral Sr_4 - or Ba_4 -voids are fully occupied (Tab. A1.3, D1-D3), but the boat terminating site (Tab. A1.3, D4) is not fully occupied and thus some germanium/tin atoms are undersaturated. Assuming ideal composition ($x = 0$) the Zintl concept can be applied giving $\text{Ae}^{2+}\text{H}^-(\text{Tt}^-)_{2/3}((\text{TtH})^-)_{1/3}$.

BaSiD_{2-x} shows a new structure type where the polyanion forms zig-zag ${}^\infty[(\text{SiH})^-]$ chains. They are isoelectronic to a poly-phosphane $(\text{PH})_x$, which is claimed to be a non-volatile yellow solid [60], but proof of its existence is still elusive [61, 62]. BaSiD_{2-x} is a non-stoichiometric compound as well with 95% of the tetrahedral Ba_4 voids occupied as well as 91% of the silicon atoms terminated by hydrogen (deuterium). In the ideal composition it could be considered as $\text{Ba}^{2+}\text{H}^-(\text{SiH})^-$.

All phases show an undersaturation at the Tt -polyanionic backbone, which needs explanation. This non-stoichiometry effect can be rationalized in two ways. First there could be additional Tt - Tt bonds and therefore more extended polyanions, which derive from the current model by further condensation along the crystallographic a direction. In case such larger units would be statistically distributed within the crystal structure, this might result in reduced deuterium occupation as observed in the structure refinements. As an alternative explanation π -bonding in the polyanion may play a role. From DFT calculations of AeSi ($\text{Ae} = \text{Ca-Ba}$) [63, 64] as well as an experimental charge density study on CaSi [65] it is well known that poor metallic behavior is caused by π -bonding due to $\text{Si}(p)$ - $\text{Ae}(d)$ -overlap and therefore depopulated π^* -bands. An oxidation by depopulating π^* -bands would result in shortened Tt - Tt bonds within the chains. Experimental data unfortunately do not allow a clear distinction between those two models. In any case Tt -D distances might be affected hereby.

From a structure refinement of neutron diffraction data the Ge-D distance is 1.521(9) Å, which is in the same region as for molecular GeD_4 at low temperatures, while the Sn-D distance of 1.858(8) Å is 8% larger than in molecular SnD_4 at low temperature [66]. Quantum chemical structure relaxation on the idealized compositions shows good agreement for Sn-D with 1.867 Å, but assumes a larger distance for Ge-D with 1.667 Å. The non-stoichiometry should have a larger effect on the calculation of $\text{SrGeD}_{4/3-x}$ since x is larger in this case. The Si-D bond length in BaSiD_{2-x} , which was determined as 1.641(5) Å, is elongated compared to similar covalently bound Si-D groups like 1.54 Å for β - KSiD_3 at low temperature [17], but a comparable bond length was determined for a hypervalent SiH_6^{2-} moiety [67]. Quantum chemical calculations suggest a 4% shorter Si-D distance, but were done on an idealized composition.

Partial density of states (pDOS) which was calculated for both structure types (i.e. for BaSiH_2 and $\text{SrGeH}_{4/3}$, Fig. A1.5) shows a strong difference between the hydrogen located in a tetrahedral alkaline earth void and the hydrogen binding to the tetrel chain. The tetrahedral site shows a sharp band with negligible contribution of electronic states of other atoms. The pDOS of hydrogen bound to tetrel is highly dispersive and mixes with tetrel states mainly arising from the p_x -orbitals pointing to the hydrogen atom. Thus a bonding interaction is assumed here.

The Ge-Ge distances change over time due to a small deuterium release which is explained in detail in a forthcoming paper [30]. While synchrotron powder diffraction was done on a freshly prepared sample neutron diffraction was done after 70 days. The Ge-Ge bonds of the zig-zag chains as predetermined by the hydrogen (deuterium) free Zintl phase are shortened. Synchrotron diffraction results fit DFT calculated distances (given in square brackets) well with $d(\text{Ge1-Ge2}) = 2.5720(16)$ Å [2.556 Å] for the hydrogen (deuterium) terminated chain and $d(\text{Ge3-Ge3}) = 2.5681(13)$ Å [2.577 Å] for the middle chain. Neutron diffraction shows a further contraction for the terminal chain with 2.511(5) Å. Therefore the bonds in chain direction are much shorter than in the hydrogen (deuterium) free Zintl phase with 2.6462(16) Å [2.613 Å]. As discussed above this shortening might be caused by depopulating π^* -bands, i. e. oxidation of the Zintl polyanion. Comparing the DFT derived values for the Zintl phase and its hydride confirms this trend (see Tab. A1.S5). The chain connecting bond running in a -direction is strongly elongated ($d(\text{Ge2-Ge3}) = 2.743(6)$ Å) compared to the other bonds. The same trend is obtained for $\text{BaSnD}_{4/3-x}$ (Tab. A1.S5). The Si-Si chain does not show a significant difference to the hydrogen (deuterium) free Zintl phase. DFT calculated distances on a fully hydrogen terminated Si-chain confirms this. For details see Tab. A1.S5.

The Si-Si-Si angle is 111.4°, while Ge-Ge-Ge and Sn-Sn-Sn angles are systematically smaller in the region of 103.37(8)°-107.9(3)° and 98.52(14)°-105.41(16)°, respectively (Tab. A1.S5). They fit DFT derived angles well and are larger than the angles in black phosphorus (102.09(8)° and 96.64(4)° [68])

or grey arsenic ($96.64(6)^\circ$ [69]) which resemble condensed armchair six-rings. The D-Ge-Ge angle is $101.8(3)^\circ$ and therefore widened compared to the DFT derived value (96.3°), which might be caused by the non-stoichiometry effect again. The D-Sn-Sn and D-Si-Si angles fit to the DFT value (Tab. A1.S6). These angles are smaller than the corresponding *Tt-Tt-Tt* angles.

Solid state NMR was performed on the ^2H nucleus of BaSiD_{2-x} and $\text{SrGeD}_{4/3-x}$ in order to avoid contamination from spurious ^1H signals. Based on the structure of the materials it appears unambiguous to assign the different crystallographic sites to our two NMR signals in Fig. A1.6. The narrow lines represent ^2H in the tetrahedral voids that have nearly cubic charge symmetry. Whereas, the broad signals are caused by ^2H nuclei attached to Si/Ge atoms. The latter sites are expected to show a substantial axially symmetric quadrupole splitting if chemically bound to Si/Ge (σ -bond). Further experimental proof for this scenario comes from the NMR intensities. For $\text{SrGeD}_{4/3-x}$, due to the tilting and the interconnected Ge chains (Fig. A1.3), the number of ^2H atoms enclosed by the Sr_4 tetrahedral voids exceeds that of the Ge chain sites by a factor of about 3. On the other hand, for BaSiD_{2-x} we expect nearly equal numbers of nuclei in either position. More independent confirmation of the assignment comes from the fact that both sites are expected to be rather similar in both materials, and that is what we find from NMR shifts and quadrupole splittings. Thus, there can be no doubt with regard to the site assignment.

Obviously, the vanishing quadrupole splitting is expected for the ^2H sites within tetrahedra for symmetry reasons. The different quadrupole splittings ($51(1)$ and $39(1)$ kHz) for the polyanionic sites fit an expected general trend that σ -bonds involving silicon are stronger than in the case of germanium.

While the width of the narrow line for BaSiD_{2-x} is in good agreement with nuclear dipole-dipole coupling, for $\text{SrGeD}_{4/3-x}$ significant additional broadening is present. Since it is field independent, a likely candidate is a weak quadrupole coupling. Indeed, the tetrahedral voids spanned by Sr atoms are much less regular compared to those made up by Ba in BaSiD_{2-x} . The resulting distortion is prone to result in a non-vanishing EFG that could explain the observed width.

The chemical shifts are very similar for both materials with a about $\delta = 0$ ppm for the polyanionic site and about $\delta = +11$ ppm for the tetrahedral site referenced to TMS. The perhaps surprisingly large positive shift for hydrogen in the tetrahedral voids is not unusual since the ^2H chemical shift in BaD_2 was reported to be about $\delta = +9$ ppm [70, 71].

Since the nuclear relaxation is rather long and similar in both systems substantial contributions from itinerant carriers are not likely. Furthermore, paramagnetic impurities such as Eu, which are common in strontium and barium, might easily explain the observed relaxation.

Conclusion

In this contribution we show the existence of two new phases $\text{SrGeD}_{4/3-x}$ and $\text{BaSnD}_{4/3-x}$. Since there are two additional hydrogen (deuterium) poor phases in the Sr-Ge- H_2 system (as shown in a forthcoming paper[30]) $\text{SrGeD}_{4/3-x}$ will be called γ - SrGeD_y as well. We also reinvestigated the compound BaSiD_{2-x} .

The existence of polyanionic hydrides (deuterides) of group 14 elements was questioned. While Ohba *et al.*[24] assume a short Si-H distance of 1.58 Å and thus a covalent bond in $\text{CaSiH}_{1.3}$ from synchrotron diffraction as well as DFT calculations, Wu *et al.*[25] found a much longer distance $d(\text{Si-D}) = 1.82$ Å from powder neutron diffraction. They support their view by neutron vibrational spectroscopy.

We now could show the existence of new polymeric main-group element-hydrogen structures with the group 14 elements Si, Ge and Sn. We prepared the deuteride phases $\text{SrGeD}_{4/3-x}$ and $\text{BaSnD}_{4/3-x}$ that resemble the structure which was proposed by Ohba *et al.*[24] for $\text{CaSiH}_{1.3}$. The polyanionic structures show similarities to the elemental structures of black phosphorus or grey arsenic, but, while these elements consist of condensed armchair six-rings, the new structures show a condensed boat motif. It is topologically related to the boron partial structure of OsB_2 [72] which is cut by the terminating hydrogen (deuterium) atoms. In addition some of the germanium and tin atoms are terminated by deuterium. The bonding length of $d(\text{Ge-D}) = 1.521(9)$ Å [1.667 Å] and $d(\text{Sn-D}) = 1.858(8)$ Å [1.867 Å] (DFT calculations in brackets) are clearly in a region of covalent bonding.

In the structure of BaSiD_{2-x} the zig-zag Si^{2-} chain as in the parent Zintl phase BaSi is retained. However it is terminated by hydrogen (deuterium) (except for the non-stoichiometry) forming a linear $(\text{SiH})^-$ -chain as we would expect from a poly-phosphane. The distance $d(\text{Si-D}) = 1.641(5)$ Å as obtained from neutron diffraction (DFT: $d = 1.573$ Å) is larger than the value proposed for $\text{CaSiH}_{1.3}$ by Ohba *et al.*[24] but much shorter than the value Wu *et al.*[25] determined by neutron diffraction for $\text{CaSiD}_{1.2}$.

We also applied solid-state NMR to BaSiD_{2-x} and $\text{SrGeD}_{4/3-x}$ and could distinguish and assign two chemically different sites. The quadrupolar interaction of the ^2H nuclei bound to Si/Ge atoms fits into the picture of a covalent bond. Therefore we can show the first well confirmed polyanionic hydrides of group 14 elements.

Supplementary Information

Technical information on the evaluation of diffraction data. Rietveld plots derived from synchrotron diffraction (Fig. A1.S1, A1.S2). Structural parameters as refined from synchrotron diffraction as well as calculated by DFT structure relaxations (Tab. A1.S1 - A1.S4). A list of *Tt-Tt* distances and *Tt-Tt-Tt* angles (Tab. A1.S5). A list of *Tt-D* distances and *Tt-Tt-D* angles (Tab. A1.S6). CIF files ($\text{BaSiD}_{1.86}$, $\text{SrGeD}_{1.20}$, $\text{BaSnD}_{1.28}$ in standard setting, please consider the rotation of the axes system) from neutron diffraction data.

Acknowledgement

The authors thank beamline staff 11-BM at Advanced Photon Source (APS) at Argonne National Laboratory (ANL) for powder synchrotron diffraction. Use of the APS at ANL was supported by the U. S. Department of Energy, Office of Science, Office of Basic Energy Sciences, under Contract No. DE-AC02-06CH11357. The Institut Laue-Langevin is acknowledged for providing beamtime, Prof. Oeckler, Universität Leipzig, Germany for providing access to SEM and TEM and Marc Wiedenmeyer and Rainer Niewa for providing access to an arc melting furnace. We thank the Deutsche Forschungsgemeinschaft (DFG, grant Ko1803/8-1) and Fond der Chemischen Industrie (FCI, grant 194371) for financial support.

A1.4 Supplement

In the following technical details regarding the evaluation of diffraction data are given. Structural parameters obtained by Rietveld refinements on the basis of powder synchrotron diffraction data and first principle calculations are listed. Important distances and angles are given. For structural parameters refined from powder neutron diffraction please consult the main manuscript.

Diffraction

The hydride (deuteride) phases show a shrinking for the a lattice parameter while b is elongated with regard to the parent Zintl phases. For powder X-ray (synchrotron) diffraction data this allows us to construct a starting model using the atomic coordinates of the Zintl phase. For BaSiD_{2-x} this $Cmcm$ (No. 63) model can explain all reflections. Our samples also contain an additional phase that is a superstructure variant of BaSiD_x with lower deuterium content and changed lattice parameter ratios, which will be explained elsewhere. Even synchrotron diffraction does not show any additional superstructure reflections (Fig. A1.S1). Including powder neutron diffraction data of the deuteride in the evaluation suggests a reduction of symmetry due to the additional (101)-reflection, which is extinct in a C -centered lattice (main paper Fig. A1.2). Thus, symmetry was reduced to $Pbnm$ (No. 62, $Pnma$) to describe deuterium positions properly. Synchrotron diffraction data show anisotropic line widths with h dominated broadening. Since the silicon binding deuterium site D2 is not fully occupied (91 %, main paper Tab. 2) there is probably some disorder in the (SiD)-zig zag chains. This undersaturation might explain the anisotropic line broadening.

$\text{SrGeD}_{4/3-x}$ and $\text{BaSnD}_{4/3-x}$ clearly show a tripled a -axis (regarding the parent Zintl phase) as known from the $\text{CaSiH}_{1,3}$ structure type [24]. Therefore an isopointal starting model was successfully used to refine these structures. The structure of $\text{SrGeD}_{4/3-x}$ was determined by powder synchrotron diffraction (Fig. A1.S2) and powder neutron diffraction (main paper Fig. A1.2). The samples change over time, which can be seen from the lattice parameters as determined from synchrotron and neutron data (see main paper Tab. 4). While synchrotron diffraction was done on a freshly prepared sample, neutron data were collected after 70 days. This effect is reproducible and can be explained by a changing hydrogen (deuterium) site occupation at D4 (main paper Tab. 3) which also influences Ge-Ge distances. This will be discussed in more detail in a forthcoming paper [30]. Thus, Rietveld refinements were done individually. The structure of $\text{BaSnD}_{4/3-x}$ was determined by laboratory powder X-ray diffraction (not shown) and powder neutron diffraction (main paper Fig. A1.2).

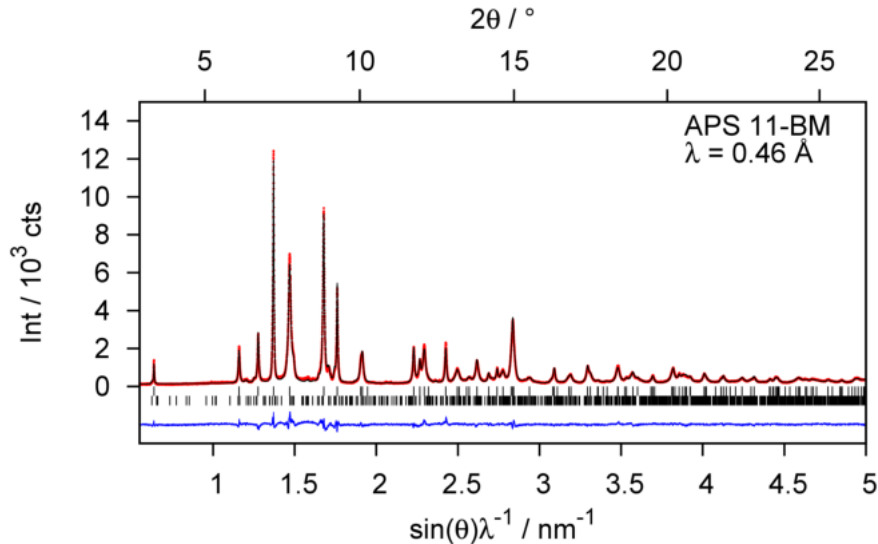


Figure A1.S1: Rietveld refinement of the crystal structure of BaSiD_{2-x} . The second phase corresponds to BaSiD_x with lower hydrogen content ($\approx 10\%$ phase fraction) and will be discussed elsewhere. Rietveld refinement was done using powder synchrotron diffraction data and the high symmetry model in space group type $Cmcm$ (No.63). $R_p = 4.88\%$, $R_{wp} = 9.31\%$, $R_{Bragg} = 3.49\%$, $\text{GoF} = 1.91$.

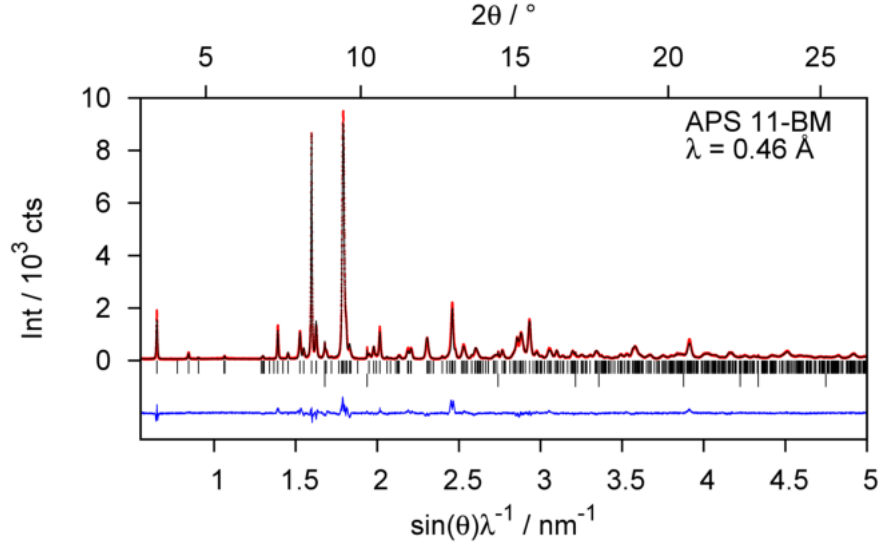


Figure A1.S2: Rietveld refinement of the crystal structure of $\text{SrGeD}_{4/3-x}$. Refinement was done using powder synchrotron diffraction data. The second phase is SrO (fraction $\approx 1\%$). $R_p = 10.66\%$, $R_{wp} = 13.02\%$, $R_{Bragg} = 5.10\%$, $\text{GoF} = 1.79$;

Table A1.S1: Structural parameters of BaSiD_{2-x} ($Cmcm$, No 63) as obtained by Rietveld refinement using powder synchrotron diffraction data.

BaSiD _{2-x}					
$Cmcm$ (No. 63), $a = 4.48485(5)$ Å, $b = 15.66599(18)$ Å, $c = 4.12256(3)$ Å					
Atom	Wyckoff	x	y	z	$B_{iso}/\text{Å}^2$
Ba1	4c	0	0.34594(2)	1/4	0.811(11)
Si1	4c	0	0.04075(12)	1/4	1.73(4)

Table A1.S2: Structural parameters of BaSiH_2 from first principle calculations. Lattice parameters as well as atomic coordinates were relaxed by DFT calculations constraining all angles to 90° . A threefold superstructure regarding to BaSi was used for initial calculation to have the same metrical ratios as for $\text{SrGeH}_{4/3}$ and $\text{BaSnH}_{4/3}$. On the relaxed structure a pseudo symmetry search was done using PSEUDO[50–52] module of the Bilbao Crystallographic Server[54–56]. $Pbnm$ (No 62, $Pnma$) pseudo symmetry was found without the superstructure of the initial model.

BaSiH ₂				
$Pbnm$ (No. 62), $a = 4.3996$ Å, $b = 15.332$ Å, $c = 4.1156$ Å				
Atom	Wyckoff	x	y	z
Ba1	4c	0.0198	0.3468	1/4
Si1	4c	0.0213	0.0449	1/4
H1	4c	0.5142	0.2548	1/4
H2	4c	0.3786	0.0410	1/4

Table A1.S3: Structural parameters of $\text{SrGeD}_{4/3-x}$, $Pbnm$ (No 62, $Pnma$) as obtained by Rietveld refinement using powder synchrotron diffraction data. Debye-Waller factors were constraint for like atoms.

SrGeD _{4/3-x}					
$Pbnm$ (No. 62), $a = 11.84848(12)$ Å, $b = 15.3938(2)$ Å, $c = 4.06561(4)$ Å					
Atom	Wyckoff	x	y	z	$B_{iso}/\text{Å}^2$
Sr1	4c	0.34206(13)	0.31423(8)	1/4	0.208(11)
Sr2	4c	0.65164(12)	0.33864(8)	1/4	0.208
Sr3	4c	0.01300(11)	0.36346(7)	1/4	0.208
Ge1	4c	0.31003(11)	0.05002(12)	1/4	0.590(15)
Ge2	4c	0.73979(12)	0.04489(12)	1/4	0.590
Ge3	4c	0.52999(14)	0.54545(9)	1/4	0.590

Table A1.S4: Structural parameters of SrGeH_{4/3} and BaSnH_{4/3} from first principle calculations. Lattice parameters as well as atomic coordinates were relaxed by DFT calculations constraining all angles to 90°. On the relaxed structure a pseudo symmetry search was done using PSEUDO[50–52] module of the Bilbao Crystallographic Server[54–56]. *Pbnm* (No. 62, *Pnma*) pseudo symmetry was found for both structures and is given below.

SrGeH _{4/3}				
<i>Pbnm</i> (No. 62), $a = 11.624 \text{ \AA}$, $b = 15.152 \text{ \AA}$, $c = 4.046 \text{ \AA}$				
Atom	Wyckoff	x	y	z
Sr1	4 <i>c</i>	0.3420	0.3112	1/4
Sr2	4 <i>c</i>	0.6502	0.3381	1/4
Sr3	4 <i>c</i>	0.0148	0.3667	1/4
Ge1	4 <i>c</i>	0.3034	0.0505	1/4
Ge2	4 <i>c</i>	0.7368	0.0483	1/4
Ge3	4 <i>c</i>	0.5313	0.5472	1/4
H1	4 <i>c</i>	0.5077	0.2217	1/4
H2	4 <i>c</i>	0.1565	0.2509	1/4
H3	4 <i>c</i>	0.8401	0.2757	1/4
H4	4 <i>c</i>	0.4458	0.0371	1/4

BaSnH _{4/3}				
<i>Pbnm</i> (No. 62), $a = 12.814 \text{ \AA}$, $b = 16.034 \text{ \AA}$, $c = 4.5564 \text{ \AA}$				
Atom	Wyckoff	x	y	z
Ba1	4 <i>c</i>	0.3422	0.3052	1/4
Ba2	4 <i>c</i>	0.6489	0.3308	1/4
Ba3	4 <i>c</i>	0.0130	0.3691	1/4
Sn1	4 <i>c</i>	0.3066	0.0574	1/4
Sn2	4 <i>c</i>	0.7310	0.0527	1/4
Sn3	4 <i>c</i>	0.5308	0.5525	1/4
H1	4 <i>c</i>	0.5064	0.2155	1/4
H2	4 <i>c</i>	0.1547	0.2518	1/4
H3	4 <i>c</i>	0.8399	0.2774	1/4
H4	4 <i>c</i>	0.4506	0.0394	1/4

Table A1.S5: Bond lengths (Tt - Tt) and angles (Tt - Tt - Tt , $Tt = \text{Si, Ge, Sn}$) as obtained from Rietveld refinement and DFT calculations. See also main paper Fig. 3 for labeling.

Bond / angle		PSD/ PXR	PND	DFT
BaSiD _{2-x}				
d(Si-Si)		2.4446(18) Å	2.489(10) Å	2.483 Å
∠(Si-Si-Si)			111.4(4) °	112.0 °
BaSi				
d(Si-Si)		2.507(3) Å		2.465 Å
∠(Si-Si-Si)		111.6(3) °		111.9 °
SrGeD _{4/3-x}				
d(Ge1-Ge2)	terminal chain	2.5720(16) Å	2.511(5) Å	2.556 Å
d(Ge3-Ge3)	middle chain	2.5681(13) Å	2.547(4) Å	2.577 Å
d(Ge2-Ge3)	chain connection	2.728(3) Å	2.743(6) Å	2.695 Å
d(average)		2.623 Å	2.600 Å	2.609 Å
∠(Ge1-Ge2-Ge3)	chain connection	103.37(8) °	105.54(13) °	100.3 °
∠(Ge2-Ge3-Ge3)	chain connection	105.96(9) °	104.76(13) °	106.6 °
∠(Ge1-Ge2-Ge1)	chain direction	104.44(12) °	107.9(3) °	103.8 °
∠(Ge3-Ge3-Ge3)	chain direction	104.66(10) °	105.68(18) °	102.5 °
SrGe				
d(Ge-Ge)		2.6462(16) Å		2.613 Å
∠(Ge-Ge-Ge)		104.48(15) °		104.9 °
BaSnD _{4/3-x}				
d(Sn1-Sn2)	terminal chain		2.893(7) Å	2.922 Å
d(Sn3-Sn3)	middle chain		2.965(6) Å	2.941 Å
d(Sn2-Sn3)	chain connection		3.085(8) Å	3.052 Å
d(average)			2.981 Å	2.972 Å
∠(Sn1-Sn2-Sn3)	chain connection		98.52(14) °	99.5 °
∠(Sn2-Sn3-Sn3)	chain connection		105.41(16) °	105.6 °
∠(Sn1-Sn2-Sn1)	chain direction		103.9(3) °	102.4 °
∠(Sn3-Sn3-Sn3)	chain direction		100.37(18) °	101.6 °
BaSn				
d(Sn-Sn)		2.9962(12) Å		2.954 Å
∠(Sn-Sn-Sn)		101.89(9) °		103.6 °

Table A1.S6: Bond lengths (Tt -D) and angles (D- Tt - Tt , $Tt = \text{Si, Ge, Sn}$) as obtained from Rietveld refinement and DFT calculations. See also main paper Fig. 3 for labeling.

Bond / angle	PND	DFT
β -KSiD ₃ @1.5K [17]		
d(Si-D)	1.537(8)- 1.545(6) Å	
BaSiD _{2-x}		
d(Si1-D2)	1.641(5) Å	1.573 Å
∠(D2-Si1-Si2)	92.0(3) °	93.1 °
GeD ₄ @5K [66]		
d(Ge-D)	1.517(3) Å	
SrGeD _{4/3-x}		
d(Ge1-D4)	1.521(9) Å	1.667 Å
∠(D4-Ge1-Ge2)	101.8(3) °	96.3 °
SnD ₄ @5K [66]		
d(Sn-D)	1.706(3) Å	
BaSnD _{4/3-x}		
d(Sn1-D4)	1.858(8) Å	1.867 Å
∠(D4-Sn1-Sn2)	93.3(2) °	94 °

A1.5 References

- (1) Zintl, E.; Kaiser, H. *Z. Anorg. Allg. Chem.* **1933**, *211*, 113–131, DOI: 10.1002/zaac.19332110113.
- (2) Zintl, E. *Angew. Chem.* **1939**, *52*, 1–6, DOI: 10.1002/ange.19390520102.
- (3) Schäfer, H.; Eisenmann, B.; Müller, W. *Angew. Chem.* **1973**, *85*, 742–760, DOI: 10.1002/ange.19730851704.
- (4) Schäfer, H. *Annu. Rev. Mater. Sci.* **1985**, *15*, 1–42, DOI: 10.1146/annurev.ms.15.080185.000245.
- (5) Nesper, R. *Angew. Chem.* **1991**, *103*, 805–834, DOI: 10.1002/ange.19911030709.
- (6) Corbett, J. D. *Angew. Chem., Int. Ed.* **2000**, *39*, 670–690, DOI: 10.1002/(SICI)1521-3773(20000218)39:4<670::AID-ANIE670>3.0.CO;2-M.
- (7) Nesper, R. *Z. Anorg. Allg. Chem.* **2014**, *640*, 2639–2648, DOI: 10.1002/zaac.201400403.
- (8) Häussermann, U.; Kranak, V. F.; Puhakainen, K. *Struct. Bond.* **2010**, *139*, 143–161, DOI: 10.1007/430_2010_20.
- (9) Fahlquist, H.; Noréus, D.; Callear, S.; David, W. I. F.; Hauback, B. C. *J. Am. Chem. Soc.* **2011**, *133*, 14574–14577, DOI: 10.1021/ja2067687.
- (10) Fahlquist, H.; Noréus, D. *Inorg. Chem.* **2013**, *52*, 7125–7129, DOI: 10.1021/ic400714e.
- (11) Fahlquist, H.; Noréus, D.; Sørby, M. H. *Inorg. Chem.* **2013**, *52*, 4771–4773, DOI: 10.1021/ic400224a.
- (12) Gingl, F.; Vogt, T.; Akiba, E. *J. Alloys Compd.* **2000**, *306*, 127–132, DOI: 10.1016/S0925-8388(00)00755-6.
- (13) Björling, T.; Noréus, D.; Häussermann, U. *J. Am. Chem. Soc.* **2006**, *128*, 817–824, DOI: 10.1021/ja054456y.
- (14) Wenderoth, P.; Kohlmann, H. *Inorg. Chem.* **2013**, *52*, 10525–10531, DOI: 10.1021/ic401480b.
- (15) Chotard, J.-N.; Tang, W. S.; Raybaud, P.; Janot, R. *Chem. - Eur. J.* **2011**, *17*, 12302–12309, DOI: 10.1002/chem.201101865.
- (16) Tang, W. S.; Chotard, J.-N.; Raybaud, P.; Janot, R. *Phys. Chem. Chem. Phys.* **2012**, *14*, 13319, DOI: 10.1039/c2cp41589e.
- (17) Tang, W. S.; Chotard, J.-N.; Raybaud, P.; Janot, R. *J. Phys. Chem. C* **2014**, *118*, 3409–3419, DOI: 10.1021/jp411314w.
- (18) Kranak, V. F.; Lin, Y.-C.; Karlsson, M.; Mink, J.; Norberg, S. T.; Häussermann, U. *Inorg. Chem.* **2015**, *54*, 2300–2309, DOI: 10.1021/ic502931e.
- (19) Kranak, V. F.; Benson, D. E.; Wollmann, L.; Mesgar, M.; Shafeie, S.; Grins, J.; Häussermann, U. *Inorg. Chem.* **2015**, *54*, 756–764, DOI: 10.1021/ic501421u.
- (20) Evans, M. J.; Holland, G. P.; Garcia-Garcia, F. J.; Häussermann, U. *J. Am. Chem. Soc.* **2008**, *130*, 12139–12147, DOI: 10.1021/ja803664y.
- (21) Evans, M. J.; Kranak, V. F.; Garcia-Garcia, F. J.; Holland, G. P.; Daemen, L. L.; Proffen, T.; Lee, M. H.; Sankey, O. F.; Häussermann, U. *Inorg. Chem.* **2009**, *48*, 5602–5604, DOI: 10.1021/ic9005423.
- (22) Lee, M. H.; Björling, T.; Hauback, B. C.; Utsumi, T.; Moser, D.; Bull, D.; Noréus, D.; Sankey, O. F.; Häussermann, U. *Phys. Rev. B* **2008**, *78*, 195209, DOI: 10.1103/PhysRevB.78.195209.
- (23) Kranak, V. F.; Evans, M. J.; Daemen, L. L.; Proffen, T.; Lee, M. H.; Sankey, O. F.; Häussermann, U. *Solid State Sci.* **2009**, *11*, 1847–1853, DOI: 10.1016/j.solidstatesciences.2009.08.007.
- (24) Ohba, N.; Aoki, M.; Noritake, T.; Miwa, K.; Towata, S.-i. *Phys. Rev. B* **2005**, *72*, 075104, DOI: 10.1103/PhysRevB.72.075104.

- (25) Wu, H.; Zhou, W.; Udovic, T. J.; Rush, J. J.; Yildirim, T. *Phys. Rev. B* **2006**, *74*, 224101, DOI: 10.1103/PhysRevB.74.224101.
- (26) Armbruster, M. M. Reaktionen von Wasserstoff mit Zintl-Phasen., Ph.D. Thesis, Zürich: Eidgenössische Technische Hochschule (ETH) Zürich, 2008, DOI: 10.3929/ethz-a-005645188.
- (27) Armbruster, M.; Wörle, M.; Krumeich, F.; Nesper, R. *Z. Anorg. Allg. Chem.* **2009**, *635*, 1758–1766, DOI: 10.1002/zaac.200900220.
- (28) Ångström, J.; Johansson, R.; Sarkar, T.; Sørby, M. H.; Zlotea, C.; Andersson, M. S.; Nordblad, P.; Scheicher, R. H.; Häussermann, U.; Sahlberg, M. *Inorg. Chem.* **2016**, *55*, 345–352, DOI: 10.1021/acs.inorgchem.5b02485.
- (29) Nedumkandathil, R.; Kranak, V. F.; Johansson, R.; Ångström, J.; Balmes, O.; Andersson, M. S.; Nordblad, P.; Scheicher, R. H.; Sahlberg, M.; Häussermann, U. *J. Solid State Chem.* **2016**, *239*, 184–191, DOI: 10.1016/j.jssc.2016.04.028.
- (30) Auer, H.; Wallacher, D.; Hansen, T. C.; Kohlmann, H. *Inorg. Chem.* **2017**, *56*, 1072–1079, DOI: 10.1021/acs.inorgchem.6b01945.
- (31) Hansen, T. C.; Henry, P. F.; Fischer, H. E.; Torregrossa, J.; Convert, P. *Meas. Sci. Technol.* **2008**, *19*, 034001.
- (32) Rietveld, H. M. *Acta Crystallogr.* **1967**, *22*, 151–152, DOI: 10.1107/S0365110X67000234.
- (33) Rietveld, H. M. *J. Appl. Crystallogr.* **1969**, *2*, 65–71, DOI: 10.1107/S0021889869006558.
- (34) Bruker AXS, TOPAS[©] version 5, www.bruker-axs.com.
- (35) Stephens, P. W. *J. Appl. Crystallogr.* **1999**, *32*, 281–289, DOI: 10.1107/S0021889898006001.
- (36) Rodriguez-Carvajal, J. *Phys. B* **1993**, *192*, 55–69, DOI: 10.1016/0921-4526(93)90108-I.
- (37) Rodríguez-Carvajal, J. FULLPROF (version 5.30): A Program for Rietveld Refinement and Pattern Matching Analysis; Institut Laue-Langevin, Grenoble (France)., 2012.
- (38) Momma, K.; Izumi, F. *J. Appl. Crystallogr.* **2011**, *44*, 1272–1276, DOI: 10.1107/S0021889811038970.
- (39) VESTA - Visualisation for Electronic and STructural Analysis, version 3.3.1.
- (40) Gelato, L. M.; Parthé, E. *J. Appl. Crystallogr.* **1987**, *20*, 139–143, DOI: 10.1107/S0021889887086965.
- (41) Hahn, E. L. *Phys. Rev.* **1950**, *80*, 580–594, DOI: 10.1103/physrev.80.580.
- (42) Powles, J.; Mansfield, P. *Phys. Lett.* **1962**, *2*, 58–59, DOI: 10.1016/0031-9163(62)90147-6.
- (43) Giannozzi, P. et al. *J. Phys.: Condens. Matter* **2009**, *21*, 395502.
- (44) <http://www.quantum-espresso.org>, QUANTUM ESPRESSO v. 5.1.2, , GNU General Public License.
- (45) Perdew, J. P.; Burke, K.; Ernzerhof, M. *Phys. Rev. Lett.* **1996**, *77*, 3865–3868, DOI: 10.1103/physrevlett.77.3865.
- (46) Blöchl, P. E. *Phys. Rev. B* **1994**, *50*, 17953–17979, DOI: 10.1103/physrevb.50.17953.
- (47) <http://www.qe-forge.org/gf/project/pslibrary>, version 0.3.1.
- (48) Marzari, N.; Vanderbilt, D.; Vita, A. D.; Payne, M. C. *Phys. Rev. Lett.* **1999**, *82*, 3296–3299, DOI: 10.1103/physrevlett.82.3296.
- (49) Blöchl, P. E.; Jepsen, O.; Andersen, O. K. *Phys. Rev. B* **1994**, *49*, 16223–16233, DOI: 10.1103/physrevb.49.16223.
- (50) Kroumova, E.; Aroyo, M. I.; Perez-Mato, J. M.; Ivantchev, S.; Igartua, J. M.; Wondratschek, H. *J. Appl. Crystallogr.* **2001**, *34*, 783–784, DOI: 10.1107/S0021889801011852.
- (51) Capillas, C.; Aroyo, M. I.; Perez-Mato, J. M. *Z. Kristallogr.* **2005**, *220*, DOI: 10.1524/zkri.220.8.691.67076.
- (52) Capillas, C.; Tasci, E. S.; de la Flor, G.; Orobengoa, D.; Perez-Mato, J. M.; Aroyo, M. I. *Z. Kristallogr. - Cryst. Mater.* **2011**, *226*, 186–196, DOI: 10.1524/zkri.2011.1321.

- (53) Bilbao Crystallographic Server, <http://www.cryst.ehu.es/>.
- (54) Aroyo, M. I.; Perez-Mato, J. M.; Capillas, C.; Kroumova, E.; Ivantchev, S.; Madariaga, G.; Kirov, A.; Wondratschek, H. *Z. Kristallogr.* **2006**, *221*, DOI: 10.1524/zkri.2006.221.1.15.
- (55) Aroyo, M. I.; Kirov, A.; Capillas, C.; Perez-Mato, J. M.; Wondratschek, H. *Acta Crystallogr., Sect. A* **2006**, *62*, 115–128, DOI: 10.1107/s0108767305040286.
- (56) Aroyo, M. I.; Perez-Mato, J. M.; Orobengoa, D.; E., T.; de la Flor, G.; Kirov, A. *Bulg. Chem. Commun.* **2011**, *43*, 183–197.
- (57) Monkhorst, H. J.; Pack, J. D. *Phys. Rev. B* **1976**, *13*, 5188–5192, DOI: 10.1103/physrevb.13.5188.
- (58) Currao, A.; Curda, J.; Nesper, R. *Z. Anorg. Allg. Chem.* **1996**, *622*, 85–94, DOI: 10.1002/zaac.19966220113.
- (59) Merlo, F.; Fornasini, M. *J. Less-Common Met.* **1967**, *13*, 603–610, DOI: 10.1016/0022-5088(67)90105-1.
- (60) Holleman, A. F.; Wiberg, N.; Wiberg, E., *Lehrbuch der Anorganischen Chemie*, 102nd ed.; de Gruyter: 2008.
- (61) Baudler, M.; Glinka, K. *Chem. Rev.* **1994**, *94*, 1273–1297, DOI: 10.1021/cr00029a005.
- (62) Carlsohn, B. Zur Frage der Existenz eines festen Phosphorwasserstoffs (PH)_x, Ph.D. Thesis, Köln: Universität zu Köln, 1976.
- (63) Reyes, E. C.; Stalder, E. D.; Mensing, C.; Budnyk, S.; Nesper, R. *J. Phys. Chem. C* **2011**, *115*, 1090–1095, DOI: 10.1021/jp106169h.
- (64) Reyes, E. C.; Nesper, R. *J. Phys. Chem. C* **2012**, *116*, 2536–2542, DOI: 10.1021/jp205825d.
- (65) Kurylyshyn, I. M.; Fässler, T. F.; Fischer, A.; Hauf, C.; Eickerling, G.; Presnitz, M.; Scherer, W. *Angew. Chem., Int. Ed.* **2014**, *53*, 3029–3032, DOI: 10.1002/anie.201308888.
- (66) Maley, I. J.; Brown, D. H.; Ibberson, R. M.; Pulham, C. R. *Acta Crystallogr., Sect. B* **2008**, *64*, 312–317, DOI: 10.1107/S0108768108010379.
- (67) Puhakainen, K.; Benson, D.; Nylén, J.; Konar, S.; Stoyanov, E.; Leinenweber, K.; Häussermann, U. *Angew. Chem., Int. Ed.* **2012**, *51*, 3156–3160, DOI: 10.1002/anie.201108713.
- (68) Schiferl, D.; Barrett, C. S. *J. Appl. Crystallogr.* **1969**, *2*, 30–36, DOI: 10.1107/S0021889869006443.
- (69) Brown, A.; Rundqvist, S. *Acta Crystallogr.* **1965**, *19*, 684–685, DOI: 10.1107/S0365110X65004140.
- (70) Nicol, A. T.; Vaughan, R. W. *J. Chem. Phys.* **1978**, *69*, 5211–5213, DOI: 10.1063/1.436475.
- (71) Jehle, M.; Hoffmann, A.; Kohlmann, H.; Scherer, H.; Röhr, C. *J. Alloys Compd.* **2015**, *623*, 164–177, DOI: 10.1016/j.jallcom.2014.09.228.
- (72) Frotscher, M.; Hölzel, M.; Albert, B. *Z. Anorg. Allg. Chem.* **2010**, *636*, 1783–1786, DOI: 10.1002/zaac.201000101.

A2 Structural and electronic flexibility in hydrides of Zintl phases with tetrel-hydrogen and tetrel-tetrel bonds

Henry Auer^a, Robert Schlegel^b, Oliver Oeckler^b, Holger Kohlmann^{a*}

^a *Leipzig University, Department of Inorganic Chemistry, Johannisallee 29, 04103 Leipzig, Germany*

^b *Leipzig University, Department of Mineralogy, Crystallography and Materials Science, Scharnhorststraße 20, 04275 Leipzig, Germany*

* *Corresponding author*

Reprinted with permission from

H. Auer, R. Schlegel, O. Oeckler, H. Kohlmann, *Angew. Chem. Int. Ed.* **2017**, *56*, 12344-12347.
DOI:10.1002/anie.201706523

© 2017 Wiley-VCH Verlag GmbH & Co. KGaA, Weinheim

This is the accepted version with minor adaptations for use with L^AT_EX and one column printing.

A German translation is published as
H. Auer, R. Schlegel, O. Oeckler, H. Kohlmann, *Angew. Chem.* **2017**, *129*, 12515-12518.
DOI:10.1002/ange.201706523

A2.1 Authors' contributions

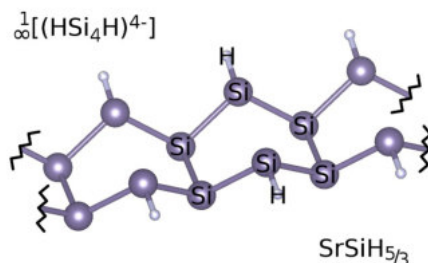
The hydrogenation behaviour of BaGe was investigated by H. Auer. He prepared the deuterated sample BaGeD_{5/3-x} and collected the neutron diffraction data. SrSiD_{5/3-x} neutron diffraction data collected by P. Wenderoth^a were re-evaluated. H. Kohlmann supervised the powder diffraction part of this work. Quantum chemical modelling and the subsequent final crystal structure evaluation of both compounds were conducted by H. Auer. Electron diffraction data of SrSiH_{5/3-x} as well as BaGeH_{5/3-x} and BaSiH_y were collected by G. Wagner (see acknowledgement) and R. Schlegel, respectively. The collected diffraction patterns were indexed and simulated by H. Auer and R. Schlegel. O. Oeckler supervised the electron diffraction part of the work.

The first draft was mainly written by H. Auer. R. Schlegel provided parts of the text regarding transmission electron microscopy. The manuscript was edited by H. Kohlmann. O. Oeckler helped to improve the text.

^a Wenderoth, P. *Untersuchungen zur Hydridbildung von Zintl-Phasen der Erdalkalimetalle mit Aluminium, Gallium und Silicium*, PhD thesis, Saarbrücken: Universität des Saarlandes, 2014.

A2.2 Abstract

The hydrogenation of Zintl phases enables the formation of new structural entities with main group element-hydrogen bonds in the solid state. The hydrogenation of SrSi, BaSi and BaGe yields the hydrides SrSiH_{5/3-x}, BaSiH_{5/3-x} and BaGeH_{5/3-x}. The crystal structures show a six-fold superstructure compared to the parent Zintl phase and were solved by a combination of X-ray, neutron and electron diffraction and the aid of DFT calculations. Layers of connected HSr₄ (HBa₄) tetrahedra containing hydride ions alternate with layers of infinite single- and double-chain polyanions, where hydrogen atoms are covalently bound to silicon and germanium. The idealized formulae $AeTtH_{5/3}$ (Ae = alkaline earth, Tt = tetrel) can be rationalized with the Zintl-Klemm concept according to $(AeTt^{2+})_3(TtH^-)(Tt_2H_2^-)(H^-)_3$, where all Tt atoms are three-binding. The non-stoichiometry (SrSiH_{5/3-x}, $x = 0.17(2)$; BaGeH_{5/3-x}, $x = 0.10(3)$) can be explained by additional π -bonding of the Tt chains.



A2.3 Article

The formation of covalent element-hydrogen bonds is a common theme in synthetic chemistry. Recently, new polymeric triel- and tetrel-hydrogen units were found in the solid state by hydrogenation of Zintl phases or by direct synthesis in hydrogen atmosphere.[1] Examples are triel based polyanions ${}^2_{\infty}[TrH^-]$ and ${}^2_{\infty}[(TrH)^-Tt^-]$ forming puckered honeycomb-layers with hydrogen bound to the triel atom in $AeTr_2H_2$ and $AeTrTtH$ ($Ae = Sr, Ba$; $Tr = Al, Ga$; $Tt = Si, Ge, Sn$), respectively,[1] and pseudo-alkane like moieties, e. g. neopentane like $[Ga(GaH_3)_4]^{5-}$. [2] Hydrogen containing tetrel based anions comprise monomeric SiH_3^- in $ASiH_3$ ($A = K-Cs$), [3, 4] infinite single chains ${}^1_{\infty}[SiH^-]$ in $BaSiH_{2-x}$, [5] and infinite triple chains ${}^1_{\infty}[HTt_6H^{6-}]$ in $CaSiH_{4/3-x}$, $SrGeH_{4/3-x}$ and $BaSnH_{4/3-x}$. [5, 6] For the latter, the parent Zintl phases $AeTt$ crystallize in the CrB structure type (space group $Cmcm$) and exhibit infinite polyanionic silicon and germanium zigzag chains ${}^1_{\infty}[Tt^{2-}]$ in agreement with the Zintl-Klemm concept. Since the hydrogenation of CaSi to $CaSiH_{4/3-x}$ is reversible, this system is a potential hydrogen storage material. [6] The hydrogenation of Zintl phases is a very promising yet barely explored synthetic pathway to new main group element-hydrogen entities in the solid state. In this contribution, we extend this approach and report on new main group-hydrogen structural units in the hydrides of SrSi, BaSi and BaGe. We will focus on the rationale behind the multitude of polyanionic structural motifs, the formation of new tetrel-tetrel and tetrel-hydrogen bonds in the solid and the hydrogen content of the hydrides.

The Zintl phases SrSi and BaGe were hydrogenated at 453 K and 473 K under hydrogen gas pressures of 9.0 and 5.0 MPa, respectively, forming $SrSiH_{5/3-x}$, $x = 0.17(2)$ (1.27 wt-% hydrogen, elemental analysis: 1.16(6) wt-%), and $BaGeH_{5/3-x}$, $x = 0.10(3)$ (0.74 wt-% hydrogen, elemental analysis: 0.73(3) wt-%, see Supplementary Information for details). The hydrides are gray powders sensitive against air and moisture. Exposed to air, they yield amorphous products. The color of $BaGeH_{5/3-x}$ changes to yellow in the course of this reaction, which is probably caused by hydrolysis to polygermene, $(GeH_2)_x$. [7] A similar color change was seen for the moisture induced decomposition of $SrAlGeH$ and $BaAlGeH$ where the formation of Ge-H bonds was followed by IR spectroscopy. [8]

The crystal structures of $SrSiH_{5/3-x}$, $x = 0.17(2)$ and $BaGeH_{5/3-x}$, $x = 0.10(3)$ were elucidated by a combination of electron, X-ray and neutron powder diffraction. The latter two clearly showed a threefold superstructure regarding the parent Zintl phase with $a_{\text{hydride}} \approx 3 a_{\text{Zintl phase}}$, i. e. perpendicular to the ${}^1_{\infty}[Tt^{2-}]$ zigzag chains. Structure solution and refinement first led to a model in space group type $Cmcm$ with two fully and two ca. 50% occupied hydrogen sites. Selected-area electron diffraction (SAED) patterns of the Sr compound indicated a further cell doubling, i.e. a six-fold superstructure (Fig. A2.1). With the help of DFT relaxations of various crystal structure candidates, a model with completely ordered hydrogen distribution was found in space group $Pnma$ ($c_{\text{hydride}} \approx 6 a_{\text{Zintl phase}}$, Fig. A2.2). Joint Rietveld refinements using laboratory X-ray and neutron diffraction data of the deuterides revealed vacancies of up to ca. 20% on some of the hydrogen sites (for details of the structure solution and refinement cf. Supplementary Information). SAED patterns of a BaSi hydride sample suggested the presence of a phase

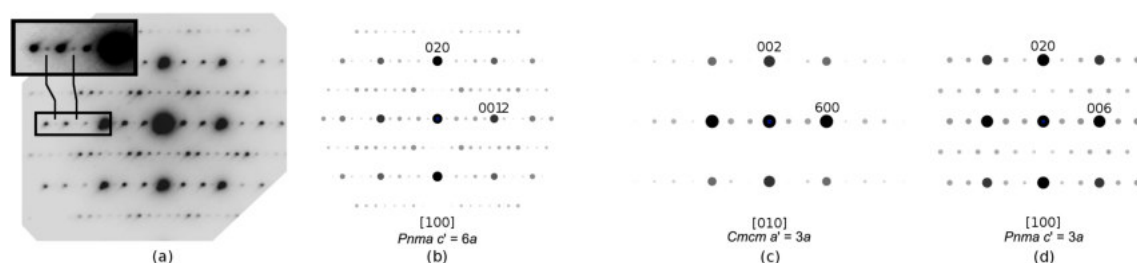


Figure A2.1: (a) SAED pattern of a $SrSiD_{5/3-x}$ crystal (inset does not scale linearly). (b) Simulation using the final model ($Pnma$, sixfold superstructure regarding the parent Zintl phase), all observed reflections are explained. (c) Simulation using the model with half-occupied hydrogen sites ($Cmcm$, threefold superstructure), rows of reflections are missing due to C -centering. (d) Simulation based on the $CaSiH_{1.3}$ structure type, additional row of reflections explained, but mismatch for position and quantity. For corresponding stereographic projection and further SAED patterns with simulations see supplementary information (Fig. A2.S4, A2.S5).

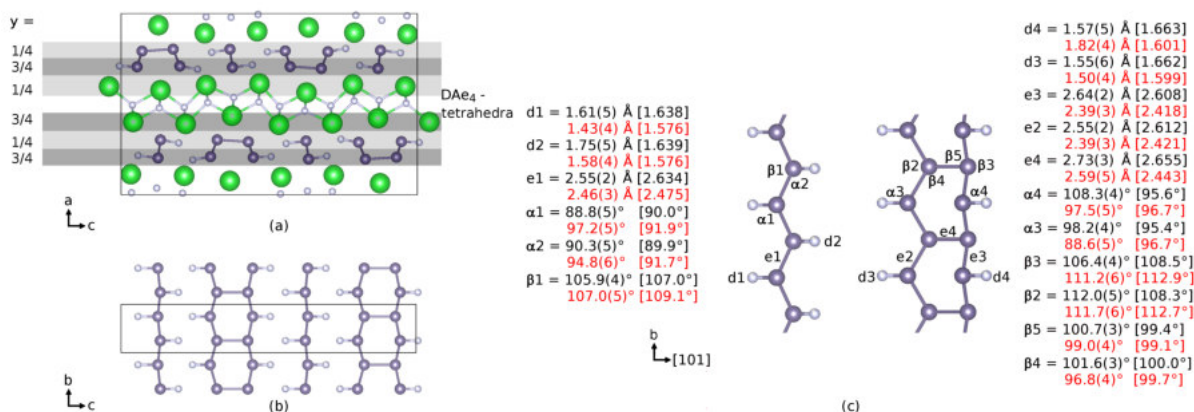


Figure A2.2: Projections of the crystal structure of BaGeD_{5/3-x} (a) and polyanionic partial structure (b), (c), large spheres (green): Ba, medium spheres (gray): Ge, small spheres (white): H (D). Experimental interatomic distances and angles in comparison to corresponding ones calculated by DFT [in brackets] (first line (black): BaGeD_{5/3-x}, second line (red): SrSiD_{5/3-x}).

isotypic to SrSiH_{5/3-x} and BaGeH_{5/3-x}. The formerly unassigned side phase in BaSiH_{2-x} samples [5] is thus identified as BaSiH_{5/3-x} (Figs. A2.S8-A2.S10).

The hydrides of SrSi and BaGe are non-stoichiometric with respect to hydrogen and crystallize in space group type *Pnma* (SrSiH_{5/3-x}, hydride: $a = 15.1009(6)$ Å, $b = 3.95121(18)$ Å, $c = 24.6298(12)$ Å, deuteride: $a = 15.070(2)$ Å, $b = 3.9503(2)$ Å, $c = 24.642(2)$ Å; BaGeH_{5/3-x}, hydride: $a = 15.8253(9)$ Å, $b = 4.2308(2)$ Å, $c = 25.8728(14)$ Å; deuteride: $a = 15.804(3)$ Å, $b = 4.2293(6)$ Å, $c = 25.855(4)$ Å,³¹ Tab. A2.S5, A2.S7, A2.S8 in Supplementary Information). The crystal structures can be rationalized in their idealized composition *AeTtH_{5/3}* according to the Zintl concept as (*AeTt²⁺*)₃(*TtH⁻*)(*Tt₂H₂⁻*)(H⁻)₃, i.e. they contain hydride anions as well as hydrogen covalently bound to the polyanions. Having a formal charge of 1-, all tetrel atoms are expected to form three covalent bonds, either to three tetrel atoms or to two tetrel and one hydrogen atom. The polyanions show two structural motifs (Fig. A2.2). In the first one, the parallel $\frac{1}{\infty}[Tt^{2-}]$ zigzag chains, which are already present in the parent Zintl phase, are inclined towards each other and form additional tetrel-tetrel bonds. This results in double chains $\frac{1}{\infty}[Tt_2H_2^-]$ ($= \frac{1}{\infty}[H Tt - Tt_2 - TtH^{4-}]$, Fig. A2.2), where every other tetrel atom covalently binds to a hydrogen atom. This polyanion may also be described as a chain of condensed six-membered rings of tetrel atoms in boat conformation. The second motif is a zigzag chain $\frac{1}{\infty}[TtH^-]$ as obtained for BaSiH_{2-x}, [5] running parallel to the double chain. The crystal structure is clearly stabilized by strong ionic bonding from additional hydride ions in *Ae₄* tetrahedra (Fig. A2.2). Crystal structure (for both) and hydrogen content (for the BaSi hydrides) contradict an earlier report of hydrides of *AeSi* Zintl phases, where, however, hydrogen positions were not determined.[9] The crystal structure shows a close relationship to the parent Zintl phase. The chain direction of the polyanions ([001] in the Zintl phase, [010] in the hydride) shrinks by 2% upon formation of the hydride. A considerable expansion of more than 30% occurs in the direction perpendicular to the *HAe₄* tetrahedra sheets ([010] in the Zintl phase, [100] in the hydride) (Fig. A2.2) due to the incorporation of hydrogen. Connecting the polyanions of the Zintl phase to double chains leads to a reduction of 15% in that direction ([100] in the Zintl phase, [001] in the hydride, accounting for the sixfold superstructure). These strongly anisotropic effects of hydrogenation certainly reflect the bonding situation, which was investigated by quantum-mechanical calculations (DFT).

In zigzag chain direction [010], tetrel-tetrel bonds are 2.41 Å [2.438 Å] (Si) and 2.58 Å [2.633 Å] (Ge) (DFT results in brackets, Fig. A2.2, e1-3) while the additional chain-connecting bond (Fig. A2.2, e4) is longer with 2.59 Å (Si) and 2.73 Å (Ge). This is not the case for DFT calculated values of the hypothetical stoichiometric composition *AeTtH_{5/3}* (2.443 Å (Si) and 2.655 Å (Ge)). The tetrel-tetrel distances are comparable to those in the pristine Zintl phases. Si-Si-Si angles range from 96° to 111° (Ge-Ge-Ge: 101° to

³¹ Further details on the crystal structure investigations may be obtained from the Fachinformationszentrum Karlsruhe, 76344 Eggenstein-Leopoldshafen, Germany (fax: (+49)7247-808-666; e-mail: crysdata@fiz-karlsruhe.de), on quoting the depository numbers CSD-433047, and -433048.

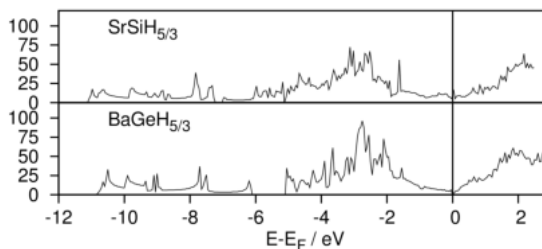


Figure A2.3: Electronic density of states of SrSiH_{5/3} (top) and BaGeH_{5/3} (bottom)

107°) and are in a similar range as in the chair configuration of black phosphorus (\angle P-P-P: 102.09(8)° and 96.34(11)°)[10] and gray arsenic (\angle As-As-As: 96.64(6)°),[11] respectively.

Refined distances Si-D / Ge-D (averaged $d(\text{Ge-D}) = 1.62 \text{ \AA}$ [1.650 \AA], averaged $d(\text{Si-D}) = 1.58 \text{ \AA}$ [1.588 \AA]; DFT results in brackets) indicate covalent interactions. Si-D distances are in between those found in β -KSiD₃ (1.537(8) - 1.545(6) \AA)[4] and BaSiD_{2-x} (1.641(5) \AA),[5] while Ge-D distances are somewhat longer than in molecular GeD₄ (1.517(3) \AA at 5 K)[12] or SrGeD_{4/3-x} (1.521(9) \AA)[5]. Sr-D and Ba-D distances reach from 2.35(4) to 2.57(4) \AA and 2.41(6) to 2.73(6) \AA , respectively, and are comparable to those in DAe_4 tetrahedra of the binary deuterides SrD₂ and BaD₂ (average 2.44 \AA and 2.62 \AA , respectively),[13] thus underlining the ionic nature of bonding within the HAe_4 tetrahedra sheets.

Hydrogen atoms covalently bound to the polyanions do not show full occupation (85(2)% in BaGeH_{5/3-x}, 77.2(8)% in SrSiH_{5/3-x}). There is no hint to further ordering, not even at low temperature, as studied by neutron diffraction on BaGeH_{5/3-x} at 10 K (Supplementary information, Fig. A2.S3). Such hydrogen-atom vacancies are an intrinsic feature of Zintl-phase hydrides $AeTtH_y$ ($Ae = \text{Ca-Ba}$, $Tt = \text{Si-Sn}$, $1 < y < 2$)[5]. They may be related to additional π -bonding due to depopulation of π^* bands upon the formation of hydride anions. The effect of π -bonding has been discussed in detail for the parent Zintl-phase silicides [14–16]. Additional π -bonding in non-stoichiometric samples can be assumed comparing DFT-derived bond lengths, which were calculated on idealized structures with full occupation. Experimentally observed tetrel-tetrel distances along the chain direction [010] are systematically shorter (π -bonded) while chain-connecting bonds are longer than calculated distances.

The density of states (DOS) (Fig. A2.3) was calculated for SrSiH_{5/3} and BaGeH_{5/3} using the relaxed structures with an idealized full hydrogen site occupation. While the DOS of BaGeH_{5/3} hints at a band gap as expected for an electron-precise Zintl-phase hydride, SrSiH_{5/3} has significant electron density at the Fermi level and shows only a pseudo-gap. This could explain the non-stoichiometry, which is more pronounced in the latter compound, by electronic effects.

BaGeH_{5/3-x} and SrSiH_{5/3-x} may be considered the missing link between SrGeH_{4/3-x} with three tetrel zigzag chains connected to form a triple-chain polyanion $\frac{1}{\infty}[\text{HGe}_6\text{H}^{6-}]$ and BaSiH_{2-x} with a single chain $\frac{1}{\infty}[\text{SiH}^-]$. They underline the rich structural chemistry of the hydrides of Zintl phases and represent new structural motifs of main-group element chemistry. Examining the hydrides of CrB type Zintl phases $AeTt$ ($Ae = \text{Ca, Sr, Ba}$; $Tt = \text{Si, Ge, Sn}$) reveals a remarkable compositional, structural and electronic flexibility. There are two main positions for hydrogen atoms, in Ae_4 tetrahedra and attached to tetrel polyanions, both of which may be under-occupied, and there are various types of polyanions in the solid state. Single tetrel zigzag chains may be saturated by hydrogen atoms like in BaSiH_{2-x} [5], or such chains may be connected to form double chains like in $AeTt_{5/3-x}$ or triple chains like in CaSiH_{1.3},[6] γ -SrGeH_{4/3-x} and BaSnH_{4/3-x} [5]. Alternatively, none of the above may occur for hydrogen-poor phases α - and β -SrGeH_{<1},[17] where the electronic balance is adjusted by the Ge-Ge bond length and the degree of π -bonding.

Thus, three types of structural and electronic compensation to the presence of hydrogen may be distinguished: (1) Increasing connectivity from two- to three-bonding by linking of single to double or triple chains, thus considering hydrogenation as an oxidation, e. g. $[\text{Si}(2b)^{2-}] + \frac{1}{2}\text{H}_2 \longrightarrow [\text{Si}(3b)^-] + \text{H}^-$; (2) covalent bonds to hydrogen, e. g. $[\text{Si}^{2-}] + \text{H}_2 \longrightarrow [\text{SiH}^-] + \text{H}^-$; (3) increasing π -bonding in the polyanionic chains by depopulating π^* bands upon formation of hydride anions. The balance between (1) and (2) strongly depends on geometrical restrictions implied by the alkaline earth atoms. With their increasing size, binding hydrogen covalently (2) outweighs the linking of polyanions (1), because of its

higher space requirements. The highest degree of condensation is found in $\text{CaSiH}_{1.3}$, [6] $\gamma\text{-SrGeH}_{4/3-x}$ and $\text{BaSnH}_{4/3-x}$ [5], where the layers of hydride-filled Ae_4 tetrahedra are strongly puckered to fit to the translational period of the polyanionic layers. Complete condensation to hydrogen-free layer-like polyanions ${}^2_{\infty}[\text{Tt}^-]$ is thus unlikely due to geometrical restrictions in these $AeTt$ compounds. For smaller hydrogen contents, however, the electronic flexibility of the π^* electron reservoir seems sufficient and only some strengthening of existing Si-Si and Ge-Ge bonds are found instead of forming new ones. Yet another solution to the optimization of space requirements and electronic structure is found in NdGaH_{1+x} , where hydrogen bridges two gallium zigzag chains approximately halfway between them [18].

To conclude this geometric reasoning, the combination of large alkaline earth and small tetrel atoms favors high hydrogen contents and single polyanionic chains, e. g. ${}^1_{\infty}[\text{SiH}^-]$ in BaSiH_{2-x} [5], while small alkaline earth and large tetrel atoms should support the maximum degree of polyanion condensation. However, the tendency of the tetrel atoms to form stable covalent bonds to hydrogen limits this endeavor as seen for the inertness towards hydrogen (SrSn) or tendency to decomposition (SrPb , BaPb) [5]. Varying the combinations of alkaline earth and tetrel atoms or substituting them by other elements gives ample opportunity to synthesize tetrel-tetrel and tetrel-hydrogen bonds in the solid. Such considerations may serve as a guide for the search for further compounds with new main group element-hydrogen entities or higher hydrogen content.

Acknowledgements

We thank Dr. Patrick Wenderoth for the synthesis of SrSi samples, Dr. Thomas Hansen for help with neutron diffraction, Dr. Gerald Wagner for help with practical TEM work, the Institute Laue-Langevin and Helmholtz Zentrum Berlin for providing beamtime and the Deutsche Forschungsgemeinschaft (Grant Ko1803/8-1) and the Fonds der Chemischen Industrie (Grant 194371) for financial support.

A2.4 Supplement

Experimental Section

Synthesis: All manipulations were done in an argon filled glove box. Moisture and oxygen content were monitored and kept below 1 ppm each. The Zintl phases SrSi and BaGe were prepared from the elements (Sr: Alfa Aesar, 99.8%; Ba: rod, 99.3% (0.7% Sr); Si: ChemPur, 6N; Ge: ChemPur, 6N). SrSi was prepared using an arc furnace and 5% excess of Sr in order to compensate losses due to evaporation. The sample was ground several times and remelted to reach homogeneity. BaGe was prepared from stoichiometric mixtures of the elements by using sealed niobium metal, which were heated under vacuum. The sample was melted at 1373 K and subsequently annealed at 1173 K for 40 h. Hydrides (deuterides) were prepared in Nicrofer[®] 5219Nb-alloy 718 autoclaves. Hydrides and deuterides of SrSi were prepared under 90 bar hydrogen and deuterium pressure, respectively (H₂: Air Liquide, 99.9%; D₂: Air Liquide, 99.8% isotope purity) at 453 K for 24 h. Hydrides and deuterides of BaGe were prepared under 50 bar hydrogen and deuterium pressure, respectively, at 473 K for 10 h. All products are air and moisture sensitive gray powders. Exposed to air, they yield amorphous products. The color of BaGeH_{5/3-x} changes to yellow in the course of this reaction, which is probably caused by hydrolysis to polygermene, (GeH₂)_x [7]. Synthesis and hydrogenation (deuteration) of BaSi are already described elsewhere [5].

Elemental analysis: The hydrogen contents of the hydrides were determined by elemental analysis with a VARIO EL (Heraeus) microanalyzer using the carrier gas-hot extraction method in triplicate repetition. The hydrogen contents of SrSiH_{5/3-x} and BaGeH_{5/3-x} were determined to be 1.36(8) and 1.54(5) mol-% (1.16(6) and 0.73(3) wt-%), respectively, in good agreement with Rietveld refinements on the corresponding deuterides (1.493(12) and 1.57(3) mol-% of deuterium). The hydrogen contents determined by elemental analysis are of the expected value for a stoichiometric composition *AeTtH*_{5/3} by four and two times the standard uncertainty of the respective measurement. The elemental analysis of the BaSiH_y sample gave 1.71(5) mol-% (1.023(3) wt-%) hydrogen content as compared to 1.83 mol-% calculated from the results of a Rietveld refinement (mixture of 92% BaSiH_{2-x1}, x1 = 0.13(2) (taken from [5]) and 8% BaSiH_{5/3-x2}, assuming x2 to be similar as in BaGeD_{5/3-x} / SrSiD_{5/3-x}).

X-ray and neutron powder diffraction: X-ray powder diffraction (XRPD) was performed using a Stoe Stadi P diffractometer with germanium monochromator, copper K_{α1} radiation, and a position sensitive detector Mythen 1K. Neutron powder diffraction (NPD) data were taken at the high-intensity diffractometer D20 [19] (Institut Laue Langevin (ILL), Grenoble, France) at 297 K with a 120° take-off angle and a wavelength $\lambda = 1.86613(16)$ Å, which was calibrated using Si-NIST 640b as external standard. Neutron powder diffraction data were also collected at the fine resolution powder diffractometer (FIREPOD) E9 [20] (neutron source BERII, Helmholtz-Zentrum, Berlin, Germany) using a dry cryostat (TroK) at 10 K and 290 K with a wavelength of $\lambda = 1.7972(2)$ Å.

Rietveld refinement of crystal structures was performed on X-ray and neutron powder diffraction data simultaneously using the *TOPAS*[®] [21] software package. Structure images were prepared using *VESTA* [22, 23]. Structural data were normalized using *STRUCTURE TIDY* [24] as implemented in *VESTA*.

Quantum chemical calculations were executed using the *QUANTUM ESPRESSO* package [25, 26] in the DFT framework with the generalized gradient approximation (GGA) and the Perdew-Burke-Ernzerhof (PBE) [27] functional. Projector augmented waves [28] were used as obtained from PSLibrary [29]. The kinetic energy cutoff was checked for convergence and set to 60 ry. Crystal structures were relaxed using Marzari-Vanderbilt cold smearing [30] at 0.005 ry and a 4x4x12 k-grid prepared according to the Monkhorst-Pack scheme [31]. Lattice parameters *a*, *b* and *c* were relaxed, while angles were fixed to 90°. Atomic coordinates were relaxed without any symmetry restraints. Density of states (DOS) were calculated on the relaxed structures using the tetrahedron method [32] and an 8x8x24 k-grid. The relaxed structure model was checked for pseudo-symmetry using the *PSEUDO* module [33–35] of the Bilbao-crystallographic server [36–39].

The samples for transmission electron microscopy (TEM) were thoroughly ground in an agate mortar in a glove box under argon atmosphere and placed on a copper TEM grid (mesh 200) with a holey carbon film. During the transfer of the sample holder into the TEM instrument the sample was exposed to air for less than 30 s. Imaging and selected-area electron diffraction (SAED) was performed with a Philips STEM CM 200 ST (point resolution 0.23 nm). The sample was moved with a double-tilt low-background sample holder. Energy-dispersive X-ray spectroscopy (EDX) was carried out with an attached EDAX-EDX system. The imaging conditions were 200 kV with energy spread 1.5 eV (9 nm), semi-convergence 1 mrad, $C_S = 1.2$ mm, $C_C = 1.2$ mm. TEM-EDX yielded compositions of 49.5(10)% for strontium and 50.5(10)% for silicon in the deuteride of SrSi and 49.4(9)% barium and 50.6(9)% germanium in the deuteride of BaGe.

Solution and refinement of the crystal structures of $\text{SrSiH}_{5/3-x}$ and $\text{BaGeH}_{5/3-x}$

The crystal structures of the hydrides of SrSi and BaGe were elucidated by a combination of selected-area electron diffraction (SAED), X-ray and neutron powder diffraction. The latter indicated a threefold superstructure regarding the parent Zintl phase with $a_{\text{hydride}} \approx 3 a_{\text{Zintl phase}}$, i. e. perpendicular to the ${}^1_{\infty}[Tt^{2-}]$ zigzag chains. Structure solution and refinement first led to a model in space group type $Cmcm$ with two fully and two about half occupied hydrogen sites. SAED patterns indicated a further cell doubling, i.e. a six-fold superstructure. With the help of DFT relaxations of various crystal structure candidates, a model with fully ordered hydrogen distribution was found in space group $Pnma$ ($c_{\text{hydride}} \approx 6 a_{\text{Zintl phase}}$). In the following, details of structure solution and refinement are given. The former model in space group $Cmcm$ will be called averaged structure model in $Cmcm$ or threefold superstructure, while the latter model will be called structure model in $Pnma$ or sixfold superstructure.

Averaged crystal structure model in $Cmcm$ (threefold superstructure)

The Zintl phases SrSi, BaSi and BaGe crystallize in the CrB type ($Cmcm$) and exhibit infinite polyanionic silicon and germanium zigzag chains ${}^1_{\infty}[Tt^{2-}]$, which run along [001]. The X-ray diffraction patterns of the hydrogenated samples of SrSi and BaGe could be indexed on the basis of orthorhombic C -centred unit cells with threefold superstructures in [100], i. e. perpendicular to the silicon and germanium zigzag chains. A structure model in space group type $Cmcm$ was derived by tripling lattice parameter a of the parent Zintl phases and crystal structures were refined on the basis of X-ray diffraction powder data. Tetrel zigzag chains are stacked along the superstructure direction at distances of 2.915(9) Å and 4.705(7) Å for the deuteride of SrSi and 3.221(6) Å and 4.853(4) Å for the deuteride of BaGe (Fig. A2.S1). Difference Fourier analysis based on neutron powder diffraction data yielded maxima in the center of Sr_4 - and Ba_4 -tetrahedra and within the large gaps between the chains (Fig. A2.S2). The latter are two well separated maxima with a short distance of 1.524(18) Å for the deuteride of SrSi, and 1.35(3) Å for the deuteride of BaGe. Rietveld refinements (Fig. A2.S3) lead to full occupation (within one standard uncertainty) for the positions D1 and D2 in the center of the DAe_4 tetrahedra (Tabs. A2.S1 and A2.S2, fixed to $\text{SOF} = 1$ during the last refinements) and about 50% occupation for each of the other two maxima (D3 and D4, Tabs. A2.S1 and A2.S2), giving chemical formulae $\text{SrSiD}_{5/3-x}$, $x = 0.112(12)$ and $\text{BaGeD}_{5/3-x}$, $x = 0.06(2)$. Si-D distance of 1.511(13) Å and 1.674(14) Å and Ge-D distances of 1.69(2) Å and 1.81(3) Å are in the typical range for covalent tetrel-hydrogen bonds. For $\text{BaGeD}_{5/3-x}$ we performed neutron diffraction experiments at 10 K to check for a possible ordering of the deuterium positions of the averaged model. Reflection intensities did not change significantly with respect to room temperature measurements (Fig. A2.S3). Therefore we assume no dynamic disorder effects for these structures.

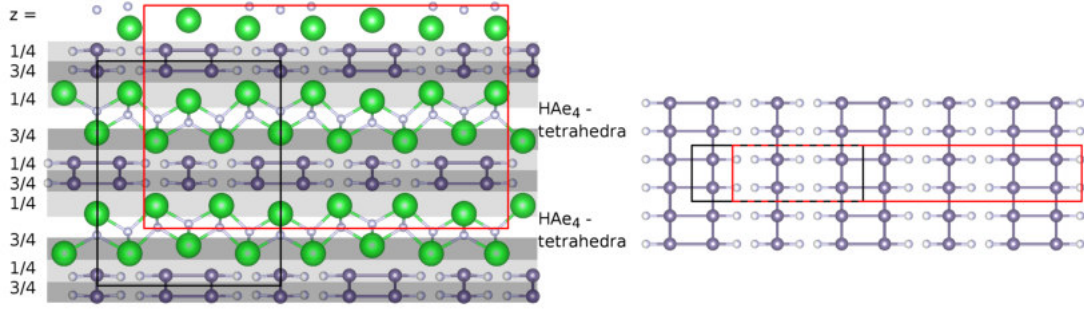


Figure A2.S1: Averaged crystal structure ($Cmcm$, threefold superstructure) of $\text{SrSiD}_{5/3-x}$, $x = 0.112(12)$ and $\text{BaGeD}_{5/3-x}$, $x = 0.06(2)$. Large green spheres: alkaline earth metal (Ae); medium gray spheres: tetrel element (Tt : silicon or germanium); small white spheres: hydrogen / deuterium. Deuterium positions are about half filled. The red unit cell corresponds to the structure model in $Pnma$ (sixfold superstructure) as shown in the main manuscript in Fig. A2.2.

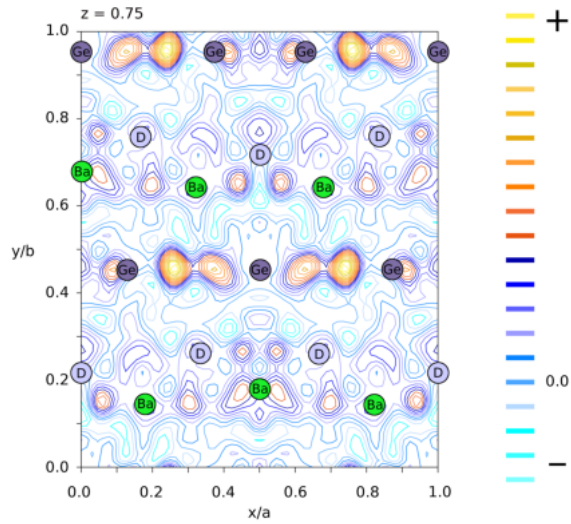


Figure A2.S2: Difference Fourier map of $\text{BaGeD}_{5/3-x}$ from the Rietveld refinement of the averaged model ($Cmcm$, threefold superstructure) on neutron powder diffraction data with maxima in tetrahedral Ba_4 voids (marked with D) and two maxima at the interchain positions.

Table A2.S1: Averaged crystal structure (threefold superstructure) of $\text{SrSiD}_{5/3-x}$, $x = 0.112(12)$, refined on neutron powder diffraction data, space group $Cmcm$ (No. 63), $a = 12.321(2)$ Å, $b = 15.084(2)$ Å, $c = 3.9521(4)$ Å, $R_p = 4.90\%$, $R_{wp} = 6.77\%$, $Gof = 3.94$.

Atom	Wyckoff site	x	y	z	$B_{\text{ios}} / \text{Å}^2$	SOF
Sr1	$4c$	0	0.3197(4)	$1/4$	0.3	1
Sr2	$8g$	0.3219(3)	0.3521(2)	$1/4$	0.3	1
Si1	$4c$	0	0.0391(8)	$1/4$	0.7	1
Si2	$8g$	0.3817(5)	0.0476(7)	$1/4$	0.7	1
D1	$4c$	0	0.7792(6)	$1/4$	1	1
D2	$8g$	0.1629(7)	0.2422(4)	$1/4$	1	1
D3	$8g$	0.1226(10)	0.0384(7)	$1/4$	1	0.414(4)
D4	$8g$	0.2459(10)	0.0385(7)	$1/4$	1	SOF(D3)

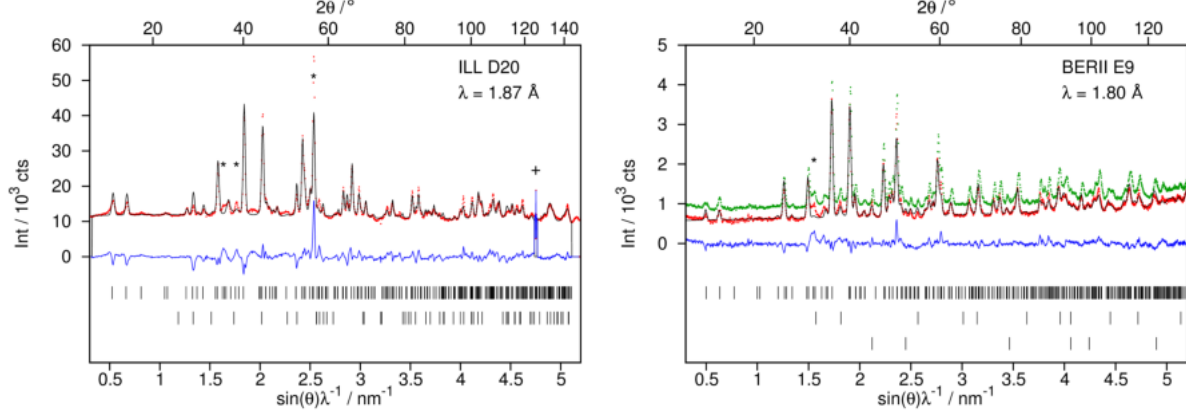


Figure A2.S3: Rietveld refinements of the averaged crystal structures ($Cmcm$, threefold superstructure) on neutron powder diffraction data, reflections that are improved or only described by the model in $Pnma$ (sixfold superstructure) marked with an asterisk. **Left:** $\text{SrSiD}_{5/3-x}$, $x = 0.112(12)$, second row of Bragg markers SrSi2 (3%), (+) detector failure, $R_p = 4.90\%$, $R_{wp} = 6.77\%$, $\text{GoF} = 3.94$. **Right:** $\text{BaGeD}_{5/3-x}$, $x = 0.06(2)$, second and third row of Bragg markers BaO (4%), Al (cryostate), $R_p = 5.67\%$, $R_{wp} = 7.46\%$, $\text{GoF} = 2.24$; green: data collected at 10 K (300 cts offset applied).

Table A2.S2: Averaged crystal structure (threefold superstructure) of $\text{BaGeD}_{5/3-x}$, $x = 0.06(2)$, refined on neutron powder diffraction data, space group $Cmcm$ (No. 63), $a = 12.927(2)$ Å, $b = 15.805(3)$ Å, $c = 4.2299(6)$ Å, $R_p = 5.67\%$, $R_{wp} = 7.46\%$, $\text{GoF} = 2.24$.

Atom	Wyckoff site	x	y	z	$B_{\text{ios}} / \text{Å}^2$	SOF
Ba1	$4c$	0	0.3206(2)	$1/4$	0.1(2)	1
Ba2	$8g$	0.3214(2)	0.35634(15)	$1/4$	B(Ba1)	1
Ge1	$4c$	0	0.0482(4)	$1/4$	0.71(14)	1
Ge2	$8g$	0.3754(3)	0.0461(3)	$1/4$	B(Ge1)	1
D1	$4c$	0	0.7750(9)	$1/4$	0.8(2)	1
D2	$8g$	0.1687(10)	0.2403(5)	$1/4$	B(D1)	1
D3	$8g$	0.1307(15)	0.0409(18)	$1/4$	B(D1)	0.450(8)
D4	$8g$	0.2351(16)	0.044(2)	$1/4$	B(D1)	SOF(D3)

Crystal structure model in *Pnma* (sixfold superstructure)

Transmission electron microscopy (TEM) studies were performed on the deuterides of SrSi and of BaGe. A short contact with air could not be avoided, which did not affect the SrSi deuteride noticeably, but yielded almost complete decomposition to an amorphous powder for the deuteride of BaGe. Selected-area electron diffraction (SAED, Figs. A2.S4, A2.S5 and A2.S6) indicated inconsistencies with the averaged structure model (threefold superstructure), i.e. no *C*-centering, doubling of lattice parameter *a* and the presence of an *n*-glide plane. DFT structure relaxations were used to aid the structure solution. Starting models were derived by doubling of *a* in the averaged model and full occupation of one of the former positions D3 and D4 (Tabs. A2.S1 and A2.S2). All atoms were slightly moved to break crystallographic symmetry. After the DFT structure relaxation, a pseudo-symmetry search [33–35, 39] led to space group type *Pnma* (No. 62) with $a' = b$, $b' = c$, $c' = 6a$ with regard to the parent Zintl phase. A DFT structure relaxation of the same starting model for BaGeD_{5/3} yielded very similar results with an isotopic structure.

Joint Rietveld refinements of the crystal structures were performed on laboratory X-ray and neutron powder diffraction data (Fig. A2.S7). The site occupation factors of deuterium were constrained to be the same for deuterium atoms in tetrahedral voids (D1-D6) and for those binding to the polyanion (D7-D10). The former did not deviate significantly from full occupation and were thus fixed to 1 in the final refinement cycles, which yielded SrSiD_{5/3-x}, $x = 0.174(19)$ and BaGeD_{5/3-x}, $x = 0.10(3)$. Debye-Waller factors were fixed to reasonable values for SrSiD_{5/3-x}, in order to obtain a stable the refinement, but could be refined for BaGeD_{5/3-x} (constrained for like atoms).

Comparing residual (R) values for the refinements of different models showed that using fixed coordinates from the DFT derived model and only refining deuterium occupation already improved the agreement between observed and calculated patterns (Tab. A2.S3). A full structure refinement further improved the fit considerably, which supports the model in *Pnma* (sixfold superstructure) to be a more suitable description of the crystal structures than the averaged model in *Cmcm* (Tabs. A2.S4, A2.S5, A2.S6 and A2.S7). SAED patterns also showed a good correspondence between measured and simulated ones and thus confirmed the so derived structural model.

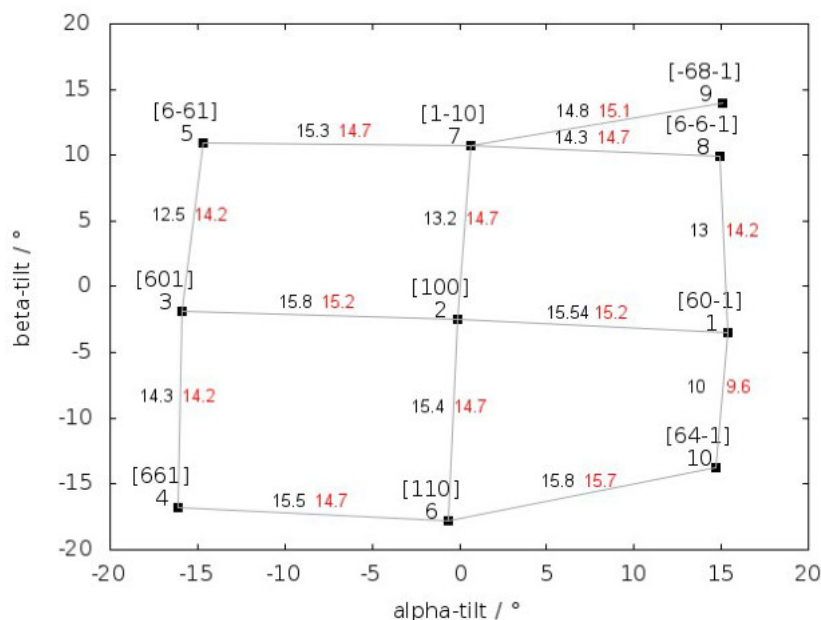


Figure A2.S4: Stereogramm as obtained by SAED of SrSiD_{5/3-x}. Directions are given with regard to the model in *Pnma* with sixfold superstructure, tilt angles between the directions are given; black angles: measured, red angles: calculated.

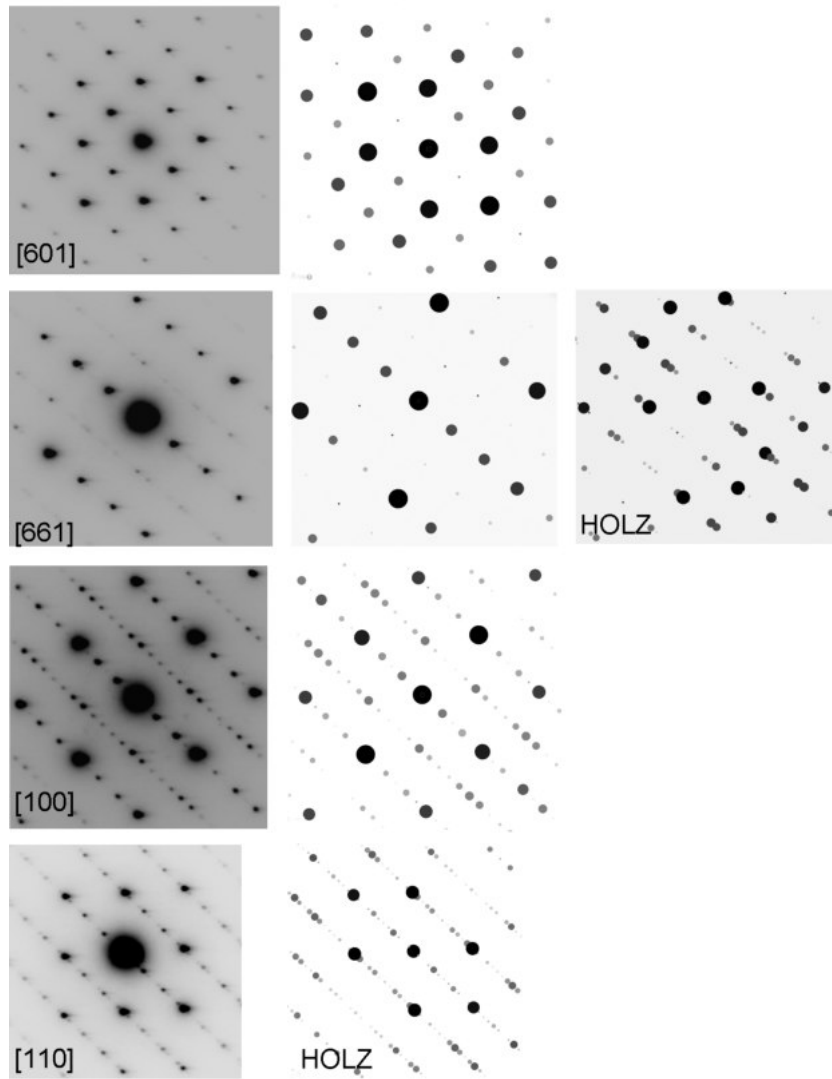


Figure A2.S5: SAED patterns of $\text{SrSiD}_{5/3-x}$ and simulated ones using the final $Pnma$ model with sixfold superstructure regarding to the parent Zintl phase. Lattice parameters were determined by a least squares fit using distances measured from the SAED patterns. $a = 15.15 \text{ \AA}$, $b = 3.96 \text{ \AA}$, $c = 24.67 \text{ \AA}$. HOLZ denotes patterns that contain contributions from higher-order Laue zones.

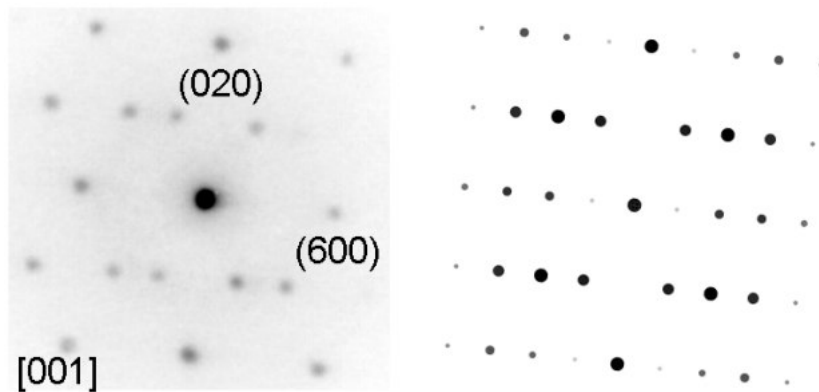


Figure A2.S6: SAED pattern of $\text{BaGeD}_{5/3-x}$ and simulation using the final $Pnma$ model with sixfold superstructure regarding to the parent Zintl phase.

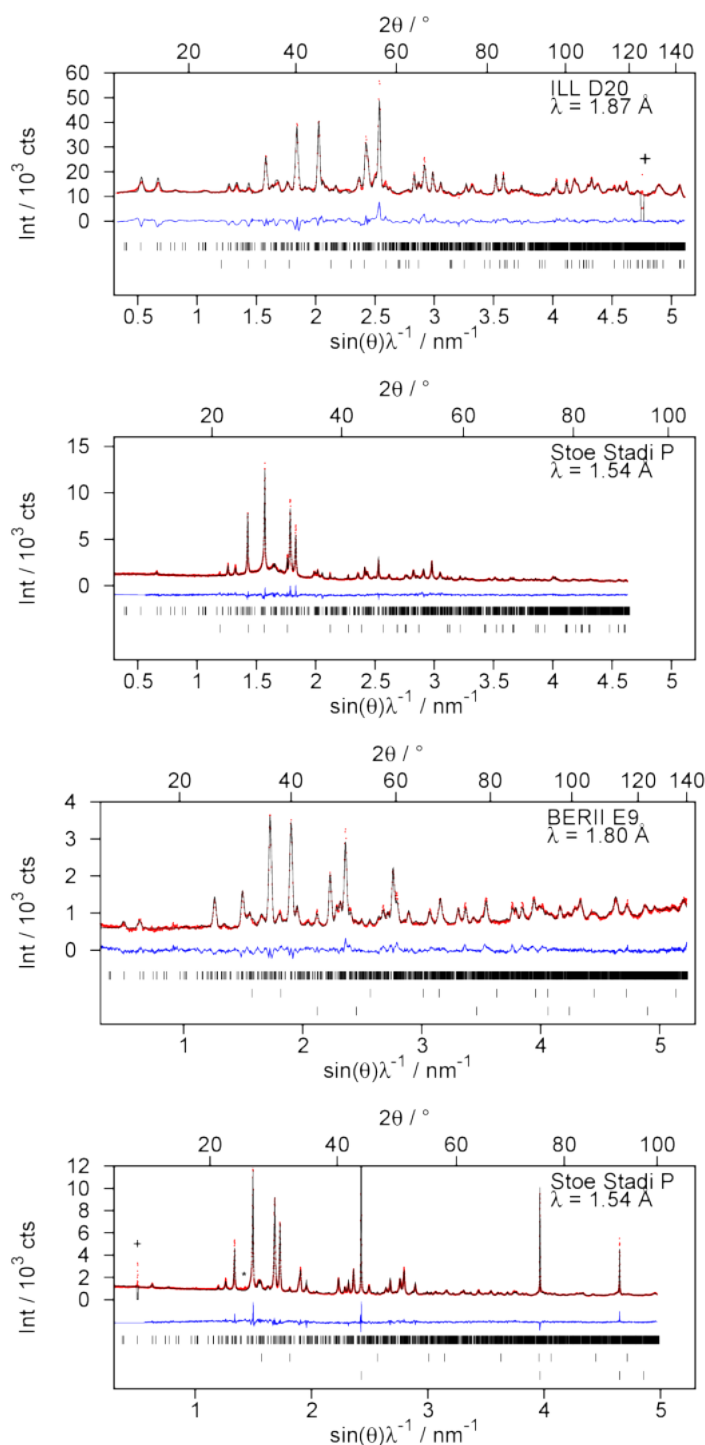


Figure A2.S7: Rietveld refinement of the crystal structure of SrSiD_{5/3-x}, x = 0.174(12) on neutron as well as laboratory X-ray powder diffraction (**top two**). Phases are (neutron / ILL D20): SrSiD_{5/3-x} and SrSi₂ (3%), (+) detector failure, (X-ray / Stoe Stadi P): SrSiD_{5/3-x}, SrSi₂ (2%). R_p = 4.00%, R_{wp} = 5.36%, GoF = 3.13. Rietveld refinement of the crystal structure of BaGeD_{5/3-x}, x = 0.10(3) on neutron powder as well as laboratory X-ray diffraction (**bottom two**). Phases are (neutron / BERII E9): BaGeD_{5/3-x}, BaO (4%), Al (cryostate), (X-ray / Stoe Stadi P): BaGeD_{5/3-x}, BaO (2%), diamond for reducing X-ray absorption, (+) Artefact from powder diffraction, (*) small amount of a third phase. R_p = 5.15%, R_{wp} = 6.71%, GoF = 2.02.

Table A2.S3: R values of Rietveld refinements for the three different models as well as nonstoichiometry term x . For all refinements the same number of profile parameters was used.

Model	x	$R_{\text{exp}} / \%$	$R_{\text{p}} / \%$	$R_{\text{wp}} / \%$
SrSiD _{5/3-x}				
averaged	0.112(12)	1.72	4.90	6.77
DFT ^a	0.179(7)	1.72	4.52	6.05
ordered	0.174(12)	1.71	4.00	5.36
BaGeD _{5/3-x}				
averaged	0.06(2)	3.33	5.67	7.46
DFT ^a	0.13(2)	3.33	5.63	7.40
ordered	0.10(3)	3.32	5.15	6.71

^a atomic coordinates from DFT as described in the text. Debye-Waller factors fixed to the same values as for the full refinements. Occupation of the deuterium positions were refined. Occupation of tetrahedral site as well as chain sites were constraint.

Table A2.S4: Structural data obtained from a DFT structure relaxation and subsequent pseudo-symmetry search of SrSiH_{5/3}; space group $Pnma$ (No 62), $a = 14.426 \text{ \AA}$, $b = 4.0311 \text{ \AA}$, $c = 23.927 \text{ \AA}$.

Atom	Wyckoff site	x	y	z
Sr1	4c	0.44398	1/4	0.37685
Sr2	4c	0.38839	1/4	0.71166
Sr3	4c	0.39931	1/4	0.03846
Sr4	4c	0.39038	1/4	0.5295
Sr5	4c	0.42988	1/4	0.87288
Sr6	4c	0.40058	1/4	0.22038
Si1	4c	0.20439	1/4	0.12201
Si2	4c	0.20489	1/4	0.82414
Si3	4c	0.20166	1/4	0.44198
Si4	4c	0.70906	1/4	0.57377
Si5	4c	0.19646	1/4	0.62744
Si6	4c	0.20705	1/4	0.30686
H1	4c	0.01869	1/4	0.21011
H2	4c	0.00748	1/4	0.53895
H3	4c	0.01734	1/4	0.03521
H4	4c	0.46637	1/4	0.62133
H5	4c	0.47686	1/4	0.12876
H6	4c	0.00716	1/4	0.71587
H7	4c	0.21832	1/4	0.24029
H8	4c	0.20883	1/4	0.05618
H9	4c	0.20014	1/4	0.69325
H10	4c	0.2095	1/4	0.50866

Table A2.S5: Crystal structure of SrSiD_{5/3-x} (sixfold superstructure), $x = 0.174(14)$, space group $Pnma$ (No. 62), $a = 15.070(2)$ Å, $b = 3.9503(2)$ Å, $c = 24.642(2)$ Å. $R_p = 4.00\%$, $R_{wp} = 5.36\%$, $GoF = 3.13$.

Atom	Wyckoff site	x	y	z	$B_{ios} / \text{Å}^2$	SOF
Sr1	4c	0.4402(8)	1/4	0.3763(9)	0.3	1
Sr2	4c	0.3910(14)	1/4	0.7100(6)	0.3	1
Sr3	4c	0.4064(12)	1/4	0.0393(6)	0.3	1
Sr4	4c	0.3925(13)	1/4	0.5329(6)	0.3	1
Sr5	4c	0.4221(8)	1/4	0.8685(6)	0.3	1
Sr6	4c	0.4015(11)	1/4	0.2221(6)	0.3	1
Si1	4c	0.209(2)	1/4	0.1141(10)	0.8	1
Si2	4c	0.221(2)	1/4	0.8256(11)	0.8	1
Si3	4c	0.208(2)	1/4	0.4462(9)	0.8	1
Si4	4c	0.707(2)	1/4	0.5696(14)	0.8	1
Si5	4c	0.1965(18)	1/4	0.6274(14)	0.8	1
Si6	4c	0.191(2)	1/4	0.3147(11)	0.8	1
D1	4c	0.023(2)	1/4	0.2130(11)	1.5	1
D2	4c	0.999(2)	1/4	0.5405(10)	1.5	1
D3	4c	0.016(2)	1/4	0.0391(10)	1.5	1
D4	4c	0.4610(14)	1/4	0.6250(13)	1.5	1
D5	4c	0.4779(14)	1/4	0.1299(10)	1.5	1
D6	4c	0.007(2)	1/4	0.7143(10)	1.5	1
D7	4c	0.220(2)	1/4	0.2429(11)	1	0.772(8)
D8	4c	0.217(2)	1/4	0.0563(9)	1	SOF(D7)
D9	4c	0.198(2)	1/4	0.6916(8)	1	SOF(D7)
D10	4c	0.214(2)	1/4	0.5069(11)	1	SOF(D7)

Table A2.S6: Structural data obtained from a DFT structure relaxation and subsequent pseudo-symmetry search of BaGeH_{5/3}; space group $Pnma$ (No 62), $a = 15.535$ Å, $b = 4.2343$ Å, $c = 25.556$ Å.

Atom	Wyckoff site	x	y	z
Ba1	4c	0.44035	1/4	0.37721
Ba2	4c	0.38589	1/4	0.71185
Ba3	4c	0.3958	1/4	0.03799
Ba4	4c	0.38686	1/4	0.52985
Ba5	4c	0.42819	1/4	0.87263
Ba6	4c	0.39631	1/4	0.22022
Ge1	4c	0.20361	1/4	0.12228
Ge2	4c	0.20148	1/4	0.8234
Ge3	4c	0.19931	1/4	0.44351
Ge4	4c	0.70592	1/4	0.57276
Ge5	4c	0.1959	1/4	0.62743
Ge6	4c	0.20513	1/4	0.30521
H1	4c	0.0168	1/4	0.21003
H2	4c	0.00693	1/4	0.53909
H3	4c	0.01667	1/4	0.03472
H4	4c	0.46438	1/4	0.62166
H5	4c	0.47557	1/4	0.12838
H6	4c	0.00757	1/4	0.71621
H7	4c	0.22026	1/4	0.24079
H8	4c	0.21285	1/4	0.05839
H9	4c	0.20487	1/4	0.69131
H10	4c	0.21141	1/4	0.50812

Table A2.S7: Crystal structure of BaGeD_{5/3-x} (sixfold superstructure), $x = 0.10(3)$; space group *Pnma* (No 62), $a = 15.804(3)$ Å, $b = 4.2293(6)$ Å, $c = 25.855(4)$ Å. $R_p = 5.15\%$, $R_{wp} = 6.71\%$, $GoF = 2.02$.

Atom	Wyckoff site	x	y	z	$B_{\text{ios}} / \text{Å}^2$	SOF
Ba1	4c	0.4359(7)	1/4	0.3742(6)	0.2(2)	1
Ba2	4c	0.3948(12)	1/4	0.7129(5)	B(Ba1)	1
Ba3	4c	0.4021(10)	1/4	0.0407(5)	B(Ba1)	1
Ba4	4c	0.3863(11)	1/4	0.5329(5)	B(Ba1)	1
Ba5	4c	0.4228(7)	1/4	0.8670(4)	B(Ba1)	1
Ba6	4c	0.3912(10)	1/4	0.2178(5)	B(Ba1)	1
Ge1	4c	0.2031(11)	1/4	0.1244(10)	0.75(17)	1
Ge2	4c	0.1966(13)	1/4	0.8244(7)	B(Ge1)	1
Ge3	4c	0.2064(14)	1/4	0.4461(7)	B(Ge1)	1
Ge4	4c	0.7074(16)	1/4	0.5704(7)	B(Ge1)	1
Ge5	4c	0.1968(12)	1/4	0.6327(7)	B(Ge1)	1
Ge6	4c	0.2104(16)	1/4	0.3019(7)	B(Ge1)	1
D1	4c	0.009(4)	1/4	0.2075(19)	1.1(3)	1
D2	4c	0.005(3)	1/4	0.538(2)	B(D1)	1
D3	4c	0.012(4)	1/4	0.035(2)	B(D1)	1
D4	4c	0.463(2)	1/4	0.620(2)	B(D1)	1
D5	4c	0.479(2)	1/4	0.129(3)	B(D1)	1
D6	4c	0.018(3)	1/4	0.713(2)	B(D1)	1
D7	4c	0.193(3)	1/4	0.2420(17)	0.5(4)	0.85(2)
D8	4c	0.217(4)	1/4	0.0572(17)	B(D7)	SOF(D7)
D9	4c	0.214(4)	1/4	0.6942(17)	B(D7)	SOF(D7)
D10	4c	0.211(3)	1/4	0.506(2)	B(D7)	SOF(D7)

Transmission electron microscopy study of $\text{BaSiH}_{5/3-x}$

In a previous study on BaSiH_{2-x} a secondary phase (approx. 10%) was found, whose crystal structure could not be solved [5]. Comparing refined lattice parameters reveals a close relationship to $\text{BaSiH}_{5/3-x}$ as described in this publication (Tab. A2.S8). SAED patterns of two crystals (A and B) were taken. Crystal B could only be indexed using the $\text{SrSiH}_{5/3-x}$ structure type (Fig. A2.S9). Crystal A is assumed to show an intergrowth of two phases with different hydrogen content in the same orientation, i.e. BaSiH_{2-x} [5] and $\text{BaSiH}_{5/3-x}$ in the $\text{SrSiH}_{5/3-x}$ -structure type (Figs. A2.S8, A2.S9 and A2.S10). For crystal A the lattice parameters of BaSiH_{2-x} and $\text{BaSiH}_{5/3-x}$ could not be distinguished since the main reflections overlap (Fig. A2.S10) and thus both possible cells are given in Tab. A2.S8. The combination of synchrotron, neutron and electron diffraction data (Tab. A2.S8 and Figs. A2.S8, A2.S9 and A2.S10) lead us to the conclusion that two hydrides of BaSi exist, BaSiH_{2-x} with its own structure type [5] and $\text{BaSiH}_{5/3-x}$ in the $\text{SrSiH}_{5/3-x}$ type structure. The latter most probably is the formerly found side phase in hydrides of BaSi [5].

Table A2.S8: Lattice parameters of hydrides of BaSi, BaGe and SrSi in space group $Pnma$. $\text{BaSiH}_{5/3-x}$ is the secondary phase assumed to have a structure like $\text{SrSiD}_{5/3-x}$. SAED (selected area electron diffraction) data refer to two crystals (A and B). SPD (data see [5]): synchrotron powder diffraction, NPD: neutron powder diffraction, XRPD: X-ray powder diffraction, “n” denotes the superstructure with regard to the Zintl phase according to $\text{Chydride} \approx n^*a_{\text{Zintl phase}}$.

sample	method	n	$a / \text{\AA}$	$b / \text{\AA}$	$c / \text{\AA}$
BaSiH_{2-x}	SPD	1	15.6924(2)	4.12222(4)	4.48848(5)
$\text{BaSiH}_{5/3-x}$	SPD	6	16.021(2)	4.1129(4)	25.819(3)
BaSiH_y (A)	SAED	1	15.6	4.12	4.42
		6			26.5
BaSiH_y (B)	SAED	6	15.6	4.08	26.1
$\text{BaGeD}_{5/3-x}$	NPD	6	15.804(3)	4.2293(6)	25.855(4)
	NPD,10K	6	15.781(2)	4.2201(4)	25.729(3)
$\text{BaGeH}_{5/3-x}$	XRPD	6	15.8253(9)	4.2308(2)	25.8728(14)
$\text{BaGeH}_{5/3}$	DFT	6	15.535	4.2343	25.556
$\text{SrSiD}_{5/3-x}$	NPD	6	15.070(2)	3.9503(2)	24.642(2)
	SAED	6	15.2	3.96	24.7
$\text{SrSiH}_{5/3-x}$	XRPD	6	15.1009(6)	3.95121(18)	24.6298(12)
$\text{SrSiH}_{5/3}$	DFT	6	14.426	4.0311	23.927

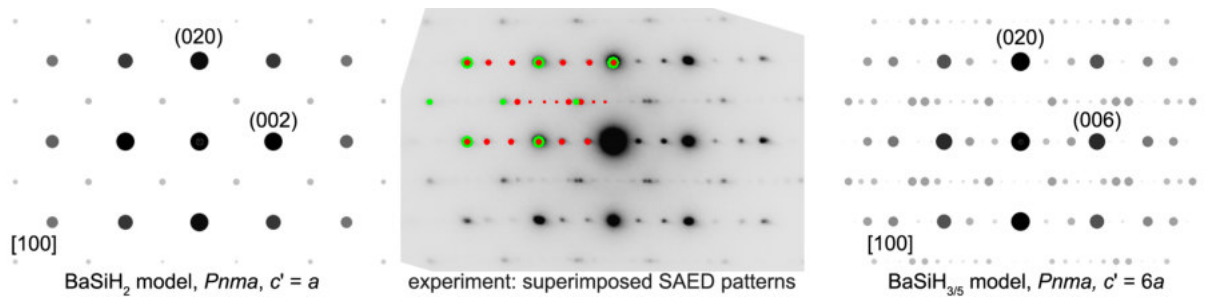


Figure A2.S8: SAED pattern of crystal A (hydride of BaSi) with view on a principal axis similar to Fig. A2.1 (main manuscript). The crystal has two domains with overlapping diffraction patterns. Due to similar lattice parameters the main reflections cannot be distinguished. Simulations of the BaSiH_{2-x} and the $\text{BaSiH}_{5/3-x}$ model are shown and marked in the SAED pattern as well.

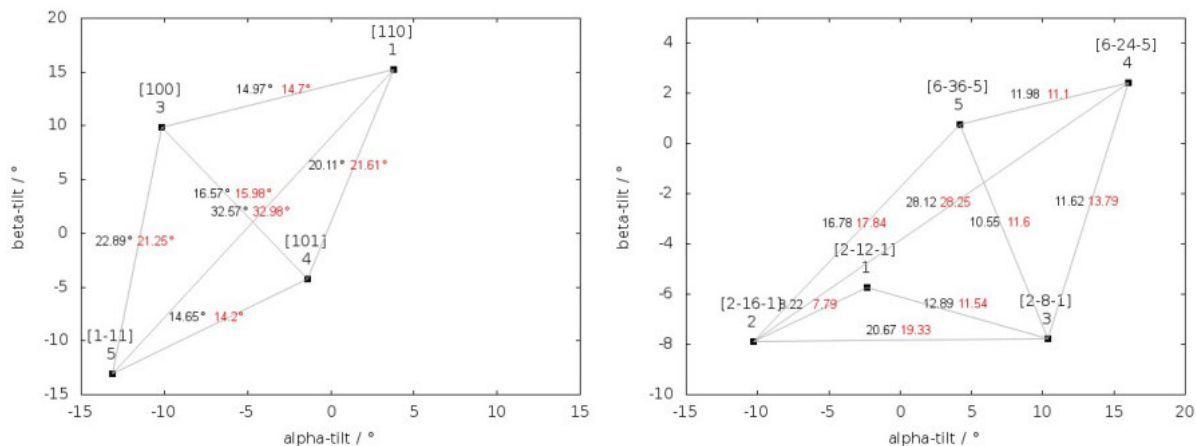


Figure A2.S9: Stereogram as obtained by SAED of BaSi-hydride crystals. Directions are given with regard to (left, crystal A) the BaSiH_{2-x} model ($Pnma$, $c' = a$ with regard to BaSi) and (right, crystal B) the $\text{BaSiH}_{5/3-x}$ model ($Pnma$, $c' = 6a$ with regard to BaSi). Tilt angles between the directions are given; black angles: measured, red angles: calculated.

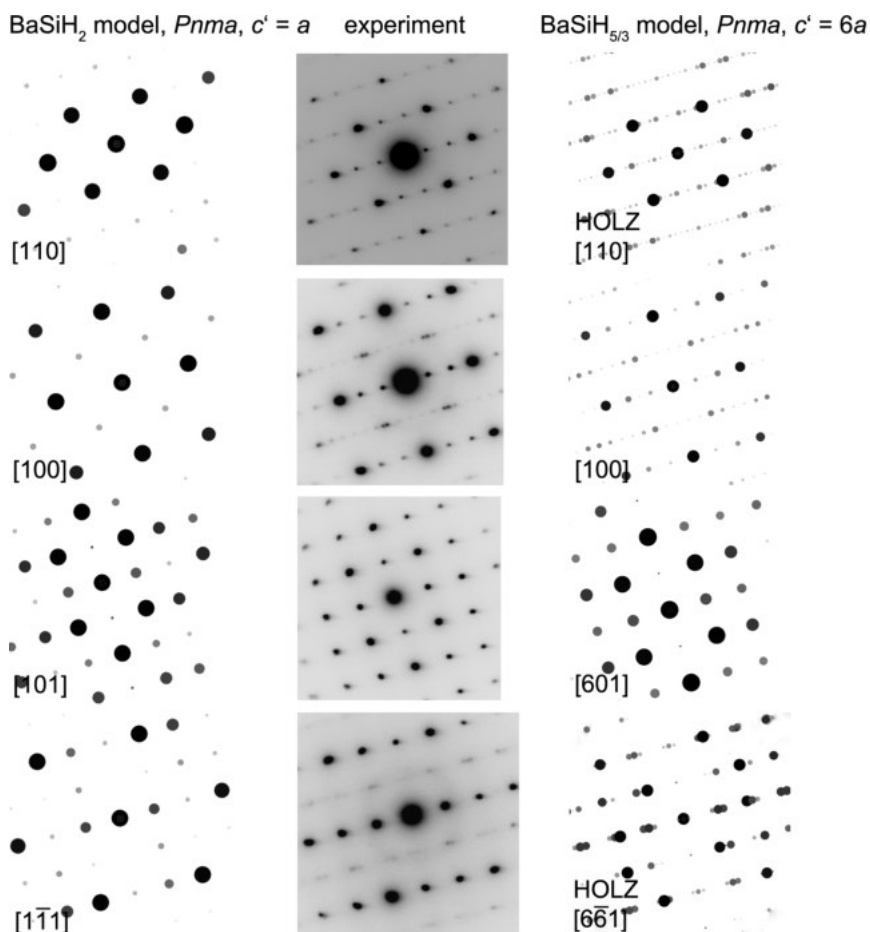


Figure A2.S10: SAED patterns of crystal A (hydride of BaSi) and simulated ones using the BaSiH_2 model and a $\text{BaSiH}_{5/3}$ model that is isotopic to the final $Pnma$ model of $\text{SrSiH}_{5/3-x}$ with sixfold superstructure regarding to the parent Zintl phase. Lattice parameters were determined by a least squares fit using distances measured from the SAED patterns. $a = 15.6 \text{ \AA}$, $b = 4.12 \text{ \AA}$, $c = 4.42 \text{ \AA}$ (BaSiH_2 model). HOLZ denotes patterns with contributions from higher-order Laue zones.

A2.5 References

- (1) Häussermann, U.; Kranak, V. F.; Puhakainen, K. *Struct. Bond.* **2010**, *139*, 143–161, DOI: 10.1007/430_2010_20.
- (2) Fahlquist, H.; Noréus, D.; Callear, S.; David, W. I. F.; Hauback, B. C. *J. Am. Chem. Soc.* **2011**, *133*, 14574–14577, DOI: 10.1021/ja2067687.
- (3) Chotard, J.-N.; Tang, W. S.; Raybaud, P.; Janot, R. *Chem. - Eur. J.* **2011**, *17*, 12302–12309, DOI: 10.1002/chem.201101865.
- (4) Tang, W. S.; Chotard, J.-N.; Raybaud, P.; Janot, R. *J. Phys. Chem. C* **2014**, *118*, 3409–3419, DOI: 10.1021/jp411314w.
- (5) Auer, H.; Guehne, R.; Bertmer, M.; Weber, S.; Wenderoth, P.; Hansen, T. C.; Haase, J.; Kohlmann, H. *Inorg. Chem.* **2017**, *56*, 1061–1071, DOI: 10.1021/acs.inorgchem.6b01944.
- (6) Ohba, N.; Aoki, M.; Noritake, T.; Miwa, K.; Towata, S.-i. *Phys. Rev. B* **2005**, *72*, 075104, DOI: 10.1103/PhysRevB.72.075104.
- (7) Royen, P.; Schwarz, R. *Z. Anorg. Allg. Chem.* **1933**, *211*, 412–422, DOI: 10.1002/zaac.19332110409.
- (8) Kranak, V. F.; Evans, M. J.; Daemen, L. L.; Proffen, T.; Lee, M. H.; Sankey, O. F.; Häussermann, U. *Solid State Sci.* **2009**, *11*, 1847–1853, DOI: 10.1016/j.solidstatesciences.2009.08.007.
- (9) Armbruster, M.; Wörle, M.; Krumeich, F.; Nesper, R. *Z. Anorg. Allg. Chem.* **2009**, *635*, 1758–1766, DOI: 10.1002/zaac.200900220.
- (10) Schiferl, D.; Barrett, C. S. *J. Appl. Crystallogr.* **1969**, *2*, 30–36, DOI: 10.1107/S0021889869006443.
- (11) Brown, A.; Rundqvist, S. *Acta Crystallogr.* **1965**, *19*, 684–685, DOI: 10.1107/S0365110X65004140.
- (12) Maley, I. J.; Brown, D. H.; Ibberson, R. M.; Pulham, C. R. *Acta Crystallogr., Sect. B* **2008**, *64*, 312–317, DOI: 10.1107/S0108768108010379.
- (13) Ting, V. P.; Henry, P. F.; Kohlmann, H.; Wilson, C. C.; Weller, M. T. *Phys. Chem. Chem. Phys.* **2010**, *12*, 2083, DOI: 10.1039/b914135a.
- (14) Reyes, E. C.; Stalder, E. D.; Mensing, C.; Budnyk, S.; Nesper, R. *J. Phys. Chem. C* **2011**, *115*, 1090–1095, DOI: 10.1021/jp106169h.
- (15) Reyes, E. C.; Nesper, R. *J. Phys. Chem. C* **2012**, *116*, 2536–2542, DOI: 10.1021/jp205825d.
- (16) Kurylyshyn, I. M.; Fässler, T. F.; Fischer, A.; Hauf, C.; Eickerling, G.; Presnitz, M.; Scherer, W. *Angew. Chem., Int. Ed.* **2014**, *53*, 3029–3032, DOI: 10.1002/anie.201308888.
- (17) Auer, H.; Wallacher, D.; Hansen, T. C.; Kohlmann, H. *Inorg. Chem.* **2017**, *56*, 1072–1079, DOI: 10.1021/acs.inorgchem.6b01945.
- (18) Ångström, J.; Johansson, R.; Sarkar, T.; Sørby, M. H.; Zlotea, C.; Andersson, M. S.; Nordblad, P.; Scheicher, R. H.; Häussermann, U.; Sahlberg, M. *Inorg. Chem.* **2016**, *55*, 345–352, DOI: 10.1021/acs.inorgchem.5b02485.
- (19) Hansen, T. C.; Henry, P. F.; Fischer, H. E.; Torregrossa, J.; Convert, P. *Meas. Sci. Technol.* **2008**, *19*, 034001.
- (20) Többens, D.; Stüßer, N.; Knorr, K.; Mayer, H.; Lampert, G. *Mater. Sci. Forum* **2001**, *378-381*, 288–293.
- (21) Bruker AXS, TOPAS[®] version 5, www.bruker-axs.com.
- (22) Momma, K.; Izumi, F. *J. Appl. Crystallogr.* **2011**, *44*, 1272–1276, DOI: 10.1107/s0021889811038970.
- (23) VESTA - Visualisation for Electronic and STructural Analysis, version 3.3.1.
- (24) Gelato, L. M.; Parthé, E. *J. Appl. Crystallogr.* **1987**, *20*, 139–143, DOI: 10.1107/s0021889887086965.

- (25) Giannozzi, P. et al. *J. Phys.: Condens. Matter* **2009**, *21*, 395502.
- (26) <http://www.quantum-espresso.org>, QUANTUM ESPRESSO v. 5.1.2, , GNU General Public License.
- (27) Perdew, J. P.; Burke, K.; Ernzerhof, M. *Phys. Rev. Lett.* **1996**, *77*, 3865–3868, DOI: 10.1103/physrevlett.77.3865.
- (28) Blöchl, P. E. *Phys. Rev. B* **1994**, *50*, 17953–17979, DOI: 10.1103/physrevb.50.17953.
- (29) <http://www.qe-forge.org/gf/project/pslibrary>, version 0.3.1.
- (30) Marzari, N.; Vanderbilt, D.; Vita, A. D.; Payne, M. C. *Phys. Rev. Lett.* **1999**, *82*, 3296–3299, DOI: 10.1103/physrevlett.82.3296.
- (31) Monkhorst, H. J.; Pack, J. D. *Phys. Rev. B* **1976**, *13*, 5188–5192, DOI: 10.1103/physrevb.13.5188.
- (32) Blöchl, P. E.; Jepsen, O.; Andersen, O. K. *Phys. Rev. B* **1994**, *49*, 16223–16233, DOI: 10.1103/physrevb.49.16223.
- (33) Kroumova, E.; Aroyo, M. I.; Perez-Mato, J. M.; Ivantchev, S.; Igartua, J. M.; Wondratschek, H. *J. Appl. Crystallogr.* **2001**, *34*, 783–784, DOI: 10.1107/s0021889801011852.
- (34) Capillas, C.; Aroyo, M. I.; Perez-Mato, J. M. *Z. Kristallogr.* **2005**, *220*, DOI: 10.1524/zkri.220.8.691.67076.
- (35) Capillas, C.; Tasci, E. S.; de la Flor, G.; Orobengoa, D.; Perez-Mato, J. M.; Aroyo, M. I. *Z. Kristallogr. - Cryst. Mater.* **2011**, *226*, 186–196, DOI: 10.1524/zkri.2011.1321.
- (36) Aroyo, M. I.; Perez-Mato, J. M.; Capillas, C.; Kroumova, E.; Ivantchev, S.; Madariaga, G.; Kirov, A.; Wondratschek, H. *Z. Kristallogr.* **2006**, *221*, DOI: 10.1524/zkri.2006.221.1.15.
- (37) Aroyo, M. I.; Kirov, A.; Capillas, C.; Perez-Mato, J. M.; Wondratschek, H. *Acta Crystallogr., Sect. A* **2006**, *62*, 115–128, DOI: 10.1107/s0108767305040286.
- (38) Aroyo, M. I.; Perez-Mato, J. M.; Orobengoa, D.; E., T.; de la Flor, G.; Kirov, A. *Bulg. Chem. Commun.* **2011**, *43*, 183–197.
- (39) Bilbao Crystallographic Server, <http://www.cryst.ehu.es/>.

**A3 From metallic $LnTt$ ($Ln = La, Nd$; $Tt = Si, Ge, Sn$) to
electron-precise Zintl phase hydrides $LnTtH$**

Anton Werwein^a, Henry Auer^a, Lena Kuske^a, Holger Kohlmann^{a*}

^a *Leipzig University, Department of Inorganic Chemistry, Johannisallee 29, 04103 Leipzig,
Germany*

** Corresponding author*

Reprinted with permission from

A. Werwein, H. Auer, L. Kuske, H. Kohlmann, *Z. Anorg. Allg. Chem.* **2018**, accepted manuscript No.
zaac.201800062, DOI:10.1002/zaac.201800062.

© 2018 Wiley-VCH Verlag GmbH & Co. KGaA, Weinheim

This is the accepted version with minor adaptations for use with L^AT_EX and one column printing.

A3.1 Authors' contributions

Preparation of LaSi was done and its hydrogenation was investigated by L. Kuske under supervision of H. Auer. The remaining samples and their hydrogenation were investigated by A. Werwein. Initial determination of the crystal structures of the hydride phases was done in parallel for a LaSiH-sample by L. Kuske and H. Auer as well as for a LaGeH-sample by A. Werwein. Neutron diffraction experiments were done by A. Werwein, H. Auer and H. Kohlmann. Furthermore, H. Auer conducted the quantum chemical calculations. A. Werwein assembled the manuscript and did the major part in writing. L. Kuske supplied a draft for the introduction and the description of the synthesis. H. Auer prepared the text and figures regarding the DFT calculations and contributed to the conclusion. The manuscript was edited by H. Kohlmann.

A3.2 Abstract

$LnTt$ ($Ln = La, Nd$; $Tt = Si, Ge, Sn$) compounds crystallize in the CrB- or the FeB-structure type with ${}^1_{\infty}[Tt^{2-}]$ -polyanionic zigzag chains and can be rationalized as $Ln^{3+}Tt^{2-}e^{-}$. They take up hydrogen at gas pressures from 10 to 160 bar and temperatures up to 750 K. The hydrides $LnTtH_{1-x}$ ($0.04 \leq x \leq 0.39$) crystallize either in a hydrogen filled CrB-structure type (ZrNiH type, C -phase, $Cmcm$: LaSiD_{0.92(1)}, LaGeD_{0.88(1)}, NdSiD, NdGeD_{0.95(1)}, LaSnH_x) or in a hydrogen filled FeB-structure type (LaGeH type, P -phase, $Pnma$: LaSiD_{0.61(3)}, LaGeD_{0.96(4)}, NdSiD_{0.88(6)}). In both cases, hydrogen atoms partially fill tetrahedral Ln_4 voids as proven by neutron powder diffraction. While CrB-structure type $LnTt$ reacts to C -phase only, FeB-structure type $LnTt$ hydrogenates to mixtures of C - (major phase) and P -type hydrides. Electronic structure calculations reveal the depopulation of Ln -d states which cause the metallic conductivity in $LnTt$ to be the main electronic effect upon hydrogenation. They further suggest Zintl phase hydrides $LnTtH$ to be still poor metallic conductors with a pseudo band gap at the Fermi level. The hydrogenation reaction from $LnTt$ to $LnTtH$ may thus be regarded as an incomplete metal to semiconductor transition.

A3.3 Article

Introduction

The chemists' view of matter is often a local one and he prefers to see chemical bonds whenever possible. In solids, valence electron rules are very useful for explaining the crystal structures and the chemical bonding situation in mainly ionic and covalent compounds. These concepts rely on electron localization and therefore, do not work in the realm of metallic bonding. Here, delocalized electrons and a nearly uncountable number of states can only be described by band structures. A fascinating class of compounds are Zintl phases which combine all of these bonding modes and often follow simple electron counting rules, at least for their structures. They are polar intermetallic compounds on the border between ionic salts and metals consisting of a group one, two or lanthanide metal and a group 13 to 16 element. Structures of the polyanions can be rationalized by the general 8-N rule [1–8]. A textbook example of a Zintl phase is CaSi. It crystallizes in the CrB-structure type exhibiting a zigzag chain ${}^1_{\infty}[\text{Si}^{2-}]$ -polyanion. In contrast to the ionic picture drawn by the Zintl-Klemm concept with full electron transfer from calcium to silicon, this phase shows poor metallic conductivity. The electronic structure was recently reinvestigated by a theoretical and experimental charge density study [9] showing considerable covalent interaction between Ca-d and Si-p states. This leads to partially depopulated π^* -states within the zigzag chain. Density functional theory (DFT) calculations of the homologue series $Ae\text{Si}$ ($Ae = \text{Ca}, \text{Sr}, \text{Ba}$) lead to the same result [10, 11]. Surprisingly, exchanging the divalent alkaline earth metal by a three-valent lanthanide (Ln) does not alter the structure type, and the Tt -zigzag chains are retained. These phases $LnTt$ are not electron-precise Zintl phases. They can be formulated as $Ln^{3+}Tt^{2-}e^-$ and indeed, these phases show increased metallic conductivity [12]. The excess electron can be attributed to Ln -d states. This again shows how different bonding modes can be combined within one compound. Depending on the combination of Ln and Tt , the compounds crystallize either in the FeB- or CrB-structure type (Figure A3.1). The concept of non electron-precise Zintl phases is also known from several other compounds e.g. A_5Pn_3 ($A = \text{Ca}, \text{Yb}, \text{Sm}, \text{Eu}$; $Pn = \text{Sb}, \text{Bi}$) phases [13–15].

The hydrogenation of Zintl phases $AeTt$ ($Ae = \text{Ca}, \text{Sr}, \text{Ba}$; $Tt = \text{Si}, \text{Ge}, \text{Sn}$) yields hydrides with diverse structure and bonding motifs. They range from hydride anions in interstitial hydrides to hydrogen containing polyanions with covalent Tt-H bonds in polyanionic hydrides, first described by Häussermann [6]. Both features may be combined in hydrides $AeTtH_{4/3}$ and $AeTtH_{5/3}$, which contain one hydride anion per formula unit and $1/3$ or $2/3$ hydrogen atoms bound to the polyanions [16, 17]. LaSi reacts with hydrogen to form a hydride whose crystal structure was not known before [18]. This work systematically investigates the oxidation of non electron-precise Zintl phases $LaTt$ ($Tt = \text{Si}, \text{Ge}, \text{Sn}$) and $NdTt$ ($Tt = \text{Si}, \text{Ge}$) by hydrogen. The reactions were monitored by thermal analysis under hydrogen pressure. Crystal structures of the hydrides were determined by neutron and X-ray powder diffraction. The electronic structures were investigated by DFT calculations.

Results and Discussion

Thermal analysis

Thermal analysis with differential scanning calorimetry (DSC) at 50 bar hydrogen pressure revealed exothermic reactions for all title compounds in the range between 573 K and 773 K suggesting a hydrogen uptake. Subsequent runs show no further signals, thus it can be assumed that reactions were complete

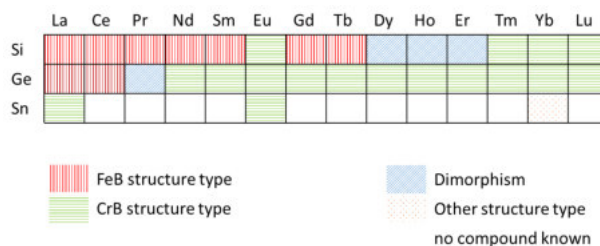


Figure A3.1: Crystal structure types of $LnTt$ (the low temperature modification of LaSi and LaGe are not considered).

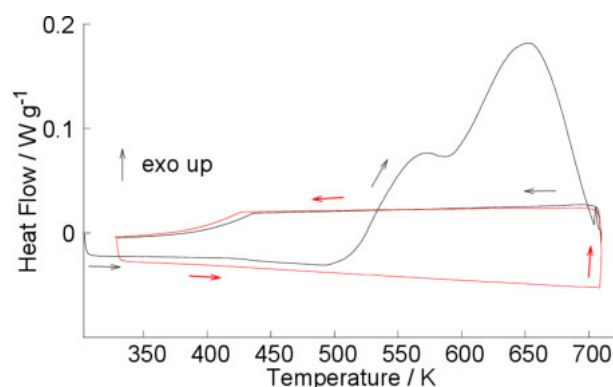


Figure A3.2: Thermal analyses of the hydrogenation of the compound NdGe at 50 bar hydrogen pressure, black line first run, red line second run.

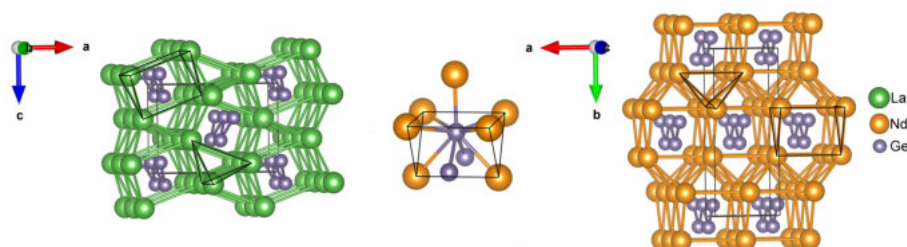


Figure A3.3: Crystal structure of LaGe (**left**, FeB-structure type), the local environment of Ge (**middle**) and the crystal structure of NdGe (**right**, CrB-structure type), a tetrahedral void and a trigonal prism are highlighted.

and not reversible under the given conditions (Figure A3.2, Figures A3.S1-A3.S3). LaSi is an exception since no thermal signals were detected.

Crystal structures

The intermetallic precursors crystallize either in the FeB- (LaSi, LaGe, NdSi) or the CrB-structure type (LaSn, NdGe) [19]. Both feature a capped trigonal prismatic coordination of the tetrelide by the lanthanide atoms complemented by two further tetrelide atoms. This results in a $7+2$ coordination (Figure A3.3). The prismatic units share trigonal faces in the CrB-structure type yielding infinite columns along crystallographic a direction. Neighboring columns share common edges to form sheets. In contrast, the FeB-structure type does not feature infinite columns (Figure A3.3). The tetrelide atoms are connected to zig-zag ${}^1_{\infty}[Tt^{2-}]$ -chains along the c direction (CrB-structure type) and b direction (FeB-structure type). The crystal structures show tetrahedral voids well suited for the occupation by hydrogen. For LaSi and LaGe a low temperature modification exists, which will not be discussed here [20, 21].

X-ray diffraction patterns of hydrogenated samples of $LnTt$ with CrB-structure type (NdGe, LaSn) show similarities to those of the intermetallic precursors. Bragg reflections are shifted to lower angles, indicating a unit cell volume increase, thus suggesting an uptake of hydrogen. The crystal structures can be successfully refined using the CrB-structure type as a starting model with increased lattice parameter b , reduced a and almost equal c (Figure A3.S7).

The remaining title compounds (LaSi, LaGe, NdSi), exhibiting the FeB-structure type, react differently. The obtained X-ray powder diffraction pattern of a hydrogenated sample of LaSi strongly resembles those of LaSiH mentioned earlier, whose crystal structure was not determined [22]. Hydrogenation at low temperatures was reported to lead to lower hydrogen contents $\text{LaSiH}_{<1}$ keeping the FeB-structure type regarding the heavy metal partial structure [22]. Assuming two phases, one based on the CrB-structure type, the other on the FeB-structure type structure, all X-ray reflections of hydrogenated LaSi sample are described well. In the following the phases with a FeB-structure type derived hydrides (LaGeH type, ($oP12$)) will be called P -phase, and the one with the CrB-structure type (ZrNiH type, ($oC12$)) will be referred to as C -phase. The lattice parameters of the P -phase show anisotropic changes regarding the

Table A3.1: Lattice parameter of the Zintl phase hydrides $LnTtH_x$ and lattice parameter changes of the hydrides with respect to the hydrogen-free Zintl phase; the lattice parameters of the deuterides can be found in the tables with crystal structure data. st - structure type: $P = \text{LaGeH}$, $C = \text{ZrNiH}$.

hydride	st	$a / \text{\AA}$	$\Delta a / \%$	$b / \text{\AA}$	$\Delta b / \%$	$c / \text{\AA}$	$\Delta c / \%$	$V / \text{\AA}^3$	$\Delta V / \%$
FeB type precursor									
LaSiH _x	P	8.2148(6)	-3.11	4.0571(3)	0.94	6.3944(5)	5.42	213.11(3)	3.19
LaSiH _x	C	4.2998(2)	-	12.3865(7)	-	4.0283(1)	-	2.1455(2)	-
LaGeH _x	P	8.2710(4)	-1.85	4.1487(2)	0.63	6.3682(3)	4.03	218.52(2)	2.74
LaGeH _x	C	4.3523(1)	-	12.2368(3)	-	4.1245(1)	-	219.66(1)	-
NdSiH _x	P	7.9709(9)	-2.29	3.9709(4)	1.55	6.1503(6)	4.47	195.06(4)	3.67
NdSiH _x	C	4.1776(1)	-	11.9136(3)	-	3.9530(1)	-	196.74(1)	-
CrB type precursor									
NdGeH _x	C	4.2230(1)	-5.21	11.8770(3)	7.54	4.0400(1)	0.29	202.81(1)	3.12
LaSnH _x	C	4.4739(1)	-6.08	12.5998(2)	5.78	4.4515(1)	0.97	250.93(1)	0.31

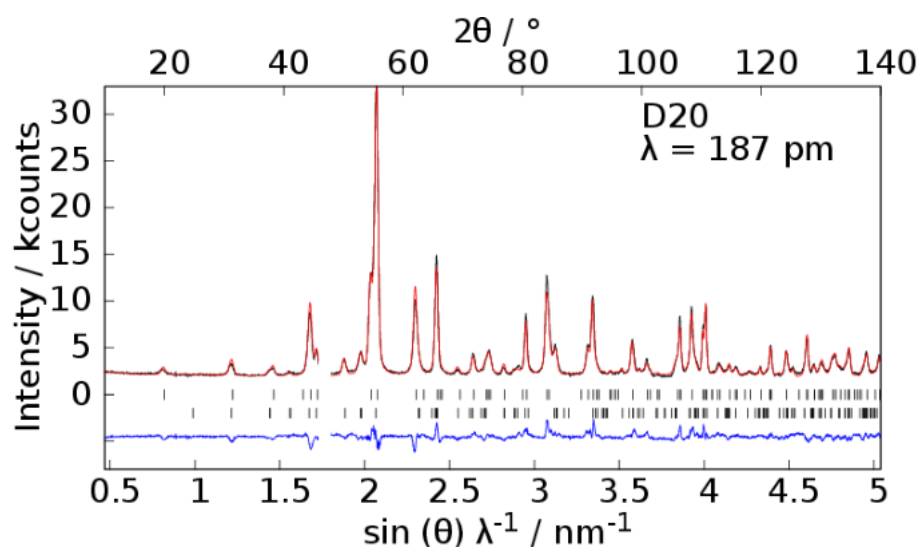


Figure A3.4: Rietveld refinement of the crystal structure of LaGe deuterides using neutron powder diffraction data, Bragg markers from top to bottom: $C\text{-LaGeD}_{0.88}$ (79.6(5) %), $P\text{-LaGeD}_{0.96}$ (20.4(5) %).

intermetallic precursor. While the lattice parameter a becomes smaller, c is getting larger and b stays roughly the same. The P -phase as well as the C -phase show a volume increase with respect to the precursor. This comparison should be taken with care since the hydrogen content between the P - and C -phases are slightly different. The presented examples contain the C -phase as major components. The unit cell volume expansion of the hydrides in respect to the parent Zintl phase is about 3% (except for LaSnH which is $< 1\%$) (Table A3.1).

To locate the hydrogen positions neutron diffraction experiments of the corresponding deuterides LaSiD_x, NdSiD_x, LaGeD_x and NdSiD_x were carried out (Figure A3.4, Figures A3.S4, A3.S5, A3.S6). Rietveld refinement was performed using the metal atom positions determined by X-ray experiments. A difference Fourier analysis was calculated to locate deuterium positions. In both structure types deuterium atoms occupy Ln_4 -tetrahedral voids. In the P -phase the tetrahedra are connected by corners and edges. In the crystallographic b direction they share edges, while in the a and c direction corners are shared. In the C -Phase all tetrahedra are connected to each other by four edges. Thus, the crystal structures can be described as interstitial hydrides resembling filled FeB (P -phase) and CrB (C -phase) type structures (Figure A3.5, Tables A3.2, A3.3, A3.S1-A3.S6, A3.S9, A3.S10).

The driving force of the reaction is the formation of strongly ionic $Ln\text{-H}$ bonds. Changing the lattice parameters reduces the distortion of the tetrahedra that are occupied by hydrogen atoms. Due to the large polarizability of hydride ions, their size depends strongly on the local environment. One possible attempt to describe the different demands in space are volume increments, which should be characteristic for different classes of compound [23, 24]. For $LnTtH$ this fails because of missing volume increments of Tt^{2-}

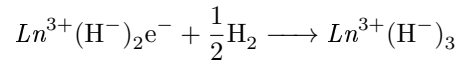
Table A3.2: Crystal structure data of $C\text{-LaGeD}_{0.88(1)}$, $Cmcm$, $a = 4.34400(18)$ Å, $b = 12.2111(8)$ Å, $c = 4.11674(15)$ Å.

atom	Wyckoff site	x	y	z	$B_{\text{iso}} / \text{Å}^2$	Occ
La	$4c$	0	0.3536(6)	$1/4$	0.13(7)	1
Ge	$4c$	0	0.0621(3)	$1/4$	0.30(7)	1
D	$4c$	0	0.7584(4)	$1/4$	1.19(11)	0.878(9)

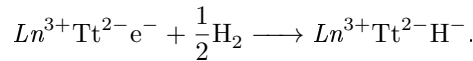
Table A3.3: Crystal structure data of $P\text{-LaGeD}_{0.96(4)}$, $Pnma$, $a = 8.2357(10)$ Å, $b = 4.1245(7)$ Å, $c = 6.4161(12)$ Å (thermal displacement parameters constrained to be the same as in $C\text{-LaGeD}_{0.88}$ (Table A3.2) due to small phase fraction).

atom	Wyckoff site	x	y	z	$B_{\text{iso}} / \text{Å}^2$	Occ
La	$4c$	0.1765(10)	$1/4$	0.130(2)	$B_{\text{iso}}(\text{La}, C\text{-LaGeD}_{0.88})$	1
Ge	$4c$	0.0144(9)	$1/4$	0.602(2)	$B_{\text{iso}}(\text{Ge}, C\text{-LaGeD}_{0.88})$	1
D	$4c$	0.3983(16)	$1/4$	0.414(3)	$B_{\text{iso}}(\text{D}, C\text{-LaGeD}_{0.88})$	0.96(4)

ions. Therefore, the difference in unit cell volume between the Zintl phase and the corresponding hydride was used to estimate the volume increment of the hydride ion. The obtained values are $1.2 \text{ cm}^3/\text{mol}$ (LaSi derived from DFT data), $0.9 \text{ cm}^3/\text{mol}$ (LaGe), $0.9 \text{ cm}^3/\text{mol}$ (NdSi), $0.7 \text{ cm}^3/\text{mol}$ (NdGe), $0.1 \text{ cm}^3/\text{mol}$ (LaSn). Thus, they are far smaller than typical values of ionic or metallic hydrides, where the expected volume increment of hydrogen is about $5\text{-}7 \text{ cm}^3/\text{mol}$ [23, 24]. This discrepancy is due to a change in the chemical bonding situation upon hydrogenation. The reason for the contraction is a further depopulation of π^* -bands regarding to the pristine Zintl phases (see below). The situation is comparable to the hydrogenation of LnH_2 to LnH_3 , where unit cell volumes decrease due to a metal to semiconductor transition [24], i.e.



and accordingly



Furthermore, the $Tt\text{-}Tt$ bond length within the zigzag chains slightly decreases (Table A3.4) for all systems. This contributes a negative volume effect. Both electronic effects reduce the expected volume expansion due to hydrogen incorporation. Neodymium containing samples have a smaller unit cell compared to the corresponding lanthanum containing compounds, which is in agreement with the lanthanide contraction. The $D\text{-}Ln$ distances are all in accordance to comparable ionic hydrides that exhibit tetrahedrally coordinated hydrogen atoms ($2.4257(13)$ Å in LaD_3 and $2.361(4)$ Å to $2.576(8)$ Å in NdH_3) [25, 26]. $D\text{-}Ln$ distances are shorter for the silicides than for the germanides and shorter in the C -phase than in the P -phase (Table A3.4).

The C -phase hydrides are isotypic to ZrNiH [27], whose small monoclinic distortion was apparently ignored for the designation of the structure type in the Inorganic Crystal Structure Database (ICSD),

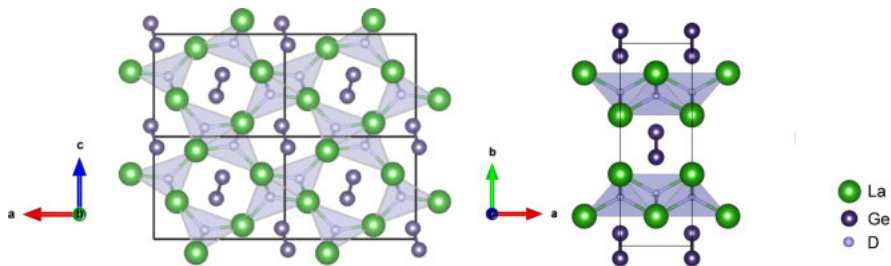


Figure A3.5: Crystal structures of $P\text{-LaGeD}_{0.96}$ (right) and $C\text{-LaGeD}_{0.88}$ (left).

Table A3.4: *Tt-Tt* and averaged *Ln-D* bond lengths in compounds *LnTt* and their hydrides (deuterides).

Precursor	d <i>Tt-Tt</i> / Å	deuteride/ hydride	d <i>Tt-Tt</i> / Å	d <i>Ln-D</i> / Å
LaSi	2.517(4)	<i>P</i> -LaSiD _{0.61(3)}	2.4438(6) ^a	2.475(7) ^a
		<i>C</i> -LaSiD _{0.92(1)}	2.426(9)	2.462(3)
NdSi	2.597(5)	<i>P</i> -NdSiD _{0.88(6)}	2.45(4)	2.3923(4)
		<i>C</i> -NdSiD	2.314(8)	2.3843(4)
LaGe	2.6673(9)	<i>P</i> -LaGeD _{0.96(4)}	2.454(10)	2.502(3)
		<i>C</i> -LaGeD _{0.88(1)}	2.577(4)	2.4671(4)
NdGe	2.685(5)	NdGeD _{0.95(1)}	2.502(5)	2.3948(3)
LaSn	2.9913(7)	LaSnH _x	2.8319(9)	

^a atomic coordinates are fixed according to the DFT model (Table A3.S9), only lattice parameters were refined.

deposition number 201426, spacegroup type *Cmcm*). It features Ni zigzag chains and HZr₄-tetrahedra. Li₂Ga with Ga zigzag chains and LiLi₄ tetrahedra [28] is isopointal, but due to major differences for lattice parameter ratios not isotypic ($b/a \approx 2.8$ (LnTtH), ≈ 3 (ZrNiH), ≈ 2 (Li₂Ga)). One of the rare examples for filled FeB-structure types is AgTlS [29], which is isopointal to the title compounds. In contrast to Zintl phase hydrides, silver atoms are shifted strongly away from the center of the tetrahedra and thallium chains are almost perfectly lying in the (*b,c*) plane. These structural differences between AgTlS and Zintl phase hydrides prevent a classification as isotypic. Therefore, crystal structures of the *P*-phase hydrides will be referred to as LaGeH type. In contrast to Zintl phase hydrides *AeTtH_x* with alkaline earth elements *Ae* combining features of both interstitial and polyanionic hydrides [6], *LnTtH* hydrides are of interstitial nature only.

Total energy calculations show, that the stabilization of the FeB-structure type LaSi as compared to CrB-structure type LaSi is only 2 meV/f.u. which corresponds to the convergence criterion of these calculations. The hydrogenation $\text{LaSi} + \frac{1}{2}\text{H}_2 \longrightarrow \text{LaSiH}$ lowers the total energy by 656 meV (LaGeH type) or 703 meV (ZrNiH type). We assume that voids of the FeB-like Zintl phase are filled first, before the crystal structure transforms into the hydrogen filled CrB-structure type at higher temperatures. Further *in situ* diffraction experiments are necessary to confirm this hypothesis.

This subtle influence of hydrogen on the crystal structure of metal hydrides, sometimes called the structure-directing effect, is well known. It plays an important role in compounds A_5Pn_3 ($A = \text{Ca, Yb, Sm, Eu}$; $Pn = \text{Sb, Bi}$), some of which are in fact ternary hydrides $A_5Pn_3\text{H}$ [13–15]. Further examples include structural change upon hydrogenation like (i) from cubic to hexagonal close packing for heavier lanthanides for the reaction $\text{LnH}_2 + \frac{1}{2}\text{H}_2 \longrightarrow \text{LnH}_3$ [30], (ii) from a crystal structure related to the doublehexagonal close packing to one related to a cubic close packing (ccp) or between different ccp related structures in palladium-rich intermetallics [31] or (iii) from a TiNiSi to the ZrNiAl or to the ZrBeSi type of structure in compounds LnNiSn [32, 33]. The structure directing effect of hydrogen is also at work in order-disorder transitions in complex transition metal hydrides and Laves phase hydrides, where the driving force for the transition is the minimization of repulsive H-H interactions [34–36].

DFT calculation

Recent experimental as well as theoretical charge density studies of CaSi show considerable covalent interaction between calcium and silicon atoms [9]. Calcium d-states interact with silicon p-states leading to the poor metallic behavior. The same trend is observed for the heavier elements Sr and Ba [10, 11, 37].

The hypothetical structure of LaSi in CrB-structure type is a good model system to study electronic changes [38]. There are polyanionic as well as lanthanum sheets that correspond well to the orientation of (molecular) p- and d-orbitals, which simplifies the interpretation of a fatband and *m*-resolved projected density of states representation. FeB- and CrB-structure type show the same coordination for the polyanionic chain, thus the effects for both structures are similar.

We calculated the density of states as well as the band structure of CrB-type LaSi, CaSi and LaGa to compare the results to the electron-precise LaSiH (*C*-phase). Furthermore density of states was calculated for FeB-structure type LaSi and the corresponding *P*-phase LaSiH. FeB-structure type LaSi as well as

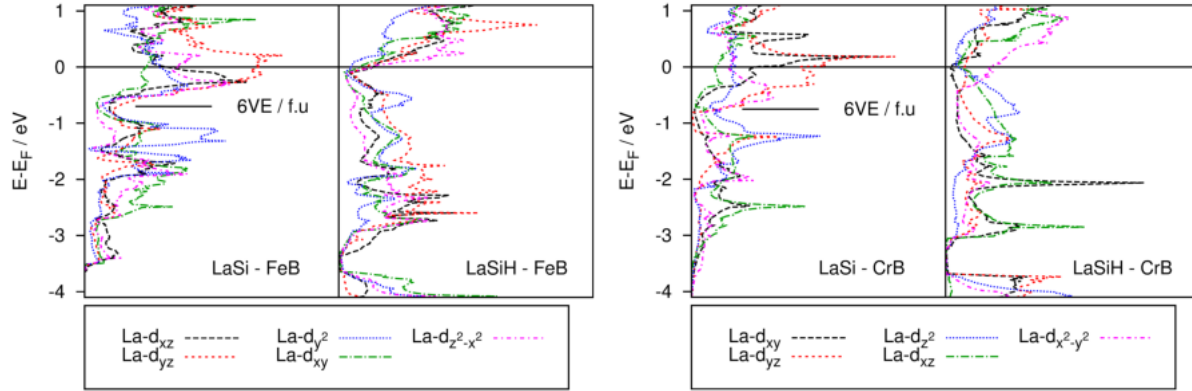


Figure A3.6: m -resolved pDOS of the lanthanum d-states. A comparable spatial orientation of orbitals of the different structure types is given in equal colors.

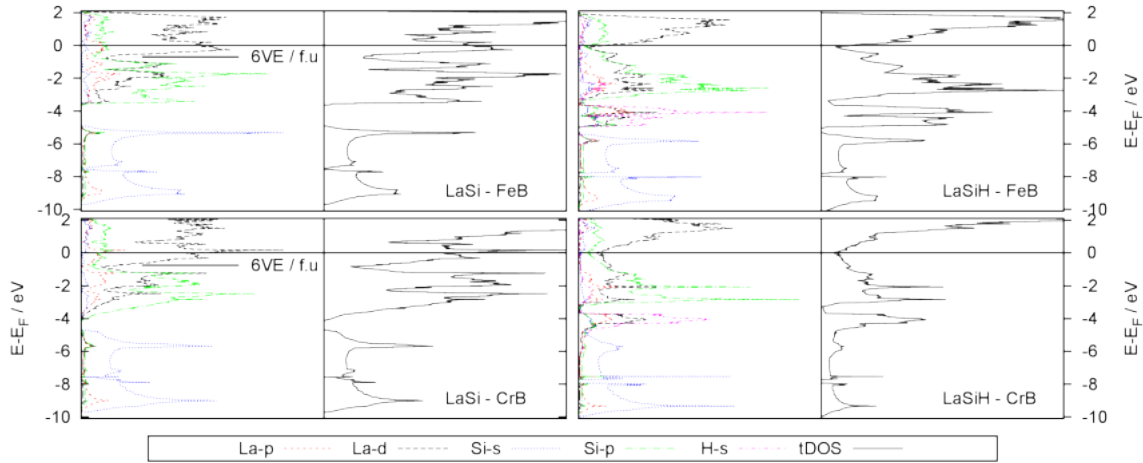


Figure A3.7: Total (tDOS) and l -resolved partial (pDOS) density of states. Energies are referenced to the Fermi level. For the hydrogen-free Zintl phases there is a pseudo gap at the electron count of 6 VE, which matches a formally electron-precise Zintl phase.

CrB-structure type LaSi show large density of states at the Fermi-level indicating the metallic property of this compound (Figure A3.6). The region around the Fermi level is dominated by lanthanum d-states (d-metallicity) and silicon p_x -states forming a π -band (π -metallicity). The fully hydrogenated compounds (both structure types) show a pseudo-gap. Mainly the La-d contributions have vanished. The hydride anion states at about -4 eV show only a small dispersion as expected from an ionic species. Silicon s- and p-states do hardly mix. Thus, hybridisation is small as well. The s-states lie almost completely below -5 eV. There is a high density of Si-p states above -4 eV from σ -bands formed by p_y - p_z interaction. Furthermore, Si- p_x states rise above the Fermi level (π -band, see Figure A3.8). There are pseudo-gaps at 0.75 eV (CrB-type) and -0.70 eV (FeB-type) which correspond to six valence electrons per formula unit and therefore matches a hypothetical Zintl-precise electron count (Figure A3.7) [38].

The d-metallicity can be further described by considering l -resolved partial density of states (pDOS) (Figure A3.7) and the fatband representation. Orbitals are differently oriented in FeB- ($Pnma$) and CrB- ($Cmcm$) type LaSi. Figure A3.6 shows similarly oriented orbitals in equal colors. La- d_{yz} states (both structure types) exhibit a large contribution at the Fermi-level. According to the fatband representation, they do not mix with Si-p states (see Figures A3.6, A3.8, A3.S9-A3.S11). The d_{z^2} -states (CrB type, d_{y^2} for FeB type) show the same behavior but with less contribution. pDOS as well as fatbands show that these states cross the Fermi level leading to metallic behavior. Both types of orbitals are oriented towards other lanthanum atoms, thus the La_4 -tetrahedra are dominated by this interaction. Upon hydrogenation HLa_4 -

units are formed that are dominated by ionic interactions. According to the pDOS the metallic d_{yz} and d_{z^2} (d_{y^2})-states are totally depopulated at the Fermi level. Additional to the metallic La-La interaction in hydrogen-free LaSi and the mainly ionic HLa_4 -moieties of LaSiH, there is covalent interaction between La and Si atoms. For LaGa and CaSi there is an interaction between La(Ca)- d_{xz} and $-d_{xy}$ orbitals and the π -band of Ga(Si) [9, 38]. The fatband representation of the model CrB type LaSi emphasizes this well. The pDOS of LaSi (CrB type) shows a large contribution of them above the Fermi level, which is the mixing part with the π^* -states (see Figure A3.7 and A3.8). This interaction might be considered as some sort of π -back-bonding towards Si(Ga) depopulating the π^* -band and leads to metallic behavior (π -metallicity) as well. Upon hydrogenation of LaSi the described La-Si interactions do not change qualitatively, but the π^* orbitals are lifted regarding the Fermi-level (Figure A3.8). Therefore, there is an overall depopulation of π^* -states, i. e. an oxidation of silicon atoms in the polyanion. This can be seen from the bond lengths, which decrease from 2.517(4) Å (LaSi) to 2.4438(6) Å (LaSiD_{0.61(3)}). The partial occupation is comparable to CaSi as seen from fatband representation. According to bond lengths the effect is even stronger since the bonds are shorter than in CaSi (2.45 Å) [38–40]. The solid solution series LaGa_xSi_{1-x} shows such an increase of the bond order for increasing gallium content [38], but the effect is superimposed by the different covalence radii of silicon and gallium. Our example clearly shows the stronger π^* -depopulation of the formally electron-precise Zintl phase. Furthermore, all systems show a mixing of La(Ca)- p_y , which is oriented towards the sheets of La(Ca)-tetrahedra, with Si(Ga)- $d_{x^2-y^2}$ (Figure A3.8). These states also show considerable contribution to the d-dominated metallicity. Upon oxidation these states do not change strongly and still cross the Fermi level. In contrast to this behavior, in CaSi and LaGa these bands are shifted above the Fermi-edge, but mixing with Si/Ga- $p_{x/y}$ states increases.

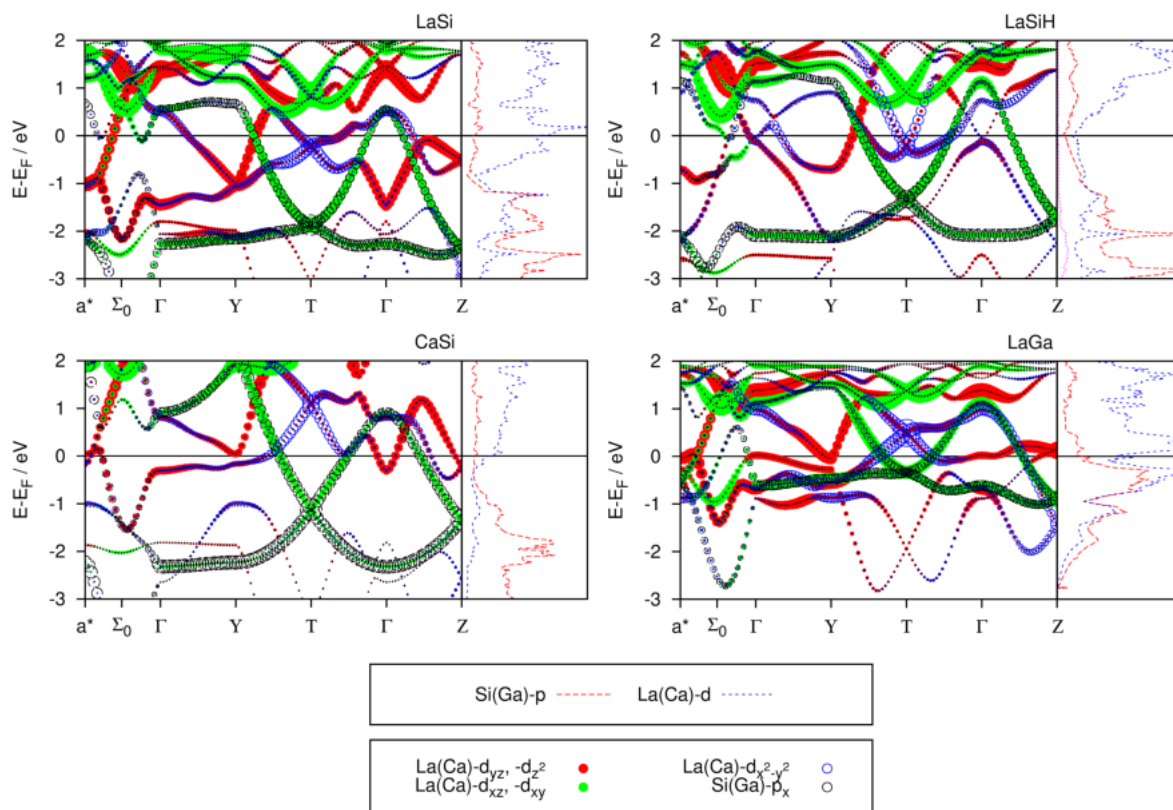


Figure A3.8: Fatband representation of the π -band (black circles) of CrB-type structures. Additionally the pDOS of Si(Ga)- p and La(Ca)- d states are shown. The contribution of La- d_{yz} and $-d_{z^2}$ (d -metallic states) are shown in red, La- d_{xz} , $-d_{xy}$ (La-Si-mixing) are shown in green. The La- $d_{x^2-y^2}$ states resemble both effects and are shown in blue. All LaSi and LaSiH fat bands are shown in the supplement.

Conclusions

Metallic Zintl phases $LnTt$ ($Ln = \text{La, Nd}$; $Tt = \text{Si, Ge, Sn}$) take up hydrogen to form the electron-precise compounds $LnTtH$. The precursor phases resemble CrB- or FeB-structure type exhibiting ${}^{\infty}[Tt]$ -zigzag chains. According to the Zintl concept, these phases can be described as $Ln^{3+} Tt^{2-} e^{-}$. The excess electron causes the metallic behavior that can be mainly attributed to Ln -d states (d-metallicity). Furthermore, there is significant covalent Ln - Tt interaction, which is also seen in the isotypic, electron-precise Zintl phases $AeSi$ ($Ae = \text{Ca, Sr, Ba}$) [10, 11, 37]. In a more local picture this interaction can be considered as π -back bonding towards Ln and leads to a depopulation of π^* -bands of the Tt -zigzag chains and poor metallic behavior (π -metallicity). Upon hydrogenation, tetrahedral Ln_4 -voids already present in the parent phase are filled with hydrogen. CrB-structure type precursors (NdGe, LaSn) lead to single-phase hydrides $LnTtH$ in ZrNiH-structure type. Thus, the topology of the parent phase is retained. This type of hydrides are called C -phase. FeB-structure type phases (ht-LaSi, LaGe, NdSi) react to form hydrides isotypic to ZrNiH as major phase as well. There is always a minor phase present, which keeps the heavy metal structure of the FeB-type and shows HLn_4 -tetrahedra as well. This new structure type is referred to as LaGeH-structure type or P -phase. In the case of $LaSiH_x$, the minor P -phase has a considerably lower hydrogen content ($x = 0.61$) compared to the C -phase ($x = 0.92$). The remaining two-phase systems show almost equal hydrogen contents for C - and P -phase. Total energy DFT calculations for LaSiH confirm the thermodynamic preference of the C -phase. Electronic structure calculations on LaSi (FeB-structure type and hypothetical structure in CrB-structure type) and their hydrides reveal the depopulation of La-d states to be the main electronic effect of hydrogenation. This leads to a pseudo band gap, i. e. the hydrides are poor metals with an electronic structure comparable to $AeSi$ ($Ae = \text{Ca, Sr, Ba}$) or LaGa. The contribution of the Si- π band is hardly effected, with only slightly stronger depopulation of π^* -states, resulting in a shortening of Tt - Tt distances within the zigzag chains. Thus, the reaction can be formally described as an incomplete metal to semiconductor transition.

Experimental Section

Synthesis: Due to the air sensitivity of the compounds all handlings were carried out in an argon filled glove box. Lanthanide metals (La, Nd; Chempur with a purity of 99.9% or better) were surface cleaned, cut into small pieces, and mixed with lumps of silicon (abcr GmbH, 99,9999%), germanium (Chempur 99,9999%) or tin (Alfa Aesar, 99,8%) in a stoichiometric 1:1 ratio. The metal lumps were fused in an arc furnace (400 mbar argon) and melted several times. For preparation of the hydrides (deuterides), well-ground samples were placed in crucibles made from hydrogen-resisting Böhler L718-V alloy and reacted with hydrogen (deuterium) gas (hydrogen: Air Liquide, 99.9%; deuterium, Air Liquide, 99.8%) at 50 bar (30 bar for LaSi) in autoclaves made from the same alloy. The temperature was increased with 100 K/h until the maximum temperature of 773 K and held for 48 h. After the annealing time, the furnace was switched off. After reaching room temperature, the autoclave was removed from the furnace.

Thermal analysis: Hydrogenation experiments were carried out in a differential scanning calorimeter (DSC) Q1000 from TA Instruments equipped with a gas pressure cell. 10-30 mg of the powdered samples were loaded in aluminium pans, which were subsequently crimped. The experiments were performed with a heating rate of 10 K/min under a hydrogen atmosphere of 50 bar at 298 K, which rose to 67 bar at the final temperature of 703 K, due to the isochore setup.

X-ray powder diffraction: X-ray powder diffraction data were collected on a Huber G670 camera with image plate system using $\text{MoK}_{\alpha 1}$ or $\text{CuK}_{\alpha 1}$ radiation. Flat transmission samples were prepared by grinding the moisture sensitive powders in an argon atmosphere, mixing with apiezon grease, and putting the sample between two sheets of capton foil.

Neutron powder diffraction: Neutron powder diffraction was carried out at the Institut Laue-Langevin in Grenoble, France, at the high-flux diffractometer D20 in high-resolution mode as well as at the E9 diffractometer at the Helmholtz Zentrum, Berlin, Germany. Powdered samples were held in indium-sealed vanadium containers with 6 mm inner diameter. The wavelengths were calibrated using silicon (NIST640b) as an external standard.

Rietveld refinement: Rietveld refinement [41, 42] were performed using TOPAS [43] or FULLPROF [44, 45]. The crystal structures were visualized with VESTA [46, 47]. Further details of the crystal structure investigations may be obtained from FIZ Karlsruhe, 76344 Eggenstein-Leopoldshafen, Germany (fax: (+49)7247-808-666; e-mail: crysdata@fiz-karlsruhe.de) on quoting the deposition numbers CSD-434191 (LaGeD_{0.88}), -434192 (LaGeD_{0.96}), -434193 (LaSiD_{0.92}), -434194 (LaSnH_x), -434195 (NdGeD_{0.95}), -434196 (NdSiD), -434197 (NdSiD_{0.88}).

DFT Calculation: DFT calculations were performed with the Abinit package [48–52] using generalized gradient approximation (GGA) and the Perdew-Burke-Ernzerhof (PBE) functional [53]. Projector augmented wave (PAW) [54] atomic data were taken from the JTH PAW atomic dataset table [55, 56]. Calculations were converged regarding kinetical energy cutoff, k-point grid and smearing of metallic occupation levels with an accuracy of 0.1 mhartree. The kinetical energy cutoff (ecut) was set to 35 hartree (pawecutdg = 70 hartree). The compounds were treated metallic with 1 mhartree Gaussian smearing (occopt = 7, tsmear = 0.001). The smearing contribution of the total energy was lower than 0.1 mhartree. Geometry optimisations and total energy calculations were performed using space group *Pnma* for FeB- as well as CrB-structure type. For the latter one this subgroup was used, to have the same degrees of freedom for both structures. The hydrogen filled structures were treated similarly. For structure relaxations a 6x12x12 Monkhorst-Pack-grid was applied [57]. Lattice parameters reproduce experimental data with less than 1% deviation. Density of states were calculated using a 12x24x24 k-grid and integration was done using the tetrahedron method [58]. Fatbands were calculated for special k-paths (Figure A3.S8).

Supporting Information: Thermal analyses of the hydrogenation reactions of LaGe, LaSn, NdSi; Rietveld refinements and crystal structures of deuterides of LaSi, NdSi, NdGe, LaSn; DFT calculated crystal structures and fatband representations of LaSi and LaSiH in different structure types.

Acknowledgements

We thank the Institute Laue-Langevin and the Helmholtz-Zentrum Berlin for providing beamtime. Furthermore, we want to thank Dr. Alexandra Franz and Dr. Thomas C. Hansen for assistance with the neutron experiments. We thank the Deutsche Forschungsgemeinschaft (DFG, grant Ko1803/8–1) and the Fonds der Chemischen Industrie (Grant 194371) for financial support.

A3.4 Supplement

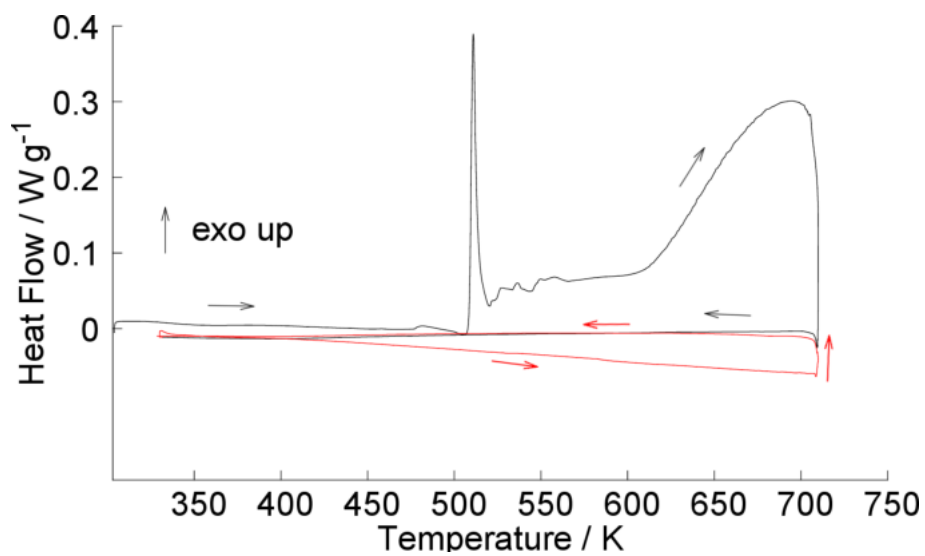


Figure A3.S1: Thermal analyses of the hydrogenation of LaGe under 50 bar hydrogen pressure, black line first run, red line second run.

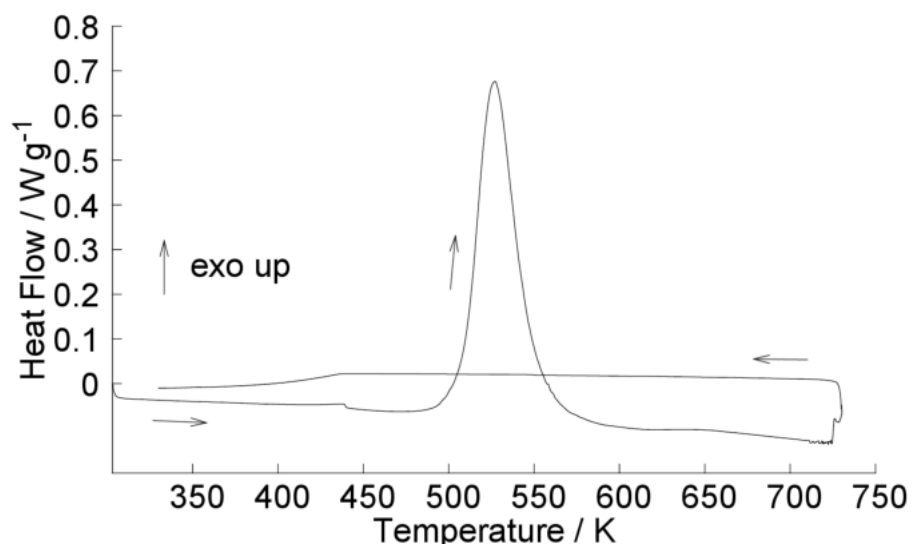


Figure A3.S2: Thermal analysis of the hydrogenation of LaSn under 50 bar hydrogen pressure.

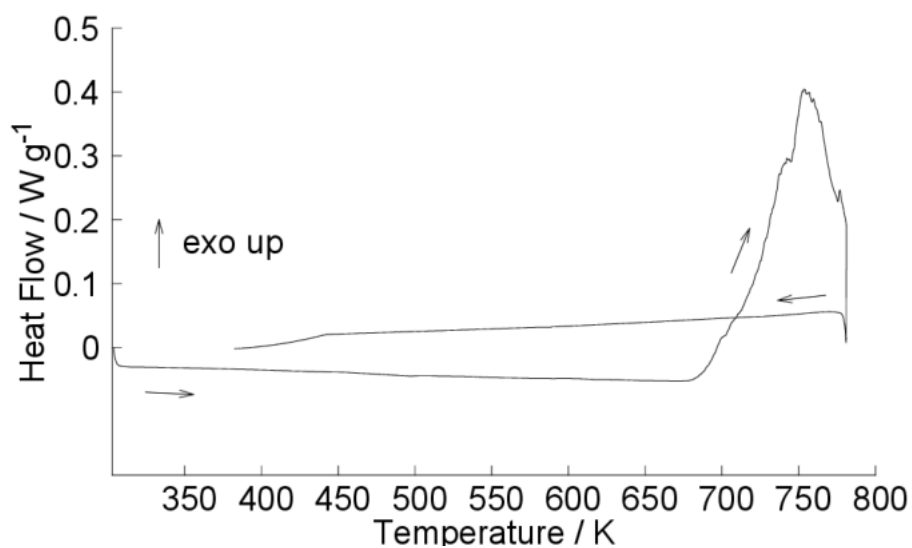


Figure A3.S3: Thermal analysis of the hydrogenation of NdSi under 30 bar hydrogen pressure.

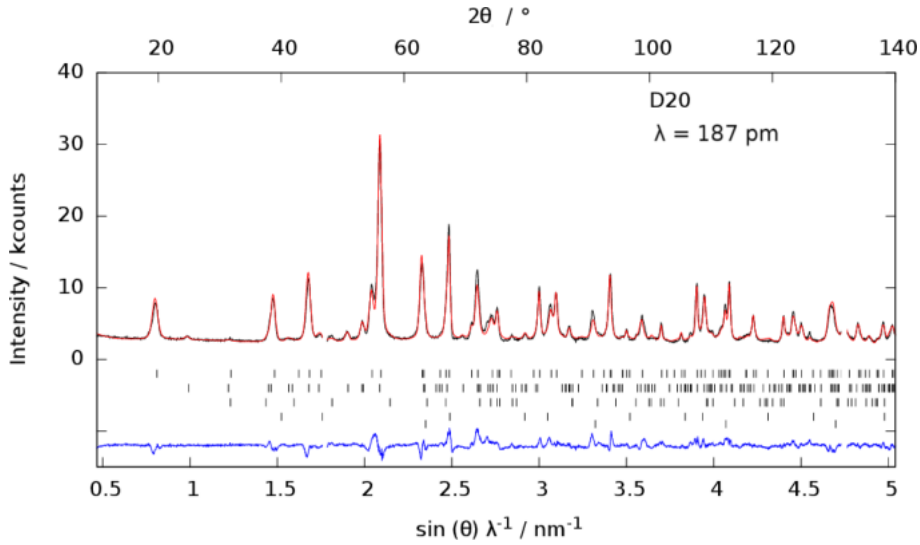


Figure A3.S4: Rietveld refinement of the crystal structures of LaSi deuterides using neutron powder diffraction data, Bragg markers from top to bottom: C -LaSiD_{0.92} (84(4)%), P -LaSiD_{0.61} (14(1)%), LaD₃ (0.2(2)%), LaSi₂ (1.8(2)%), V (sample holder).

Table A3.S1: Crystal structure of C -LaSiD_{0.92(1)}, $Cmcm$, $a = 4.2963(6)$ Å, $b = 12.3419(18)$ Å, $c = 4.0279(6)$ Å.

atom	Wyckoff site	x	y	z	$B_{\text{iso}} / \text{Å}^2$	Occ
La	$4c$	0	0.3561(2)	$1/4$	0.20(10)	1
Si	$4c$	0	0.0548(6)	$1/4$	0.40(12)	1
D	$4c$	0	0.7597(3)	$1/4$	0.60(12)	0.918(11)

Table A3.S2: Crystal structure of P -LaSiD_{0.61(3)}, $Pnma$, $a = 8.200(3)$ Å, $b = 4.0489(13)$ Å, $c = 6.395(2)$ Å (atomic positions fixed to values obtain from DFT calculation and thermal displacement parameters constrained to be the same as in C -LaSiD _{x} (Tab. A3.S1) due to small phase fraction, see Fig. A3.S4).

atom	Wyckoff site	x	y	z	$B_{\text{iso}} / \text{Å}^2$	Occ
La	$4c$	0.17466	$1/4$	0.122	$B_{\text{iso}}(\text{La}, C\text{-LaSiD}_{0.92})$	1
Si	$4c$	0.02353	$1/4$	0.603	$B_{\text{iso}}(\text{Si}, C\text{-LaSiD}_{0.92})$	1
D	$4c$	0.3758	$1/4$	0.421	$B_{\text{iso}}(\text{D}, C\text{-LaSiD}_{0.92})$	0.61(3)

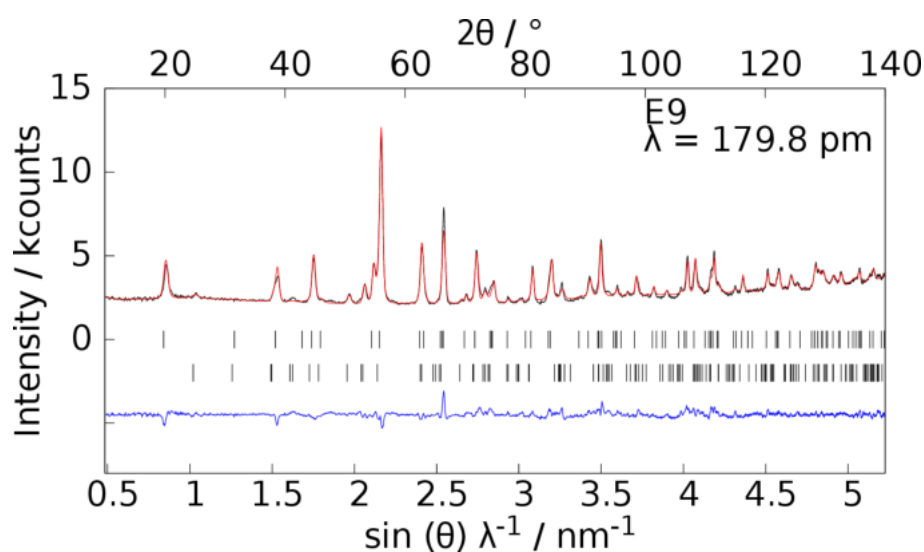


Figure A3.S5: Rietveld refinement of the crystal structures of NdSi deuterides using neutron powder diffraction data, Bragg markers from top to bottom: $P\text{-NdSiD}_{0.94}$ (78.1(8)%), $C\text{-NdSiD}_{0.96}$ (21.9(8)%).

Table A3.S3: Crystal structure of $C\text{-NdSiD}$, $Cmcm$, $a = 4.1713(4)$ Å, $b = 11.8902(14)$ Å, $c = 3.9494(3)$ Å.

atom	Wyckoff site	x	y	z	$B_{\text{iso}} / \text{Å}^2$	Occ
Nd	$4c$	0	0.3547(3)	$1/4$	0.20(10)	1
Si	$4c$	0	0.0507(8)	$1/4$	0.60(12)	1
D	$4c$	0	0.7586(4)	$1/4$	1.00(16)	1

Table A3.S4: Crystal structure of $P\text{-NdSiD}_{0.88(6)}$, $Pnma$, $a = 7.954(3)$ Å, $b = 3.9587(14)$ Å, $c = 6.221(4)$ Å (thermal displacement parameters constrained to be the same as in $C\text{-NdSiD}_x$ (Tab. A3.S3) due to small phase fraction, see Fig. A3.S5).

atom	Wyckoff site	x	y	z	$B_{\text{iso}} / \text{Å}^2$	Occ
Nd	$4c$	0.172(2)	$1/4$	0.119(3)	$B_{\text{iso}}(\text{Nd}, C\text{-NdSiD})$	1
Si	$4c$	0.037(4)	$1/4$	0.606(6)	$B_{\text{iso}}(\text{Si}, C\text{-NdSiD})$	1
D	$4c$	0.383(3)	$1/4$	0.427(5)	$B_{\text{iso}}(\text{La}, C\text{-NdSiD})$	0.88(6)

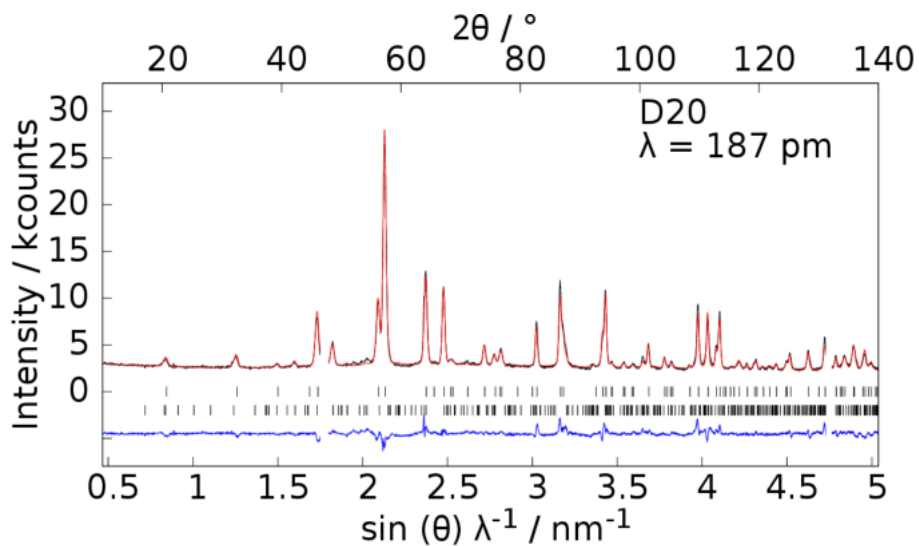


Figure A3.S6: Rietveld refinement of the crystal structure of $\text{NdGeD}_{0.96}$ using neutron powder diffraction data, Bragg markers from top to bottom $\text{NdGeD}_{0.96}$ (86.8(4)%), Nd_4Ge_7 (13.2(4)%).

Table A3.S5: Crystal structure of $C\text{-NdGeD}_{0.95(1)}$, $Cmcm$, $a = 4.21033(33)$ Å, $b = 11.8512(4)$ Å, $c = 4.03149(13)$ Å.

atom	Wyckoff site	x	y	z	$B_{\text{iso}} / \text{Å}^2$	Occ
Nd	4c	0	0.3527(2)	$1/4$	0.27(8)	1
Ge	4c	0	0.0625(3)	$1/4$	0.50(8)	1
D	4c	0	0.7566(3)	$1/4$	0.90(11)	0.951(13)

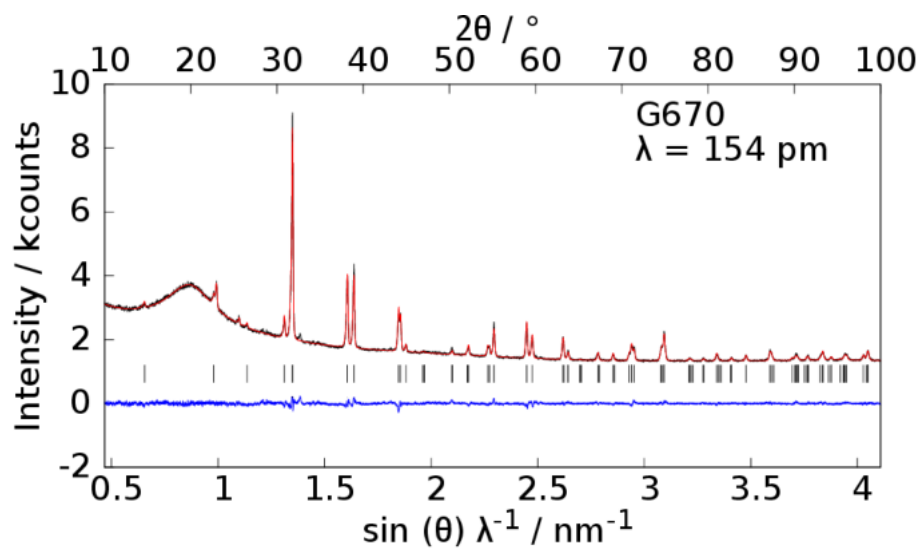


Figure A3.S7: Rietveld refinement of the crystal structure of LaSnH_x using X-ray powder diffraction data ($\text{CuK}\alpha_1$ radiation).

Table A3.S6: Crystal structure of $C\text{-LaSnH}_x$, $Cmcm$, $a = 4.47388(6) \text{ \AA}$, $b = 12.59978(17) \text{ \AA}$, $c = 4.45146(6) \text{ \AA}$ (negative thermal displacement parameters probably due to strong X-ray absorption).

atom	Wyckoff site	x	y	z	$B_{\text{iso}} / \text{\AA}^2$
La	4c	0	0.34668(5)	$1/4$	-0.30(3)
Sn	4c	0	0.06949(8)	$1/4$	-0.23(3)

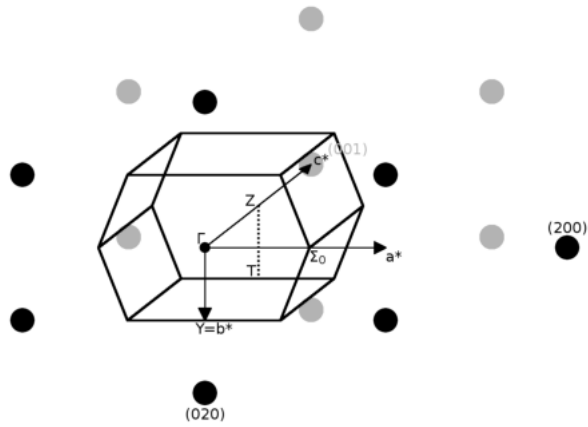


Figure A3.S8: Reciprocal lattice with the first Brillouin zone, $hk1$ are highlighted by grey points, $hk0$ by black points.

Table A3.S7: Crystal structure of hT-LaSi derived from DFT, $Pnma$, $a = 8.4556 \text{ \AA}$, $b = 4.0109 \text{ \AA}$, $c = 6.0662 \text{ \AA}$; $d(\text{Si-Si}) = 2.518 \text{ \AA}$, $\angle(\text{Si-Si-Si}) = 105.6^\circ$, $d(\text{La-La}) = 3.827 - 4.541 \text{ \AA}$.

atom	Wyckoff site	x	y	z
La	$4c$	0.17948	$1/4$	0.11344
Si	$4c$	0.03318	$1/4$	0.61672

Table A3.S8: Crystal structure of hypothetical CrB-type LaSi derived from DFT, $Cmcm$, $a = 4.5782 \text{ \AA}$, $b = 11.2922 \text{ \AA}$, $c = 3.9801 \text{ \AA}$; $d(\text{Si-Si}) = 2.514 \text{ \AA}$, $\angle(\text{Si-Si-Si}) = 104.7^\circ$, $d(\text{La-La}) = 3.912 - 4.511 \text{ \AA}$.

atom	Wyckoff site	x	y	z
La	$4c$	0	0.35936	$1/4$
Si	$4c$	0	0.06804	$1/4$

Table A3.S9: Crystal structure of P -LaSiH derived from DFT, $Pnma$, $a = 8.2433 \text{ \AA}$, $b = 4.0767 \text{ \AA}$, $c = 6.3592 \text{ \AA}$, $d(\text{Si-Si}) = 2.451 \text{ \AA}$, $\angle(\text{Si-Si-Si}) = 112.5^\circ$, $d(\text{La-La}) = 3.858 - 4.428 \text{ \AA}$, $d(\text{La-H}) = 2.445 - 2.518 \text{ \AA}$.

atom	Wyckoff site	x	y	z
La	$4c$	0.17465	$1/4$	0.12285
Si	$4c$	0.02353	$1/4$	0.60256
H	$4c$	0.37579	$1/4$	0.42088

Table A3.S10: Crystal structure of C -LaSiH derived from DFT, $Cmcm$, $a = 4.3226 \text{ \AA}$, $b = 12.2980 \text{ \AA}$, $c = 4.0498 \text{ \AA}$, $d(\text{Si-Si}) = 2.427 \text{ \AA}$, $\angle(\text{Si-Si-Si}) = 113.1^\circ$, $d(\text{La-La}) = 3.918 - 4.323 \text{ \AA}$, $d(\text{La-H}) = 2.439 - 2.475 \text{ \AA}$.

atom	Wyckoff site	x	y	z
La	$4c$	0	0.35425	$1/4$
Si	$4c$	0	0.0544	$1/4$
H	$4c$	0	0.75624	$1/4$

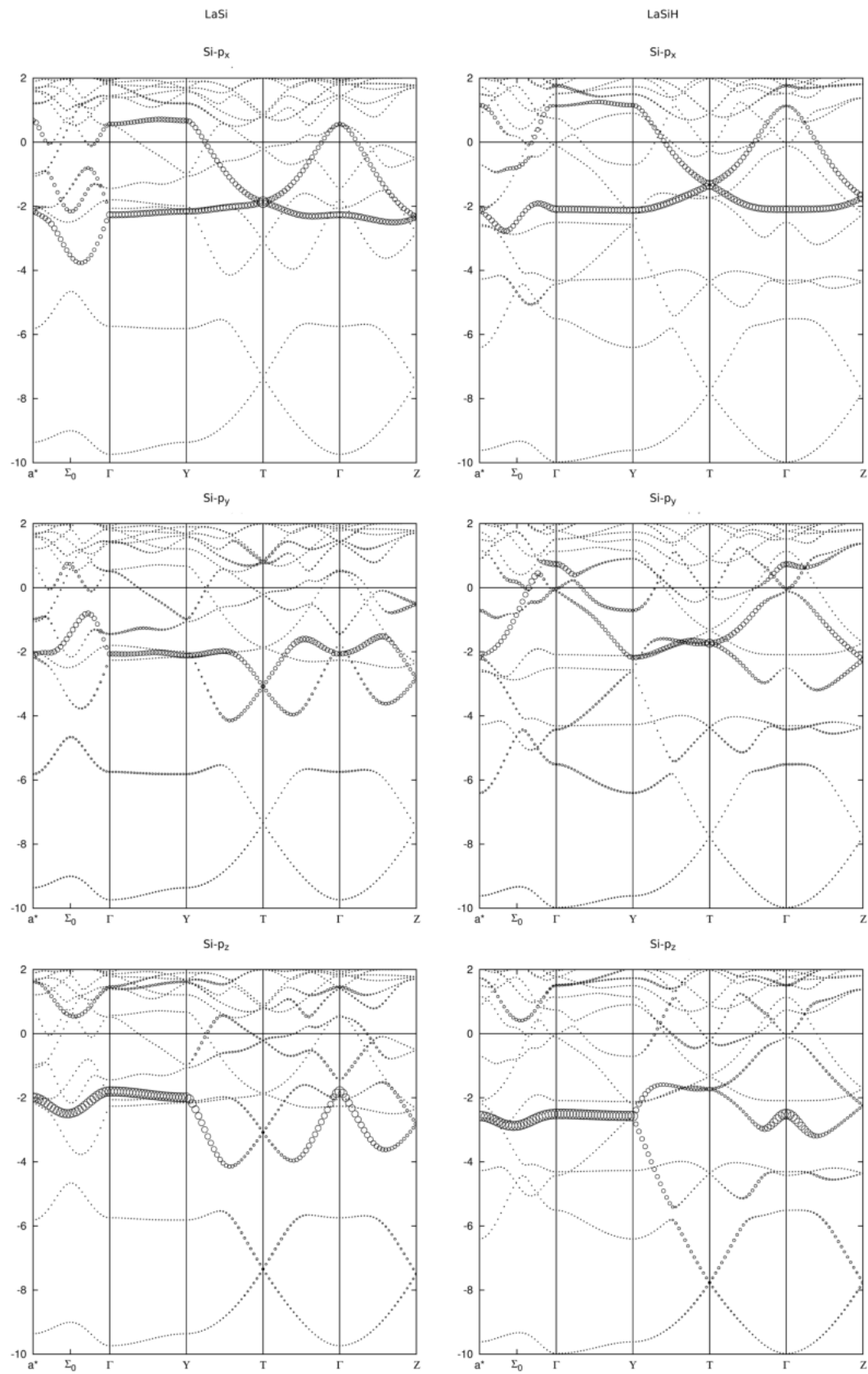


Figure A3.S9: Fatband representation of p_x (top) p_y (middle) and p_z (bottom) states for LaSi (left) and LaSiH (right).

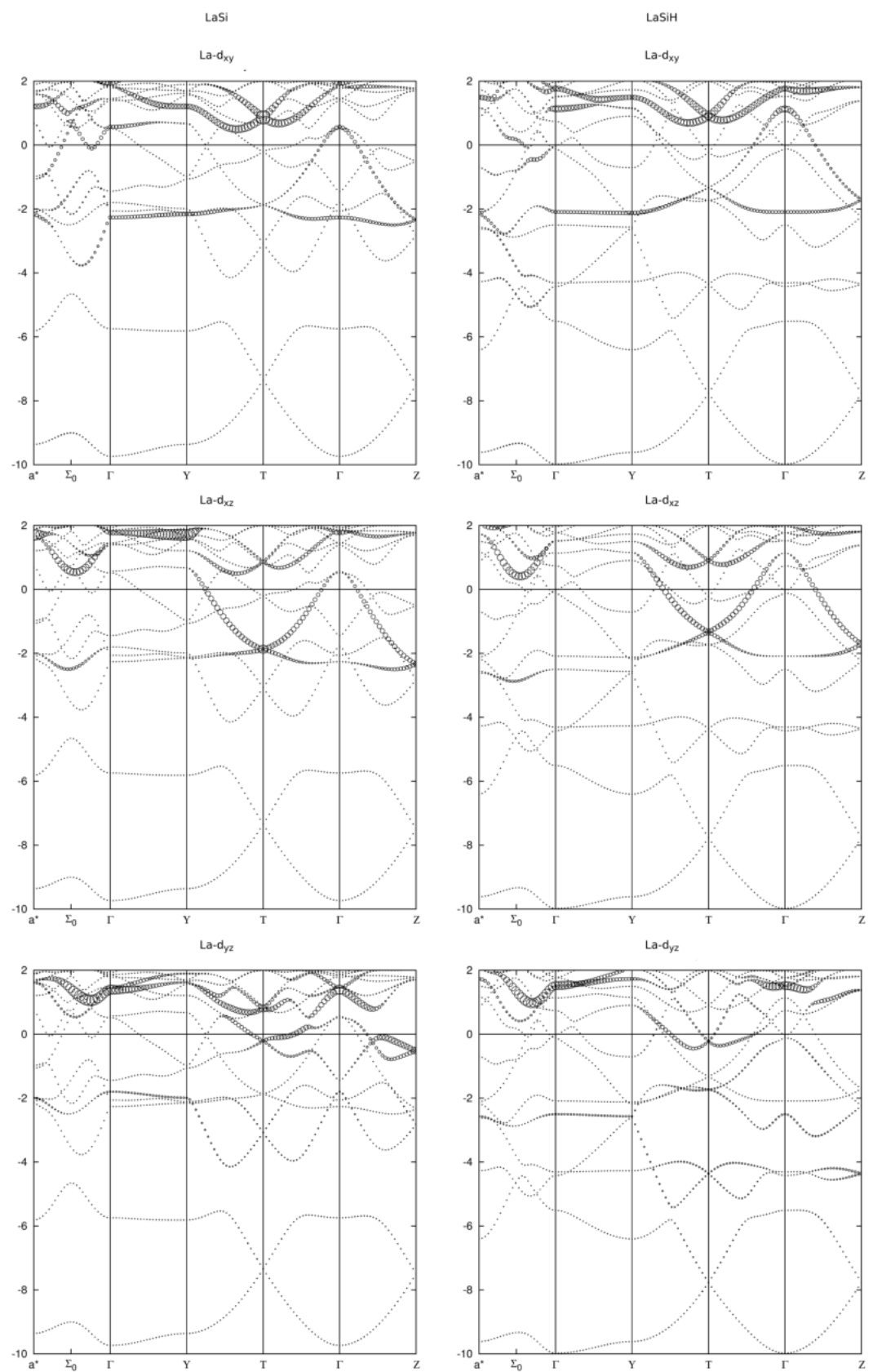


Figure A3.S10: Fatband representation of d_{xy} (top) d_{xz} (middle) and d_{yz} (bottom) states for LaSi (left) and LaSiH (right).

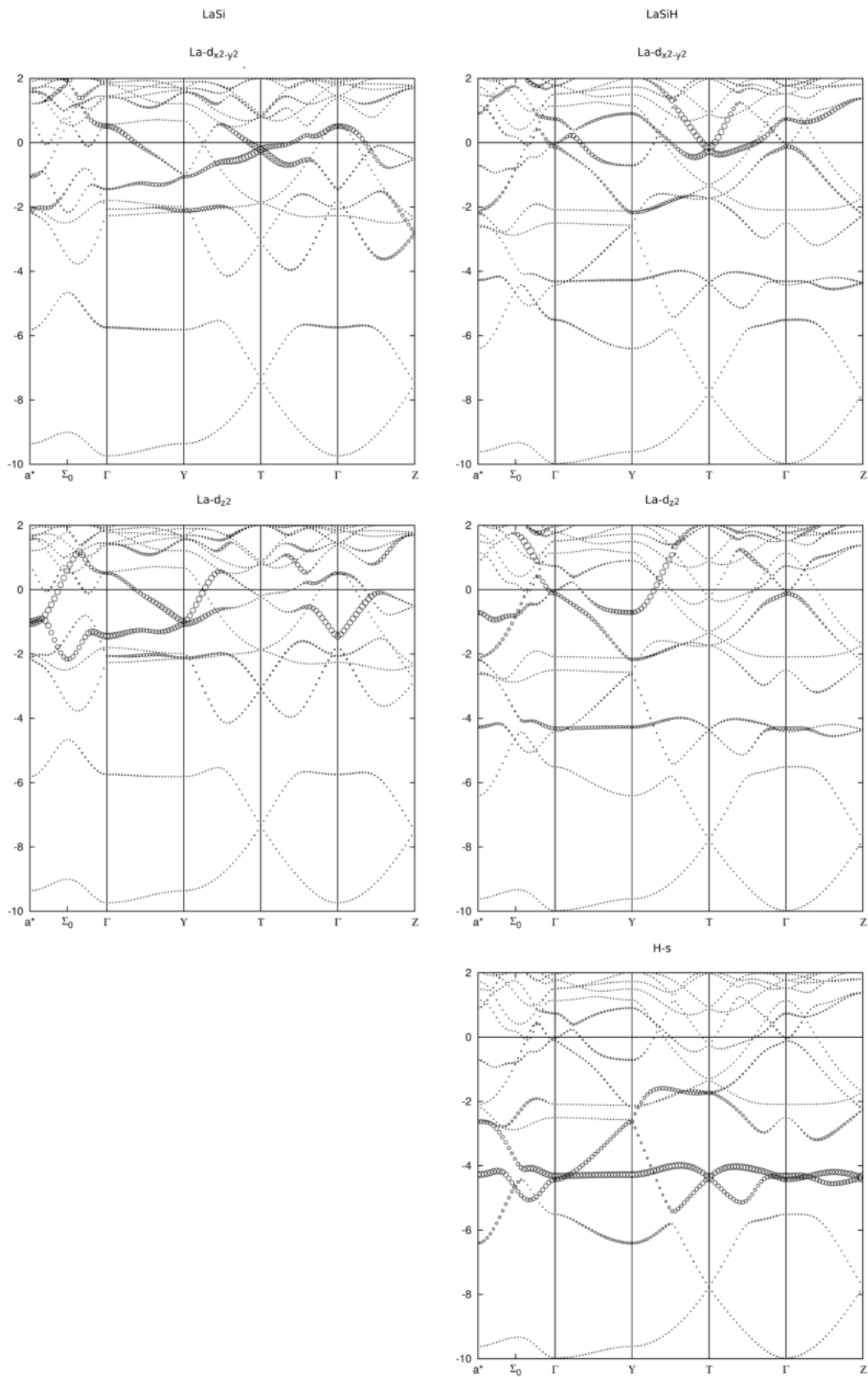


Figure A3.S11: Fatband representation of $d_{x^2-y^2}$ (top) d_{z^2} (middle) and H_s (bottom) states for LaSi (left) and P-LaSiH (right).

A3.5 References

- (1) Zintl, E.; Kaiser, H. *Z. Anorg. Allg. Chem.* **1933**, *211*, 113–131, DOI: 10.1002/zaac.19332110113.
- (2) Zintl, E. *Angew. Chem.* **1939**, *52*, 1–6, DOI: 10.1002/ange.19390520102.
- (3) Schäfer, H.; Eisenmann, B.; Müller, W. *Angew. Chem.* **1973**, *85*, 742–760, DOI: 10.1002/ange.19730851704.
- (4) Nesper, R. *Angew. Chem.* **1991**, *103*, 805–834, DOI: 10.1002/ange.19911030709.
- (5) *Chemistry, Structure, and Bonding of Zintl Phases and Ions*; Kauzlarich, S. M., Ed.; Wiley-VCH: 1996.
- (6) Häussermann, U.; Kranak, V. F.; Puhakainen, K. *Struct. Bond.* **2010**, *139*, 143–161, DOI: 10.1007/430_2010_20.
- (7) Nesper, R. *Z. Anorg. Allg. Chem.* **2014**, *640*, 2639–2648, DOI: 10.1002/zaac.201400403.
- (8) Corbett, J. D. *Angew. Chem., Int. Ed.* **2000**, *39*, 670–690, DOI: 10.1002/(SICI)1521-3773(20000218)39:4<670::AID-ANIE670>3.0.CO;2-M.
- (9) Kurylyshyn, I. M.; Fässler, T. F.; Fischer, A.; Hauf, C.; Eickerling, G.; Presnitz, M.; Scherer, W. *Angew. Chem., Int. Ed.* **2014**, *53*, 3029–3032, DOI: 10.1002/anie.201308888.
- (10) Reyes, E. C.; Nesper, R. *J. Phys. Chem. C* **2012**, *116*, 2536–2542, DOI: 10.1021/jp205825d.
- (11) Evers, J.; Weiss, A. *Solid State Commun.* **1975**, *17*, 41–43, DOI: 10.1016/0038-1098(75)90330-0.
- (12) Hashimoto, K.; Kurosaki, K.; Imamura, Y.; Muta, H.; Yamanaka, S. *J. Appl. Phys.* **2007**, *102*, 063703, DOI: 10.1063/1.2778747.
- (13) Leon-Escamilla, E.; Corbett, J. D. *J. Alloys Compd.* **1998**, *265*, 104–114, DOI: 10.1016/S0925-8388(97)00320-4.
- (14) Leon-Escamilla, E. A.; Dervenagas, P.; Stassis, C.; Corbett, J. D. *J. Solid State Chem.* **2010**, *183*, 114–119, DOI: 10.1016/j.jssc.2009.10.024.
- (15) Leon-Escamilla, E. A.; Corbett, J. D. *Chem. Mater.* **2006**, *18*, 4782–4792, DOI: 10.1021/cm0612191.
- (16) Auer, H.; Guehne, R.; Bertmer, M.; Weber, S.; Wenderoth, P.; Hansen, T. C.; Haase, J.; Kohlmann, H. *Inorg. Chem.* **2017**, *56*, 1061–1071, DOI: 10.1021/acs.inorgchem.6b01944.
- (17) Auer, H.; Schlegel, R.; Oeckler, O.; Kohlmann, H. *Angew. Chem., Int. Ed.* **2017**, *56*, 12344–12347, DOI: 10.1002/anie.201706523.
- (18) Bohmhammel, K.; Henneberg, E. *Solid State Ionics* **2001**, *141-142*, 599–602, DOI: 10.1016/S0167-2738(01)00774-3.
- (19) Hohnke, D.; Parthé, E. *Acta Crystallogr.* **1966**, *20*, 572–582, DOI: 10.1107/S0365110X66001282.
- (20) Mattausch, H.; Oeckler, O.; Simon, A. *Z. Anorg. Allg. Chem.* **1999**, *625*, 1151–1154, DOI: 10.1002/(SICI)1521-3749(199907)625:7<1151::AID-ZAAC1151>3.0.CO;2-4.
- (21) Mattausch, H.; Simon, A. *Z. Naturforsch., B: Chem. Sci.* **2004**, DOI: 10.1515/znb-2004-0513.
- (22) Henneberg, E. Thermodynamische und kinetische Untersuchung im System La-Si-H-(Cl), Ph.D. Thesis, Freiberg: Technische Universität Bergakademie Freiberg, 2003.
- (23) Biltz, W., *Raumchemie der festen Stoffe*; Verlag von Leopold Voss: Leipzig, 1934.
- (24) Bronger, W. *Z. Anorg. Allg. Chem.* **1996**, *622*, 9–16, DOI: 10.1002/zaac.19966220103.
- (25) Fischer, P.; Hälgl, W.; Schlapbach, L.; Yvon, K. *J. Less-Common Met.* **1978**, *60*, 1–9, DOI: 10.1016/0022-5088(78)90084-x.
- (26) Renaudin, G.; Fischer, P.; Yvon, K. *J. Alloys Compd.* **2000**, *313*, L10–L14, DOI: 10.1016/S0925-8388(00)01200-7.

- (27) Westlake, D.; Shaked, H.; Mason, P.; McCart, B.; Mueller, M.; Matsumoto, T.; Amano, M. *J. Less-Common Met.* **1982**, *88*, 17–23, DOI: 10.1016/0022-5088(82)90005-4.
- (28) Müller, W.; Stöhr, J. *Z. Naturforsch., B* **1977**, *32*, DOI: 10.1515/znb-1977-0607.
- (29) Soulard, M.; Tournoux, M. *Sciences Chimiques* **1971**, *273*, 1251–1253.
- (30) Udovic, T. J.; Huang, Q.; Santoro, A.; Rush, J. J. *Z. Kristallogr.* **2008**, *223*, DOI: 10.1524/zkri.2008.1139.
- (31) Götze, A.; Hansen, T.; Kohlmann, H. *J. Alloys Compd.* **2018**, *731*, 1001–1008, DOI: 10.1016/j.jallcom.2017.10.107.
- (32) Yartys, V.; Isnard, O.; Riabov, A.; Akselrud, L. *J. Alloys Compd.* **2003**, *356-357*, 109–113, DOI: 10.1016/s0925-8388(03)00106-3.
- (33) Chevalier, B.; Bobet, J.-L.; Pasturel, M.; Bauer, E.; Weill, F.; Decourt, R.; Etourneau, J. *Chem. Mater.* **2003**, *15*, 2181–2185, DOI: 10.1021/cm0213669.
- (34) Kohlmann, H.; Yvon, K. *J. Alloys Compd.* **2000**, *309*, 123–126, DOI: [http://dx.doi.org/10.1016/S0925-8388\(00\)01040-9](http://dx.doi.org/10.1016/S0925-8388(00)01040-9).
- (35) Riabov, A.; Yartys, V. *J. Alloys Compd.* **2002**, *330-332*, 234–240, DOI: 10.1016/s0925-8388(01)01672-3.
- (36) Kohlmann, H.; Moyer, R.; Hansen, T.; Yvon, K. *J. Solid State Chem.* **2003**, *174*, 35–43, DOI: 10.1016/s0022-4596(03)00171-3.
- (37) Reyes, E. C.; Stalder, E. D.; Mensing, C.; Budnyk, S.; Nesper, R. *J. Phys. Chem. C* **2011**, *115*, 1090–1095, DOI: 10.1021/jp106169h.
- (38) Dürr, I.; Bauer, B.; Röhr, C. *Z. Naturforsch. B* **2011**, *66*, 1107–1121.
- (39) Rieger, W.; Parthé, E. *Acta Crystallogr.* **1967**, *22*, 919–922, DOI: 10.1107/s0365110x67001793.
- (40) Currao, A.; Curda, J.; Nesper, R. *Z. Anorg. Allg. Chem.* **1996**, *622*, 85–94, DOI: 10.1002/zaac.19966220113.
- (41) Rietveld, H. M. *Acta Crystallogr.* **1967**, *22*, 151–152, DOI: 10.1107/S0365110X67000234.
- (42) Rietveld, H. M. *J. Appl. Crystallogr.* **1969**, *2*, 65–71, DOI: 10.1107/S0021889869006558.
- (43) Bruker AXS, TOPAS[®] version 5, www.bruker-axs.com.
- (44) Rodríguez-Carvajal, J. *Phys. B* **1993**, *192*, 55–69, DOI: 10.1016/0921-4526(93)90108-I.
- (45) Rodríguez-Carvajal, J. FULLPROF (version 5.30): A Program for Rietveld Refinement and Pattern Matching Analysis; Institut Laue-Langevin, Grenoble (France), 2012.
- (46) VESTA - Visualisation for Electronic and Structural Analysis, version 3.3.1.
- (47) Momma, K.; Izumi, F. *J. Appl. Crystallogr.* **2011**, *44*, 1272–1276, DOI: 10.1107/s0021889811038970.
- (48) <http://www.abinit.org>, Abinit v. 8.2.2, GNU General Public License.
- (49) Gonze, X. et al. *Comput. Mater. Sci.* **2002**, *25*, 478–492, DOI: 10.1016/s0927-0256(02)00325-7.
- (50) Gonze, X. *Z. Kristallogr.* **2005**, *220*, DOI: 10.1524/zkri.220.5.558.65066.
- (51) Gonze, X. et al. *Comput. Phys. Commun.* **2009**, *180*, 2582–2615, DOI: 10.1016/j.cpc.2009.07.007.
- (52) Gonze, X. et al. *Comput. Phys. Commun.* **2016**, *205*, 106–131, DOI: 10.1016/j.cpc.2016.04.003.
- (53) Perdew, J. P.; Burke, K.; Ernzerhof, M. *Phys. Rev. Lett.* **1996**, *77*, 3865–3868, DOI: 10.1103/physrevlett.77.3865.
- (54) Blöchl, P. E. *Phys. Rev. B* **1994**, *50*, 17953–17979, DOI: 10.1103/physrevb.50.17953.
- (55) <https://www.abinit.org/downloads/PAW2>, JTH PAW atomic datasets, version 1.0.
- (56) Jollet, F.; Torrent, M.; Holzwarth, N. *Comput. Phys. Commun.* **2014**, *185*, 1246–1254, DOI: 10.1016/j.cpc.2013.12.023.

- (57) Monkhorst, H. J.; Pack, J. D. *Phys. Rev. B* **1976**, *13*, 5188–5192, DOI: 10.1103/physrevb.13.5188.
- (58) Blöchl, P. E.; Jepsen, O.; Andersen, O. K. *Phys. Rev. B* **1994**, *49*, 16223–16233, DOI: 10.1103/physrevb.49.16223.

A4 *In situ* hydrogenation of the Zintl phase SrGe

Henry Auer^a, Dirk Wallacher^b, Thomas Christian Hansen^c, Holger Kohlmann^{a*}

^a *Leipzig University, Department of Inorganic Chemistry, Johannisallee 29, 04103 Leipzig, Germany*

^b *Helmholtz Zentrum Berlin für Materialien und Energie, Hahn-Meitner-Platz 1, 14109 Berlin, Germany*

^c *Institut Laue-Langevin, 71 Avenue des Martyrs, CS 20156, 38042 Grenoble cedex 9, France*

* *Corresponding author*

— Dedicated to Prof. Lothar Beyer on the occasion of his 80th birthday. —

Reprinted with permission from

H. Auer, D. Wallacher, T. C. Hansen, H. Kohlmann, *Inorg. Chem.* **2017**, *56*, 1072-1079,
DOI:10.1021/acs.inorgchem.6b01945.

© 2017 American Chemical Society.

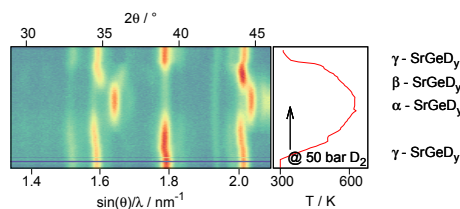
This is the accepted version with minor adaptations for use with L^AT_EX and one column printing.

A4.1 Authors' contributions

The SrGe sample was prepared and the reaction was precharacterised using thermal analysis by H. Auer. H. Kohlmann and H. Auer conducted the *in situ* neutron diffraction experiment. T. C. Hansen assisted during the beamtime. The sample environment of the *in situ* synchrotron diffraction experiment was mainly set up by D. Wallacher. The experiment itself was conducted by H. Auer. Furthermore H. Auer evaluated all data, assembled and edited the manuscript. H. Kohlmann revised the text prior to submission.

A4.2 Abstract

Hydrides (deuterides) of CrB-type Zintl phases $AeTt$ ($Ae =$ alkaline earth; $Tt =$ tetrel) show interesting bonding properties with novel polyanions. In $SrGeD_{4/3-x}$ (γ -phase) three zig-zag chains of Ge atoms are condensed and terminated by covalently bound deuterium atoms. A combination of *in situ* techniques (thermal analysis, synchrotron and neutron powder diffraction) revealed the existence of two further hydride (deuteride) phases with lower H(D) content (called α - and β -phases). Both are structurally related to the parent Zintl phase SrGe and to the ZrNiH-structure type containing variable amounts of hydrogen (deuterium) in Sr_4 tetrahedra. For α - $SrGeD_y$ the highest D content $y = 0.29$ was found at 575(2) K under 5.0(1) MPa deuterium pressure, β - $SrGeD_y$ shows a homogeneity range of $0.47 < y < 0.63$. Upon decomposition of $SrGeD_{4/3-x}$ (γ - $SrGeD_y$) tetrahedral Sr_4 -voids stay filled while the germanium bound D4-site loses deuterium. When reaching the lower D content limit, $SrGeD_{4/3-x}$ (γ -phase), $0.10 < x < 0.17$ decomposes to the β -phase. All three hydrides (deuterides) of SrGe show variable H(D) content.



A4.3 Article

Introduction

Zintl phases build a bridge between solid state and molecular chemistry. These polar intermetallic compounds exhibit polyanionic partial structures that resemble molecular analogues. Structures of Zintl phases can be explained by a simple concept where the less electronegative partner formally transfers all its valence electrons to the more electronegative one [1–7]. As expected this concept lacks to describe the true electronic situation, e.g. CaSi crystallizes in CrB-structure type and is a textbook example of a Zintl phase, where the formally Si^{2-} forms a zig-zag chain-like partial structure that is coordinated by Ca^{2+} cations. In contrast to this ionic picture that suggests semi-conducting properties all the isotopic compounds $AeTt$ ($Ae = \text{Ca-Ba}$, $Tt = \text{Si, Ge}$) are poor metals [8, 9], i.e., the Zintl-Klemm formalism is a very useful crystal chemistry concept, which, however often lacks a proper description of the electronic structure. DFT and experimental charge density studies could show significant covalent contribution for the Ca-Si bonding [10].

Introducing hydrogen (deuterium) into these systems complicates this picture even further. There are several hydride (deuteride) phases that derive from CrB-type structures like $\text{CaSiH}_{1.2}$ [11–14], $\text{SrSiH}_{1.6}$ [14], BaSiH_{2-x} [14, 15], $\text{SrGeH}_{4/3-x}$ [15], $\text{BaSnH}_{4/3-x}$ [15], $\text{NdGaH}_{1.66}$ [16], GdGaH_y [17]. Common features in these phases are salt like layers of hydrogen (deuterium) filled M_4 -tetrahedra ($M = \text{Ca-Ba, Nd, Gd}$) as well as hydrogen (deuterium) positions that coordinate the polyanionic chain. For BaSiD_{2-x} , $\text{SrGeD}_{4/3-x}$ and $\text{BaSnD}_{4/3-x}$ we could show that these positions correspond to covalent $Tt\text{-H(D)}$ ($Tt = \text{Si-Sn}$) bonds using neutron diffraction, solid state NMR spectroscopy as well as DFT calculations [15]. In view of the variety of different related crystal structures it seemed promising to follow the uptake of hydrogen (deuterium) by time-resolved studies. *In situ* diffraction techniques in general [18, 19] can help to probe phases that occur during a reaction. Especially intermediate products that cannot be quenched are accessible. Moreover composition changes can be followed to estimate homogeneity ranges for different phases.

In this contribution we present *in situ* powder neutron diffraction (*in situ* PND) data on reactions in the $\text{SrGe-H}_2(\text{D}_2)$ system. The findings are correlated to a thermal analysis of SrGe under different hydrogen pressures as well as *in situ* powder synchrotron diffraction. *In situ* investigations on SrGe shows, in addition to $\text{SrGeD}_{4/3-x}$ (called $\gamma\text{-SrGeD}_y$), the existence of two hydrogen (deuterium) poorer phases (α - and β -phase), that both are structurally related to the ZrNiH -structure type[20]. They exhibit a large homogeneity range of their hydrogen (deuterium) content. The same applies to $\text{SrGeD}_{4/3-x}$ with a large homogeneity range for the hydrogen (deuterium) position covalently bound to germanium.

Experimental

Synthesis

All handlings were done in an argon filled glovebox. Oxygen and moisture level were kept below 1 ppm. SrGe and $\text{SrGeD}_{4/3-x}$ ($\gamma\text{-SrGeD}_y$) were prepared from the elements (Sr: chemPUR, 99%, packed under oil and washed in hexane; Ge: chemPUR, 99.9999%) and subsequent deuteration (D_2 : Air Liquide, 99.8% isotope purity) of the Zintl phase as described before [15].

Thermal Analysis

Differential scanning calorimetry (DSC) was performed with a Q1000 DSC (TA Instruments) equipped with a gas pressure chamber. DSC experiments were done under several hydrogen pressures in the region of 2 to 5 MPa to follow the hydrogenation reaction. Aluminum crucibles were filled with about 15 mg SrGe and crimped within a glovebox. The sample was placed in the pressure chamber of the DSC, which was subsequently flushed with hydrogen and afterwards filled to the desired hydrogen pressure. Samples were heated at a rate of $10 \text{ K}\cdot\text{min}^{-1}$ to a maximum temperature of 700 K. The temperature was usually held for 10 minutes. In subsequent runs lower maximum temperatures were used depending on the occurring signals. The heating was then stopped right after a reaction step, the temperature held there for 10 minutes before cooling down to room temperature.

Structural Characterization

Powder Neutron Diffraction (PND) was done at the Institut Laue Langevin (ILL), Grenoble, France at the high-intensity two-axis diffractometer D20 [21]. Measurements were done at a take off angle of 120° and a wavelength of $\lambda = 1.86832(7)$ Å which was calibrated using a silicon NIST640b standard sample in a 5 mm vanadium container. *Ex situ* measurements were conducted in indium sealed 6 mm vanadium containers. *In situ* experiments were done in (leuco-)sapphire single crystal cells with 6 mm inner diameter, which were connected to a gas supply system (for more details see Kohlmann *et al.* [22]). For the *in situ* investigation the sapphire cell filled with SrGe or SrGeD_{4/3-x} (γ -SrGeD_y) was pressurized with 5.0(1) MPa D₂ (Air Liquide, 99.8% isotope purity) at ambient temperature. Heating up to a maximum temperature of 623 K was realized using two laser beams. Data were collected with 2 min time resolution. For sequential Rietveld refinement a summation over 5 data sets was done giving a time resolution of 10 min. Sequential data are presented with error bars corresponding to 3 e.s.u. as obtained from Rietveld refinement. For more clarity 2D-diffraction patterns are truncated to a small angular range. The total measured angular range is presented in Fig. A4.S2 (SrGe) and Fig. A4.S3 (γ -SrGeD_y).

All data sets obtained at the ILL D20 instrument are presented with an additional label according internal raw data labeling (NUMOR-labeling). Data refer to proposal 5-22-734 [23].

Ex situ PND was also performed at the neutron source BER II at Helmholtz-Zentrum Berlin (HZB), Germany at the high resolution powder diffractometer E9 (FIREPOD) [24]. Measurements were done at a wavelength of 1.7972(2) Å in a copper sealed 6 mm vanadium container.

***In situ* Powder Synchrotron Diffraction (*in situ*-PSD)** was realized at BESSY II, Helmholtz-Zentrum Berlin (HZB), Germany at beamline KMC-2 [25]. A novel *in situ* setup for diffraction under hydrogen pressure and elevated temperatures was used, which allows a qualitative analysis of the reactions. Data do not allow Rietveld refinement yet due to static samples yielding poor crystallite statistics. Details will be published elsewhere.

Rietveld refinement was done using FULLPROF [26, 27]. *In situ* data sets were evaluated in sequential refinements. If a phase showed a fraction less than 10% the atomic structure was kept fixed. When lattice parameters of such a phase diverged or showed unreasonable behavior the phase was removed from the refinement. Profile parameters were constrained to be the same for all phases. Structure pictures were prepared by VESTA [28, 29]. Structural data were normalized using STRUCTURE TIDY [30] as implemented in VESTA.

Results and Discussion

Structures of α - and β -SrGeD_y

The thermal behavior of γ -SrGeH_y (SrGeH_{4/3-x}) suggested the existence of two hydrogen poorer phases, which will be called α - and β -SrGeH_y. Structural studies reveal that the Zintl phase SrGe and the hydrogen (deuterium) richest phase γ -SrGeD_y [15] can be considered as compositional and structural boundaries for these phases. They have in common main structural features as tetrahedral Sr₄-voids and Ge-Ge zig-zag chains. While γ -SrGeD_y has filled tetrahedral voids and partially connected Ge-Ge-chains, the voids are empty and the chains are well separated for SrGe. This suggests, that the intermediate phases may either show features of the parent Zintl phase or the hydrogen rich hydride (deuteride). Using *in situ* neutron diffraction data, two new phases, α - and β -SrGeD_y, could be indexed in the orthorhombic crystal system. In regard to the axes-system of SrGe a systematic contraction in *a*-direction and an elongation in *b*-direction can be seen with increasing deuterium content. The *c* axis only slightly contracts.

α -SrGeD_y: The structure of α -SrGeD_y can be described in orthorhombic *Cmcm* (No. 63) symmetry. Lattice parameter *a* is contracted while *b* is elongated in regard to the Zintl phase. According to a difference Fourier map there is only one deuterium site in the center of the Sr₄ tetrahedral voids, which could be confirmed by a Rietveld refinement, based on the *in situ* collected data at 5.0(1) MPa D₂-pressure and 618(2) K as shown in Fig. A4.1. This phase has the lowest hydrogen content which was refined to $y = 0.204(4)$. Structural data are summarized in Tab. A4.1.

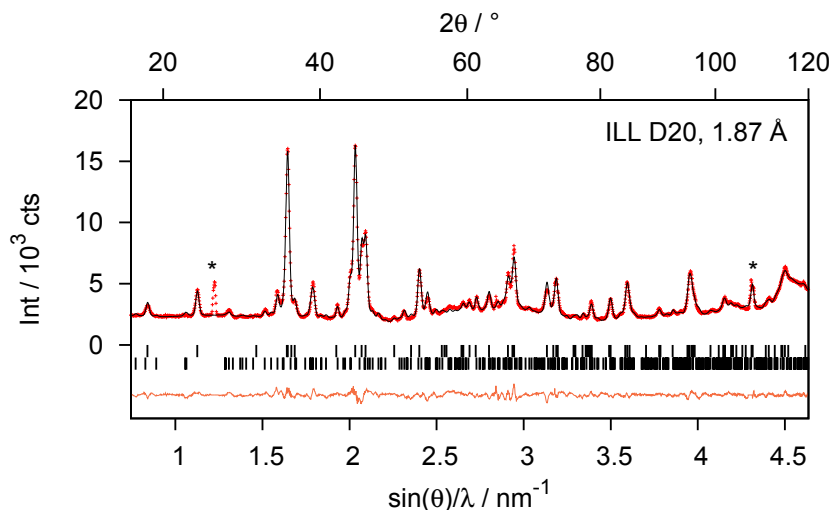


Figure A4.1: Rietveld refinement of the crystal structure of α -SrGeD_y ($y = 0.204(4)$, $Cmcm$, No. 63, $a = 4.7659(5)$ Å, $b = 11.8280(14)$ Å, $c = 4.1542(5)$ Å) based on *in situ* PND data at 618(2) K and 5.0(1) MPa D₂. A summation was done from numor 926991 to 927020 [23], with an overall measuring time of 60 min. The additional phase is γ -SrGeD_y ($\approx 20\%$, bottom marker); (*) denotes reflections of the sapphire cell. Background corrected reliability factors are: $R_p = 13.6\%$, $R_{wp} = 13.0\%$, $S = 2.45$.

Table A4.1: Structural data and selected distances (< 3 Å) of α -SrGeD_y, $y = 0.204(4)$ at 618(2) K, 5.0(1) MPa D₂ pressure. Space group $Cmcm$ (No.63), $a = 4.7659(5)$ Å, $b = 11.8280(14)$ Å, $c = 4.1542(5)$ Å.

Atom	Wyckoff	x	y	z	$B_{iso} / \text{Å}^2$	SOF
Sr	4c	0	0.3568(2)	1/4	4.82(17)	
Ge	4c	0	0.0679(3)	1/4	2.66(13)	
D	4c	0	0.7509(11)	1/4	2.1(6)	0.204(4)
Atom 1	Atom 2	d / Å				
Sr	D	2.437(8) - 2.692(7)				
Ge	Ge	2.626(3)				
Ge	D	2.985(11)				

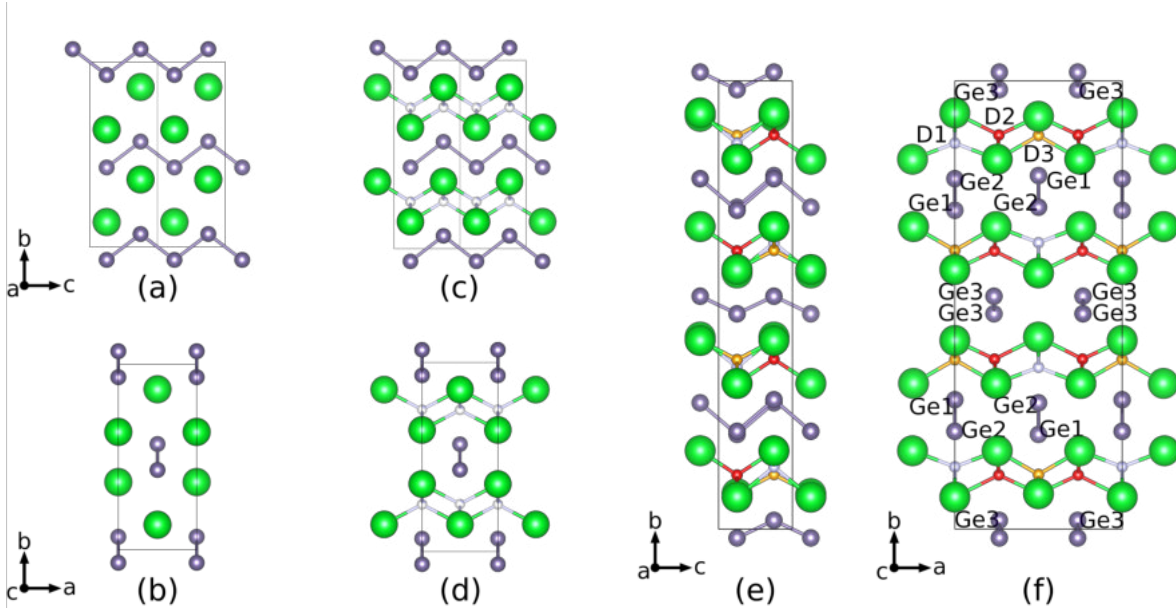


Figure A4.2: Different projections of the crystal structures of the Zintl phase SrGe (a/b), α - (c/d) and β -SrGeD_y (e/f). Tetrahedral Sr₄-voids of α - and β -SrGeD_y are partially filled with deuterium. Large spheres: Sr; Medium spheres: Ge; Small spheres D.

The structure looks quite similar to the parent Zintl phase SrGe (Fig. A4.2 (a/b)), but has a partial occupation of tetrahedral Sr₄-voids by deuterium of 20.4(4)% (Fig. A4.2 (c/d)). α -SrGeD_y can be classified as an interstitial hydride (deuteride) according to Häussermann [31]. Applying an extended Zintl concept that includes hydrogen (deuterium) it can be considered as Sr²⁺(H⁻)_{0.2}Ge^{1.8-}. Although the polyanion is formally oxidized, it keeps the structure we know from the hydrogen (deuterium) free Zintl phase.

As Fig. A4.2 (d) shows, the germanium chains stay parallel and well separated. The distance $d(\text{Ge-Ge}) = 2.626(3) \text{ \AA}$ at 618(2) K is slightly shorter than in the hydrogen free Zintl phase ($d(\text{Ge-Ge}) = 2.6462(16) \text{ \AA}$) at ambient temperature. Assuming a normal temperature effect, the bond length decreases upon hydrogenation. The Zintl phases themselves are poor metals. For the silicides this is explained in detail by π -bonding in the zig-zag chains [9, 10, 32] due to a partial depopulation of π^* -bands. The reduced electron count at the polyanion in the hydride (deuteride) strengthens this effect further, therefore the decreased bond length can be correlated with increased π -bonding. The Ge-Ge-Ge angle does not change and is $104.57(18)^\circ$ (SrGe: $104.48(15)^\circ$).

β -SrGeD_y: The structure is more complex than the α - and γ - phase. In a first approach it can be described in the basis structure of the Zintl phase with deuterium occupying tetrahedral Sr₄ voids again.

Fig. A4.3 shows the Rietveld plot. A superstructure reflection at low angles is marked and corresponds to a 2x2 super cell in crystallographic *a*- and *b*-direction. See also Fig. A4.S5 for corresponding 2D-diffraction data. Rietveld refinement was done on the *in situ* data at 5.0(1) MPa D₂-pressure and 538(2) K. Due to the limited quality and the occurrence of the other phases a structure solution was difficult. Thus, considering the superstructure, a high symmetry model in *Cmcm* (No. 63) is suggested (Tab. A4.2/Fig. A4.2 (e/f)). The deuterium content could be refined to give the chemical formula β -SrGeD_y, $y = 0.53(4)$, which implies a half filling of the tetrahedral voids. The proposed model shows a preferred filling but allows no total ordering due to limited degrees of freedom. Different low symmetry models have been tested, but none gave a much better refinement result than the model as shown in Fig. A4.2 (e/f). From a Zintl point of view this phase can be considered as Sr²⁺(H⁻)_{0.53}Ge^{1.47-} \approx Sr²⁺(H⁻)_{0.5}(Ge²⁻)_{0.5}(Ge⁻)_{0.5}.

The proposed model shows two different types of Ge zig-zag chains with $d(\text{Ge1-Ge2}) = 2.71(3) \text{ \AA}$ and $d(\text{Ge3-Ge3}) = 2.280(11) \text{ \AA}$ at 538(2) K. The former is not significantly different from the value of the hydrogen (deuterium) free Zintl phase ($d(\text{Ge-Ge}) = 2.6462(16) \text{ \AA}$) and therefore corresponds to a single bond. The value $d(\text{Ge3-Ge3})$ is much smaller and therefore might be dominated by additional π -bonding.

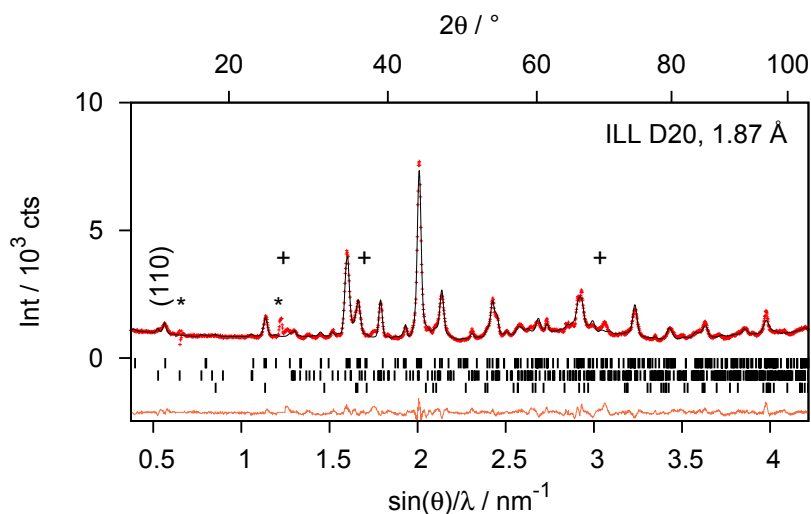


Figure A4.3: Rietveld refinement of the crystal structure of β -SrGeD_y ($y = 0.53(4)$, $Cmcm$, No. 63, $a = 9.3368(19)$ Å, $b = 25.001(6)$ Å, $c = 4.1164(8)$ Å,) based on *in situ* PND data at 538(2) K and 5.0(1) MPa D₂. A summation was done from numor 927072 to 927082 [23], with an overall measuring time of 22 min. Additional phases are γ -SrGeD_y ($\approx 25\%$, middle marker), α -SrGeD_y ($\approx 8\%$, bottom marker); (*) denotes a detector deficiency and reflections of the sapphire cell. (+) denotes the largest misfits. Background corrected reliability factors are: $R_p = 20.2\%$, $R_{wp} = 18.6\%$, $S = 2.17$.

Table A4.2: Structural data and selected distances (< 3 Å) of β -SrGeD_y, $y = 0.53(4)$, at 538(2) K, 5.0(1) MPa D₂ pressure. Space group $Cmcm$ (No.63), $a = 9.3368(19)$ Å, $b = 25.001(6)$ Å, $c = 4.1164(8)$ Å. Debye-Waller-factors were constrained for like atoms.

Atom	Wyckoff	x	y	z	B _{iso} / Å ²	SOF
Sr1	4c	0	0.5792(11)	1/4	4.9(2)	
Sr2	4c	0	0.0716(13)	1/4	4.9	
Sr3	8g	0.247(3)	0.3250(7)	1/4	4.9	
Ge1	4c	0	0.7112(12)	1/4	6.7(3)	
Ge2	4c	0	0.2183(15)	1/4	6.7	
Ge3	8g	0.234(2)	0.4804(7)	1/4	6.7	
D1	4c	0	0.860(4)	1/4	2.1(4)	0.24(4)
D2	4c	0	0.3858(15)	1/4	2.1	0.65(4)
D3	8g	0.263(5)	0.1206(8)	1/4	2.1	0.61(3)
Atom 1	Atom 2	d / Å				
Sr	D	2.237(18)-2.75(5)				
Ge1	Ge2	2.71(3)				
Ge3	Ge3	2.280(11)				
Ge	D	2.86(7) and > 3				

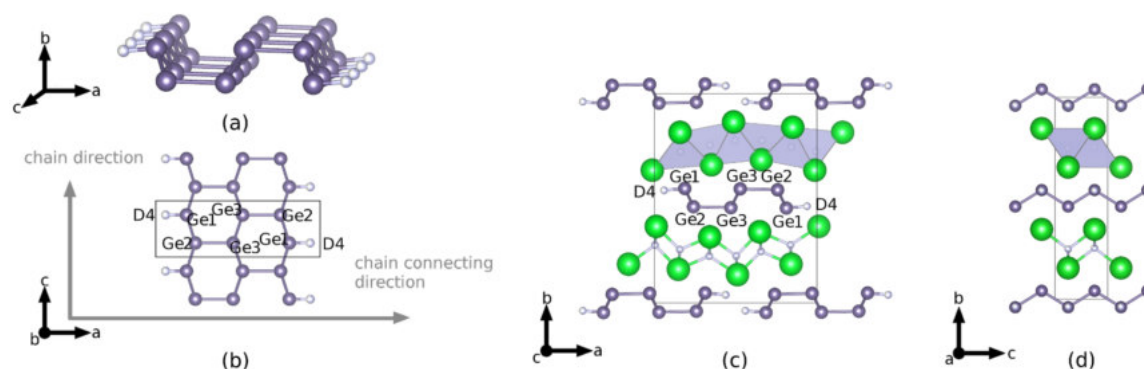


Figure A4.4: Polyanionic partial structure (a/b) and crystal structure (c/d) of γ -SrGeD_y following [15]. Large spheres: Sr; Medium spheres: Ge; Small spheres D.

Table A4.3: Lattice parameters and site occupancy factor (SOF) of the germanium bound D4 atom for γ -SrGeD_y right after the preparation, during the *in situ* experiment and after 70 days under inert atmosphere. SOF of D1-D3 (tetrahedral voids) are not affected. For complete structural data see supplementary information (Tab. S1).

	1	2	3	4	5
institute ^a	BER II	ILL [15]	ILL	ILL	ILL
container	vanadium	vanadium	sapphire cell 0.3(1) MPa D ₂ 298(2) K	sapphire cell 5.0(1) MPa D ₂ 503(2) K	sapphire cell 5.0(1) MPa D ₂ 313(4) K
time after preparation	+ 3 days	+ 70 days	+ 70 days	during <i>in situ</i>	after <i>in situ</i>
Space group	<i>Pbnm</i> (No. 62)	<i>Pbnm</i> (No. 62)	<i>Pbnm</i> (No. 62)	<i>Pbnm</i> (No. 62)	<i>Pbnm</i> (No. 62)
<i>a</i> / Å	11.8176(10)	11.9113(9)	11.9028(11)	11.9435(10)	11.8283(9)
<i>b</i> / Å	15.3772(14)	15.2692(11)	15.2807(13)	15.3252(13)	15.3534(11)
<i>c</i> / Å	4.0603(3)	4.0600(2)	4.0607(3)	4.0728(3)	4.0617(2)
V / Å ³	737.85(18)	738.41(14)	738.57(19)	745.47(18)	737.62(15)
SOF(D4)	0.684(10)	0.592(8)	0.616(12)	0.642(12)	0.672(10)

^a BER II - Helmholtz-Zentrum Berlin, Germany; ILL - Institut Laue Langevin, France

The corresponding Ge3-Ge3-Ge3 angle is 129.1(15)° compared to the chain angle Ge1-Ge2-Ge1 of the long chain with 98.9(6)°.

Long term stability of γ -SrGeD_y

The structure of γ -SrGeD_y was presented elsewhere and discussed in detail [15]. It shows *Pbnm* (No 62) symmetry. (A nonstandard setting is used, thus, the axes do not need to be rotated in regard to the Zintl phase SrGe. Standard setting is *Pnma*; $a' = b$, $b' = c$, $c' = a$.) In contrast to the other phases γ -SrGeD_y has completely filled tetrahedral Sr₄-voids. The Ge-Ge chains are tilted and two thirds of the germanium atoms form an additional Ge-Ge bond. The last third of the germanium atoms is hydrogen (deuterium) terminated (site D4) or neighboring a void since the hydrogen (deuterium) site D4 is underoccupied.

Lattice metrics as well as deuterium content at the chain terminating position D4 change over time as shown by PND (Tab. A4.3, for complete structural data see Tab. S1). Over 70 days a hydrogen (deuterium) release at site D4 from 68% to 60% occupation can be seen. After the *in situ* experiment the D4-site has a comparable filling as the freshly prepared sample. Following the general trend, lattice parameter *a* shrinks while *b* gets larger during the hydrogen (deuterium) uptake. In contrast the overall volume effect is negative. Rietveld refinement plots for different data sets can be found in the supporting information file Fig. A4.S1.

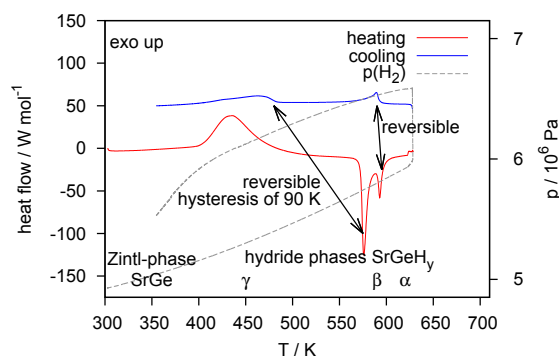


Figure A4.5: Hydrogen pressure DSC of the hydrogenation reaction of SrGe. Further heating (not shown) leads to a slow and irreversible decomposition resulting in SrH_2 and SrGe_2 . This last step did not give a proper DSC signal.

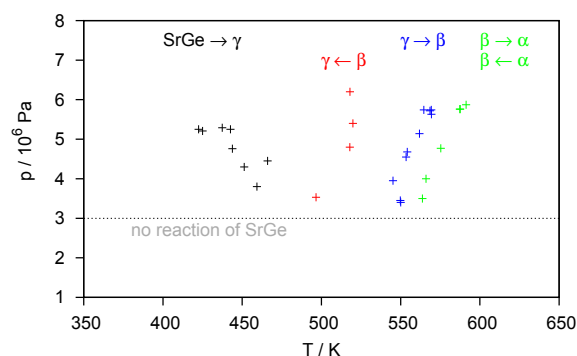


Figure A4.6: Onset temperatures for the different reaction steps in DSC experiments at various hydrogen gas pressures. The onset of the formation of $\gamma\text{-SrGeH}_y$ from SrGe is not well defined and varies for different experiments. Below 3 MPa no reaction of SrGe was obtained.

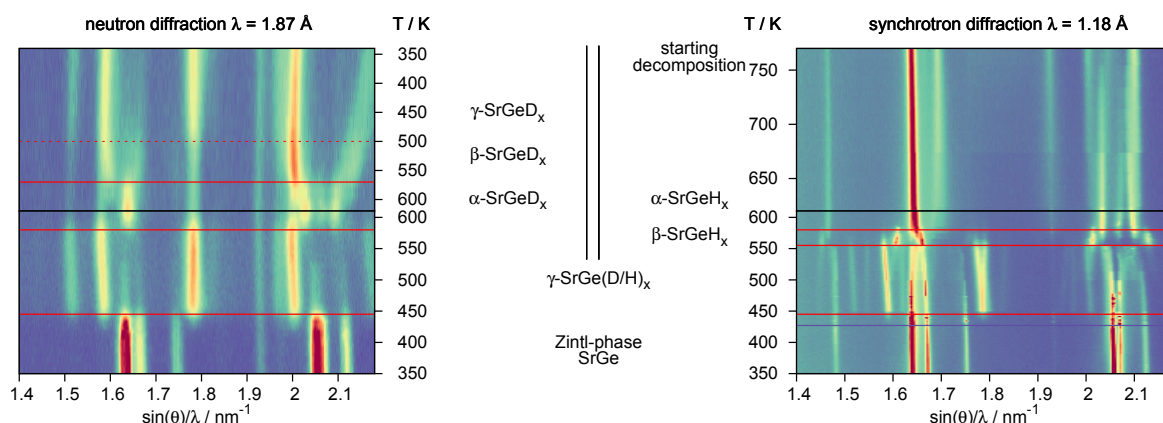


Figure A4.7: *In situ* powder neutron and synchrotron diffraction. Data were normalized to get a linear temperature scale. Both experiments were done at 5.0(1) MPa H_2 (D_2) pressure. Synchrotron data were collected by 14 s exposure time and heating up to 770 K while using neutron diffraction the reversibility was probed heating to 623 K and cooling down afterwards.

Overview of the hydrogenation of SrGe followed *in situ*

The hydrogenation of the Zintl phase SrGe was investigated under *in situ* conditions. Hydrogen pressure DSC shows three prominent signals. Fig. A4.5 shows the heat flow during the reaction at 5 MPa H_2 starting pressure. At 405 K a first strong exothermic reaction starts. The product of this step can be characterized *ex situ*, which has been published elsewhere as $\text{SrGeD}_{4/3-x}$ ($\gamma\text{-SrGeD}_y$) [15]. Afterwards two endothermic reactions follow at 570 K and 590 K, respectively. Both of these steps are reversible and none of the products can be quenched for *ex situ* characterization yet. While the second endothermic step is reversible with negligible hysteresis, the first one shows a hysteresis of 90 K. Running the reaction under 5 MPa H_2 pressure at temperatures above 700 K we get the formation of SrH_2 and of the germanium richer Zintl phase SrGe_2 . The DSC measurements were done several times at different pressure conditions. Fig. A4.6 shows the pressure dependency of the different reaction steps. The exothermic formation step of $\gamma\text{-SrGeH}_y$ shifts to higher temperatures on lowering the pressure. On the other hand the two subsequent endothermic steps shift to lower temperatures indicating a hydrogen loss. Thus, the hydrogen poorer phases β - and $\alpha\text{-SrGeH}_y$ are subsequently formed. The results of the precharacterization using a hydrogen pressure DSC can directly be correlated to *in situ* diffraction experiments. Fig. A4.7 shows *in situ* powder synchrotron and neutron diffraction at 5.0(1) MPa isobaric hydrogen (for synchrotron) or deuterium (for neutron diffraction) pressure. It can be clearly seen that the formation of $\gamma\text{-SrGeD}_y$ (H_y)

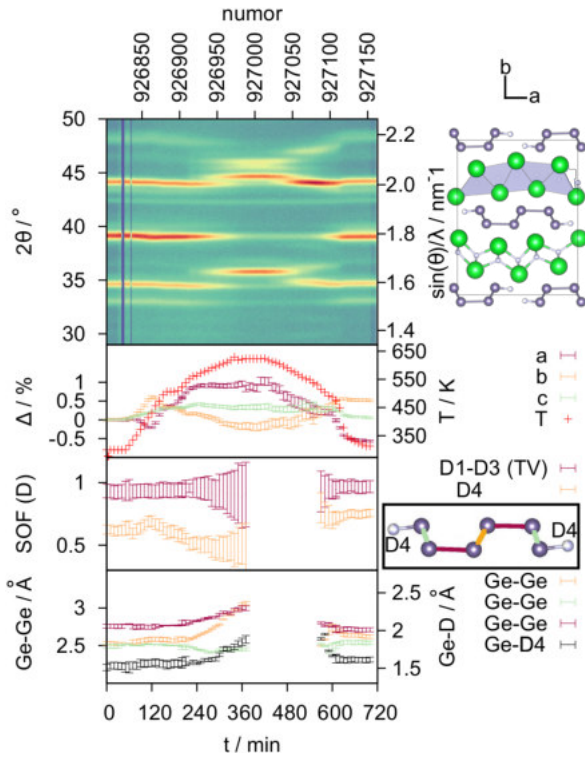


Figure A4.8: *In situ* PND data of γ -SrGeD_y under 5.0(1) MPa D₂ pressure from D20 beamline, ILL ($\lambda = 1.87$ Å) [23]. Error bars correspond to 3 e.s.u. as obtained by Rietveld refinement. SOF of the deuterium atoms in the tetrahedral voids (D1-D3(TV)) are averaged over all three positions. The different Ge-Ge bonds are drawn in the corresponding color (see inset box).

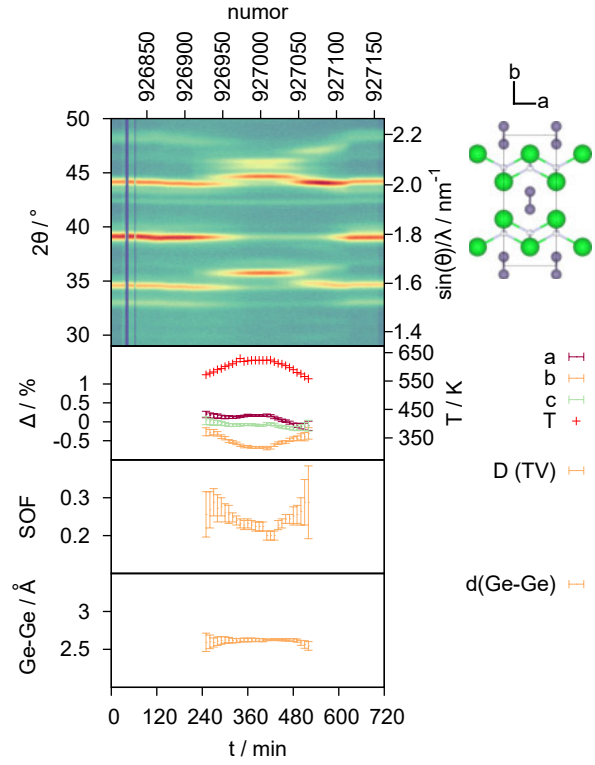


Figure A4.9: *In situ* PND data of the formation of α -SrGeD_y under 5.0(1) MPa D₂ pressure from D20 beamline, ILL ($\lambda = 1.87$ Å) [23]. Error bars correspond to 3 e.s.u. as obtained by Rietveld refinement. D(TV) = deuterium atom in tetrahedral Sr₄ voids.

is a one step reaction at 435 K which fits DSC data reasonably. Using synchrotron diffraction the first hydrogen release step can be monitored at 555 K. Neutron diffraction cannot resolve this step, which could be caused by the small temperature window of this reaction and a stronger temperature inhomogeneity due to the large amount of sample. During the neutron diffraction experiment the reversibility was tested. The transition from α - to β -phase is reversible at 5 MPa D₂ and approximately 575 K. Due to the hysteresis during the reformation of γ -SrGeD_y the β -phase can be resolved here. The decomposition into SrGe₂ and SrH₂ as seen in *ex situ* experiments is quite slow and could not be seen in the *in situ* synchrotron experiment.

Structural changes during deuterium release and uptake

The temperature dependent reaction of γ -SrGeD_y under 5.0(1) MPa isobaric D₂-pressure is discussed in more detail now. From the 2D-diffraction pattern it can be clearly seen that regions corresponding to the three distinct phases are present. Phase fractions and volume changes are shown in detail in Fig. A4.S4.

γ -SrGeD_y: During the heating ramp lattice parameter a contracts while b is increased. This reaches a maximum at 423 K (frame 60 /numor 926865 [23]) and corresponds to a small deuterium uptake. The tetrahedral Sr₄-voids are totally filled with deuterium within 3 e.s.u., thus the deuterium uptake corresponds to an increased occupation on site D4. This emphasizes the effect again, that γ -SrGeD_y has a homogeneity range and releases some deuterium over time. After this maximum is reached, the lattice parameters show an inverse trend and the site corresponding to the Ge-D bond releases deuterium again. A minimal occupation of 48(4)% at site D4 is refined before this phase collapses into α -SrGeD_y. The intensity decrease of the (110) reflection while the (200) reflection stays constant is a clear indication of

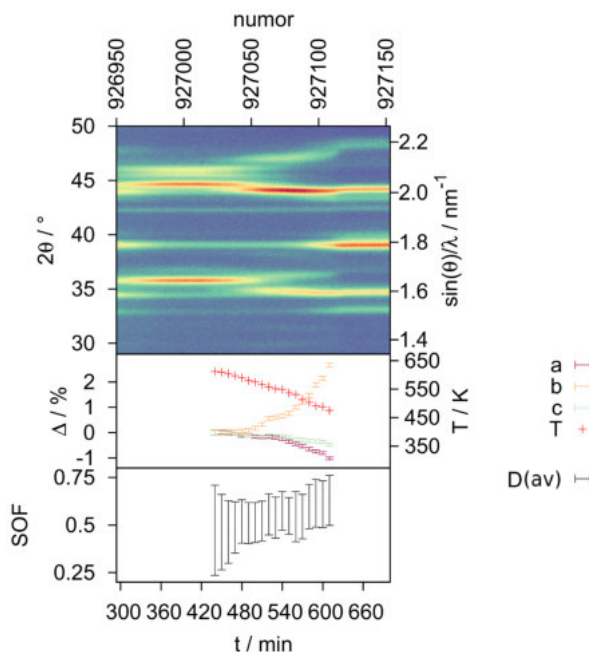


Figure A4.10: *In situ* PND data of the formation of β -SrGeD_y under 5.0(1) MPa D₂ pressure from D20 beamline, ILL ($\lambda = 1.87$ Å) [23]. Error bars correspond to 3 e.s.u. as obtained by Rietveld refinement. Due to the averaged model only a limited number of parameters is evaluated. $D(av) = SOF$ averaged over all deuterium sites.

the deuterium loss as well (see Fig. A4.S5). Within 3 e.s.u. the occupation of the tetrahedral voids does not change at all. The total breakup of the Ge-D bond during the formation of α -SrGeD_y at 575 K is close to the decomposition temperature of polymeric germane, (GeH_y)_∞, which decomposes under H₂ release at 470-520 K [33].

The Ge-Ge bond lengths depend on the changed deuterium occupation as well. While some of the Ge-D bonds break, the middle Ge3-Ge3 chain opens, thus reaching Ge-Ge distances close to the interchain distance Ge2-Ge3. During the deuterium release the Ge-D bond is slightly stretched as well.

Upon cooling γ -SrGeD_y is reformed from β -SrGeD_y. At the end of the *in situ* experiment a final diffraction data set was measured at 313 K. Lattice parameters a and b show a deviation of ± 0.5 % compared to the starting material. This can be correlated to the increased deuterium content after the redeuteriation. The average Ge-Ge bond is 2.627(8) Å, which is the same value as for the unhydrogenated Zintl phase SrGe. The terminal chain shows the shortest bond with $d(\text{Ge1-Ge2}) = 2.539(8)$ Å. The middle chain is $d(\text{Ge3-Ge3}) = 2.630(8)$ Å and chain connecting bond is $d(\text{Ge2-Ge3}) = 2.712(9)$ Å. The Ge-D length reaches a slightly longer value than before with 1.609(11) Å. The bond lengths in this freshly formed γ -SrGeD_y fit very well to the DFT calculations of a recently published study [15].

α -SrGeD_y: Fig. A4.9 shows the evaluation of α -SrGeD_y during the *in situ* experiment. Upon heating lattice parameter b contracts. At the maximum temperature of 623 K a minimal deuterium content was reached with 20.0(4)% occupation of the tetrahedral Sr₄-voids. When α -SrGeD_y reacts reversibly at 575 K a maximum deuterium content of 28.8(7)% can be reached. The Ge-Ge chain does not change during this small deuterium release.

β -SrGeD_y: The averaged model we suggest for β -SrGeD_y allows some interpretation of deuterium occupations. The lattice parameters show the strongest effect within the SrGe-D₂ system. The b lattice parameter strongly expands by 2.66(3)% upon cooling from 613 K to 475 K, while the overall deuterium content of the tetrahedral Sr₄-voids increases from 47(8)% to 63(4)%. Due to data quality a more thorough evaluation of *in situ* diffraction data on β -SrGeD_y is still elusive.

Conclusion

We recently reported about the existence of the hydrogen (deuterium) rich $\text{SrGeD}_{4/3-x}$ ($\gamma\text{-SrGeD}_y$) phase where the occurrence of a polyanionic hydride partial structure could be proven [15]. Here, two additional phases in the $\text{SrGe-H}_2/\text{D}_2$ system with lower hydrogen (deuterium) content are presented. From *ex situ* as well as *in situ* neutron diffraction data it was found that $\gamma\text{-SrGeD}_y$ has a homogeneity range. Tetrahedral Sr_4 -voids stay filled while the germanium bound D4-site loses hydrogen (deuterium). A maximal occupation of 68(1)% for a freshly prepared sample was found. During the *in situ* experiment a minimal occupation of 48(4)% was reached for the D4-site before the phase decomposed. Thus, the chemical formula can be established as $\text{SrGeD}_{4/3-x}$ with phase boundaries of at least $0.10 < x < 0.17$.

From hydrogen pressure DSC we could show a pressure dependent decomposition above 540 K in several steps. *In situ* diffraction proved that the first step results from breaking of Ge-D bonds forming $\beta\text{-SrGeD}_y$. The β -phase releases hydrogen (deuterium) reversibly to form $\alpha\text{-SrGeD}_y$ under 5 MPa D_2 pressure at 575 K. Upon cooling it takes up hydrogen (deuterium) and $\gamma\text{-SrGeD}_y$ is formed again below 520 K. Within this hysteresis region $\beta\text{-SrGeD}_y$ shows a homogeneity range of at least $0.47 < y < 0.63$ with the highest hydrogen (deuterium) content at the lowest temperature.

For $\alpha\text{-SrGeD}_y$, $y = 0.288(12)$ we find the highest hydrogen (deuterium) content at 575 K under 5 MPa hydrogen (deuterium) pressure. Upon further heating the hydrogen (deuterium) content further decreases. The highest measured temperature at 5 MPa D_2 was 623 K with $y = 0.200(4)$.

Ex situ experiments showed that under 5 MPa H_2 pressure an irreversible reaction occurs at temperatures above 700 K forming SrGe_2 and SrH_2 . Thus, hydrides of Zintl phases show a rich crystal chemistry with a variety of bonding situations and may be described with an extended Zintl-Klemm concept. As shown in this study, however, phase widths due to hydrogen vacancies may occur, which might be compensated by π -bonding within the polyanionic chains. It further demonstrates the potential of *in situ* studies, since both α - and β -phase in the SrGe-D_2 system could only be found and studied this way.

Dedication

Dedicated to Prof. Lothar Beyer on the occasion of his 80th birthday.

Supplementary Information

The supporting information file contains the following data: Tab. A4.S1: Five sets of crystal structure data of $\gamma\text{-SrGeD}_y$; Fig. A4.S1: Rietveld refinement of the crystal structure of $\gamma\text{-SrGeD}_y$ of 5 data sets; Fig. A4.S2: Total angular range of *in situ* neutron diffraction of SrGe; Fig. A4.S3: Total angular range of *in situ* neutron diffraction of $\gamma\text{-SrGeD}_y$; Fig. A4.S4: Phase content and corresponding volumes of the different phases regarding to Fig. A4.S3; Fig. A4.S5: Low angle reflections regarding Fig. A4.S3. CIF files for α - and $\beta\text{-SrGeD}_y$ are deposited as well.

Acknowledgement

This work has been supported by the Deutsche Forschungsgemeinschaft (DFG, grant Ko1803/8-1) and by Fonds der Chemischen Industrie (FCI, grant 194371). The Institut Laue-Langevin (ILL) as well as Helmholtz-Zentrum Berlin (HZB, BER II and BESSY II) are acknowledged for providing beamtime. We thank Daniel Toebbens for general support at KMC-2 beamline, BESSY II and Alexandra Franz for support at E9 beamline, BER II.

A4.4 Supplement

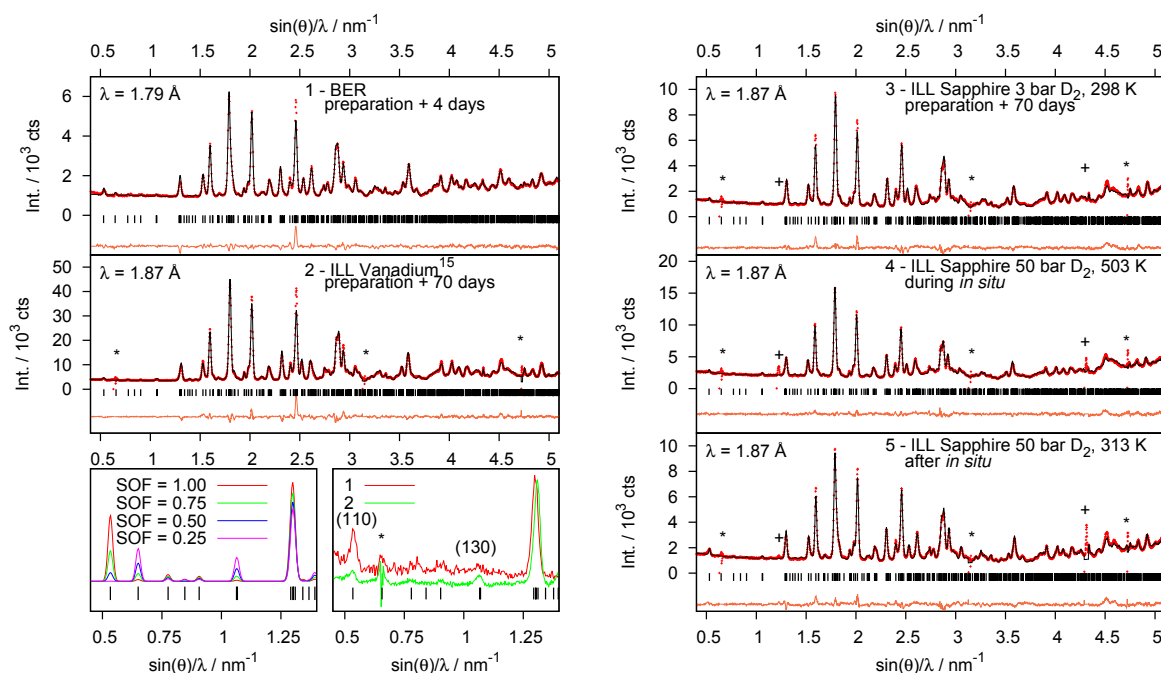


Figure A4.S1: Rietveld refinement of the crystal structure of γ -SrGeD_y based on PND data at different times after the preparation and during the *in situ* experiment. (*) denotes a detector deficiency; (+) denotes reflections of the sapphire cell. The deuterium occupation at site D4 which terminates the Ge-Ge chains is reduced over time (Tab. A4.S1) and can be repopulated during the *in situ* experiment. **Lower left:** Simulation of different occupations for the D4 site and comparison of measurements 1 and 2. Reflections are labeled regarding *Pbnm* setting. The (110) reflection decreases while (130) increases over time. Correlating this behavior with the simulation underlines the deuterium loss on D4 position which was already estimated for isopointal CaSiD_y by Wu *et.al* [13]. An underoccupation of the tetrahedral voids does not correspond to the intensity changes and can be excluded. **R-Values** (corrected for background): **1**: $R_p = 7.94$, $R_{wp} = 9.72$, $S = 1.50$, **2** (published elsewhere [15]) (numor: 924726-727, 30 min [23]): $R_p = 8.42$, $R_{wp} = 10.2$, $S = 4.80$, **3** (numor: 926803-817, 30 min [23]): $R_p = 12.7$, $R_{wp} = 13.4$, $S = 2.24$, **4** (numor: 926882-895, 28 min [23]): $R_p = 16.5$, $R_{wp} = 14.7$, $S = 2.57$, **5** (numor: 927144-160, 34 min [23]): $R_p = 12.5$, $R_{wp} = 12.9$, $S = 2.32$.

Table A4.S1: Crystal structure data of γ -SrGeD_y at different times after the preparation and from the *in situ* PND experiment. For the BER II data set Debye-Waller factors were kept at reasonable values. Measurements 2 and 3 were done on the same sample and instrument. It can be noticed, that in this case Debye-Waller factors are strongly overestimated using the sapphire cell. In contrast the site occupancy factors (SOF) match well between these two experiments, thus, a strong correlation with the SOF can be excluded. This effect can be seen for the whole *in situ* experiment. Thus, we assume a systematical error from the sapphire cell set up that is compensated by the Debye-Waller factors. Therefore B-values lose their physical meaning and need to be considered cautiously. The SOF values for D1-D3 were equal to full occupation within 1 e.s.u. and therefore they were fixed to 1.0. Data are given in non-standard setting *Pbnm* (No. 62, *Pnma* with $a' = b$, $b' = c$, $c' = a$).

institute: container:	BER II vanadium	ILL [15] vanadium	ILL sapphire cell 0.3(1)MPa D ₂ 298(2) K	ILL sapphire cell 5.0(1) MPa D ₂ 503(2) K	ILL sapphire cell 5.0(1) MPa D ₂ 313(4) K
time after preparation:	+ 3 days	+ 70 days	+ 70 days	during <i>in situ</i>	after <i>in situ</i>
Space group: (standard setting)	<i>Pbnm</i> (No. 62, <i>Pnma</i>)	<i>Pbnm</i> (No. 62, <i>Pnma</i>)	<i>Pbnm</i> (No. 62, <i>Pnma</i>)	<i>Pbnm</i> (No. 62, <i>Pnma</i>)	<i>Pbnm</i> (No. 62, <i>Pnma</i>)
Sr1	x 0.3413(8)	x 0.3415(7)	x 0.3467(11)	x 0.3434(11)	x 0.3376(8)
	y 0.3119(4)	y 0.3153(4)	y 0.3173(6)	y 0.3169(7)	y 0.3100(6)
	z 1 / 4	z 1 / 4	z 1 / 4	z 1 / 4	z 1 / 4
	B _{iso} / Å ² 0.2	B _{iso} / Å ² 0.35(9)	B _{iso} / Å ² 1.35(11)	B _{iso} / Å ² 2.65(11)	B _{iso} / Å ² 1.62(10)
Sr2	x 0.6463(7)	x 0.6480(7)	x 0.6541(9)	x 0.6501(9)	x 0.6520(8)
	y 0.3408(4)	y 0.3398(4)	y 0.3349(6)	y 0.3380(7)	y 0.3422(6)
	z 1 / 4	z 1 / 4	z 1 / 4	z 1 / 4	z 1 / 4
	B _{iso} / Å ² 0.2	B _{iso} / Å ² 0.35	B _{iso} / Å ² 1.35	B _{iso} / Å ² 2.65	B _{iso} / Å ² 1.62
Sr3	x 0.0134(7)	x 0.0122(4)	x 0.0134(7)	x 0.0096(8)	x 0.0118(7)
	y 0.3682(6)	y 0.3655(4)	y 0.3657(6)	y 0.3658(7)	y 0.3648(7)
	z 1 / 4	z 1 / 4	z 1 / 4	z 1 / 4	z 1 / 4
	B _{iso} / Å ² 0.2	B _{iso} / Å ² 0.35	B _{iso} / Å ² 1.35	B _{iso} / Å ² 2.6	B _{iso} / Å ² 1.62
Ge1	x 0.7384(4)	x 0.7410(4)	x 0.7429(4)	x 0.7391(6)	x 0.7367(4)
	y 0.0409(7)	y 0.0403(4)	y 0.0418(7)	y 0.0426(8)	y 0.0440(7)
	z 1 / 4	z 1 / 4	z 1 / 4	z 1 / 4	z 1 / 4
	B _{iso} / Å ² 0.4	B _{iso} / Å ² 0.66(7)	B _{iso} / Å ² 1.50(10)	B _{iso} / Å ² 3.33(11)	B _{iso} / Å ² 1.36(7)
Ge2	x 0.3109(4)	x 0.3125(4)	x 0.3103(6)	x 0.3055(7)	x 0.3017(6)
	y 0.0483(6)	y 0.0470(4)	y 0.0447(7)	y 0.0466(8)	y 0.0452(7)
	z 1 / 4	z 1 / 4	z 1 / 4	z 1 / 4	z 1 / 4
	B _{iso} / Å ² 0.4	B _{iso} / Å ² 0.66	B _{iso} / Å ² 1.50	B _{iso} / Å ² 3.33	B _{iso} / Å ² 1.36
Ge3	x 0.5318(6)	x 0.5288(4)	x 0.5299(6)	x 0.5304(7)	x 0.5353(6)
	y 0.5492(4)	y 0.5451(4)	y 0.5461(6)	y 0.5468(7)	y 0.5475(6)
	z 1 / 4	z 1 / 4	z 1 / 4	z 1 / 4	z 1 / 4
	B _{iso} / Å ² 0.4	B _{iso} / Å ² 0.66	B _{iso} / Å ² 1.50	B _{iso} / Å ² 3.33	B _{iso} / Å ² 1.36
D1	x 0.5064(8)	x 0.5040(6)	x 0.5045(8)	x 0.5040(11)	x 0.5043(9)
	y 0.2227(6)	y 0.2240(4)	y 0.2272(6)	y 0.2245(7)	y 0.2245(7)
	z 1 / 4	z 1 / 4	z 1 / 4	z 1 / 4	z 1 / 4
	B _{iso} / Å ² 1	B _{iso} / Å ² 1.21(10)	B _{iso} / Å ² 3.08(14)	B _{iso} / Å ² 4.74(17)	B _{iso} / Å ² 3.11(12)
D2	x 0.1580(8)	x 0.1570(7)	x 0.1592(11)	x 0.1551(14)	x 0.1569(11)
	y 0.2559(6)	y 0.2546(4)	y 0.2507(7)	y 0.2531(8)	y 0.2520(7)
	z 1 / 4	z 1 / 4	z 1 / 4	z 1 / 4	z 1 / 4
	B _{iso} / Å ² 1	B _{iso} / Å ² 1.21	B _{iso} / Å ² 3.08	B _{iso} / Å ² 4.74	B _{iso} / Å ² 3.11
D3	x 0.8421(8)	x 0.8383(7)	x 0.8464(11)	x 0.8412(13)	x 0.8463(9)
	y 0.2767(6)	y 0.2765(4)	y 0.2719(7)	y 0.2722(8)	y 0.2699(7)
	z 1 / 4	z 1 / 4	z 1 / 4	z 1 / 4	z 1 / 4
	B _{iso} / Å ² 1	B _{iso} / Å ² 1.21	B _{iso} / Å ² 3.08	B _{iso} / Å ² 4.74	B _{iso} / Å ² 3.11
D4	x 0.4406(9)	x 0.4397(7)	x 0.4371(11)	x 0.43014(14)	x 0.4440(11)
	y 0.0396(9)	y 0.0380(8)	y 0.0363(11)	y 0.03687(14)	y 0.0322(11)
	z 1 / 4	z 1 / 4	z 1 / 4	z 1 / 4	z 1 / 4
	B _{iso} / Å ² 1	B _{iso} / Å ² 1.21	B _{iso} / Å ² 3.08	B _{iso} / Å ² 4.74	B _{iso} / Å ² 3.11
	SOF 0.684(10)	SOF 0.598(8)	SOF 0.616(12)	SOF 0.642(12)	SOF 0.672(10)

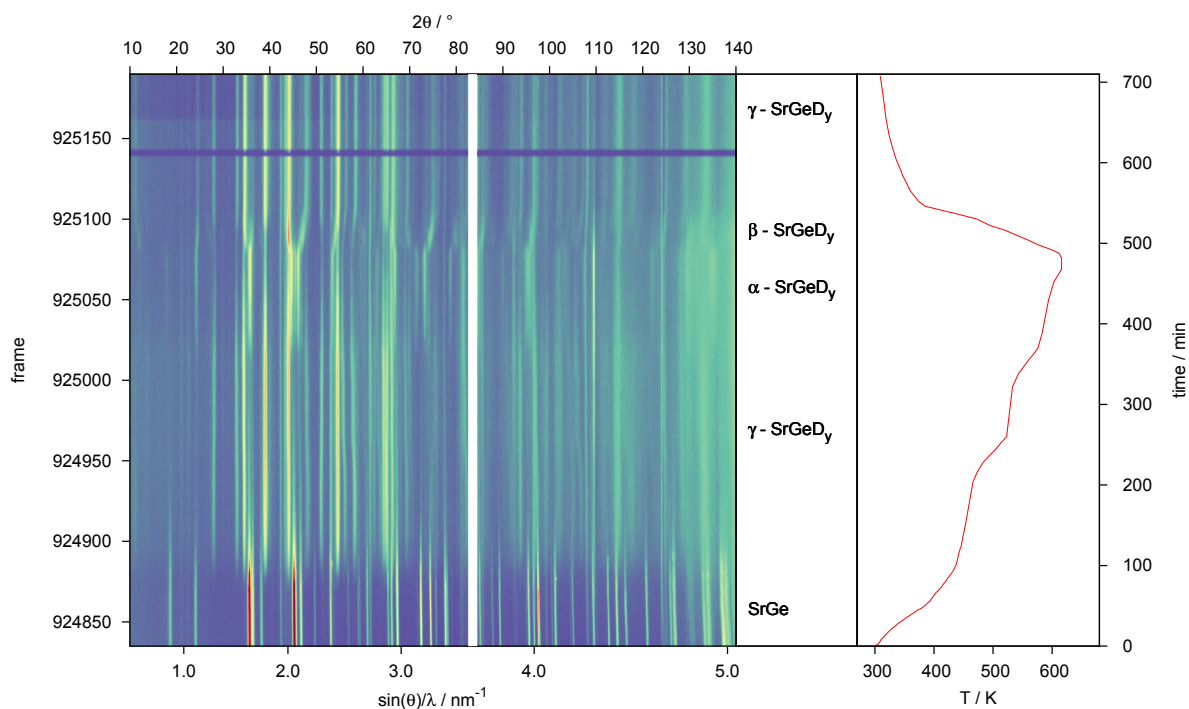


Figure A4.S2: *In situ* neutron diffraction (ILL, D20, $\lambda = 1.87 \text{ \AA}$) of SrGe under 5.0(1) MPa deuterium pressure; overview of the whole angular range. The white bar excludes a single crystal reflection of the sapphire cell. Frame numbers correspond to the ILL numbering[23].

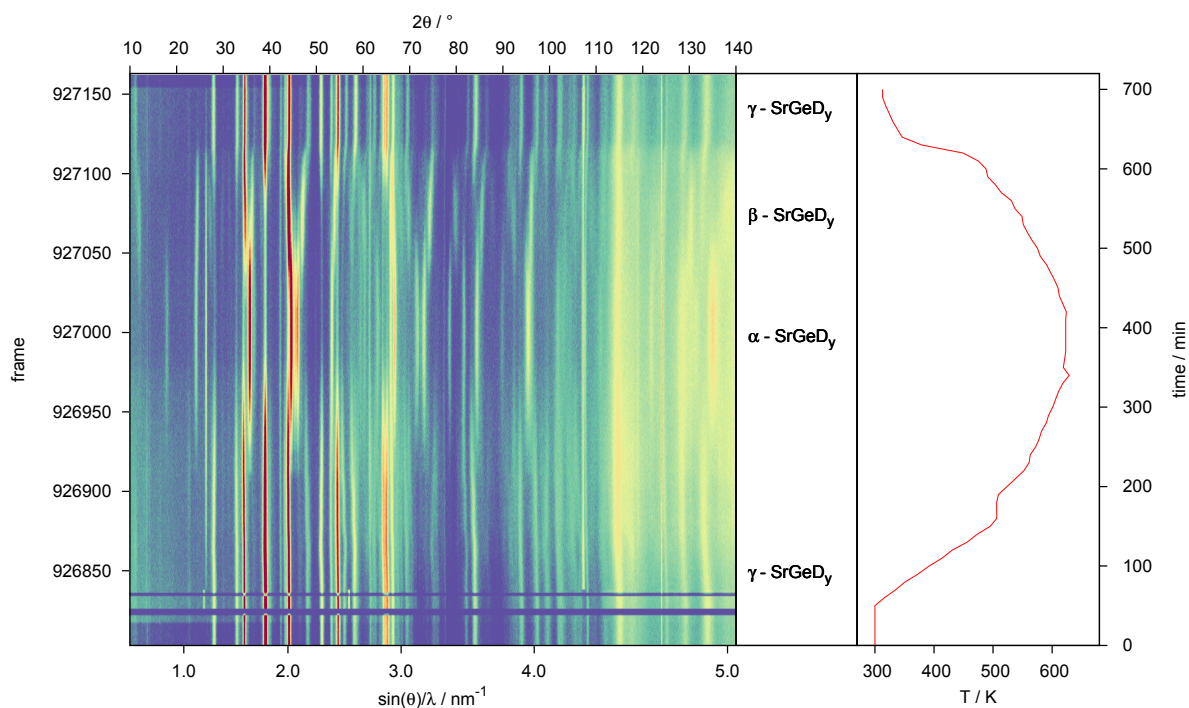


Figure A4.S3: *In situ* neutron diffraction (ILL, D20, $\lambda = 1.87 \text{ \AA}$) of γ -SrGeD_x under 5.0(1) MPa deuterium pressure; overview of the whole angular range. Frame numbers correspond to the ILL numbering[23].

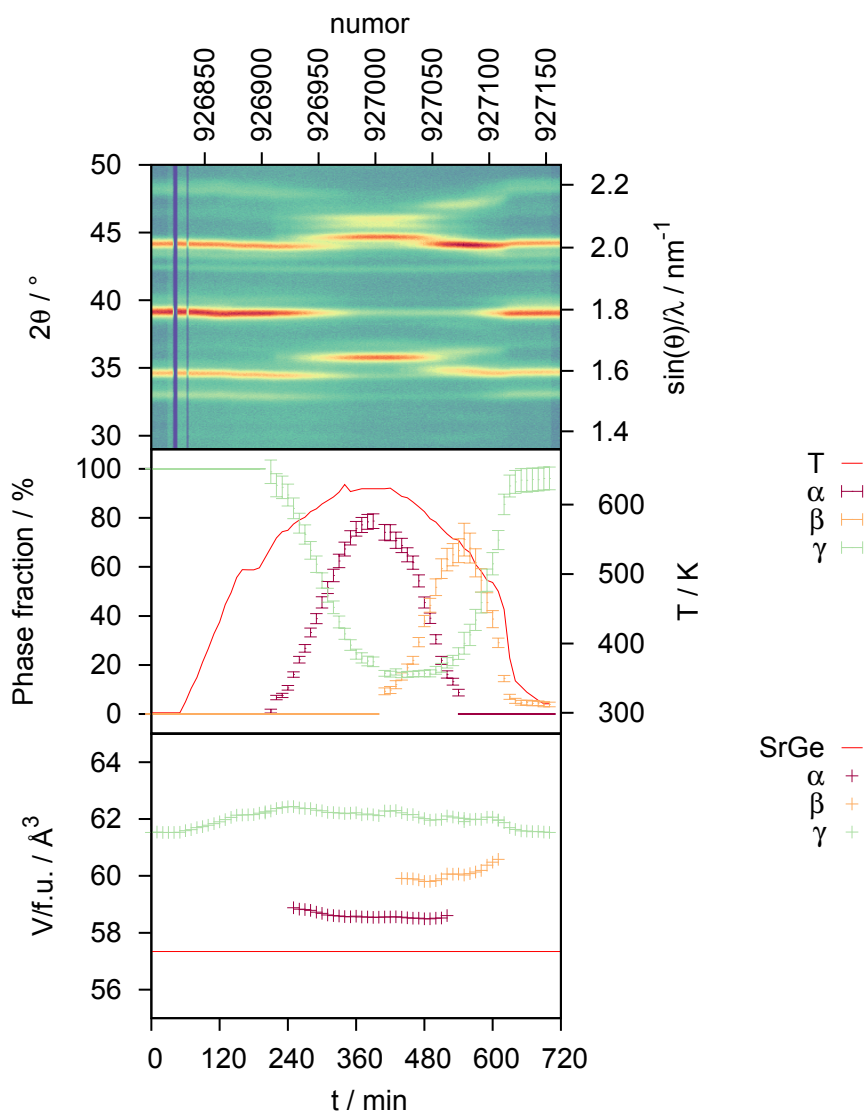


Figure A4.S4: *In situ* PND data (ILL D20, $\lambda = 1.87 \text{ \AA}$, $p = 5.0(1) \text{ MPa D}_2$) starting from γ -SrGeD_y. Phase fractions and volumes correspond to α -, β - and γ -SrGeD_y, respectively. Error bars are shown as 3 e.s.u. as obtained from Rietveld refinement. Numor-labeling corresponds to the ILL numbering[23].

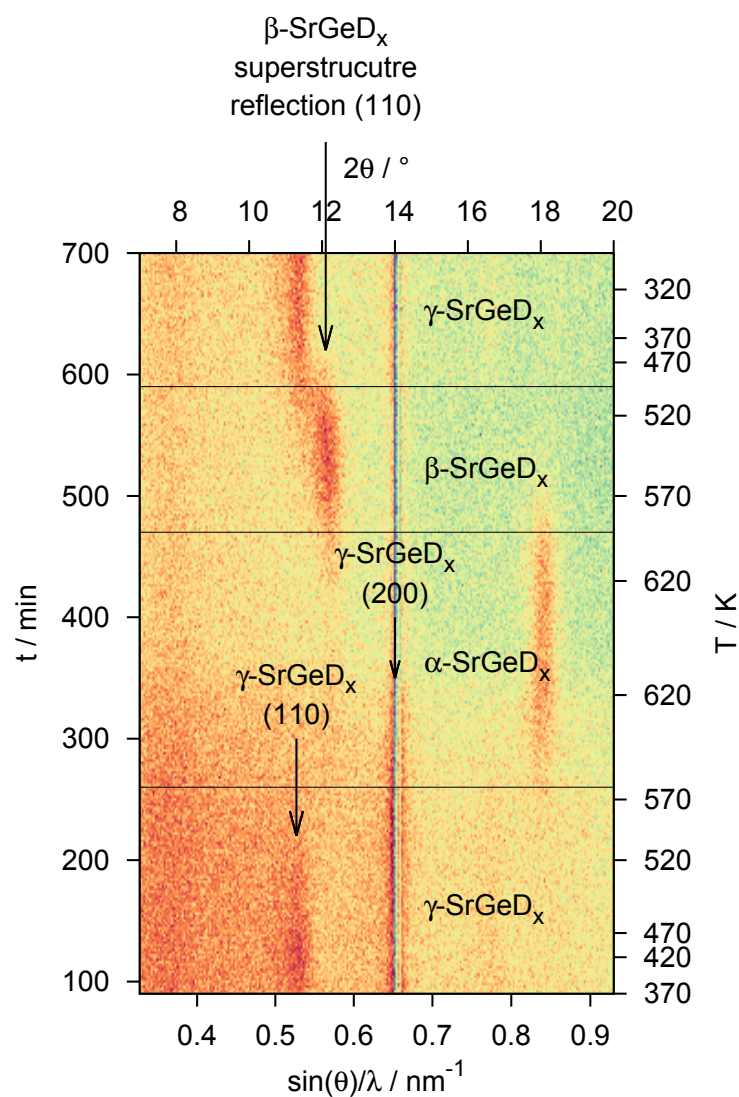


Figure A4.S5: Low angle reflections from *in situ* PND measurement (ILL D20, $\lambda = 1.87 \text{ \AA}$, 5.0(1) MPa D₂). During the formation of β -SrGeD_y the occurrence of the superstructure reflection (110) can be seen. The supercell corresponds to a doubling of a and b lattice parameter. The depopulation of the D4-site of γ -SrGeD_y is accounted for by the vanishing of the (110) reflection while the (200) reflection keeps constant intensity (compare to inset Fig. A4.S1). Unfortunately there are some deficient detector cells at the (200) reflection position.

A4.5 References

- (1) Zintl, E.; Kaiser, H. *Z. Anorg. Allg. Chem.* **1933**, *211*, 113–131, DOI: 10.1002/zaac.19332110113.
- (2) Zintl, E. *Angew. Chem.* **1939**, *52*, 1–6, DOI: 10.1002/ange.19390520102.
- (3) Schäfer, H.; Eisenmann, B.; Müller, W. *Angew. Chem.* **1973**, *85*, 742–760, DOI: 10.1002/ange.19730851704.
- (4) Schäfer, H. *Annu. Rev. Mater. Sci.* **1985**, *15*, 1–42, DOI: 10.1146/annurev.ms.15.080185.000245.
- (5) Nesper, R. *Angew. Chem.* **1991**, *103*, 805–834, DOI: 10.1002/ange.19911030709.
- (6) Corbett, J. D. *Angew. Chem., Int. Ed.* **2000**, *39*, 670–690, DOI: 10.1002/(SICI)1521-3773(20000218)39:4<670::AID-ANIE670>3.0.CO;2-M.
- (7) Nesper, R. *Z. Anorg. Allg. Chem.* **2014**, *640*, 2639–2648, DOI: 10.1002/zaac.201400403.
- (8) Evers, J.; Weiss, A. *Solid State Commun.* **1975**, *17*, 41–43, DOI: 10.1016/0038-1098(75)90330-0.
- (9) Reyes, E. C.; Nesper, R. *J. Phys. Chem. C* **2012**, *116*, 2536–2542, DOI: 10.1021/jp205825d.
- (10) Kurylyshyn, I. M.; Fässler, T. F.; Fischer, A.; Hauf, C.; Eickerling, G.; Presnitz, M.; Scherer, W. *Angew. Chem., Int. Ed.* **2014**, *53*, 3029–3032, DOI: 10.1002/anie.201308888.
- (11) Aoki, M.; Ohba, N.; Noritake, T.; Towata, S. *Appl. Phys. Lett.* **2004**, *85*, 387–388, DOI: 10.1063/1.1773930.
- (12) Ohba, N.; Aoki, M.; Noritake, T.; Miwa, K.; Towata, S.-i. *Phys. Rev. B* **2005**, *72*, 075104, DOI: 10.1103/PhysRevB.72.075104.
- (13) Wu, H.; Zhou, W.; Udovic, T. J.; Rush, J. J.; Yildirim, T. *Phys. Rev. B* **2006**, *74*, 224101, DOI: 10.1103/PhysRevB.74.224101.
- (14) Armbruster, M.; Wörle, M.; Krumeich, F.; Nesper, R. *Z. Anorg. Allg. Chem.* **2009**, *635*, 1758–1766, DOI: 10.1002/zaac.200900220.
- (15) Auer, H.; Guehne, R.; Bertmer, M.; Weber, S.; Wenderoth, P.; Hansen, T. C.; Haase, J.; Kohlmann, H. *Inorg. Chem.* **2017**, *56*, 1061–1071, DOI: 10.1021/acs.inorgchem.6b01944.
- (16) Ångström, J.; Johansson, R.; Sarkar, T.; Sørby, M. H.; Zlotea, C.; Andersson, M. S.; Nordblad, P.; Scheicher, R. H.; Häussermann, U.; Sahlberg, M. *Inorg. Chem.* **2016**, *55*, 345–352, DOI: 10.1021/acs.inorgchem.5b02485.
- (17) Nedumkandathil, R.; Kranak, V. F.; Johansson, R.; Ångström, J.; Balmes, O.; Andersson, M. S.; Nordblad, P.; Scheicher, R. H.; Sahlberg, M.; Häussermann, U. *J. Solid State Chem.* **2016**, *239*, 184–191, DOI: 10.1016/j.jssc.2016.04.028.
- (18) Möller, K. T.; Hansen, B. R. S.; Dippel, A.-C.; Jørgensen, J.-E.; Jensen, T. R. *Z. Anorg. Allg. Chem.* **2014**, *640*, 3029–3043, DOI: 10.1002/zaac.201400262.
- (19) Hansen, T. C.; Kohlmann, H. *Z. Anorg. Allg. Chem.* **2014**, *640*, 3044–3063, DOI: 10.1002/zaac.201400359.
- (20) Westlake, D.; Shaked, H.; Mason, P.; McCart, B.; Mueller, M.; Matsumoto, T.; Amano, M. *J. Less-Common Met.* **1982**, *88*, 17–23, DOI: 10.1016/0022-5088(82)90005-4.
- (21) Hansen, T. C.; Henry, P. F.; Fischer, H. E.; Torregrossa, J.; Convert, P. *Meas. Sci. Technol.* **2008**, *19*, 034001.
- (22) Kohlmann, H.; Kurtzemann, N.; Weihrich, R.; Hansen, T. *Z. Anorg. Allg. Chem.* **2009**, *635*, 2399–2405, DOI: 10.1002/zaac.200900336.
- (23) Kohlmann, H.; Auer, H.; Götze, A.; Hansen, T.; Weber, S. Reaction pathways to the Zintl phase hydrides CaSiH and MGeH_x (M = Sr, Ba), Institut Laue-Langevin, 2015, DOI: 10.5291/ILL-DATA.5-22-734.
- (24) Többens, D.; Stüßer, N.; Knorr, K.; Mayer, H.; Lampert, G. *Mater. Sci. Forum* **2001**, *378-381*, 288–293.

-
- (25) Többsens, D. M.; Zander, S. *Journal of large-scale research facilities* **2016**, *2*, A49, DOI: 10.17815/jlsrf-2-65.
- (26) Rodriguez-Carvajal, J. *Phys. B* **1993**, *192*, 55–69, DOI: 10.1016/0921-4526(93)90108-I.
- (27) Rodríguez-Carvajal, J. FULLPROF (version 5.30): A Program for Rietveld Refinement and Pattern Matching Analysis; Institut Laue-Langevin, Grenoble (France)., 2012.
- (28) Momma, K.; Izumi, F. *J. Appl. Crystallogr.* **2011**, *44*, 1272–1276, DOI: 10.1107/s0021889811038970.
- (29) VESTA - Visualisation for Electronic and STructural Analysis, version 3.3.1.
- (30) Gelato, L. M.; Parthé, E. *J. Appl. Crystallogr.* **1987**, *20*, 139–143, DOI: 10.1107/s0021889887086965.
- (31) Häussermann, U.; Kranak, V. F.; Puhakainen, K. *Struct. Bond.* **2010**, *139*, 143–161, DOI: 10.1007/430_2010_20.
- (32) Reyes, E. C.; Stalder, E. D.; Mensing, C.; Budnyk, S.; Nesper, R. *J. Phys. Chem. C* **2011**, *115*, 1090–1095, DOI: 10.1021/jp106169h.
- (33) Bianco, E.; Butler, S.; Jiang, S.; Restrepo, O. D.; Windl, W.; Goldberger, J. E. *ACS Nano* **2013**, *7*, 4414–4421, DOI: 10.1021/nn4009406.

A5 A sapphire single-crystal cell for *in situ* neutron powder diffraction of solid-gas reactions

André Götze^a, Henry Auer^a, Raphael Finger^a, Thomas Christian Hansen^b,
Holger Kohlmann^{a*}

^a *Leipzig University, Department of Inorganic Chemistry, Johannisallee 29, 04103 Leipzig, Germany*

^b *Institut Laue-Langevin, 71 Avenue des Martyrs, CS 20156, 38042 Grenoble cedex 9, France*

* *Corresponding author*

The final version is published as

A. Götze, H. Auer, R. Finger, T. C. Hansen, H. Kohlmann, *Physica B: Condensed Matter* **2018**,
accepted Nov. 11, 2017, DOI:10.1016/j.physb.2017.11.024

This is the accepted version with minor adaptations for use with L^AT_EX and one column printing.

© 2017. This manuscript version is made available under the CC-BY-NC-ND 4.0 license.

<http://creativecommons.org/licenses/by-nc-nd/4.0/>

A5.1 Authors' contributions

This article results from a conference talk of Holger Kohlmann who assembled the manuscript. The description of the *in situ* neutron diffraction cell was done by R. Finger. The shown examples of hydrogenation of palladium rich intermetallics and of Zintl phases were described by A. Götze and H. Auer, respectively. They also conducted the corresponding experiments. T. Hansen assisted during the experiments at the beamline.

A5.2 Abstract

Solid-gas reactions play an important role in many technologically important processes from ore smelting to hydrogen storage and the synthesis of functional materials. *In situ* investigations are very useful for unravelling basic steps of such reactions, rationalize them and gain control. For investigating time-resolved solid-gas reactions, we have constructed a gas pressure cell for elastic neutron diffraction. By proper orientation of a single-crystal sapphire tube as sample holder Bragg peaks from the container material can be completely avoided, thus yielding high-quality powder diffraction data with very clean diffraction background. This enables the extraction of high precision crystal structure data as a function of gas pressure and temperature (laser heating) in time-resolved studies. The potential of the gas pressure cell is demonstrated by *in situ* studies of the reaction of solids with hydrogen, which yielded detailed models of the reaction pathways including high quality crystal structures of reaction intermediates and products. These were used to predict successfully the existence of further metal hydrides, to explain unusual bonding properties, and to optimize the synthesis of metastable compounds.

A5.3 Article

Introduction

The importance of solid-gas reactions in science and in everyday life can hardly be overrated. They play a crucial role in many technologically important processes such as ore smelting (Fig. A5.1), heterogeneous catalysis, combustion of solid fuels, and the synthesis of solid materials. Solid-gas reactions are the basic step of gas storage, e.g. CO₂ sequestration or hydrogen storage, of corrosion of metals and alloys (Fig. A5.1) or their hardening procedures. They are thus key for the production, use and wear of many functional materials. The study of such reactions is often technically demanding due to the often times harsh conditions and the difficulty to find suitable probes. This is probably the reason, why despite being subject of research for many decades, only model systems are well understood and a deeper knowledge of reaction mechanisms in solids allowing control over processes is often lacking [1–5].

Neutron diffraction is ideally suited to serve as a probe for such reactions because of several reasons. The gases most often used, e.g. H₂, N₂, O₂, H₂O, CO, CO₂, contain light elements, which can often be better located in crystal structures by neutron as compared to X-ray diffraction. Studying solid-gas reactions by *in situ* methods allowing control over external parameters such as pressure and temperature often requires bulky sample environment. This is easier to penetrate by neutrons than by X-rays due to the smaller absorption coefficients for most elements. Further, neutrons can probe many properties of materials, e.g. crystal structure, diffusion, magnetism, vibrational properties, and thus yield extensive information. In this contribution, we will focus on crystal structure evolution during solid-gas reactions by elastic neutron powder diffraction. Time-resolved *in situ* investigations are very useful for unravelling basic steps of such reactions and understanding reaction pathways. This is the key to rationalize them and gain better control over reactions and processes. The potential of *in situ* neutron diffraction for the study of solid-gas reactions is intimately connected to the development of high-flux diffractometers and has increased accordingly over the past decades [6–9]. Here, we will briefly describe a single-crystal based sapphire cell and show the potential and limitations of this piece of sample environment for time-resolved *in situ* neutron powder diffraction.

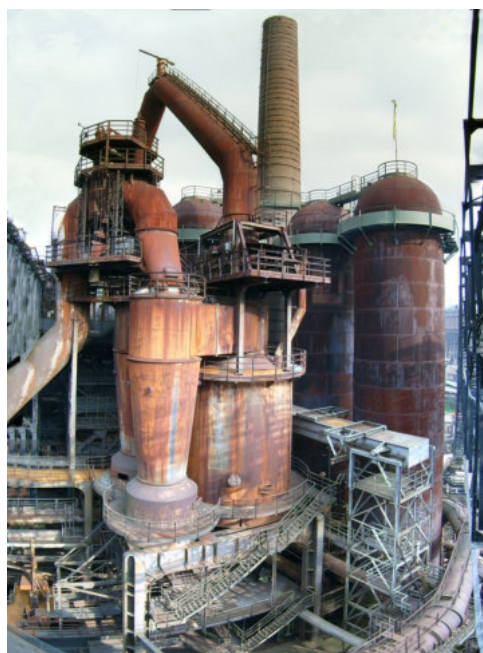


Figure A5.1: Ironworks in Völklingen, Germany (UNESCO World Heritage Site since 1994), as an example for two different kinds of solid-gas reactions, iron ore smelting (reaction of iron oxides with gaseous carbon monoxide; when operating \leq 1986) and corrosion of steel in air (after closing in 1986); By Lokilech - Own work, CC BY-SA 3.0, <https://commons.wikimedia.org/w/index.php?curid=1331378>, downloadAugust8, 2017.

Materials and Methods

Chemical syntheses

MgPd₃ was synthesized by solid-state reaction of the elements (3.1% excess of magnesium powder, 99.8%, abcr; palladium powder, 99.95%, $\leq 150 \mu\text{m}$, Goodfellow; 25 Kh^{-1} to 868 K, held for 4.5 d, quenched in air) in evacuated glass ampoules with iodine as mineralization agent (few crystals) [10]. The product was annealed for another 3 d at 868 K after regrinding and yielded α -MgPd₃ with about 1% of MgO as minor phase. SrGe was prepared from the elements in sealed tantalum ampoules [11].

A sapphire single-crystal cell for *in situ* neutron diffraction

In situ neutron diffraction for solid-gas reaction requires dedicated sample environment. It has to hold the sample in place, give control over temperature and gas pressure, and allow neutron diffraction to be carried out. Specifically, the sample environment should fulfill the following requirements:

- chemical inertness (corrosion, hydrogen embrittlement)
- pressure stability
- temperature stability
- free optical access for the neutron beam
- low incoherent neutron scattering
- low neutron absorption
- low background
- no parasitic reflections

High-strength alloys seem to be good candidates for the material of an *in situ* cell in view of temperature and pressure stability, and are often used [12–16]. For detailed structural investigations, however, they show some disadvantages. Most severely, such materials as steel, Inconel, aluminum alloys etc. are polycrystalline and evidently diffract the neutron beam, thus contributing to the diffraction pattern. This may lead to overlap of reflections from sample and container, especially for low-symmetry compounds in the sample, disturbing the data analysis by Rietveld refinement. Amorphous container materials (e.g. the widely used silica for high-temperature diffraction) are not an ideal choice either, because they produce a strong structured diffraction background. The degree of these problems of course scales with the neutron scattering lengths in the materials of use. Therefore, zero-scattering alloys such as Ti₅₂Zr₄₈ are suitable materials and are used for gas-pressure cells [17]. Due to hydrogen embrittlement, unfortunately, it cannot be used when studying hydrogenation reactions. This problem can be solved by using an inner liner, preventing hydrogen contact to the alloy. However, either pressure-temperature conditions are limited, e.g. in copper-coated vanadium cans [18] or the lining material will again produce neutron reflections.

The intrinsic flaws of amorphous and polycrystalline materials have prompted us to aim for another concept. In a powder diffraction experiment, most often the detector operates in a plane and is of limited height, i.e. measures only a thin slice of reciprocal space. Debye-Scherrer rings from a polycrystalline container material will inevitably be measured by such a detector (Fig. A5.2, left). In case of a single crystalline material, however, diffraction intensities are confined to small spots in reciprocal space. Having a single-crystalline container material should therefore enable a mode of operation where by proper orientation the detector in a powder diffraction experiment will measure only reciprocal space between rows of diffraction spots and therefore not see the container material (Fig A5.2, right). A material available as large single crystals and fulfilling the above-mentioned requirements is synthetic α -Al₂O₃, also known as leuco-sapphire, and is thus chosen. A 10 cm long sapphire is machined to have a borehole of 6 mm inner diameter to hold the powder sample. A flange at the upper end of the single crystal in combination with an endcap machined from steel (Fig. A5.3) allows hermetical sealing and realization of high gas pressures. The latter also provides a free optical access of the neutron beam. Due to the design with separated endcaps, no further supports in the diffraction plane are necessary, which

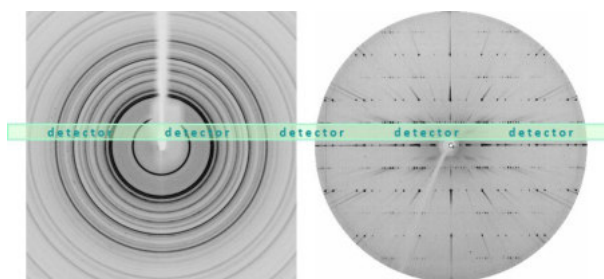


Figure A5.2: Diffraction patterns of a polycrystalline material (**left**) and a single crystal (**right**) with a thin slice of reciprocal space mapped in a typical powder diffraction experiment marked in green.

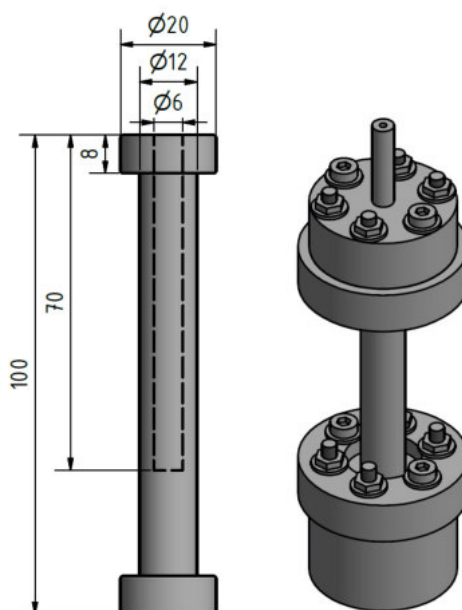


Figure A5.3: Schematic drawings of the machined single-crystal sapphire (**left**, measures in mm, crystallographic c axis along cylinder axis or slightly inclined) and fully assembled cell (**right**).

might disturb the diffraction experiment by neutron absorption. A similar design using a single-crystal sapphire cell was described before for inelastic scattering on gas hydrates at low temperatures [19] and inspired our development. The use of leuco-sapphire has the further advantage of optical transparency, which makes visual control of the reaction progress and heating by a laser possible. Neutron diffraction measurements of the empty cell and of reference samples inside the cell show that the concept of avoiding Bragg reflections from the container by using a single crystal with proper orientation with respect to the diffractometer works well. Diffraction data are comparable in quality to *ex situ* data due to the absence of enhanced background or parasitic reflections. In some cases incoherent scattering in the vicinity of strong single-crystal reflections of the sapphire cannot be avoided completely and a few degrees in 2θ have to be excluded [8, 20, 21].

Typical operating conditions for the sapphire single-crystal cell for *in situ* investigations of solid-gas reactions with hydrogen (deuterium) are $T \leq 700$ K, $p_{\text{gas}} \leq 16$ MPa, and time resolution of $10 \text{ s} \leq t \leq 300$ s. For avoiding mechanical failure of the flanges at the end of the container (Fig. A5.3), seals have to be chosen according to their hardness and assembled carefully. Due to thermal conductivity of sapphire and hydrogen gas, seals warm up, i.e. their temperature stability is also a major concern. Depending on gas pressure and temperature suitable seals consist of indium, lead or polymeric materials.

For the latter O-rings of Viton GLT70 with 70 shore (15 mm outer diameter, 2 mm thickness, operating temperature according to manufacturer $293 \text{ K} \leq T \leq 493 \text{ K}$, 21 Dichtungstechnik, Germany [22]) and NBR flat seal with 65 shore (17 mm outer diameter, 9 mm inner diameter, 2 mm thickness, operating temperature according to manufacturer $243 \text{ K} \leq T \leq 373 \text{ K}$, IDT-Flachdichtungen, Germany [23]) were

tested successfully. Leak rates are below 1 kPa/h at room temperature for pressures up to 10 MPa. The tube attached to the upper steel cap (Fig. A5.3, right) is connected to a gas delivery system. This and the laser heating can be controlled remotely while the *in situ* experiment is running. It consists of two laser diode modules (LNT, 808 nm, 40 W each), 5 m long glass fibres and divergent optics to widen the beam to an area of 6x20 mm² at the sample inside the sapphire single-crystal cell. For safety reasons, the cell is operated inside an enclosure made from aluminium installed on the diffractometer (D20, Institut Laue-Langevin, Grenoble, France). From experience over eight years, an average lifetime of sapphire crystals is estimated to be more than five *in situ* neutron diffraction experiments. Test measurements with the empty cell and reference samples for hydrogenation have been described already [8, 20, 21]. Herein, we report on new application of *in situ* neutron diffraction experiments of the sapphire single-crystal cell, probing its potential and limits.

Results and discussion

Hydrogenation of palladium-rich intermetallic compounds

Compounds of palladium and palladium-rich intermetallics with hydrogen are archetypical examples for metallic hydrides with variable hydrogen content. Ordered palladium-rich intermetallic compounds show a very interesting interplay between hydrogen-palladium interactions and atomic order. In MPd_3 ($M = \text{Mg}$ [24], In [25, 26], Tl [27], Sn , Pb [28], Bi [29]) hydrogen induces a rearrangement between different ordered variants of close packing of M and Pd atoms for which the maximization of the number of octahedral $[\text{Pd}_6]$ voids plays an important role. These interstices are preferred by hydrogen and provide the highest bonding energy in their hydrides $MPd_3\text{H}_x$ (in general $x \leq 1$). For $M = \text{Mg}$ the crystal structure is retained when removing the hydrogen by gentle heating in vacuum [24]. This concept provides a soft-chemical route (*chimie douce*) to new polymorphs of intermetallic compounds. Some of the hydrides cannot be quenched to ambient conditions, i.e. *in situ* investigations are mandatory for their investigation. As an example, we present here a study on the hydrogen uptake of MgPd_3 , which crystallizes in the tetragonal ZrAl_3 type structure (ordered variant of cubic close packing, Fig. A5.4 top right), at room temperature. The crystal structure exhibits three suitable interstitial sites for hydrogen (deuterium) atoms, each of them surrounded in a slightly distorted octahedral arrangement by varying numbers of magnesium and palladium atoms, $[\text{Pd}_6]$, $[\text{MgPd}_5]$, and $[\text{Mg}_2\text{Pd}_4]$. Deuterium uptake starts at room temperature when flushing the cell with deuterium gas (1 MPa, frame 1, Fig. A5.4). At this point, half of $[\text{Pd}_6]$ and one quarter of $[\text{MgPd}_5]$ are occupied while $[\text{Mg}_2\text{Pd}_4]$ are empty. During the isothermal deuteration up to frame 17 (corresponding to 112 minutes) both lattice parameters increase ($\Delta a = +1.3\%$, $\Delta c = +0.9\%$). The development of lattice parameter a and the occupation of $[\text{MgPd}_5]$ are strongly correlated as evident from the very similar dependence on time (Fig. A5.4). This is most probably caused by the structural arrangement of $[\text{MgPd}_5]$ octahedra, which share edges and form sheets perpendicular to the crystallographic c axis (Fig. A5.4 top right). A volume increase by deuterium occupation in these voids will therefore be highly anisotropic and cause a larger increase in a than in c . This effect is less pronounced for $[\text{Pd}_6]$ voids, which share edges with $[\text{Mg}_2\text{Pd}_4]$ to form similar octahedral sheets. $[\text{Mg}_2\text{Pd}_4]$ are unoccupied in the beginning of the experiment, thus working as a buffer and soothing the effect of deuterium occupation in $[\text{Pd}_6]$ on the lattice parameter a . Only when the lattice and thus the size of $[\text{Mg}_2\text{Pd}_4]$ voids has increased considerably (after one hour, frame ≥ 11), they are occupied by deuterium, however, at low rates ($\leq 1/4$) during the whole experiment. The beginning of $[\text{Mg}_2\text{Pd}_4]$ occupation seems to mark the end of a short two-phase region. This suggests a small miscibility gap for hydrogen in $\alpha\text{-MgPd}_3$ near the composition $\alpha\text{-MgPd}_3\text{H}$, i.e. distinct hydride phases with and without $[\text{Mg}_2\text{Pd}_4]$ occupation. Further investigations will be necessary, however, to confirm this hypothesis.

In order to probe the pressure dependence of deuterium occupation, it was first decreased to 0.1 MPa (frames 18 to 21) and then the cell was evacuated (≈ 10 Pa, frames 22 to 35). Lattice parameters and deuterium content decrease only slightly (Fig. A5.4). The change to lower pressures is accompanied by a considerable decrease in reflection width. The broad reflections at higher pressure (1 MPa deuterium) indicate a wider distribution of phases, most probably differing in deuterium content, which suggests that the sample is not at thermodynamic equilibrium. By reducing the pressure, fractions with higher deuterium content apparently quickly release some deuterium. This effect is reversible as proven by broadening of reflections, increasing lattice parameters and deuterium content upon raising the pressure again to 1 MPa (frames ≥ 36 , Fig. A5.4). Strain by incorporated hydrogen may also contribute somewhat to reflection width, however, it cannot explain the marked differences between two states with very similar

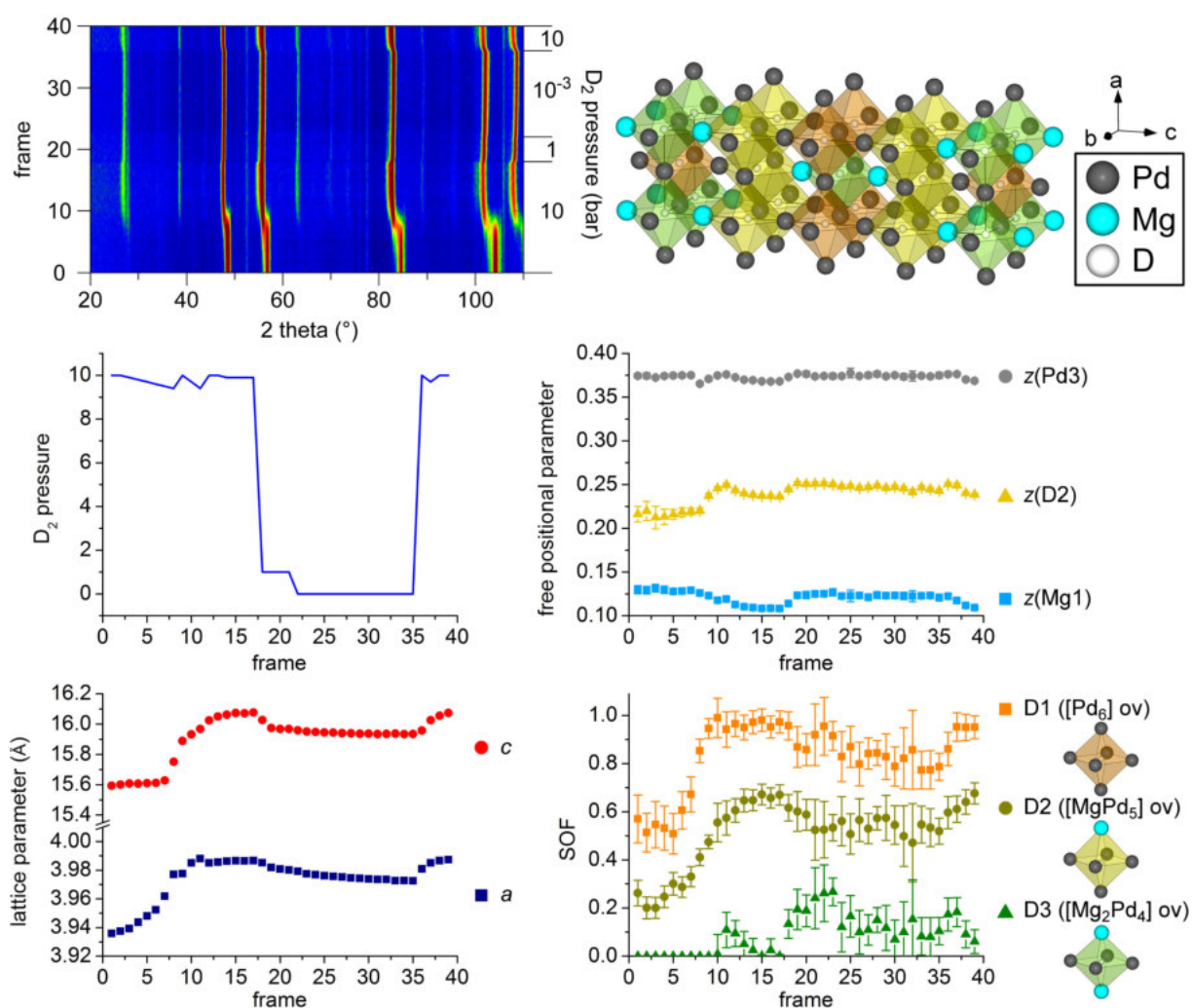


Figure A5.4: *In situ* neutron powder diffraction data (**top left**; intensities in false colors, each frame six minutes data collection time) of the deuteration of MgPd_3 (filled ZrAl_3 type; **top right**) taken on diffractometer D20 at $\lambda = 1.86786(3)$ Å in a sapphire single-crystal cell with NBR flat seal (see chapter 2.2) at $T = 297(1)$ K under various deuterium pressures (**middle left**, frames 22-35: vacuum); lattice parameters (**bottom left**), free positional parameters (**middle right**) and site occupation factors (SOF) of deuterium atoms (**bottom right**, SOF(D3) fixed to zero for frames 1 to 9) determined by sequential Rietveld refinement.

overall deuterium content. The maximum deuterium concentration is reached at the last frame of this experiment according to the formula $\alpha\text{-MgPd}_3\text{D}_{1.18(9)}$ (Tab. A5.1) with full occupation of $[\text{Pd}_6]$ voids (within three e.s.u.s). The free positional parameter z of Pd3 stays nearly constant through the whole *in situ* experiment. However, $z(\text{Mg1})$ decreases during the deuteration (vice-versa during applying vacuum) and $z(\text{D2})$ increases on the first deuteration and stays nearly constant afterwards. These changes in z parameters result in growing Mg1-D2-distances within the $[\text{MgPd}_5]$ octahedral void (from 1.4(2) Å at frame 1 to 2.06(2) Å at frame 17). The stretching of Mg-D distances conforms to those observed before (1.901(8)-2.29(2) Å) [20] and is primarily due to the increasing deuterium uptake in $[\text{MgPd}_5]$ octahedral voids.

The tetragonal $\alpha\text{-MgPd}_3\text{H}_x$ phases described here are metastable intermediates of the hydrogenation reaction of ZrAl_3 type $\alpha\text{-MgPd}_3$ to cubic $\beta\text{-MgPd}_3\text{H}_x$ with an anti-perovskite like structure [24]. Their characterization by *in situ* methods yields structural details needed for accurate modelling of total energies, which are indispensable for the evaluation of different reaction mechanisms such as hydrogen assisted gliding [30].

Table A5.1: Crystal structure parameters of α -MgPd₃D_{1.18(9)} ($I4/mmm$, filled ZrAl₃ type, $a = 3.9873(4)$ Å, $c = 16.073(2)$ Å, frame 39).

atom	Wyckoff position	x	y	z	SOF	B_{iso} (Å ²)
Mg1	$4e$	0	0	0.1093(9)	1	0.9(2)
Pd1	$4c$	0	$1/2$	0	1	0.86(9)
Pd2	$4d$	0	$1/2$	$1/4$	1	$B_{\text{iso}}(\text{Pd1})$
Pd3	$4e$	0	0	0.3686(11)	1	$B_{\text{iso}}(\text{Pd1})$
D1	$2b$	0	0	$1/2$	0.95(5)	3.1(2)
D2	$4e$	0	0	0.2386(13)	0.68(4)	$B_{\text{iso}}(\text{D1})$
D3	$2a$	0	0	0	0.06(5)	$B_{\text{iso}}(\text{D1})$

Hydrogenation of Zintl phases

The hydrogenation of Zintl phases leads to the formation of different types of hydrides, i.e. interstitial hydrides, where hydrogen is coordinated by the cationic partial structure or polyanionic hydrides, with hydrogen binding to the polyanion [31]. For the system SrGe-H₂(D₂) three phases are known. The hydrogen-rich γ -SrGeH_{>1} shows features of both types with hydride anions tetrahedrally surrounded by four strontium atoms (interstitial type) and hydrogen covalently bound to germanium polyanions (polyanionic type) [11]. Two hydrogen poor hydrides, α - and β -SrGeH_{<1}, are of the interstitial type without Ge-H bonds, and cannot be quenched to ambient conditions [32]. Thus, *in situ* investigations are necessary for determination of their crystal structures, hydrogen content and hydrogen uptake and release. The reaction of SrGe at 4-5 MPa deuterium pressure and temperatures $300 \text{ K} \leq T \leq 620 \text{ K}$ was followed by *in situ* neutron powder diffraction with 1 min data collection time per pattern. Fig. A5.5 shows a section of the 2θ range that represents the main changes during the reaction. There are three distinct phases formed during the heating and cooling cycle. The deuterium content of all phases was evaluated for all patterns by serial Rietveld refinement (FullProf [33]) using the crystal structure models described earlier [11, 32].

Due to their metastable character, *in situ* diffraction was required to discover and characterize the interstitial hydrides α - and β -SrGeH_x. This study proves that α -, β -, and γ -hydrides of SrGe are three distinct phases, each with a more or less pronounced phase width with respect to hydrogen content. Vacancies on hydrogen positions may be compensated for by π -bonding within the polyanionic chains [11, 32]. This underlines the rich crystal chemistry of hydrides of Zintl phases with a variety of bonding situations, crystal structures and hydrogen contents. It further demonstrates the potential of *in situ* studies for these otherwise inaccessible reaction intermediates.

Further solid-gas reactions

The sapphire single-crystal cell described here has been used for *in situ* neutron powder diffraction studies on further systems. Zintl phases SrGa₂, KSi and CsSi show a single-step reaction to their hydrides SrGa₂H₂, KSiH₃ and CsSiH₃ without any noticeable phase width with respect to hydrogen content [34, 35], in contrast to SrGe (see above). Various binary and ternary nitrides, imides and amides are formed by hydrogenation-dehydrogenation in the light-weight hydrogen storage material Li₃N-MgH₂ [36]. Hydrogen-induced amorphization is observed for Dy₅Pd₂ [37] and SmCo₅ [38]. The latter is a crucial part of the widely used hydrogenation-disproportionation-desorption-recombination (HDDR) process for the production of strong permanent magnetic materials. For binary and ternary intermetallic lithium aluminium compounds, the formation of lithium hydride is frequently observed, e.g. $\text{LiAl} + x/2\text{H}_2 \rightleftharpoons \text{Li}_{1-x}\text{Al} + x\text{LiH}$ [39] and for the half-Heusler compound LiAlSi according to $\text{LiAlSi} + 1/2\text{H}_2 \rightleftharpoons \text{LiH} + \text{Al} + \text{Si}$ [40]. A wealth of structural data on α - and β -palladium hydride at various temperature-pressure conditions have been extracted from a single *in situ* neutron diffraction experiment [21].

Conclusion

The sapphire single-crystal cell has proven its usefulness and provides access to high-quality diffraction data and thus to accurate crystal structure information. Real-time *in situ* neutron powder diffraction of solid-gas reactions, where diffraction intensity is measured as a function of scattering angle, gas pressure,

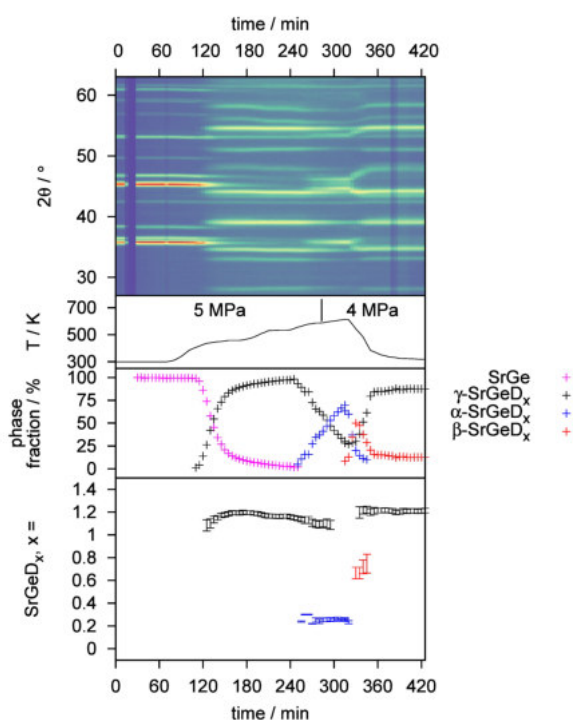


Figure A5.5: *In situ* neutron powder diffraction (ILL, D20, $\lambda = 1.86832(7)$ Å) of the reaction of SrGe to γ -SrGeD_x ($1.10(1) \leq x \leq 1.233(7)$) at 5.0 MPa deuterium pressure in a sapphire single-crystal cell with lead seal, the subsequent decomposition and reformation under 4.0 MPa deuterium pressure showing the additional phases α -SrGeD_x ($0.23(1) \leq x \leq 0.30(2)$) and β -SrGeD_x ($0.67(5) \leq x \leq 0.75(8)$).

temperature and time, can efficiently be performed. The cell material has a negligible contribution to the diffraction background and the typically achievable time resolution in the order of a minute is well suited to many solid-gas reactions. The main difference to other cell designs is the use of a single crystal as sample holder, which for a proper orientation does not contribute to the diffraction pattern, because the detector does not pick up the single crystal reflections. It is thus powder diffraction in a single crystal! Its main limitation at present is the danger of mechanical failure at temperatures above 700 K. The weak point is the end of the sapphire tube where the steel caps with the seals are attached (Fig. A5.3). New cell designs are currently being explored in order to avoid these problems and to extend the capabilities to higher temperatures. The sapphire single-crystal cell has been applied to the study of reaction pathways of hydrogenation and dehydrogenation reactions. Their understanding has contributed to the characterization of otherwise inaccessible metastable compounds, processes of hydrogen uptake and release in hydrogen storage materials and unravelling reaction pathways in industrial processes such as HDDR. With often hundreds of data sets collected in a single *in situ* diffraction experiment, a wealth of structural information is gathered. This is particularly useful as it often characterizes functional materials at non-ambient, close to their operational conditions.

Acknowledgement

We acknowledge the Institut Laue Langevin for provision of beamtime at the high-intensity powder diffractometer D20. Funding: This work was supported by the Deutsche Forschungsgemeinschaft [grant numbers Ko1803/4-1 and Ko1803/8-1] and the Fonds der Chemischen Industrie [grant number FCI 194371].

A5.4 References

- (1) Schäfer, H. *Angew. Chem.* **1971**, *83*, 35–42, DOI: 10.1002/ange.19710830105.
- (2) Szekley, J.; Evans, J. W.; Shon, H. Y., *Gas-Solid Reactions*; Academic Press: 1976.
- (3) Schmalzried, H. *Solid State Phenom.* **1997**, *56*, 13–36, DOI: 10.4028/www.scientific.net/ssp.56.13.
- (4) Pienack, N.; Bensch, W. *Angew. Chem.* **2011**, *123*, 2062–2083, DOI: 10.1002/ange.201001180.
- (5) Pienack, N.; Bensch, W. *Angew. Chem., Int. Ed.* **2011**, *50*, 2014–2034, DOI: 10.1002/anie.201001180.
- (6) Pannetier, J. *Chem. Scr.* **1986**, *26A*, 131–139.
- (7) Isnard, O. *C. R. Phys.* **2007**, *8*, 789–805, DOI: <http://dx.doi.org/10.1016/j.crhy.2007.10.002>.
- (8) Widenmeyer, M.; Niewa, R.; Hansen, T. C.; Kohlmann, H. *Z. Anorg. Allg. Chem.* **2013**, *639*, 285–295, DOI: 10.1002/zaac.201200299.
- (9) Hansen, T. C.; Kohlmann, H. *Z. Anorg. Allg. Chem.* **2014**, *640*, 3044–3063, DOI: 10.1002/zaac.201400359.
- (10) Wannek, C.; Harbrecht, B. *J. Solid State Chem.* **2001**, *159*, 113–120, DOI: 10.1006/jssc.2001.9138.
- (11) Auer, H.; Guehne, R.; Bertmer, M.; Weber, S.; Wenderoth, P.; Hansen, T. C.; Haase, J.; Kohlmann, H. *Inorg. Chem.* **2017**, *56*, 1061–1071, DOI: 10.1021/acs.inorgchem.6b01944.
- (12) Bailey, I. F.; Done, R.; Dreyer, J. W.; Gray, E. M. *High Pressure Res.* **2004**, *24*, 309–315, DOI: 10.1080/08957950410001722028.
- (13) Kuhs, W. F.; Hensel, E.; Bartels, H. *J. Phys.: Condens. Matter* **2005**, *17*, S3009.
- (14) Stepanov, G. N.; Telepnev, A. S.; Simkin, V. G. *Crystallogr. Rep.* **2007**, *52*, 558–560, DOI: 10.1134/s1063774507030406.
- (15) Yartys, V.; Denys, R.; Maehlen, J. P.; Webb, C. J.; Gray, E. M.; Blach, T.; Poletaev, A. A.; Solberg, J. K.; Isnard, O. *Mater. Res. Soc. Symp. Proc.* **2010**, *1262*, DOI: 10.1557/proc-1262-w04-01.
- (16) Klotz, S., *Techniques in High Pressure Neutron Scattering*; CRC Press - Taylor and Francis: 2013.
- (17) Knorr, K.; Annighöfer, B.; Depmeier, W. *J. Appl. Crystallogr.* **1999**, *32*, 373–374, DOI: 10.1107/s0021889898011674.
- (18) Flacau, R.; Bolduc, J.; Bibienne, T.; Huot, J.; Fritzsche, H. *J. Appl. Crystallogr.* **2012**, *45*, 902–905, DOI: 10.1107/s002188981202938x.
- (19) Rondinone, A. J.; Jones, C. Y.; Marshall, S. L.; Chakoumakos, B. C.; Rawn, C. J.; Lara-Curzio, E. *Can. J. Phys.* **2003**, *81*, 381–385, DOI: 10.1139/p03-027.
- (20) Kohlmann, H.; Kurtzemann, N.; Weihrich, R.; Hansen, T. *Z. Anorg. Allg. Chem.* **2009**, *635*, 2399–2405, DOI: 10.1002/zaac.200900336.
- (21) Kohlmann, H.; Kurtzemann, N.; Hansen, T. C. *Powder Diffr.* **2013**, *28*, S242–S256.
- (22) www.21-dichtungstechnik.de/download/o-ringe.pdf, August 9, 2017.
- (23) idt-dichtungen.de/download.php?f=&fname=IDT_Katalog_2016_deutsch.pdf, August 9, 2017.
- (24) Kohlmann, H.; Renaudin, G.; Yvon, K.; Wannek, C.; Harbrecht, B. *J. Solid State Chem.* **2005**, *178*, 1292–1300, DOI: 10.1016/j.jssc.2005.02.001.
- (25) Kohlmann, H.; Ritter, C. *Z. Anorg. Allg. Chem.* **2009**, *635*, 1573–1579, DOI: 10.1002/zaac.200900053.
- (26) Kohlmann, H.; Skripov, A.; Soloninin, A.; Udovic, T. *J. Solid State Chem.* **2010**, *183*, 2461–2465, DOI: 10.1016/j.jssc.2010.08.015.

-
- (27) Kurtzemann, N.; Kohlmann, H. *Z. Anorg. Allg. Chem.* **2010**, *636*, 1032–1037, DOI: 10.1002/zaac.201000012.
- (28) Götze, A.; Sander, J. M.; Kohlmann, H. *Z. Naturforsch., B* **2016**, *71*, DOI: 10.1515/znb-2016-0003.
- (29) Götze, A.; Hansen, T.; Kohlmann, H. *J. Alloys Compd.* **2018**, *731*, 1001–1008, DOI: 10.1016/j.jallcom.2017.10.107.
- (30) Kunkel, N.; Sander, J.; Louis, N.; Pang, Y.; Dejon, L. M.; Wagener, F.; Zang, Y. N.; Sayede, A.; Bauer, M.; Springborg, M.; Kohlmann, H. *Eur. Phys. J. B* **2011**, *82*, 1–6, DOI: 10.1140/epjb/e2011-10916-5.
- (31) Häussermann, U.; Kranak, V. F.; Puhakainen, K. *Struct. Bond.* **2010**, *139*, 143–161, DOI: 10.1007/430_2010_20.
- (32) Auer, H.; Wallacher, D.; Hansen, T. C.; Kohlmann, H. *Inorg. Chem.* **2017**, *56*, 1072–1079, DOI: 10.1021/acs.inorgchem.6b01945.
- (33) Rodríguez-Carvajal, J. FULLPROF (version 5.30): A Program for Rietveld Refinement and Pattern Matching Analysis; Institut Laue-Langevin, Grenoble (France), 2012.
- (34) Wenderoth, P.; Kohlmann, H. *Inorg. Chem.* **2013**, *52*, 10525–10531, DOI: 10.1021/ic401480b.
- (35) Auer, H.; Kohlmann, H. *Z. Anorg. Allg. Chem.* **2017**, *643*, 945–951, DOI: 10.1002/zaac.201700164.
- (36) Behrendt, G.; Reichert, C.; Kohlmann, H. *J. Phys. Chem. C* **2016**, *120*, 13450–13455, DOI: 10.1021/acs.jpcc.6b04902.
- (37) Kohlmann, H.; Talik, E.; Hansen, T. *J. Solid State Chem.* **2012**, *187*, 244–248, DOI: 10.1016/j.jssc.2012.01.029.
- (38) Belener, K. L.; Kohlmann, H. *J. Magn. Magn. Mater.* **2014**, *370*, 134–139, DOI: 10.1016/j.jmmm.2014.06.066.
- (39) Reichert, C. Untersuchungen zu Synthese und Hydrierverhalten von Verbindungen der Triele (B, Al, Ga) mit Lithium und Kalium., Ph.D. Thesis, Saarbrücken: Universität des Saarlandes, 2013.
- (40) Kunkel, N.; Reichert, C.; Springborg, M.; Wallacher, D.; Kohlmann, H. *J. Solid State Chem.* **2015**, *221*, 318–324, DOI: 10.1016/j.jssc.2014.10.021.

A6 Reversible hydrogenation of the Zintl phases BaGe and BaSn studied by *in situ* diffraction

Henry Auer^a, Sebastian Weber^a, Thomas Christian Hansen^b, Daniel Maria Többens^c, Holger Kohlmann^{a*}

^a *Leipzig University, Department of Inorganic Chemistry, Johannisallee 29, 04103 Leipzig, Germany*

^b *Institut Laue-Langevin, 71 Avenue des Martyrs, CS 20156, 38042 Grenoble cedex 9, France*

^c *Helmholtz Zentrum Berlin für Materialien und Energie, Albert-Einstein-Str. 15, 12489 Berlin, Germany*

* *Corresponding author*

Reprinted with permission from

H. Auer, S. Weber, T. C. Hansen, D. M. Többens, H. Kohlmann, Reversible hydrogenation of the Zintl phases BaGe and BaSn studied by *in situ* diffraction, *Z. Kristallogr. - Cryst. Mater.*, in press, Berlin, Boston: Walter De Gruyter GmbH, *accepted Dec. 20, 2017*. DOI:10.1515/zkri-2017-2142.

Copyright and all rights reserved. Material from this publication has been used with permission of Walter De Gruyter GmbH.

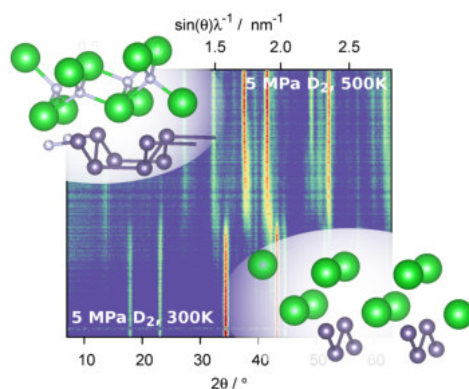
This is the accepted version with minor adaptations for use with L^AT_EX and one column printing.

A6.1 Authors' contributions

Preparation of BaSn and the thermal analysis of the hydrogenation reaction were done by S. Weber. *In situ* diffraction was conducted by S. Weber under the supervision of H. Kohlmann. BaGe was prepared by H. Auer. He also conducted *in situ* synchrotron as well as neutron diffraction of this compound. D. M. Többens and T. C. Hansen assisted during the synchrotron and neutron beam time, respectively. Data evaluation concerning BaGe was done by H. Auer. S. Weber handled data of BaSn. The manuscript was mainly written and assembled by H. Auer. S. Weber contributed figures and texts dealing with the hydrogenation of BaSn. H. Kohlmann edited the manuscript.

A6.2 Abstract

Hydrogenation products of the Zintl phases $AeTt$ (Ae = alkaline earth; Tt = tetrel) exhibit hydride anions on interstitial sites as well as hydrogen covalently bound to Tt which leads to a reversible hydrogenation at mild conditions. *In situ* thermal analysis, synchrotron and neutron powder diffraction under hydrogen (deuterium for neutrons) pressure was applied to $BaTt$ ($Tt = Ge, Sn$). $BaTtH_y$ ($1 < y < 1.67$, γ -phases) were formed at 5 MPa hydrogen pressure and elevated temperatures (400 - 450 K). Further heating (500 - 550 K) leads to a hydrogen release forming the new phases β -BaGeH_{0.5} ($Pnma$, $a = 1319.5(2)$ pm, $b = 421.46(2)$ pm, $c = 991.54(7)$ pm) and α -BaSnH_{0.19} ($Cmcm$, $a = 522.72(6)$ pm, $b = 1293.6(2)$ pm, $c = 463.97(6)$ pm). Upon cooling the hydrogen rich phases are reformed. Thermal decomposition of γ -BaGeH_y under vacuum leads to β -BaGeH_{0.5} and α -BaGeH_{0.13} ($Cmcm$, $a = 503.09(3)$ pm, $b = 1221.5(2)$ pm, $c = 427.38(4)$ pm). At 500 K the reversible reaction α -BaGeH_{0.23} (vacuum) \rightleftharpoons β -BaGeH_{0.5} (0.2 MPa deuterium pressure) is fast and was observed with 10 s time resolution by *in situ* neutron diffraction. The phases α -BaTtH_y show a pronounced phase width (at least $0.09 < y < 0.36$). β -BaGeH_{0.5} and the γ -phases appear to be line phases. The hydrogen poor (α - and β -) phases show a partial occupation of Ba₄ tetrahedra by hydride anions leading to a partial oxidation of polyanions and shortening of Tt - Tt bonds.



A6.3 Article

Introduction

Zintl phases gained some interest as reversible hydrogen storage materials since they react under mild conditions, e.g. $\text{CaSiH}_{1.3}$ [1, 2], KSiH_3 [3, 4] or SrAl_2H_2 [5, 6]. Chemisorbed hydrogen storage materials can be divided into (i) ionic (e.g. MgH_2) or (ii) complex metal hydrides (e.g. NaAlH_4 , or LiBH_4) or (iii) molecular hydrides (e.g. NH_3BH_3) [7–12]. Ionic metal hydrides like MgH_2 exhibit strong Coulomb interactions of the hydride anions with metal cations and thus, show high desorption temperatures. In complex metal hydrides like alanates or boronates, however, hydrogen is covalently bound to an element forming a complex anion. Unfortunately, these systems show poor rehydrogenation properties and often need catalysts to react in a reasonable temperature-pressure regime.

Zintl phase hydrides can either incorporate hydrogen on interstitial sites or covalently bound to the polyanion (review: [13]), thus showing features of ionic as well as complex hydrides. Furthermore, both bonding schemes can appear next to each other and might help to overcome the problems mentioned above. Additionally, they allow the use of light and inexpensive elements like calcium, potassium, aluminium, silicon, etc. Since Zintl phase hydrides features both, salt-like and complex hydride moieties, decomposition occurs usually at moderate temperatures, e.g. 414 K for KSiH_3 [3] and 523 K for $\text{CaSiH}_{1.3}$ [1] at 0.1 MPa, and show good reversibility.

In situ diffraction has proven to be a valuable tool to study such solid-state gas reactions (recent reviews: [14] for neutron, [15] for X-ray diffraction.) To investigate the incorporation of hydrogen into crystalline structures the use of neutron radiation is often mandatory to localize hydrogen (or more often deuterium) positions. There are several examples demonstrating the benefit of such studies. *In situ* diffraction of the reaction of $\text{Li}_3\text{N} + \text{H}_2 \rightleftharpoons \text{LiNH}_2 + 2\text{LiH}$, which is an example of a hydrogen storage system due to its reversibility, showed quite different reaction paths depending on the temperature-pressure conditions [16, 17]. Previous studies on the reaction of Zintl phases with hydrogen revealed that reactions happen in one step forming line phases [18, 19] or show intermediate phases with large homogeneity ranges regarding hydrogen [20].

The *AeTt*- H_2 (*Ae* = Ca-Ba, *Tt* = Si-Sn) systems show hydrogen rich phases incorporating ionic hydride anions as well as hydrogen covalently bound to the *Tt*-polyanions [2, 21–23]. For the SrGe-H_2 system it was shown that the breaking of covalent Ge-H bonds is accompanied by a release of ionic hydrogen from interstitial sites [20, 24].

This contribution extends the mechanistic understanding of hydrogen uptake and release of Zintl phases using *in situ* thermal analysis and diffraction. We use the heavy element representatives of the *AeTt* system, i.e. BaGe and BaSn, since they show better reactivity than the silicides. Three new, hydrogen poor compounds ($y < 1$) are described that are intermediates in the formation and decomposition of the hydrogen rich phases BaTtH_y , $1 < y < 2$.

Experimental

Synthesis

All preparations were done in an argon filled glove box (< 1 ppm H_2O , O_2). The Zintl phases BaGe and BaSn were prepared from the elements (Ba: rod, 99.3% (ca. 0.7% Sr); Ge: ChemPur, 99.9999%; Sn: powder, ChemPur, 99+%). Stoichiometric mixtures of barium and germanium or barium and tin were sealed inside a niobium (BaGe) or stainless steel (BaSn) metal jacket, which was heated under primary vacuum (0.1 Pa, active pumping). BaGe was melted at 1373 K and subsequently annealed at 1173 K for 40 h. BaSn was annealed at 1273 K for 48 h, then ground and annealed at 1273 K for 48 h again.

Thermal analysis

Differential scanning calorimetry was done *in situ* under hydrogen pressure (H_2 -DSC). Measurements were performed with a Q1000 DSC (TA Instruments) equipped with a gas pressure chamber. Aluminum crucibles were filled with about 15–20 mg of the Zintl phase and crimped within a glovebox. Thus, the container was tight against air but still allows hydrogen to penetrate. Samples were placed in the pressure chamber, which was then flushed with hydrogen (Air Liquide, 99.9%) for three times before it was set to the desired starting pressure. Due to isocore set up, the pressure increased during a measurement as shown in the corresponding figures. Samples were heated at a rate of 10 Kmin^{-1} to a maximum temperature of

700 K. The temperature was usually held for 10 min. In subsequent runs, lower maximum temperatures were used depending on the occurring signals. The heating was then stopped right after a reaction step, and the temperature was held there for 10 min before cooling to room temperature and *ex situ* XRPD characterisation.

Laboratory X-ray powder diffraction (XRPD)

Ex situ XRPD was done using monochromatic Cu-K $_{\alpha 1}$ -radiation either on a Huber G670 Guinier diffractometer with image plate detector or on a Stoe Stadi P Debye-Scherrer diffractometer with Mythen 1K detector.

In situ synchrotron powder diffraction (*in situ* SPD)

SPD was done at KMC-2 beamline [25] of BESSY II at Helmholtz-Zentrum Berlin (HZB), Germany, using radiation with $\lambda = 118.08(2)$ pm (10.5 keV). For *in situ* measurements 0.3 mm fused silica capillaries were used, glued into $1/4$ in. VCR-fittings using two component epoxy glue, and attached to a gas handling system (H $_2$: 99.999%). Heating was realised using a hot air jet. As sample rotation was not yet possible, the resulting poor crystallite statistics allowed qualitative evaluation of the reaction only.

In situ neutron powder diffraction (*in situ* NPD)

In situ NPD was done at the high intensity D20 instrument [26] at the Institut Laue Langevin (ILL), Grenoble, France. Measurements were done at $\lambda = 186.819(3)$ pm, which was calibrated by an external silicon NIST640b standard sample in a 5 mm vanadium container. *In situ* experiments were done in (leuco-)sapphire single-crystal cells with 6 mm inner diameter, which were connected to a gas supply system (for more details, see [24, 27]). Due to the single-crystalline character of the cell a proper orientation leads to almost no background contribution of the container. For the *in situ* investigations, the sapphire cell was filled with the Zintl phase within a glove box. After attaching to the gas supply system on the diffractometer the reaction chamber was pressurized with D $_2$ (Air Liquide, 99.8% isotope purity) at ambient temperature. Heating was realized using two laser beams.

All data sets obtained on the ILL D20 instrument are presented with an additional label according to internal raw data labelling (NUMOR labelling). Data refer to proposal 5-22-734 [28].

Rietveld refinement and crystal structure pictures

Crystal structures were Rietveld refined [29, 30] using *FULLPROF* [31, 32] (BaSn-D2 experimentes) or *TOPAS* [33] (BaGe-D2 experiments). *In situ* data set were evaluated in sequential refinements. Structure pictures were prepared by *VESTA* [34, 35]. Structural data were normalized using *STRUCTURE TIDY* [36] as implemented in *VESTA*.

Results and Discussion

Preliminary Considerations

The *AeTt* Zintl-phase family (*Ae* = alkaline earth metal, *Tt* = tetrel / group 14 element) shows a rich hydrogenation chemistry. For the SrGe-H $_2$ system three hydride phases are known already. There are hydrogen rich γ -SrGeH $_y$, $1.10 < y < 1.23$ [20, 21, 24], as well as two hydrogen poor phases α -SrGeH $_y$, $y < 0.3$ and β -SrGeH $_y$, that shows a homogeneity range of at least $0.47 < y < 0.75$ [20, 24].

The Zintl phases *AeTt*, *Ae* = Ca-Ba *Tt* = Si-Pb, crystallize in CrB-structure type (space group type *Cmcm*, No. 63). According to the Zintl-Klemm concept we suspect two-binding Si $^{2-}$ -ions, which form $^1_{\infty}$ [Si $^{2-}$]-zigzag chains. Alkaline earth metal atoms form sheets of connected *Ae* $_4$ tetrahedra that are compressed along the crystallographic *b* direction. Upon formation of α - and β -phases with less than one equivalent hydrogen per formula unit, tetrahedral *Ae* $_4$ -voids are occupied and the *Tt* $^{2-}$ polyanions are partially oxidized. As DFT calculations of the hydrogen free phases have shown, there are already partially filled (oxidized) π^* -bands at the Fermi edge [37–39], due to *Tt*-p-*Ae*-d interaction. Upon incorporation of hydrogen these bands are further oxidized increasing bond strength within the zigzag chain and shortening the bond lengths [20–23]. A similar effect was described for the solid solutions CaGa $_x$ Tt $_{1-x}$ (*Tt* = Si ($x \leq 0.6$), Sn ($x \leq 0.4$)) [40] where electron poor Zintl phases are formed since gallium ions formally have

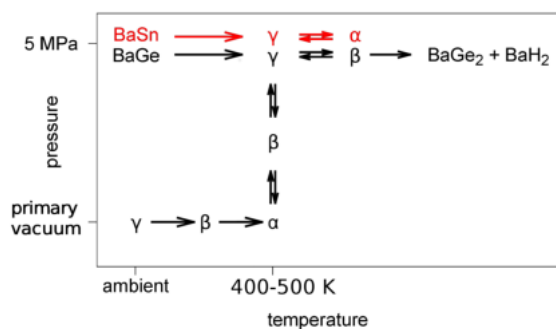


Figure A6.1: Reaction scheme of the hydrogenation of BaGe (black) and BaSn (red) showing irreversible and reversible formation steps. Approximate compositions are α -BaTtH_y ($0 < y < 0.36$), β -BaGeH_y ($y = 0.5$) and γ -BaTtH_y ($1 < y < 1.67$), ($Tt = \text{Ge or Sn}$, no β -BaSnH_y obtained).

Table A6.1: Structural data of the α -phase BaGeD_{0.131(5)}, 325(6) K, sapphire cell, primary vacuum (10 Pa), $Cmcm$, $a = 503.09(3)$ pm, $b = 1221.5(2)$ pm, $c = 427.38(4)$ pm, $d(\text{Ge-Ge}) = 261.6(6)$ pm, $\angle(\text{Ge-Ge-Ge}) = 109.5(3)^\circ$. Structural data of α -BaGeD_{0.095(7)} are given in Tab. A6.S3.

Table A6.2: Structural data of the α -phase BaSnD_{0.188(4)}, 478(5) K, sapphire cell, 5.2(1) MPa D₂ pressure, $Cmcm$, $a = 522.72(6)$ pm, $b = 1293.60(15)$ pm, $c = 463.97(6)$ pm, $d(\text{Sn-Sn}) = 294.0(3)$ pm, $\angle(\text{Sn-Sn-Sn}) = 104.2(3)^\circ$.

atom	x	y	z	$B_{\text{iso}} / 10^4 \text{ pm}^2$	SOF	atom	x	y	z	$B_{\text{iso}} / 10^4 \text{ pm}^2$	SOF
Ba	0	0.3578(3)	1/4	0.62(13)		Ba	0	0.3530(3)	1/4	3.58(6) ^a	
Ge	0	0.0618(4)	1/4	1.80(10)		Ge	0	0.0698(4)	1/4	3.58	
D	0	0.767(3)	1/4	0.7(8)	0.131(5)	D	0	0.7531(12)	1/4	4.58	0.188(4)

^a Due to similar molar mass (Ba and Sn) and some problems with adjustment of the single crystal cell, constraints were set to $B_{\text{iso}}(\text{Ba}) = B_{\text{iso}}(\text{Sn}) = B_{\text{iso}}(\text{D})$ -offset; offset = 1.0. Varying the offset did not change the SOF(D) significantly (offset = 0.0 to 2.0: 2 e.s.u. variation, offset = 3.0: 3 e.s.u.)

only 5 valence electrons instead of 6. Replacing the alkaline earth metal by an alkaline metal in $AeTt$ has a similar effect as partial oxidation by hydrogen. Thus, a bond length shortening within the chain was found in Na_{0.14}Sr_{0.86}Ge [41].

Thermal analysis (see below) of the reaction of BaGe and BaSn with gaseous hydrogen suggests the occurrence of similar hydrogen poor phases as obtained for the SrGe-H₂ system, i.e. α -BaGeH_y and α -BaSnH_y ($y < 0.4$) and β -BaGeH_y ($y = 0.5$). Therefore, the recently described phases BaGeH_{5/3-x} [22, 23] and BaSnH_{4/3-x} [21] will be called γ -BaGeH_y and γ -BaSnH_y, respectively. α - and β -phases are typical decomposition products at high temperatures. γ -phases release hydrogen under vacuum conditions as well as under hydrogen pressure forming the hydrogen poor phases. Fig. A6.1 gives a schematic overview of the conditions where the different phases are obtained. Before the reactions are discussed as determined by *in situ* thermal analysis and diffraction, the structures of the new compounds will be discussed in detail.

Crystal structures of α -BaGeD_y, α -BaSnD_y and β -BaGeD_y, $y < 1.0$

Using *in situ* neutron diffraction data the crystal structures (see Fig. A6.2) of the deuterides α -BaGeD_y, α -BaSnD_y and β -BaGeD_y, $y < 1.0$ were determined and refined [42].

The crystal structures of the α -phases of the BaTt-H₂ system ($Tt = \text{Ge, Sn}$) were Rietveld refined using a model isotopic to α -SrGeH_y (Fig. A6.3 and A6.S3; Tab A6.1, A6.2 and A6.S3). Due to technical issues (see description of the *in situ* experiment below) the refinement of α -BaSnD_y shows some misfits. The crystal structure of the parent Zintl phases is preserved, but especially lattice parameter b is elongated when tetrahedral Ba₄-voids are partially filled with hydrogen.

They appear as decomposition products of the more hydrogen rich β - and γ -BaGeH_y or γ -BaSnH_y

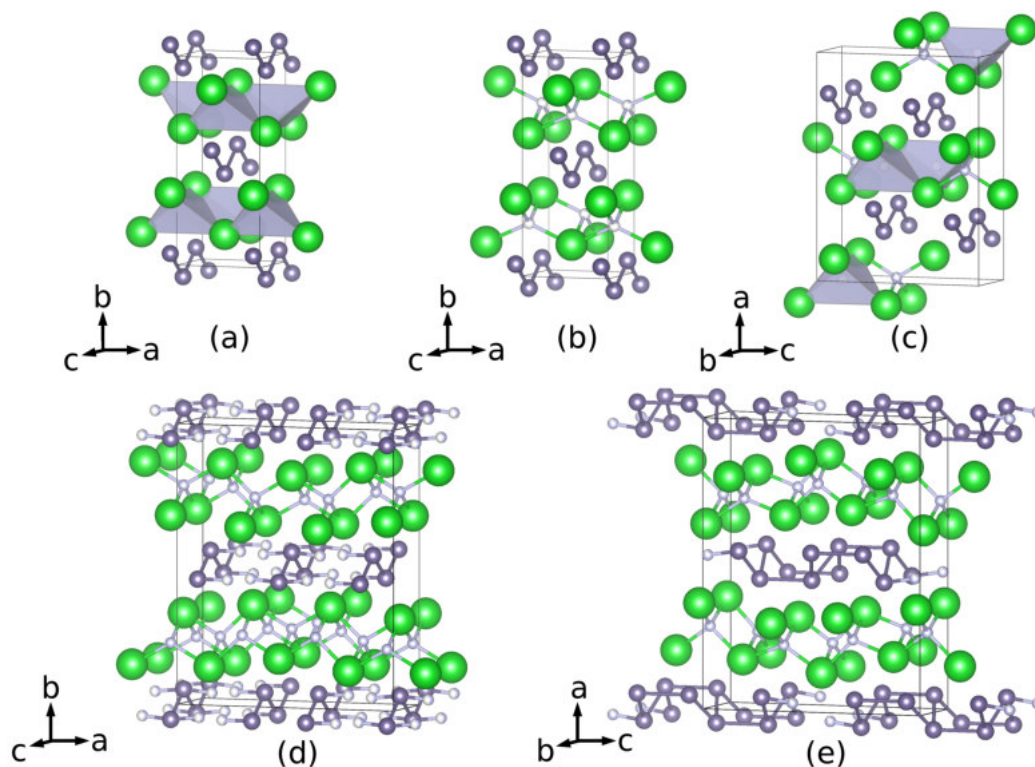


Figure A6.2: Crystal structures of (a) BaGe / BaSn ($Cmcm$), (b) α -BaGeD_y / α -BaSnD_y ($Cmcm$), (c) β -BaGeD_y ($Pnma$, $a' = b$, $b' = c$, $c' = 2a$; $(1/4, 1/4, 0)$), (d) γ -BaGeD_y (averaged $Cmcm$ -model, the germanium binding D sites are about half occupied (see [22, 23], $a' = 3a$) and (e) γ -BaSnD_y ($Pnma$, $a' = b$, $b' = c$, $c' = 3a$). Grey tetrahedra show voids of the hydrogen free Zintl phase and the almost free deuterium site (D2, SOF = 0.05(3), see Tab A6.4) of β -BaGeD_y. Space groups are given in regard to the parent Zintl phase. Large, green spheres: Ba; medium, grey spheres: Ge / Sn; small white spheres: H/D.

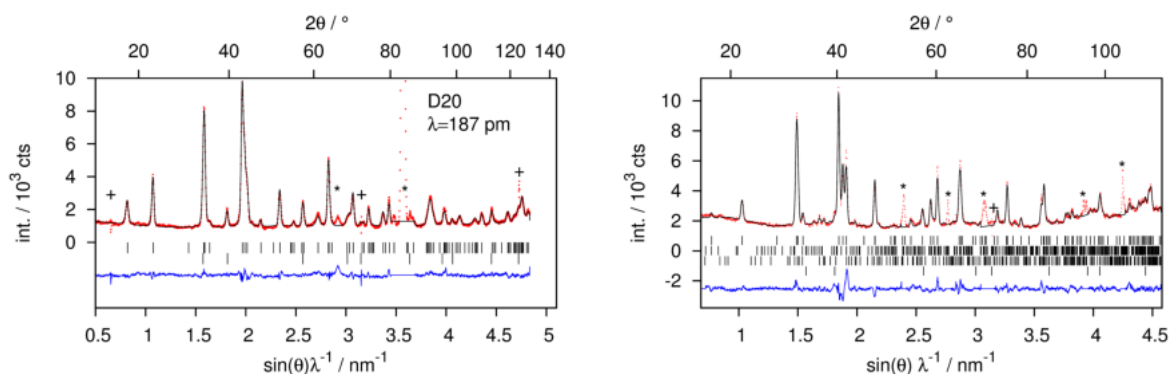


Figure A6.3: Rietveld refinement of the crystal structures of (left) α -BaGeD_{0.131(5)} ($Cmcm$, $a = 503.09(3)$ pm, $b = 1221.5(2)$ pm, $c = 427.38(4)$ pm; 325(6) K, primary vacuum; Bragg-marker from top: α -BaGeD_{0.13}, BaO (6 wt-%); $R_{wp} = 6.9\%$, $R_p = 4.9\%$, $S = 2.7$) and (right) α -BaSnD_{0.188(4)} ($Cmcm$, $a = 522.72(6)$ pm, $b = 1293.6(2)$ pm, $c = 463.97(6)$ pm; 478(5) K, 5.2(1) MPa D₂ pressure; Bragg-marker from top: α -BaSnD_{0.19}, γ -BaSnD_{1.3} (2 wt-%), Ba₃Sn₅ (4 wt-%), BaO (1 wt-%); $R_{wp} = 5.5\%$, $R_p = 4.2\%$, $S = 2.7$). Diffraction data are taken from the *in situ* experiment, thus some reflections of the sapphire cell (*) are present. Defect detector cells are marked with (+).

Table A6.3: Lattice parameters of the parent Zintl phases, α - and β -Ba TtD_y ($Tt = \text{Ge}, \text{Sn}$) determined by neutron powder diffraction.

Phase ^a	y	T / K	a / pm	b / pm	c / pm	b/c	d($Tt-Tt$) / pm
BaGe		298(2)	506.58(2)	1195.5(2)	430.27(2)	2.78	267.6(4)
BaGe		502(2)	507.50(4)	1206.0(2)	431.65(4)	2.79	269.5(4)
α -BaGeD _y	0.095(7)	502(2)	505.66(4)	1218.0(2)	429.85(4)	2.83	266.5(6)
α -BaGeD _y ^b	0.131(5)	325(6)	503.09(3)	1221.5(2)	427.38(4)	2.86	261.6(6)
β -BaGeD _y ^c	0.488(11)	502(2)	$1/2c' =$ 495.77(4)	$a' =$ 1319.5(2)	$b' =$ 421.46(2)	$a'/b' =$ 3.13	257.1(7)
BaSn		298(2)	532.79(5)	1251.10(10)	465.89(4)	2.69	301.0(5)
α -BaSnD _y	0.188(4)	478(5)	522.72(6)	1293.6(2)	463.97(6)	2.79	294.0(3)

^a All phases crystallize in spacegroup $Cmcm$, except β -BaGeH_y which crystallizes in space group type $Pnma$.

^b Dehydrogenated at $T_{\max} = 450(2)$ K.

^c Axes reordered and normalised with respect to the CrB-structure type to gain comparability.

under reduced pressure or at high temperatures (Fig. A6.1). Depending on preparation conditions, the deuterium content is variable indicating a homogeneity range. α -BaGeD_{0.131(5)} was formed from γ -BaGeD_y under vacuum (ca. 10 Pa) and a maximum temperature of 450(2) K. It was recovered at room temperature. Heating β -BaGeD_y for at least 30 min at the same pressure and 502(2) K leads to α -BaGeD_{0.095(7)}. γ -BaSnD_y decomposes at ca. 430 K and 5.0(1) MPa D₂ (*in situ* diffraction, see below) into α -BaSnD_{0.188(4)} or at ca. 450 K and 5.5(1) MPa H₂ (H₂-DSC, see below). This phase was not recovered at room temperature since a reversible formation of γ -BaSnD_y occurred upon cooling under 5 MPa D₂ at ca. 425 K.

Within the whole $Ae Tt\text{-H}_2$ system, lattice parameter c regarding the CrB-type Zintl phases (direction of the zigzag chains) is hardly affected by the hydrogenation. The other lattice parameters strongly change. Therefore, the b/c -ratio is a good measure for a structural change. Hydrogen free BaGe shows $b/c = 2.78\text{-}2.79$ depending on the temperature. This value increases to 2.83 and finally to 2.86 with increasing hydrogen content of the α -phase (Tab. A6.3). The b/c -ratio increases from 2.69 in hydrogen free BaSn to 2.79 in α -BaSnD_{0.188(4)}. Thus, it is a proper measure for the hydrogen incorporation in low concentrations.

The Ge-Ge distance of BaGe was evaluated as 267.6(4) pm (298(2) K) and 269.5(4) pm (502(2) K). The angle within the zigzag chain is 106.4(2) $^\circ$ or 107.0(2) $^\circ$ respectively. BaSn shows a Sn-Sn distance of 301.0(5) pm and a chain angle of 101.4(3) $^\circ$ (298(2) K). Upon formation of the α -phases, the chains are partially oxidized (e.g. $\text{Ge}^{2-} + y/2\text{H}_2 \longrightarrow \text{Ge}^{(2-y)-} + y\text{H}^-$). Thus, a shortening of the bond lengths is observed. The change in BaGe is small with $d(\text{Ge-Ge}) = 261.6(6)$ pm for α -BaGeD_{0.131(5)} at 325(6) K and 266.5(6) pm for α -BaGeD_{0.095(7)} at 502(2) K. The corresponding chain angles are 109.5(3) $^\circ$ and 107.5(3) $^\circ$, respectively. The formal germanium-electron count of α -BaGeD_{0.131(5)} is comparable to Na_{0.14}Sr_{0.86}Ge, which shows a similar bond length $d(\text{Ge-Ge}) = 260.2(3)$ pm (293 K) [41]. The shortening of the Sn-Sn bond length is similar and reaches $d(\text{Sn-Sn}) = 294.0(3)$ pm (478(5) K). The chain angle increases to 104.2(3) $^\circ$. The data are summarized in Tab. A6.3. Ba-D distances are slightly larger than in binary BaH₂ (262 pm [43]) with 261(3)-279(3) pm in α -BaGeD_{0.095(7)} and 269.5(9)-291.6(8) pm in α -BaSnD_{0.188(4)}.

While the α -phases show a statistical occupation of tetrahedral voids, the β -phases show hydrogen ordering. For β -SrGeH_y a 2x2-fold superstructure regarding the parent Zintl phase was found [20]. Due to data quality only a preliminary structure model was presented. β -BaGeH_y shows a twofold superstructure along crystallographic a direction regarding the parent Zintl phase. The structure was determined with the aid of group-subgroup relations [44]. To reach a doubling of lattice parameter a staying in orthorhombic crystal system at least two transitions of type $k2$ (*klassengleiche* transition of index two) are necessary. These symmetry reductions lead to seven space group type candidates. Four of them describe all superstructure reflections according to profile fitting. Only one structure model led to an ordered deuterium site occupation. Thus, the structure is described in space group type $Pnma$ ($a' = b, b' = c, c' = 2a$). The symmetry reduction leads to two independent crystallographic sites within Ba₄-tetrahedra as possible deuterium positions. Rietveld refinement (Fig. A6.4, Tab. A6.4) of the crystal structure of β -BaGeD_y results in one site (D1, Tab. A6.4) with 92.5(13)% occupation and one nearly empty site (D2, Tab. A6.4) with 5.0(10)% occupation giving an approximate composition of β -BaGeD_{0.5}.

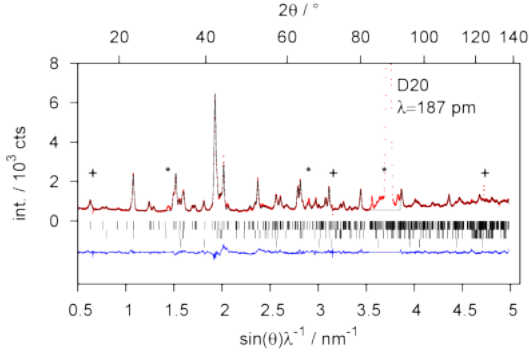


Figure A6.4: Rietveld refinement of the crystal structure of β -BaGeD_{0.488(12)} ($Pnma$, $a = 1319.5(2)$ pm, $b = 421.46(2)$ pm, $c = 991.54(7)$ pm; 502(2) K, 0.20(5) MPa D₂; Bragg-marker from top: β -BaGeD_{0.49}, α -BaGeD_{0.22} (25 wt-%), BaO (6 wt-%); $R_{wp} = 6.9\%$, $R_p = 4.9\%$, $S = 2.7$). Diffraction data are taken from the *in situ* experiment, thus some reflections of the sapphire cell (*) are present. Defect detector cells are marked with (+)

Table A6.4: Structural data of the β -phase BaGeD_{0.488(12)}, 502(2) K, sapphire cell, 0.20(5) MPa D₂ pressure, $Pnma$, $a = 1319.5(2)$ pm, $b = 421.46(2)$ pm, $c = 991.54(7)$ pm, $d(\text{Ge1-Ge2}) = 257.1(7)$ pm, $\angle(\text{Ge1-Ge2-Ge1}) = 110.1(5)^\circ$.

atom	x	y	z	$B_{\text{iso}} / 10^4 \text{ pm}^2$
Ba1	0.1050(7)	$1/4$	0.1471(13)	0.8(2)
Ba2	0.1040(9)	$1/4$	0.6095(17)	$B_{\text{iso}}(\text{Ba1})$
Ge1	0.3237(6)	$1/4$	0.3893(9)	1.7(2)
Ge2	0.2820(6)	$1/4$	0.8758(10)	$B_{\text{iso}}(\text{Ge1})$
D1	0.0031(7)	$1/4$	0.3768(11)	0.7(3)
			SOF(D1) = 0.925(13)	
D2 ^a	$x(\text{D1})^{+1/2}$	$3/4$	$z(\text{D1})$	$B_{\text{iso}}(\text{D1})$
			SOF(D1) = 0.050(10)	

^a Symmetry condition as inherited from the original super group to fix this nearly empty site within the tetrahedral void.

The filled tetrahedra are more regular than the nearly empty ones with typical Ba-D distances of 254.1(9) pm to 266(2) pm. These values are comparable to the binary hydride BaH₂ with 262 pm on average [43] and they are 5-10% smaller than in the α -phases. The irregular, hardly filled tetrahedral voids show one strongly elongated Ba-D distance longer than 300 pm and a strongly opened Ba-Ba edge.

While the effect on the inter-chain distances of the α -phases is small, the shortening of the Ge-Ge distance in β -BaGeH_{0.5} from 267.6(4) pm in BaGe to 257.1(7) pm in the hydride is much stronger. The bond length compares well to Li₄Ge₂H, which shows Ge-Ge zigzag chains as well with a Ge-Ge distance of 253 pm [45, 46]. Both examples can be described as Zintl phases with formally Ge^{1.5-}-polyanions, which are oxidized in regard to the assumed Ge²⁻ of a zigzag chain according to the Zintl concept. Thus, the shortened bond lengths correspond to an increased π -bonding due to a depopulation of π^* -bands upon hydrogenation.

Thermal analysis

In situ thermal analysis under hydrogen pressure (H₂-DSC) was conducted under several pressure conditions to investigate the reactions of BaGe and BaSn with hydrogen. The hydrogenation of BaGe shows the first strong exothermic signal above 373 K (Fig. A6.5). Between 3 to 5 MPa starting pressure the signal does not significantly shift, but since it is broad the onset is not well defined. According to *in situ* diffraction (see below) and *ex situ* characterisation, this effect corresponds to the formation of γ -BaGeH_y. The partially formation of the β -phase already takes place at room temperature (see below, *in situ* NPD) but does not give any DSC signal. Since the reaction is quite slow and a heating range of 10 K min⁻¹ was applied, the exothermic signal might mainly show the direct reaction of $\text{BaGe} + y/2\text{H}_2 \longrightarrow \gamma\text{-BaGeH}_y$. Subsequent cycles ($T_{\text{max}} = 475$ K) did not result in further signals.

At 553 K and 5.7 MPa H₂ pressure an endothermic decomposition step occurs. With decreasing hydrogen pressure it shifts to 523 K at 3.4 MPa. From *ex situ* characterisation the decomposition product is not clear. Either γ -BaGeH_y (although a reversible DSC signal could never be obtained) or a poorly crystalline product was present. Further heating at elevated pressures leads to the formation of BaH₂ and BaGe₂ as seen for the SrGe-H₂ system before [20]. *In situ* synchrotron diffraction showed

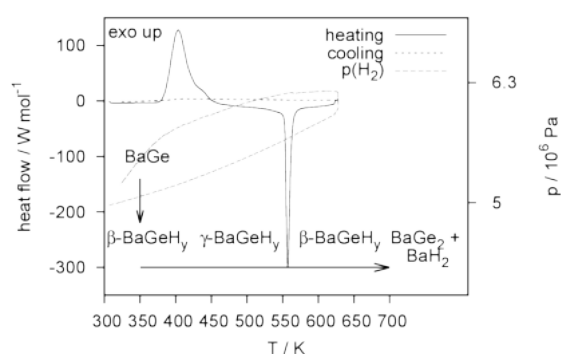


Figure A6.5: *In situ* thermal analysis (H_2 -DSC) of the hydrogenation of BaGe.

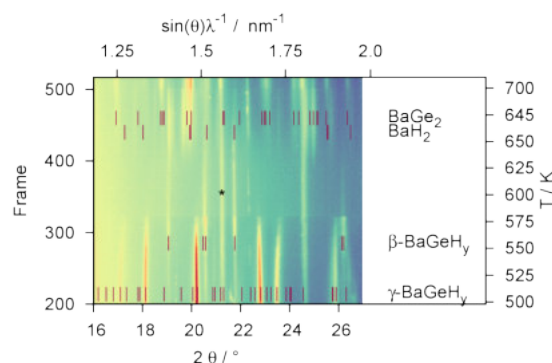


Figure A6.6: 2D plot of *in situ* synchrotron powder diffraction (*in situ* SPD) of the hydrogenation of BaGe showing the high temperature region at 5 MPa H_2 and 2 K min^{-1} heating rate (20s / frame data collection). (*) marks BaO.

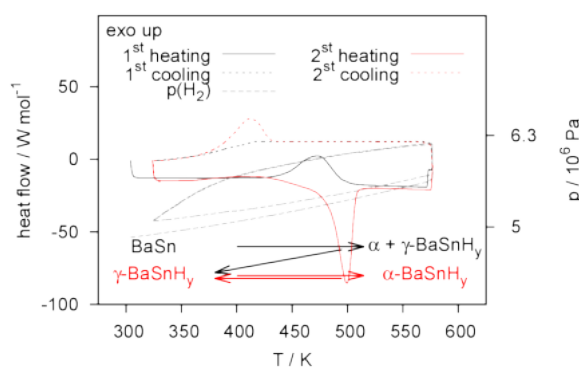


Figure A6.7: *In situ* thermal analysis (H_2 -DSC) of the hydrogenation of BaSn. A measurement starting directly from $\gamma\text{-BaSnH}_y$ reproduces run two (Fig. A6.S5).

that $\beta\text{-BaGeH}_y$ is formed and subsequently the decomposition in the germanium rich phase and binary hydride takes place (Fig A6.6). At pressures below 3 MPa H_2 $\gamma\text{-BaGeH}_y$ was not formed from BaGe.

H_2 -DSC experiments of the hydrogenation of BaSn give different signals in the first cycle compared to the subsequent ones (Fig. A6.7). The first run at 5.0 MPa starting pressure shows an exothermic signal at 470 K. Upon cooling no further signal is observed. Subsequent cycles show an endothermic signal at 500 K which was not observed during the first run. A corresponding exothermic signal at 410 K is obtained upon cooling. *Ex situ* characterised samples after one cycle show a mixture of α - and $\gamma\text{-BaSnH}_y$. After the second and subsequent cycles $\gamma\text{-BaSnH}_y$ is the main phase. Using $\gamma\text{-BaSnH}_y$ as starting material for the H_2 -DSC experiment, the same pattern as for the second cycle is obtained (Fig. A6.S5). According to *in situ* neutron diffraction (see below) the reversible decomposition step accounts for the formation of $\alpha\text{-BaSnH}_y$.

In situ diffraction

In situ diffraction experiments were done starting from the CrB-structure type Zintl phases BaGe and BaSn (Rietveld refinement: Fig A6.S1, A6.S2 and A6.S4; Tab. A6.S1, A6.S2 and A6.S4). The deuteration and dedeuteration of BaGe was studied under 5 MPa deuterium pressure and primary vacuum, respectively, using neutron diffraction, while the decomposition at high temperatures was studied by synchrotron diffraction at 5 MPa hydrogen pressure. The reversible reaction between α - and $\beta\text{-BaGeD}_y$ was investigated isothermally at 502 K. The reaction of BaSn was observed under 5 MPa isobaric deuterium pressure.

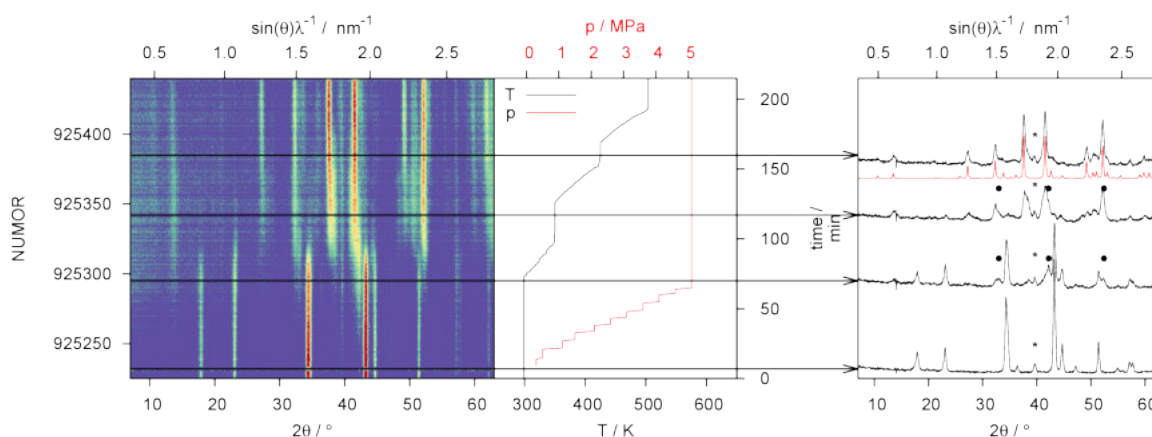


Figure A6.8: 2D plot of *in situ* neutron powder diffraction starting with BaGe under D₂ pressure (left) as well as selected diffraction patterns (right). The diffraction patterns show BaGe (bottom), the partially formation of β -BaGeD_y (middle, marked as a bullet) and the formation of γ -BaGeH_y (top, a simulation is given as red curve). (*) marks BaO (right). ILL raw data labelling (NUMOR) is given [28].

In situ diffraction of the reaction of BaGe

In situ neutron powder diffraction (NPD) of the reaction of BaGe under deuterium pressure and heating was done with 1 min time resolution. A first reaction step already happens at room temperature and low pressures of about 1-2 MPa (Fig. A6.8). As stated above, this is an effect that was not seen in the H₂-DSC experiment. The obtained phase was indexed in the orthorhombic crystal system ($a = 1309.1(13)$ pm, $b = 423.4(3)$ pm, $c = 998.7(8)$ pm, 298(2) K, 5.1(1) MPa, about 30% phase fraction) and therefore, corresponds to β -BaGeD_y. The reflections are broad and Rietveld refinement of the structure was not possible. The phase fraction was estimated using the β -BaGeD_{0.5}-model described above. Thus, the deuteration reaction could not be evaluated using sequential Rietveld refinement.

After reaching 5 MPa deuterium pressure, isobaric heating was started. The amount of β -BaGeD_y did not increase, but at about 350 K γ -BaGeD_y starts to form, which corresponds to the exothermic DSC signal. In the beginning of this reaction the reflections are broad as well while they sharpen when higher temperatures are reached. The isothermic step at 425 K already shows a total formation of γ -BaGeD_y (except for some BaO impurity). Isobaric heating was stopped at 505 K.

The decomposition at 5 MPa hydrogen pressure and high temperatures was observed by *in situ* SPD (Fig. A6.6). At 580 K a hydrogen poor phase in the orthorhombic crystal system is formed. Metrical relations clearly indicate β -BaGeH_y. There is no sign towards the formation of the α -phase. Upon further heating, the phase segregates into the germanium rich Zintl phase BaGe₂ and BaH₂ above 650 K.

The *in situ* generated γ -BaGeD_y-phase was dedeuterated under primary vacuum (10 Pa), which was studied by *in situ* NPD (Fig. A6.9). Since crystallinity improved during the first heating cycle, sequential Rietveld refinement was possible. Phase fraction as well as hydrogen content was evaluated. At about 365 K β -BaGeD_y is formed again but is only stable in a small temperature window. Already at 400 K α -BaGeD_y is formed. For the evaluation of γ -BaGeD_y a simplified model with three-fold superstructure ($a' = 3a$) with regard to the hydrogen free Zintl phase BaGe and space group type *Cmcm* was used as described elsewhere (Fig. A6.2, for more details see Ref. [22, 23] and its Supporting Information). Since there is no evidence for a deuterium release from tetrahedral voids, their occupation was kept fixed at 100%. The occupation of the two about 50% filled chain binding deuterium sites (split position) were constraint to the same value and refined. Fig. A6.9 shows the sum of these sites which is constant up to 365 K and shows no sign for a homogeneity range. The averaged composition is γ -BaGeD_y, $y = 1.61(2)$, which is about the previously published value $y = 1.57(3)$ [22, 23].

The temperature region from 365 K to 425 K is characterised by severe overlap of all three deuteride phases. Therefore, all parameters of γ -BaGeD_y except for the scaling were kept fixed. Nonetheless, deuterium occupations of β -BaGeD_y strongly correlate with the occurrence of α -BaGeD_y and the residual γ -BaGeD_y. The occupation of D1 (Tab. A6.4) goes down a bit, but shows full occupation after γ -BaGeD_y was removed from the sequential refinement. The second tetrahedral void site (D2, Tab. A6.4) stays empty. Therefore, the varying occupation might be an artefact of the refinement and this phase might

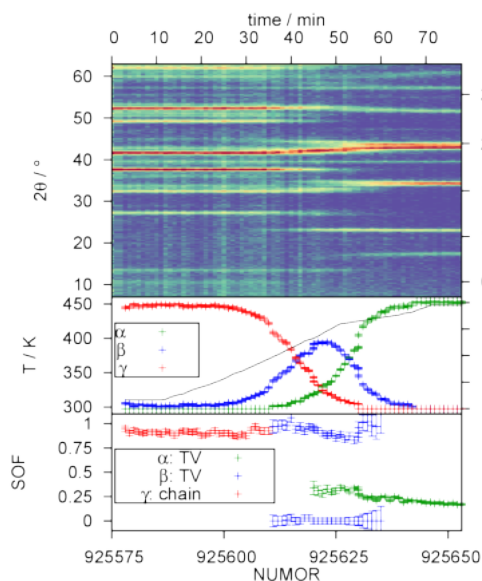


Figure A6.9: 2D diffraction plot of the decomposition of *in situ* formed γ -BaGeD_{1.61} under primary vacuum (**top**), temperature and phase fraction profiles (**middle**) and deuterium site occupation factors (SOF, **bottom**). γ -BaGeD_y: sum of the split position of the chain binding sites (chain); α - and β -BaGeD_y: tetrahedral voids (TV). ILL raw data labelling (NUMOR) is given [28].

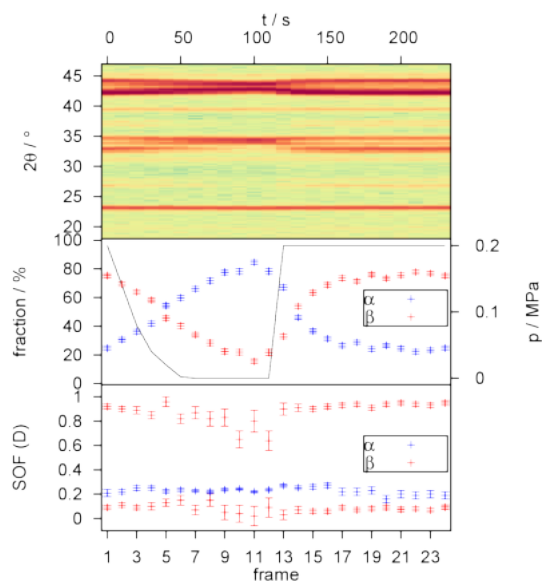


Figure A6.10: Pressure dependent cyclic formation of α - (primary vacuum) and β -BaGeD_y (0.2 MPa D₂) at isothermal conditions at 502 K (**top**), pressure and phase fraction profiles (**middle**) and deuterium site occupation factors (SOF) of tetrahedral voids (**bottom**). ILL raw data labelling (NUMOR) is given [28].

show no homogeneity range or only a small one in contrast to β -SrGeH_y [20].

Above 400 K, α -BaGeD_y is formed starting with $y = 0.32(3)$ ($b/c = 2.94$, cf. Tab. A6.3). During the heating process, deuterium is slowly released going down to $y = 0.167(10)$ ($b/c = 2.87$, cf. Tab. A6.3) at the maximum temperature of 450 K. Rietveld refinement after cooling down to 325 K showed a composition α -BaGeD_{0.131(5)}.

Under isothermic conditions at 502 K the deuterium pressure was cycled between vacuum (10 Pa) and 0.2 MPa. Diffraction patterns were collected with 10 s time resolution. To improve counting statistics, the experiment was repeated five times and diffraction patterns of equal pressure conditions were summed (Fig. A6.10). Starting from α -BaGeD_y, the β -phase was allowed to form for 2 min at 0.2 MPa to have the same starting conditions for each repetition.

The reaction from β - to α -BaGeD_y is fully reversible and only depends on the applied pressure. On this time scale the occupation of the tetrahedral voids stays constant (Fig. A6.10). The D1 site of the β -phase shows an occupation of 0.90(4) averaged over the whole experiment except for the points with less than 25% phase content. The occupation of the empty D2 site was refined as well and shows no additional deuterium incorporation (averaged SOF = 0.029(13)). α -BaGeD_y shows a constant deuterium occupation on this time scale (averaged SOF = 0.23(2)). A hint pointing towards a phase width is a small volume jump of 0.6% when the sample is pressurized. The b/c -ratio decreases during evacuation from 2.94 to 2.90 and jumps back to 2.95 when the sample is pressurized with deuterium to 0.2 MPa. The volume of β -BaGeD_y is not effected at all (< 0.1% volume change). After a further dehydrogenation under vacuum for 30 min, a composition of α -BaGeD_{0.095(7)} was reached, clearly indicating a homogeneity range of this phase.

***In situ* neutron diffraction of the reaction of BaSn**

In situ neutron diffraction of BaSn_y was done under 5.0(1) MPa isobaric deuterium pressure and heating. Diffraction patterns were collected with 1 min time resolution. For serial Rietveld refinement a summation over five frames was applied. The orientation of the single-crystal cell was inadequate and needed correction. Due to this technical issue the experiment was interrupted for about 100 min at

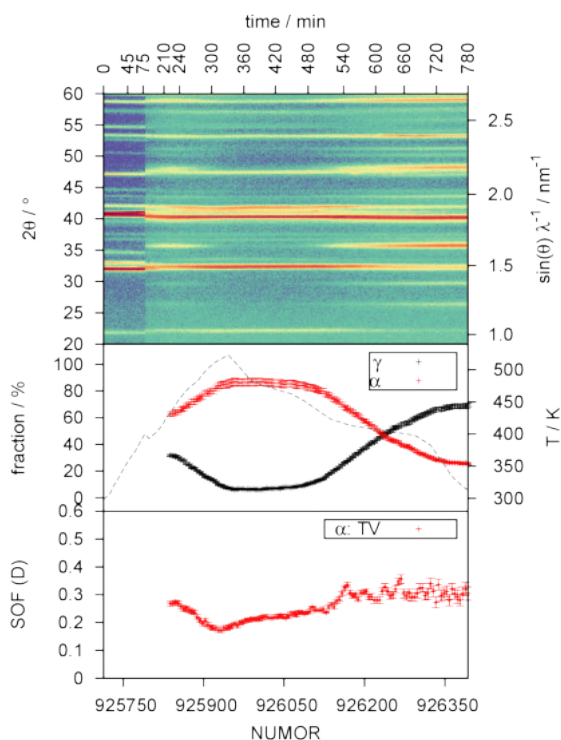


Figure A6.11: 2D *in situ* diffraction plot of the reaction of BaSn at 5 MPa D₂ pressure (**top**), temperature and phase fractions (**middle**) and deuterium site occupation factors (SOF) of tetrahedral voids (TV, **bottom**). SOF(D) of γ -BaSnD_y (chain-binding and TV) are constant (not shown). Due to technical issues (see text) the evaluation starts at $t = 200$ min. ILL raw data labelling (NUMOR) is given [28].

elevated temperatures. After the correction some container reflections were still present. Furthermore, a significant fraction of γ -BaSnD_y was already formed. Due to severe overlap with γ -BaSnD_y and the broadness of the reflections the formation of α -BaSnD_y at low temperatures cannot be evaluated unambiguously. Therefore, sequential Rietveld refinement results are shown, starting with the decomposition of γ -BaSnD_y (Fig. A6.11). At 423 K the decomposition of γ -BaSnD_y starts, which is well below the endothermic DSC signal at 500 K. The reformation of the γ -phase is reversible without hysteresis and the phase fraction starts to increase again after the temperature was below 423 K. The reformation step fits to the exothermic signal obtained in the DSC experiment.

The structure of γ -BaSnD_y was kept fixed during the serial refinement and only the occupation of the tin binding deuterium site was refined. Considering estimated standard uncertainties (e.s.u.) this value stays constant over the whole experiment. The first formation leads to an averaged chemical formula γ -BaSnD_y, $y = 1.273(13)$. The reformation during the cooling process results in a slightly larger value of $y = 1.291(3)$. Both evaluations fit the published value $y = 1.278(2)$ [21] reasonably well. Thus, no homogeneity range is assumed here.

Starting with the decomposition of γ -BaSnD_y, the α -phase is present during the rest of the experiment. The deuterium occupation is sensitive to temperature. It goes down to $y = 0.172(4)$ ($b/c = 2.78$) at the highest measured temperature of 519(2) K. Right after the γ -phase started to decompose (430(2) K) about one quarter of the tetrahedral voids is filled ($y = 0.260(8)$; $b/c = 2.80$). This value is reached again upon cooling (430(2) K, $y = 0.248(4)$, $b/c = 2.80$). After the reformation of γ -BaSnD_y, at the end of the *in situ* experiment the α -phase is still present with 31(2) wt-% and reaches a maximum deuterium occupation of $y = 0.36(3)$ (317(2) K, $b/c = 2.81$). The formation of a β -phase was not observed.

Conclusions

The formation and decomposition of different types of BaTtH_y-phases, $Tt = \text{Ge, Sn}$, were observed by *in situ* diffraction and thermal analysis under several conditions. It could be shown that another two

representatives of the system $AeTt\text{-H}_2$ show almost reversible hydrogenation properties. Upon decomposition under pressure as well as under vacuum some residual hydrogen stays in tetrahedral voids forming $\alpha\text{-Ba}Tt\text{H}_y$ phases. These show a homogeneity range and a hydrogen occupation sensitive to pressure and temperature. This contribution establishes compositional limits for $\alpha\text{-BaGeH}_y$ of at least $0.095(7) \leq y \leq 0.32(3)$ and for $\alpha\text{-BaSnH}_y$ of at least $0.172(4) \leq y \leq 0.36(3)$.

The α -phases show slightly shorter $Tt\text{-}Tt$ distances than the hydrogen free phases due to a depopulation of π^* -bands and, therefore increased π -bonding within zigzag chains. This correlates well with the electron poor CrB-structure type phase $\text{Na}_{0.14}\text{Sr}_{0.86}\text{Ge}$ [41] or $\alpha\text{-SrGeH}_y$, $y < 0.3$, [20, 24] which have a similar electron count per anion.

Another intermediate phase exists in the BaGe-H_2 system, which can be related to the SrGe-H_2 system [20]. In contrast to $\beta\text{-SrGeH}_y$, $\beta\text{-BaGeH}_{0.5}$ appears to be a line phase with ordered hydrogen occupation. It already appears at room temperature, when BaGe is set under hydrogen pressure and is a decomposition product of $\gamma\text{-BaGeH}_y$ at elevated temperature. Due to stronger oxidation compared to the α -phase, $\beta\text{-BaGeH}_{0.5}$ shows stronger π -bonding and thus decreased Ge-Ge distance. Therefore, the phase can be related to $\text{Li}_4\text{Ge}_2\text{H}$ [45, 46]. Switching between 0.2 MPa D_2 pressure and primary vacuum (10 Pa) at 500 K the formation of α - and $\beta\text{-BaGeD}_y$ can be cycled. At 2 MPa the uptake is fast and $\alpha\text{-BaGeD}_y$ reacts almost completely to form $\beta\text{-BaGeD}_{0.5}$ within 1 min. The corresponding deuterium release is slower.

Upon heating to moderate temperatures (< 400 K) and hydrogen pressures above 3 MPa, BaGe and BaSn form hydrogen rich γ -phases as published earlier [21–23]. These phases are characterised by ionic hydride ions that are incorporated into sheets of tetrahedral Ba_4 -voids and hydrogen bound covalently to the polyanion. The formation of γ -phases can be rationalised using a hypothetical intermediate $\text{Ba}Tt\text{H}$, where according to the Zintl-Klemm concept Tt^- is supposed to form three-binding polyanions. Due to the rigid hydride filled cationic sheets, the Tt^- -atoms cannot solely form bonds to other Tt^- -ions but need to additionally form $Tt\text{-H}$ bonds (see Fig. A6.2e). Filling tetrahedral voids is thus directly related to the formation of $Tt\text{-H}$ bonds and vice versa. Since Ge-H and Sn-H bonds are thermally labile, the γ -phases decompose at moderate temperatures under vacuum or 5 MPa hydrogen pressure and need to release additional hydrogen from tetrahedral Ba_4 -sites. The decomposition temperatures fit the thermal decomposition of polygermane $(\text{GeH}_y)_\infty$ at 470-520 K [47] reasonably well. Therefore these phases show a good (partial) reversibility relating them to classical interstitial hydrides combined with moderate decomposition temperatures due to thermally labile $Tt\text{-H}$ bonds. In addition to the almost complete reversibility the filling of tetrahedral voids shows fast kinetics as shown by the reaction of α - to $\beta\text{-BaGeH}_y$. This might serve as a starting point for the search of proper hydrogen storage systems within the class of Zintl phases.

Acknowledgements

We thank the Institute Laue-Langevin (ILL) for providing neutron (proposal 5-22-734) and the Helmholtz Zentrum Berlin (HZB) for providing synchrotron beam time (proposal 15202481). Furthermore, we want to thank Dr. Dirk Wallacher and Nico Grimm for set up and support with the *in situ* experiment at BESSY II. We thank the Deutsche Forschungsgemeinschaft (DFG, grant Ko1803/8-1) and the Fonds der Chemischen Industrie (Grant 194371) for financial support.

A6.4 Supplement

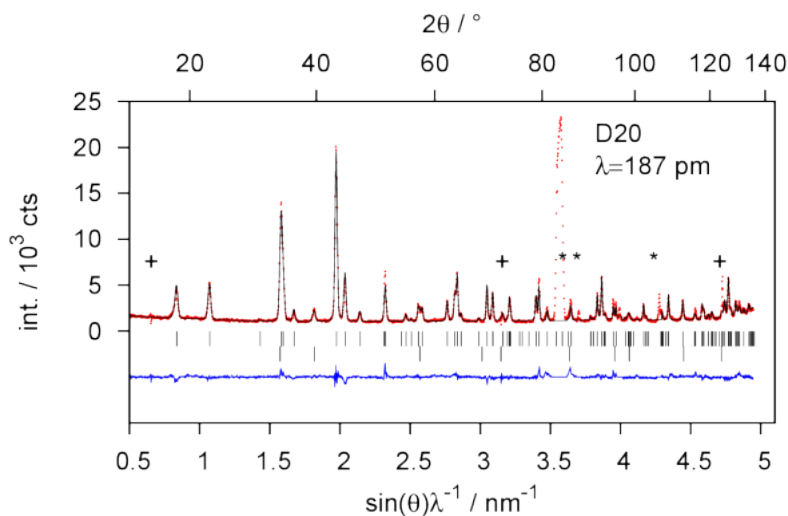


Figure A6.S1: Rietveld refinement of the crystal structure of the precursor Zintl phase BaGe, 298(2) K, sapphire cell, argon atmosphere:

Bragg marker top:	BaGe
Bragg marker bottom:	BaO (6 wt-%)
(+)	corrupt detector cells
(*)	reflections from the sapphire cell
Rwp:	8.4%
Rp:	6.3%
S:	2.0

Table A6.S1: Structural data of the precursor Zintl phase BaGe, 298(2) K, sapphire cell, argon atmosphere:

Space group:	<i>Cmcm</i>
$a =$	506.58(2) pm
$b =$	1195.52(6) pm
$c =$	430.27(2) pm
$d(\text{Ge-Ge}) =$	267.6(4) pm
$\angle(\text{Ge-Ge-Ge}) =$	107.0(2)°

atom	x	y	z	$B_{\text{iso}} / 10^4 \text{ pm}^2$
Ba	0	0.3610(3)	$1/4$	0.86(8)
Ge	0	0.0662(2)	$1/4$	1.55(6)

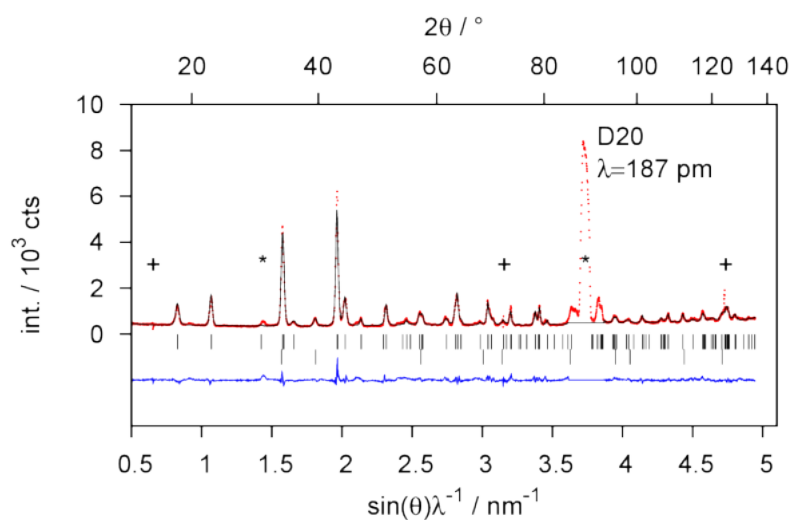


Figure A6.S2: Rietveld refinement of the crystal structure of the precursor Zintl phase BaGe, 502(2) K, sapphire cell, primary vacuum (10Pa):

Bragg marker top:	BaGe
Bragg marker bottom:	BaO (6 wt-%)
(+)	corrupt detector cells
(*)	reflections from the sapphire cell
Rwp:	8.3%
Rp:	6.3%
S:	2.1

Table A6.S2: Structural data of the precursor Zintl phase BaGe, 502(2) K, sapphire cell, primary vacuum (10Pa):

Space group:	<i>Cmcm</i>
$a =$	507.50(4) pm
$b =$	1206.0(2) pm
$c =$	431.65(4) pm
$d(\text{Ge-Ge}) =$	269.5(4) pm
$\angle(\text{Ge-Ge-Ge}) =$	106.4(2)°

atom	x	y	z	$B_{\text{iso}} / 10^4 \text{ pm}^2$
Ba	0	0.3600(4)	$1/4$	1.6(2)
Ge	0	0.0669(3)	$1/4$	1.47(12)

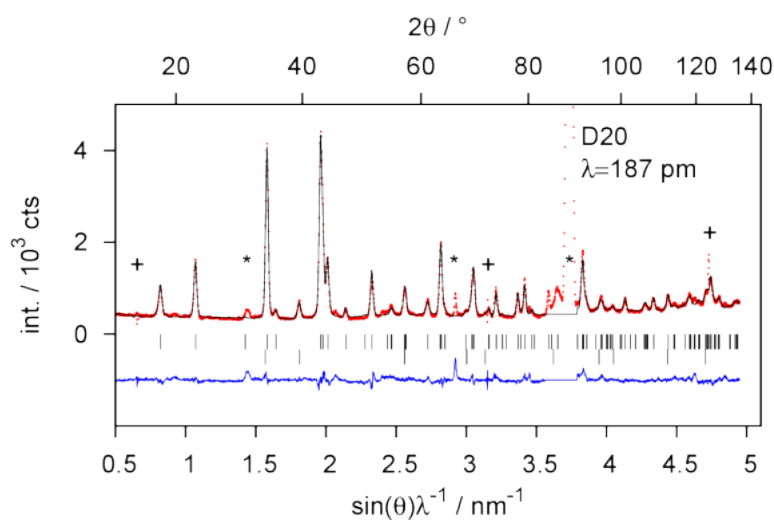


Figure A6.S3: Rietveld refinement of the crystal structure of α -BaGeD_{0.095(7)}, 502(2) K, sapphire cell, primary vacuum (10 Pa):

Bragg marker top:	α -BaGeD _{0.095(7)}
Bragg marker bottom:	BaO (6 wt-%)
(+)	corrupt detector cells
(*)	reflections from the sapphire cell
Rwp:	8.3%
Rp:	5.7%
S:	2.0

Table A6.S3: Structural data of α -BaGeD_{0.095(7)}, 502(2) K, sapphire cell, primary vacuum (10 Pa):

Space group:	<i>Cmcm</i>
$a =$	505.66(4) pm
$b =$	1218.0(2) pm
$c =$	429.85(4) pm
$d(\text{Ge-Ge}) =$	266.5(6) pm
$\angle(\text{Ge-Ge-Ge}) =$	107.5(3) $^\circ$

atom	x	y	z	$B_{\text{iso}} / 10^4 \text{ pm}^2$	SOF
Ba	0	0.3593(4)	$1/4$	1.34(14)	
Ge	0	0.0647(4)	$1/4$	1.76(10)	
D	0	0.762(4)	$1/4$	0.8(8)	0.095(7)

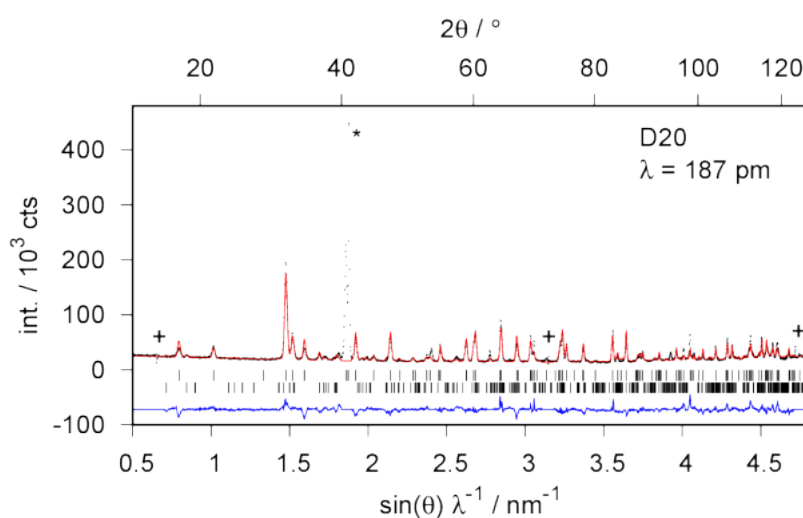


Figure A6.S4: Rietveld refinement of the crystal structure of the precursor Zintl phase BaSn, 298(2) K, sapphire cell, argon atmosphere:

Bragg marker top:	BaSn
Bragg marker bottom:	Ba ₃ Sn ₅ (11 wt-%)
(+)	corrupt detector cells
(*)	reflections from the sapphire cell
Rwp:	13.9%
Rp:	10.1%
S:	3.3

Table A6.S4: Structural data of the precursor Zintl phase BaSn, 298(2) K, sapphire cell, argon atmosphere:

Space group:	<i>Cmcm</i>
<i>a</i> =	532.78(5) pm
<i>b</i> =	1251.09(10) pm
<i>c</i> =	465.88(4) pm
d(Ge-Ge) =	301.0(5) pm
∠(Ge-Ge-Ge) =	101.4(3)°
overall-B =	2.75(14) · 10 ⁴ pm ²

(due to similar molar mass and some problems with adjustment of the single crystal cell, only an overall Debye-Waller factor was used)

atom	<i>x</i>	<i>y</i>	<i>z</i>
Ba	0	0.3668(4)	1/4
Sn	0	0.0762(3)	1/4

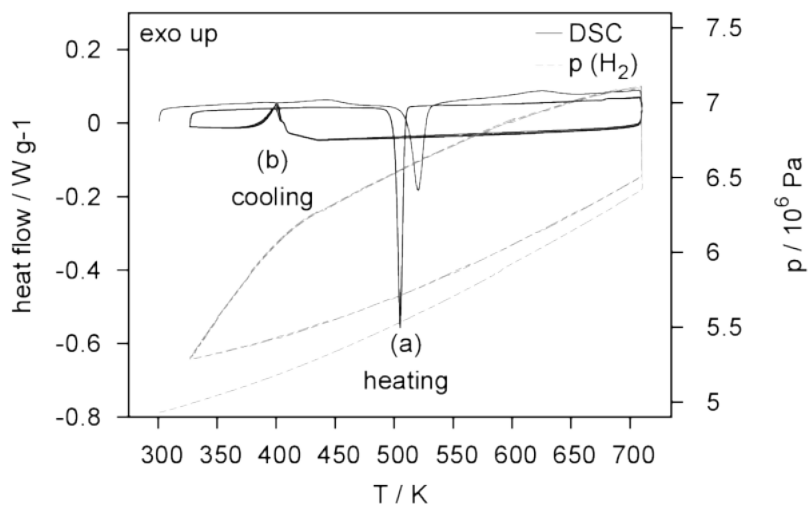


Figure A6.S5: *In situ* thermal analysis (H₂-DSC) starting from γ -BaSnH_y: The endothermic signal (a, heating) corresponds to the decomposition into α -BaSnH_y, which is reversible upon cooling (b). Subsequent runs are similar. The shift corresponds to different pressures caused by an overall warming of the pressure cell and the isocore set up.

A6.5 References

- (1) Aoki, M.; Ohba, N.; Noritake, T.; Towata, S. *Appl. Phys. Lett.* **2004**, *85*, 387–388, DOI: 10.1063/1.1773930.
- (2) Ohba, N.; Aoki, M.; Noritake, T.; Miwa, K.; Towata, S.-i. *Phys. Rev. B* **2005**, *72*, 075104, DOI: 10.1103/PhysRevB.72.075104.
- (3) Chotard, J.-N.; Tang, W. S.; Raybaud, P.; Janot, R. *Chem. - Eur. J.* **2011**, *17*, 12302–12309, DOI: 10.1002/chem.201101865.
- (4) Zhang, J.; Yan, S.; Qu, H.; Yu, X.; Peng, P. *Int. J. Hydrogen Energy* **2017**, *42*, 12405–12413, DOI: 10.1016/j.ijhydene.2017.03.132.
- (5) Gingl, F.; Vogt, T.; Akiba, E. *J. Alloys Compd.* **2000**, *306*, 127–132, DOI: 10.1016/S0925-8388(00)00755-6.
- (6) Zhu, Y.; Zhang, W.; Liu, Z.; Li, L. *J. Alloys Compd.* **2010**, *492*, 277–281, DOI: 10.1016/j.jallcom.2009.11.065.
- (7) Orimo, S.-i.; Nakamori, Y.; Eliseo, J. R.; Züttel, A.; Jensen, C. M. *Chem. Rev.* **2007**, *107*, 4111–4132, DOI: 10.1021/cr0501846.
- (8) Stephens, F. H.; Pons, V.; Baker, R. T. *Dalton Trans.* **2007**, 2613–2626, DOI: 10.1039/B703053C.
- (9) Sakintuna, B.; Lamari-Darkrim, F.; Hirscher, M. *Int. J. Hydrogen Energy* **2007**, *32*, 1121–1140, DOI: 10.1016/j.ijhydene.2006.11.022.
- (10) Jain, I.; Lal, C.; Jain, A. *Int. J. Hydrogen Energy* **2010**, *35*, 5133–5144, DOI: 10.1016/j.ijhydene.2009.08.088.
- (11) Rusman, N.; Dahari, M. *Int. J. Hydrogen Energy* **2016**, *41*, 12108–12126, DOI: 10.1016/j.ijhydene.2016.05.244.
- (12) Wang, H.; Lin, H.; Cai, W.; Ouyang, L.; Zhu, M. *J. Alloys Compd.* **2016**, *658*, 280–300, DOI: 10.1016/j.jallcom.2015.10.090.
- (13) Häussermann, U.; Kranak, V. F.; Puhakainen, K. *Struct. Bond.* **2010**, *139*, 143–161, DOI: 10.1007/430_2010_20.
- (14) Hansen, T. C.; Kohlmann, H. *Z. Anorg. Allg. Chem.* **2014**, *640*, 3044–3063, DOI: 10.1002/zaac.201400359.
- (15) Möller, K. T.; Hansen, B. R. S.; Dippel, A.-C.; Jørgensen, J.-E.; Jensen, T. R. *Z. Anorg. Allg. Chem.* **2014**, *640*, 3029–3043, DOI: 10.1002/zaac.201400262.
- (16) Bull, D. J.; Weidner, E.; Shabalina, I. L.; Telling, M. T. F.; Jewell, C. M.; Gregory, D. H.; Ross, D. K. *Phys. Chem. Chem. Phys.* **2010**, *12*, 2089–2097, DOI: 10.1039/B903821N.
- (17) Behrendt, G.; Reichert, C.; Kohlmann, H. *J. Phys. Chem. C* **2016**, *120*, 13450–13455, DOI: 10.1021/acs.jpcc.6b04902.
- (18) Wenderoth, P.; Kohlmann, H. *Inorg. Chem.* **2013**, *52*, 10525–10531, DOI: 10.1021/ic401480b.
- (19) Auer, H.; Kohlmann, H. *Z. Anorg. Allg. Chem.* **2017**, *643*, 945–951, DOI: 10.1002/zaac.201700164.
- (20) Auer, H.; Wallacher, D.; Hansen, T. C.; Kohlmann, H. *Inorg. Chem.* **2017**, *56*, 1072–1079, DOI: 10.1021/acs.inorgchem.6b01945.
- (21) Auer, H.; Guehne, R.; Bertmer, M.; Weber, S.; Wenderoth, P.; Hansen, T. C.; Haase, J.; Kohlmann, H. *Inorg. Chem.* **2017**, *56*, 1061–1071, DOI: 10.1021/acs.inorgchem.6b01944.
- (22) Auer, H.; Schlegel, R.; Oeckler, O.; Kohlmann, H. *Angew. Chem., Int. Ed.* **2017**, *56*, 12344–12347, DOI: 10.1002/anie.201706523.
- (23) Auer, H.; Schlegel, R.; Oeckler, O.; Kohlmann, H. *Angew. Chem.* **2017**, *129*, 12515–12518, DOI: 10.1002/ange.201706523.
- (24) Götze, A.; Auer, H.; Finger, R.; Hansen, T.; Kohlmann, H. *Phys. B* **2018**, DOI: 10.1016/j.physb.2017.11.024.

- (25) Többing, D. M.; Zander, S. *Journal of large-scale research facilities* **2016**, *2*, A49, DOI: 10.17815/jlsrf-2-65.
- (26) Hansen, T. C.; Henry, P. F.; Fischer, H. E.; Torregrossa, J.; Convert, P. *Meas. Sci. Technol.* **2008**, *19*, 034001.
- (27) Kohlmann, H.; Kurtzemann, N.; Wehrich, R.; Hansen, T. *Z. Anorg. Allg. Chem.* **2009**, *635*, 2399–2405, DOI: 10.1002/zaac.200900336.
- (28) Kohlmann, H.; Auer, H.; Götze, A.; Hansen, T.; Weber, S. Reaction pathways to the Zintl phase hydrides CaSiH and MGeH_x (M = Sr, Ba)., Institut Laue-Langevin, 2015, DOI: 10.5291/ILL-DATA.5-22-734.
- (29) Rietveld, H. M. *Acta Crystallogr.* **1967**, *22*, 151–152, DOI: 10.1107/S0365110X67000234.
- (30) Rietveld, H. M. *J. Appl. Crystallogr.* **1969**, *2*, 65–71, DOI: 10.1107/S0021889869006558.
- (31) Rodríguez-Carvajal, J. *Phys. B* **1993**, *192*, 55–69, DOI: 10.1016/0921-4526(93)90108-I.
- (32) Rodríguez-Carvajal, J. FULLPROF (version 5.30): A Program for Rietveld Refinement and Pattern Matching Analysis; Insitut Laue-Langevin, Grenoble (France)., 2012.
- (33) Bruker AXS, TOPAS[®] version 5, www.bruker-axs.com.
- (34) Momma, K.; Izumi, F. *J. Appl. Crystallogr.* **2011**, *44*, 1272–1276, DOI: 10.1107/s0021889811038970.
- (35) VESTA - Visualisation for Electronic and STructural Analysis, version 3.3.1.
- (36) Gelato, L. M.; Parthé, E. *J. Appl. Crystallogr.* **1987**, *20*, 139–143, DOI: 10.1107/s0021889887086965.
- (37) Reyes, E. C.; Stalder, E. D.; Mensing, C.; Budnyk, S.; Nesper, R. *J. Phys. Chem. C* **2011**, *115*, 1090–1095, DOI: 10.1021/jp106169h.
- (38) Reyes, E. C.; Nesper, R. *J. Phys. Chem. C* **2012**, *116*, 2536–2542, DOI: 10.1021/jp205825d.
- (39) Kurylyshyn, I. M.; Fässler, T. F.; Fischer, A.; Hauf, C.; Eickerling, G.; Presnitz, M.; Scherer, W. *Angew. Chem., Int. Ed.* **2014**, *53*, 3029–3032, DOI: 10.1002/anie.201308888.
- (40) Harms, W.; Wendorff, M.; Röhr, C. *J. Alloys Compd.* **2009**, *469*, 89–101, DOI: 10.1016/j.jallcom.2008.02.020.
- (41) Xie, Q.-X.; Nesper, R. *Z. Kristallogr. - New Cryst. Struct.* **2003**, *218*, 291–292, DOI: 10.1524/ncrs.2003.218.3.291.
- (42) Further details of the crystal structure investigations may be obtained from FIZ Karlsruhe, 76344 Eggenstein-Leopoldshafen, Germany (fax: (+49)7247-808-666; e-mail: crysdata(at)fiz-karlsruhe(dot)de, on quoting the deposition numbers CSD-433794 (α -BaGeD_{0.09}), CSD-433795 (α -BaGeD_{0.13}), CSD-433796 (α -BaSnD_{0.19}), CSD-433797 (β -BaGeD_{0.49}).
- (43) Ting, V. P.; Henry, P. F.; Kohlmann, H.; Wilson, C. C.; Weller, M. T. *Phys. Chem. Chem. Phys.* **2010**, *12*, 2083, DOI: 10.1039/b914135a.
- (44) Bärnighausen, H. *MATCH: Commun. Math. Comput. Chem.* **1980**, *9*, 139–175.
- (45) Wu, H.; Zhou, W.; Udovic, T. J.; Rush, J. J.; Yildirim, T.; Hartman, M. R.; Bowman, R. C.; Vajo, J. J. *Phys. Rev. B* **2007**, *76*, 224301, DOI: 10.1103/PhysRevB.76.224301.
- (46) Wu, H.; Hartman, M. R.; Udovic, T. J.; Rush, J. J.; Zhou, W.; Bowman Jr, R. C.; Vajo, J. J. *Acta Crystallogr., Sect. B* **2007**, *63*, 63–68, DOI: 10.1107/s0108768106046465.
- (47) Bianco, E.; Butler, S.; Jiang, S.; Restrepo, O. D.; Windl, W.; Goldberger, J. E. *ACS Nano* **2013**, *7*, 4414–4421, DOI: 10.1021/nn4009406.

A7 *In situ* investigations on the formation and decomposition of
KSiH₃ and **CsSiH₃**

Henry Auer^a, Holger Kohlmann^{a*}

^a *Leipzig University, Department of Inorganic Chemistry, Johannisallee 29, 04103 Leipzig, Germany*

** Corresponding author*

— Dedicated to Prof. Evamarie Hey-Hawkins on the occasion of her 60th birthday —

Reprinted with permission from

H. Auer, H. Kohlmann, *Z. Anorg. Allg. Chem.* **2017**, *643*, 945-951. DOI:10.1002/zaac.201700164

© 2017 Wiley-VCH Verlag GmbH & Co. KGaA, Weinheim

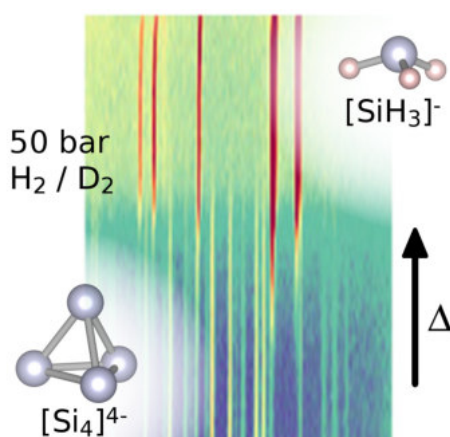
This is the accepted version with minor adaptations for use with L^AT_EX and one column printing.

A7.1 Authors' contributions

The experimental work was done by H. Auer. He also prepared the draft of the manuscript. H. Kohlmann supervised the work and edited the manuscript.

A7.2 Abstract

The system KSi-KSiH_3 stores 4.3 mass-% of hydrogen and shows a very good reversibility at mild conditions of 0.1 MPa hydrogen pressure and 414 K [1]. We followed the reaction pathways of the hydrogenation reactions of KSi and its higher homologue CsSi by *in situ* methods in order to check for possible intermediate hydrides. *In situ* diffraction at temperatures up to 500 K and gas pressures up to 5.0 MPa hydrogen gas for X-ray and deuterium gas for neutron reveal that both KSi and CsSi react in one step to the hydrides KSiH_3 and CsSiH_3 and the respective deuterides. Neither do the Zintl phases dissolve hydrogen (deuterium), nor do the hydrides (deuterides) show any signs for non-stoichiometry, i. e. all phases involved in the formation are line phases. Heating to temperatures above 500 K shows that at 5.0 MPa hydrogen pressure only the reaction $2\text{CsSi} + 3\text{H}_2 \rightleftharpoons 2\text{CsSiH}_3$ is reversible. Under these conditions, KSiH_3 decomposes to a clathrate and potassium hydride according to $46\text{KSiH}_3 \rightleftharpoons \text{K}_8\text{Si}_{46} + 38\text{KH} + 50\text{H}_2$.



A7.3 Article

Introduction

The system KSi-KSiH₃ recently gathered interest as a potential hydrogen storage material with 4.3 wt-% hydrogen capacity and good reversibility at mild conditions of 0.1 MPa hydrogen pressure and 414 K [1]. KSiH₃ is prepared either by solution chemistry using silane, SiH₄, and elemental potassium [2] or by reaction of the Zintl phase KSi with gaseous hydrogen. Starting from the Zintl phases the homologue series *M*Si as well as its solid solutions *M*_{0.5}*M'*_{0.5}Si (*M*, *M'* = K, Rb, Cs) react accordingly to form *M*SiH₃ and *M*_{0.5}*M'*_{0.5}SiH₃, respectively, in a solid gas reaction under 5 MPa hydrogen pressure and 373 K [3, 4]. In contrast, the Zintl phases LiSi and NaSi decompose to LiH and Si or NaH + Na₈Si₄₆, respectively [5, 6], under comparable hydrogenation conditions.

KSi and CsSi are typical Zintl phases and exhibit Si₄⁴⁻ tetrahedra [7–9], which are isoelectronic to P₄ in white phosphorous. Both compounds crystallize in the KGe type structure with the center of gravity of the Si₄⁴⁻ tetrahedra lying on the corners, the body center and two on each face of the cubic unit cell (Fig. A7.1). This arrangement of Si₄⁴⁻ tetrahedra is analogous to the Cr₃Si type structure [10]. Alkaline metal atoms cap each triangular face of the Si₄⁴⁻ tetrahedra and thus complete the polyhedra to *stellae quadrangulae* [9]. Hydrogenation of KSi at 5 MPa hydrogen pressure and 373 K yields α-KSiH₃, which crystallizes in an NaCl type arrangement with disordered SiH₃⁻ units (Fig. A7.1). These pyramidal anions are isoelectronic to phosphane, PH₃, and show Si-D distances of 154 pm as typically found in silanes [11]. Below 200 K a modification (β) with ordered SiH₃⁻ units exist (Fig. A7.1) [3]. Such order-disorder phase transitions at low temperatures are well known in the structural chemistry of metal hydrides including binary hydrides [12, 13], hydridoborates [14], Laves phase hydrides [15, 16] or transition metal complexes [17, 18], just to name a few. The α-β transition in ASiH₃ (*A* = K, Rb) is a typical order-disorder rotator phase transition accompanied by a large unit cell volume increase of about 14% [19, 20]. From its occurrence close to room temperature, it was concluded that the SiH₃⁻ are only weakly bound to the alkaline metal cations [20]. In contrast to ASiH₃ (*A* = K, Rb, Cs), most other hydrides of Zintl phases based on silicon contain infinite silicon chains, which can be single as in Li₄Si₂H [21] and BaSiH_{2-x} [22] or double chains as in SrSiH_{5/3-x} and BaGeH_{5/3-x} [23, 24] or triple chains as in CaSiH_{4/3-x} and SrGeH_{4/3-x} [22, 25].

It is of fundamental interest to understand the process of hydrogen uptake and release in Zintl phases both from the standpoint of basic research and in view of possible application as hydrogen storage materials. Rationalizing hydrogen containing structural units will allow the synthesis of new materials and enrich main group chemistry, while unravelling reaction pathways of hydrogen uptake and release will help in optimizing hydrogen storage properties. In regard to the hydrogenation of ASi to ASiH₃ (*A* = K, Rb, Cs) the reaction pathway from the structural units of the Si₄⁴⁻ tetrahedra to the formation of four SiH₃⁻ anions is uncertain. The reaction Si₄⁴⁻ + 6H₂ ⇌ 4SiH₃⁻ may be rationalized as the insertion of H₂ in all six Si-Si bonds of the tetrahedron. One of the central questions is, whether there are intermediates with lower insertion rate, where Si-Si bonds are left and oligomeric anions may occur. This is a fundamental question in view of the structural richness of hydrogen containing polyanions shown above.

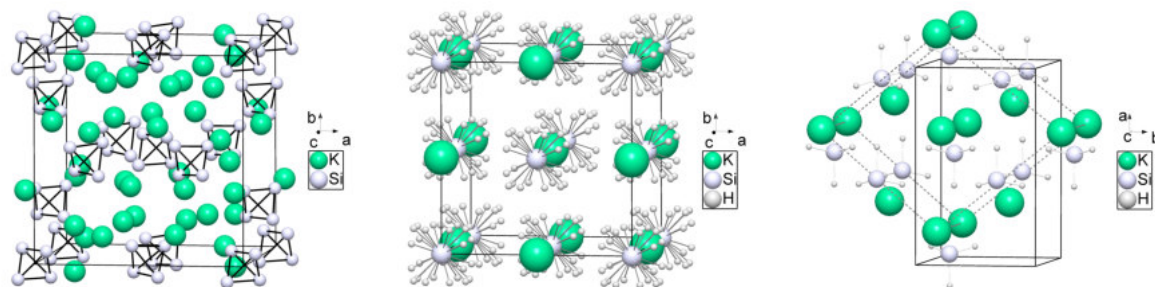


Figure A7.1: The crystal structures of KSi (**left**), α-KSiH₃ with rotationally disordered anions in NaCl like arrangement (**middle**) and part of the crystal structure of β-KSiH₃ with ordered anions emphasizing the structural relationship to the NaCl type (**right**); green, large spheres: K, grey, middle sized spheres: Si, white, small spheres: H.

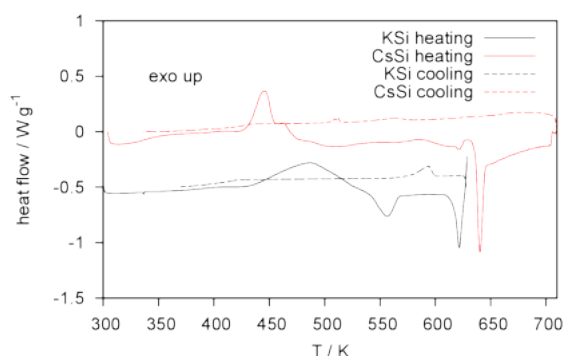


Figure A7.2: *In situ* differential scanning calorimetry (DSC) of the hydrogenation of KSi and CsSi at 5.0 MPa hydrogen pressure (starting pressure at 300 K, increasing to 7.0 MPa at the maximum temperature). The *ex situ* characterized (XRPD) products are $\text{K}_8\text{Si}_{146}$ and KH as well as CsSiH_3 .

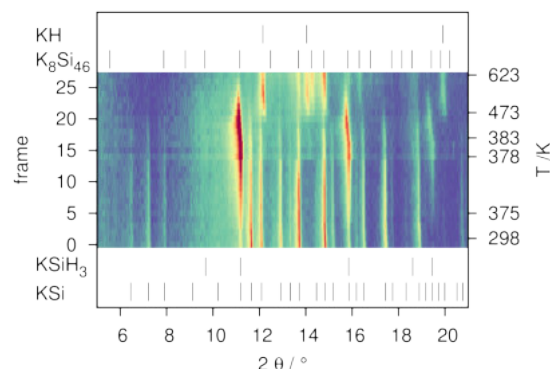


Figure A7.3: *In situ* laboratory X-ray powder diffraction ($\text{Mo-K}\alpha_1$ radiation) of the hydrogenation of KSi under 5.0 MPa hydrogen pressure. Diffraction patterns were collected isothermally with 15 min counting time per frame. Vertical bars indicate Bragg reflection positions of the respective phases.

In situ neutron diffraction has shown a huge potential for unravelling reaction pathways of solid-gas reactions in general [26, 27] and for Zintl phases in particular [28, 29]. The huge advantage of neutron scattering over other solid-state probes is the low neutron absorption of many materials. This enables the use of bulky environment as often needed for controlling physical parameters of the sample, such as temperature, pressure, gas atmospheres, electrical or magnetic fields [30, 31]. This applies for example to the study of hydrogen storage since both temperature and hydrogen gas pressure need to be controlled and the sample has to be enclosed in a pressure vessel. The reaction $\text{Li}_3\text{N} + 2\text{H}_2 \rightleftharpoons \text{LiNH}_2 + 2\text{LiH}$ is considered to be of interest for hydrogen storage due to the partial reversibility and high weight capacity for hydrogen. *In situ* studies revealed a strong pressure dependence of the reaction pathway for hydrogen uptake and release, which is of great importance to the ideal pressure-temperature protocol in the application [32, 33]. Studying electrode materials inside an electrochemical cell is also possible by neutron diffraction. This lead to further insight into electrode processes during charge and discharge cycles [31, 34, 35], where for example discontinuous intercalation reactions were identified causing unfavourable capacity fading [36]. The technologically important *HDDR* process (hydrogenation decomposition desorption recombination) for improving the magnetic properties of permanent magnets is largely based on empirical grounds [37]. *In situ* studies showed that different reaction pathways with or without a hydrogen-induced amorphization may occur depending on the crystallite size of the starting material [38, 39]. These examples illustrate that unravelling the reaction pathway is often crucial for controlling technical processes, chemical syntheses or gas uptake and release in a wide variety of materials. *In situ* studies are thus of fundamental importance for development in the field of solid state sciences and functional materials.

In this contribution we therefore investigated the reaction of KSi with gaseous hydrogen to form $\alpha\text{-KSiH}_3$ and the analogous reaction of CsSi with various *in situ* methods at hydrogen pressures of 5.0 MPa. *In situ* thermal analysis (differential scanning calorimetry, DSC) under hydrogen pressure may yield information on thermodynamic and kinetic properties [40, 41], whereas *in situ* diffraction methods give structural information on crystalline phases. *In situ* X-ray powder diffraction was performed to follow the development of crystal structures during the reaction. In order to locate hydrogen in the crystal structures, *in situ* neutron powder diffraction data were also taken.

Results and Discussion

The synthesis of KSi and CsSi from the elements yielded grey powders with a metallic lustre. According to X-ray powder diffraction (XRPD) the samples were single phase and refined lattice parameters ($a_{\text{KSi}} = 1262.33(3)$ pm, $a_{\text{CsSi}} = 1350.96(5)$ pm) were in good agreement with literature data. *In situ* thermal analysis (DSC) under 5.0 MPa hydrogen pressure gave a broad exothermic signal for KSi, which, however, could not be attributed to the formation of KSiH_3 (Fig. A7.2). This was proven by X-ray diffraction on

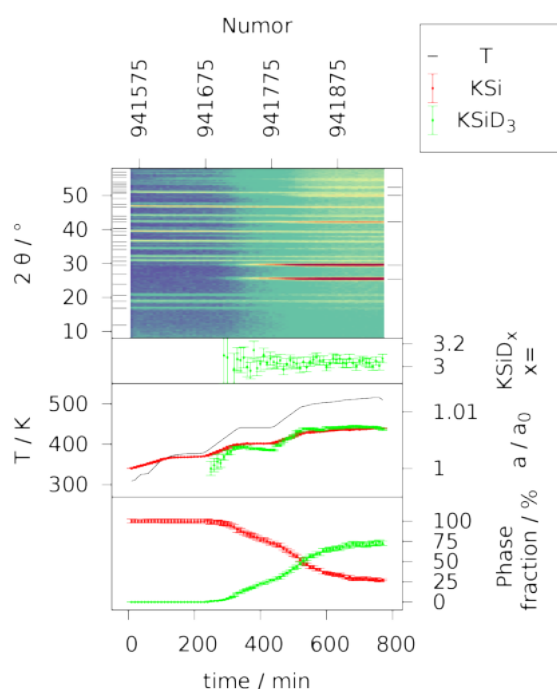


Figure A7.4: *In situ* neutron powder diffraction (D20, Institut Laue-Langevin (ILL), $\lambda = 186.719(2)$ pm) of the hydrogenation of KSi under 5.0 MPa deuterium pressure in a single-crystal sapphire cell with a time resolution of 2 min per pattern (= NUMOR, ILL's internal numbering of experimental data [42]). Serial Rietveld refinement was done using a summation over 5 patterns. Vertical bars indicate Bragg reflection positions of KSi (top left) and α -KSiD₃ (top right).

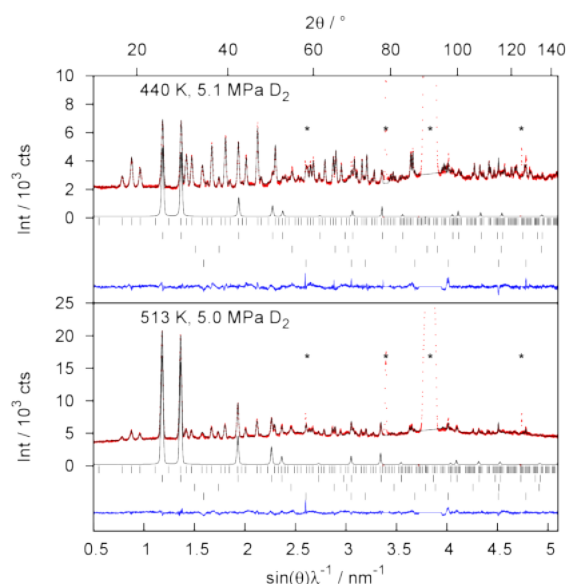


Figure A7.5: Rietveld refinement (*in situ* NPD, $\lambda = 186.719(2)$ pm) of the crystal structure of KSi (top row Bragg marker) and α -KSiD₃ (second row) with minor impurity phases KD (third row) and Si (bottom row). The calculated diffraction pattern shown above the Bragg markers belongs to α -KSiD₃. Structural data and R values are summarized in Tab. A7.1. The asterisks (*) mark reflections from the sapphire cell.

a sample whose hydrogenation reaction was stopped after the first exothermic signal. The endothermic signal at higher temperatures belongs to the partial formation of the clathrate K_8Si_{46} . Since $KSiH_3$ could not be detected in the DSC experiment, the clathrate formation probably stems from the direct reaction of KSi with hydrogen gas. The reaction of CsSi to $CsSiH_3$ showed a very broad weak exothermic signal (Fig. A7.2). The endothermic signal at higher temperatures probably belongs to the decomposition of $CsSiH_3$, but an unambiguous assignment to the reactions observed by other methods (vide infra) is not possible. Upon cooling, $CsSiH_3$ is formed again but did not show a significant DSC signal. The product right after the exothermic step as well as after the whole cycle is $CsSiH_3$ and was determined by XRPD. The fact that no $KSiH_3$ is formed in the DSC experiment may be attributed to the rather high heating rates of 10 K/min typical for thermal analysis. It was already reported that fast absorption of hydrogen by KSi leads rather to a mixture of the clathrate phase K_8Si_{46} and potassium hydride instead of $KSiH_3$ [6].

The hydrogenation of KSi was also followed by *in situ* X-ray powder diffraction under isobaric conditions of 5.0 MPa hydrogen pressure and temperatures up to 623 K (Fig. A7.3). Under these conditions, KSi starts to form $KSiH_3$ in a one-step reaction at 375 K, which proceeds only sluggishly. Above 473 K α - $KSiH_3$ decomposes to the clathrate K_8Si_{46} and KH (Fig. A7.3). We note a difference to the behavior at 0.1 MPa, where a full reversibility for the reaction $2KSi + 3H_2 \rightleftharpoons 2KSiH_3$ was found, and KSi is reformed from $KSiH_3$ at temperatures above 414 K [1, 3]. Higher hydrogen pressure as applied in our experiments, apparently favors decomposition to hydrogen containing products (KH).

Details of hydrogen positions within the crystal structures cannot be resolved well by XRPD. Therefore, similar *in situ* experiments were performed with neutron radiation. Two questions were of particular interest: Does KSi dissolve hydrogen in the solid before the reaction to $KSiH_3$? Does $KSiH_3$ show hydro-

Table A7.1: Selected crystal structure data of KSiD₃ and CsSiD₃

Atom	<i>x</i>	<i>y</i>	<i>z</i>	B_{iso} 10^4 pm^2	SOF
KSiD _{3.27(7)} (440 K, 5.1 MPa D ₂ , fraction = 18%), d(Si-D) = 143(2) pm, <i>a</i> = 729.83(6) pm, R _{Bragg} = 3.2% R _p = 20.6%, R _{wp} = 18.3%, $\chi^2 = 4.35$.					
K	0	0	0	5.6(5)	
Si	1/2	1/2	1/2	6.5(4)	
D	0.5838(10)	<i>x</i>	0.6556(16)	8.0(6)	0.136(3)
KSiD _{3.23(5)} (513 K, 5.0 MPa D ₂ , fraction = 70%), d(Si-D) = 145.4(7) pm, <i>a</i> = 733.03(9) pm, R _{Bragg} = 2.5% R _p = 26.3%, R _{wp} = 17.3%, $\chi^2 = 4.78$.					
K	0	0	0	7.6(4)	
Si	1/2	1/2	1/2	9.3(3)	
D	0.5845(6)	<i>x</i>	0.6583(10)	10.5(5)	0.134(2)
CsSiD _{3.22(8)} (378 K, 5.0 MPa D ₂ , fraction = 15%), d(Si-D) = 149(3) pm, <i>a</i> = 787.68(13) pm, R _{Bragg} = 10.4% R _p = 18.7%, R _{wp} = 24.4%, $\chi^2 = 9.03$.					
Cs	0	0	0	6.7(6) ^a	
Si	1/2	1/2	1/2	9.2 ^a	
D	0.583(2)	<i>x</i>	0.649(3)	9.2 ^a	0.134(3)
CsSiD _{3.05(3)} (450 K, 5.1 MPa D ₂ , fraction = 100%), d(Si-D) = 148.8(7) pm, <i>a</i> = 791.09(14) pm, R _{Bragg} = 4.6% R _p = 25.6%, R _{wp} = 18.5%, $\chi^2 = 8.98$.					
Cs	0	0	0	8.2(3)	
Si	1/2	1/2	1/2	8.4(3)	
D	0.5849(7)	<i>x</i>	0.6448(8)	9.1(4)	0.1271(13)

^a Due to small fraction Biso values were set to literature values [3] and only one overall B value was refined and added.

gen defects in the early stages of the formation or the decomposition? *In situ* neutron powder diffraction (NPD) was carried out using sapphire single-crystal cells, which provide a very low scattering background [26]. In order to avoid the strong incoherent scattering, deuterium was used instead of the natural isotopic mixture of hydrogen. The reaction of KSi with deuterium (5.0 MPa) at temperatures up to 500 K is rather slow and even after more than 13 hours the turnover does not surpass 75% (Fig. A7.4). The only significant changes in the crystal structure of KSi during the reaction concern lattice parameters. They increase with temperature but do not show any additional expansion effects during isothermal steps. The neutron reflections of KSi do not vary significantly in intensity and Rietveld refinements gave no hint to the presence of any deuterium in the crystal structure. We therefore conclude that the solubility for deuterium in KSi is negligible. In agreement with the *in situ* XRPD experiment, *in situ* NPD showed a one-step reaction to KSiD₃ without any intermediates (Fig. A7.4).

At two (quasi) isothermic steps at 440 K and at 513 K frames were summed to get about 80 min counting time per pattern (Fig. A7.5). These two diffraction patterns characterize the start of KSiD₃ formation and the maximum temperature reached in the experiment. The crystal structures could be refined by the Rietveld method using the crystal structure model of α -KSiD₃ (Fig. A7.1, [1]). The SiD₃⁻ moieties are rotationally disordered and thus, the deuterium atoms were set to a 96k site as suggested by earlier studies [1]. A thorough investigation of the fractional coordinates showed the existence of at least two minima in the least squares refinement. The lower one led to fractional coordinates that deviate slightly from literature values (Tab. A7.1). Due to the rotational disorder it is not unexpected that the minimization functional is quite flat with several local minima, which may also depend on the dynamical behaviour and thus change with temperature. There are no significant changes to the crystal structure of KSiD₃ during the *in situ* experiment. The deuterium occupation of α -KSiD₃ is constant within one estimated standard uncertainty and yields an average composition of KSiD_{3.04(4)}. Raising the deuterium pressure to 9 MPa at 550 K (not shown) did not increase the deuterium content either. Thus, α -KSiD₃ is a line phase as expected for an electron precise compound.

The reaction of CsSi was much faster and completed in less than six hours. The formation of CsSiD₃ already started at 373 K in agreement with earlier work (Fig. A7.6) [6]. Further heating increased the reaction rate and leads to single phase CsSiD₃. Rietveld refinement results are shown for 378 K

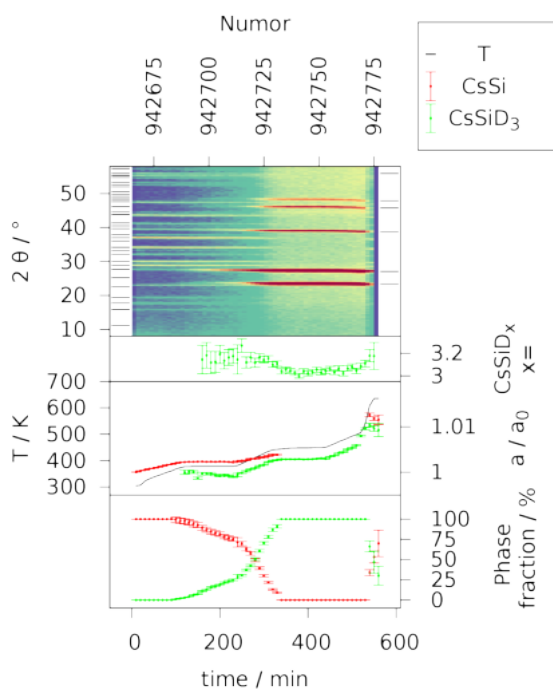


Figure A7.6: *In situ* neutron powder diffraction (D20, Institut Laue-Langevin, $\lambda = 186.719(2)$ pm) of the hydrogenation of CsSi under 5.0 MPa deuterium pressure in a single-crystal sapphire cell. Time resolution was 5 min per pattern (= NUMOR, ILL's internal numbering of experimental data [42]). Serial Rietveld refinement was done using a summation over two patterns. Vertical bars indicate Bragg reflection positions of CsSi (top left) and α -CsSiD₃ (right).

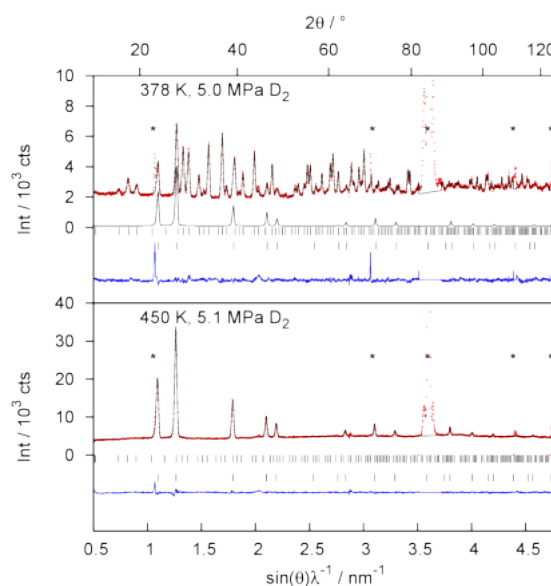


Figure A7.7: Rietveld refinement (*in situ* NPD, $\lambda = 186.719(2)$ pm) of the crystal structure of CsSi (top row Bragg marker) and α -CsSiD₃ (bottom row). The calculated diffraction pattern shown above the Bragg markers belongs to CsSiD₃ (378 K). Structural data and R values are summarized in Tab A7.1. The asterisks (*) mark reflections from the sapphire cell.

and 450 K explicitly (Fig. A7.7, Tab. A7.1). As for the analogous KSi-KSiD₃ system the crystal structures of CsSi and CsSiD₃ did not change significantly during the *in situ* NPD experiment except thermal lattice expansion and there were no hints for a solubility of deuterium in CsSi. Refined deuterium occupation factors did not change significantly during the course of the reaction and yielded a composition of CsSiD_{3.08(4)} at average. Therefore, CsSiD₃ is considered to be a line phase as well. Heating above 500 K led to the decomposition of CsSiD₃, i. e. the reaction $2\text{CsSi} + 3\text{H}_2 \rightleftharpoons 2\text{CsSiH}_3$ is fully reversible even at 5.0 MPa hydrogen pressure in contrast to KSiH₃. The preference of the irreversible formation of the clathrate in the case of KSi according to the formula $46\text{KSiH}_3 \rightleftharpoons \text{K}_8\text{Si}_{46} + 38\text{KH} + 50\text{H}_2$ might be attributed to the higher formation enthalpy of potassium hydride in comparison to cesium hydride.

Conclusions

In situ investigations on the hydrogenation of KSi and CsSi to KSiH₃ and CsSiH₃, respectively, were carried out at 5.0 MPa by thermal analysis, X-ray and neutron powder diffraction. They resulted in a deeper insight into the reaction pathways of these potential reversible hydrogen storage materials. Neither KSi nor CsSi dissolve hydrogen in their crystal structures. The reactions to KSiH₃ and CsSiH₃ are one-step reactions without any intermediates. While the reaction to CsSiH₃ can be completed in less than six hours, the formation of KSiH₃ proceeds rather sluggishly. Both KSiH₃ and CsSiH₃ are line phases with refined compositions of KSiD_{3.04(4)} and CsSiD_{3.08(4)} (determined on the deuterides). At 5.0 MPa hydrogen pressure, KSiH₃ decomposes to K₈Si₄₆ and KH at temperatures above 473 K, while CsSiH₃ releases hydrogen to reversibly form CsSi above 500 K.

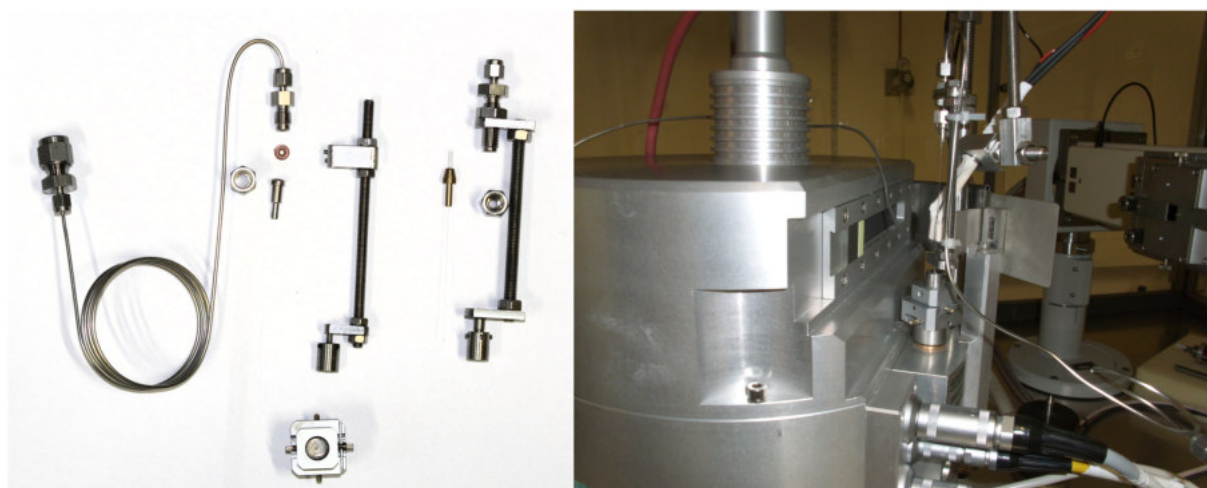


Figure A7.8: *In situ* XRD setup with VCR and Swagelok attachments to the gas supply system (left) and Huber G670 Guinier chamber with resistivity sample heater (right).

Experimental Section

All preparations were done in an argon filled glove box. Oxygen and moisture contents were monitored and kept below 1 ppm. The Zintl phases KSi and CsSi were prepared from the elements (Si: 99.9999% abcr; K: 99.95% abcr; Cs: 99.98%, abcr) with an excess of 3-5 mol-% silicon. The starting materials were placed into sealed stainless steel jackets and heated with 0.5 K min^{-1} to 825 K. The temperature was kept for 60 h. KSiH_3 , KSiD_3 and CsSiD_3 were prepared *in situ* under 5.0 MPa hydrogen (Air Liquide 99.9%) or deuterium (Air Liquide, 99.8% isotope purity) gas pressure and elevated temperatures (Figs. A7.3, A7.4, A7.6).

Differential scanning calorimetry (DSC) was performed with a Q1000 DSC (TA Instruments) equipped with a gas pressure chamber. DSC experiments were done under 5 MPa hydrogen pressure. Aluminum crucibles were filled with about 15 mg KSi or CsSi and crimped within a glovebox. The sample was placed in the pressure chamber of the DSC, which was subsequently flushed with hydrogen and afterwards filled to the desired hydrogen pressure. Samples were heated at a rate of 10 K min^{-1} .

For laboratory *in situ* X-ray powder diffraction (XRPD) a home build setup (inspired by [43]). A quartz capillary is attached to a gas supply system using VCR or Swagelok connections. Either a $1/8$ inch VCR or a $1/8$ inch Swagelok dummy plug were modified with a bore hole (3.5 mm at top, 1mm at the bottom). The hole on top was wide enough to house the cone of a 0.3 mm or 0.5 mm quartz capillary, which was glued with two component epoxy glue into the fitting. Pressures up to 200 bar H_2 were tested at room temperature and up to 100 bar H_2 at 700 K. A capillary holder that allows mounting the hydrogen line attached capillary from top was built to fit the standard goniometer head. A standard Huber capillary resistivity heater was modified to allow attachment from top (Fig. A7.8). Measurements were done in a static setup without capillary rotation.

In situ neutron powder diffraction (NPD) was performed at the Institut Laue Langevin (ILL), Grenoble, France, at the high intensity diffractometer D20 [44]. Measurements were done at a take-off angle of 120° and a wavelength of $\lambda = 186.719(2) \text{ pm}$, which was calibrated using an external silicon NIST-640b standard sample. *In situ* experiments were done in (leuco-)sapphire single crystal cells with 6 mm inner diameter which were connected to a gas supply system [45]. *In situ* data were collected with 2 min (KSi) or 5 min (CsSi) time resolution. All data sets obtained at the ILL are presented with an additional label according to internal raw data labelling (NUMOR labelling). Data refer to Proposal 5-21-1096 [42].

Rietveld refinement was done using FULLPROF [46, 47]. For serial refinements datasets were added to get an overall measurement time of 10 min per pattern. Since the heavy atom partial structure of ASiH_3 ($A = \text{K}, \text{Cs}$) has NaCl-structure type only the partially occupied Wyckoff site 96k of deuterium shows positional degrees of freedom. These two fractional coordinates were investigated thoroughly and showed no significant change during the *in situ* experiment. They were kept fixed during the final serial refinement. Debye-Waller factors show large e.s.u., thus they were set to literature values [3] and the overall factor was refined to account for the increase during the heating.

Acknowledgements

The Institut Laue-Langevin is acknowledged for providing beamtime and Dr. Thomas Hansen for help with the neutron diffraction measurements. We thank the Deutsche Forschungsgemeinschaft (DFG, grant Ko1803/8-1) and the Fonds der Chemischen Industrie (Grant 194371) for financial support.

A7.4 References

- (1) Chotard, J.-N.; Tang, W. S.; Raybaud, P.; Janot, R. *Chem. - Eur. J.* **2011**, *17*, 12302–12309, DOI: 10.1002/chem.201101865.
- (2) Ring, M. A.; Ritter, D. M. *J. Phys. Chem.* **1961**, *65*, 182–183, DOI: 10.1021/j100819a506.
- (3) Tang, W. S.; Chotard, J.-N.; Raybaud, P.; Janot, R. *J. Phys. Chem. C* **2014**, *118*, 3409–3419, DOI: 10.1021/jp411314w.
- (4) Tang, W. S.; Dimitrievska, M.; Chotard, J.-N.; Zhou, W.; Janot, R.; Skripov, A. V.; Udovic, T. J. *J. Phys. Chem. C* **2016**, *120*, 21218–21227, DOI: 10.1021/acs.jpcc.6b06591.
- (5) Tang, W. S.; Chotard, J.-N.; Janot, R. *J. Electrochem. Soc.* **2013**, *160*, A1232–A1240, DOI: 10.1149/2.089308jes.
- (6) Tang, W. S.; Chotard, J.-N.; Raybaud, P.; Janot, R. *Phys. Chem. Chem. Phys.* **2012**, *14*, 13319, DOI: 10.1039/c2cp41589e.
- (7) Busmann, E. *Naturwissenschaften* **1960**, *47*, 82, DOI: 10.1007/BF00628474.
- (8) Busmann, E. *Z. Anorg. Allg. Chem.* **1961**, *313*, 90–106, DOI: 10.1002/zaac.19613130108.
- (9) Von Schnering, H. G.; Schwarz, M.; J.-H., C.; Peters, K.; E.-M., P.; Nesper, R. *Z. Kristallogr. - New Cryst. Struct.* **2005**, *220*, 525, DOI: 10.1524/ncrs.2005.220.4.525.
- (10) Nuss, J.; Hönle, W.; Peters, K.; Schnering, H. G. V. *Z. Anorg. Allg. Chem.* **1996**, *622*, 1879–1885, DOI: 10.1002/zaac.19966221112.
- (11) Kranak, V. F.; Lin, Y.-C.; Karlsson, M.; Mink, J.; Norberg, S. T.; Häussermann, U. *Inorg. Chem.* **2015**, *54*, 2300–2309, DOI: 10.1021/ic502931e.
- (12) Flanagan, T. B.; Oates, W. A. *Annu. Rev. Mater. Sci.* **1991**, *21*, 269–304, DOI: 10.1146/annurev.ms.21.080191.001413.
- (13) Vajda, P. *Solid State Ionics* **2004**, *168*, 271–279, DOI: 10.1016/j.ssi.2002.11.001.
- (14) Filinchuk, Y.; Chernyshov, D.; Dmitriev, V. *Z. Kristallogr.* **2008**, *223*, DOI: 10.1524/zkri.2008.1021.
- (15) Somenkov, V.; Irodova, A. *J. Less-Common Met.* **1984**, *101*, 481–492, DOI: [http://dx.doi.org/10.1016/0022-5088\(84\)90124-3](http://dx.doi.org/10.1016/0022-5088(84)90124-3).
- (16) Kohlmann, H.; Yvon, K. *J. Alloys Compd.* **2000**, *309*, 123–126, DOI: [http://dx.doi.org/10.1016/S0925-8388\(00\)01040-9](http://dx.doi.org/10.1016/S0925-8388(00)01040-9).
- (17) Yvon, K.; Renaudin, G. In, (Ed.), R. B. K., Ed.; Wiley, New York: 2005, pp 1814–1846.
- (18) Kohlmann, H. *Z. Kristallogr.* **2009**, *224*, DOI: 10.1524/zkri.2009.1179.
- (19) Österberg, C.; Fahlquist, H.; Häussermann, U.; Brown, C. M.; Udovic, T. J.; Karlsson, M. *J. Phys. Chem. C* **2016**, *120*, 6369–6376, DOI: 10.1021/acs.jpcc.6b00363.
- (20) Nedumkandathil, R.; Jaworski, A.; Fischer, A.; Österberg, C.; Lin, Y.-C.; Karlsson, M.; Grins, J.; Pell, A. J.; Edén, M.; Häussermann, U. *J. Phys. Chem. C* **2017**, *121*, 5241–5252, DOI: 10.1021/acs.jpcc.6b12902.
- (21) Wu, H.; Hartman, M. R.; Udovic, T. J.; Rush, J. J.; Zhou, W.; Bowman Jr, R. C.; Vajo, J. J. *Acta Crystallogr., Sect. B* **2007**, *63*, 63–68, DOI: 10.1107/s0108768106046465.
- (22) Auer, H.; Guehne, R.; Bertmer, M.; Weber, S.; Wenderoth, P.; Hansen, T. C.; Haase, J.; Kohlmann, H. *Inorg. Chem.* **2017**, *56*, 1061–1071, DOI: 10.1021/acs.inorgchem.6b01944.
- (23) Auer, H.; Schlegel, R.; Oeckler, O.; Kohlmann, H. *Angew. Chem., Int. Ed.* **2017**, *56*, 12344–12347, DOI: 10.1002/anie.201706523.
- (24) Auer, H.; Schlegel, R.; Oeckler, O.; Kohlmann, H. *Angew. Chem.* **2017**, *129*, 12515–12518, DOI: 10.1002/ange.201706523.
- (25) Wu, H.; Zhou, W.; Udovic, T. J.; Rush, J. J.; Yildirim, T. *Phys. Rev. B* **2006**, *74*, 224101, DOI: 10.1103/PhysRevB.74.224101.
- (26) Widenmeyer, M.; Niewa, R.; Hansen, T. C.; Kohlmann, H. *Z. Anorg. Allg. Chem.* **2013**, *639*, 285–295, DOI: 10.1002/zaac.201200299.

- (27) Hansen, T. C.; Kohlmann, H. *Z. Anorg. Allg. Chem.* **2014**, *640*, 3044–3063, DOI: 10.1002/zaac.201400359.
- (28) Auer, H.; Wallacher, D.; Hansen, T. C.; Kohlmann, H. *Inorg. Chem.* **2017**, *56*, 1072–1079, DOI: 10.1021/acs.inorgchem.6b01945.
- (29) Wenderoth, P.; Kohlmann, H. *Inorg. Chem.* **2013**, *52*, 10525–10531, DOI: 10.1021/ic401480b.
- (30) Pannetier, J. *Chem. Scr.* **1986**, *26A*, 131–139.
- (31) Isnard, O. *C. R. Phys.* **2007**, *8*, 789–805, DOI: <http://dx.doi.org/10.1016/j.crhy.2007.10.002>.
- (32) Bull, D. J.; Weidner, E.; Shabalyn, I. L.; Telling, M. T. F.; Jewell, C. M.; Gregory, D. H.; Ross, D. K. *Phys. Chem. Chem. Phys.* **2010**, *12*, 2089–2097, DOI: 10.1039/B903821N.
- (33) Behrendt, G.; Reichert, C.; Kohlmann, H. *J. Phys. Chem. C* **2016**, *120*, 13450–13455, DOI: 10.1021/acs.jpcc.6b04902.
- (34) Bardé, F.; Palacin, M. R.; Chabre, Y.; Isnard, O.; Tarascon, J.-M. *Chem. Mater.* **2004**, *16*, 3936–3948, DOI: 10.1021/cm0401286.
- (35) Latroche, M.; Chabre, Y.; Decamps, B.; Percheron-Guégan, A.; Noreus, D. *J. Alloys Compd.* **2002**, *334*, 267–276, DOI: [http://dx.doi.org/10.1016/S0925-8388\(01\)01799-6](http://dx.doi.org/10.1016/S0925-8388(01)01799-6).
- (36) Bianchini, M.; Leriche, J. B.; Laborier, J.-L.; Gendrin, L.; Suard, E.; Croguennec, L.; Masquelier, C. *J. Electrochem. Soc.* **2013**, *160*, A2176–A2183, DOI: 10.1149/2.076311jes.
- (37) Takeshita, T. *J. Alloys Compd.* **1995**, *231*, 51–59, DOI: [http://dx.doi.org/10.1016/0925-8388\(95\)01873-5](http://dx.doi.org/10.1016/0925-8388(95)01873-5).
- (38) Bulyk, I.; Panasyuk, V.; Trostianchyn, A. *J. Alloys Compd.* **2004**, *379*, 154–160, DOI: <http://dx.doi.org/10.1016/j.jallcom.2004.02.022>.
- (39) Belener, K. L.; Kohlmann, H. *J. Magn. Magn. Mater.* **2014**, *370*, 134–139, DOI: 10.1016/j.jmmm.2014.06.066.
- (40) Füglein, E.; Léon, A. In *Hydrogen Technology: Mobile and Portable Applications*, Léon, A., Ed.; Springer Berlin Heidelberg: Berlin, Heidelberg, 2008, pp 501–521, DOI: 10.1007/978-3-540-69925-5_20.
- (41) Kohlmann, H. *J. Solid State Chem.* **2010**, *183*, 367–372, DOI: <http://dx.doi.org/10.1016/j.jssc.2009.11.029>.
- (42) Kohlmann, H.; Auer, H.; Götze, A.; Hansen, T.; Werwein, A. Formation and decomposition of deuterides of the Zintl phases KSi and CsGe., Institut Laue-Langevin, 2015, DOI: 10.5291/ILL-DATA.5-21-1096.
- (43) Jensen, T. R.; Nielsen, T. K.; Filinchuk, Y.; Jørgensen, J.-E.; Cerenius, Y.; Gray, E. M.; Webb, C. J. *J. Appl. Crystallogr.* **2010**, *43*, 1456–1463, DOI: 10.1107/S0021889810038148.
- (44) Hansen, T. C.; Henry, P. F.; Fischer, H. E.; Torregrossa, J.; Convert, P. *Meas. Sci. Technol.* **2008**, *19*, 034001.
- (45) Kohlmann, H.; Kurtzemann, N.; Wehrich, R.; Hansen, T. *Z. Anorg. Allg. Chem.* **2009**, *635*, 2399–2405, DOI: 10.1002/zaac.200900336.
- (46) Rodríguez-Carvajal, J. FULLPROF (version 5.30): A Program for Rietveld Refinement and Pattern Matching Analysis; Institut Laue-Langevin, Grenoble (France), 2012.
- (47) Rodríguez-Carvajal, J. *Phys. B* **1993**, *192*, 55–69, DOI: 10.1016/0921-4526(93)90108-I.

U1 *In situ* neutron powder diffraction of the Zintl phase NdGa

Henry Auer^a, Ulrich Häussermann^b, Holger Kohlmann^{a*}

^a *Leipzig University, Department of Inorganic Chemistry, Johannisallee 29, 04103 Leipzig, Germany*

^b *Stockholm University, Department of Materials and Environmental Chemistry, 10691 Stockholm, Sweden*

* *Corresponding author*

— This is an unpublished manuscript. —

U1.1 Authors' contributions

This is an unpublished manuscript written by H. Auer. The *in situ* diffraction experiment was conducted by H. Auer and H. Kohlmann. Data evaluation was done by H. Auer. The manuscript run through some editing by H. Kohlmann. It is not approved by U. Häussermann yet.

U1.2 Manuscript

Introduction

Zintl phase hydrides gained some interest due to their novel binding motives. While interstitial hydride atoms which are coordinated by the less electronegative metal are well known, the occurrence of polyanions with element-hydrogen bonds is a more recently found feature. The first example of such a polyanionic hydride given in the year 2000 is SrAl_2H_2 exhibiting a two-dimensional net of puckered honeycomb-like six-rings that are saturated by hydrogen [1]. Especially gallium shows a rich Zintl phase hydride chemistry i.e. featuring polyethylene like $\frac{1}{\infty}[(\text{GaH}_2)^-]$ [2, 3], propane-like $(\text{Ga}_3\text{H}_8)^{3-}$ [4] or neopentane-like $(\text{Ga}(\text{GaH}_3)_4)^{5-}$ [5]. The hydrogenation of Zintl phases AeGa_2 or AeGaTt (Ae = alkaline earth metal, Tt = tetrel / group 14 element) leads to the formation of polyanionic hydrides AeGa_2H_2 or $\text{Ae}(\text{GaH})\text{Tt}$, respectively [6–12]. Typical Ga-H bond lengths in these compounds reach from 169 to 173 pm.

Recently the hydrogenation of NdGa and GdGa led to the formation of $\text{NdGaH}_{1.66}$ and $\text{GdGaH}_{1.66}$ [13, 14]. Hydrogen positions were determined for the first compound. This phase shows one hydrogen per formula unit located in Nd_4 -tetrahedra. The additional hydrogen coordinates $2/3$ of the gallium zigzag chains. In contrast to the previously named Zintl phase hydrides, the Ga-H distance is considerably longer with about 200 pm and therefore, longer than expected for a conventional covalent bond. $\text{NdGaH}_{1.66}$ is structurally related to AeTtH_y (Ae = Ca - Ba, Tt = Si - Sn). In contrast, these phases show covalent Tt-H interaction [15–17].

This manuscript aims to characterise the hydrogenation of NdGa. It investigates the compositional range for hydrogen incorporation. Furthermore, the bonding distance towards gallium is reinvestigated. The reaction was monitored *in situ* by neutron powder diffraction. While the first issue can be addressed the latter one still needs further investigations. Since the sample contains an unidentified impurity phase the results are considered preliminary and need further clearance. Thus, the manuscript is not considered for publication yet.

Experimental

NdGa is an air and moisture stable, grey compound. It was provided by the *Häussermann*-group³². The sample contains an unidentified impurity phase³³. A Rietveld refinement plot is shown in the Supplement of this Manuscript (Fig. U1.S1).

In situ neutron powder diffraction

In situ neutron powder diffraction (NPD) was done at the high-intensity two-axis diffractometer D20 [18] at the Institut Laue-Langevin (ILL), Grenoble, France. Measurements were done at $\lambda = 186.764(9)$ pm. The wavelength was calibrated using an external silicon NIST640b standard sample in a 5 mm vanadium container. Time resolved neutron diffraction was done under hydrogen pressure and heating. These *in situ* experiments were carried out in (leuco-)sapphire single-crystal cells with 6 mm inner diameter connected to a gas supply system. Details are given elsewhere [19], [A5]. The sample cell is filled with NdGa within an glove box. After attaching to the gas supply system on the diffractometer the reaction chamber opened to the D_2 -line at atmospheric pressure and ambient temperature (D_2 : Air Liquide, 99.8% isotope purity). Heating was realized using two laser beams. Data sets were obtained with 2 min time resolution. They are presented with an additional label according to internal raw data labelling (NUMOR labelling). Data refer to proposal 5-24-576 [20].

Rietveld Refinement

Powder diffraction data were evaluated by the Rietveld method [21, 22]. Crystal structure refinements were conducted sequential. The converged result regarding a diffraction pattern was used as input for the following one. Rietveld refinement was done with the *TOPAS* software package [23].

³² Prof. Ulrich Häusserman, Department of Materials and Environmental Chemistry, Stockholm University, SE-10691 Stockholm, Sweden.

³³ Due to peak overlap with the impurity phase, reasonable Rietveld refinements are difficult to achieve. Especially Debye-Waller-factors tend to behave abnormally and needed to be constraint or fixed. This is one major issue, why the manuscript is considered to be preliminary and further experiments are necessary to confirm the results.

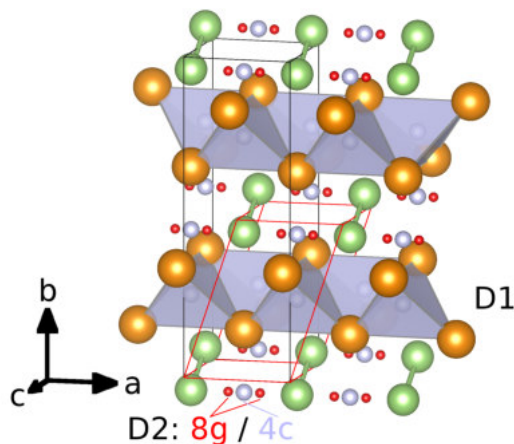


Figure U1.1: Crystal structure of $\text{NdGaD}_{1.66}$ given in space group $Cmcm$ (black unit cell) without superstructure regarding NdGa . Nd shown as large, yellow sphere and Ga as medium, green sphere. D1 occupies tetrahedral voids (shaded in grey). D2 is located on a $4c$ site ($\text{SOF} \approx 2/3$, grey spheres), or on a $8g$ site as split position ($\text{SOF} \approx 1/3$, red spheres). The unit cell in $P2_1/m$ sub-group representation is shown as well (red unit cell).

Results and Discussion

Preliminary considerations

$\text{NdGaH}_{1.66}$ was described to crystallize in space group type $Cmcm$ or its monoclinic sub-group $P2_1/m$ [13]. The crystal structure can be derived from the parent Zintl phase NdGa which crystallizes in CrB-structure type. It shows trigonal prismatically coordinated gallium atoms. All three faces are capped by an additional Nd atom and two Ga atoms. According to the Zintl-concept gallium forms zigzag chain ${}_{\infty}[\text{Ga}^{3-}]$ -polyanions. The parent Zintl phase shows tetrahedral Nd_4 -voids that become filled with one hydrogen per formula unit during the formation of $\text{NdGaH}_{1.66}$. The additional hydrogen occupies sites bridging two gallium-chains. These sites are partially occupied. According to the refined hydrogen content and DFT calculations the formation of a ${}_{\infty}[(\text{Ga}-\text{H}-\text{Ga}-\text{H}-\text{Ga})^{6-}]$ -moiety seems most favourable [13]. Such a description demands (at least) a three-fold superstructure in crystallographic a direction regarding the parent phase. The above mentioned models deal with a simple CrB-like unit cell. The $Cmcm$ -description shows gallium on a $4c$ site that has a fixed x -coordinate. Hydrogen is described on an $8g$ site leading to two hydrogen atoms between two gallium chains (Fig. U1.1). This results in a short H-H distance and can be considered as a split position of the corresponding $4c$ site which lies in the middle of these hydrogen atoms. Locally only one of these hydrogen atoms can be present. This leads to a short and a long Ga-H distance of 180 and 235 pm. The sub-group description in space group type $P2_1/m$ leads to an ordered hydrogen occupation almost in the middle of two chains. Furthermore gallium atoms have an additional degree of freedom allowing the chains to tilt out of the original b - c -plane of the parent phase. Fig. U1.1 shows the different crystal structure models.

Reaction of NdGa monitored by *in situ* neutron diffraction

The deuteration of NdGa was investigated isothermally at 480 K under increasing gas pressure. Afterwards the sample was cooled to ambient temperature, set under vacuum (active pumping) and reheated. Diffraction data were evaluated using the Rietveld method sequentially. The reaction of NdGa with D_2 -gas leads to the formation a deuteride. All phases NdGaD_{1+x} , $x \leq 0.799(11)$ occurring during the *in situ* diffraction experiment are described in the $Cmcm$ -model without a superstructure (Fig. U1.1), since there is no hint towards a monoclinic distortion of the unit cell. Further, the chain-bridging deuterium site is described as a $4c$ position and, thus, fixed in the middle of two chains. Refinements using the proposed $8g$ split-site show the tendency to move towards each other leading to the higher symmetry site. The independent atomic parameter $y(\text{D2})$ was constraint to the gallium atom to prevent a movement

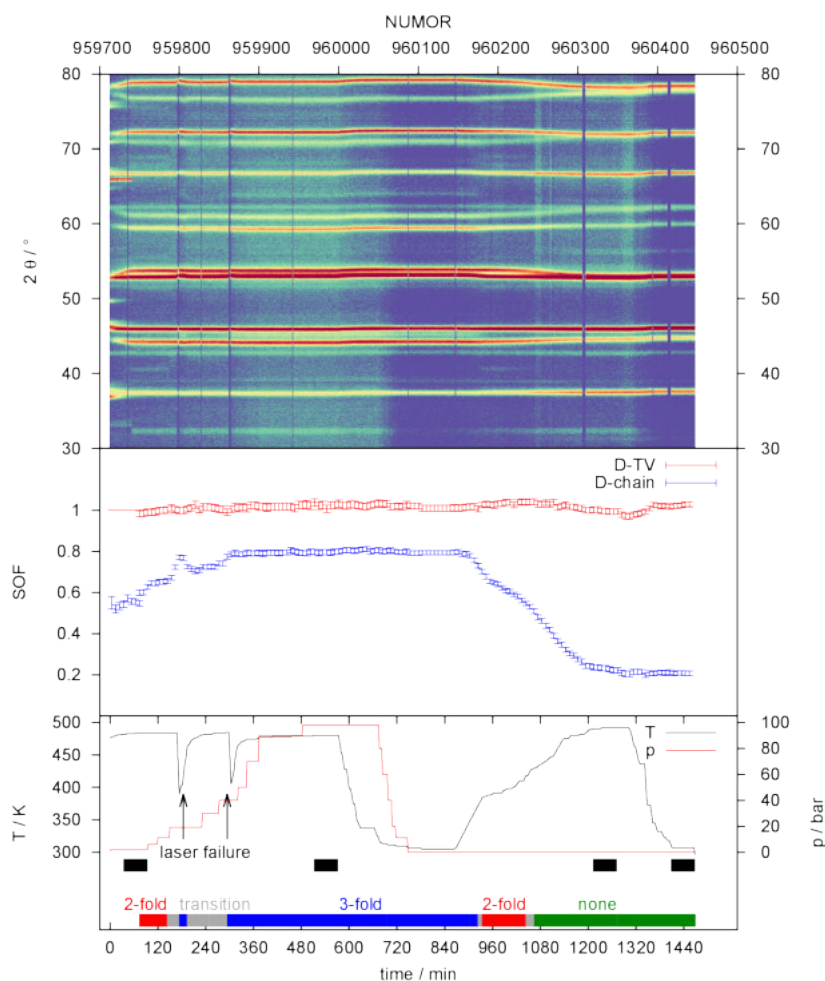


Figure U1.2: *In situ* NPD of the reaction of NdGa with D_2 (top). Overview of the isothermal deuteration step after the formation of $NdGaD_{1.5}$ and the dedeuteration reaction. The occupations of the tetrahedral Nd_4 -voids (D-TV) and the gallium chain bridging site (D-chain) of $NdGaD_{1+x}$, $x < 1$, (middle) and the temperature and pressure programm (bottom) are shown. The black bars indicate frames that were summed and are given in Fig. U1.6, U1.5, U1.S2 and U1.S3. The coloured bars indicate regions where superstructure reflections were present.

towards the DNd_4 -tetrahedra for low occupations. Otherwise a short D-D distance (< 200 pm) regarding the deuterium of the tetrahedral void was obtained.

The formation of $NdGaD_{1.5}$: The experiment was started at room temperature. The gas handling system was flushed with deuterium several times. Finally the pressure was released. Thus, about 0.1 MPa D_2 pressure remains in the system. The sample in the sapphire cell remained under argon, but the connecting valve was opened and gas diffusion was possible. Thus, the sample started taking up deuterium during the heating process leading to 26 wt-% phase fraction of $NdGaD_{1+x}$. Then the pressure was increased stepwise starting at 0.2 MPa D_2 . Within one hour the whole sample reacted to form $NdGaD_{1+x}$. The tetrahedral Nd_4 -voids are filled with deuterium showing no sign towards an under occupation. The chain coordinating position is about half filled (SOF = 0.52(2)-0.539(13) NUMOR 959715-750) during this first reaction step.

Deuteration at increased pressure and dedeuteration: Sequential Rietveld refinement results are shown for the isothermal part of the experiment and the dedeuteration step (Fig. U1.2). Increasing the

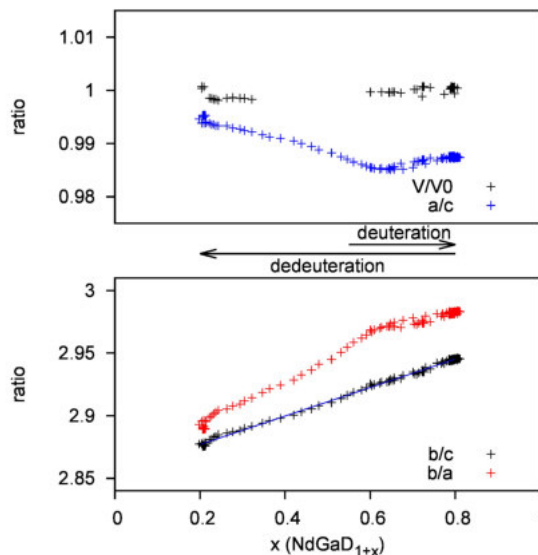


Figure U1.3: Lattice parameter ratios and relative volume regarding the occupation of gallium chain coordinating deuterium sites ($x = \text{SOF}(\text{D2})$ regarding Fig. U1.1). The relative volume is given regarding the first refined frame of Fig. U1.2 using datasets $T > 470$ K. Lattice parameter ratios are given for all temperatures.

pressure stepwise from 0.2 to 4.0 MPa D_2 leads to deuterium uptake. During the hydrogen uptake a two-fold and a three-fold superstructure can be identified. They occur for compositions of about $\text{NdGaD}_{1.55}$ to $\text{NdGaD}_{1.66}$ and $\text{NdGaD}_{>1.76}$, respectively as indicated in Fig. U1.2 (for details see below).

The maximum uptake was reached at a composition of $\text{NdGaD}_{1.799(11)}$. Increasing the pressure up to 9.8 MPa and a total equilibration time of 300 min did not help to increase the deuterium content. There were two failures of the laser heating system, that led to a drop of temperature. During these steps the deuterium content increased to the maximum we obtained during this experiment. After restarting the heating a decrease was observed. Thus, lower temperatures seem more favorable for the deuterium uptake. After 600 min isothermal heating, the sample was cooled at 9.8 MPa D_2 pressure, but no additional deuterium uptake was obtained.

When 310 K were reached, a subsequent desorption experiment was done applying vacuum. The sample cell was actively pumped (≈ 0.1 Pa) and heating was started again. The chain coordinating site releases deuterium. The maximum temperature of 490 K was kept for 60 min. During this last step the deuterium content only slowly decreased from NdGaD_{1+x} , $x = 0.232(13)$ to $x = 0.207(13)$. After cooling down to 300 K the composition reaches $x = 0.172(8)$. An *ex situ* characterisation afterwards leads to a final composition of $\text{NdGaD}_{1.137(7)}$.

Phase width of NdGaD_{1+x} , $x < 1$: NdGa already takes up deuterium at room temperature and D_2 partial pressures below 0.1 MPa. NdGaD_{1+x} covers a large range of deuterium incorporation reaching at least from $x = 0.137(7)$ to $0.799(11)$. Nevertheless the volume effect is much lower than 1% change from $\text{NdGaD}_{1.2}$ to $\text{NdGaD}_{1.8}$ (evaluated for diffraction patterns at like temperatures, i.e. $T > 470$ K, see Fig. U1.3). Lattice parameter ratios are given for all temperature. Unless there is an anisotropic thermal expansion, the ratios are independent of the temperature. This can be assumed since dedeuteration started at much lower temperatures than deuteration but ratios are still equal for like deuterium contents (Fig. U1.3). Lattice parameter b shows the strongest effect, while c is hardly effected. Thus, the b/c -ratio is a good measure for the deuterium content, showing a linear behaviour independent of the temperature. An empirical formula for NdGaD_{1+x} can be fitted by regression:

$$b/c = 0.1138(4) + 2.8542(2)x.$$

Furthermore, a shows a non-linear development with increasing refined deuterium content. It decreases until a composition NdGaD_{1+x} , $x \approx 2/3$ is reached and stays almost equal then.

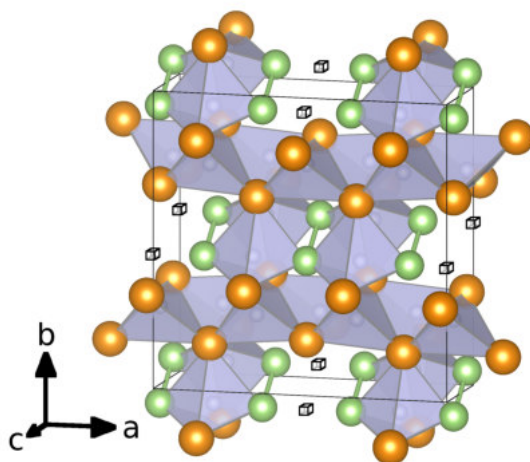


Figure U1.4: Crystal structure of $\text{NdGaD}_{1.66}$ given in space group $Cmcm$ ($a' = 3a$ regarding NdGa). D1 and D2 are coordinated tetrahedrally by Nd_4 . D3 is coordinated trigonal-pyramidally by Nd_3Ga_2 . A non-occupied void between the gallium zigzag chains is marked as \square . Labels are given according to Tab. U1.1. Large, yellow spheres: Nd; medium, green spheres: Ge; small, white sphere inside the shaded polyhedra: D.

Superstructures and the desorption product

During the *in situ* diffraction experiment different superstructures occur. They were neglected for sequential Rietveld refinement. Considering low-angle reflections they can be assigned to a doubling or tripling of the unit cell along crystallographic a direction. The superstructures are evaluated qualitatively by visual inspection of the diffraction patterns and indicated as a coloured bar in Fig. U1.2 (bottom). There are transition regions where the two- and three-fold superstructure reflections have vanished. There only a very weak reflection occurs that cannot be assigned unambiguously. The two-fold superstructure occurs for refined deuterium occupations of the chain coordination site (SOF(D2), see Fig. U1.1) of about 0.53 to 0.66. The threefold one can be assigned to occupation larger than about 0.73. Due to hydrogen contents and unit cell size the superstructures might lead to phases $\text{NdGaD}_{1+1/2}$ and $\text{NdGaD}_{1+2/3}$ with deuterium order. The refined deuterium contents are higher which might arise from a partial order or a phase mixture of ordered and unordered phases.

A three-fold superstructure is refined using a summation of *in situ* diffraction data as indicated in Fig. U1.2 (bottom, black bar at 9 MPa D_2 and 480 K). The refined composition using a non-superstructure model is $\text{NdGaD}_{1.799(11)}$. Considering all reflections, the diffraction pattern can be indexed in space group type $Cmcm$ with $a' = 3a$. Thus, it shows chemically and structural similarities to $\text{SrSiH}_{5/3-x}$ and $\text{BaGeH}_{5/3-x}$ which show a six-fold superstructure regarding the CrB-structure type [16, 17]. Nevertheless, a description in the ordered $\text{SrSiH}_{5/3-x}$ -structure type does not lead to satisfactory refinement results. In contrast it shows only a single $8g$ site almost in the middle of two gallium chains that is fully occupied leading to $\text{NdGaD}_{1.66}$ (Structure: Fig. U1.4, Rietveld plot: Fig. U1.5, structural data: Tab. U1.1).

This model leads to reasonable Ga-Ga distances of 257 pm and 259 pm within the chain and Ga-D distances of 205 pm and 225 pm. The remaining Ga-Ga distance perpendicular to the chain that is not bridged by deuterium is 374 pm. The bonds within the zigzag chains resemble the previously published value (259 pm [13]). It is shortened compared to the parent phase which shows $d(\text{Ga-Ga}) = 262.0(3)$ pm. The same work [13] presented a DFT derived structure model with a $\frac{1}{\infty}[(\text{Ga-H-Ga-H-Ga})^{6-}]$ -moiety with a short (190 pm) and a long (244 pm) Ga-H distance which fits our findings qualitatively.

The ordered superstructure model deviates from the non-superstructure model by 0.13 formula units of hydrogen. Adding an additional deuterium site within the remaining chain gap yields unreasonable interatomic distances.

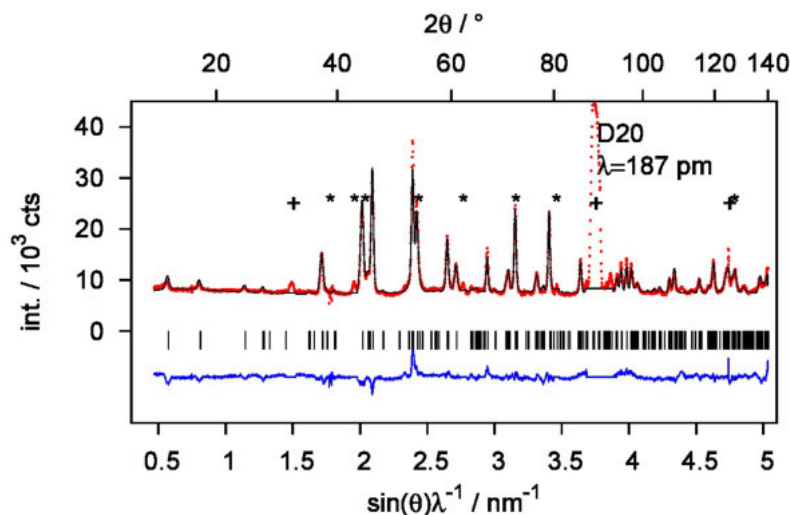


Figure U1.5: Rietveld refinement of the crystal structure of $\text{NdGaD}_{1.66}$ ($T = 480(2)$ K, $p = 9.8(1)$ Mpa D_2 , sapphire cell; $R_{\text{exp}} = 1.03\%$, $R_{\text{wp}} = 5.50\%$, $R_p = 4.25\%$, $\text{GoF} = 5.30$). Structural data are given in Tab. U1.1. (+) denotes a defect detector cell; (*) denoted the position of reflections of an unidentified side phase as already seen from the diffraction pattern of the parent phase (Fig. U1.S1).

Table U1.1: Structural data of $\text{NdGaH}_{1.66}$ at $T = 480(2)$ K, $p = 9.8(1)$ MPa D_2 (sapphire cell); $Cmcm$ ($a' = 3a$ regarding NdGa), $a = 1235.99(7)$ pm, $b = 1229.23(13)$ pm, $c = 417.25(3)$ pm; $R_{\text{exp}} = 1.03\%$, $R_{\text{wp}} = 5.50\%$, $R_p = 4.25\%$, $\text{GoF} = 5.30$; ${}_{\infty}[\text{Ga}]$ -chains: $d(\text{Ga1-Ga1}) = 259.0(12)$ pm, $d(\text{Ga2-Ga2}) = 257.2(9)$ pm; ${}_{\infty}[(\text{Ga2-D3-Ga1-D3-Ga2})^{6-}]$ -moiety: $d(\text{Ga1-D3}) = 225.9(12)$ pm, $d(\text{Ga2-D3}) = 205.5(14)$ pm; perpendicular to the chain: $d(\text{Ga2-Ga2}) = 373.8(11)$ pm (separated by a void), $d(\text{Ga1-Ga2}) = 431.1(8)$ pm (separated by D3); SOF of D1, D2 and D3 were unity within 3 e.s.u. and, thus, fixed during the last refinement.

atom	Wyck.	x	y	z	$B_{\text{iso}}/10^4 \text{ pm}^2$	SOF
Ga1	4c	0	0.0624(11)	$1/4$	0.27(12)	
Ga2	8g	0.3488(6)	0.0612(8)	$1/4$	$= B_{\text{iso}}(\text{Ga1})$	
Nd1	4c	0	0.3276(8)	$1/4$	0.12(14)	
Nd2	8g	0.3306(9)	0.3550(5)	$1/4$	$= B_{\text{iso}}(\text{Nd1})$	
D1	4c	0	0.7377(13)	$1/4$	1.68(14)	1
D2	8g	0.1702(12)	0.2508(9)	$1/4$	$= B_{\text{iso}}(\text{D1})$	1
D3	8g	0.1826(9)	0.0554(9)	$1/4$	2.7(2)	1

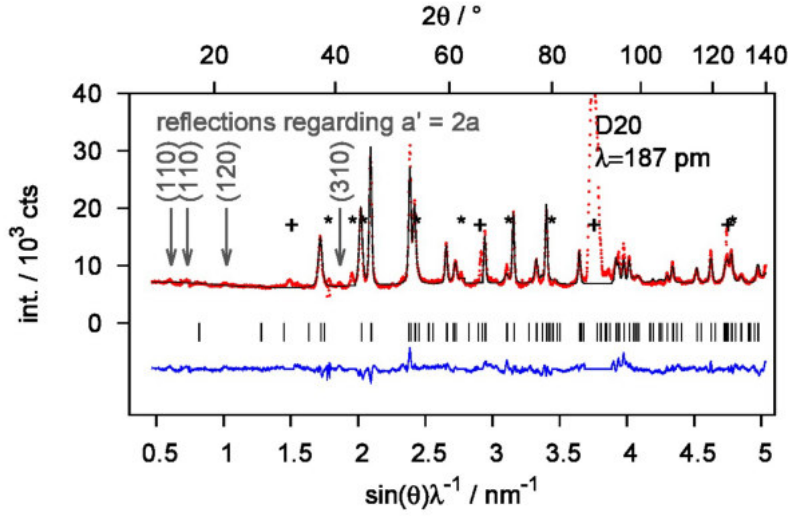


Figure U1.6: Rietveld refinement of the crystal structure of NdGaD_{1.56} (T = 480(2) K, p = 0.2(1) Mpa D₂, sapphire cell; $R_{\text{exp}} = 1.10\%$, $R_{\text{wp}} = 5.43\%$, $R_{\text{p}} = 4.21\%$, GoF = 4.93). Structural data are given in Tab. U1.2 (+) denotes a defect detector cell; (*) denoted the position of reflections of an unidentified side phase as already seen from the diffraction pattern of the parent phase (Fig. U1.S1).

Table U1.2: Structural data of NdGaH_{1.595(11)} at T = 480(2) K, p = 0.2(1) MPa D₂ (sapphire cell); *Cmcm* (no superstructure), $a = 412.46(3)$ pm, $b = 1223.02(13)$ pm, $c = 418.37(3)$ pm; $R_{\text{exp}} = 1.10\%$, $R_{\text{wp}} = 5.43\%$, $R_{\text{p}} = 4.21\%$, GoF = 4.93; $d(\text{Ga-Ga}) = 245.5(5)$ pm, $d(\text{Ga-D2}) = 209.0(2)$ pm. $B_{\text{iso}}(\text{Nd})$ needed to be kept at a reasonable value. *SOF* and B_{iso} of D2 strongly correlate, thus, B_{iso} was constraint to be equal to $B_{\text{iso}}(\text{D2})$.

atom	Wyck.	x	y	z	$B_{\text{iso}} / 10^4 \text{ pm}^2$	<i>SOF</i>
Ga	4 <i>c</i>	0	0.0525(5)	1/4	0.59(11)	
Nd	4 <i>c</i>	0	0.3560(3)	1/4	0.2	
D1	4 <i>c</i>	0	0.7545(6)	1/4	2.65(12)	1
D2	4 <i>c</i>	0	0.5801(7)	1/4	$B_{\text{iso}}(\text{D1})$	0.595(11)

The two-fold superstructure shows quite small superstructure reflections. According to group subgroup relations there are seven orthorhombic space groups that allow to double lattice parameter a (see supplement, Tab. U1.S1). They are not maximal subgroups, but can be derived by two klassengeiche transitions of index two ($2x \ k2$). Two out of the seven subgroups describe all super structure reflections:

$$Pbcm \text{ (No. 57): } P = \begin{pmatrix} 2 & 0 & 0 & 1/4 \\ 0 & 1 & 0 & 1/4 \\ 0 & 0 & 1 & 0 \end{pmatrix} \quad Pmma \text{ (No. 51): } P = \begin{pmatrix} 0 & 2 & 0 & 0 \\ 0 & 0 & 1 & 0 \\ 1 & 0 & 0 & 0 \end{pmatrix}$$

(Transformation matrix according to *International Tables of Crystallography* [24]). None of these two models leads to an ordering of deuterium. Thus, a structure model in space group type *Cmcm* without superstructure was refined using a summation of *in situ* diffraction data as indicated in Fig. U1.2 (bottom, black bar at 0.2 Mpa D₂ and 480 K). The superstructure reflections are small and additionally labelled in the Rietveld profile plot (Fig. U1.6). The chain bridging deuterium is described as a 4*c* position and, thus, fixed in the middle of two chains ($d(\text{Ga-D}) = 209.0(2)$ pm). Refinements using the proposed 8*g* split-site show the tendency to move towards each other leading to the higher symmetry site. Within the gallium zigzag chain the distance is 245.5(5) pm which is much shorter than in the parent phase or in the NdGaD_{1.66}-superstructure model. Structural data are given in Tab. U1.2.

Desorption product Upon deuterium desorption superstructures vanish for compositions NdGaD_{<1.5}. The desorption product was characterised using a summation of *in situ* diffraction data as indicated in Fig. U1.2 (bottom, black bar at vacuum and 500 K / 300 K, see Supplement: Fig. U1.S2 / Fig. U1.S3 and Tab. U1.S3 / Tab. U1.S4). The composition reaches NdGaD_{1+x} with $x = 0.226(9)$ to 0.172(8). An *ex situ*

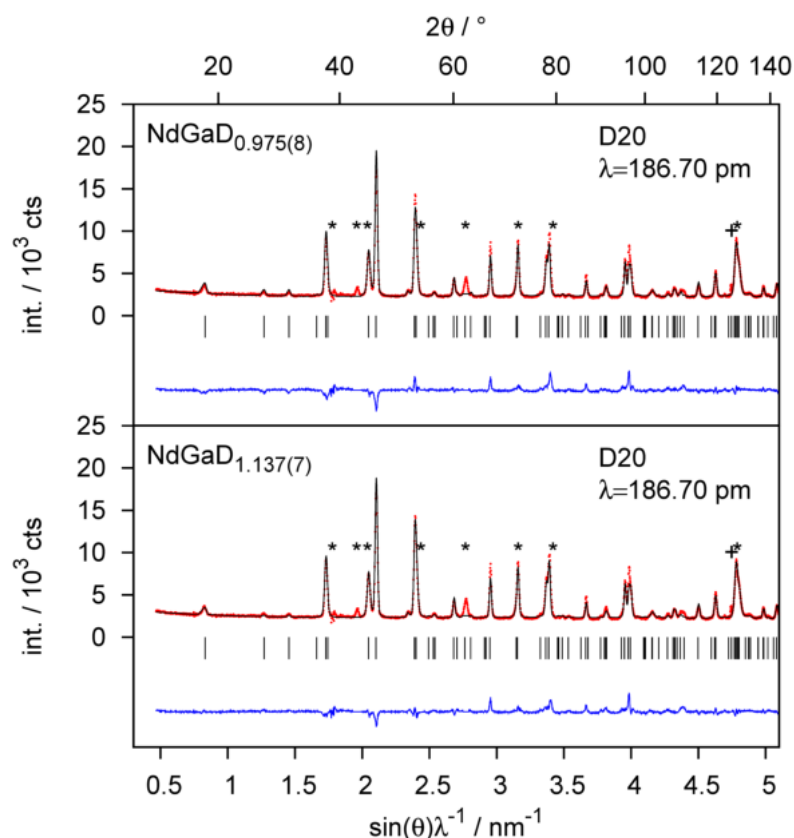


Figure U1.7: Rietveld refinement of the crystal structures of $\text{NdGaD}_{0.98}$ (**top**, $R_{\text{exp}} = 1.83\%$, $R_{\text{wp}} = 6.33\%$, $R_{\text{p}} = 4.55\%$, $\text{GoF} = 3.45$;) and $\text{NdGaD}_{1.14}$ (**bottom**, $R_{\text{exp}} = 1.83\%$, $R_{\text{wp}} = 5.89\%$, $R_{\text{p}} = 4.14\%$, $\text{GoF} = 3.22$;) using the same data set (298(2) K, vanadium cylinder). The difference between a model with and without a gallium chain coordinating deuterium site (D2) is shown. Structural data are given in Tab. U1.3 and U1.4, respectively. (+) denotes a defect detector cell; (*) denoted the position of reflections of an unidentified side phase as already seen from the diffraction pattern of the parent phase (Fig. U1.S1). The corresponding structural data are given in Tab. U1.3 ($\text{NdGaD}_{0.98}$) and Tab. U1.4 ($\text{NdGaD}_{1.14}$).

diffraction after recovering the desorption product at ambient temperature leads to $\text{NdGaD}_{1.137(7)}$. The Rietveld refinement was done using a structure model with and without deuterium between the chains (Fig. U1.7, Tab. U1.4 and U1.3). Profile fit as well as reliability factors degrade for the latter model. *Ångström* et. al could show in absorption experiments the immediate formation of a phase NdGaH_{1+x} , $x > 0$ [13] that might correspond to the desorption product as lower limit for hydrogen incorporation. Furthermore, they showed a two-step desorption until NdGa was reformed. We stopped the reaction after the first desorption step and showed that hydrogen remains on the gallium chain coordination D2 site. The phases with low D2 occupation, i.e. NdGaD_{1+x} with $x = 0.14 - 0.17$, show a Ga-Ga distance within the zigzag chain of 247 - 250 pm which is smaller than in the phases of higher hydrogen content (259 pm). This trend was predicted by DFT calculations comparing hypothetical NdGaH_1 ($d(\text{Ga-Ga}) = 251$ pm) and NdGaH_2 ($d(\text{Ga-Ga}) = 257$ pm) [13].

Conclusion

The Zintl phases AeTt ($\text{Ae} = \text{Ca-Ba}$, $\text{Tt} = \text{Si-Sn}$) and NdGa are isotopic. Furthermore the polyanions are composed of pseudo-pnicogens, i.e. Tt^{2-} and Ga^{3-} , forming zigzag chains. The hydrogenation products show similarities as well, like $\text{HAe}_4(\text{HNd}_4)$ -tetrahedra and additional hydrogen atoms between the polyanionic chains. Nevertheless the bonding situation towards the Tt and gallium is quite different. While the existence of a covalent Tt-H bond was established [15–17], the Ga-H distance is quite long (≈ 200 pm) and the coordination can be described as trigonal bipyramidal by Nd in the equatorial plane

Table U1.3: Structural data of NdGaD_{0.975(8)} at 298(2) K (vanadium cylinder); *Cmcm* (no superstructure), $a = 416.62(3)$ pm, $b = 1203.33(10)$ pm, $c = 418.65(2)$ pm; $R_{\text{exp}} = 1.83\%$, $R_{\text{wp}} = 6.33\%$, $R_{\text{p}} = 4.55\%$, GoF = 3.45; The structure model with additional deuterium between the gallium chains according to Tab. U1.4 improves the refinement. $d(\text{Ga-Ga}) = 247.5(4)$ pm. $B_{\text{iso}}(\text{Nd})$ was fixed at a value comparable to the refinement using a D2-site. Otherwise it becomes negative but deviation from 0 is less than 2 e.s.u.

atom	Wyck.	x	y	z	$B_{\text{iso}}/10^4 \text{ pm}^2$	SOF
Ga	4c	0	0.0549(4)	$1/4$	0.27(7)	
Nd	4c	0	0.3453(3)	$1/4$	0.1	
D1	4c	0	0.7510(3)	$1/4$	0.96(7)	1

Table U1.4: Structural data of NdGaD_{1.137(7)} at 298(2) K (vanadium cylinder) *Cmcm* (no superstructure), $a = 416.63(8)$ pm, $b = 1203.50(9)$ pm, $c = 418.63(2)$ pm; $R_{\text{exp}} = 1.83\%$, $R_{\text{wp}} = 5.89\%$, $R_{\text{p}} = 4.14\%$, GoF = 3.22; $d(\text{Ga-Ga}) = 249.5(3)$ pm. SOF and B_{iso} of D2 strongly correlate. Free refinement of $B_{\text{iso}}(\text{D2})$ leads to a value $> 15 \cdot 10^4 \text{ pm}^2$ and, thus, was fixed. Refinement of $z(\text{D2})$ leads to a movement towards the DNd_4 -tetrahedron and a short D-D distance. Thus, it was constraint to be at the same y coordinate as Ga.

atom	Wyck.	x	y	z	$B_{\text{iso}}/10^4 \text{ pm}^2$	SOF
Ga	4c	0	0.0564(3)	$1/4$	0.14(7)	
Nd	4c	0	0.3451(2)	$1/4$	0.05(7)	
D1	4c	0	0.7492(3)	$1/4$	1.02(6)	1
D2	4c	0	$= y(\text{Ga})+0.5$	$1/4$	3	0.137(7)

and Ga on top and bottom [13].

This work elucidates another major difference: NdGaH_{1+x} shows a large phase width with x reaching at least from 0.1 to 0.8. By contrast, the *AeTh_y*-systems show distinct structure types without or with only a small variability in hydrogen occupation. Furthermore, hydrogen poor $\text{NdGaH}_{<1}$ phases were not observed. The changing hydrogen content shows no volume effect, but lattice parameter ratios change. There is a linear behaviour of the b/c -ratio in regard to the occupation of chain coordination hydrogen site (x in NdGaH_{1+x}). In contrast, a/c decreases linear up to $x \approx 0.6$ and then starts to increase slightly again. The Ga-Ga distance in crystallographic a direction in the hydrogen free phase NdGa is similar to the distance in a Ga-H-Ga-moiety, while $d(\text{Ga-Ga})$ decreases if no hydrogen is incorporated as seen from the crystal structure of $\text{NdGaD}_{1.66}$.

Superstructures occur for special hydrogen occupations. They lead to a doubling or tripling of lattice parameter a . A possible interpretation is that at least partial ordering of hydrogen between the zigzag chains occurs. For the two-fold superstructure no proper model could be determined due to the small intensities of the superstructure reflections and the presence of an non-determined side phase. A model of the three-fold superstructure was refined showing a $\frac{1}{\infty}[(\text{Ga-H-Ga-H-Ga})^{6-}]$ -moiety as predicted by DFT calculations [13]. This structure shows hydrogen bridging two gallium-chains almost in the middle confirming the previous discussion.

U1.3 Supplement

Subgroup candidates for two-fold superstructures

Table U1.S1: Space group type candidates of a twofold superstructure ($a' = 2a$) derived from the crystal structure of NdGa by group-subgroup relations. There are seven possible paths that keep the orthorhombic crystal system and centro-symmetry. Transformation matrices P are given according to the *International Tables of Crystallography* [24].

$$Cmcm \longrightarrow Pbcm \longrightarrow Pnma$$

$$Pnma \text{ (No. 62): } P = \begin{pmatrix} 0 & 0 & 2 & 1/4 \\ 1 & 0 & 0 & 1/4 \\ 0 & 1 & 0 & 0 \end{pmatrix}$$

$$Cmcm \longrightarrow Pbcm \longrightarrow Pbca$$

$$Pbca \text{ (No. 61): } P = \begin{pmatrix} 2 & 0 & 0 & 1/4 \\ 0 & 1 & 0 & 1/4 \\ 0 & 0 & 1 & 0 \end{pmatrix}$$

$$Cmcm \longrightarrow Pbcm \longrightarrow Pbcn$$

$$Pbcn \text{ (No. 60): } P = \begin{pmatrix} 0 & 2 & 0 & 1/4 \\ 0 & 0 & 1 & 1/4 \\ 1 & 0 & 0 & 0 \end{pmatrix}$$

$$Cmcm \longrightarrow Pbcm \longrightarrow Pbcm$$

$$Pbcm \text{ (No. 57): } P = \begin{pmatrix} 2 & 0 & 0 & 1/4 \\ 0 & 1 & 0 & 1/4 \\ 0 & 0 & 1 & 0 \end{pmatrix}$$

$$Cmcm \longrightarrow Pmma \longrightarrow Pmnn$$

$$Pmnn \text{ (No. 59): } P = \begin{pmatrix} 0 & 2 & 0 & 0 \\ 0 & 0 & 1 & 0 \\ 1 & 0 & 0 & 0 \end{pmatrix}$$

$$Cmcm \longrightarrow Pmma \longrightarrow Pmna$$

$$Pmna \text{ (No. 53): } P = \begin{pmatrix} 2 & 0 & 0 & 0 \\ 0 & 1 & 0 & 0 \\ 0 & 0 & 1 & 0 \end{pmatrix}$$

$$Cmcm \longrightarrow Pmma \longrightarrow Pmma$$

$$Pmma \text{ (No. 51): } P = \begin{pmatrix} 0 & 2 & 0 & 0 \\ 0 & 0 & 1 & 0 \\ 1 & 0 & 0 & 0 \end{pmatrix}$$

NdGa, vanadium-cylinder, 298(2) K:

There is a non-described side phase present in the sample of NdGa. Still, the Rietveld refinement leads to the same structural data as described before [13].

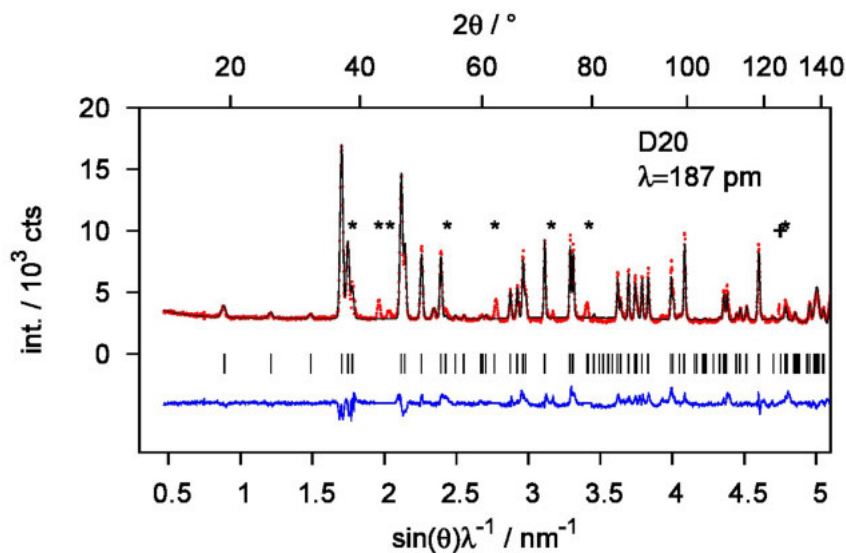


Figure U1.S1: Rietveld refinement of the crystal structure of NdGa. (*) denotes a non-described side phase; (+) denotes a defect detector cell.

Table U1.S2: Structural data of NdGa $Cmcm$, $a = 443.05(2)$ pm, $b = 1125.14(5)$ pm, $c = 418.15(2)$ pm; $R_{\text{exp}} = 1.67\%$, $R_{\text{wp}} = 6.52\%$, $R_{\text{p}} = 4.88\%$, $\text{GoF} = 3.90$; $d(\text{Ga-Ga}) = 262.0(3)$ pm; $B_{\text{iso}}(\text{Nd})$ refined to about $0.0(2)$ and was fixed at a reasonable value.

atom	Wyck.	x	y	z	$B_{\text{iso}} / 10^4 \text{ pm}^2$	SOF
Ga	$4c$	0	0.0702(2)	$1/4$	0.64(8)	
Nd	$4c$	0	0.35606(15)	$1/4$	0.2	

NdGaD_{1,23}, sapphire-cell, 500(2) K, vacuum:

Rietveld refinement results of the desorption product at high temperature. *In situ* diffraction data are summed as indicated in Fig. U1.2 (bottom, black bar)

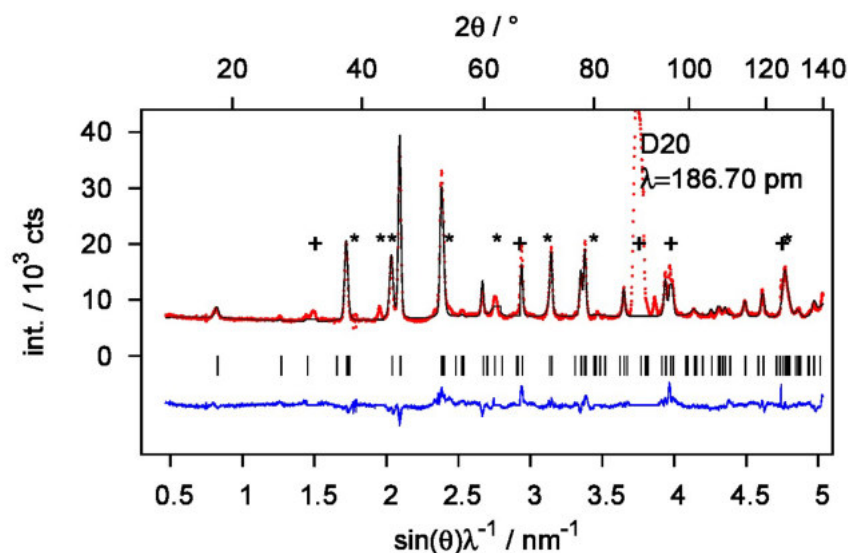


Figure U1.S2: Rietveld refinement of the crystal structure of NdGaD_{1,23}. (*) denotes a non-described side phase; (+) denotes sapphire-cell reflections.

Table U1.S3: Structural data of NdGaD_{1,23} *Cmcm* (no superstructure), $a = 416.69(4)$ pm, $b = 1207.99(12)$ pm, $c = 419.15(4)$ pm; $R_{\text{exp}} = 1.09\%$, $R_{\text{wp}} = 5.92\%$, $R_{\text{p}} = 4.62\%$, $\text{GoF} = 5.42$; $d(\text{Ga-Ga}) = 250.4(4)$ pm. SOF and B_{iso} of D2 strongly correlate. Free refinement of $B_{\text{iso}}(\text{D2})$ leads to a value $> 15 \cdot 10^4 \text{ pm}^2$ and thus, was fixed at a reasonable value. Refinement of $y(\text{D2})$ leads to a movement towards the DNd_4 -tetrahedron und a short D-D-distance, thus, it was constraint to be on the same y coordinate as Ga. $B_{\text{iso}}(\text{Nd})$ and $B_{\text{iso}}(\text{Ga})$ needed to be fixed at reasonable values.

atom	Wyck.	x	y	z	$B_{\text{iso}} / 10^4 \text{ pm}^2$	SOF
Ga	$4c$	0	0.0567(4)	$1/4$	0.8	
Nd	$4c$	0	0.3465(3)	$1/4$	0.2	
D1	$4c$	0	0.7465(4)	$1/4$	2.57(11)	1
D2	$4c$	0	$= y(\text{Ga}) + 0.5$	$1/4$	3	0.226(9)

NdGaD_{1.17}, sapphire-cell, 300(5) K, vacuum:

Rietveld refinement results of the desorption product after cooling down. *In situ* diffraction data are summed as indicated in Fig. U1.2 (bottom, black bar)

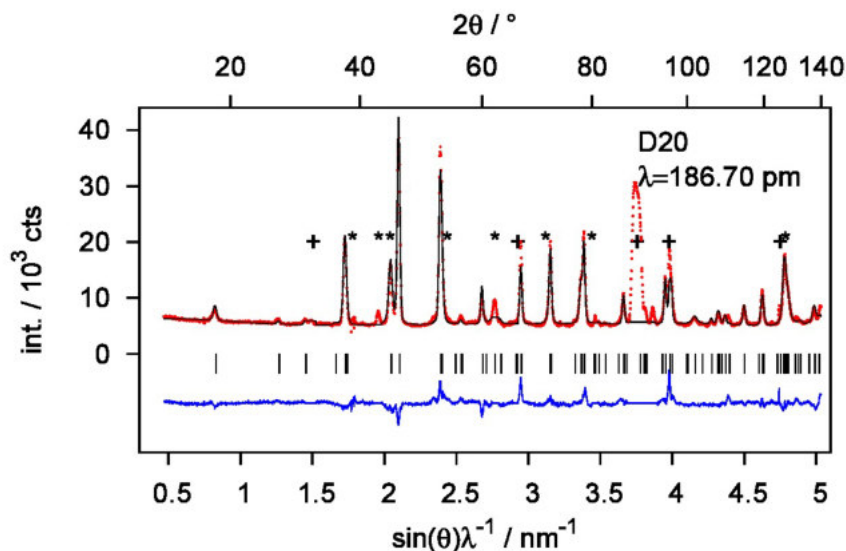


Figure U1.S3: Rietveld refinement of the crystal structure of NdGaD_{1.17}. (*) denotes a non-described side phase; (+) denotes sapphire-cell reflections.

Table U1.S4: Structural data of NdGaD_{1.17} *Cmcm* (no superstructure), $a = 416.17(4)$ pm, $b = 1202.22(12)$ pm, $c = 418.06(3)$ pm; $R_{\text{exp}} = 1.19\%$, $R_{\text{wp}} = 7.00\%$, $R_p = 5.19\%$, $\text{GoF} = 5.86$; $d(\text{Ga-Ga}) = 247.2(4)$ pm. *SOF* and B_{iso} of D2 strongly correlate. Free refinement of $B_{\text{iso}}(\text{D2})$ leads to a value $> 15 \cdot 10^4$ pm² and thus, was fixed at a reasonable value. Refinement of $y(\text{D2})$ leads to a movement towards the DNd₄-tetrahedron und a short D-D distance, thus, it was constraint to be on the same y coordinate as Ga. $B_{\text{iso}}(\text{Nd})$ and $B_{\text{iso}}(\text{Ga})$ needed to be fixed at reasonable values.

atom	Wyck.	x	y	z	$B_{\text{iso}} / 10^4 \text{ pm}^2$	<i>SOF</i>
Ga	$4c$	0	0.0549(4)	$1/4$	0.8	
Nd	$4c$	0	0.3455(3)	$1/4$	0.2	
D1	$4c$	0	0.7487(4)	$1/4$	1.88(11)	1
D2	$4c$	0	$= y(\text{Ga})+0.5$	$1/4$	3	0.172(8)

U2 Collection of unpublished results

U2.1 Hydrogenation of CaGa

Introduction

In contrast to the electron-rich $LnTt$ or electron-precise $AeTt$, Ln = lanthanoid, Ae = alkaline earth metal, Tt = tetrel, CaGa is an electron poor system. It still shows ${}^1_\infty[Tt]$ -zigzag chains (CrB-structure type as the phases above). Band structure calculations have shown that π -states completely lie above the Fermi-level and chains start to interact σ -like perpendicular to the chains [25]. According to the Zintl concept CaGa is supposed to contain three-binding Ga^{2-} -atoms. The situation is therefore comparable to the hypothetical $AeTtH$ -phases (Sec. 4.3.3). Thus, the incorporation of hydrogen between the chains of CaGa is likely.

Synthesis

All manipulations were done in an argon-filled glove box. CaGa shows a peritectic decomposition at 1068 K [26]. A stoichiometric mixture of calcium and gallium was sealed inside a niobium-metal jacket. The container was heated under vacuum (active pumping) to 1275 K (1 K min^{-1}) and quenched in cold water. Afterwards, the metal jacket with the sample was annealed for another 24 h at 1000 K.

Thermal analysis

Differential scanning calorimetry was done *in situ* (H_2 -DSC, Q1000 TA Instruments) under hydrogen pressure to monitor the hydrogenation reaction of CaGa (Fig. U2.1). There is a strong exothermic signal above 500 K which can be attributed to the decomposition into CaH_2 and Ca_3Ga_8 . Especially the formation of an ionic hydride usually leads to strong H_2 -DSC signals. There is a reaction at lower temperatures that gives no signal at all (see below).

A H_2 -DSC experiment (5 MPa H_2) was stopped at 475 K right before the exothermic signal occurs. *Ex situ* characterisation showed already the decomposition into an amorphous product. Stopping an experiment at even lower temperature (420 K) still shows the precursor phase as well as a starting decomposition into an amorphous phase and small reflections of a new phase.

In situ diffraction

In situ diffraction was done using the laboratory set up of a Huber G670 Guinier diffractometer. Given temperatures are calibrated according to $T_{\text{sample}} = 0.85 T_{\text{HTC}}$ (HTC = high temperature controller). Experiments were done at 5 MPa hydrogen pressure and repeated several times. Stepwise heating with 0.85 K per 15 min leads to the formation of a new phase at about 415 K (Fig. U2.2, marked as (*)). At the

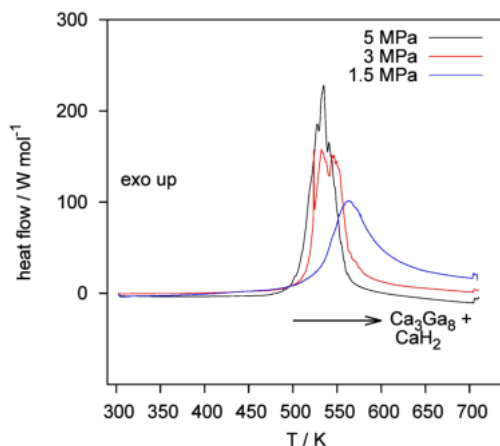


Figure U2.1: H_2 -DSC of CaGa at several hydrogen gas pressures.

same time a broad peak of an amorphous decomposition product appears (Fig. U2.2, $2\theta \approx 15^\circ$). Keeping the temperature for 10 h at 420 K increases the amount of new phase compared to the amorphous phase. Going to higher temperatures (> 500 K) leads to the formation of CaH_2 and Ca_3Ga_8 (Fig. U2.3) which corresponds to the exothermic signal of the H_2 -DSC experiment. Finally, the reaction was investigated isothermally at 420 K and 5 MPa H_2 with 30 min time resolution per frame (Fig. U2.4). Already after 4 h the intensities do not change any longer. The new phases is forming only as long as precursor phase is present. Thus, a crystallisation from the amorphous phase can be excluded.

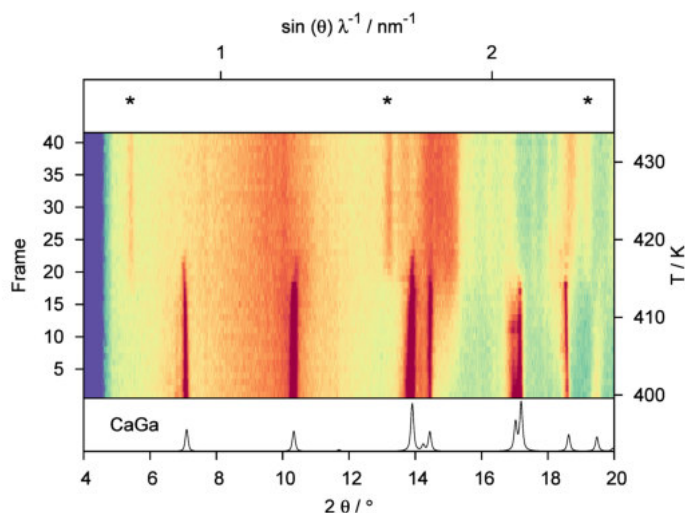


Figure U2.2: *In situ* diffraction (Mo- $\text{K}_{\alpha 1}$ -radiation) of the reaction of CaGa at 5 MPa H_2 . Diffraction patterns were collected with 15 min exposition time. The heating rate was 0.85 K per frame (1 K/frame at HTC). The precursor phase is shown below. Characteristic reflections of the new phase are marked above (*, see Fig. U2.5 for reference). The broad peak occurring at $2\theta \approx 15^\circ$ corresponds to an amorphous phase.

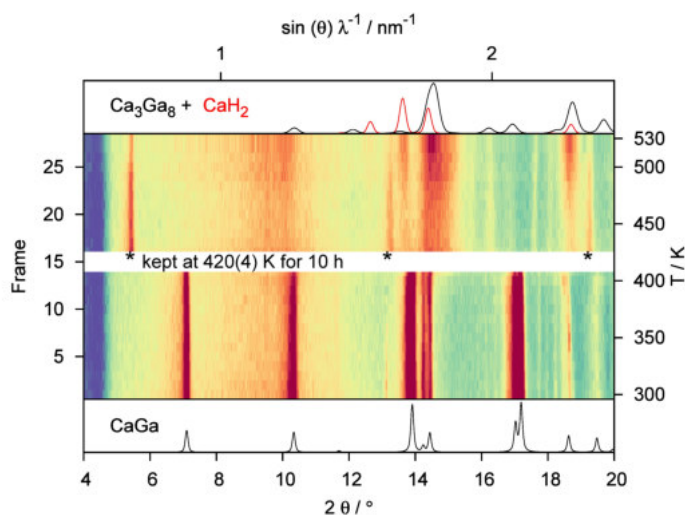


Figure U2.3: *In situ* diffraction (Mo- $\text{K}_{\alpha 1}$ -radiation) of the reaction of CaGa at 5 MPa H_2 . Diffraction patterns were collected with 15 min exposition time. The heating rate was 8.5 K per frame (10 K/frame at HTC). The sample was kept for 10h at 420(4) K (443 K at HTC) without collecting diffraction patterns. The precursor phase is shown below. Characteristic reflections of the new phase are marked in the middle (*, see Fig. U2.5 for reference). Additionally the crystalline decomposition products CaH_2 and Ca_3Ga_8 are shown above.

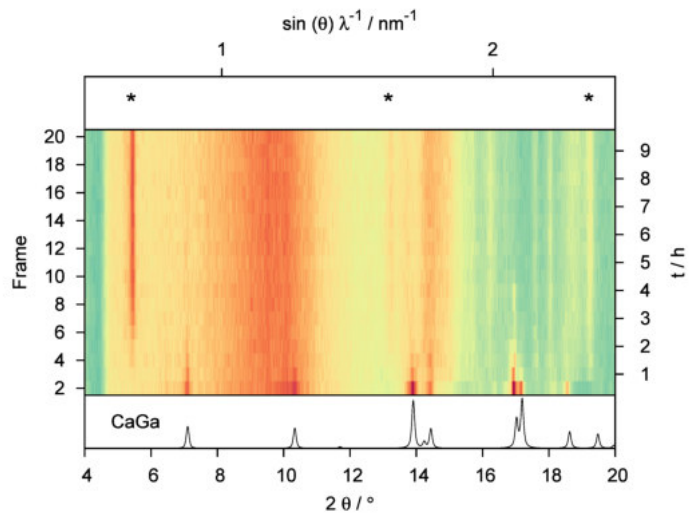


Figure U2.4: *In situ* diffraction (Mo- $K_{\alpha 1}$ -radiation) of the isothermal reaction of CaGa at 420(4) K (443 K at HTC) and 5 MPa H_2 . Diffraction patterns were collected with 30 min exposition time. The precursor phase is shown below. Characteristic reflections of the new phase are marked above (*, see Fig. U2.5 for reference).

Overview of diffraction patterns

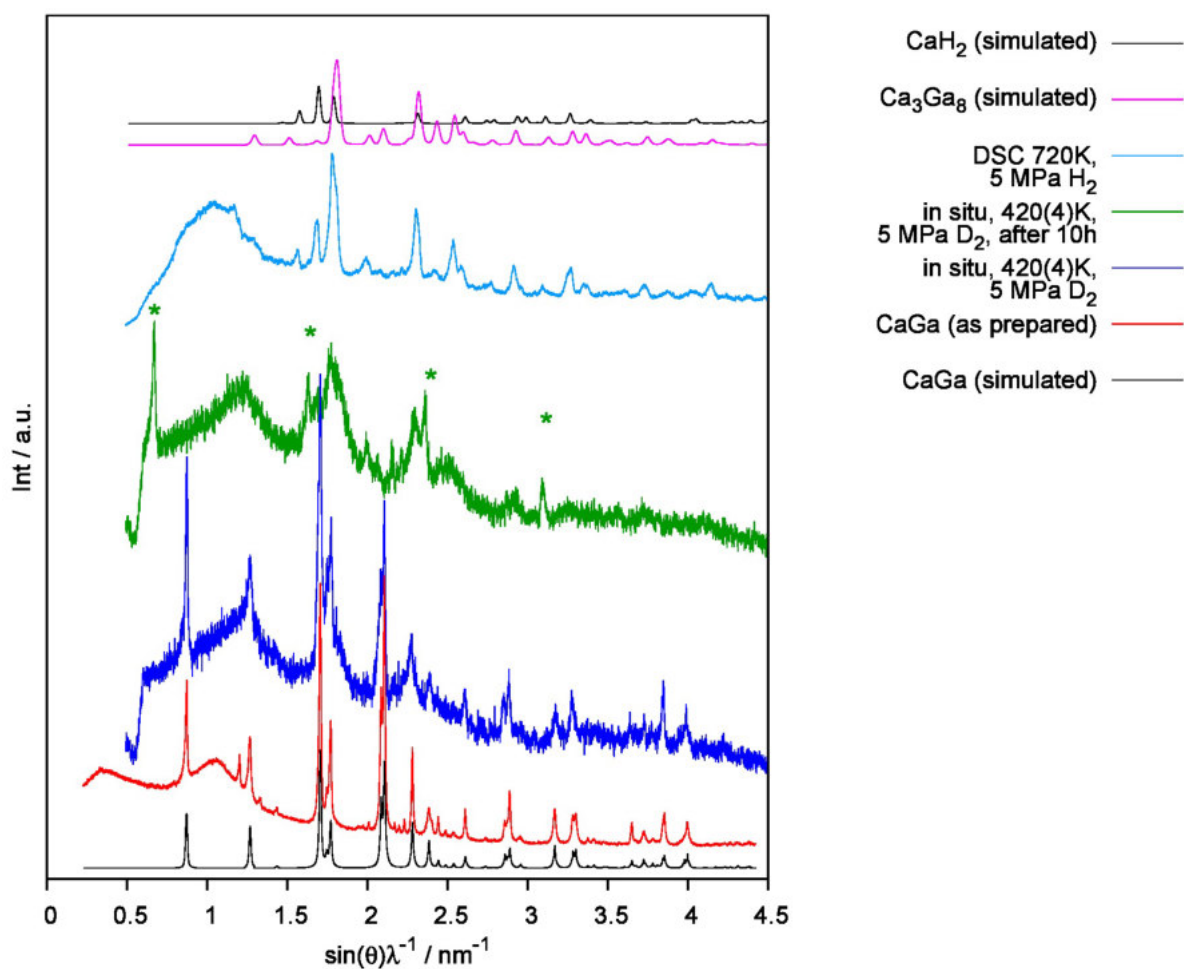


Figure U2.5: Different steps of the reaction of CaGa under hydrogen pressure. During the *in situ* (Fig. U2.4) experiment a new phase occurs (green, marked with *). The first reflection corresponds to a d -spacing of about 750 pm. The formation of the intermediate phase and the decomposition to an amorphous, already Ca_3Ga_8 -like phase occur at similar temperatures. Thus, *ex situ* preparation was not possible yet.

Summary

There are some preliminary result on the hydrogenation of CaGa. At 5 MPa hydrogen pressure and low temperatures (420 K) the formation of a new phase can be observed. This formation is accompanied by a decomposition into an amorphous product. Further heating at 5 MPa H_2 leads to the crystallisation of CaH_2 and Ca_3Ga_8 .

U2.2 Hydrogenation of Ae_8Ga_7 , $Ae = Sr, Ba$

Introduction

There are no phases $AeGa$ for $Ae = Sr$ or Ba . Instead the isotypic compounds Ae_8Ga_7 are formed. These phases show two types of polyanions, Ga_4^{8-} -tetrahedra (*nido*-cluster) and Ga_3^{8-} -three-membered rings (electron deficient *arachno*-cluster). Tetrahedral polyanions also occur in the phases ASi ($A = K - Cs$) which are reactive towards hydrogen. Furthermore, electronically imbalanced Zintl phases appear as a good starting point for hydrogenation experiments [27].

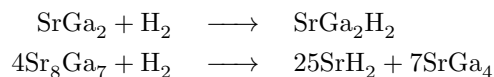
Synthesis

All preparations were done in an argon-filled glove box. Stoichiometric mixtures of the elements were placed in niobium-metal jackets. Samples were heated under vacuum to 1270 K and quenched in cold water. According to the phase diagrams the phases Ba_8Ga_7 and Sr_8Ga_7 show a peritectic decomposition at 857 K and 983 K, respectively [28, 29]. Samples were annealed about 50 K below the decomposition temperature for 24h.

Hydrogenation of Sr_8Ga_7

The prepared sample of Sr_8Ga_7 shows a high content of $SrGa_2$ (about 50 wt-% phase fraction, Fig. U2.6). Still, this sample was used for preliminary experiments to test the reactivity towards hydrogen. *In situ* differential scanning calorimetry (H_2 -DSC) at 5 MPa H_2 pressure shows two strong exothermic signals during the first cycle and a small reversible one at high temperatures that is present during a second cycle as well (Fig. U2.7).

The *in situ* DSC experiment heating up to 700 K leads to the formation of $SrGa_4$ and SrH_2 (XRPD: Fig. U2.8). An other *in situ* DSC experiment at the same pressure was stopped after the first exothermic signal at 550 K. *Ex situ* characterisation shows the formation of $SrGa_2H_2$ as well as SrH_2 and $SrGa_4$ (Fig. U2.9). Thus, for the first exothermic DSC signal two reactions can be distinguished:



The corresponding phase fractions fit well, i.e. the molar ratio $SrH_2:SrGa_4$ is 0.80:0.20. The theoretical ratio is 0.78:0.22. The formation of $SrGa_2H_2$ from $SrGa_2$ at this temperature fits literature results [30]. The second DSC signal, thus corresponds to the decomposition of $SrGa_2H_2$ into SrH_2 and $SrGa_4$ which was reported before as well. The reversible effect shown by the *in situ* DSC at 670 K needs to be related to the decomposition products and was not investigated any further.

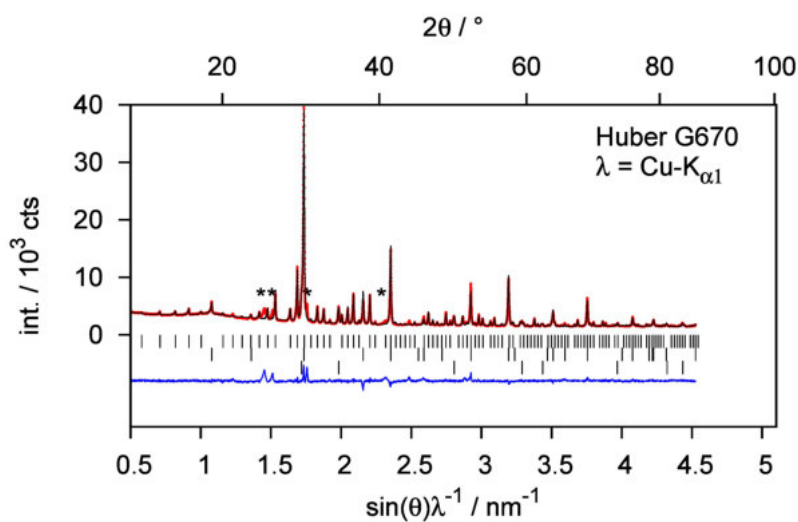


Figure U2.6: Phase analysis of the Sr_8Ga_7 -sample. The phases according to Bragg-markers from top to bottom are: Sr_8Ga_7 (44 wt-%), SrGa_2 (50 wt-%) and SrO (6 wt-%). (*) marks an unidentified phase, that does not change during the hydrogenation reactions.

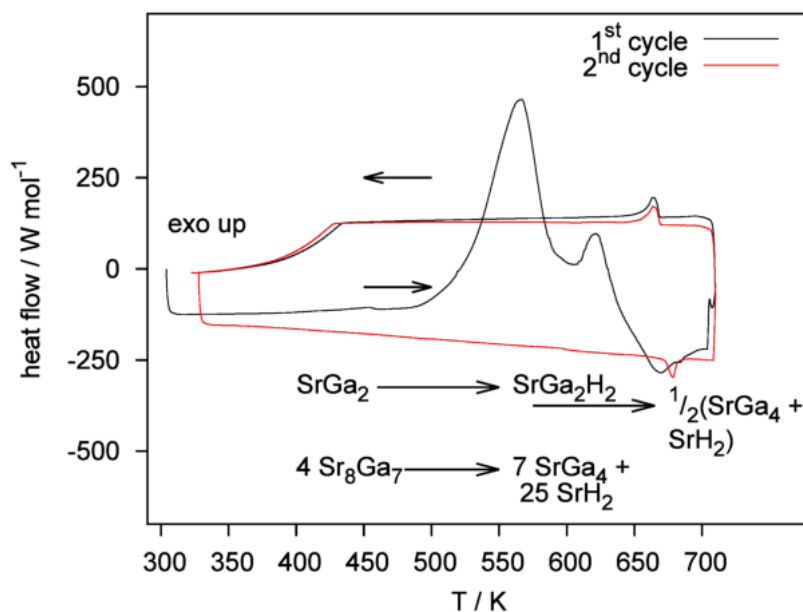


Figure U2.7: H_2 -DSC of the Sr_8Ga_7 -sample (50 wt-% SrGa_2) at 5 MPa H_2 pressure. *Ex situ* characterisation the product of this experiment (Fig. U2.8) and of another experiment stopped at 550 K (Fig. U2.9) leads to the assignment of the different reactions.

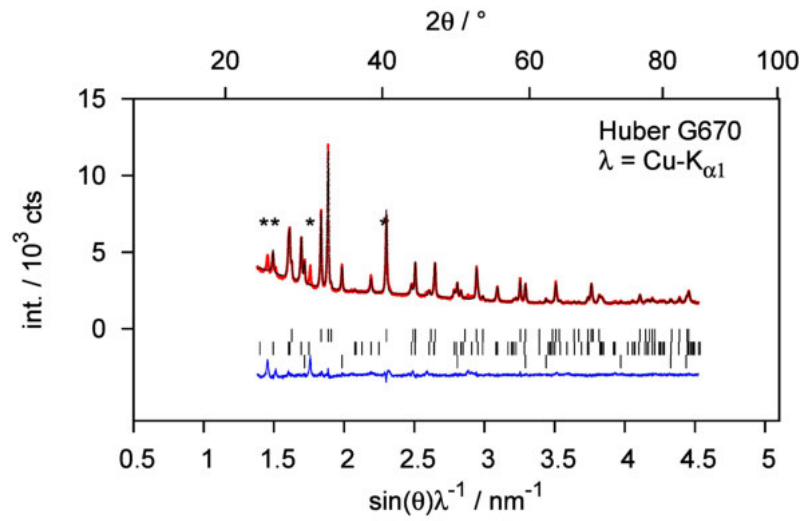


Figure U2.8: Phase analysis of the Sr_8Ga_7 -sample after hydrogenation at 700 K and 5 MPa H_2 pressure. The phases according to Bragg-markers from top to bottom are: SrGa_4 (64 wt-%), SrH_2 (26 wt-%) and SrO (10 wt-%). (*) marks an unidentified phase, that did not change during the hydrogenation.

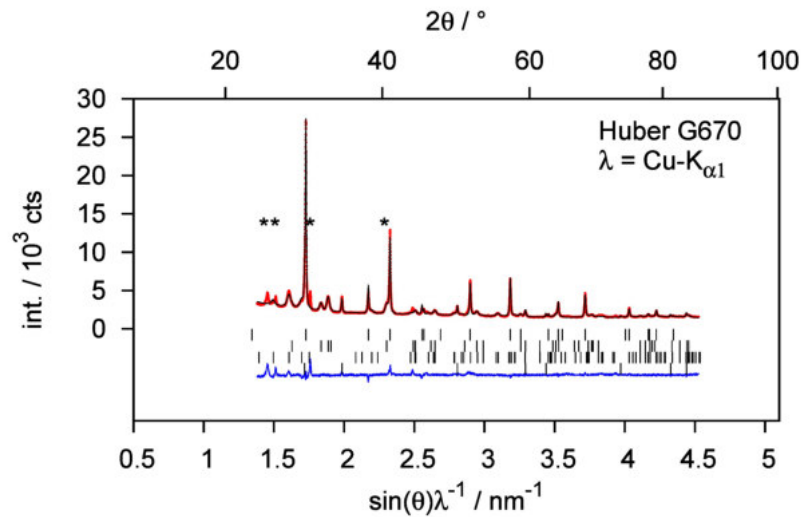


Figure U2.9: Phase analysis of the Sr_8Ga_7 -sample after hydrogenation at 550 K and 5 MPa H_2 pressure. The phases according to Bragg-markers from top to bottom are: SrGa_2H_2 (54 wt-%) SrGa_4 (20 wt-%), SrH_2 (20 wt-%) and SrO (6 wt-%). (*) marks an unidentified phase, that did not change during the hydrogenation.

Hydrogenation of Ba_8Ga_7

The sample of Ba_8Ga_7 is phase pure except for about 6 wt-% BaO (Fig. U2.10). *In situ* differential scanning calorimetry (H_2 -DSC) at 5 MPa H_2 pressure shows one strong exothermic signal at even lower temperatures than the Sr_8Ga_7 -sample (Fig. U2.11). *Ex situ* characterisation of the reaction product shows the decomposition into BaGa_4 and BaH_2 (Fig. U2.12). The molar ratio of the decomposition products determined by Phase analysis ($\text{BaGa}_4:\text{BaH}_2 = 0.22:0.78$) fit the theoretical ratio (0.25:0.75) reasonably.

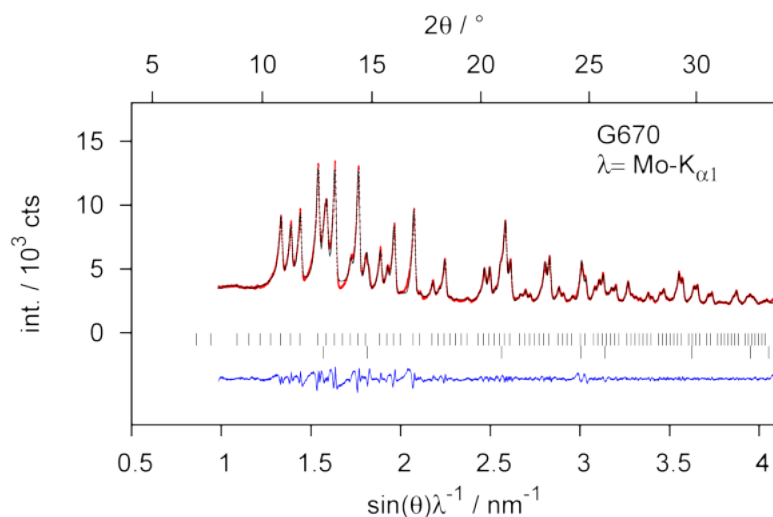


Figure U2.10: Phase analysis of the Ba_8Ga_7 -sample. The phases according to Bragg-markers from top to bottom are: Ba_8Ga_7 (94 wt-%) and BaO (6 wt-%).

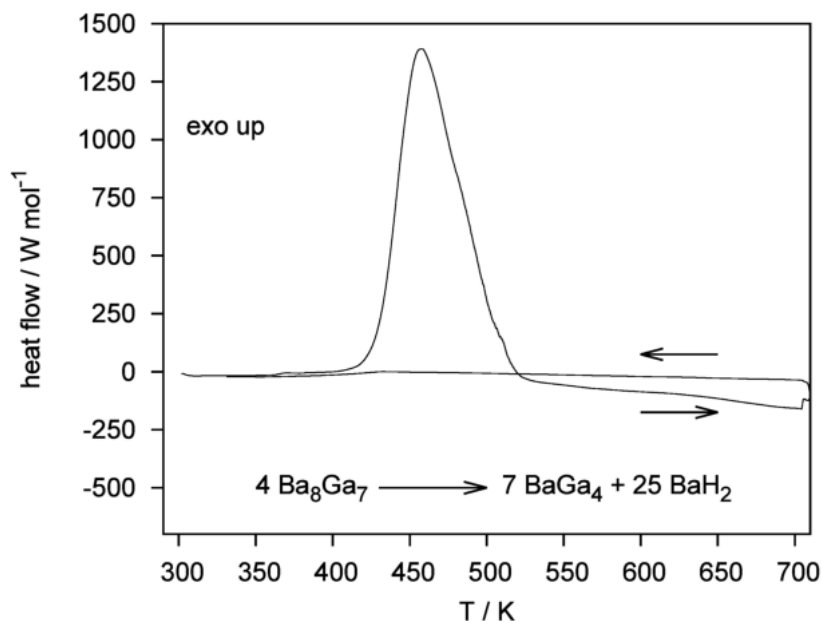


Figure U2.11: H_2 -DSC of the Ba_8Ga_7 -sample at 5 MPa H_2 pressure. *Ex situ* characterisation the product of this experiment (Fig. U2.12) shows a decomposition according to the reaction given in the graph.

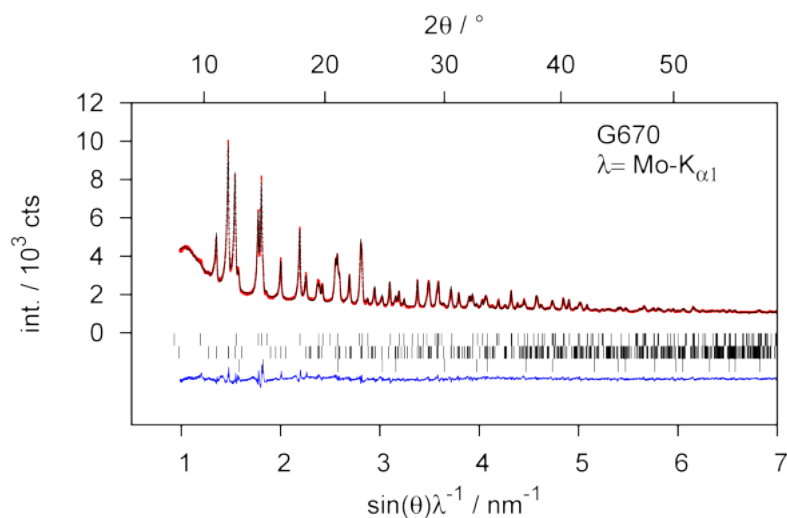


Figure U2.12: Phase analysis of the Ba_8Ga_7 -sample after H_2 -DSC (Fig. U2.11). The phases according to Bragg-markers from top to bottom are: $BaGa_4$ (47 wt-%), BaH_2 (48 wt-%) and BaO (5 wt-%).

Summary

The Phases Sr_8Ga_7 and Ba_8Ga_7 show a decomposition into binary hydride and a gallium-rich phase. According to Scheme 2.1 (Sec. 2.3.1, p. 10) this might be interpreted as the final step after an interstitial hydride formation. The formation and incorporation of a hydride anion typically shows a strong exothermic H_2 DSC Signal. Reactions can be assigned to all thermal analysis peaks. Thus, the formation of an interstitial hydride as intermediate phase is not likely.

Furthermore the formation of a polyanionic hydride is possible, i.e. similar to the reaction of KSi which shows tetrahedral polyanions as well. Reactions at low temperatures, i.e. below the DSC peaks, were not conducted, yet.

U2.3 Hydrogenation of $AeTt_2$ ($Ae = Ca, Sr, Ba$; $Tt = Si, Ge$)

Introduction

The $AeTt_2$ -systems exhibit several structure types. They show three-binding polyanions as expected from the Zintl concept. The $BaSi_2$ -structure type exhibits Si_4^{4-} -tetrahedra. $BaGe_2$ and $SrGe_2$ are isotyp. The polyanion of the $SrSi_2$ -structure type shows a three-dimensional net. $CaSi_2$ and $CaGe_2$ show layered structures with two-dimensional polyanionic nets similar to the structure of grey arsenic. The anions of these systems are highly interconnected. Thus, they were considered as promising candidates for polyanionic hydride formation since hydrogen can insert into element-element bonds. For $CaSi_2$ a hydrogen-mediated phase transition from the layered 6R- to the 3R-polymorph is described [31].

Synthesis

All manipulations were done in an argon-filled glove box. The compounds $AeTt_2$, $Ae = Sr, Ba$, $Tt = Si, Ge$, all show congruent melting points above 1370 K [32–35]. $CaGe_2$ has a melting point of 1118 K [36]. The corresponding samples were prepared from stoichiometric mixtures which were placed in a niobium or corundum container which were then sealed under argon atmosphere inside a fused-silica tube. Samples were annealed at 1275 K for about three days.

Results and summary

A hydrogenation of $AeTt_2$, $Ae = Sr, Ba$, $Tt = Si, Ge$ was attempted at 5 MPa H_2 and temperatures up to 700 K. The reaction heat was monitored *in situ* using differential scanning calorimetry (H_2 -DSC). There are no signals present at all (Fig. U2.13). Furthermore $BaSi_2$ and $BaGe_2$ were placed in an autoclave at 18 MPa H_2 and 500 K for 10h. Powder diffraction patterns were taken before and after all the hydrogenation attempts. They were identical and neither showed significant changes in intensity nor new reflections. Thus, these samples are considered to be non-reactive towards hydrogen at the given conditions.

It needs to be mentioned, that $AeTt_2$ is a typical decomposition product of $AeTtH_y$ under hydrogen pressure and high temperatures above 700 K. These decomposition products also show no signs of hydrogen uptake.

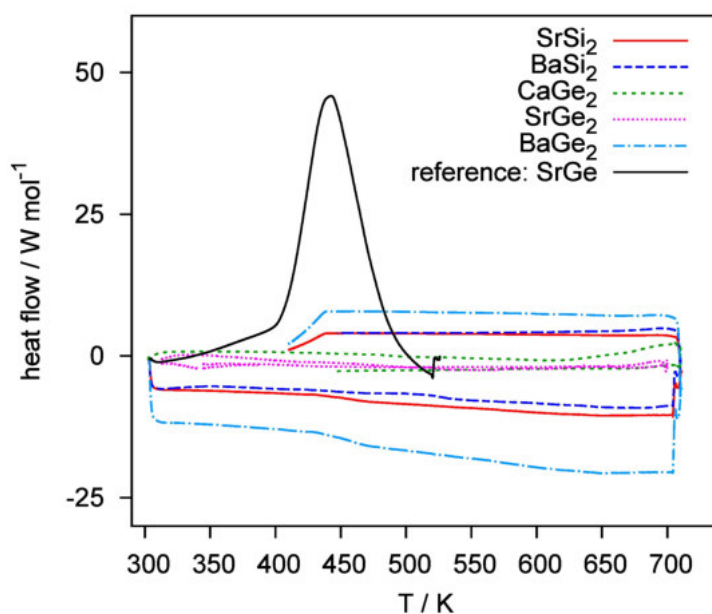


Figure U2.13: H_2 -DSC of the different $AeTt_2$ -samples ($Ae = (Ca), Sr, Ba$, $Tt = Si, Ge$) at 5 MPa H_2 pressure. There are no DSC signals detected. Diffraction patterns taken after the experiments do not show any changes. The H_2 -DSC trace of the reaction of $SrGe$ to form $SrGeH_y$ at 5 MPa H_2 is shown for reference.

U2.4 Hydrogenation of AGe, A = K, Cs

Introduction

The phases ASi and AGe ($A = \text{K, Rb, Cs}$) are isotypic and crystallize in KGe- structure type. They feature tetrahedral Si_4^{4-} (Ge_4^{4-}) polyanions, which is the structure of isovalence-electronic white phosphorous. Furthermore, the corresponding hydride phases ASiH_3 (AGeH_3) are well known from solution chemistry [37–41]. The solid-gas reaction of ASi at 5 MPa H_2 and 375 K also leads to ASiH_3 [42]. A solid state route to form AGeH_3 was not described yet. This section shows that the reaction of KGe and CsGe with hydrogen does not lead to the desired products. There are hints that the clathrate phase $\text{Cs}_8\text{Ge}_{44}\square_2$ can be formed at 5 MPa H_2 and temperatures above 700 K.

Synthesis

All manipulations were done in an argon-filled glove box. Stoichiometric mixtures of the alkaline element and germanium were placed in a corundum crucible which was sealed under argon within a fused silica tube. The samples were annealed at 775 K (KGe) or 825 K (CsGe) for 5 h.

Results

Differential scanning calorimetry was done at 5 MPa hydrogen pressure to monitor the reaction heat (H_2 -DSC, Q1000, TA Instruments). The samples show a broad but weak exothermic signal below 470 K (Fig. U2.14). This signal is reproducible with different samples and was also seen in the case of KSi [A7]. The signal occurs only during the first heating cycle of the DSC experiment. Still, *ex situ* powder diffraction shows no hint of any reaction as shown for a KGe sample (Figure U2.15). Similar problems occurred for KSi [A7]. Only CsSi [A7] and RbSi [43] showed good reactivity using the H_2 -DSC. Keeping the temperature up to 10h at 470 K still does not lead to any changes in the diffraction pattern. KGe does not show any reactivity towards hydrogen up to 5 MPa H_2 and 710 K.

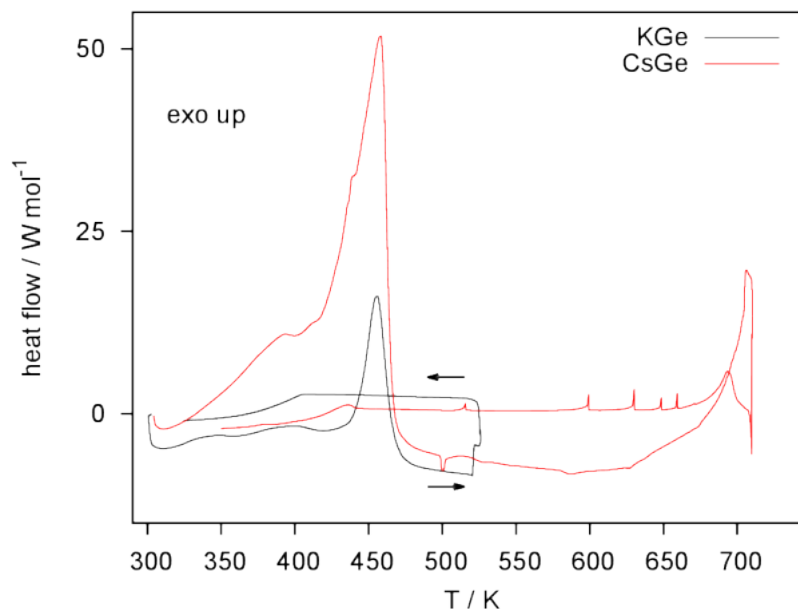


Figure U2.14: H_2 DSC of KGe and CsGe at 5 MPa H_2 pressure. The exothermic signals below 470 K are typical for the ATt -systems ($A = \text{K, Cs}$, $Tt = \text{Si, Ge}$) but cannot be assigned to any reaction. In the case of CsGe at high temperatures a decomposition into the clathrate $\text{Cs}_8\text{Ge}_{44}\square_2$ is possible (see text, Fig. U2.17).

CsGe shows no reactivity at low temperatures as well. During the H₂-DSC experiment at 700-710 K a decomposition occurs. Keeping the maximum temperature for at least 20h (two heating cycles, 10h at 710 K each) leads to a crystalline product. The diffraction pattern shows high background and several unidentified reflections (Fig. U2.17). The main reflections can be assigned to Cs₈Ge₂₂□₂ which is a clathrate phase. This is remarkable since this phase was only accessible from CsGe and Ge via high pressure high temperature synthesis [44]. The lattice parameter of the phase prepared by H₂-DSC (*Pm* $\bar{3}$ *n*, $a = 1090.99(3)$ pm) is longer than the values from the literature reaching from 1080.70(2) pm to 1084.93(3) pm [44]. Clathrate formation was described for the hydrogenation of KSi as well [45], [A7]. The sample from the DSC shows a germanium rich phase. The formation of CsH, which is most likely during the decomposition, was not obtained. The reaction could not be reproduced using an autoclave at several conditions (5.5 MPa 675 K, 10 MPa 775 K, 24 MPa 775 K, temperatures given as set point of the oven, calibrated temperature is about 70 K to 90 K below). Higher temperatures could not be realised using the available autoclaves. Increasing the pressure could not facilitate the reaction. Diffraction patterns showed no changes compared to the precursor sample.

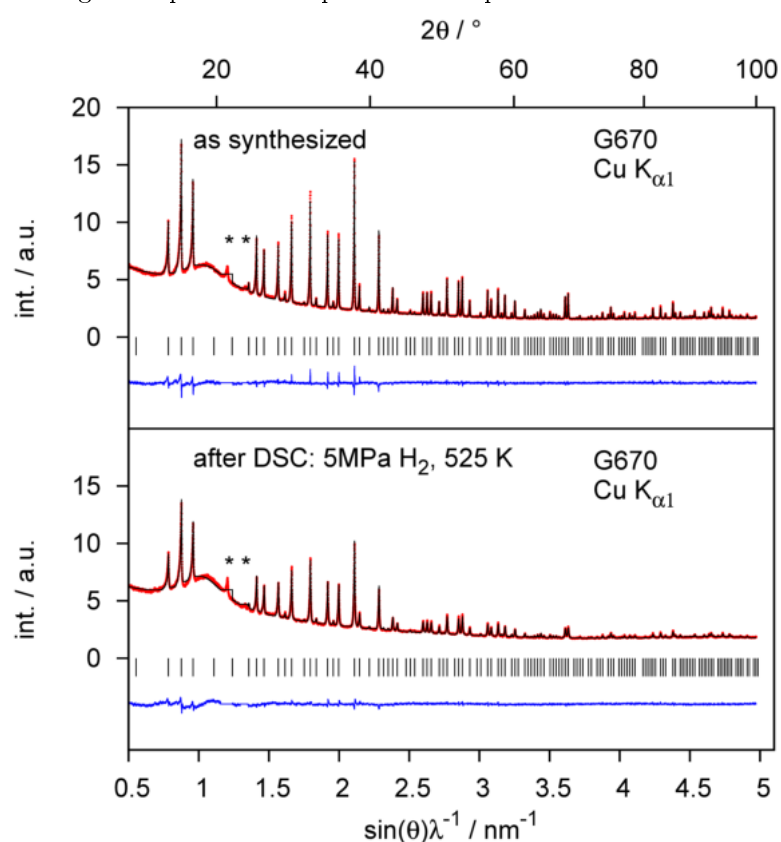


Figure U2.15: Phase analysis of the KGe-sample before and after hydrogenation. There are no other phases present. (*) marks peaks caused by the foil used for flat-sample preparation.

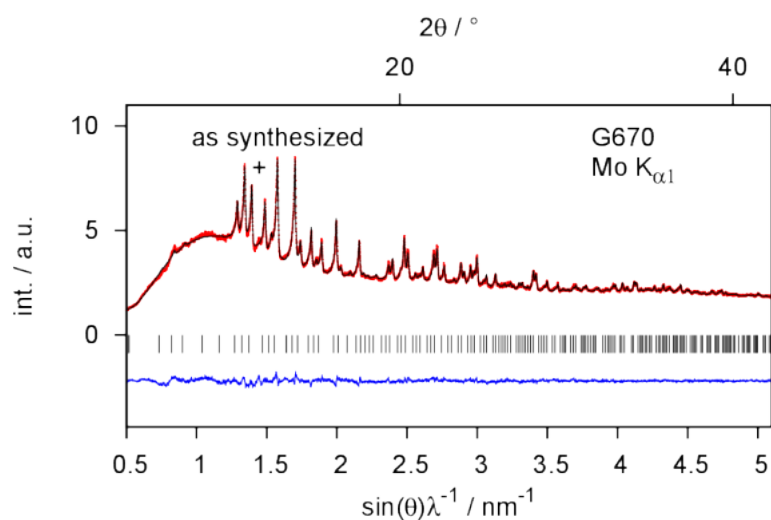


Figure U2.16: Phase analysis of the CsGe-sample. (+) marks a peak caused by the foil used for flat-sample preparation.

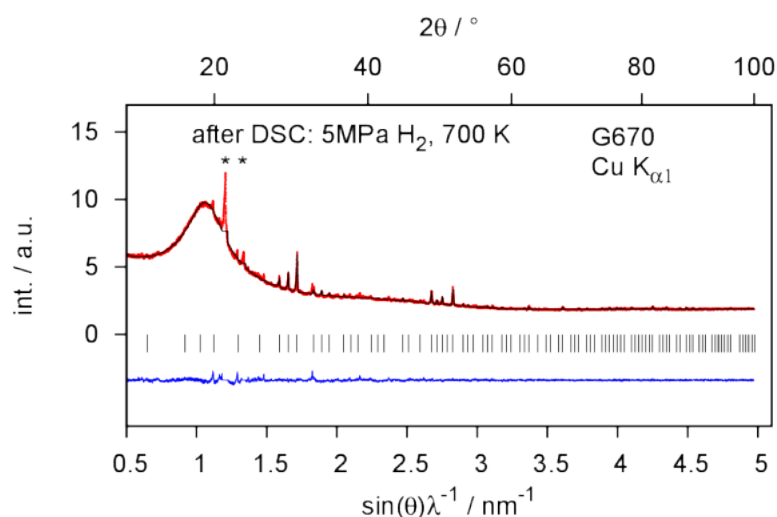


Figure U2.17: Phase analysis of the CsGe-sample after hydrogenation within the H₂-DSC. The identified phase is Cs₈Ge₄₄□₂ ($Pm\bar{3}n$, $a = 1090.99(3)$ pm). (*) marks peaks at positions typically caused by the foil used for flat-sample preparation. The peaks are unusually large, thus they might correspond to another phase.

Summary

The germanium-containing homologues of ASi ($A = \text{K}, \text{Cs}$) do not show any reactivity towards hydrogen. Even increasing the heating time did not lead any product formation. Clathrate formation known from KSi at hydrogen pressure and high temperatures was not observed in the case of KGe. There was a H₂-DSC experiment of CsGe that indicated the formation of Cs₈Ge₄₄□₂. Further experimental evidence is still missing since *ex situ* preparation was not possible yet.

U2.5 References

- (1) Gingl, F.; Vogt, T.; Akiba, E. *J. Alloys Compd.* **2000**, *306*, 127–132, DOI: 10.1016/S0925-8388(00)00755-6.
- (2) Fahlquist, H.; Noréus, D.; Sørby, M. H. *Inorg. Chem.* **2013**, *52*, 4771–4773, DOI: 10.1021/ic400224a.
- (3) Reichert, C. Untersuchungen zu Synthese und Hydrierverhalten von Verbindungen der Triele (B, Al, Ga) mit Lithium und Kalium., Ph.D. Thesis, Saarbrücken: Universität des Saarlandes, 2013.
- (4) Fahlquist, H.; Noréus, D. *Inorg. Chem.* **2013**, *52*, 7125–7129, DOI: 10.1021/ic400714e.
- (5) Fahlquist, H.; Noréus, D.; Callear, S.; David, W. I. F.; Hauback, B. C. *J. Am. Chem. Soc.* **2011**, *133*, 14574–14577, DOI: 10.1021/ja2067687.
- (6) Björling, T.; Noréus, D.; Jansson, K.; Andersson, M.; Leonova, E.; Edén, M.; Hålenius, U.; Häussermann, U. *Angew. Chem., Int. Ed.* **2005**, *44*, 7269–7273, DOI: 10.1002/anie.200502090.
- (7) Björling, T.; Noréus, D.; Häussermann, U. *J. Am. Chem. Soc.* **2006**, *128*, 817–824, DOI: 10.1021/ja054456y.
- (8) Evans, M. J.; Holland, G. P.; Garcia-Garcia, F. J.; Häussermann, U. *J. Am. Chem. Soc.* **2008**, *130*, 12139–12147, DOI: 10.1021/ja803664y.
- (9) Lee, M. H.; Björling, T.; Hauback, B. C.; Utsumi, T.; Moser, D.; Bull, D.; Noréus, D.; Sankey, O. F.; Häussermann, U. *Phys. Rev. B* **2008**, *78*, 195209, DOI: 10.1103/PhysRevB.78.195209.
- (10) Kranak, V. F.; Evans, M. J.; Daemen, L. L.; Proffen, T.; Lee, M. H.; Sankey, O. F.; Häussermann, U. *Solid State Sci.* **2009**, *11*, 1847–1853, DOI: 10.1016/j.solidstatesciences.2009.08.007.
- (11) Evans, M. J.; Lee, M. H.; Holland, G. P.; Daemen, L. L.; Sankey, O. F.; Häussermann, U. *J. Solid State Chem.* **2009**, *182*, 2068–2073, DOI: 10.1016/j.jssc.2009.05.023.
- (12) Evans, M. J.; Kranak, V. F.; Garcia-Garcia, F. J.; Holland, G. P.; Daemen, L. L.; Proffen, T.; Lee, M. H.; Sankey, O. F.; Häussermann, U. *Inorg. Chem.* **2009**, *48*, 5602–5604, DOI: 10.1021/ic9005423.
- (13) Ångström, J.; Johansson, R.; Sarkar, T.; Sørby, M. H.; Zlotea, C.; Andersson, M. S.; Nordblad, P.; Scheicher, R. H.; Häussermann, U.; Sahlberg, M. *Inorg. Chem.* **2016**, *55*, 345–352, DOI: 10.1021/acs.inorgchem.5b02485.
- (14) Nedumkandathil, R.; Kranak, V. F.; Johansson, R.; Ångström, J.; Balmes, O.; Andersson, M. S.; Nordblad, P.; Scheicher, R. H.; Sahlberg, M.; Häussermann, U. *J. Solid State Chem.* **2016**, *239*, 184–191, DOI: 10.1016/j.jssc.2016.04.028.
- (15) Auer, H.; Guehne, R.; Bertmer, M.; Weber, S.; Wenderoth, P.; Hansen, T. C.; Haase, J.; Kohlmann, H. *Inorg. Chem.* **2017**, *56*, 1061–1071, DOI: 10.1021/acs.inorgchem.6b01944.
- (16) Auer, H.; Schlegel, R.; Oeckler, O.; Kohlmann, H. *Angew. Chem., Int. Ed.* **2017**, *56*, 12344–12347, DOI: 10.1002/anie.201706523.
- (17) Auer, H.; Schlegel, R.; Oeckler, O.; Kohlmann, H. *Angew. Chem.* **2017**, *129*, 12515–12518, DOI: 10.1002/ange.201706523.
- (18) Hansen, T. C.; Henry, P. F.; Fischer, H. E.; Torregrossa, J.; Convert, P. *Meas. Sci. Technol.* **2008**, *19*, 034001.
- (19) Kohlmann, H.; Kurtzemann, N.; Weihrich, R.; Hansen, T. *Z. Anorg. Allg. Chem.* **2009**, *635*, 2399–2405, DOI: 10.1002/zaac.200900336.
- (20) Kohlmann, H.; Auer, H.; Götze, A.; Hansen, T.; Werwein, A. Reaction pathways to the Zintl phase hydride NdGaD_{1.66} by *in situ* neutron diffraction., Institut Laue-Langevin, 2016, DOI: 10.5291/ill-data.5-24-576.
- (21) Rietveld, H. M. *Acta Crystallogr.* **1967**, *22*, 151–152, DOI: 10.1107/S0365110X67000234.
- (22) Rietveld, H. M. *J. Appl. Crystallogr.* **1969**, *2*, 65–71, DOI: 10.1107/S0021889869006558.

- (23) Bruker AXS, TOPAS[®] version 5, www.bruker-axs.com.
- (24) *International Tables for Crystallography*; Aroyo, M. I., Ed.; International Union of Crystallography: 2016, DOI: 10.1107/97809553602060000114.
- (25) Harms, W.; Wendorff, M.; Röhr, C. *J. Alloys Compd.* **2009**, *469*, 89–101, DOI: 10.1016/j.jallcom.2008.02.020.
- (26) Itkin, V. P.; Alcock, C. B. *J. Phase Equilib.* **1992**, *13*, 273–277, DOI: 10.1007/bf02667555.
- (27) Häussermann, U.; Kranak, V. F.; Puhakainen, K. *Struct. Bond.* **2010**, *139*, 143–161, DOI: 10.1007/430_2010_20.
- (28) Itkin, V.; Alcock, C. *J. Phase Equilib.* **1991**, *12*, 575–577, DOI: 10.1007/bf02645073.
- (29) Itkin, V. P.; Alcock, C. B. *J. Phase Equilib.* **1992**, *13*, 190–192, DOI: 10.1007/bf02667486.
- (30) Wenderoth, P.; Kohlmann, H. *Inorg. Chem.* **2013**, *52*, 10525–10531, DOI: 10.1021/ic401480b.
- (31) Nedumkandathil, R.; Benson, D. E.; Grins, J.; Spektor, K.; Häussermann, U. *J. Solid State Chem.* **2015**, *222*, 18–24, DOI: 10.1016/j.jssc.2014.10.033.
- (32) Okamoto, H. *J. Phase Equilib. Diffus.* **2006**, *27*, 204–204, DOI: 10.1361/154770306x97768.
- (33) Okamoto, H. *J. Phase Equilib. Diffus.* **2008**, *29*, 464–464, DOI: 10.1007/s11669-008-9361-5.
- (34) Okamoto, H. *J. Phase Equilib. Diffus.* **2008**, *30*, 114–114, DOI: 10.1007/s11669-008-9428-3.
- (35) Okamoto, H. *J. Phase Equilib. Diffus.* **2012**, *33*, 423–423, DOI: 10.1007/s11669-012-0081-5.
- (36) Okamoto, H. *J. Phase Equilib. Diffus.* **2012**, *34*, 172–173, DOI: 10.1007/s11669-012-0179-9.
- (37) Emeleus, H. J.; Mackay, K. M. *J. Chem. Soc.* **1961**, 2676–2680, DOI: 10.1039/JR9610002676.
- (38) Ring, M. A.; Ritter, D. M. *J. Am. Chem. Soc.* **1961**, *83*, 802–805, DOI: 10.1021/ja01465a013.
- (39) Amberger, E.; Römer, R.; Layer, A. *J. Organomet. Chem.* **1968**, *12*, 417–423, DOI: 10.1016/S0022-328X(00)88694-5.
- (40) Thirase, G.; Weiss, E. *Z. Naturforsch., B* **1974**, *29*, 800.
- (41) Thirase, G.; Weiss, E.; Hennig, H. J.; Lechert, H. *Z. Anorg. Allg. Chem.* **1975**, *417*, 221–228, DOI: 10.1002/zaac.19754170306.
- (42) Chotard, J.-N.; Tang, W. S.; Raybaud, P.; Janot, R. *Chem. - Eur. J.* **2011**, *17*, 12302–12309, DOI: 10.1002/chem.201101865.
- (43) Kemmesies, P. Untersuchung von Alkali-Silizium-Zintl-Phasen mit Germaniummischbesetzungen, und deren Verhalten bei Hydrierung., Practical course, Leipzig: Universität Leipzig, 2017.
- (44) Veremchuk, I.; Wosylus, A.; Böhme, B.; Baitinger, M.; Borrmann, H.; Prots, Y.; Burkhardt, U.; Schwarz, U.; Grin, Y. *Z. Anorg. Allg. Chem.* **2011**, *637*, 1281–1286, DOI: 10.1002/zaac.201100187.
- (45) Tang, W. S.; Chotard, J.-N.; Raybaud, P.; Janot, R. *Phys. Chem. Chem. Phys.* **2012**, *14*, 13319, DOI: 10.1039/c2cp41589e.

Part III

Curriculum vitae and list of publications

Curriculum vitae

Name: Henry Auer
Date of Birth: 09.07.1989
Place of Birth: Leipzig, Germany

Education:

2008	Abitur, Martin-Rinckart Gymnasium, Eilenburg
2008 - 2011	B.Sc. Studies in Chemistry, Leipzig University
20.09.2011	Bachelor of Science, Thesis on <i>Numerische Analyse zur Anwendbarkeit von Tensorformaten in Post-Hartree-Fock-Methoden</i> supervised by Dr. Mike Espig, Max-Planck Institute for Mathematics in Sciences, Leipzig
2011 - 2013	M.Sc. Studies, Chemie, Leipzig University
02.2012 - 08.2012	ISAP exchange semester, Monash University, Melbourne, Australia, with Prof. Doug MacFarlane on ionic liquids and Dr. Katya Pas on quantum chemistry
22.08.2013	Master of Science, Thesis on <i>Synthese und strukturelle Charakterisierung von Kupferhydrid</i> supervised by Prof. Holger Kohlmann, Leipzig University
since 27.01.2014	Ph.D. at Leipzig University, supervised by Prof. Holger Kohlmann

Awards:

04.12.2009	Arthur-Hantsch-Preis 2009 des Freundeskreises der Fakultät f. Chemie und Mineralogie, Leipzig
04.12.2013	Hermann-Kolbe-Preis 2013 des Freundeskreises der Fakultät f. Chemie und Mineralogie, Leipzig

List of publications

- (12) Werwein, A.; Auer, H.; Kuske, L.; Kohlmann, H.
From metallic $LnTt$ ($Ln = La, Nd$; $Tt = Si, Ge, Sn$) to electron-precise Zintl phase hydrides $LnTtH$,
Z. Anorg. Allg. Chem., **2018**, *accepted*,
DOI: 10.1002/zaac.201800062.
- (11) Auer, H.; Weber, S.; Hansen, T. C.; Töbrens, D. M.; Kohlmann, H.
Reversible hydrogenation of the Zintl phases BaGe and BaSn studied by *in situ* diffraction,
Z. Kristallogr. - Cryst. Mater., **2018**, *in press*,
DOI: 10.1515/zkri-2017-2142
- (10) Götze, A.; Auer, H.; Finger, R.; Hansen, T.; Kohlmann, H.
A sapphire single-crystal cell for *in situ* neutron powder diffraction of solid-gas reactions,
Phys. B, **2018**, *in press*,
DOI: 10.1016/j.physb.2017.11.024
- (9) Auer, H.; Kohlmann, H.
In situ Investigations on the Formation and Decomposition of $KSiH_3$ and $CsSiH_3$,
Z. Anorg. Allg. Chem., **2017**, *643*, 945-951.
DOI: 10.1002/zaac.201700164.
- (8) Auer, H.; Schlegel, R.; Oeckler, O.; Kohlmann, H.
Structural and Electronic Flexibility in Hydrides of Zintl Phases with Tetrel-Hydrogen and Tetrel-Tetrel Bonds,
Angew. Chem., Int. Ed., **2017**, *56*, 12344-12347,
DOI: 10.1002/anie.201706523
- (8a) Auer, H.; Schlegel, R.; Oeckler, O.; Kohlmann, H.
Strukturelle und elektronische Flexibilität in Hydriden von Zintl-Phasen mit Tetrel-Wasserstoff- und Tetrel-Tetrel-Bindung,
Angew. Chem., **2017**, *129*, 12515-12518,
DOI: 10.1002/ange.201706523.
- (7) Auer, H.; Wallacher, D.; Hansen, T. C.; Kohlmann, H.
In Situ Hydrogenation of the Zintl Phase SrGe,
Inorg. Chem., **2017**, *56*, 1072-1079,
DOI: 10.1021/acs.inorgchem.6b01945.
- (6) Auer, H.; Guehne, R.; Bertmer, M.; Weber, S.; Wenderoth, P.; Hansen, T.; Haase, J.; Kohlmann, H.
Hydrides of Alkaline Earth-Tetrel ($AeTt$) Zintl Phases: Covalent Tt -H Bonds from Silicon to Tin,
Inorg. Chem., **2017**, *56*, 1061-1071,
DOI: 10.1021/acs.inorgchem.6b01944.
- (5) Auer, H.; Kohlmann, H.
Reinvestigation of Crystal Structure and Non-Stoichiometry in Copper Hydride, CuH_{1-x} ($0 \leq x \leq 0.26$),
Z. Anorg. Allg. Chem., **2014**, *640*, 3159-3165,
DOI: 10.1002/zaac.201400236.
- (4) Frank, R.; Adhikari, A. K.; Auer, H.; Hey-Hawkins, E.
Electrophile-Induced Nucleophilic Substitution of the *nido*-Dicarbaundecaborate Anion *nido*-7,8- $C_2B_9H_{12}^-$ by Conjugated Heterodienes,
Chem. - Eur. J., **2014**, *20*, 1440-1446,
DOI: 10.1002/chem.201303762.
- (3) Icker, M.; Fricke, P.; Grell, T.; Hollenbach, J.; Auer, H.; Berger, S.
Experimental boundaries of the quantum rotor induced polarization (QRIP) in liquid state NMR,
Magn. Reson. Chem., **2013**, *51*, 815-820,
DOI: 10.1002/mrc.4021.

-
- (2) Frank, R.; Auer, H.; Hey-Hawkins, E.
Functionalisation of the *nido*-dicarbaborate anion *nido*-7,8-C₂B₉H₁₂⁻ by hydride abstraction,
J. Organomet. Chem., **2013**, *747*, 217 - 224,
DOI: 10.1016/j.jorganchem.2013.04.031.
- (1) Benedikt, U.; Auer, H.; Espig, M.; Hackbusch, W.; Auer, A. A.
Tensor representation techniques in post-Hartree Fock methods: matrix product state tensor format,
Mol. Phys. **2013**, *111*, 2398-2413,
DOI: 10.1080/00268976.2013.798433.

Conference contributions

Poster presentations and talks given on conferences. The presenting author is underlined.

- (11) Talk:
Auer, H.; Guehne R.; Bertmer, M; Haase, J.; Kohlmann H.
Polyanions with covalent Si-H, Ge-H and Sn-H bonds in Zintl phase hydrides
26th Annual Meeting of the German Crystallographic Society (DGK),
Essen, Germany, **2018**,
DOI: 10.1515/9783110595994-004(S03-05)
- (10) Poster presentation:
Guehne, R.; Lindel, M.; Auer, H.; Kohlmann, H.; Haase, J.; Bertmer M.
Solid-state ²H NMR of Zintl Phase Deuterides - Determination of Bonding Situations
39th FGMR Annual Discussion Meeting,
Bayreuth, Germany, **2017**.
- (9) Talk:
Werwein, A.; Auer, H.; Kuske, L.; Kohlmann, H.
Die Zintl-Phasen-Hydride $LnTtH_x$ ($Ln = La, Nd$; $Tt = Si, Ge, Sn$)
15. Mitteldeutsches Anorganiker-Nachwuchssymposium (MANS-15),
Leipzig, Germany, **2017**.
- (8) Poster presentation:
Auer, H.; Kohlmann, H.
Covalent Tt -H bonds ($Tt = Si, Ge, Sn$) in Zintl Phases
18. Vortragstagung der Wöhler-Vereinigung für Anorganische Chemie
Berlin, Germany, **2016**.
- (7) Poster presentation:
Auer, H.; Kohlmann, H.
Hydrides of CrB-structure type Zintl phases - An *in situ* investigation
Challenges and Prospects for Solid State Chemistry (CPSSC 16),
Sevilla, Spain, **2016**.
- (6) Talk:
Auer, H.; Kohlmann, H.
Time resolved diffraction study of the Zintl phase SrGe under 50 bar hydrogen pressure and elevated temperatures
24th Annual Meeting of the German Crystallographic Society (DGK),
Stuttgart, Germany, **2016**,
DOI: 10.1515/9783110476620-014(MS13-T02)
- (5) Talk:
Auer, H.; Kohlmann, H.
Strukturen der homologen Reihe $EaTtH_x$, $Ea = Sr, Ge$, $Tt = Si - Sn$, $1 \leq x \leq 2$
42. Festkörperchemiesymposium Hirschegg,
Hirschegg, Austria, **2016**.
- (4) Poster presentation:
Auer, H.; Weber, S.; Kohlmann H.
Reactions in the $AeTt$ -hydrogen system ($Ae = Sr, Ba$, $Tt = Ge - Pb$)
GDCH Wissenschaftsforum Chemie 2015,
Dresden, Germany, **2015**.
- (3) Talk:
Auer, H.; Weber, S.; Kohlmann H.
Hydrierverhalten der Zintl Phasen $EaTt$ ($Ea = Ba, Sr$; $Tt = Ge, Sn, Pb$)
13. Mitteldeutsches Anorganiker-Nachwuchssymposium (MANS-13),
Chemnitz, Germany, **2015**.

(2) Talk:

Auer, H.; Wenderoth, P.; Kohlmann, H.

Oxidation behaviour of Zintl phases MTt , $M = \text{Sr, Ba}$; $Tt = \text{Si, Ge}$; under hydrogen pressure

23rd Annual Meeting of the German Crystallographic Society (DGK),

Göttingen, Germany, **2015**,

DOI: 10.1515/9783110415377-017(MS16-T02)

(1) Poster presentation:

Auer, H.; Kohlmann, H.

Metric Shifts and Non-Stoichiometry in Copper Hydride $\text{CuH}_{(1-x)}$

17. Vortragstagung der GDCh Fachgruppe Festkörperchemie und Materialforschung,

Dresden, Germany, **2014**.

Kurzfassung der wissenschaftlichen Ergebnisse
zur Dissertation

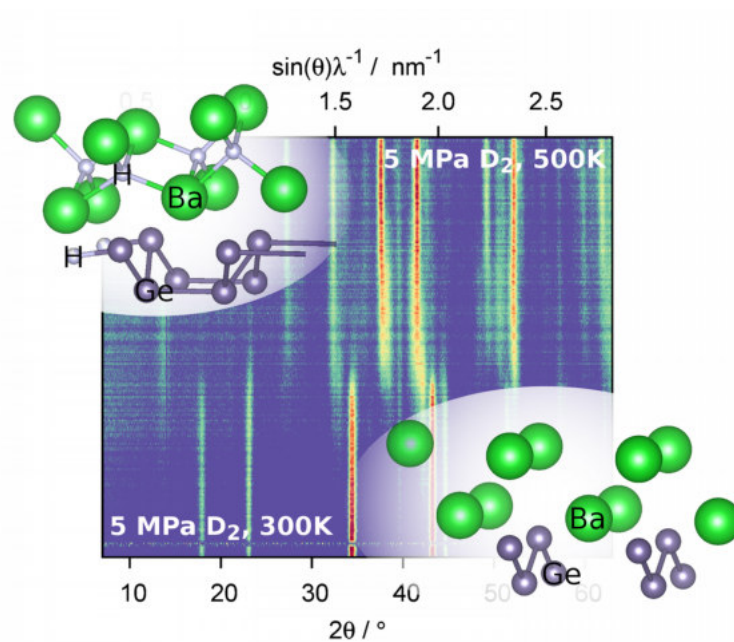
In Situ and *Ex Situ* Hydrogenation Studies of Zintl Phases
Containing Tetrelides or Gallium

Der Fakultät für Chemie und Mineralogie der Universität Leipzig
vorgelegt von

M. Sc. Henry Auer

im
März 2018

angefertigt im Institut für Anorganische Chemie



Zeitaufgelöste *in situ*-Neutronenpulverbeugung zeigt an
der Reaktion von BaGe mit Wasserstoff-(Deuterium-)gas.

Einleitung und Motivation

Zintl-Phasen sind eine Stoffklasse am Übergang von salzartigen zu intermetallischen Verbindungen aus einem Metall der ersten oder zweiten Gruppe des Periodensystems oder oft auch einem Element der Lanthanoide (einschließlich La) mit geringer Elektronegativität und einem p-Block Element. Die Verbindungen lassen sich verstehen, indem man alle Valenzelektronen dem stärker elektronegativen Partner zuschreibt. Das führt zur Ausbildung polyanionischer Strukturen, die sich in der Regel von den isovalenzelektronischen Elementen ableiten lassen (Zintl-Konzept).

Die Hydrierung von Zintl-Phasen kann zu verschiedenen Strukturmotiven führen. Da Wasserstoff eine ähnliche Elektronegativität wie die p-Block Elemente besitzt, verhält er sich in den Strukturen auch analog. Dabei kann er als monoatomiges Anion ausschließlich von Kationen koordiniert vorliegen (Einlagerungshydrid) oder kovalent an das Polyanion binden (polyanionisches Hydrid). Vor allem der zweite Fall ist interessant, da hier neue Struktur motive möglich sind, die sich von binären Element-Wasserstoffverbindungen ableiten lassen.

Polyanionische Hydride sind vor allem für Elemente der Gruppe 13 bekannt. Ein fundierter experimenteller Beleg für ein Anion mit einer Tt -H- neben einer Tt - Tt -Bindung (Tt = Tetrel, hier Si, Ge, Sn oder Pb) war jedoch noch offen. Das einzige Beispiel war $CaSiH_{1.3}$, in dem Wasserstoff sowohl in Ca_4 -Tetraedern zu finden ist (Einlagerungshydrid) als auch an das Silizium des Polyanions koordiniert. Die Bindungssituation der letzteren Position ist in der Literatur jedoch umstritten und reicht von einer kovalenten Beschreibung mit kurzem Si-H-Abstand von 158 pm bis zu einer ionischen Auffassung mit 184 pm Si-H-Abstand.

Diese Arbeit schließt diese Lücke, indem schwerpunktmäßig das System $EaTt$ - H_2 (Ea = Erdalkalimetall oder divalentes Lanthanoid, Tt = Tetrel / Element der Gruppe 14) untersucht wurde. Dabei tritt eine Reihe von polyanionischen Hydriden auf, für die eine kovalente Tt -H-Bindung bestätigt werden kann. *In situ*-Neutronenpulverdiffraktion (*in situ*-NPD) zeigt das Auftreten weiterer wasserstoffhaltiger Phasen in diesen Systemen.

Außerdem wurden die beiden literaturbekannten Reaktionen $2 KSi + 3 H_2 \rightarrow 2 KSiH_3$ und $2 NdGa + (1+x) H_2 \rightarrow 2 NdGaH_{1+x}$, $x < 1$, mit *in situ*-Methoden charakterisiert, um Einblick in den Reaktionsverlauf zu gewinnen.

Methoden

Die Zintl-Phasen wurden aus den Elementen im stöchiometrischen Verhältnis hergestellt. Die Synthese erfolgte in der Regel durch Aufschmelzen bei Temperaturen > 1250 K in Metallampullen (Niob, Tantal oder Stahl). Hydride oder Deuteride wurden durch Umsetzung der Zintl-Phasen mit dem entsprechenden Gas im Autoklaven bei typischen Bedingungen von 5 MPa und 480 K dargestellt.

Kristallstrukturen wurden aus Pulverbeugungsmessungen bestimmt. Die Lagen aller Atome außer Wasserstoff können dabei aus Laborröntgen- oder Synchrotrondaten erhalten werden. Wasserstoffpositionen wurden mittels Neutronenpulverdiffraktion (NPD) bestimmt, da hier der Streukontrast deutlich höher ist. Es wurden vollständig deuterierte Proben eingesetzt, da Wasserstoff stark inkohärent streut, was den Untergrund signifikant erhöht.

Kernspinresonanzspektren wurden an Pulvern gemessen. Die Experimente wurden in Kooperation mit dem Institut für Experimentelle Physik II, Leipzig durchgeführt. Die erhaltenen Daten konnten mittels selbst durchgeführter Dichtefunktionaltheorie- (DFT-) Rechnungen interpretiert werden. In diesem Zuge wurde auch die elektronische Struktur der Verbindungen berechnet.

Dynamische Differenzkalorimetrie (DDK) wurde genutzt um Hydrierreaktionen zu beobachten. Dazu stand ein Gerät zur Verfügung, das mit einer Druckkammer ausgerüstet ist, die mit bis zu 7 MPa Wasserstoffdruck beladen werden kann. Für eine typische Messung wurden 10-20 mg pulverige Probe in einen Aluminiumtiegel gefüllt, der so verbördelt werden kann, dass er gegen Luft abdichtet, jedoch Wasserstoff hindurch lässt.

In situ-Pulverbeugungsexperimente wurden durchgeführt, um die Reaktionsverläufe ausführlich zu charakterisieren. Dazu wurden Proben direkt auf einem Diffraktometer Wasserstoff- oder Deuteriumgasdruck ausgesetzt und geheizt. Im Zuge dieser Dissertation wurde auch ein Laboraufbau realisiert, der die Reaktionsverfolgung mittels Röntgenpulverbeugung ermöglicht. *In situ*-NPD wurde am Institut Laue-Langevin (ILL) am Gerät D20 durchgeführt. Die benötigte Probenumgebung wurde in unserer Gruppe entwickelt und konnte direkt genutzt werden.

Ergebnisse

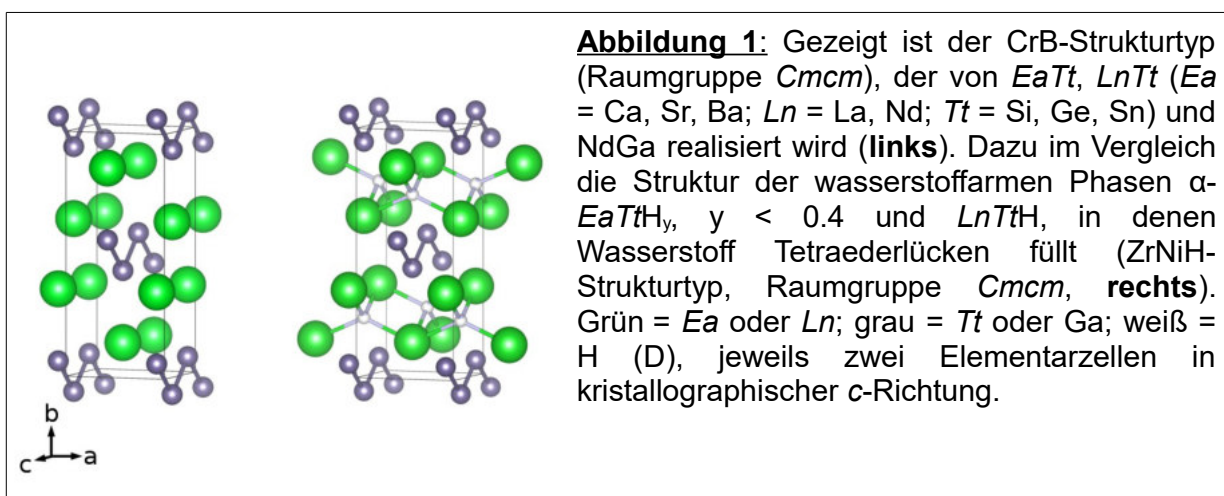
Hydride von Zintl-Phasen im CrB-Strukturtyp

Diese Arbeit beschäftigt sich schwerpunktmäßig mit der Hydrierung von binären Zintl-Phasen AB im CrB-Strukturtyp. Diese sind durch das Auftreten von Polyanionen als $^{1-}_{\infty}[B]$ -Zickzackketten charakterisiert (Abb. 1). Es wurde die Hydrierung von Zintl-Phasen untersucht, die sich als Valenzverbindungen auffassen lassen, als auch von Verbindungen, die zusätzliche, formal metallische Elektronen aufweisen. Für die Dissertation relevante Systeme sind:

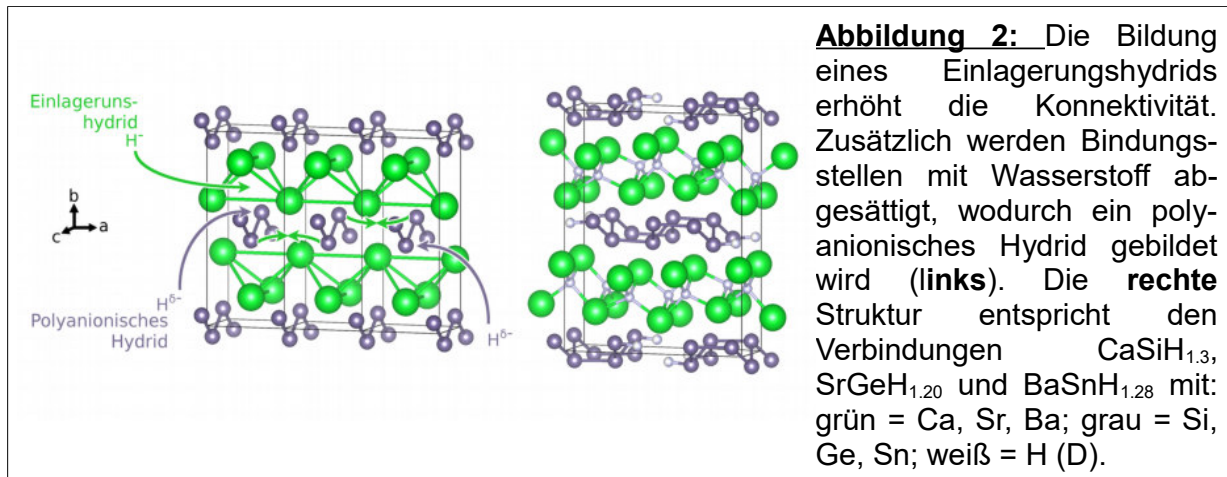
- $Ea^{2+}Tt^{2-}$ mit $Ea = Ca, Sr, Ba$ und $Tt = Si, Ge, Sn$
- $Ln^{3+}Tt^{2-e}$ mit $Ln = La, Nd$ und $Tt = Si, Ge, Sn^a$
- $Nd^{3+}Ga^{3-}$

Die gebildeten Hydride ABH_y lassen sich in wasserstoffarme Phasen mit $y \leq 1$ und wasserstoffreiche Phasen mit $1 < y \leq 2$ einteilen.

Verbindungen des ersten Typs kann man durch das Auffüllen von A_4 -Tetraedern mit Wasserstoff beschreiben. Dabei wird die Topologie der CrB-Struktur erhalten (Abb. 1). Die so gebildeten Hydride sind dann isotyp zur $ZrNiH$ -Struktur (Raumgruppe $Cmcm$). Im Fall von $LnTt$ führt das zu elektronenpräzisen Verbindungen $LnTtH$. Dabei werden hauptsächlich metallische Ln -d-Zustände depopuliert. Die polyanionische Teilstruktur ist dennoch von der Oxidationsreaktion betroffen, was man an der Verkürzung der Atomabstände innerhalb der Zickzackkette um ca. 5% erkennen kann. Die Erdalkaliverbindungen $EaTt$ zeigen wasserstoffarme Phasen in zwei Ausprägungen. Die Verbindungen α - $EaTtH_y$ ($EaTt = SrGe, BaGe, BaSn$) bauen Wasserstoff bis zu einem

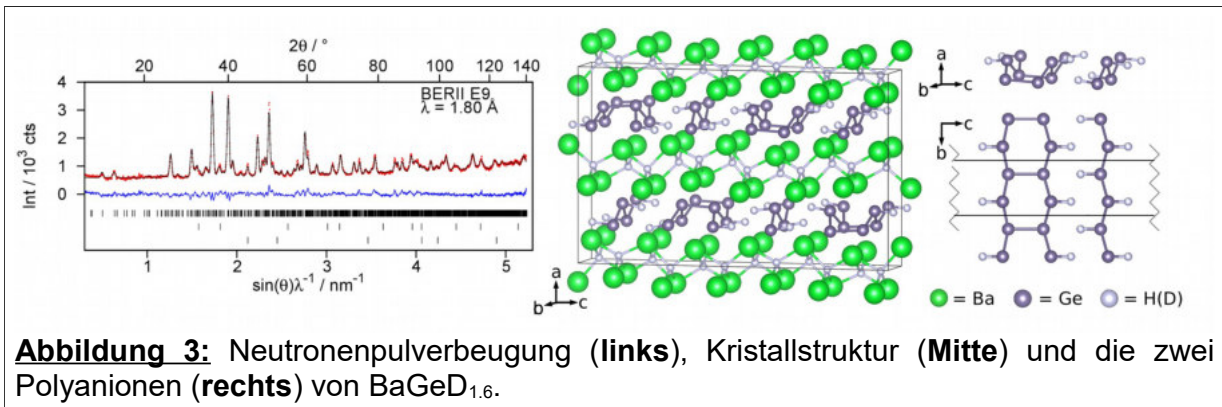


a Diese Phasen kristallisieren auch im strukturell eng verwandten FeB-Strukturtyp oder im LaSi-Strukturtyp. Diese sind für die Diskussion der Hydride nicht relevant und deren Beschreibung wird ausgelassen.



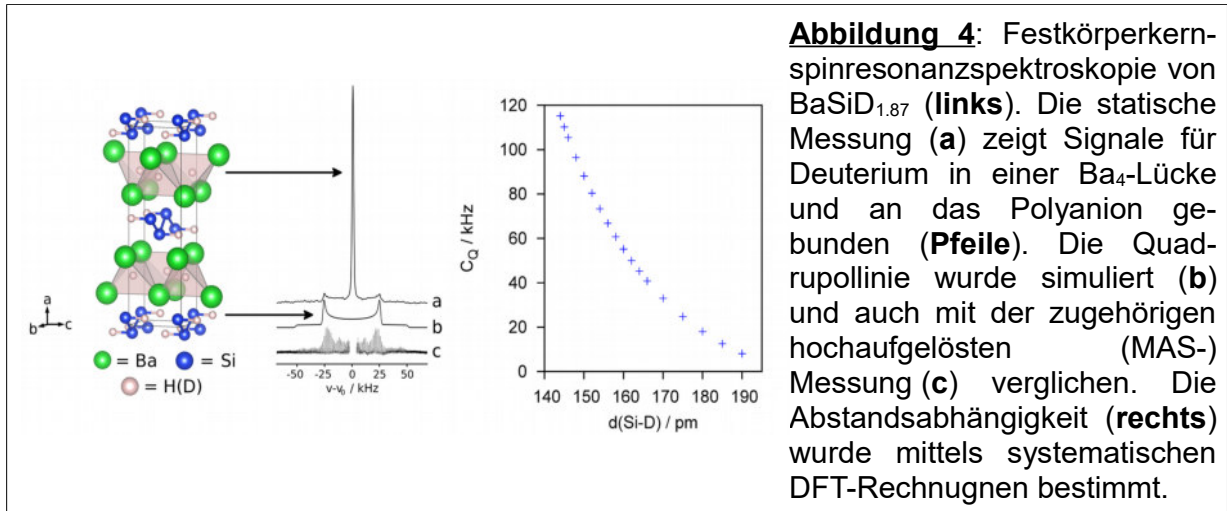
Gehalt von $y < 0.4$ ein. Der lückenlose Übergang bis $y = 0$ konnte noch nicht gezeigt werden, erscheint aber plausibel. Der Wasserstoff besetzt analog zu LnTtH Tetraederlücken im CrB-Strukturtyp. Anhand von NPD-Experimenten wird davon ausgegangen, dass eine statistische Verteilung von Hydridionen in den Lücken vorliegt. Bei etwas größeren Wasserstoffgehalten tritt Ordnung ($\beta\text{-BaGeH}_{0.5}$) oder zumindest partielle Ordnung ($\beta\text{-SrGeH}_y$ mit $0.47 \leq y \leq 0.75$) auf. Da die Mutterphasen bereits elektronenpräzise Verbindungen sind, wird in diesem Fall hauptsächlich das Polyanion oxidiert. Dabei werden antibindende π^* -Zustände der Zickzackketten depopuliert, was zu einer Verkürzung des Atomabstandes innerhalb der Kette führt. Für die Hydrierung von NdGa sind keine wasserstoffarmen Verbindungen bekannt.

Die wasserstoffreichen Phasen sind durch die Kombination von Einlagerungs- und polyanionischen Hydridmotiven gekennzeichnet. Dabei wird die Topologie des CrB-Strukturtyps weitestgehend erhalten und verschiedene Überstrukturen ausgebildet. Wie im Fall der wasserstoffarmen Verbindungen werden Tetraederlücken der kationischen Teilstruktur befüllt. Im Fall der EaTtH_y -Phasen mit $1 < y \leq 2$, zur Abgrenzung auch γ -Phasen genannt, führt die vollständige Besetzung dieser Lage zu einer intermediären Formel „ EaTtH_1 “. Demnach ist das Polyanion vollständig zu Tt^- oxidiert und isoelektronisch zu Elementen der Gruppe 15. Dadurch erhöht sich die Konnektivität des Polyanions und die Zickzackketten verknüpfen sich senkrecht zu ihrer Laufrichtung (Abb. 2). Das führt zu einer hypothetischen zweidimensionalen Schicht aus kondensierten Sechsringen in Wannenkongformation. Aus geometrischen Gründen wird die beschriebene Polyanionenschicht jedoch so nicht ausgebildet, sondern die Bindungsstellen senkrecht zur Kettenrichtung werden teilweise mit Wasserstoff abgesättigt (Abb. 2). Dadurch erhält man mindestens drei Struktur motive. In $\text{BaSiH}_{1.87}$ sind alle Si-Atome durch Wasserstoff



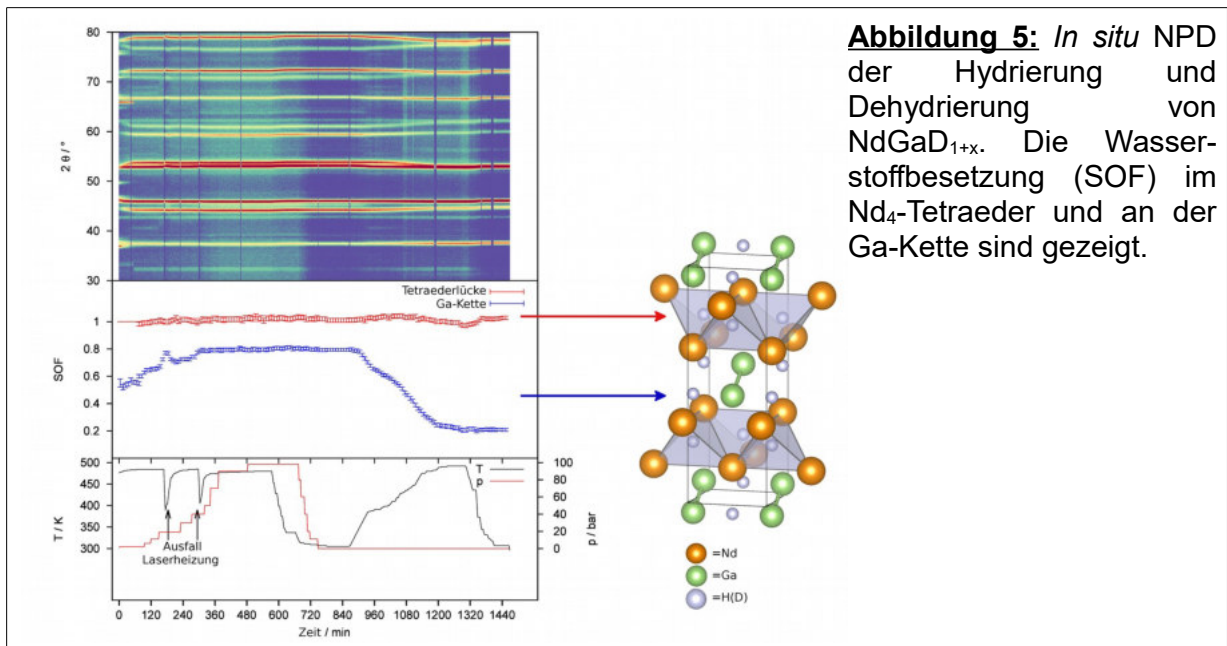
abgesättigt. Dadurch ergibt sich eine $^1_{\infty}[\text{SiH}]$ -Zickzackkette, die isoelektronisch zu Polyphosphen, $(\text{PH})_{\infty}$, ist. In den isotypen Strukturen von $\text{SrSiH}_{1.5}$ und $\text{BaGeH}_{1.6}$ treten die gleichen Einzelketten auf. Zusätzlich werden jeweils zwei der Zickzackketten senkrecht verknüpft. Damit erhält man eine eindimensionale Reihe kondensierter Sechsringe, die senkrecht zur Laufrichtung mit Wasserstoff terminiert sind (Abb. 3). In den Strukturen von $\text{CaSiH}_{1.3}$, $\text{SrGeH}_{1.20}$ und $\text{BaSnH}_{1.28}$ werden jeweils drei Zickzackketten verknüpft was zu dem polyanionischen Hydrid in Abb. 2 führt. Die Strukturen weisen alle eine Unterbesetzung der Wasserstoffposition am Polyanion auf. Das führt entweder zu ungesättigten Tt -Ionen oder partiell zu einer zusätzlichen Verknüpfung von Ketten, die durch Pulverbeugung jedoch nicht aufgeklärt werden konnte.

Eine wichtige Fragestellung war der Charakter der Bindung zwischen Wasserstoff und Polyanion. Die Abstände, die aus NPD-Daten ermittelt wurden, legen bereits den kovalenten Charakter nahe. Um diesen Befund weiter zu untermauern, wurden theoretische Rechnungen und spektroskopische Messungen durchgeführt. Die mit DFT-Methoden ermittelte elektronische Zustandsdichte wurde an Strukturen mit idealisierter Wasserstoffbesetzung bestimmt und zeigt sehr kleine oder pseudo-Bandlücken. Dieses metallische Verhalten ist wahrscheinlich auch der Grund, dass weder Infrarot- noch Ramanspektroskopie ein Signal liefern. Ausschließlich im Fall von $\text{BaSiH}_{1.87}$ wurde eine schwache Bande bei 1757 cm^{-1} gemessen, die auf eine schwächere Bindung als im SiH_4 ($\nu = 2200 \text{ cm}^{-1}$) hinweist. Festkörperkernspinresonanzspektroskopie hat sich hier als wertvolle Methode herausgestellt. Die Quadrupolwechselwirkung des Deuteriumkerns mit dem annähernd axialsymmetrischen elektrischen Feldgradienten (EFG) einer kovalenten Bindung bewirkt eine Signalaufspaltung (C_Q in kHz), die charakteristisch für die Bindungslänge ist (Abb. 4). Zusammen mit DFT-Rechnungen lassen sich so die Abstände auf $d(\text{Si-H}) = 155(2) \text{ pm}$, $d(\text{Ge-H}) = 163(2) \text{ pm}$ und $d(\text{Sn-H}) = 186(1) \text{ pm}$ bestimmen. Sie



sind damit ca. 10% länger als in den entsprechenden TtH_4 -Molekülen und können als kovalent betrachtet werden.

Die literaturbekannte Phase $\text{NdGaH}_{1.66}$ ist isoelektronisch zu den oben beschriebenen Systemen. Die Bindungssituation ist jedoch stark verschieden. Wasserstoff verbrückt zwei Zickzackketten fast äquidistant in der Mitte. Das führt zu sehr langen Ga-H Abständen von ca. 200 pm. Damit erwartet man hier keine kovalente 2-Elektronen-2-Zentren-Bindung. Das System NdGa-H_2 wurde für diese Arbeit mit *in situ*- NPD untersucht. Dabei zeigt sich direkt die Bildung einer wasserstoffreichen Phase NdGaH_{1+x} , $x < 1$. Der Wasserstoffgehalt kann hier lückenlos mindestens von $x = 0.14$ bis 0.8 variiert werden (Abb. 5), wobei ausschließlich die Lage zwischen den Ga-Ketten betroffen ist. Das steht



klar im Kontrast zu den $EaTtH_y$ -Phasen mit $1 < y \leq 2$, die weitestgehend fix in ihrer Zusammensetzung sind. Das ist ein weiterer Beleg dafür, dass hier keine klassische kovalente Bindung zu den Ketten vorliegt.

Im $LnTt-H_2$ System sind bisher keine wasserstoffreichen Verbindungen bekannt.

Charakterisierung von Reaktionsverläufen durch *in situ*-Studien

Das Reaktionsverhalten im $EaTt-H_2$ wurde mittels DDK unter Wasserstoffdruck und *in situ*-Pulverbeugung untersucht. Dabei kann man das Reaktionsverhalten wie folgt zusammenfassen (Abb. 6):

1. Bei erhöhten Wasserstoffdrücken (5 MPa) und nur leicht erhöhten Temperaturen (< 370 K) werden bereits wasserstoffarme Phasen gebildet. Diese Reaktion ist nicht vollständig und läuft oft nur stark gehemmt ab. Mögliche Gründe sind Partikelgrößen der Edukte oder fehlende Aktivierungsenergie für die Dissoziation von H_2 .
2. Beim Erhöhen der Temperatur (5 MPa H_2 , 430 - 530 K) werden die wasserstoffreichen γ -Phasen gebildet.
3. Verringerung des Wasserstoffdruckes oder weiteres Erhöhen der Temperatur führt zum Bruch der $Tt-H$ Bindung. Zusätzlich wird Wasserstoff aus den Ea_4 -Tetraedern abgegeben. Damit werden wieder wasserstoffarme α - oder β -Phasen gebildet.
4. Weiteres Heizen (> 700 K) unter Wasserstoffdruck führt zur Zersetzung in binäres Hydrid EaH_2 und elementreiche Zintl-Phase $EaTt_2$.

Die Reaktionen zwischen α -, β - und γ -Phase sind reversibel. Die Thermolabilität der $Tt-H$ -Bindung ist auch für z.B. Polygerman GeH_x bekannt.

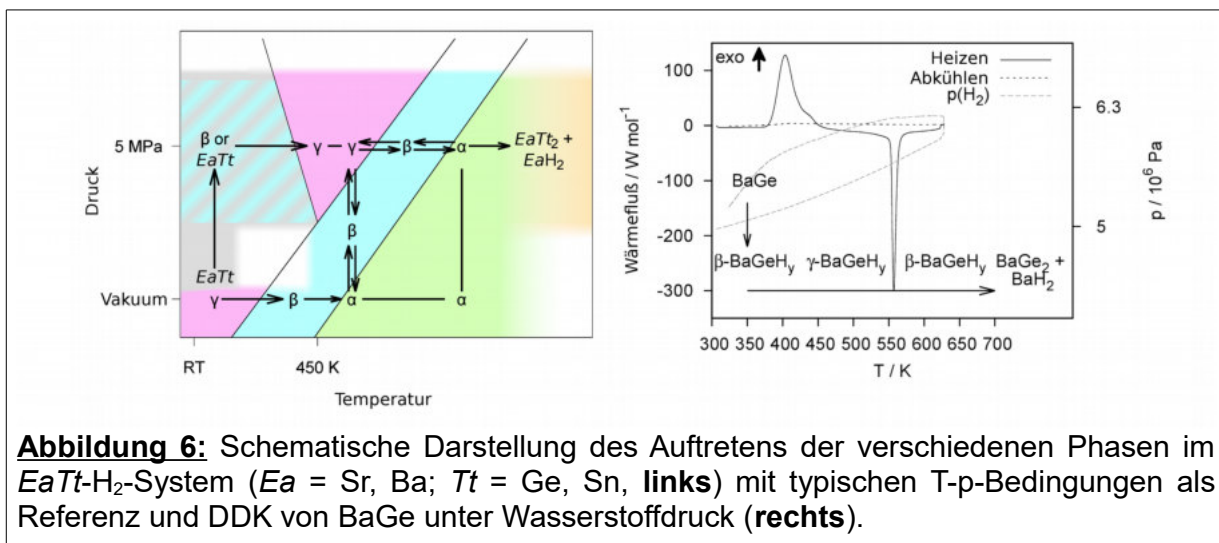


Abbildung 6: Schematische Darstellung des Auftretens der verschiedenen Phasen im $EaTt-H_2$ -System ($Ea = Sr, Ba; Tt = Ge, Sn$, links) mit typischen T-p-Bedingungen als Referenz und DDK von BaGe unter Wasserstoffdruck (rechts).

Außerdem wurde die Reaktion $2 \text{KSi} + 3 \text{H}_2 \rightarrow 2 \text{KSiH}_3$ mit *in situ*-NPD untersucht. Es konnte gezeigt werden, dass die Zintl-Phase in einem Schritt zum Hydrid reagiert. KSiH_3 ist eine Linienphase, die monomere SiH_3 -Einheiten enthält. Die Verbindung zeigt keine Variabilität beim Wasserstoffeinbau. Außerdem weist die Zintl-Phase selbst keine Löslichkeit für Wasserstoff auf.

Fazit

Diese Arbeit erweitert unser Bild von Zintl-Phasenhydriden indem das Auftreten von polyanionischen Hydriden mit einer *Tt*-H-Bindung neben *Tt-Tt*-Bindungen das erste Mal eindeutig belegt werden kann. Es werden neue Beispiele gezeigt, in denen Wasserstoff als Oxidationsmittel auf die polyanionische Teilstruktur der Zintl-Phasen wirkt und deren Konnektivität beeinflusst. Der CrB-Strukturtyp hat sich hier als geeignete Mutterstruktur gezeigt. Durch Variieren von Kation und Anion kann man die Komplexität der polyanionischen Hydride steuern. Die Bildung eines Einlagerungshydrids erhöht die Konnektivität, was zur Ausbildung zusätzlicher Element-Element-Bindungen führt. Der Bedarf an einer zusätzlichen Bindung kann jedoch auch von Wasserstoffatomen erfüllt werden, wobei ein polyanionisches Hydrid gebildet wird. Damit kann die Hydrierung von Zintl-Phasen genutzt werden, um zu neuen Motiven von pseudo-Elementstrukturen oder pseudo-binären Hydridstrukturen zu gelangen. Außerdem kombiniert der Einbau von Wasserstoff als ionisches Einlagerungshydrid und als kovalent gebundenes polyanionisches Hydrid zwei Struktur motive, die typisch für Wasserstoffspeichermaterialien sind. Dahingehend kann die Hydrierung von Zintl-Phasen neue Impulse für die Suche nach Verbindungen mit hohem Wasserstoffgehalt, guter Kinetik und Reversibilität liefern. *In situ*-Pulverbeugungsstudien liefern dabei einen Einblick in die Bildung intermediärer, z.T. metastabiler Phasen. Damit können Reaktionsmechanismen für die ablaufenden Fest-Gas-Reaktionen besser verstanden werden. Das Wissen um die bevorzugte Besetzung einer Lage der Kristallstruktur mit Wasserstoff kann helfen, die Systeme für die Reaktivität gegenüber Wasserstoff zu optimieren.

Publikationen zum Promotionsthema:

- A. Werwein, H. Auer, L. Kuske, H. Kohlmann
From metallic $LnTt$ ($Ln = La, Nd$; $Tt = Si, Ge, Sn$) to electron-precise Zintl phase hydrides $LnTtH$
Z. Anorg. Allg. Chem. **2018**, akzeptiert
- H. Auer, S. Weber, T. C. Hansen, D. M. Többens, H. Kohlmann
Reversible hydrogenation of the Zintl phases BaGe and BaSn studied by *in situ* diffraction
Z. Kristallogr. - Cryst. Mater. **2018**, DOI: 10.1515/zkri-2017-2142, im Druck
- A. Götze, H. Auer, R. Finger, T. C. Hansen, H. Kohlmann
A sapphire single-crystal cell for *in situ* neutron powder diffraction of solid-gas reactions
Phys. B **2018**, DOI: 10.1016/j.physb.2017.11.024, im Druck
- H. Auer, H. Kohlmann
In situ Investigations on the Formation and Decomposition of $KSiH_3$ and $CsSiH_3$
Z. Anorg. Allg. Chem. **2017**, 643, 945 - 951.
- H. Auer, R. Schlegel, O. Oeckler, H. Kohlmann
Structural and Electronic Flexibility in Hydrides of Zintl Phases with Tetrel-Hydrogen and Tetrel-Tetrel Bonds
Angew. Chem., Int. Ed. **2017**, 56, 12344 - 12347, *Angew. Chem.* **2017**, 129, 12515 - 12518.
- H. Auer, D. Wallacher, T. C. Hansen, H. Kohlmann
In Situ Hydrogenation of the Zintl Phase SrGe
Inorg. Chem. **2017**, 56, 1072 - 1079.
- H. Auer, R. Guehne, M. Bertmer, S. Weber, P. Wenderoth, T. C. Hansen, J. Haase, H. Kohlmann
Hydrides of Alkaline Earth-Tetrel ($AeTt$) Zintl Phases: Covalent $Tt-H$ Bonds from Silicon to Tin
Inorg. Chem. **2017**, 56, 1061 - 1071.

weitere Publikationen:

- H. Auer, H. Kohlmann
Reinvestigation of Crystal Structure and Non-Stoichiometry in Copper Hydride, CuH_{1-x} ($0 \leq x \leq 0.26$)
Z. Anorg. Allg. Chem. **2014**, *640*, 3159 - 3165.
- R. Frank, A. K. Adhikari, H. Auer, E. Hey-Hawkins
Electrophile-Induced Nucleophilic Substitution of the *nido*-Dicarbaundecaborate Anion *nido*-7,8- $\text{C}_2\text{B}_9\text{H}_{12}^-$ by Conjugated Heterodienes
Chem. - Eur. J. **2014**, *20*, 1440 - 1446.
- M. Icker, P. Fricke, T. Grell, J. Hollenbach, H. Auer, S. Berger
Experimental boundaries of the quantum rotor induced polarization (QRIP) in liquid state NMR
Magn. Reson. Chem. **2013**, *51*, 815-820.
- R. Frank, H. Auer, E. Hey-Hawkins
Functionalisation of the *nido*-dicarbaborate anion *nido*-7,8- $\text{C}_2\text{B}_9\text{H}_{12}^-$ by hydride abstraction
J. Organomet. Chem. **2013**, *747*, 217 - 224.
- U. Benedikt, H. Auer, M. Espig, W. Hackbusch, A. A. Auer
Tensor representation techniques in post-Hartree Fock methods: matrix product state tensor format
Mol. Phys. **2013**, *111*, 2398 - 2413.